

Millimeter-wave Rat-race Balun in a CMOS 65 nm Technology with Slow-wave Transmission Lines and Innovative Topology

F. Burdin, F. Podevin, B. Blampey, N. Corrao, E. Pistono, and P. Ferrari
IMEP-LAHC, University of Grenoble, France

Abstract—An integrated rat-race coupler for balun applications based on high quality factor Slow-wave CoPlanar Waveguides transmission lines (S-CPW Tlines) at millimeter wave frequencies was realized in the 65-nm CMOS technology from STMicroelectronics. Optimized criteria for a CPW phase-inverter and Tlines' characteristic impedance enable to minimize insertion loss and surface on the die. The various building blocs were designed thanks to 3D full wave EM software coupled to a circuit simulator. Thanks to the S-CPW Tlines, the device occupies a small area of 0.085 mm^2 . From 51 GHz till a minimum of 67 GHz, i.e., a 16 GHz bandwidth, the measurements show the return loss is lower than -15 dB . The magnitude imbalance of the measured couplings are included between to -4.2 and -4.1 dB and -6.5 and -6 dB , respectively, and are really flat over a wide bandwidth. Finally, in the bandwidth the phase shift between the output ports is kept very flat, equal to $175.9^\circ \pm 0.4^\circ$, while the isolation is better than -26 dB . The rings are smaller than $290 \mu\text{m}$ on a side. It shows the potential of this approach for further increasing working frequencies.

1. INTRODUCTION

Baluns are passive components widely spread in the microwave and millimeter-wave frequency ranges. They are commonly used in many applications such as amplification, mixing or differential measurements. They can be realized in several manners, with lumped coupled inductors or transformers, or with distributed, transmission line's based circuits. The key issue for CMOS RFICs is the chip area. While in RF, say until tens of GHz, the use of transformers is obvious and easy to implement, and on the other hand distributed circuits are size consuming, the situation becomes different when dealing with working frequencies of 60–100 GHz and above. The design of the transformers becomes more difficult because of the low efficiency of the coupled inductors, the insertion loss increase and the phase and amplitude imbalance become difficult to control. This lumped approach needs the development of very accurate electrical models taking into account all the parasitic elements, in particular the capacitors. On the other hand, the design of transmission lines (TLines) is made easier because of less parasitic, and they are well suited for millimeter-wave devices. In that context, the distributed rat-race coupler is an interesting candidate to be used as a balun [1] for millimeter-wave frequencies. However it suffers from a small bandwidth when used as a balun, in particular concerning the phase imbalance. In [2], a balun was implemented in a $0.13\text{-}\mu\text{m}$ SiGe BiCMOS technology. A phase-inverter in one of the arms of the hybrid ring leads to very small variation of the phase imbalance over a wide bandwidth. The authors used classical grounded CPW TLines. A coupling factor of -5.7 dB was measured at 60 GHz with a 0.11 mm^2 chip area. Results carried out in [2] are very good in term of phase imbalance ($184^\circ \pm 1^\circ$ in the targeted bandwidth). However, such low insertion loss was obtained thanks to the use of a thick Back-End-Of-Line (BEOL) of $10 \mu\text{m}$. For more advanced technologies, like the 65-nm and in the next future the 28-nm CMOS technology, the BEOL thickness is lower, in the order of $5 \mu\text{m}$. Hence the use of grounded CPW is no more suitable because very narrow strips have to be used, leading to increased attenuation loss. Microstrip TLines also suffer from high attenuation loss when dealing with thin BEOLs.

In this paper, in order to address this issue of thin BEOLs, the same topology of balun was implemented with slow-wave CPW (S-CPW) TLines, as firstly described in [3] and by the authors in [4]. Higher quality factor can be obtained using these particular TLines, not depending on the BEOL thickness. Moreover, the slow-wave behaviour leads to shorter TLines, leading to even smaller devices. Based on these TLines, thanks to the size reduction technique described in [5] and with a phase-inverter inserted in the $3\lambda/4$ arm, a 60-GHz balun was implemented in the 65-nm CMOS technology from STMicroelectronics. The principle of the designed balun is explained in part II. Then the design of each bloc, such as TLines (S-CPW and microstrip), transitions (S-CPW to microstrip) or phase-inverter is described in part III. Finally, part IV gives the measurement results. Small phase imbalance and good isolation are obtained.

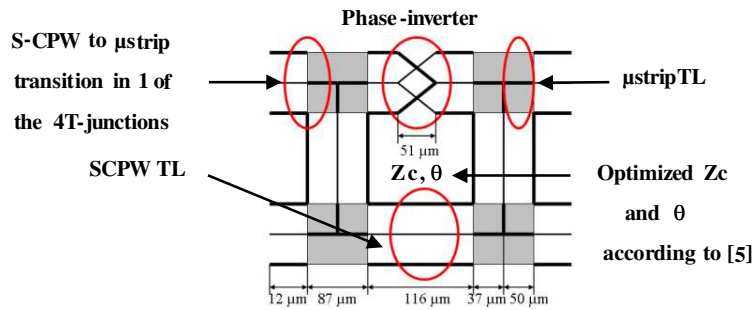


Figure 1: Compact low-loss rat-race balun description (not at scale).

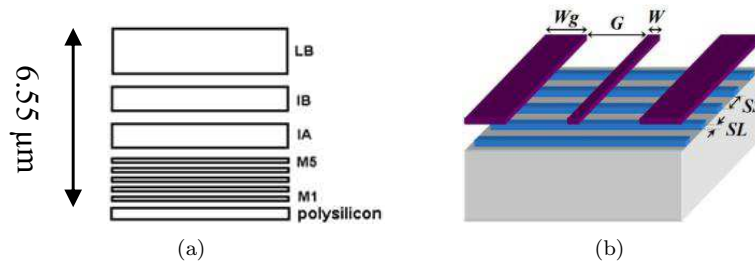


Figure 2: (a) CMOS 65-nm technology description. LB is the cap layer, IA and IB, the two thick top metal layers. (b) S-CPW 3D view.

2. RAT-RACE DESIGN

Figure 1 gives the balun's topology.

The rat-race balun was implemented in the 65-nm STMicroelectronics CMOS technology which BEOL is described in Fig. 2(a).

The design of the rat race is divided in several blocs simulated individually thanks to a 3D full-wave EM software (Ansoft HFSS). In a second step, the S -parameters are all gathered to be simulated thanks to a circuit simulator (Agilent ADS). In [5], it is reported that an infinite number of electrical lengths exists for the design of a 3 dB hybrid coupler. Whatever the arms characteristic impedance is, below the conventional value of $Z_0\sqrt{2}$, the ring electrical length may be less than 1.5λ . This is very interesting, because (i) the rat-race ring can be shortened, and (ii) the characteristic impedance of the S-CPW TLines can be chosen in order to reach the highest quality factor. Next, in order to (i) reduce the ring physical length, (ii) equate the insertion loss, and (iii) improve the phase imbalance between the two output ports, an adequate phase-inverter was designed to be inserted in the longest arm of the rat-race, as shown in Fig. 1.

Finally, T -junctions were designed and optimized in order to reach low insertion loss and return loss. The blocs' simulation and optimization are described in the next section.

3. BLOCKS SIMULATION

3.1. S-CPW TLines

S-CPW TLines are based on conventional coplanar CPW TLines with a patterned floating shield, including floating metallic strips underneath the CPW strips, as shown in Fig. 2(b). The signal conductor and the ground planes of the CPW are on the thick top metal layer IB in order to reduce the metallic losses whereas the floating strips are realized on the highest thin metal layer M5. Previous papers already proved that the simulation and measurement results of such a topology are in really good agreement and provided TLines with very high quality factors equal to more than twice those reached with classical CPW or microstrip TLines [6, 7]. The floating shield dimensions are $0.1\ \mu\text{m}$ for the strip width (SL) and $0.55\ \mu\text{m}$ for the strip spacing (SS). A parametric study involving the signal conductor width (W), the signal-to-ground gap (G) and the ground plane width (Wg) concluded to the highest Q factor value at 60 GHz for $W = 20\ \mu\text{m}$, $G = 25\ \mu\text{m}$ and $Wg = 12\ \mu\text{m}$, respectively, leading to a $45\ \Omega$ characteristic impedance. This TLine, and the microstrip Tline used in the T -junctions (Fig. 1) were realized in the CMOS 65 nm technology. The

S-CPW Tline was measured and its characteristic impedance Z_c and effective dielectric constant ε_{reff} were extracted. A really good agreement was obtained between measurement and simulation results. The value of the characteristic impedance is $45\ \Omega$ and ε_{reff} reaches 12.5 as expected. At 60 GHz, the S-CPW TLine quality factor reaches 24 which is twice bigger than that of a classical CPW TLine, and six times higher compared to the microstrip line designed for the T -junctions. The electrical lengths of the branches of a conventional rat-race built with a characteristic impedance of $70.7\ \Omega$ are $90^\circ(\lambda/4)$ and $270^\circ(3\lambda/4)$. According to [5], considering a $45\ \Omega$ characteristic impedance, the electrical lengths become 52° and 232° , respectively. Thus, while choosing the Tline with the best quality factor as possible, not only the rat race will present better loss performances but it will also be miniaturized.

3.2. T -junctions: Microstrip Lines and S-CPW/Microstrip Transitions

Because of the high memory computing needs due to the presence of the very thin strips of the floating shield, the T -junctions based on S-CPW TLines are heavy to simulate and optimize with a full-wave electromagnetic tool. Hence, T -junctions were designed in a microstrip technology. The signal strip and ground layers as well as the dimensions were optimized in order to get a microstrip Tline characteristic impedance of $45\ \Omega$. The microstrip Tline was placed on the thickest metal layer LB to reduce the metallic losses whereas the ground strip was coated on metal layer M1. The microstrip width is $6.2\ \mu\text{m}$. The extracted parameters Z_c and ε_{reff} from the measurement of the microstrip Tline fit well with the simulations, $45\ \Omega$ and 3.8, respectively. The S-CPW/microstrip transition brings about 0.11 dB of insertion loss at 60 GHz with S_{11} equal to $-28\ \text{dB}$ in simulation. The T -junction's model is taken into account in the global rat-race model.

3.3. Phase-Inverter

A phase-inverter (Fig. 1) was considered in the middle of the 232° branch in order to reduce the length of the Tline. With this approach, the same TLines are placed in the four branches, hence leading to very small phase imbalance versus frequency, thus increasing the bandwidth. The topology is based on a symmetrical design as in [2]. The wider is the overlap between signal and ground conductors and the bigger is its parasitic capacitor value when ground and signal strips are overlapping. Thus, the narrowest width limited by the technology was fixed to minimize the parasitic capacitor. The phase shift is about 199° at 60 GHz. This value is greater than 180° , due to in-out inductive parasitic effects, and the capacitive loading due to the overlap between the strips. It was compensated with smaller TLines apart to reach the targeted value of 232° .

4. RAW MEASURED RESULTS FOR THE RAT RACE BALUN

The layout of the achieved rat-race balun is shown in Fig. 3.

The raw measured results are shown in Fig. 4. Measurements were carried out with a 4 ports Agilent Vector Network Analyzer, from 10 GHz till 67 GHz. The return loss S_{11} and S_{22} show a shift in the working frequency compared to S_{33} ; indeed best matching is around 67 GHz with $-33\ \text{dB}$ for S_{11} and S_{22} , and 55 GHz for S_{33} with $-38\ \text{dB}$, (Fig. 4(a)). Both ports 1 and 2 are directly connected with the arm containing the phase-inverter. First measurements on the phase-inverter alone show unexpected mismatch. It is possible that the mismatched phase-inverter at the expected frequency degrades the global matching at the two involved ports. This point is under investigation. The pads at the inputs/outputs of the component which are equivalent to loaded capacitors at each port shift the working frequency at lower frequency. The value of these equivalent capacitors is

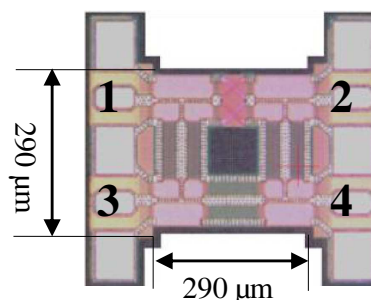


Figure 3: Layout of the rat-race balun with phase-inverter, S-CPW and microstrip TLines in 65-nm CMOS technology.

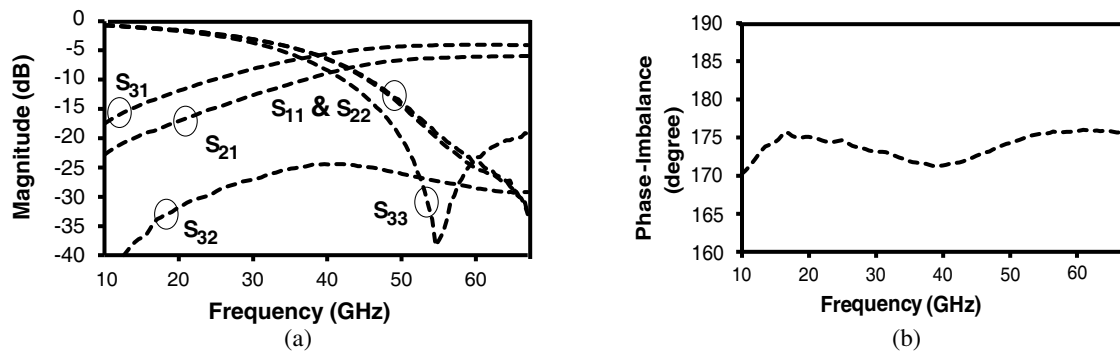


Figure 4: S -parameters measurement. (a) S_{11} , S_{22} , S_{33} , S_{21} , S_{31} , S_{32} . (b) Phase imbalance between the outputs (port 2 and port 3).

evaluated around 39 fF. If the bandwidth is defined by considering -15 dB for any return loss, then a minimum of 26% is obtained (between 51 GHz and 67 GHz minimum) with a phase imbalance equal to $175.9^\circ \pm 0.4^\circ$, as shown in Fig. 4(b). There is a shift of 4.1° compared to the perfect phase imbalance, but it is very flat over the whole bandwidth. In this frequency band, the insertion loss of the rat-race balun lies between 6.5 and 6 dB for the phase-inverted arm (S_{21}) and between 4.2 and 4.1 dB for the other one (S_{31}), Fig. 4(a). In the arm without phase-inverter the extra insertion loss is 1.2 dB compared to a lossless ideal rat-race. This is a very attractive result. In the phase-inverted arm, the increase of the insertion loss seems to be due to the phase-inverter under investigation. The transmission parameters are robust with very flat curves. Isolation S_{32} is better than -24 dB over a very large frequency band, at least from 10 GHz to 67 GHz (see Fig. 4(a)).

Finally, the chip area is equal to 0.085 mm^2 . Improving the phase-inverter, the rat race could probably be balanced in magnitude and have a better return loss, in addition to its good sturdiness, good isolation, small phase imbalance in a large frequency range, and compactness. The performances obtained in [2] are better in term of insertion loss, think this was obtained with a thicker BEOL. The other parameters are comparable, and our design leads to a 20% smaller chip area.

5. CONCLUSION

In this paper, an integrated CMOS millimeter-wave rat-race coupler for balun applications has been proposed. It is based on the use of high quality factor and compact S-CPW TLines. The design procedure in a 65 nm CMOS technology was detailed. S-CPW TLines together with the use of a phase-inverter in the longer rat-race arm enables to reach a very compact device. Measurements show a small variation in the phase imbalance, a good isolation and robust transmission parameters for a compact device. The improvement of the phase-inverter could probably improve the balanced magnitude between the output ports. To the best of our knowledge, it is the first demonstration of a millimetre-wave rat-race balun based on S-CPW TLines. As stated in the introduction, these TLines conserve good performances while the BEOL thickness is reduced. Hence the present design could serve as a proof-of-concept for the design of further baluns at higher frequencies and with advanced CMOS technologies, where the design of transformers becomes very hard due to small loops and thin BEOLs.

ACKNOWLEDGMENT

The research leading to these results has been conducted in the frame of the European ENIAC MIRANDELA project and it received funding from the ENIAC Joint Undertaking under grant agreement number 120221 together with funding from the “French Direction Générale de la Compétitivité, de l’Industrie et des services” under convention No. 102930164.

REFERENCES

1. Pon, C., “Hybrid-ring directional coupler for arbitrary power division,” *IEEE Trans. Microw. Theory Tech.*, Vol. 9, No. 6, 529–535, Nov. 1961.
2. Chirala, M. K. and B. A. Floyd, “Millimeter-wave lange and ring hybrid couplers in a silicon technology for E-band applications,” *IEEE MTT-S International Microwave Symposium Digest*, San Francisco, California, USA, June 11–16, 2006.

3. Cheung, T.-S. D. and J. Long, “Shielded passive devices for silicon-based monolithic microwave and millimeter-wave integrated circuits,” *IEEE Journal of Solid State Circuits*, Vol. 41, No. 5, 1183–1199, May 2006.
4. Kaddour, D., H. Issa, A.-L. Franc, N. Corrao, E. Pistono, F. Podevin, J.-M. Fournier, J.-M. Duchamp, and P. Ferrari, “High-Q slow-wave coplanar transmission lines on 0.35 μm CMOS process,” *IEEE Microw. and Components Letters*, Vol. 19, No. 9, 1183–1199, Sep. 2009.
5. Mandal, M. K. and S. Sanyal, “Reduced-length rat-race couplers,” *IEEE Trans. Microw. Theory Tech.*, Vol. 55, No. 12, 2593–2598, Dec. 2007.
6. Franc, A.-L., E. Pistono, D. Gloria, and P. Ferrari, “High-performance shielded coplanar waveguides for the design of CMOS 60-GHz band-pass filters,” *IEEE Trans. on Electron Device*, Vol. 59, No. 5, 1219–1226, May 2012.
7. Franc, A.-L., E. Pistono, and P. Ferrari, “Compact high rejection notch and DBR designed with slow-wave,” *Proceedings of the Asia-Pacific Microwave Conference*, 7–10, Yokohama, Japan, Dec. 2010.

Parametric Design of Stop Band Pass Filter Based on RF Metamaterials in LTCC Technology

M. Morata¹, I. Gil², and R. Fernández-García²

¹Escuela Universitaria Salesiana de Sarriá, Barcelona 08017, Spain

²Departament of Electronic Engineering, Universitat Politècnica de Catalunya, Terrassa 08222, Spain

Abstract— This paper presents a novel approach to design a parametric RF stop band pass filter based on Low Temperature Co-fired Ceramic (LTCC) Technology. The LTCC technology enables to miniaturize and development compact structures using not only the standard xy -planar circuit dimensions but also the z -height dimension. The proposed filters topologies are based on a stripline loaded with one or several complementary rings resonator (CSRRs). Specifically, a parametric study z -location of the stripline respect to the CSRRs is carried out in order to determine the optimum configurations operating in the Ku-band.

1. INTRODUCTION

Efficient filtering microwave techniques are crucial in order to design microwave circuit applications in many areas such as signal processing, wireless communications, military uses or biomedical engineering. Specifically, several works have been developed in order to design new microwave Ku-band filters [1]. Recently, metamaterial transmission lines (TLs) (i.e., artificial lines consisting of a host line loaded with reactive elements) have been used to develop microwave filters in printed circuit board (PCB) [2]. Alternatively, complementary split ring resonators (CSRRs) have been revealed as good candidates in order to improve the performance of conventional microwave filters [3]. On the other hand, the Low Temperature Co-fired Ceramic (LTCC) technology (Fig. 1) has become an alternative platform for implementing RF passive components and circuits due to its high performance, reliability and low losses [4]. Therefore, LTCC technology enables further miniaturization and development of compact structures using not only the standard xy -planar circuit dimension but also the z -height dimension [5].

The aim of this work is to develop a parametric design of several RF metamaterial stop-band filters based on a stripline loaded with complementary split ring resonators (CSRRs) in LTCC technology in order to show an alternative way to implement stop band pass filter based on RF metamaterials. The analysis of the influence of the different parameters such as the relative xyz -location of CSRRs with regard to the host transmission line has been performed in terms of frequency response. Specifically, an electromagnetic simulation parametric study has been carried out by means of the commercial *Agilent Momentum* software. A 6-metal layer LTCC technology has been used. Fig. 1 shows a cross section scheme of the Ferro A6 used substrates (dielectric constant, $\epsilon_r = 5.96$, thickness = 3.7 mil). Several layers have been interconnected by means of vias.

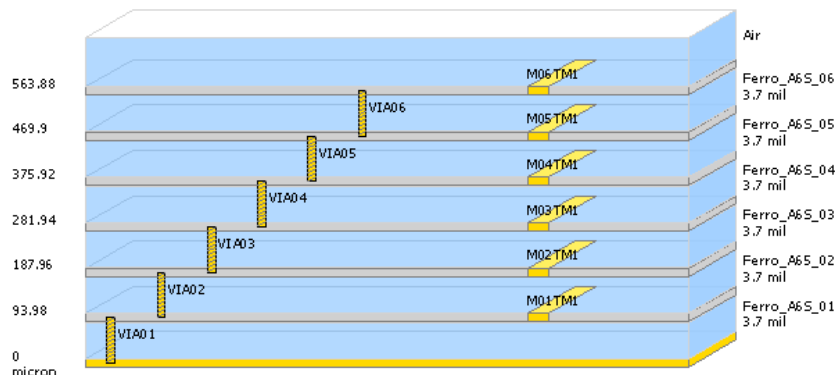


Figure 1: Cross section of the 6 metal layer LTCC technology.

2. INFLUENCE OF THE STRIPLINE RESPECT TO THE Z-POSITION

Before integrating the geometries of the complementary split ring resonators (CSRRs), the stripline itself has been defined. The initial device consists of two $50\ \Omega$ access lines etched on the layer number 6 combined with two connections through vias shortcutting the stripline which has been defined in several layers. In this sense, the influence of the position of the stripline and vias in the xyz plane is studied. Fig. 2 shows the two initial symmetrical and non-symmetrical considered topologies. The electromagnetic simulations are devoted to obtain the insertion losses (S_{21} parameter) in several cases. As a generic result a 3 dB better mismatching performance is observed in symmetrical topologies. Therefore, in order to improve the frequency response of the designed Ku-band filters, it has been sought for symmetrical geometries which reduce this mismatching degree and losses. The designed stripline is patterned on different LTCC layers but with the same dimensions that correspond to $10580 \times 200\ \mu\text{m}^2$. Fig. 3 depicts the parametric electromagnetic simulation results corresponding to the insertion losses with regard to the layer position. As can be observed, the mismatching is higher if the layer position is deeper. In addition, the rejection level has been reduced from 6 dB to 2.4 dB which implies a 60% reduction in comparison to the initial symmetrical geometry. Finally, to implement the complementary ring resonators, the designed stripline has been patterned on the LTCC layer number 3 that supposes a rejection level lower than 1 dB.

3. INFLUENCE OF THE NUMBER OF CSRRS IN TERMS OF THE LAYER POSITION

According to the previous results, the filter stripline has been located in the third LTCC layer. As next step, the influence of the number of CSRRs with regard to the layer position has been studied. The CSRRs and the stripline dimensions correspond to $2000 \times 2000\ \mu\text{m}^2$ and $10580 \times 200\ \mu\text{m}^2$, respectively. First it has been analyzed the electromagnetic simulation response when the geometry

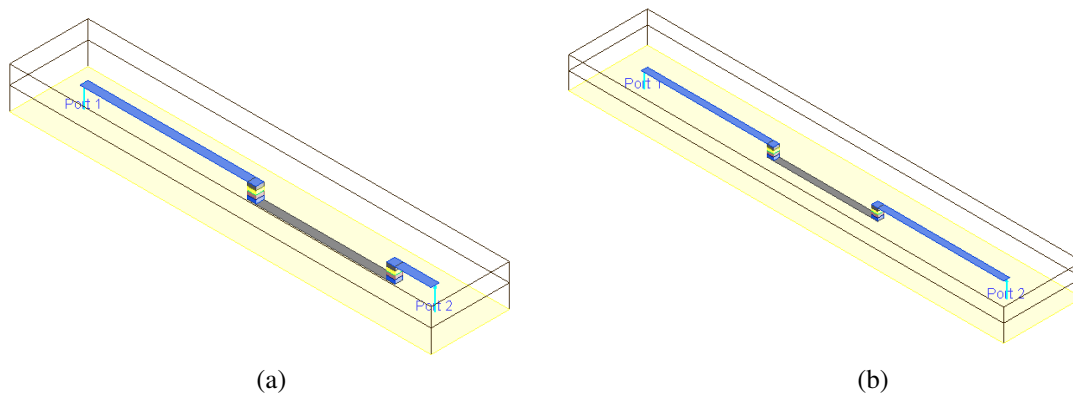


Figure 2: Comparison between (a) symmetrical and (b) non-symmetrical implementation.

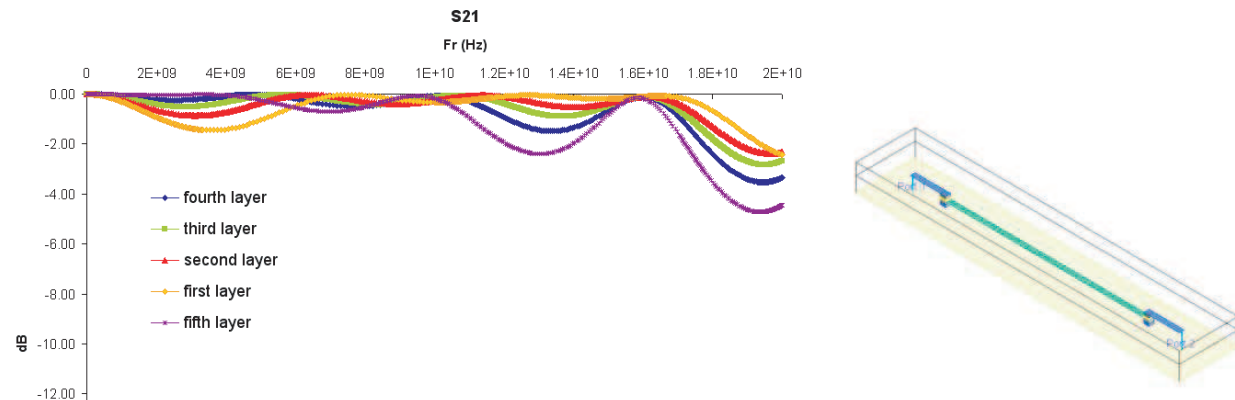


Figure 3: Electromagnetic simulation of the insertion losses of the considered stripline with regard to the layer position in the z -plane.

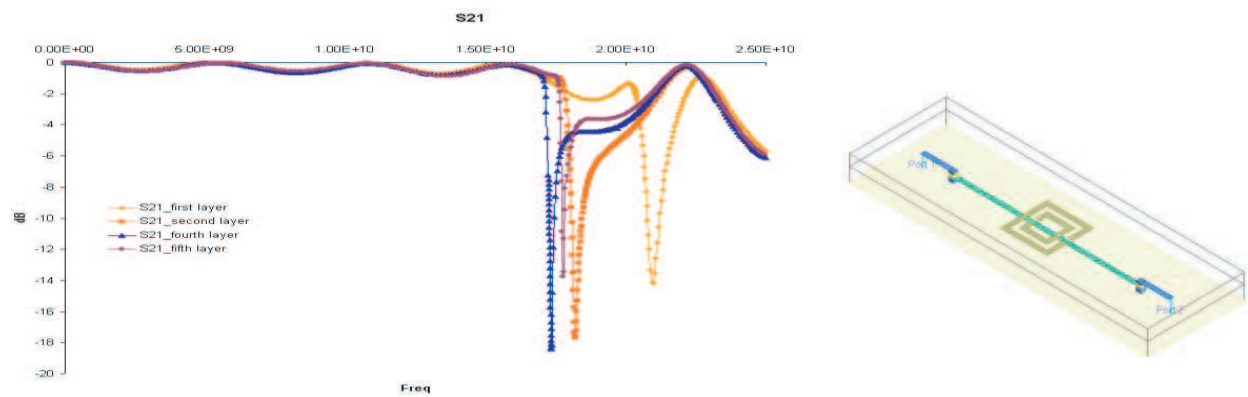


Figure 4: Electromagnetic simulation insertion losses for one CSRR with regard to the layer position.

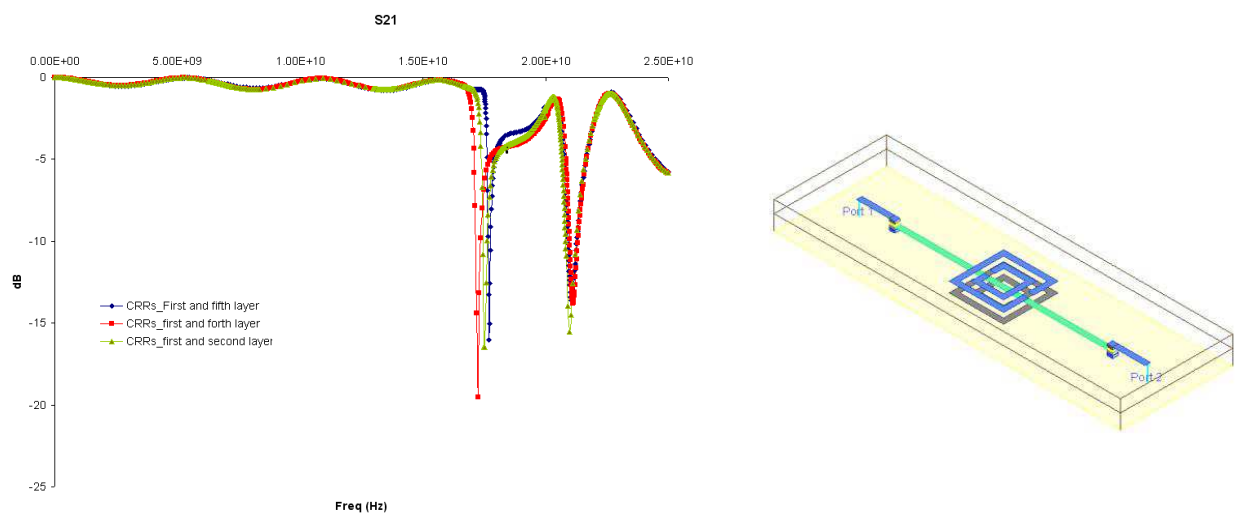


Figure 5: Electromagnetic simulation insertion losses for two CSRR located in different layers.

includes one CSRR in the first, second, fourth and fifth layer. Fig. 4 shows the electromagnetic simulation insertion losses for those different cases. It can be observed that the nearer the CSRR to the host line (layers 2 and 4) the higher the resonance frequency, because of the higher level of electrical coupling. Moreover, the resonance frequency of 2 and 4 layers are quite similar, because the involved equivalent inductors and capacitors are symmetrical. The average level of rejection corresponds to 15 dB.

Secondly, it has been considered the electromagnetic simulation response when the geometry includes two CSRRs located in the same xy position and etched in two different layers (variable z -axis). Fig. 5 shows the electromagnetic simulation insertion losses in those cases. It is observed two resonance peaks at different frequencies due to both CSRR1-host line and CSRR2-host line electrical coupling. Again, the rejection level corresponds to an average value of 15 dB and the undesired presence of an extra resonance implies that those topologies are not optimum.

As third step, the behavior of a structure composed by two CSRRs etched in the same layer has been studied. As depicted in Fig. 6, the best configurations in terms of rejection are obtained for CSRRs located on layers second and fifth by obtaining rejection levels of 40 and 27 dB, respectively,. Therefore, in order to improve the rejection level of the proposed stop-band filters it is recommended to use at least two CSRRs in each layer.

A final improved topology is presented in Fig. 7. The best case corresponds to a 2-CSRRs stage etched on layers 2 and 5 simultaneously. The obtained rejection level corresponds to 40 dB achieved around 17.8 GHz, whereas the rest of the band remains matched.

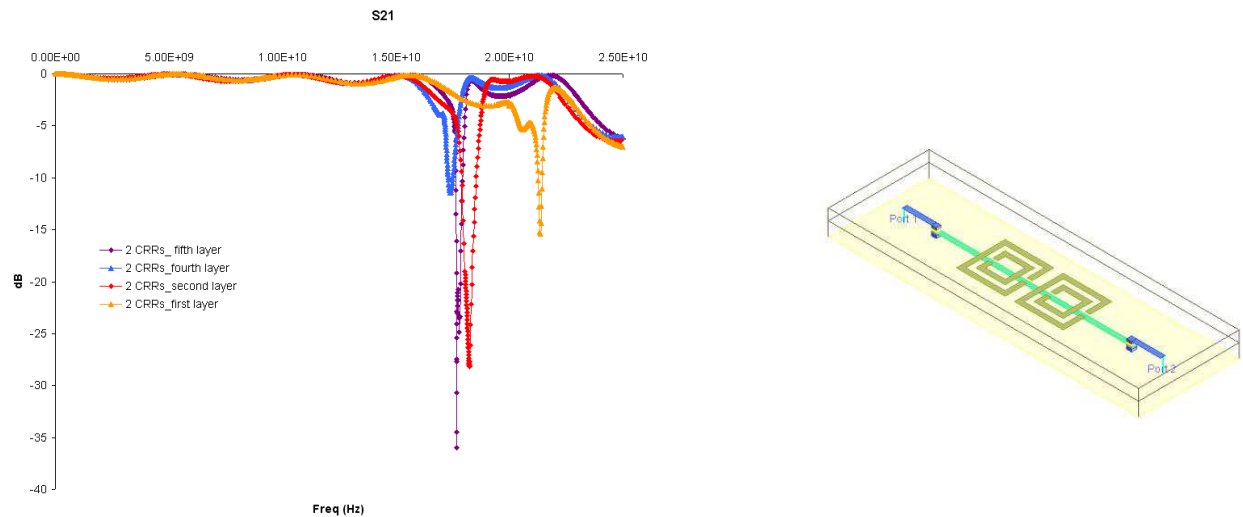


Figure 6: Electromagnetic simulation insertion losses for two CSRRs located in the same layer.

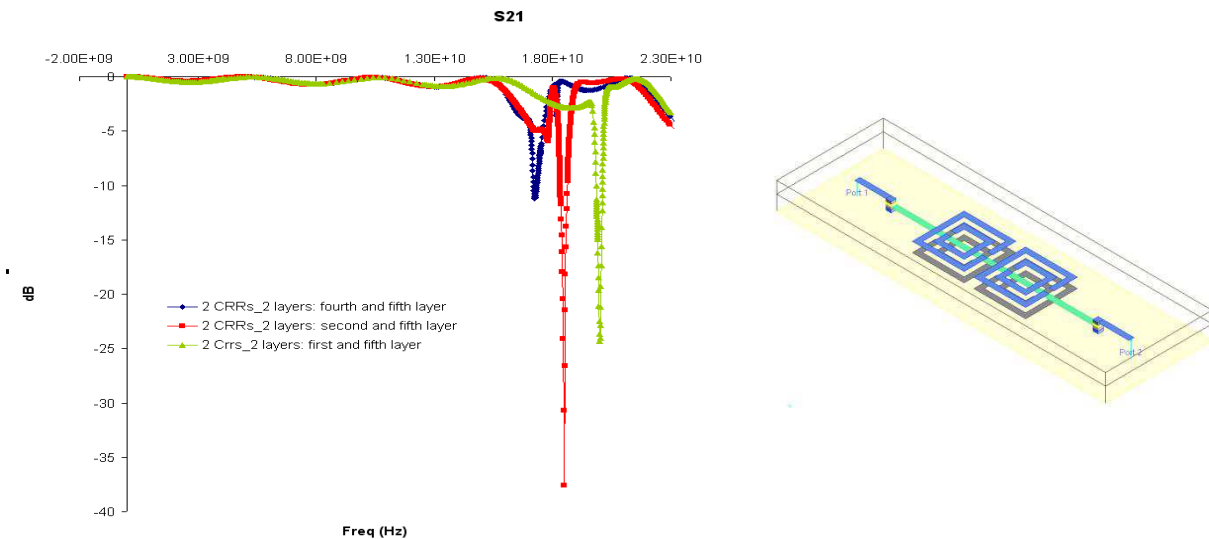


Figure 7: Electromagnetic simulation insertion losses for two CSRRs stage combined in two LTCC layers.

4. CONCLUSIONS

In summary, a parametric design of a Ku-band stop-band pass filter based on RF metamaterials on LTCC technology has been proposed. In order to reduce the number of parameters, the stripline is patterned in the LTCC layer number 3 whereas two CSRRs are etched on layers number 2 and number 5. It has been demonstrated, that these structures open the door to design filters based to stripline RF metamaterials in LTCC technology.

ACKNOWLEDGMENT

This work has been supported by the Spain-MINECO under Project TEC2010-18550 and AGAUR 2009 SGR 1425.

REFERENCES

1. Zhou, J., M. Wei, and B. Li, "Ku-band filters using open-loop and quarter-wavelength resonators based on LTCC technology," *International Conference on Consumer Electronics, Communications and Networks*, 1104–1107, April 2012.
2. Mohra, A. S. and O. F. Siddiqui, "Tunable bandpass filter based on capacitor-loaded metamaterial lines," *Electronics Letters*, Vol. 45, 470–472, April 2009.

3. Pérez, D., I. Gil, J. Gago, R. Fernández, J. Balcells, D. González, N. Berbel, and J. Mon, “Reduction of EMI susceptibility in circuits based on operational amplifiers using complementary split-ring resonators,” *IEEE Transactions on Components, Packaging and Manufacturing Technology*, Vol. 2, 240–247, February 2012.
4. Li, Y., Y. Liu, H. Zhang, D. Lu, L. Bian, and Z. Yang, “The design and fabrication of RF band pass filter by LTCC technology,” *International Conference on Electronic Packaging Technology & High Density, Packaging (ICEPT-HDP 2008)*, 1–4, August 2008.
5. Yang, T., M. Tamura, and T. Itoh, “Super compact low-temperature co-fired ceramic band pass filters using the hybrid resonator,” *IEEE Transaction on Microwave Theory and Techniques*, Vol. 58, 2896–2907, November 2010.

Radiofrequency Interference Filters Design Based on Complementary Split Rings Resonators

D. Pérez, I. Gil, and R. Fernández-García

Department of Electronic Engineering, Universitat Politècnica de Catalunya
Colom 1, Terrassa 08222, Spain

Abstract— Low frequency analog and digital electronic circuits are susceptible to radiofrequency interference (RFI). This disturbance is produced when the coupled RF signal is rectified by the non-linear behavior of the semiconductors used in the small signal analog input stages of the electronic system. These circuits present an AM demodulation effect produced by nonlinearity of internal transistors, generating parasitic signals in the low-frequency range and undesired offset voltage. In this paper, an alternative to the current standard EMI filters is presented by combining the conventional printed circuit board layout with complementary split ring resonators (CSRRs), in order to reduce the output offset impact due to RFI. An operational amplifier circuit has been designed with a 4-stage CSRR filter, electromagnetically simulated and experimentally tested. Two prototypes have been implemented, with and without CSRRs in order to compare the filter properties in standard FR4 substrate. The resonance frequency of the CSRRs has been designed in the vicinity of 2.4 GHz in order to prevent susceptibility in the ISM band. Electromagnetic and electrical equivalent circuit model simulations are also provided and compared with experimental results. Measurement data show an effective rejection of the undesired RF demodulation without affecting the signal integrity out of the filter band, and therefore a significant reduction concerning output offset voltage impact in terms of RFI amplitude with no-extra cost in terms of the device area or manufacturing process.

1. INTRODUCTION

Electronic systems are usually disturbed by high frequency radiofrequency (RF) electromagnetic interference (EMI), whose amplitudes change randomly in time. This out of frequency band electromagnetic compatibility (EMC) issue is produced when the RF signal is coupled to sensors and cabling of the system, conducting the EMI to signal-conditioning, and causing errors or malfunction due to the rectification by the non-linear behavior of the semiconductors used in the electronic systems [1].

To solve this problem, effective filtering techniques must be implemented at the input stages of the system in order to avoid the non-desired rectification effect. Standard solutions are based on design robustness (involving a higher number of electronic components) or layout shielding (involving extra metal layers or area) [2]. Recently, specific multilayer layout techniques based on electromagnetic band gaps (EBGs) have appeared in order to filter EMI in several applications with good performance [3]. EBGs belong to a broad family of artificial media with electromagnetic properties generally not found in nature, called metamaterials. A second type of metamaterials, the so-called effective media (i.e., metamaterials satisfying the condition: signal wavelength ($\lambda \ll$ period) have shown some excellent notch filtering properties. Among them, the group called single negative media (SNG) are used in this work in order to implement a filter technique to mitigate RFI.

Physically, SNG (i.e., effective media with negative magnetic permeability $\mu < 0$, or electric permittivity, $\varepsilon < 0$) can be implemented by using so called split-ring resonators (SRRs) and their dual counterparts, the complementary split-ring resonators (CSRRs) [4, 5]. In this paper, a filter developed by means of effective media metamaterials based on CSRRs is used to reduce RFI in a conventional analog circuit constituted of a differential amplifier based on an OPAMP.

2. CSRRs

Essentially, CSRRs (Fig. 1(a)) are the negative images of SRRs. SRRs consist of a pair of metal rings etched on a dielectric slab with apertures in opposite sides which can be mainly excited by means of a parallel magnetic-field along its axis. If an array of SRRs is located close to a transmission line, some current loops can be induced in the rings and they reflect the incident host signal at resonance. Therefore they behave as an LC tank magnetically coupled to the host line [6]. From duality arguments based on an approximation of the Babinet's principle for dielectric boards, it is demonstrated that the CSRRs, roughly behave as their dual counterparts (i.e., their resonance

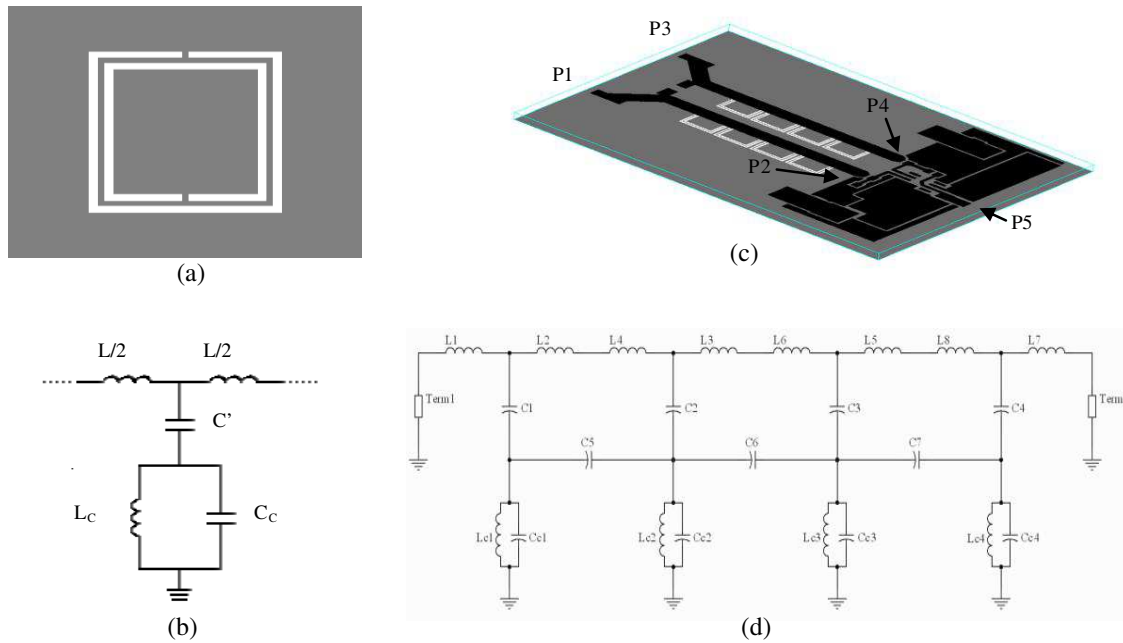


Figure 1: (a) Topology of the CSRR. Metallization zones are depicted in grey. (b) Lumped-element equivalent circuit of the CSRR coupled to a transmission line. (c) Designed layout. The black layer corresponds to the top layer, whereas the grey layer corresponds to ground, where the CSRRs have been etched. (d) Equivalent circuit model of the implemented filter.

frequency is approximately equal to that of the corresponding equivalent SRRs). An efficient way to achieve stop-band frequency responses is to etch CSRRs in the ground plane of a structure such as a microstrip line (or similar) or even in the conductor strip. CSRRs are coupled electrically to the host line according to the model shown in Fig. 1(b). The main advantage of these sub-wavelength particles are their low implementation cost (no extra components, neither PCB layers are required or special etching techniques) and the quasi-non-area consumption, since they are located in the ground plane of the overall structure. With regard to the filtering effectiveness a trade-off between the rejection level and the number of CSRR stages appears.

3. PROPOSED STRUCTURE

The test circuit consists of a conventional differential amplifier. The configuration corresponds to a basic instrumentation amplifier with an output voltage approximately equal to the input voltage difference. In order to avoid RFI reaching the OPAMP input, a 4-CSRR filter has been designed and combined in the final prototype. Fig. 1(c) shows the PCB designed layout. It can be observed two CSRR arrays located in the ground plane, underneath the input transmission lines carrying the signal of interest to the differential input. Notice that this distribution implies effective non-area consumption with respect to a conventional 1-layer design. Moreover, no extra lumped circuitry is needed and no series stage filter is required.

The resonance frequency of the CSRRs has been designed in the vicinity of 2.4 GHz, by means of the *Agilent ADS* and *Momentum* software in order to prevent susceptibility in the Industry-Scientific-Medical (ISM) radio band. In fact, the involved single resonator dimensions have been slightly detuned in order to achieve a wider stop-band bandwidth (i.e., single CSRRs with close resonance frequencies). Therefore, a final simulation step based on a multiple tuning procedure has been developed. EMI filter simulations have been performed between external input ports (P1 and P3) and internal ports (P2 and P4) before OPAMP and circuitry stage (output port corresponds to P5) (Fig. 1(c)).

Figure 1(d) depicts the corresponding full lumped circuit model by taking into account the electrical model illustrated in Fig. 1(b). The inter-resonator coupling between adjacent CSRRs has been modelled by means of capacitances $C5, C6, C7$.

By analyzing a single CSRR coupled to the line (i.e., no inter-resonator coupling), two resonance frequencies arise: the frequency that nulls the shunt impedance (i.e., transmission zero frequency),

given by (1) and the resonance frequency of the CSRR given by (2):

$$f_z = \frac{1}{2\pi\sqrt{L_C \cdot [C_C + C']}}. \quad (1)$$

$$f_0 = \frac{1}{2\pi\sqrt{L_C C_C}}. \quad (2)$$

On the other hand, the periodic structure under study by neglecting inter-resonator coupling, satisfies (3),

$$\cos \varphi = 1 + \frac{Z_S(j\omega)}{Z_P(j\omega)}. \quad (3)$$

This equation allows the analysis of periodic circuits based on the cell depicted in Fig. 1(b) with the help of the dispersion relation and Bloch impedance. φ denotes the phase shift of the elemental cell, and Z_P and Z_S correspond to the shunt and series impedance, respectively, of the T-circuit model. By combining electromagnetic simulation results and Equations (1)–(3) the parameters of the overall model can be extracted.

4. FABRICATED PROTOTYPES

Two experimental prototypes have been fabricated and tested. Both implementations present the same top level metal layer layout and are differentiated from the ground plane (a conventional one in the first case and a ground plane disturbed by etched CSRR arrays in the second case). Fig. 2 shows the prototype setup consisting of a 3-port 4-stage CSRR loaded parallel transmission lines, which have been designed to obtain a stop band filter around 2.4 GHz. The OPAMP used in the prototypes is a UA741CD, supplied by two voltage regulators, a MC78M15BDTG (15 V) and aMC79M15CDTG (−15 V). All resistor values are 1 k Ω . Decoupling capacitors (100 nF and 10 μ F) have been also used to complement the supply lines. The substrate corresponds to the commercial MC 100 FR4. Specifically, 50 Ω two microstrip access lines are considered with dimensions: width $W = 2.84$ mm, length $l = 4$ cm, and separation $s = 6.55$ mm. The total circuit area is 6.9×4.8 cm².

5. EXPERIMENTAL AND SIMULATION RESULTS

In order to test the overall performance of the proposed CSRR prototype, a RFI coupling has been emulated by means of a signal modulated in AM (with carrier frequency $f_C = 2.4$ GHz) with a low frequency tone (modulated frequency $f_m = 10$ kHz). The direct power injection carrier amplitude, corresponds to −10 dBm and the modulation index to 50%. The experimental output spectrum at the low operation frequency (10 kHz) reveals a disturbance on the order of 20 dB for the conventional case (Fig. 3(a)), which is produced by the non-linear behavior of OPAMP. However, the CSRRs prototype completely removes this EMI effect, since the impact of resonators notably filters the undesired noise signal at this frequency. In order to evaluate the effectiveness of the proposed implementation, the DC offset voltage in terms of interference amplitude has also been tested and shown in Fig. 3(b). When the noise signal is injected, a significant increase of the offset with EMI amplitudes higher than −5 dBm is observed in the conventional circuit, whereas in the same conditions, the offset of the prototype equipped with the CSRR filter remains constant (−1.19 mV). Notice also that the offset level is almost 4 times lower in CSRR filtered prototype, since the best offset level for the conventional device is approximately −4 mV.

With regard to the filter performance, Fig. 4(a) shows the detailed fitting between the proposed equivalent circuit frequency response, the electromagnetic simulation and the equivalent circuit

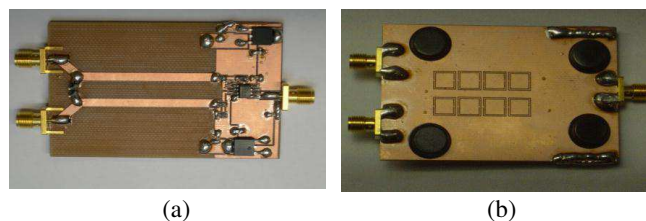


Figure 2: Fabricated prototype device. (a) Top side. (b) Bottom side including CSRRs.

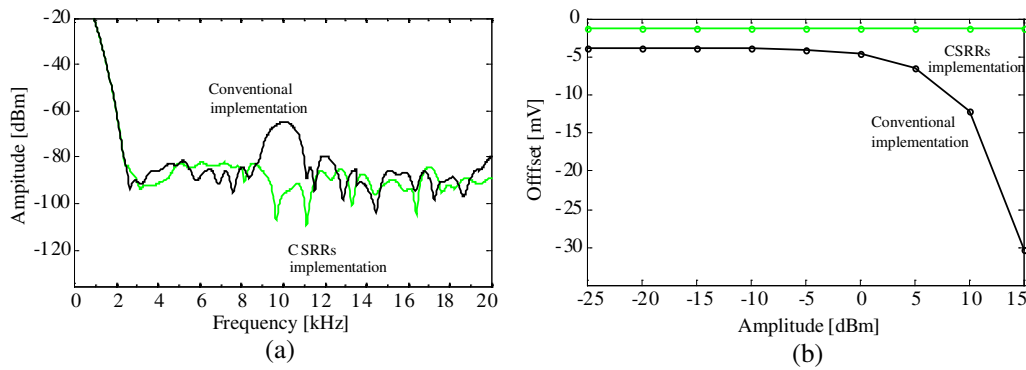


Figure 3: (a) Measured demodulation output device spectrum for conventional and CSRRs prototypes. (b) Measured DC offset vs. RF interference amplitude for conventional and CSRRs prototypes ($m = 50\%$).

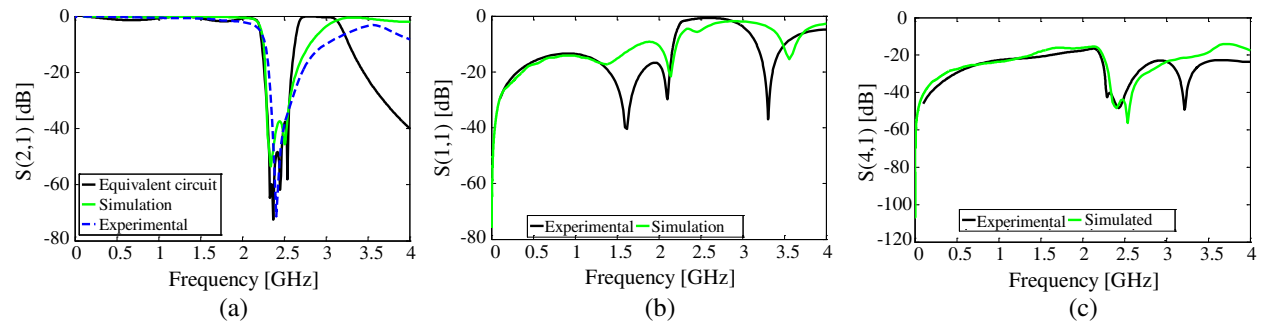


Figure 4: (a) Insertion losses $|S_{21}|$. (b) Return losses $|S_{11}|$. (c) Coupling losses $|S_{41}|$.

model behaviour. As can be observed, a significant rejection level is obtained ($|S_{21}| < -40$ dB) at the frequency band of interest. Fig. 4(b) depicts the CSRRs filter electromagnetic return losses (S_{11}), whereas the crosstalk has been obtained by measuring S_{41} . According to the results, the crosstalk is reduced in the rejection band of the CSRR RFI filter adding an extra benefit in terms of the immunity (coupling reduction).

Moreover, the obtained signal integrity (SI) of the device has been analyzed by means of the eye diagram test including eye width (EW) and eye high (EH). An input test signal of 1 V operating at 50 MHz has been used. The eye diagrams corresponding to the prototype without CSRRs simulated and measured are depicted in Figs. 5(a)–(b). In this case, the obtained values are $EW = 10$ ns and $EH = 999$ mV for simulation and $EW = 10$ ns and $EH = 1.04$ V for measurements. Likewise Figs. 5(c)–(d) show the eye diagram for the prototype with CSRRs. The obtained values by simulation (Fig. 5(c)) are $EW = 9.98$ ns and $EH = 999$ mV and $EW = 10$ ns and $EH = 1.032$ V for measurements (Fig. 5(d)). Thus, the experimental degradation between the prototype with CSRRs and a continuous ground plane reference board of the EW is null whereas a 0.77% difference is observed for the EH . Therefore, an extremely low SI degradation (negligible) is achieved with CSRRs by obtaining with a good filtering response. Therefore, those results reveal an excellent behavior in terms of SI.

6. CONCLUSIONS

In summary, it has been demonstrated that EMI effects due to random RF disturbance signals reaching the OPAMP input circuits, which present an inherent non-linear behavior, can be significantly reduced by means of filters based on CSRR with no impact in terms of signal integrity. Basically, the demodulated low frequency signal attenuation as well as DC offset minimization has been tested, both by simulation and experimentally. In fact, ground loaded CSRR transmission lines can be a compact-low-cost method in order to significantly decrease the PCB RF coupling interference at the ISM band. Simulated and experimental results show a 45 dB coupling reduction at 2.4 GHz. Moreover, it has been demonstrated that CSRRs do not affect the signal integrity out of the filter band since no significant impact is measured in the eye diagram concerning the comparison between both fabricated prototypes.

The authors are confident about the application of these structures for EMI reduction in planar

electronic circuits operating at high frequencies/data-transmission rates.

ACKNOWLEDGMENT

This work has been supported by the Spain-MINECO under Project TEC2010-18550 and AGAUR 2009 SGR 1425.

REFERENCES

1. Gago, J., J. Balcells, D. González, M. Lamich, J. Mon, and A. Santolaria, “EMI susceptibility model of signal conditioning circuits based on operational amplifiers,” *IEEE Transactions on Electromagnetic Compatibility*, Vol. 49, 849–859, Nov. 2007.
2. Lovat, G. and S. Celozzi, “Shielding effectiveness of planar negative-permeability screens,” *IEEE International Symposium on Electromagnetic Compatibility*, 1–6, Detroit, USA, Aug. 2008.
3. Iravani, B. M. and O. M. Ramahi, “Design, implementation and testing of miniaturized electromagnetic bandgap structures for broadband switching noise mitigation in high-speed PCBs,” *IEEE Transactions on Advanced Packaging*, Vol. 30, 171–179, May 2007.
4. Gil, I. and R. Fernández, “Comparison between complementary split ring resonators and electromagnetic band-gap as EMI reduction structures,” *Proceedings of the European Symposium on EMC*, 895–898, Wrocław, Poland, Sep. 2010.
5. Liu, K. Y., C. Li, and F. Li, “A new type of microstrip coupler with complementary split-ring resonator (CSR),” *PIERS Online*, Vol. 3, No. 5, 603–606, 2007.
6. Baena, J. D., J. Bonache, F. Martín, R. Marqués, F. Falcone, T. Lopetegui, M. A. G. Laso, J. García-García, I. Gil, M. Flores Portillo, and M. Sorolla, “Equivalent-circuit models for split-ring resonators and complementary split-ring resonators coupled to planar transmission lines,” *IEEE Transactions on Microwave Theory and Techniques*, Vol. 53, 1451–1461, Apr. 2005.

Occupational Exposure to Extremely Low Frequency Electric Fields in Office Work

R. Pääkkönen¹, H. Tarao^{2,3}, F. Gobba⁴, and L. Korpinen²

¹Finnish Institute of Occupational Health, Tampere, Finland

²Environmental Health, Tampere University of Technology, Finland

³Department of Electrical and Computer Engineering
Kagawa National College of Technology, Japan

⁴Department of Public Health Sciences, University of Modena and Reggio Emilia, Italy

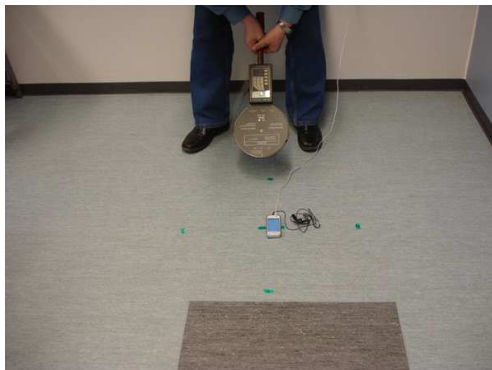
Abstract— The aim of this study is to investigate occupational exposure to extremely low frequency (ELF) electric fields (EF) in office work. The background electric fields ($n = 4$) were 2–25 V/m and the highest electric field measured was 1000 V/m. Different devices found in the office environment were measured for EF exposure. Results included, e.g., (1) spot lamps: 400 V/m and 1000 V/m (from surface) and 30 V/m (distance 50 cm), (2) coffee maker: 10–20 V/m (from surface), (3) the transformer of a computer: 100–200 V/m (from surface), (4) the alternator of a cellular phone: 40–60 V/m, (5) a UPS (uninterruptible power supply): 300 V/m (from surface) and 5 V/m (distance 1 m), (6) a PC table speaker: 250 V/m (from surface). The measured values obtained are clearly below 10 000 V/m threshold stipulated in the guidelines of ICNIRP (The International Commission on Non-ionizing Radiation Protection).

1. INTRODUCTION

Previous studies have presented the measurement results of exposure to extremely low frequency (ELF) magnetic fields in different work environments e.g., the office work environment. Electric fields (EF) have been studied at substations where there are high voltages, but are given less coverage in other settings.

The International Commission on Non-ionizing Radiation Protection (ICNIRP) has published guidelines for limiting exposure to time-varying EMFs (1 Hz–100 kHz) [1]. According to these guidelines, the reference level for general public EF exposure (50 Hz) is 5 kV/m and for occupational exposure (50 Hz), 10 kV/m. Basic restrictions of the internal electric fields (at 50 Hz) for occupational exposure are set at 0.1 V/m (for the central nervous system (CNS) tissues of the head) and 0.8 V/m (for all tissues of the head and body) [1].

In Finland, the occupational exposure to EF has been measured during various work tasks at switching and transforming stations of 110 kV substations, and analyzed to determine if the reference values of ICNIRP guidelines were exceeded. A study investigating this found the average value of all EF measurements taken was 3.6 kV/m and the maximum value was 15.5 kV/m ($n = 765$) [3]. A related study [4] showed that the highest maximum average current density in the neck was 1.8 mA/m² (calculated internal electric field 9.0–18.0 mV/m) during various work tasks at 110 kV substations. Additionally it found that all measured values were lower than the basic restrictions (0.1 and 0.8 V/m for central nervous system tissues of the head, and all tissues of the head and body, respectively), set out in the guidelines of the ICNIRP.



(a) measurement around a phone



(b) measurement from surface of a transformer

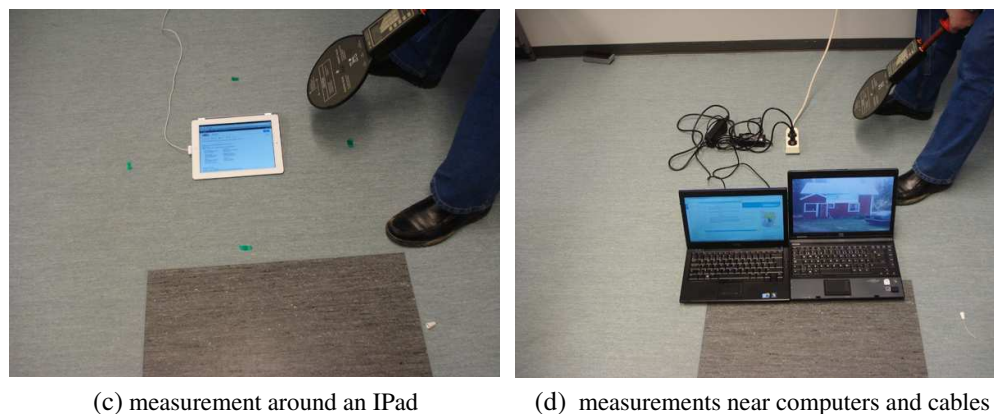


Figure 1: Examples of our measurement situations (distances are 30 cm in photographs (a), (c) and (d)).

Table 1: The summary of EF measurement results from different devices..

Site	Sensor	Electric field, V/m
Office Room — background	in room ($n = 4$)	2–25
Spot light 1	surface of lamp	1000
Spot light 1	50 cm	30
Coffee maker	surface	10–20
PC-transformers	surface	100–200
Charger of a mobile phone	surface	50–60
230 V/50 Hz plug	surface	170
Spot light 2	surface	400
UPS 1	surface	300
UPS 2	1 m	5
PC loudspeaker for table use	surface	250
MP3 player	20 cm	11–30
Chargers (camera, IPAD, etc)	20 cm	1–50
Heating radiator, 1.6 kW	20 cm	2–13
Mobile phones	20 cm	2–6
Mobile phones	surface	50–100
IPAD	20 cm	40–55
IPAD	surface	500–1000
Mixer with whisks	20 cm	50–100
Microwave oven	20 cm	4–6
Electric kettle	20 cm	12–30
Guidelines of ICNIRP for general population	exposure	5000

It is however important to monitor the EF exposure at work places where voltages are low, in order to gain some understanding of the disturbances or minor effects, such as the electrical interference to equipment or medical aids, which may result from EF exposure. The objective of this study was to investigate the occupational exposure to ELF EF in the office work setting.

2. MEASUREMENT METHODS

Measurements were taken using Holaday HI3604 (accuracy $\pm 10\%$) and Wandel&Golterman EFA-3 (accuracy $\pm 5\%$) meters. Figure 1 shows examples of our measurement situations.

3. RESULTS

Table 1 shows the summary of our measurements. The background electric fields ($n = 4$) were 2–25 V/m. Different devices were sampled, for example: (1) spot lamps — 400 V/m and 1000 V/m (from surface) and 30 V/m (distance 50 cm), (2) coffee maker — 10–20 V/m (from surface), (3) the transformers of a computer — 100–200 V/m (from surface), (4) the alternator of a cellular phone — 40–60 V/m, (5) a UPS (uninterruptible power supply) — 300 V/m (from surface) and 5 V/m (distance of 1 m), (6) a PC table speaker — 250 V/m (from surface). The highest electric field measured was 1000 V/m. From mobile phones, we also measured the exposure when the phone is in radio mode, but this was found to be on a level with the background electric field.

4. DISCUSSION

The amount of measurements was limited so it is important to conduct further measurements before stronger conclusions can be drawn. In addition, both the sizes of the measured objects and the size of the sensor used can cause erroneous results. The results however still may provide some guidance. As the values show that disturbances to radios and TVs or other sensible devices are possible. On the other side however, the measured values were so low, that no adverse effects to humans are possible during the sensible use of normal electrical devices, found in the office environment.

5. CONCLUSION

The measured values obtained are clearly below the ICNIRP guideline values of 5 000 V/m [1] and do not exceed the newly proposed EC directive (2011/0152) [2] for electric field exposure.

REFERENCES

1. International Commission on Non-Ionizing Radiation Protection (ICNIRP), “Guidelines for limiting exposure to time-varying electric and magnetic fields (1 Hz to 100 kHz),” *Health Physics*, Vol. 99, No 6, 818–836, Dec. 2010.
2. European Commission, “Proposal for a directive of the european parliament and of the council on the minimum health and safety requirements regarding the exposure of workers to the risk arising from physical agents (electromagnetic fields) (XXth individual directive within the meaning of article 16(1) of directive 89/391/EEC),” <http://eur-lex.europa.eu/LexUriServ/LexUriServ.do?uri=COM:2011:0348:FIN:EN:PDF>.
3. Korpinen, L., H. Kuisti, R. Pääkkönen, P. Vanhala, and J. Elovaara, “Occupational exposure to electric an magnetic fields while working at switching and transforming stations of 110 kV,” *Ann. Occup. Hyg.*, Vol. 55, No. 5, 526–536, 2011.
4. Korpinen, L. H., H. A. Kuisti, H. Tarao, and J. A. Elovaara, “Occupational exposure to electric fields and currents associated with 110 kV substation tasks,” *Bioelectromagnetics*, Vol. 33, No. 5, 438–442, Feb. 14, 2012.

Analysis, Design and Implementation of a Useful Broadband Coaxial-to-microstrip Transition

Gholamreza Askari, Hoda Fadakar, and Hamid Mirmohammad-Sadeghi

Information and Communication Technology Institute
Isfahan University of Technology, Isfahan 84156, Iran

Abstract— In this paper, two useful, simplex and broadband coaxial-to-microstrip transitions using CB-CPW, simple pre-transition, are designed and implemented. The CB-CPW, pre-transition section is utilized to provide a smooth transition from coaxial to microstrip. In these two transitions the effects of the field and impedance matching with considering possible fabrication errors in total performance are completely analyzed. Experimental results are in good agreement with simulation results. The results of back-to-back transition show that a wideband transition with return loss better than -10 dB and total insertion loss less than 2 dB up to 16 GHz is obtained.

1. INTRODUCTION

A coaxial-to-microstrip transition is required in the most planner structures to extract accurate measurement results. The coaxial-to-microstrip transition must support only a single propagating mode over a broad frequency band for proper de-embedding of the transition from the measurement results [1]. Furthermore it is important to have simplex, low-cost and wideband coaxial-to-microstrip transition.

There have been several studies on the end lunch microstrip to coaxial transition [2–5]. However in these transitions, the impedance is match only in the narrow frequency band [2]. In addition Eisenhart's transition that is discussed in [3], exhibits optimum performance but complicated structure, high cost and large size make it undesirable. Besides in [4] and [5] only vertical mounted configuration of coaxial-to-microstrip transition are considered.

In this paper, two broadband transitions between SMA connector and microstrip are proposed. These transitions are designed by the use of conductor back coplanar waveguide (CB-CPW). The CPW and its various configurations such as CB-CPW have several attractive features in comparison with microstrip line. For example these lines have low wave propagation dispersion up to very high frequency [6]. There have been intensive studies on transition from CPW to other planner transmission lines [7–12]. In this work CB-CPW, pre-transition section is used to improve the matching of electromagnetic field distribution at the transition. The design of signal and ground current paths through a transition are also critical and these paths must often be continuous and as near as possible to suppress radiation [2]. In these two transitions the effects of the field and impedance matching on the bandwidth are discussed. Moreover the influence of the fabrication and assembly error such as slightly gap, solder paste in connections at input and output, misalignment between microstrip and center of SMA connector, excitation of higher order modes of SMA in connections and uncertainty of measurement instruments are considered. The simulation results using CST and HFSS software indicate that the bandwidth is increased to maximum operating frequency of SMA connector. The experimental results are in good agreement with simulation results. Insertion loss less than 2.5 dB and return loss better than -10 dB are obtained from 2 to 18 GHz.

2. FIRST PROPOSED TRANSITION

It is important to design a broadband coaxial-to-microstrip transition since the transition bandwidth determines the bandwidth over which the effects of the transition can properly be de-embedded from measurement results [1]. The goal of this work is to develop a coaxial-to-microstrip transition that works up to 18 GHz. The material used in the design is Rogers RT Duroid 6010 with $\epsilon_r = 10.2$. The metal thickness is 0.035 mm and the substrate thickness is 0.635 mm. The SMA connector used in the design is 23_SMA-50-0-52/199_N from Huber-Suhner Company. This connector works at frequencies up to 18 GHz [13]. As it is shown in Fig. 1, center conductor of SMA has rectangular cross section with dimensions of 1.23 mm * 0.15 mm. The width of microstrip line is chosen 0.6 mm to yield characteristics impedance of 50 ohm within the desired frequency band. As it is seen center conductor of SMA is wider than microstrip line and therefore direct

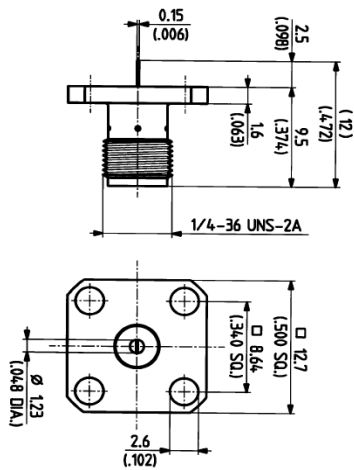


Figure 1: SMA connector [13].

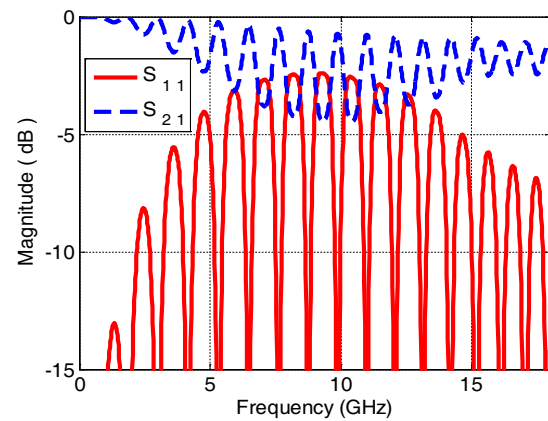
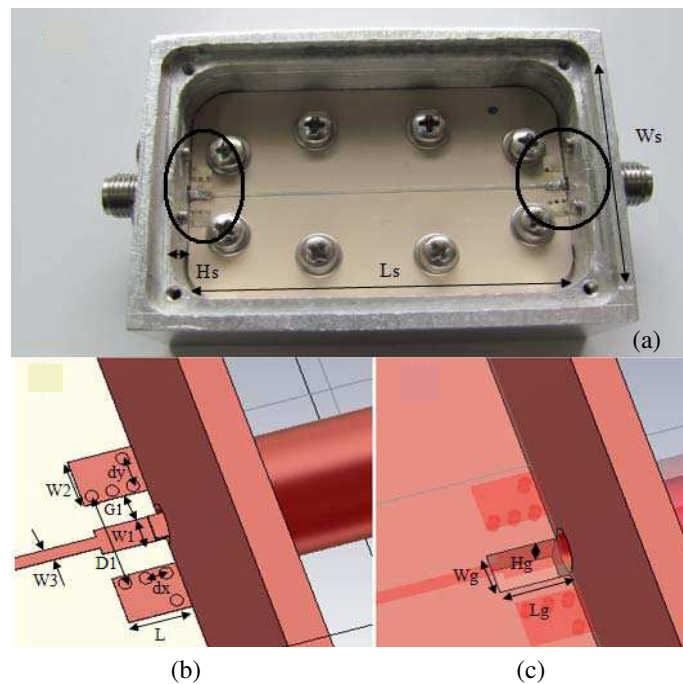

 Figure 2: S -parameters of direct soldering the SMA connector to the microstrip line.


Figure 3: First proposed transition, (a) back to back configuration, (b) top view, (c) bottom view.

soldering them cause an impedance mismatch. S -parameters obtained from CST simulation for direct soldering the SMA connector to the microstrip line of back to back transition are shown in Fig. 2. The length of microstrip line is 50 mm. The results show very high reflection and a very narrow bandwidth due to large mismatch of impedances.

2.1. Transition Design

First microstrip to coaxial transition that is proposed in this work is shown in Fig. 3. The structure includes CB-CPW pre-transition section that ensures proper field match between coaxial and microstrip lines. The center conductor of CB-CPW section should have the same width as the SMA center conductor in order to reach good impedance matching and robust solder connection. However without considering Fig. 3(c) the CB-CPW line with $W_1 = 1.3$ mm and different value of G_1 (distance between central conductor and ground conductor) on the selected substrate has maximum characteristic impedance of 37 ohm, thus there is impedance mismatch between the CB-CPW and microstrip line.

In the proposed transition, this problem is solved by means of a hole under the removed metal in the ground plane just below the CB-CPW section. Because some of the electric field lines are

placed in the air region, transmission line capacitance is reduced and according to $Z = \sqrt{L/C}$ the characteristic impedance is increased. In other words, substrate of CB-CPW section acts as a two layer substrate with less effective permeability. The dimensions of the hole are optimized to maximize the bandwidth of the transition. The parameters of transition are $W_g = 2$, $L_g = 3.4$, $H_g = 2$, $W_1 = 1.3$, $W_2 = 2.4$, $W_3 = 0.6$, $D_1 = 4.8$, $G_1 = 2$, $L_1 = 3.1$, $d_x = 1$ and $d_y = 1.5$ (all in millimeter).

This transition can be placed in the box or on the fixture. Here only the box is considered. Some portion of SMA center conductor crosses the box wall. By making circular hole in the box wall this section acts as coaxial with rectangular center conductor. The radius of the circular hole is chosen 1.2 mm to achieve characteristic impedance of 50 ohm. The dimensions of the box should be chosen so that the first resonance frequency occurs beyond the interest frequency range. Therefore the dimensions of box are chosen as: $W_S = 30$, $L_S = 50$ and $H_S = 8$ (all in millimeter) which have the first resonance frequency of 19.64 GHz.

The vias equalize the potential difference between the upper and lower ground planes consequently the placements of via through a transition are critical and impact the energy leakage and the transition band width. For a transition to function properly, the signal path and the ground path must often be continuous and in close proximity to suppress radiation [2]. Therefore in this transition the placement of vias are chosen as much as possible near the center conductor of CB-CPW. Furthermore by placing vias in the x -direction and y -direction, radiation and parallel plate mode propagation in the CB-CPW section are highly decreased [1].

2.2. Simulation and Measurement Results

The S -parameters of this structure with back to back transition are obtained from CST. Simulation and experimental results are shown in Fig. 4. The experimental bandwidth of 2 dB insertion loss and -15 dB return loss is up to 16 GHz. Two different sets of simulated results are shown in Fig. 4(a). The first set shows the original transition and the second set is for a similar transition with a slightly gap in the connection of board and box walls and also with little solder to model the real fabricated board (that are shown with circles in Fig. 3(a)).

As it is shown in Fig. 4(a) the measurement results are in good agreement with simulation results and the differences between simulation and experimental results are due to some reasons such as gap, solder paste in connections at input and output, SMA connector insertion loss, excitation of higher order modes of SMA in connections and uncertainty of measurement instruments. It is seen that due to these reasons the loss and resonances are increased.

3. SECOND PROPOSED TRANSITION

3.1. Transition Design

The structure of second proposed transition is shown in Fig. 5. In this transition center conductor of SMA is firmly cut from the butt to achieve impedance matching. This structure is very simplex and has good results compared with previous transition. Fig. 5(a) shows a back-to-back fabricated transition. The length of microstrip line is 50 mm. The parameters of the transition are $W_1 = 0.6$, $W_2 = 2.1$, $D_1 = 3.8$, $D_2 = 1.2$, $G_1 = 1.13$, $L_1 = 3$ and $d_x = 1$ (all in millimeter). In the CB-CPW

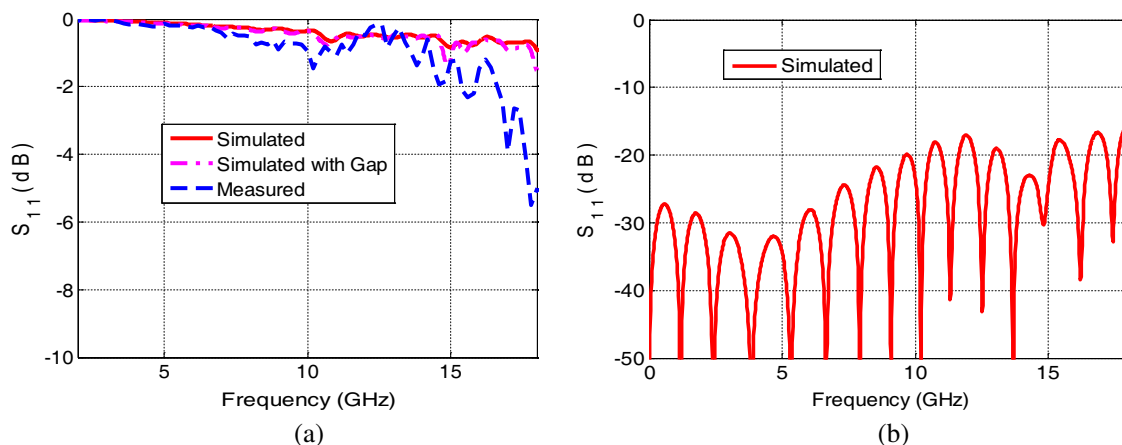


Figure 4: S -parameters for the first proposed transition.

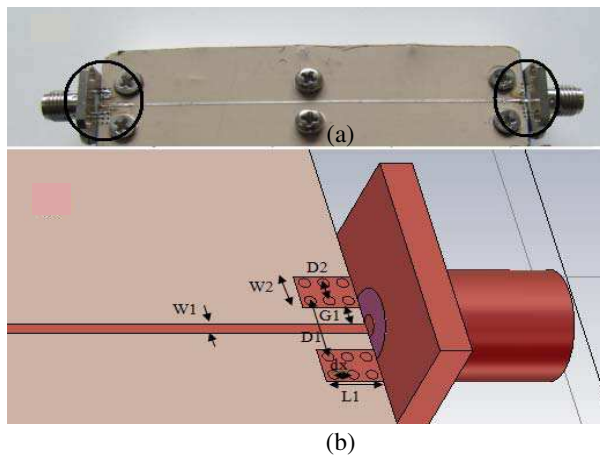


Figure 5: Second proposed transition, (a) back configuration, (b) top view.

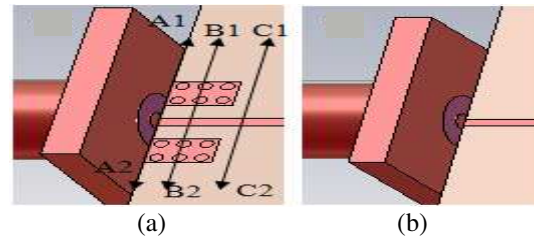


Figure 6: (a) Second proposed transition with CB-CPW section, (b) transition without CB-CPW section.

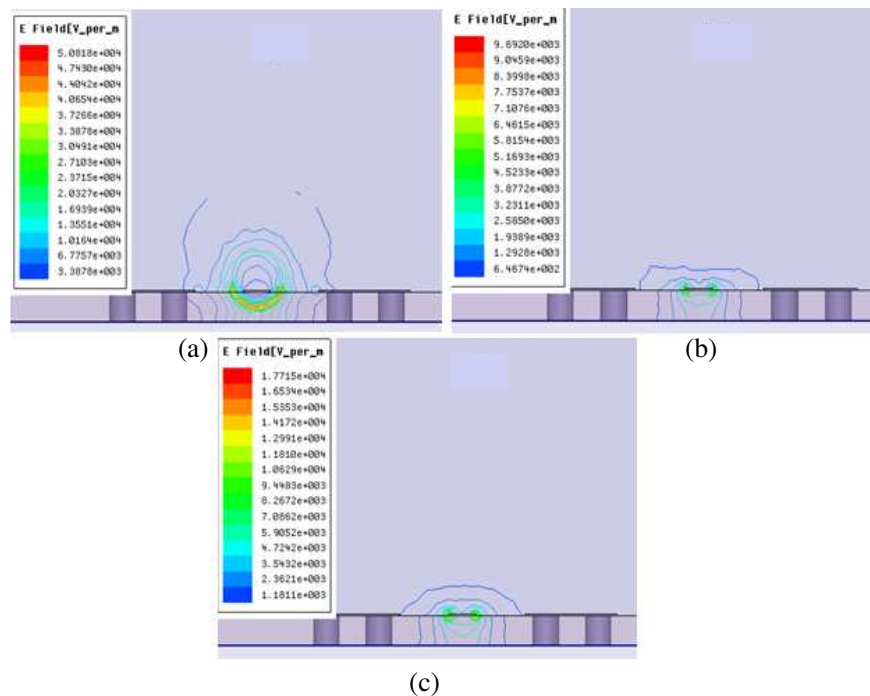


Figure 7: Magnitude of the electric field at 10 GHz, (a) along A1-A2, (b) along B1-B2, (c) along C1-C2 of transition shown in Fig. 6(a).

section the value of W_1 and the value of G_1 are chosen in order to yield a characteristic impedance of 50 ohm along the transition within the desired frequency band. The value of W_1 is chosen equal to the width of microstrip line to avoid any abrupt discontinuity and to minimize the reflection along the transition. In this transition also the number of via and placement of them are optimized to suppress parallel plate mode and radiation loss and to obtain maximum band width.

3.2. Electromagnetic Field Matching Study

Having the same characteristic impedance does not always guarantee a good transition between two transmission line at higher frequencies and the field distributions of the transmission line must also be matched. Therefore the CB-CPW section is used as an interface to match the electromagnetic field distributions at the coaxial-to-microstrip transition. To study the effects of CB-CPW section on the transitions, electromagnetic fields of two transition structures shown in the Fig. 6 are analyzed with HFSS. The first structure (Fig. 6(a)) is the proposed transition and the second structure (Fig. 6(b)) is the transition without CB-CPW section. Fig. 7 shows the magnitude of the

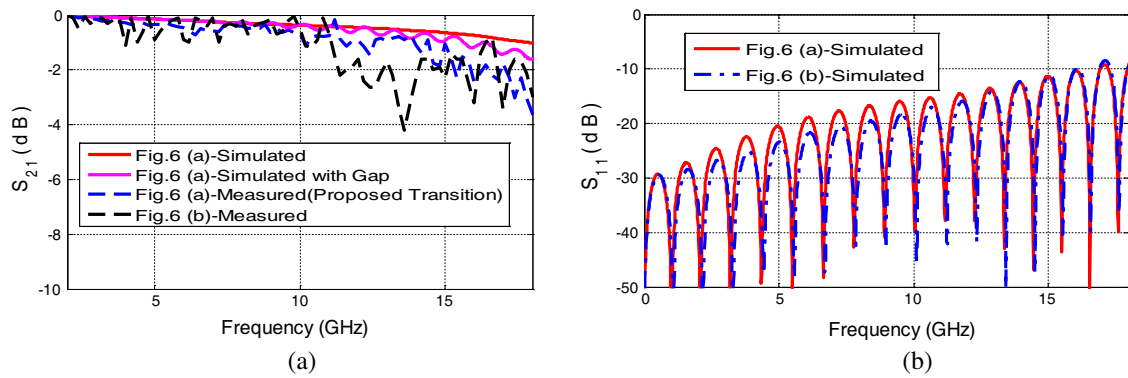


Figure 8: S -parameters for the second proposed transition and the transition without CB-CPW section shown in Fig. 6.

electric fields at A1-A2, B1-B2 and C1-C2 cross-sections. This figure indicates that in the presence of CB-CPW section, the electric field distributions are concentrated along the center conductor providing a good match to the field distribution of the coaxial connector.

3.3. Simulation and Measurement Results

Figure 8 compares the S -parameters of the back to back transition structures with and without CB-CPW. Adding CB-CPW section affects the overall bandwidth of transition such that the insertion loss bandwidth is wider in the presence of CB-CPW section. The experimental bandwidth of 2 dB insertion loss in transition without CB-CPW section is 12 GHz and in the presence of CB-CPW section is 16 GHz.

Simulation results of the transition with a slightly gap and solder paste in the In/Out connections (that are shown with circles in Fig. 5(a)) and also with misalignment between microstrip and center of SMA connector are shown in Fig. 8(a). As can be seen from Fig. 8(a), the measurement results are in good agreement with simulation results and the differences between simulation and experimental results are due to the reasons that were discussed in the previous section. It is seen that due to these reasons the loss and resonances are increased.

Comparing Fig. 4 and Fig. 8 shows that first proposed transition has more resonance within the frequency band of interest with respect to the second proposed transition. Second proposed transition is very simple more desirable and less complicated than first one. On the other hand the first proposed structure has more robust solder connection.

4. CONCLUSION

In this paper, two simplex, low-cost, useful and wideband coaxial-to-microstrip transitions were presented. The effects of CB-CPW sections on the transition bandwidth were discussed. In these two transitions the effects of the field and impedance matching with considering other practical effects in total performance were completely analyzed. The measured and simulated results of back-to-back transition were showed good agreement. The simulation and measurement results verified that the fabricated back-to-back coaxial-to-microstrip transition can achieve a 3 dB bandwidth of 18 GHz and return loss better than -10 dB. Other transitions to improve bandwidth and reduce resonances in frequency response are under investigation and will be presented in future works.

REFERENCES

1. Zhou, Z. and K. L. Melde, "Development of a broadband coplanar waveguide-to-microstrip transition with vias," *IEEE Trans. Adv. Package.*, Vol. 31, No. 4, 861–872, Nov. 2008.
2. Holzman, E., *Essentials of RF and Microwave Grounding*, Artech House, Norwood, MA, 2006.
3. Gupta, K. C., R. Garg, I. Bahl, and P. Bhartia, *Microstrip Lines and Slotlines*, Artech House, Norwell, MA, 1996.
4. Agarwal, K. and R. Harlan, "Coax-to-microstrip transition," U.S. Patent, 5552753, Sep. 1996.
5. Quan, C., S. W. Drost, M. Y. Hashimoto, and R. M. Jorgenson, "Microstrip to coax vertical launcher using fuzz button and solderless interconnects," U.S. Patent, 5886590, Mar. 1999.
6. Simons, R. N., *Coplanar Waveguide Circuits, Components, and Systems*, Wiley, New York, 2001.

7. Hung, C. F., A. S. Liu, C. H. Chien, C. L. Wang, and R. B. Wu, “Bandwidth enhancement on waveguide transition to conductor backed CPW with high dielectric constant substrate,” *IEEE Microw. Wireless Components. Lett.*, Vol. 15, No. 2, 128–130, Feb. 2005.
8. Chiu, T. and Y. Shen, “A broadband transition between microstrip and coplanar stripline,” *IEEE Microw. Wireless Components. Lett.*, Vol. 13, No. 2, 66–68, Feb. 2003.
9. Ma, K. P., Y. Qian, and T. Itoh, “Analysis and applications of a new CPW-slotline transition,” *IEEE Trans. Microw. Theory Tech.*, Vol. 47, No. 4, 426–432, Apr. 1999.
10. Nedil, M., T. A. Denidni, and A. Djaiz, “Ultra-wideband microstrip to CB-CPW transition applied to broadband filter,” *IEEE Electronics Lett.*, Vol. 43, No. 8, Apr. 2007.
11. Mao, S. G., C. T. Hwang, R. B. Wu, and C. H. Chen, “Analysis of coplanar waveguide-to-coplanar stripline transitions,” *IEEE Trans. Microw. Theory Tech.*, Vol. 48, No. 1, 23–29, Jan. 2000.
12. Kamei, T., Y. Utsumi, N. Q. Dinh, and N. Thanh, “Wide-band coaxial-to-coplanar transition,” *IEICE Trans. Electron.*, Vol. E90-C, No. 10, 2030–2036, Oct. 2007.
13. Data sheet, <http://www.hubersuhner.co.th>.

Radar Absorbing Structure with Periodic Pattern Surface for Wind Blade

J. Kim

Korea Institute of Materials Science, Composites Research Center, Korea

Abstract— The wind turbine blade, owing to its huge size and height with the rotational motion, is emerging to be a big threat to the radar systems. To reduce the radar interference, this work presents radar absorbing structures with a periodic pattern surface applicable on the surface of the blade considering the configuration of the cross sectional characteristics of the wind turbine blades. The optimal design was performed to get the design parameters along with the thickness of the substrate of the radar absorbing structure, which is the composite structure composing the wind turbine blade structure.

1. INTRODUCTION

Wind turbine blade is one of the largest composite structures in the world. For the 3 MW wind turbine system which is very popular grade in these days, the blade is over 10 ton in weight and over 40 m in length. Most of rotors of wind turbines have 3 blades and the size of rotor disks is larger than Airbus A380 wing span of 80 m. The rotating speed of the rotors of 3 MW wind turbines is about 15 ~ 16 RPM. Even though the angular velocity seems to be not so high, the rotor tip speed is over 250 km/h which is equivalent to the take-off and/or landing speeds of a jumbo airplane. Recently, the radar interference is a hot issue for the construction of the wind farms due to the fact that traditional turbine blades cause interference to radar screens. This paper presents radar absorbing structure (RAS) with periodic pattern surface for wind blades. The RAS is composed of the periodic pattern surface and dielectric substrate grounded with PEC. The dielectric substrate is the glass fibre-reinforced polymer composite for wind blade structure. The surface conductivity of the pattern is controlled with the thickness of the pattern made with the electrical conductive material [1]. The periodic pattern is optimally designed for X-band band by using CST MICROWAVE STUDIO. The optimal dimensions and surface conductivity of the pattern are obtained for the various thickness of the composite substrate determined by the internal configuration of the wind blade structure.

2. SECTIONAL CONFIGURATION OF WIND TURBINE BLADES

The wind turbine blade structure is composed with several parts including leading edge, trailing edge, spar caps, shear webs and the other wing skins. Figure 1 shows the cross sectional configuration of the ordinary wind turbine blade of 3 MW grade. The external structure of the wind turbine blade exposed to the radar signal consists of GRE and Sandwich. Figure 2 shows the schematic drawing of Sandwich and GRE. Sandwich is composed of two skins of glass/epoxy composite laminate and a core of Balsa wood or PVC foam. GRE is all composed of glass/epoxy composite laminate from skins to the core. The skins of Sandwich and GRE are continuously connected. Due to the inherent laminated structure, the glass/epoxy composite laminate is very suitable to be used as a part of the multi-layered structure. Moreover, since the materials used in wind turbine blade are all dielectric materials, we can use a part of the external structure as the substrate of the Circuit Analog absorber with a periodic pattern surface. It can be done by placing electrically conductive carbon fabric as a ground material inside of the wind turbine blade. But, due to the difference of the dielectric constant between the glass/epoxy composite laminate and Balsa wood or PVC foam, the thickness of the substrate for the absorber will be different depending on the substrate material and it will make discontinuity of the ground material at every transition area among Leading edge-wing skin, wing skin-Spar Cap, etc.. To prevent this discontinuity, the ground material can be placed between the outer skin and core. The thickness of the skin is different depending on the position in wing span direction. In this work, we designed RASs of 1 mm ~ 3 mm thick substrates composed of the glass/epoxy composite laminate.

3. DESIGN OF RADAR ABSORBING STRUCTURE

CA absorber-type RASs are designed using Periodic Pattern Surface (PPS) of the solid square patches. Figure 3 shows the schematic configuration of RAS. RASs are designed only for the

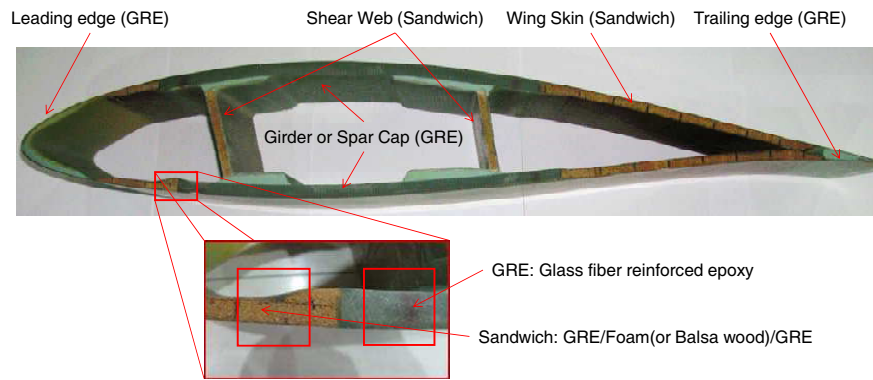


Figure 1: Cross sectional view of a wind turbine blade of 3MW grade (section at 70 ~ 80% in wing span direction of 44 m long wind blade).

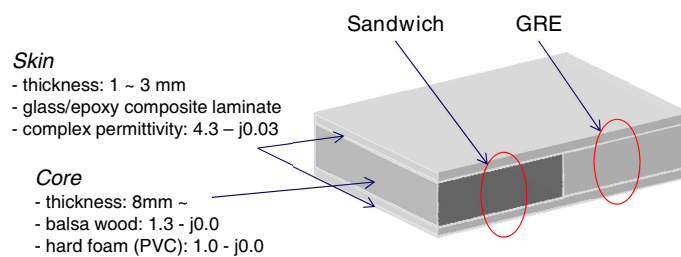


Figure 2: Sandwich and GRE for the external structure of wind turbine blades.

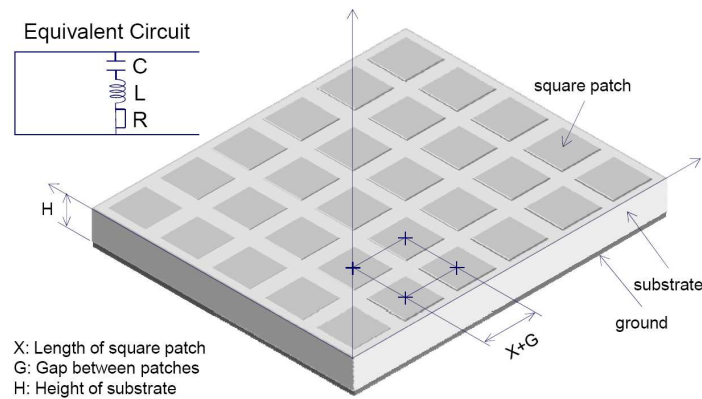


Figure 3: Schematic configuration of CA-type radar absorbing structure with periodic pattern surface (PPS).

normal incident case at the target frequency of 10 GHz. The solid square patches are composed of conductive material having an appropriate conductivity to bring out ohmic loss [1]. When the thickness of substrate is prescribed, the optimization parameters are the thickness T , and length X of square patch, gap G between the patches. Table 1 shows the parameters for the design of the RASs.

CST MICROWAVE STUDIO with transient solver was used to calculate the reflection loss of the RASs. As shown in Figure 4, a single unit cell of a square patch is used to minimize the computational cost by applying the magnetic and electric boundary condition, which mirror the structure in x and y direction to infinity. TEM wave from waveguide port 1 is normally incident on the surface of the RAS model.

4. RESULT AND DISCUSSION

The glass/epoxy composite laminate has determined discretely by number of glass ply and ply thickness ($\cong 0.5$ mm). In the screen-type RAS, the thickness of the substrate depends on the electromagnetic characteristics of the screen [2]. In CA-type RAS, the PPS can be treated as a

Table 1: Parameters for design of radar absorbing structure.

Fixed parameters	Parameters to be optimized
Target frequency: 10.0 GHz Substrate material: glass/epoxy composite laminate ($4.3 - j0.03$, constant over all frequency) Electrical conductivity of patch: 1,000 S/m	T : Thickness of patch G : Gap between patches X : Length of square patch
	Prescribed parameter H : Height of substrate (1.0, 1.5, 2.0, 2.5 and 3.0 mm)

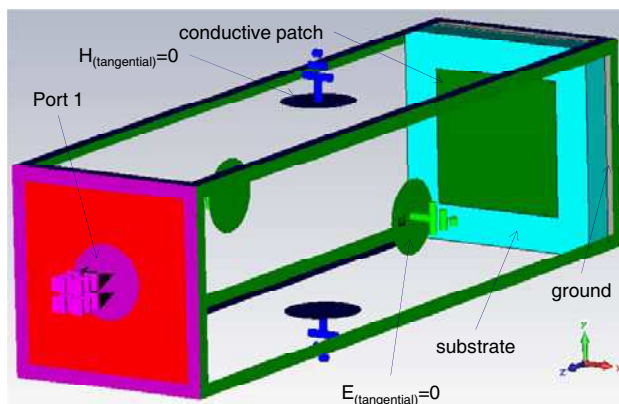
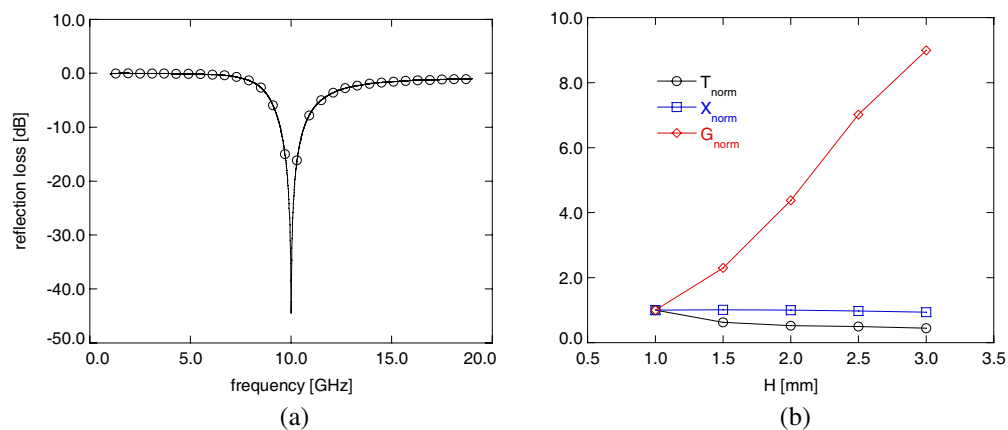


Figure 4: Numerical model to design radar absorbing structure with periodic pattern surface using CST MICROWAVE STUDIO.

Figure 5: (a) Reflection loss of RAS of $H = 1.0$ mm. (b) Variation of the design parameters (normalized by the parameters for $H = 1.0$ mm).

R, L and C equivalent circuit as shown in Figure 3 and the best configuration of PPS can be achieved through the optimization process provided by the CST MICROWAVE STUDIO [3]. The Parameters for the RASs are obtained for the prescribed $H = 1.0, 1.5, 2.0, 2.5$ and 3.0 mm. For $H = 1.0$ mm, T , X and G are obtained to be 0.1006 mm, 5.88075 mm and 1.32011 , respectively. Figure 5(a) shows the reflection loss of the RAS for $H = 1.0$ mm. The designed RAS has minimal reflection at the frequency = 10.0 GHz. Figure 5(b) shows the variation of the design parameters normalized by the corresponding values for $H = 1.0$ mm. Design parameters for the other H values are obtained with the least variation of the T . While the variation of X is very marginal, G increases rapidly along with H . This means that, to get the thinner substrate, the gap between the patches needs to be narrower. Since the gap size is related to the capacitance of the PPS, the wide gap for thick substrate makes low effective dielectric constant of PPS. This result agrees well

with the conclusion of Kim's study [2]. The thickness of patch, T decreases slowly along with H and we have to use higher surface resistance for the patches of PPS.

5. CONCLUSIONS

In this work, the CA-type RASs were designed by using PPS of square conductive patches applicable into composite blade structures of wind turbines. The RAS can be integrated into the blade structure by using the external skin of blade structure as the substrate of the RAS and inserting the ground material inside of the blade structure. To get the continuity of the ground, various RASs are designed for the thickness of glass/epoxy composite substrate of 1.0 ~ 3.0 mm thick. When the size of square patch is almost maintained, the gap increases greatly and the thickness of the patch decrease slightly along with the thickness of substrate.

ACKNOWLEDGMENT

This work was supported by the New and Renewable Energy R & D Program 2008-N-WD08-P-02 under the Korea Ministry of Knowledge Economy.

REFERENCES

1. Jang, H., J. Shin, C. Kim, S. Shin, and J. Kim, "Semi-cylindrical radar absorbing structures using fiber-reinforced composites and conductive polymers in the X-band," *ACM*, Vol. 20, 215–229, 2011.
2. Kim, J. and J. Byun, "Salisbury screen absorbers of dielectric lossy sheets of carbon nanocomposite laminate," *IEEE TEMC*, Vol. 54, 37–42, 2012.
3. Munk, B. A., *Frequency Selective Surface: Theory and Design*, Wiley-Interscience, New York, 2000.

Metastructure to Achieving of Voltage Tunable Magnetic Resonance in a Single Longitudinal Cut-wire

Galina Kraftmakher, Valery Butylkin, and Yury Kazantsev

Kotelnikov Institute of Radioengineering & Electronics RAS, Fryazino Branch, Russia

Abstract— In this presentation it is observed that varactor loaded nonmagnetic single split longitudinal cut-wire arranged in necessary planar metastructure can show a voltage tunable magnetic resonance response. Previously like metastructure has been investigated without varactor in waveguides and free space [1, 2]. It has been shown by experiment at microwaves that metastructure containing cut-wire grating and longitudinal cut-wire of resonant length can provide strong magnetic resonant response of a single nonmagnetic cut-wire in dependence on configuration and sizes t, s, l_p, l_m . Metastructure is oriented along the direction of wave propagation and cut-wires of grating are parallel to the electric field of a plane electromagnetic wave. It has been shown a practical way to the excitation of a magnetic resonance in nonmagnetic longitudinal line cut-wire which is arranged perpendicularly to the electric field of incident electromagnetic wave near a grating of cut-wires. It is suggested a concept of magnetic response based on antiparallel resonant currents excited by magnetic field of surface polaritons in many spatial *LC-circuits* created from cut-wire pairs of a grating and section of longitudinal cut-wire. Three separately observed resonant effects connected with grating, *LC-circuits* and with longitudinal cut-wire have been identified applying measurements in waveguides, cutoff waveguides and free space. The first resonance is due to parallel currents induction in grating's wires l_p , the second resonance effect is due to excitation of antiparallel currents in *LC-circuits* and the third resonance is due to contribute of total currents from *LC-circuits* along longitudinal cut-wire l_m . It is special interest to study a metastructure using varactor diodes. In [8], it has been demonstrated that the resonant frequency of split ring resonators (SRRs) can be tuned using varactor diodes. The resulting particle has been called a varactor-loaded split ring resonator (VLSRR). In this paper, we use varactor diodes to tune resonance response related to cut-wires in metastructures. With varactor one can also match the resonance minima of transmission T to concrete resonant elements with certainty what is important for multi-resonance system.

1. INTRODUCTION

In this presentation, it is observed that varactor loaded nonmagnetic single split longitudinal cut-wire arranged in necessary planar metastructure can show a voltage tunable magnetic response. Previously like metastructure without varactor (Fig. 1(a)) has been investigated in waveguides and free space [1, 2]. It has been shown by experiment at microwaves that metastructure containing cut-wire grating and longitudinal cut-wire of resonant length ("*Gr-LCW*" metastructure) can provide strong magnetic resonant response of a single nonmagnetic cut-wire in dependence on configuration and sizes t, s, l_p, l_m .

Magnetic metamaterials (i.e., metamaterials possessing magnetic response) are of interest in dispersion engineering [3].

As it is known, metamaterials containing chiral inclusions, can at microwaves possess an effective resonant magnetic polarizabilities and permeability which depends on the orientation of inclusions relative to the magnetic field \mathbf{h} of the incident electromagnetic wave [4, 5]. Resonance phenomena are caused by the excitation of resonance currents by the microwave field \mathbf{h} . Presently extensive investigations are directed toward the development of magnetic metamaterials containing technologically simple line wires. The main attention is devoted to a cut-wire pair that possesses both the electric and magnetic response due to the possibility of parallel currents induction by the wave electric field and antiparallel currents induction by the magnetic field [6, 7]. Since the magnetic and electric resonant responses are generated practically at the same frequency, it is difficult to separate these signals and evaluate the magnetic contribution.

In paper [1], it is suggested a new way to create separately a strong microwave magnetic response using cut-wires. It was found in waveguides that a line wire which is oriented along waveguide axis parallel to the direction of propagation of an electromagnetic wave (and perpendicularly to transverse electric field which is the main part of electric field \mathbf{E} , just that participates in microwave energy transfer along the grating) and arranged asymmetrically near a cut-wire grating forming surface polaritons, can exhibit a resonant response that has a magnetic nature. A giant resonance

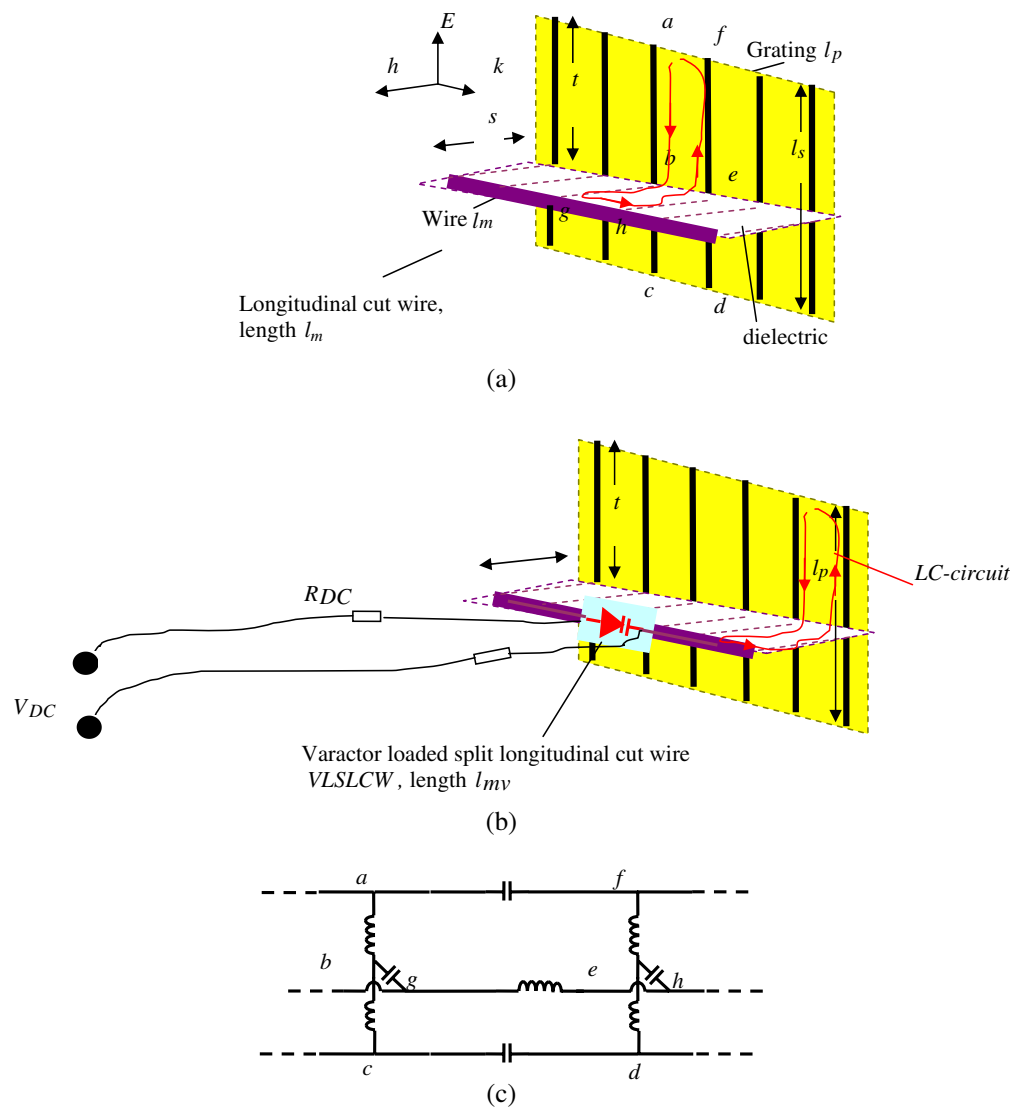


Figure 1: (a) "Gr-LCW" and (b) "Gr-VLSLCW" metastructures and (c) equivalent electric diagram.

is observed in longitudinal single cut-wire of a definite (resonant) length l_m (see Fig. 1(a)) in a certain frequency range corresponding to the existence of surface polaritons (below the resonant frequency of the polariton-generating grating of cut-wires parallel to the \mathbf{E} -field). We suggest and verify a concept of magnetic response.

In [8], it has been demonstrated that the resonant frequency of split ring resonators (*SRRs*) can be tuned using varactor diodes. The resulting particle has been called a varactor-loaded split ring resonator (*VLSRR*). Here we show that magnetic response can be controlled by external electric field in the case when a single nonmagnetic split cut-wire is loaded with varactor diode (Fig. 1(b)). In this paper, we use varactor diodes to tune resonant response related to cut-wires in metastructures "Grating-varactor loaded split longitudinal cut wire" ("Gr-VLSLCW" metastructure). We give a practical way to the excitation of a voltage tunable magnetic resonance in nonmagnetic longitudinal line cut-wire which is arranged perpendicularly to the electric field of incident electromagnetic wave near a grating of cut-wires. With varactor one can also match the resonance minima of transmission T to concrete resonant elements with certainty what is important for multi-resonance system.

2. INVESTIGATED METASTRUCTURES. MAIN EXPERIMENTAL RESULTS

We investigate two kinds of metastructures; they are presented in Fig. 1. In the first case metastructure contains a grating of cut-wires (wire length l_p) and a single longitudinal cut-wire or strip (wire length l_m) orthogonal to grating's wires l_p . Experimental investigations at microwaves show these structures can provide strong magnetic resonant response of a single nonmagnetic cut-wire

in dependence on configuration and sizes in the case when metastructures are oriented along the direction of wave propagation and cut-wires of grating are parallel to the electric field of a plane electromagnetic wave. Obtained results allow to suggesting and verifying a concept of magnetic response based on antiparallel resonant currents excited by magnetic field of surface polaritons in many spatial *LC-circuits* (such as *abghefa* and *cdehgbc* created from cut-wire pairs of a grating and section of *LCW*) and like-directed currents along *LCW*. Equivalent electric diagram is shown in Fig. 1(c).

Directions of currents which run in many *LC-circuits abghefa* are the same along wire l_m and opposed to currents of circuits *cdehgbc*. In the case of symmetrically located wire $l_m (t = l_p/2)$ these opposed currents along *LCW* of circuits *abghefa* and *abghefa* are practically quenched. In the case of asymmetrically location, if *LCW* length l_m is resonant the wave of current along wire l_m and the resonance response are very strong. Resonance response of a *LCW* (l_m) can be detected separately because its resonance frequency depends on length and distance s and is different from frequencies of grating and *LC-circuits* created from cut-wire pairs of a grating and a section of longitudinal cut-wire. Three separately observed resonant effects **I**, **II** and **III** in transmission connected with grating (**I**), *LC-circuits* (**II**) and with longitudinal cut-wire (**III**) have been identified applying measurements in waveguides, cutoff waveguides and free space. The first resonance **I** is due to parallel currents induction in grating's wires l_p , the second resonance effect **II** is due to excitation in *LC-circuits* of antiparallel currents under electromotive forces induced by microwave magnetic field and the third resonance **III** is due to summation of currents induced similarly in each of *LC-circuits* along longitudinal cut-wire l_m . The resonance **I** is identified as electric type while the resonance **II** and **III** exhibit magnetic excitation and can be excited by magnetic field of surface polaritons.

We use method of resonance type identification based on comparative analysis of the signal transmission spectra in the main and below-cutoff waveguide section [9]. In the case of magnetic excitation (magnetic resonance in WGD, **MR**) the transparency band in Cut WGD is observed above the **MR** frequency. In addition, the magnetic excitation is characterized by the presence of super-forbidden band below the **MR**. In the case of electric excitation (electric resonance, **ER**), the transparency band in Cut WGD is observed below the **ER** frequency. Resonance **III** of l_m is not depicted in free space in propagation direction, but one can observe resonant response in transverse direction by measurement of cross-polarized reflected wave from l_m wire. A strong resonance **III** is observed when the l_m wire is arranged asymmetrically relative to l_p wire grating, its intensity decreases when l_m wire shifts to symmetrically location. In the case of $t = l_p/2$ resonance response **III** is absent. Strong **MR III** is observed if the l_m value is close to half-wavelength in the frequency range adjoining resonance **I** from the side of lower frequencies, which is the region of existence of surface polaritons generated by wire grating l_p . The position of **MR III** depends on wire length l_m . Resonance **III** shifts toward higher frequencies with decreasing l_m and a pass-band of the below-cutoff section in this case exhibits the corresponding shift. We can make out resonances **I**, **II** and **III** using measurements in waveguide, cutoff waveguide and in free space.

The second kind of investigated metastructures allows to tune and mark resonance of longitudinal cut wire *LCW* or strip. In this case, we use varactor loaded split cut-wire (or strip). To this effect we split *LCW* (length l_m) into two wires of the same length $l_m/2$ placed on the substrate (laminated bakelite insulation with thickness of 0.5 mm or textolite with thickness of 1.5 mm) and slide apart and then place varactor diode in the gap (gap width is 1.5 mm) between wires $l_m/2$ and solder pins of varactor to wires $l_m/2$, Fig. 1(b). The resulting wire with length l_{mv} we will call a varactor-loaded split longitudinal cut wire (*VLSLCW*). Varactor introduces a voltage controllable effective nonlinear gap capacitance which depends on reverse bias and can tune resonance frequency of *VLSLCW* when reverse bias is applied between varactor's pins. In this configuration with resistors $R_{DC} = 100 \text{ k}\Omega$ parasitic effects through lead wires are very small.

We measured frequency dependences of the transmission coefficient T of electromagnetic wave of metastructures arranged along the axis and oriented parallel to the side wall of a standard waveguide, and a below-cutoff rectangular section. To prepare Cut WGD a fragment of the main WGD is divided into three sections by metal spacers parallel to the direction of wave propagation. Investigated metastructure is placed into a central cutoff WGD section.

Here we show experimental results for second kind of investigated metastructures "*Gr-VLSLCW*" prepared for *VLSLCW* resonance observation in range 3–6 GHz. Metastructures contain grating of parallel copper wires with lengths $l_p = 16 \text{ mm}$ and varactor-loaded split longitudinal cut copper wire or strip (*VLSLCW* with length $l_{mv} = 33 \text{ mm}$ and diameter 0.3 mm or *VLSLCS* with length

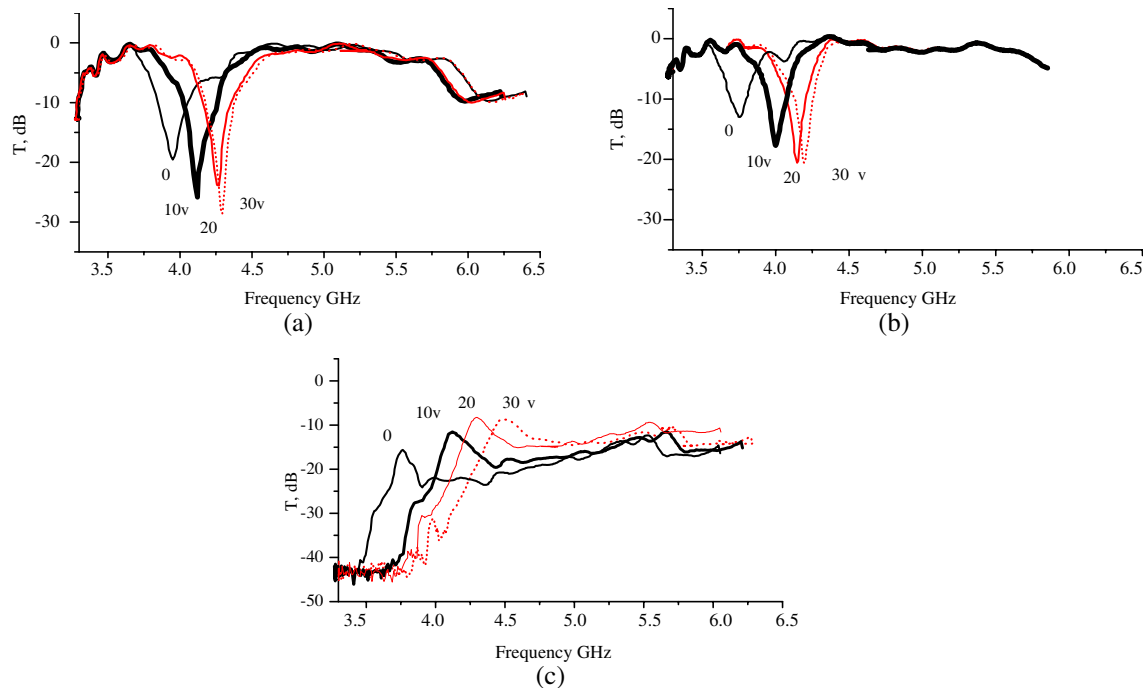


Figure 2: (a), (b) Frequency dependences of Transmission T of metastructures “*Gr-VLSLCW*” corresponding to Fig. 1(b) under different bias conditions in rectangular waveguide and (c) in cutoff waveguide section in area of resonance **III** related (a) to longitudinal cut wire loaded with varactor and (b), (c) to longitudinal cut strip loaded with varactor.

$l_{mv} = 28$ mm and width 2 mm). Distance s between longitudinal wire or strip and grating of wires l_p is 2 mm. The results have been obtained by measurements in rectangular WGD (48×24 mm) and cutoff WGD (16×24 mm) under different bias conditions. Varactors the Infineon BB857 with a low series resistance of 1.5Ω and wide tuning range are used. Varactor capacitance is 6.5 and 0.5 pF at 1 and 28 V reverse bias, respectively. It is observed that by tuning varactor resonance frequency of the *VLSLCW* can be shifted of 10% in waveguide and of 15% in cutoff waveguide section as one can see in Fig. 2.

Figure 2 shows measured frequency dependence of transmission T of metastructure and evolution of this dependence with applying of electrostatic field in area of resonance **III** (related to longitudinal cut wire or strip). We see that applying reverse bias from 0 to 30 V strong resonance curve shifts from 3.9 to 4.3 GHz (Fig. 2(a)) in the case of longitudinal cut wire and from 3.7 to 4.2 GHz (Fig. 2(b)) in the case of longitudinal cut strip when metastructure is placed in rectangular waveguide. Metastructures exhibit high resonance levels: 15–20 dB and 20–28 dB in a 0.4 and 0.5 GHz tuning range. When metastructure is placed in cutoff waveguide section we observe pass-band (Fig. 2(c)) with shift of maxima from 3.75 to 4.5 GHz applying reverse bias from 0 to 30 V. Comparative analysis of the transmission spectra in the main and below-cutoff waveguide section show that pass-bands in cutoff waveguide are observed above the frequency resonance minima of transmission in main waveguide what confirms magnetic resonance excitation in a longitudinal wire (or in a strip) and respectively electronically tunable magnetic resonance. The observed strong dependence of resonance frequency on distance s between longitudinal wire and grating of wires indicates also in favour of h-excitation of the resonance **III**. In addition it was found that the longitudinal component of electric field of surface polaritons supported by cut wire grating practically absents at measurements using resonant effects in double split ring [10].

3. CONCLUSION

In this paper, it is observed that nonmagnetic single split longitudinal cut-wire (strip) loaded with varactor and arranged in necessary planar metastructure can show in rectangular waveguide and cutoff waveguide electronically tunable magnetic resonance response in 10% tuning range centered at 3.7–4 GHz.

ACKNOWLEDGMENT

This study was supported by the RFBR, projects Nos. 10-08-00018, and 11-02-90403.

REFERENCES

1. Butylkin, V. S. and G. A. Kraftmakher, “Magnetic type resonance in nonmagnetic line wire excited by surface plasmons in microwave range,” *Tech. Phys. Letters*, Vol. 37, No. 4, 399–312, 2011; See also in *Proceedings of Metamaterials’2010*, Karlsruhe, Germany, 450–452, 2011.
2. Kraftmakher, G. and V. Butylkin, “Cut-wires grating — Single longitudinal wire, planar metas-structure to achieve microwave magnetic resonance in a single wire,” *Proc. of AES’2012*, 382–389, Paris, France, Apr. 16–19, 2012.
3. Caloz, C., “Metamaterial dispersion engineering: A new paradigm in microwave science and technology,” *Proceedings of Metamaterials’2010*, 13–18, Karlsruhe, Germany, Sep. 1–2, 2010.
4. Tretyakov, S. A., F. Mariotte, C. R. Simovski, T. G. Kharina, and J.-P. Heliot, “Analytical antenna model for chiral scatterers: Comparison with numerical and experimental data,” *IEEE Trans. on Antennas and Propagation*, Vol. 44, No. 7, 1006–1014, 1996.
5. Pendry, J. B., A. J. Holden, D. J. Robbins, and W. J. Stewart, “Magnetism from conductors and enhanced nonlinear phenomena,” *IEEE Trans. Microwave Theory Tech.*, Vol. 47, No. 11, 2075–2084, 1999.
6. Shalaev, V. M. and S. Kawata, *Advances in Nano-optics and Nano-photonics. Nanophotonics with Surface Plasmons*, Elsevier, 2007.
7. Dolling, G., C. Enkrich, M. Wegener, at al., “Cut-wire pairs and plate pairs as magnetic atoms for optical metamaterials,” *Optics Letters*, Vol. 30, No. 23, 3198–3200, 2005.
8. Gil, I., J. Garcia-Garcia, J. Bonache, F. Martin, M. Sorolla, and R. Marques, “Varactor-loaded split ring resonators for tunable notch filters at microwave frequencies,” *Electronics Letters*, Vol. 40, No. 21, 1347–1348, 2004.
9. Kraftmakher, G., “New realization and microwave properties of double negative material,” *Int. Journal of Applied Electromagnetics and Mechanics*, Vol. 19, Nos. 1–4, 57–61, 2004.
10. Butylkin, V. S., G. A. Kraftmakher, and S. L. Prosvirnin, “Method of surface polariton field structure measurement using resonance excited in a single planar double split ring,” *Tech. Phys. Letters*, Vol. 38, No. 2, 147–150, 2012.

A Full-band High Linearity CMOS T/R Switch for UWB Systems

Ro-Min Weng, Yun-Chih Lu, and Huo-Ying Chang

Department of Electrical Engineering, National Dong Hwa University, Hualien, Taiwan

Abstract— A transmitter/receiver (T/R) Switch in radio frequency front-end for 3.1 ~ 10.6 GHz ultra-wideband Systems is presented. The design focuses on the techniques to increase both power handling capability and isolation using deep n-well and floating bulk technology. The proposed switch achieves P1dB of 9 dBm and IIP3 of 20 dBm in transmitting (TX) mode which represents higher linearity than other CMOS T/R switches. The proposed T/R switch provides the TX and receiving (RX) paths with different switching topologies. Different signal paths can minimize the power leakage into the RX/TX path during TX/RX mode selection so as to improve the linearity. The proposed T/R switch uses a 1.8 V digital control signal for TX/RX mode selection. The simulated insertion loss is less than 2.3 dB and return loss is less than -10 dB during 3.1 ~ 10.6 GHz full-band operation.

1. INTRODUCTION

In commercial applications, there are advantages in ultra-wideband (UWB) systems such as low power, high integration, high transfer data rate, and low cost [1]. Transmitter/receiver (T/R) switches are one of the key blocks in radar and wireless communication systems. The abilities for T/R switch to be fully integrated with other circuits and to be operated with wide bandwidths are required to enable wideband systems on chip. As the bandwidths of radar and wireless communication systems are extended wider or required to cover multi-bands, the need of UWB CMOS T/R switches becomes more critical [2].

There are many challenging for the design T/R switches. Firstly, insertion loss is increased because of signal loss in the substrate and signal paths. Conventional structures of T/R switches are single-pole-double-throw (SPDT). Interference between an output port of transmitter and an input port of a receiver is inevitably introduced. Hence, the isolation during TX/RX mode selection is one of key design specifications. Moreover, the detrimental effects from silicon substrates bring down the power handling capability of the T/R switches. Trade-offs among design parameters is insertion loss, isolation, and power handling capability. Also wide frequency operation range is required in the design of UWB T/R switches.

In this paper, the development of a CMOS fully-integrated T/R switch is proposed. The presented T/R switch employs an ultra-wideband topology. This paper consists of four sections, beginning with this introduction. The design of UWB T/R switch is discussed in Section 2. Simulation results are given in Section 3. Finally, this switch is summarized in Section 4.

2. PROPOSED UWB T/R SWITCH

2.1. CMOS T/R Switch Design

Figure 1 shows the schematic of the proposed UWB T/R switch. The control voltage V_c for the MOS switch are either 0 V or 1.8 V so that the T/R switch can be driven directly by digital circuitry. Mn_2/Mn_3 and Mn_1/Mn_4 as MOS switch are controlled by V_c and the complimentary signal of V_c , respectively.

In TX/RX ports, the characteristic impedances of the previous/next stage circuits are equal to $50\ \Omega$ so that the TX/RX ports must match to $50\ \Omega$. Usually, the impedance of antenna port is matched to $50\ \Omega$ for measurement purpose. However, the maximum output power transfer is not achieved at output impedance of $50\ \Omega$ to antenna port. In the proposed circuit, there are only four transistors. When the signals pass through the transistor, the loss is caused. Increasing the conductance of signal transmission path can eliminate insertion loss. Furthermore, linearity and power handling capability are enhanced by using floating and applying negative bias to the bulk. The inverter is effective to control nMOS transistors and to reduce the number of the control signals.

2.2. Deep n-Well Process and Body-floating Technique

Recently, T/R switches are implemented to be fully-integrated with other integrated circuits using deep n-type well (DNW) process as shown in Fig. 2. The body resistances can be minimized with the source and drain junctions open to ground by floating the body. Hence, a smaller resistive

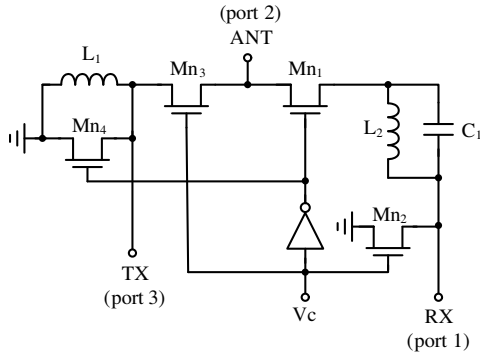


Figure 1: Schematic of the proposed UWB T/R switch.

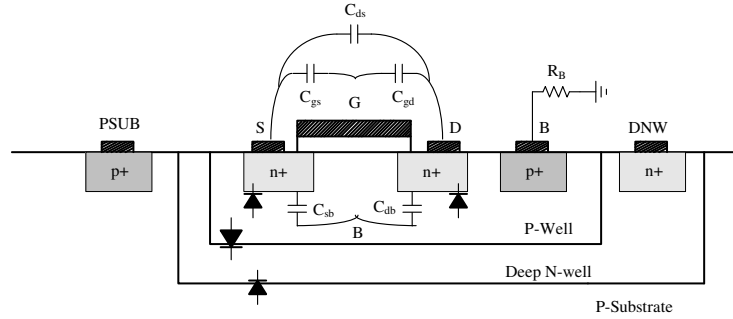


Figure 2: Simplified model of transistor using deep n-well process.

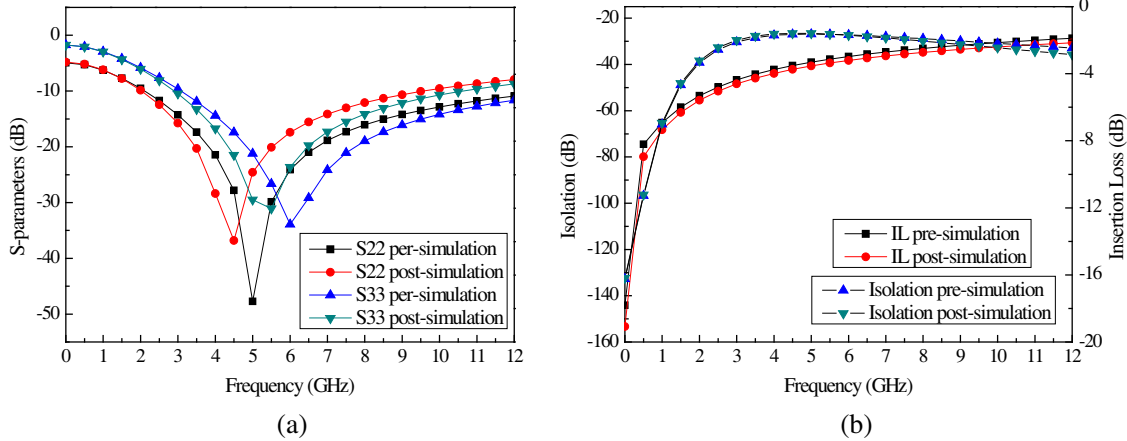


Figure 3: Per/post-simulation results in TX mode. (a) Return loss, (b) isolation and IL.

loss is obtained. Better performances of insertion loss, isolation, and power handling capability are achieved. In such a body-floating structure, large resistors can be applied directly to the body of nMOS devices, making it floating to increase the capacitance between source and drain. Latch-up problems is solved by separating the bulk of nMOS transistors from the p-substrate. The equivalent capacitance of transistors between drain and source with larger resistive in source can be expressed as

$$C_{DS} = \frac{C_{gs} \cdot C_{gd}}{C_{gs} + C_{gd}} \quad (1)$$

The equivalent parasitic capacitance of transistors between drain and source using DNW process can be expressed as

$$C'_{DS} = \frac{C_{gs} \cdot C_{gd}}{C_{gs} + C_{gd}} + \frac{C_{sb} \cdot C_{db}}{C_{sb} + C_{db}} \quad (2)$$

In order to endure large signal swing, the bias resistors should be large enough for nMOSs. The triple-well devices can also be applied to nMOSs while the substrate is floating effectively.

3. SIMULATION RESULTS

The proposed T/R switch is designed with tsmc 0.18 μm CMOS process with the control voltage of 1.8 V. The input operation frequency is from 3.1 GHz to 10.6 GHz. Both pre-simulation and post-simulation results are provided.

Figure 3(a) shows the simulation results of return loss in TX mode. Fig. 3(b) illustrates the simulation results of insertion loss (IL) and isolation in TX mode. Fig. 4(a) shows the simulation results of return loss in RX mode. Fig. 4(b) depicts the simulation results of insertion loss and isolation in RX mode. Insertion losses are less than 2.2 dB and 2.3 dB within full-band in TX mode and RX mode, respectively. The simulated return losses at the antenna and receiver/transmitter ports are better than 10 dB.

Figure 5 shows the simulation results of input third-order intercept point (IIP3) at 6 GHz. As shown in Fig. 6, the chip and core area of the T/R switch is $0.64 \times 0.71 \text{ mm}^2$ and $0.37 \times 0.56 \text{ mm}^2$.

Table 1 lists the performance summary of the proposed T/R switch along with other published T/R switches. As obtained from Table 1, the overall performance of the proposed T/R switch is better than those of others.

4. CONCLUSIONS

A 3.1 ~ 10.6 GHz fully-integrated CMOS T/R switch has been developed for ultra-wideband systems. The proposed T/R switch is implemented with standard 0.18- μm CMOS process. The deep n-well process enables the negative bias to the bulk to be simultaneously floated. The body-floating

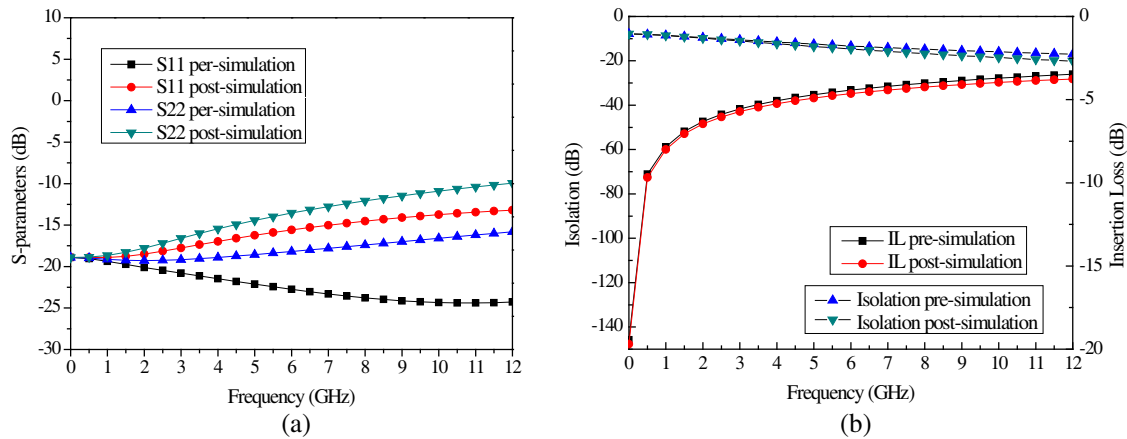


Figure 4: Per/post-simulation results in RX mode. (a) Return loss, (b) isolation and IL.

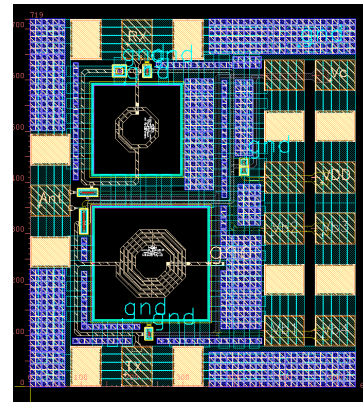
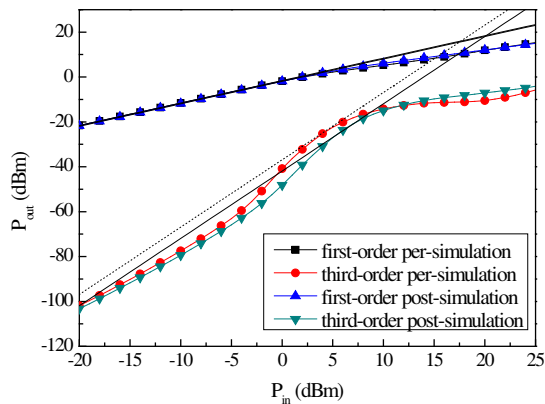


Figure 5: Per/post-simulation results of IIP3 in TX mode at 6 GHz.

Figure 6: Layout of the proposed UWB T/R switch.

Table 1: Performance comparison of T/R switches.

	This work		[3]	[4]	[5]	
	Rx	TX			Rx	TX
CMOS process (μm)	0.18		0.18	0.13	0.18	
Frequency (GHz)	3.1 ~ 10.6		3 ~ 10	DC ~ 20	5.2	
Input return loss (dB)	< -17.04	< -11.56	< -12	N/A	< -10	< -10
Input return loss (dB)	< -12.63	< -10.86	< -20	N/A	< -10	< -10
Insertion loss (dB)	< -2.2	< -2.3	< -4.4	< -2.0	< -1.56	< -2.02
Isolation (dB)	< -30.30	< -35.38	< -27	< -22	< -17.15	< -31.05
P _{1dB} (dBm@6 GHz)	8.5	9	N/A	27	11.2	29.6
IIP3 (dBm@6 GHz)	17	20	18	N/A	N/A	N/A
Chip area (mm ²)	0.21 (core)		0.63	0.18	N/A	

technique is adopted to achieve both high linearity and high power-handling capability. Unlike other T/R switches, the designed UWB T/R switch has an asymmetric structure for signals of transmission and receiving paths to obtain better input/output impedance matching and isolation. The proposed UWB T/R switch has the performances of low insertion loss, low return loss, and high isolation for wireless communication systems. The proposed UWB T/R switch is proved to be suitable for full-integration into system-on-chip of UWB systems.

ACKNOWLEDGMENT

The authors wish to thank the Chip Implementation Center (CIC) of the National Applied Research Laboratories, Taiwan, R.O.C., for supporting the tsmc CMOS process, the chip implementation, and the further performance measurement.

REFERENCES

1. Wu, C. C., A. Yen, and J. C. Chang, "A 0.13 m CMOS T/R switch design for ultra-wideband wireless applications," *IEEE International Symposium on Circuits and Systems*, 3758–3761, Dec. 2006.
2. Jin, Y. and C. Nguyen, "Ultra-compact high-linearity high-power fully integrated DC-20-GHz 0.18 m CMOS T/R switch," *IEEE Trans. on Microwave Theory and Techniques*, Vol. 55, No. 3, 30–36, 2007.
3. Pao, K.-H., C.-Y. Hsu, H.-R. Chuang, C.-L. Lu, and C.-Y. Chen, "A 3–10 GHz broadband CMOS T/R switch for UWB applications," *The 1st European Microwave Integrated Circuits Conference*, 452–454, Sep. 2006.
4. Li, Q. and Y.-P. Zhang, "CMOS T/R switch design: Towards ultra-wideband and higher frequency," *IEEE J. Solid-State Circuits*, Vol. 42, No. 3, 563–570, Mar. 2007.
5. Wang, J.-H., H.-H. Hsieh, and L.-H. Lu, "A 5.2-GHz CMOS T/R switch for ultra-low-voltage operations," *IEEE Trans. on Microwave Theory and Techniques*, Vol. 56, No. 8, 1774–1782, Aug. 2008.

A Novel Defected Microstrip Structure (DMS) Coupled Line Band Pass Filter in C Band

S. R. Hosseini, R. Sarraf Shirazi, and Gh. Moradi

Wave Propagation & Microwave Measurement Research Lab., Department of Electrical Engineering
Amirkabir University of Technology, 424 Hafez Avenue, Tehran 15914, Iran

Abstract— Novel coupled line band pass filter using defected microstrip structure (DMS) was designed which has nearly 11% relative bandwidth in *C* frequency band. HFSS full wave simulation was confirmed by ADS momentum module. A circuit model based on coupled line concept was developed to validate full wave simulation behavior.

1. INTRODUCTION

Band pass filters are one of most usable structures in microwave engineering. Band pass filters have found numerous applications in approximately all aspects of microwave engineering and communication technology.

Satellite communications are one of important and specific ways for sending and receiving data. *C* frequency band contains frequency range from 4 GHz to 8 GHz which is suitable for satellite communications.

There are various techniques for microwave filters implementation [1].

Since Planar filter structures are shapeable, light, easily fabrication and etc. can be appropriate ones for satellite communications.

Some important and practical method for designing Microstrip filters are provided in [2].

Newer methods for designing filters such as Defected ground structures (DGS), defected microstrip structures (DMS), coupled resonator and etc have found specific attentions among microwave structure designers [7–9].

Novel bandpass filter which designed in this paper is based on defected microstrip structure (DMS) method.

2. DEFECTS ON MICROSTRIP STRUCTURES

Defecting process firstly was made in microstrip ground (defected ground structure, DGS) which reported in [3].

DGS disturbs current distribution on ground plane. This Turbulence creates some resonators which will be added to main structure. Added poles caused by DGS resonances change main structure features [4]. DGS can be used for size reduction, harmonic suppression and etc. [5–7].

DMS is new defect process which adds defects to planar strips. DMS has no unwanted radiation from its ground, so it has less EMI index in comparison to DGS.

These defects disturb current distributions too. As a very simple method, each DMS can be modeled by LC resonator.

The defect shape can not affect its circuit resonator modeling concept. Thus, a T-shape defect was assumed for further analysis simplicity.

The analysis is based on *ABCD* matrix.

$$[ABCD]_T = [ABCD]_{TL_1} [ABCD]_{DMS} [ABCD]_{TL_2} \quad (1)$$

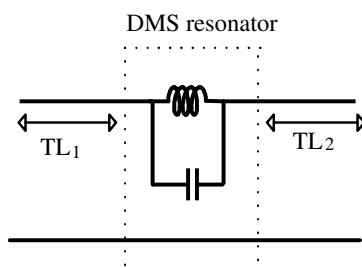


Figure 1: DMS modeling by as simple LC resonator.

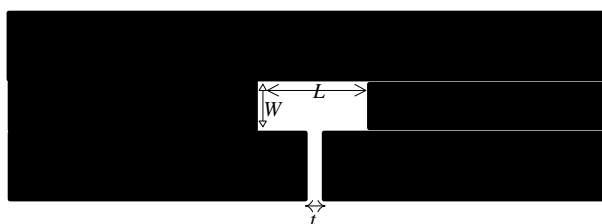


Figure 2: Typical microstrip defect.

From Equation (1) we have

$$[ABCD]_T = \begin{bmatrix} \cos(\gamma l_1) & Z_0 \sin(\gamma l_1) \\ \frac{\sin(\gamma l_1)}{Z_0} & \cos(\gamma l_1) \end{bmatrix} \begin{bmatrix} 1 & Z \\ 0 & 1 \end{bmatrix} \begin{bmatrix} \cos(\gamma l_2) & Z_0 \sin(\gamma l_2) \\ \frac{\sin(\gamma l_2)}{Z_0} & \cos(\gamma l_2) \end{bmatrix} \quad (2)$$

where $Z = (j\omega L) \parallel \frac{1}{(j\omega C)}$ and L, C are respectively the inductance and the capacitance caused by DMS.

The scattering parameters are achieved by [1].

$$S_{11} = \frac{A + \frac{B}{Z_0} - CZ_0 - D}{A + \frac{B}{Z_0} + CZ_0 + D} \quad S_{21} = \frac{2}{A + \frac{B}{Z_0} + CZ_0 + D} \quad (3)$$

which Z_0 is characteristic impedance. Simple transmission line is a low pass filter which its cutoff frequency is limited by higher order modes. One LC series resonator cause bandstop feature to TL. This modeling means each defect traps energy in itself at a certain frequency.

The idea was developed from this concept which cascading high pass filter and bandstop filter can lead to bandpass filter.

A novel coupled line band pass filter was presented using DMS concept. The designed filter is shown in Fig. 3.

This novel structure was analyzed by 3D full wave Ansoft HFSS v13 and also by Momentum module of ADS.

The scattering parameters of this band pass filters are

Figure 5 shows a good agreement between Momentum and HFSS full wave simulation. Filter is bandpass in Neighborhood of center frequency at 6 GHz.

Considering 3 dB signal transition index, the filter bandwidth is approximately 700 MHz which provide 11% relative band width.

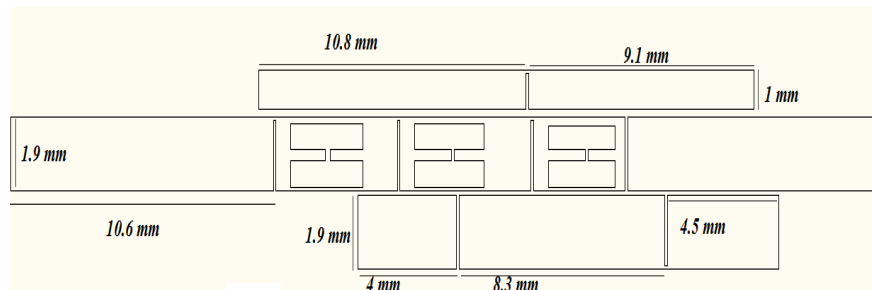


Figure 3: Coupled line DMS filter layout.

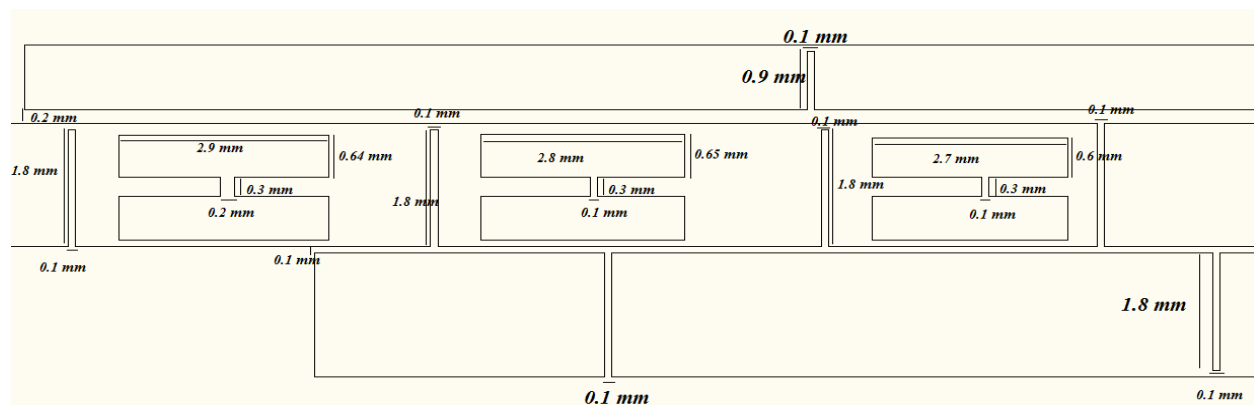


Figure 4: Coupled line DMS filter layout details.

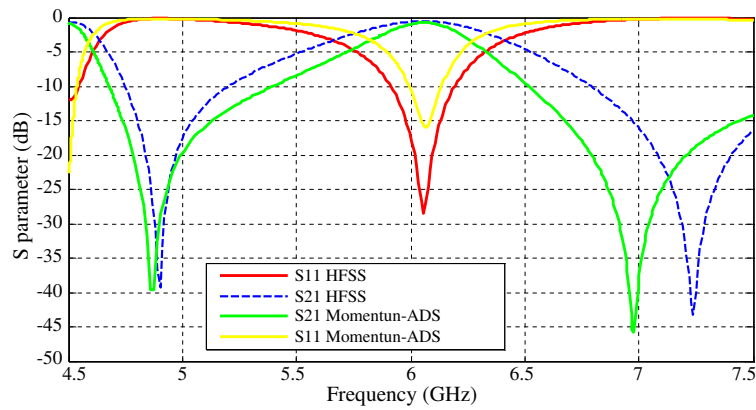


Figure 5: Coupled line DMS filter S -parameters.

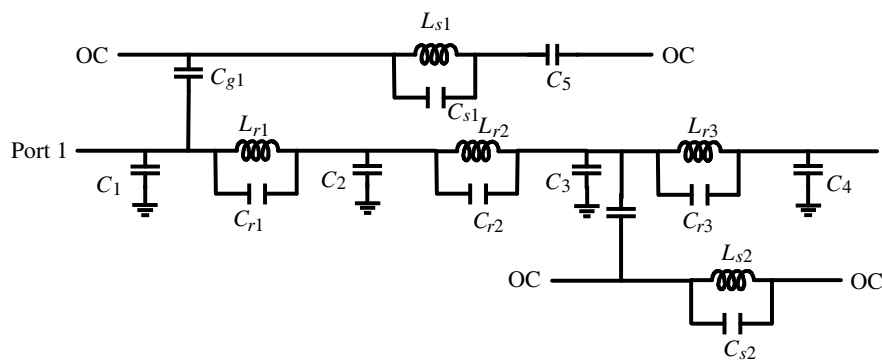


Figure 6: Circuit representation of coupled line DMS filter.

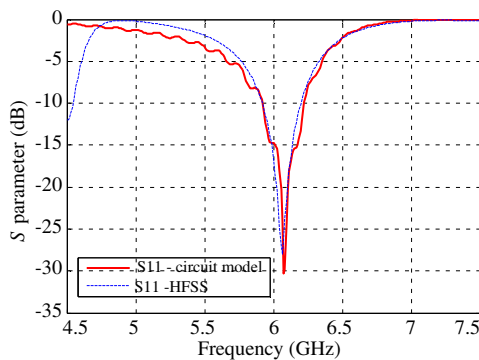


Figure 7: S_{11} comparison between full wave simulation and circuit modeling.

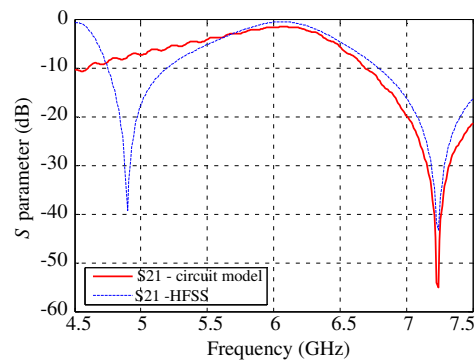


Figure 8: S_{21} comparison between full wave simulation and circuit modeling.

3. MODELLING

Circuit modeling can be used for desired structure using LC resonator concept of DMS. Each defect was modeled by lossless resonator and each gap represents capacitor as a simple way for circuit modeling. Coupling between each coupled line was modeled by coupling capacitor.

The our circuit representation is in Fig. 6.

The circuit elements were calculated via optimization process which two results have maximum agreement over desired frequency band.

Table 1 shows circuit elements values after optimization process.

It was obvious which coupling capacitors and coupled line branch inductances should have less value against main capacitors and Inductances. This expectation was confirmed after optimization process as shown in Table 1.

Table 1: Circuit modeling elements values after optimization process.

Circuit element	C_1	C_2	C_3	C_4	C_5	C_{r1}	C_{r2}	C_{r3}	C_{g1}
value	0.183665	14.1471	19.6922	19.9285	15.0342	0.50938	2.60473	9.86308	1.50868
unit	pF	fF							
Circuit element	C_{g2}	C_{s1}	C_{s2}	L_{r1}	L_{r2}	L_{r3}	L_{s1}	L_{s2}	
value	4.34636	2.60084	14.6314	0.950167	0.58837	9.98867	9.95165	3.13976	
unit	fF	pF	pF	nH	nH	nH	pH	pH	

4. CONCLUSIONS

Bandpass coupled line filter based on DMS method was analyzed in full wave simulation. Circuit model based on resonator concept of DMS confirmed full wave simulation results. Extracted circuit elements values showed farther defects from main line have less values in comparison to main defects.

ACKNOWLEDGMENT

The authors would like to thank the Iran Telecom Research Center for the support of this work.

REFERENCES

1. Pozar, D. M., *Microwave Engineering*, 486–517, Addison-Wesley, Reading, MA, 1990.
2. Hong, J.-S. and M. J. Lancaster, *Microstrip Filters for RF/Microwave Applications*, Wiley, 2001.
3. Kim, C. S., J. S. Park, D. Ahn, and J. B. Lom, “A novel 1-D periodic defected ground structure for planar circuits,” *IEEE Microwave and Wireless Components Letters*, Vol. 10, No. 4, 131–133, 2000.
4. Ahn, D., J. S. Park, C. S. Kim, J. Kim, Y. Qian, and T. Itoh, “A design of the low-pass filter using the novel microstrip defected ground structure,” *IEEE Transactions on Microwave Theory and Techniques*, Vol. 49, 86–93, Jan. 2001.
5. Sung, Y. J., C. S. Ahn, and Y.-S. Kim, “Size reduction and harmonic suppression of rat-race hybrid coupler using defected ground structure,” *IEEE Microwave and Wireless Components Letters*, Vol. 14, No. 1, Jan. 2004.
6. Lim, J.-S., J.-S. Park, Y.-T. Lee, D. Ahn, and S. Nam, “Application of defected ground structure in reducing the size of amplifiers,” *IEEE Microwave and Wireless Components Letters*, Vol. 12, 261–263, 2002.
7. El-Shaarawy, H. B., F. Coccetti, R. Plana, M. El Said, and E. A. Hashish, “Compact bandpass ring resonator filter with enhanced wide-band rejection characteristics using defected ground structures,” *IEEE Microwave and Wireless Components Letters*, Vol. 18, 500–502, 2008.
8. Wang, X.-H., B.-Z. Wang, H. Zhang, and K. J. Chen, “A tunable bandstop resonator based on a compact slotted ground structure,” *IEEE Transactions on Microwave Theory and Techniques*, Vol. 55, No. 9, Sep. 2007.
9. Baik, J.-W., S.-M. Han, C. Jeong, J. Jeong, and Y.-S. Kim, “Compact ultra-wideband bandpass filter with EBG structure,” *IEEE Microwave and Wireless Components Letters*, Vol. 18, No. 10, 671, Oct. 2008.

Optimized Rat-race Coupler with Different Shapes of Defected Ground Structure

M. Shirazi, R. Sarraf Shirazi, and Gh. R. Moradi
School of Electrical Engineering, Amirkabir University of Technology, Iran

Abstract— In this paper, a new type of Rat-Race ring coupler with different shapes of DGS is presented. Three shapes of defect on ground plane have been investigated and after optimization with Genetic Algorithm (GA) the best one is presented. Changing the shapes and dimensions of the defect on ground will lead to better performance of a rat-race coupler such as less return loss, smaller size or wider bandwidth than conventional rat-race coupler with DGS. All designs are validated by using the full-wave electromagnetic simulator. At first a circular DGS have been designed and investigated. After optimization we can see the advantages of this type to the conventional one. The next type is triangular DGS; the optimum case of this type is presented. Based on the triangular DGS results and distribution of electromagnetic current on the ground plane, a fractal DGS have been designed and simulated. After optimization with Genetic Algorithm the optimum shape and dimension of the defect on ground plane is proposed. Simulations are carried out using HFSS 13, a commercial electromagnetic simulator based on a finite element method.

1. INTRODUCTION

Microstrip rat-race ring couplers are important structures in microwave. They are widely used in power amplifiers, mixers, and antenna systems due to their simplicity and wide bandwidth in power dividing distribution [2, 3]. Hybrid ring couplers are also used in isolated power dividers where a high level of isolation between the ports is required. However, this isolation is generally limited in bandwidth by the phase balance performance of the hybrid. The conventional 180 hybrid ring coupler has several shortcomings. It is inherently narrow-band, large in size, and it requires impractically high-impedance line sections for large power-split ratios.

Recently, there has been an increasing interest in microwave and millimeter-wave applications of the PBG [4, 5] and the DGS [1, 6]. In [1] a dumbbell shape DGS have been proposed which has both size reduction and 3rd harmonic suppression in comparison with conventional Rat-Race coupler. The proposed structure in [1] is not optimum neither in shape nor in size and dimensions. Fig. 1 shows the conventional Rat-Race coupler with dumbbell shape (rectangular) DGS and new proposed structures.

In this paper, we propose three other shapes of defect on ground plane and find the optimum case based on GA. Each of the proposed rat-races is verified by full wave HFSS simulator and is compared with the conventional rat-race.

2. CONVENTIONAL RAT-RACE WITH/WITHOUT DGS

In this section we examine the S -parameters of Rat-Race coupler with and without DGS. Substrate with dielectric constant of 2.5 and thickness of 25 mil has been used. Fig. 2(a) shows return loss,

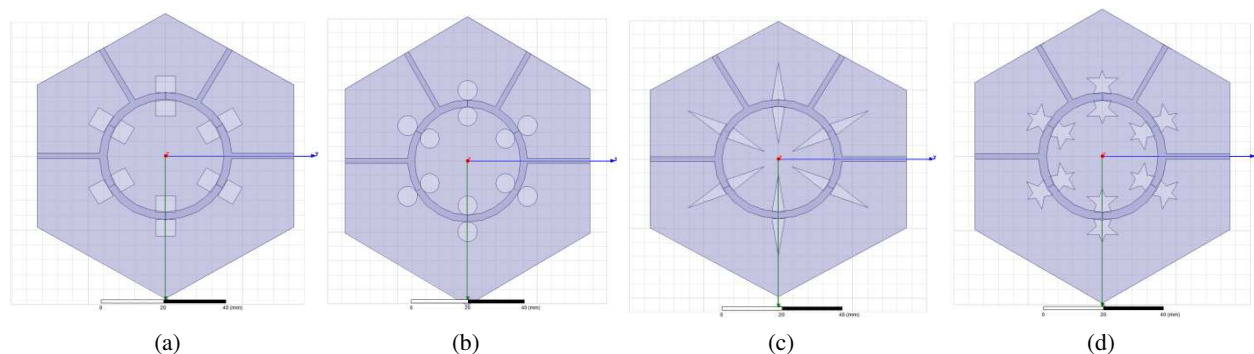


Figure 1: Four different shapes of DGS. (a) Conventional, (b) Rat-Race with Circular DGS, (c) Rat-Race with triangular DGS and (d) Rat-Race with fractal DGS.

insertion loss and isolation for the conventional Rat-Race coupler. In this paper, we follow three criteria to compute the coupler bandwidth.

1. Return loss and isolation better than 20 dB.
2. Magnitude difference between output ports should not exceed 1 dB.
3. Phase difference between output ports should not exceed 5 degree.

With these qualifications the bandwidth of conventional Rat-race coupler is about 15% with the central frequency of 2.36 GHz. Utilizing a rectangular DGS will result in 3rd harmonic suppression and size reduction as reported in [1], but the dimensions of DGS section proposed in [1] is not optimum. After optimization with GA the length width and gap distance of rectangular DGS sections were $a = 7$ mm, $b = 5.2$ mm and $g = 0.2$ mm, respectively. The S -parameters of this type of DGS has been shown in Fig. 2(b).

The central frequency of Rat-Race coupler with rectangular DGS is 1.59 GHz and the bandwidth of this type of DGS is about 13.5%, as you can see the bandwidth is 1.5% less than the bandwidth of conventional Rat-Race.

3. RAT-RACE WITH CIRCULAR DGS

A new shape that can be used as defect on ground plane is circular DGS. As shown in Fig. 1(b) six similar circular parts have been etched from ground plane. After optimization the radial of each circle and the width of strip became 3.5 mm and 2.6 mm, respectively. Fig. 3 shows the S -parameters of this kind of defect. Central frequency and bandwidth of this type has not been changed in comparison with the previous type, but much better return loss and isolation between output ports have been achieved.

4. RAT-RACE WITH TRIANGULAR DGS

The next type of DGS that will be investigated is triangular DGS. In this type six triangular sections with optimized base and height have been etched from ground plane. Fig. 4(a) shows S -parameters of coupler with triangular DGS and Fig. 4(b) illustrates the phase difference between output ports. The limiting condition for bandwidth of coupler is almost its phase imbalance between output ports. Therefore, Fig. 2(b) has been depicted to determine the bandwidth of Rat-Race coupler with triangular DGS.

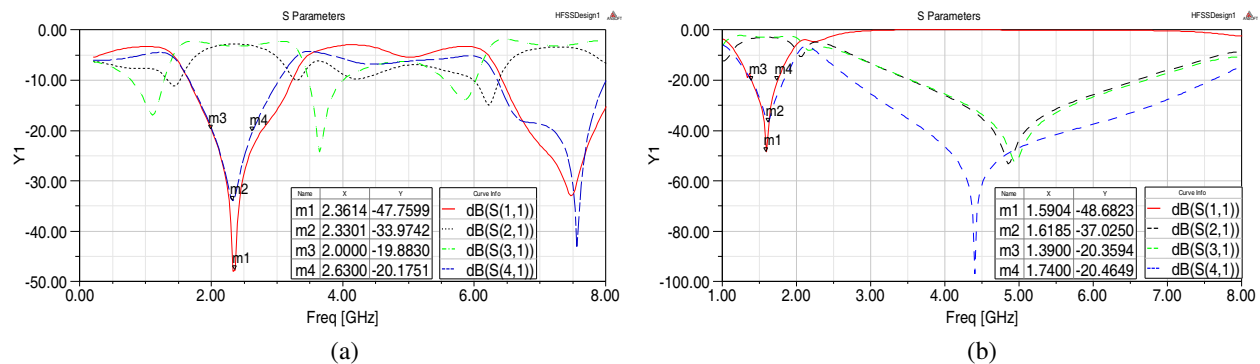


Figure 2: S -Parameters of conventional Rat-Race coupler. (a) Coupler without DGS, (b) coupler with DGS.

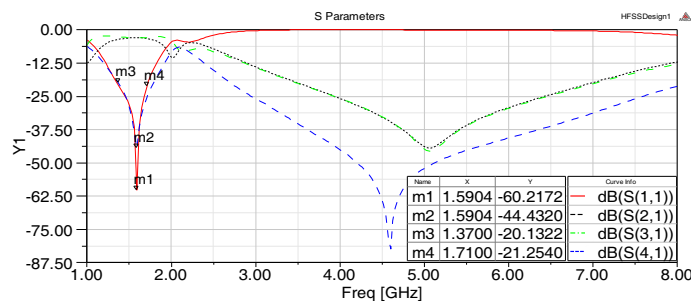


Figure 3: S -parameters of Rat-Race coupler with circular DGS.

The central frequency of this type of DGS is around 1.54 GHz and its bandwidth is almost 14%. It can be seen that the 3rd harmonic suppression of the coupler has not been affected by changing the DGS shapes and dimensions.

5. RAT-RACE WITH FRACTAL DGS

With a careful examination of current distribution of coupler with triangular DGS and the S -parameters of previous DGS types, we examined and simulated a Rat-Race coupler with fractal DGS, the shape of this kind of DGS has been depicted in Fig. 1(d). Fig. 5(a) shows the S -parameters of new proposed structure. As can be seen the central frequency is 1.51 GHz which is 90 MHz less than conventional Rat-Race with rectangular DGS. It means that the proposed hybrid ring reduce the size of coupler. The occupied area of coupler with fractal DGS is 40% of conventional Rat-Race coupler. Also with the change in the dimension of fractal section we can achieve much better return

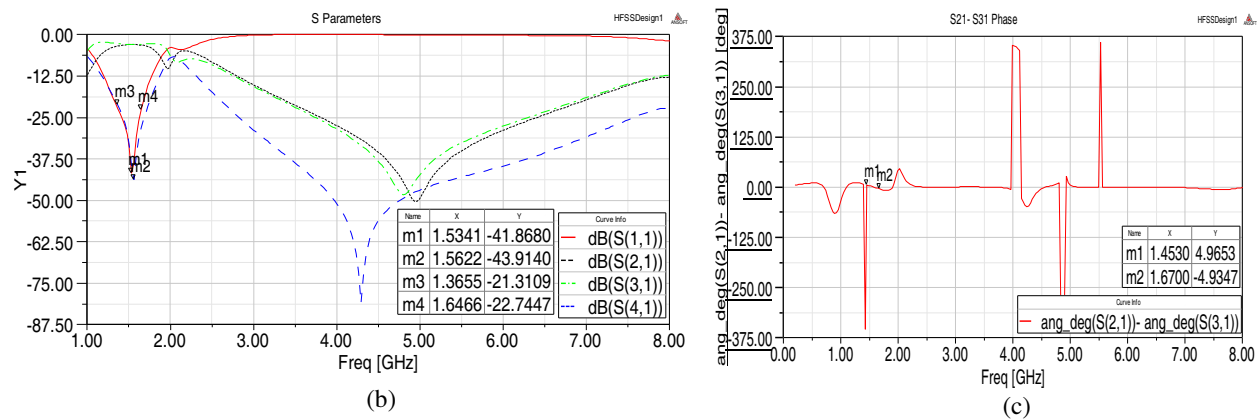


Figure 4: Rat-Race with triangular DGS. (a) S -parameters, (b) phase difference between output ports.

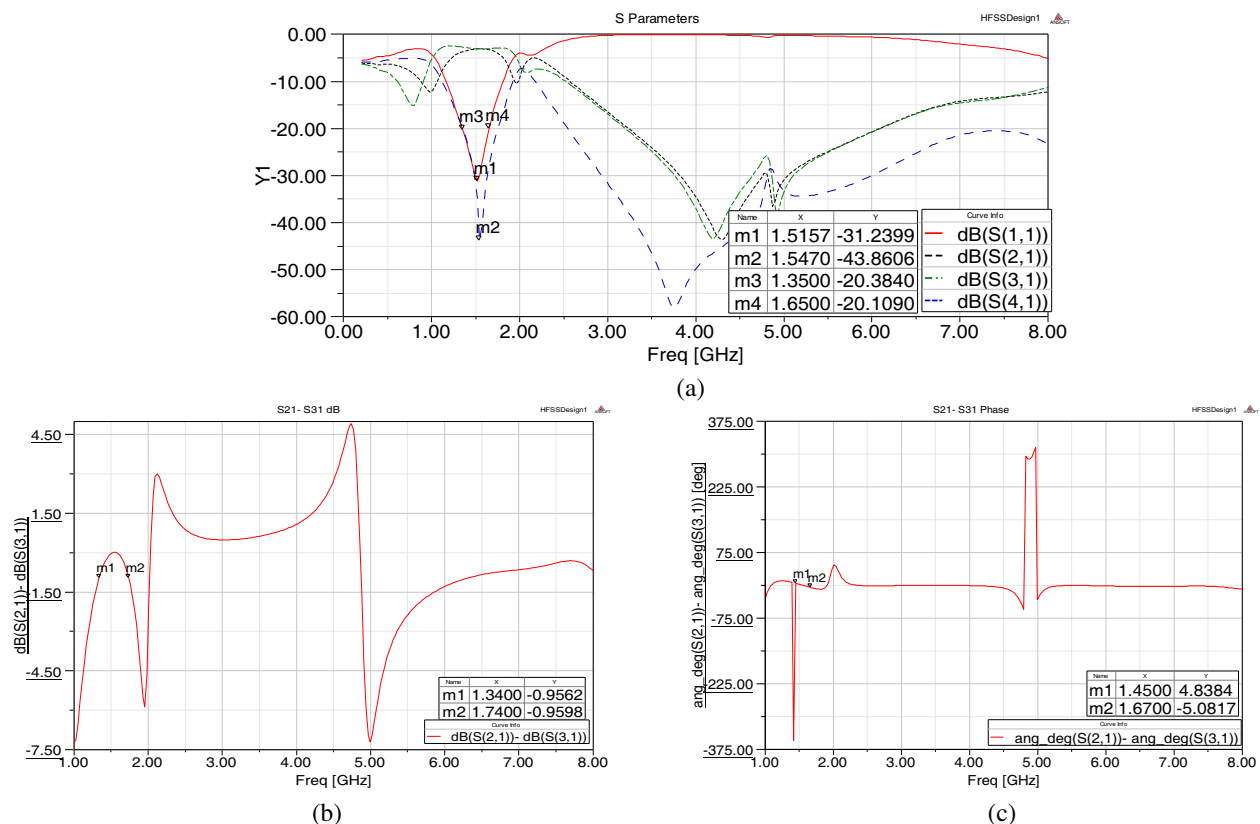


Figure 5: Rat-Race with fractal DGS. (a) S -parameters, (b) magnitude difference between output ports, (c) phase difference between output ports.

loss or isolation, but near 1.6 GHz. Fig. 5(b) and Fig. 5(c) show magnitude difference and phase difference of output ports, respectively. It can be seen that the limitative factor to determine the bandwidth is phase imbalance between output ports.

6. CONCLUSIONS

Presented is a new hybrid ring Rat-Race coupler with different types of DGS. Photography of the presented structures is shown in Fig. 1. All slots and gaps are 0.2 mm or wider and easy for fabrication. It has demonstrated that lower central frequency, as well as very good performance at the designed frequency, has been achieved in these types of a rat-race coupler with DGS. All proposed structures have been optimized with Genetic Algorithm. It is well suited to compact low-cost active circuit applications for microwave and millimeter-wave integrated-circuits.

REFERENCES

1. Sung, Y. J., C. S. Ahn, and Y. S. Kim, "Size reduction and harmonic suppression of Rat-Race hybrid ring coupler using defected ground structure," *IEEE Microwave Wireless Comp. Lett.*, Vol. 14, No. 1, 7–9, January 2004.
2. Kim, D. I. and Y. Naito, "Broad-band design of improved hybrid-ring 3-dB directional couplers," *IEEE Trans. Microwave Theory Tech.*, Vol. 30, 2040–2046, November 1982.
3. Pozar, D. M., *Microwave Engineering*, Wiley, New York, 1998.
4. Shum, K. M., Q. Xue, and C. H. Chan, "A novel microstrip ring hybrid incorporating a PBG cell," *IEEE Microwave Wireless Comp. Lett.*, Vol. 11, 258–260, June 2001.
5. Caloz, C. and T. Itoh, "Multilayer and anisotropic planar compact PBG structures for microstrip applications," *IEEE Trans. Microwave Theory Tech.*, Vol. 50, 2206–2208, September 2002.
6. Lim, J. S., J. S. Park, Y. T. Lee, D. Ahn, and S. Nam, "Application of defected ground structure in reducing the size of amplifiers," *IEEE Microwave Wireless Comp. Lett.*, Vol. 12, No. 7, 261–263, July 2002.

New Wilkinson Power Dividers Using Dual and T-shaped Transmission Lines

Sung-Yen Juang, Li-Chi Dai, Yu-Ta Chen, Wen-Chian Lai, and Pu-Hua Deng
 Department of Electrical Engineering, National University of Kaohsiung, Taiwan

Abstract— The conventional single uniform transmission line can be equivalent to the dual and the T-shaped transmission lines, which have been proposed in the previous works. This paper proposes two new compact Wilkinson power dividers. The first power divider uses dual and T-shaped transmission lines to replace the two quarter-wavelength ($\lambda/4$) transmission lines in the conventional equal-split Wilkinson power divider. The second divider utilizes new dual transmission line section, which is composed of one single uniform and one T-shaped transmission lines, to replace each $\lambda/4$ transmission line in the conventional equal-split Wilkinson power divider. The result of each proposed new Wilkinson power divider can demonstrate a compact size and similar frequency responses as the conventional Wilkinson power divider around the operating band.

1. INTRODUCTION

Recently, Wilkinson power divider is an important component in wireless communication system due to its good performance for power division and isolation. For the practical purpose, several types of Wilkinson power dividers have been studied in [1–5]. Conventional Wilkinson power divider [1] has two essential quarter-wavelength ($\lambda/4$) transmission lines for transforming required impedance matching at each port. However, the $\lambda/4$ transformer is occupied a large circuit size. Therefore, some studies discuss how to reduce the $\lambda/4$ transmission for achieving compact circuit size. For example, the miniaturized dual-frequency power divider [2] utilized the DGS structure to realize a small circuit area. Similarly, the compact dual-band power divider [3] used slow-wave structure to reduce its size. Besides, the miniaturized power dividers [4] and [5] utilized dual and T-shaped transmission lines to replace the $\lambda/4$ transmission lines in conventional Wilkinson power divider, respectively. In this paper, two new types of Wilkinson power dividers using mixed dual and T-shaped transmission lines are presented for realizing compact circuit size.

2. THE PROPOSED WILKINSON POWER DIVIDERS

In this paper, two new Wilkinson power dividers using dual and T-shaped transmission lines are presented. Figure 1 shows the equivalent circuit of the conventional equal-split Wilkinson power divider composed of a $\lambda/4$ transformer in each transmission path. The first proposed divider, as shown in Figure 2, uses dual transmission line [4] and T-shaped transmission line [5] to replace the two $\lambda/4$ transformers of the conventional equal-split Wilkinson power divider (Figure 1). The dual transmission-line section can be easily folded for the purpose of reducing circuit size since the characteristic impedance of each line is high. Besides, the length of T-shaped transmission line can achieve an effective reduction compared with the $\lambda/4$ transformer while the T-shaped line is properly designed.

The equal-split power divider as shown in Figure 1 can be designed by following design parameters. Z_1 and R are equal to $\sqrt{2}Z_0$ and $2Z_0$, respectively, where the Z_1 is the characteristic

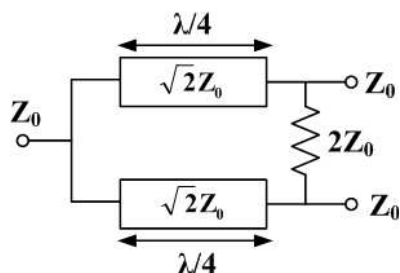


Figure 1: Conventional Wilkinson power divider.

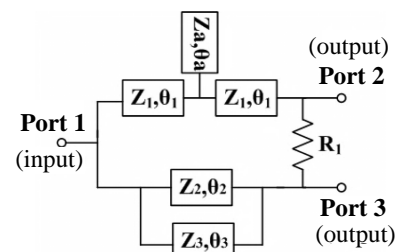


Figure 2: The proposed first power divider with T-shaped and dual transmission lines.

insertion loss are approximately 0.93 GHz and 3.4 dB ($-|S_{21}|$), respectively. The measured isolation is greater than 20 dB around the desired band.

In general, dual transmission lines can effectively reduce the circuit size because it is composed of two uniform high characteristic impedance transmission lines which can be easily folded. However, it is not suit for power divider system due to one of the high impedance lines is longer than the other line, in other words, it usually needs meander path for achieving a compact size. Therefore, the second power divider is proposed to relax this problem, as shown in Figure 5. The proposed second power divider utilizes new dual transmission line section, which is composed of one uniform and one T-shaped transmission lines, to replace each $\lambda/4$ transmission line in the conventional equal-split Wilkinson power divider. Figure 6 shows the layout of Figure 5, and it demonstrates an obvious

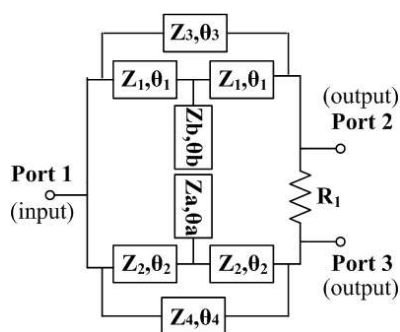


Figure 5: The second proposed power divider with new dual transmission line sections.

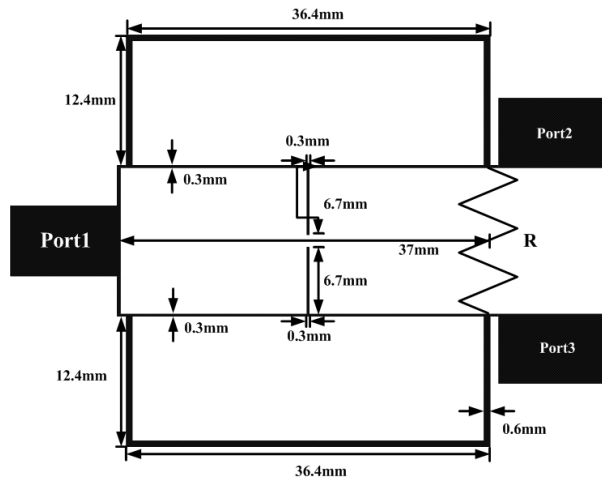


Figure 6: Layout of the proposed second power divider.

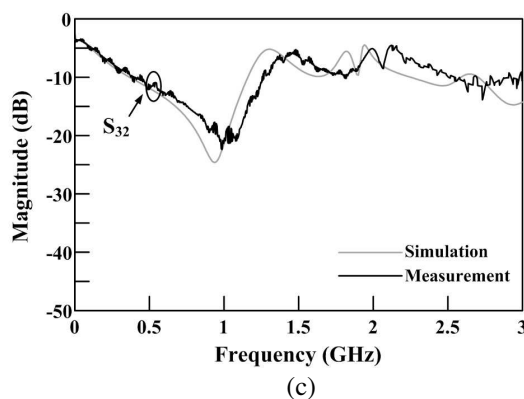
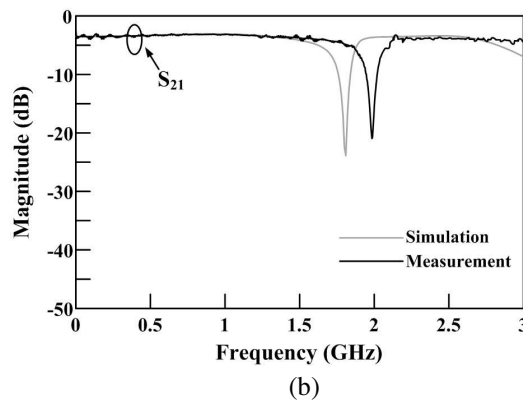
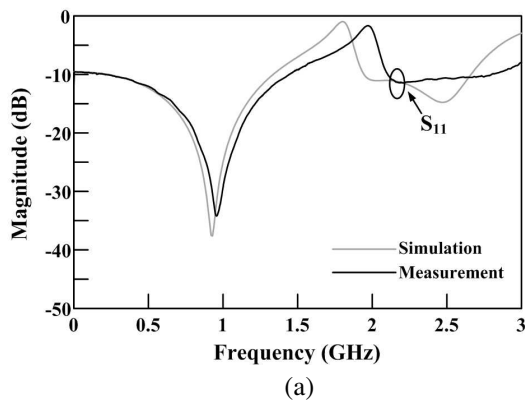


Figure 7: Simulated and measured results of Figure 6. (a) $|S_{11}|$. (b) $|S_{21}|$. (c) $|S_{32}|$.

reduction. The center frequency of the second power divider is approximately 1 GHz. The design parameters of the proposed second divider are $Z_1 = Z_2 = Z_a = Z_b = 170 \Omega$, $Z_3 = Z_4 = 141.4 \Omega$, $\theta_1 = \theta_2 = 39.8^\circ$, $\theta_3 = \theta_4 = 89^\circ$, $\theta_a = \theta_b = 20.33^\circ$, and $R_1 = 100 \Omega$, where Z_1 , Z_2 , Z_3 , Z_4 , Z_a , or Z_b and θ_3 , θ_4 , θ_a , or θ_b are the characteristic impedances and electrical lengths of the proposed new dual transmission line section, respectively. Figure 7 shows the simulated and measured results of Figure 6. The measured results of center frequency and minimal insertion loss are approximately 0.96 GHz and 3.2 dB ($-|S_{21}|$), respectively. The measured isolation is greater than 16 dB around the desired band.

3. CONCLUSIONS

In this study, two new types of Wilkinson power dividers using mixed dual and T-shaped transmission lines are presented for compact circuits. The first proposed power divider utilizes dual and T-shaped transmission lines to replace each of the $\lambda/4$ transmission line in the conventional Wilkinson power divider, and the result indicates the dual and T-shaped transmission lines has similar levels of power division and isolation. The second proposed power divider uses a new dual transmission line section composed of one uniform and one T-shaped transmission lines to replace each $\lambda/4$ transmission line in the conventional equal-split Wilkinson power divider. It successfully demonstrates a simple circuit design and an effective size reduction.

ACKNOWLEDGMENT

This work was supported by the National Science Council of Taiwan under Grant NSC 98-2221-E-390-041, Grant NSC 99-2221-E-390-007, and Grant NSC 100-2221-E-390-027. Besides, we are also grateful to the National Center for High-performance Computing for computer time and facilities.

REFERENCES

1. Pozar, D. M., *Microwave Engineering*, 2nd Edition, Chapters 7–8, Wiley, New York, 1998.
2. Hedayati, M. K., G. Moradi, A. Abdipour, and M. Mosalanejad, "A miniaturized dual-frequency Wilkinson power divider using defected ground structure," *Applied Electromagnetics, APACE*, 1–5, Nov. 2010.
3. Chou, T., C. M. Peng, and I. F. Chen, "A dual-band Wilkinson power divider with microstrip slow-wave structures," *Electromagnetic Compatibility, APEMC*, 723–726, Apr. 2010.
4. Yu, B., Z. Gao, L. Yi, and F. Gao, "A minimized Wilkinson power divider using dual transmission line," *Wireless Communications, Networking and Mobile Computing*, 24–26, Sep. 2009.
5. Srisathit, K., P. Jadhav, and W. Surakamponorn, "Miniature Wilkinson divider and hybrid, coupler with harmonic suppression, using T-shaped transmission line," *Asia-Pacific Microwave Conference*, 1–4, Dec. 2007.

Design of Bandpass Filter with Transmission Zeros Using Zeroth-order Resonator and U-shaped Resonator

X.-G. Huang, Q.-Y. Feng, Q.-Y. Xiang, and D.-H. Jia
 School of Information Science and Technology
 Southwest Jiaotong University, Chengdu, Sichuan 610031, China

Abstract— In this article, a novel bandpass filter using symmetrical composite right/left-handed transmission lines (CRLH TL) ZOR and U-shaped resonator with three transmission zeros (TZs) is proposed. The design concept of the proposed filter is based on the zeroth-order resonator (ZOR) and half-wavelength open-ended resonator with opposite phase response around the resonant frequency and, therefore, one TZ can be achieved by using a ZOR parallel-coupled with a conventional resonant circuit. To improve the selectivity, two L-shaped coupling arms connected to feed lines are introduced to provide additional two TZs. Both simulated and measured results have been presented to demonstrate the presence of one TZ on high side of the stopband and two TZs on low side of stopband.

1. INTRODUCTION

Recently, more and more devices are designed using the metamaterial concept. Especially, CRLH metamaterial transmission lines have been studied for the microwave applications [1–3]. Among these applications, the ZOR have been proposed based on CRLH TL [4]. The resonant frequency of ZOR is independent of the physical length so that the resonator has much smaller size compared to conventional resonator [5]. Thus, the ZOR is very attractive for design of compact bandpass filter. Since then, the various novel ZORs such as CRLH coplanar waveguide (CPW) ZOR [6], simplified composite right/left-handed (SCRLH) ZOR [7], and complementary split ring resonator (CSRR) ZOR [8] have been designed to synthesize bandpass filters with compact size.

In this paper, a new instructive method of filter design based on ZOR and half-wavelength open-ended resonator is discussed. The method starts from the phase shift of ZOR and traditional resonator. By adding the signal of ZOR into the traditional resonator signal path, TZs can be obtained. However, it is hard to get two TZs by the method of combine ZOR with traditional resonator since the phase shift are not opposite at every frequency around resonance frequency for the reality two resonators. Then, two L-shaped coupling arms are introduced to improve the selectivity. To validate the proposed method, the bandpass filter (centre frequency 2.20 GHz) composed of symmetrical CRLH TL ZOR and U-shaped resonator (half-wavelength open-ended resonator) is presented, providing a pair of TZs at 2.07 (provided by U-shaped resonant circuit) and 2.25 GHz, thus featuring steep roll-off at both edges of the passband.

2. ANALYSES OF ZOR AND CONVENTIONAL RESONATOR

2.1. Phase Shift of Lossy ZOR and Half-wavelength Open-ended Resonator

Figures 1(a) and (b) show the unit cell of lossy CRLH TL model and equivalent circuit of open-ended ZOR. Figure 1(b) also can be the model of conventional resonator, and the transfer impedance Z_{BA}

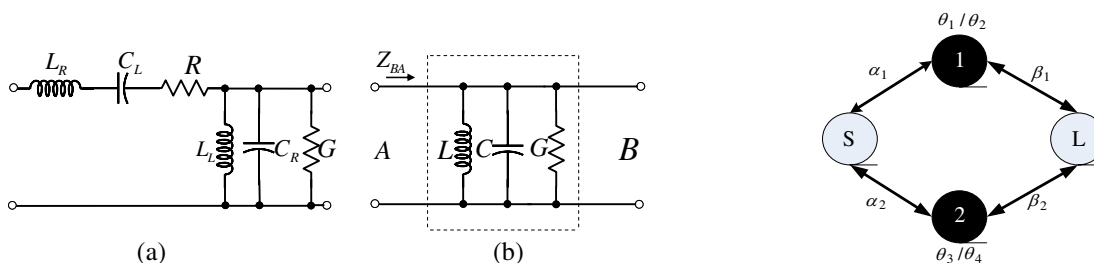


Figure 1: (a) Equivalent circuit of a unit cell of lossy CRLH TL. (b) Two-port network lossy model of ZOR and conventional resonator.

Figure 2: Coupling scheme of creating transmission zeros.

form A toward B (see Figure 1(b)) is given as

$$Z_{BA} = \frac{1}{\frac{1}{j\omega L} + j\omega C + G} = \frac{\omega^2 L^2 G + j\omega L(1 - \omega^2 LC)}{(1 - \omega^2 LC)^2 + \omega^2 L^2 G^2} \quad (1)$$

For the case the equivalent circuit shown in Figure 1(b) is ZOR, according to Eq. (1), the phase shift is 0° when $\omega = \omega_0$, θ_1 ($0^\circ < \theta_1 < 90^\circ$) when $\omega < \omega_0$ and θ_2 ($-90^\circ < \theta_2 < 0^\circ$) when $\omega > \omega_0$ because of $\text{Re}(Z_{AB}) \neq 0$. For the case the equivalent circuit shown in Figure 1(b) is half-wavelength open-ended resonator, the phase shift is 180° when $\omega = \omega_0$, θ_3 ($-180^\circ < \theta_3 < -90^\circ$) when $\omega < \omega_0$ and θ_4 ($90^\circ < \theta_4 < 180^\circ$) when $\omega > \omega_0$ because the resonator frequency of conventional resonator is at positive first order mode.

2.2. Transmission Zeros

Based on the above discussion, the TZs can be obtained by the coupling scheme as shown in Figure 2, where S and L denote the input and output ports respectively; node 1 denote the ZOR and node 2 for the conventional half-wavelength open-ended resonator. Since there is no coupling between the two resonators, the signal from form S to L has two separately parallel-coupling paths. The TZs can be obtained when the total phase shift of the upper and lower paths is 0° .

$$\begin{cases} \alpha_1 + \theta_1 + \beta_1 + \alpha_2 + \theta_3 + \beta_2 = 0^\circ & \text{when } \omega < \omega_0 \\ \alpha_1 + \theta_2 + \beta_1 + \alpha_2 + \theta_4 + \beta_2 = 0^\circ & \text{when } \omega > \omega_0 \end{cases} \quad (2a)$$

$$\begin{cases} \alpha_1 + \theta_1 + \beta_1 + \alpha_2 + \theta_3 + \beta_2 = 0^\circ & \text{when } \omega < \omega_0 \\ \alpha_1 + \theta_2 + \beta_1 + \alpha_2 + \theta_4 + \beta_2 = 0^\circ & \text{when } \omega > \omega_0 \end{cases} \quad (2b)$$

Therefore, a TZ on the lower stopband is get if the Eq. (2a) is met. Similarly, a TZ on the higher stopband is get if the Eq. (2b) is met. When Eq. (2a) and Eq. (2b) are both satisfied, two TZs are obtained, and the Eq. (3) is deduced:

$$\theta_1 + \theta_3 = \theta_2 + \theta_4 \quad (3)$$

The Eq. (3) is met only when the phase shift is $\theta_1 = -\theta_3 = 90^\circ$ when $\omega < \omega_0$ and $\theta_2 = -\theta_4 = -90^\circ$ when $\omega > \omega_0$, which means only the ZOR and conventional resonator is lossless, or it can not be got two TZs.

3. BANDPASS FILTERS APPLICATION

To demonstrate the usefulness of the proposed method, a symmetrical CRLH TL ZOR and U-shaped resonator is designed shown in Figure 3. It is designed on a substrate with a relative dielectric constant of 3.48 and thickness of 0.5 mm, and a loss tangent of 0.003. The ZOR consist of three parts, which are interdigital capacitors, a shunt stub inductors and interdigital capacitors. To improve the strength of coupling between input port and ZOR, the coupling line l of ZOR is extended to 8 mm, and has the same length with the coupling line between input port and U-shaped resonator as shown Figure 3. Basic coupling structures can be seen in Figure 2 where no coupling between two resonators. To excite the two resonators simultaneously, two ports with simple coupling lines are coupled to the resonators. The simulated results are plotted in Figure 6 for three different value of W . As can be seen, for $W = 0.4$ mm, two resonators exhibit the same

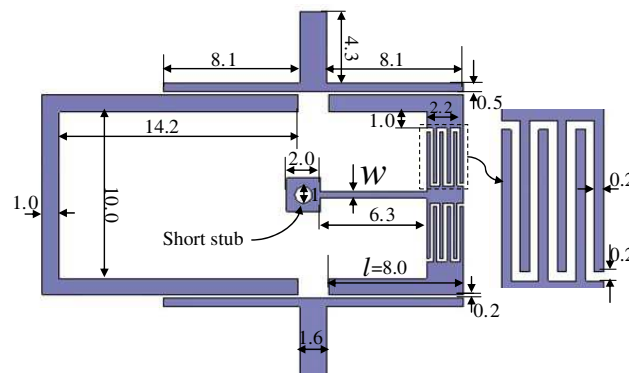


Figure 3: Layout of the two resonators on a 0.5-mm-thick dielectric substrate with a relative dielectric constant of 3.48 (All dimensions are in millimeters).

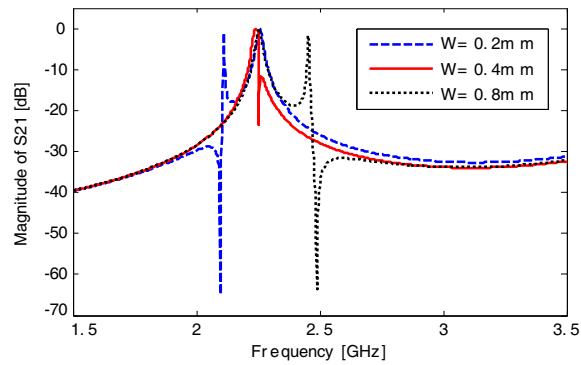


Figure 4: Resonant frequencies under different width W of shunt stub.

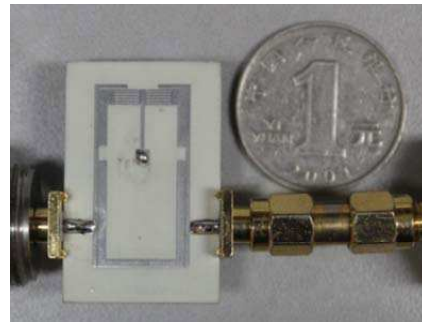


Figure 5: Photograph of the bandpass filter.

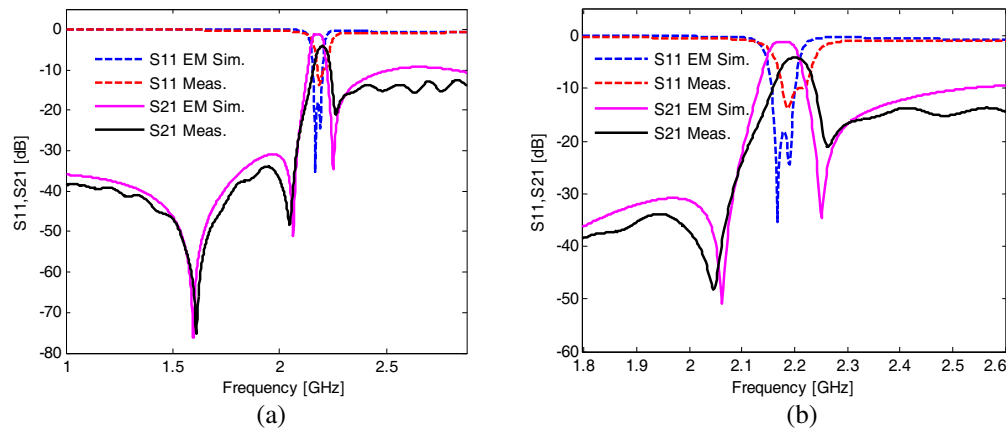


Figure 6: Measured and simulated frequency response of the proposed filter. (a) Wide-band. (b) Narrow-band

resonant frequency. When W is decreased or increased from this value, the two resonant frequencies split. This is shown in Figure 4 for $W = 0.2$ mm and $W = 0.8$ mm. The smaller W results in the ZOR being shifted to a lower frequency, while the larger W shifts the ZOR to a higher frequency, because the value of W affects the shunt inductor L_L .

It is also interesting to notice from Figure 4 that there is a TZ when the two resonant frequencies split. The TZ is allocated on the high side of two resonant frequencies when the frequency of ZOR is higher than U-shaped resonator. On the other hand, the TZ is on the lower of the two resonant frequencies when the frequency of ZOR is lower than U-shaped resonator. Thus, the TZ appears to be closely associated with the frequency of ZOR.

To improve the passband characteristics proposed in Figure 4, L-shaped coupling arms are introduced to two ports shown in Figure 3. The L-shaped coupling arms not only enhance the strength of coupling, but also create additional two TZs on the lower stopband.

The proposed filter is simulated and fabricated on the Rogers 4350B substrate with a relative dielectric constant of 3.48 and a thickness of 0.5 mm. The photograph of fabricated filter is shown in Figure 5 and the physical dimensions are described in Figure 3. The size of the filter is about 18 mm \times 28 mm \times 0.5 mm. The measured results, obtained using Agilent 5071C network analyzer, and the full EM simulated results are both plotted in Figure 6. The simulated/measured center frequency at 2.18 GHz/2.20 GHz. Three TZs are successfully acquired in both the simulation and measurement, and they are allocated at 1.58 GHz, 2.07 GHz and 2.25 GHz. Some differences between the simulation and measured data may be attributed to the short stub and the fabrication tolerances.

4. CONCLUSIONS

In this paper, a novel bandpass filter with three TZs based on the ZOR and U-shaped resonator has been presented. The lossy models of the ZOR and conventional resonator are provided to analyze the phase shift below and above the resonant frequency. By introducing L-shaped coupling

arms to two ports, a high selectivity filter using CRLH TL ZOR and U-shape resonator is designed, fabricated, and measured. In comparison with the cross-coupled filter, the filter using two resonators can provide a sharp cut-off frequency response. The filter circuit size has been significantly reduced. As a result, the compact-size filter is suitable for use in wireless communication system.

ACKNOWLEDGMENT

This work is supported by the National Natural Science Foundation of China (NSFC) under Grant 60990320, 60990323, and the National 863 Project of China under Grant 2012AA012305.

REFERENCES

1. Gil, M., J. Bonache, J. Garcia-Garcia, et al., "Composite right/left-handed metamaterial transmission lines based on complementary split-rings resonators and their applications to very wide-band and compact filter design," *IEEE Transactions on Microwave Theory and Techniques*, Vol. 55, No. 6, 1296–1304, 2007.
2. Islam, R. and G. V. Eleftheriades, "Compact corporate power divider using metamaterial NRI-TL coupled-line couplers," *IEEE Microwave and Wireless Components Letters*, Vol. 18, No. 7, 440–442, 2008.
3. Changjun, L. and W. Menzel, "Broadband via-free microstrip balun using metamaterial transmission lines," *IEEE Microwave and Wireless Components Letters*, Vol. 18, No. 7, 437–439, 2008.
4. Caloz, C. and T. Itoh, "Novel microwave devices and structures based on the transmission line approach of meta-materials," *2003 IEEE MTT-S International Microwave Symposium Digest*, Vol. 1, 195–198, 2003.
5. Sanada, A., C. Caloz, and T. Itoh, "Novel zeroth-order resonance in composite right/left-handed transmission line resonators," *Proc. Asia-Pacific Microwave Conf.*, 1588–1591, 2003.
6. Li, C., K. Y. Liu, and F. Li, "Composite right/left-handed coplanar waveguide band-pass filter using capacitively-coupled zeroth-order resonators," *Applied Physics A: Materials Science & Processing*, Vol. 87, No. 2, 317–319, 2007.
7. Gong, J.-Q. and Q.-X. Chu, "Miniaturized microstrip bandpass filter using coupled SCRLH zeroth-order resonators," *Microwave and Optical Technology Letters*, Vol. 51, 2985–2989, Dec. 2009.
8. Li, C. and F. Li, "Microstrip bandpass filters based on zeroth-order resonators with complementary split ring resonators," *IET Microwaves, Antennas & Propagation*, Vol. 3, No. 2, 276–280, 2009.

Substrate Integrated Waveguide (SIW) Filters and Its Application to Switchable Filters

Q.-Y. Xiang, Q.-Y. Feng, X.-G. Huang, and D.-H. Jia

School of Information Science and Technology
Southwest Jiaotong University, Chengdu, Sichuan 610031, China

Abstract— In this paper, novel substrate integrated waveguide (SIW) and half mode substrate integrated waveguide (HMSIW) structures for bandpass filter and switchable bandpass filter applications are proposed. The SIW resonators are realized by etching the electrical coupled complementary resonators on the surface of waveguide, and the resonances are generated below the characteristic waveguide cut-off frequency. Lumped equivalent circuit analysis models are developed. The half mode configuration of the proposed SIW bandpass filter is open structure, and this kind of HMSIW filter is easy to load with the control elements. By using a floating capacitor with mechanical switches loaded on the HMSIW resonators, a 1-bit HMSIW switchable bandpass filter is demonstrated. The simulated and measured results for the filter are provided. The prototype with compact core size of $16\text{ mm} \times 12\text{ mm}$ was designed and fabricated so as to validate the new structure. The measured central frequency is 2.1 GHz and 2.6 GHz, the fractional bandwidth is 7.3% and 7.6%, and the insertion loss is 2.5 dB and 1.5 dB, at switch-on state and switch-off state, respectively.

1. INTRODUCTION

Recently, new guided wave structures called substrate integrated waveguide (SIW) and the half-mode substrate integrated waveguide (HMSIW) which can be synthesized on a planar substrate have been used for implementing planar resonator and filter applications with the features of good power capability, high Q factor, low cost and compact volume size comparable to that of the bulky waveguide based implementations [1–4]. The concept of HMSIW is attractive for filter design since it has been proposed aiming at a further reduction of the size of the SIW, and more importantly, it is very convenient to etch the tunable elements on the waveguide surface of HMSIW. Complementary split ring resonators (CSRRs) are sub-wavelength planar structure introduced by Falcone as new metamaterial resonators, and it can be viewed as electric dipole. According to the theory of evanescent mode propagation or a waveguide loaded by electric dipoles, a passband below the waveguide cutoff frequency can be obtained by loading the CSRRs. Both SIW and HMSIW are suitable for loading the CSRRs on the waveguide surface, therefore, the SIW/HMSIW loaded complementary resonators such as CSRRs will be suitable for bandpass filter design [5].

With the rapid development of broadband, multi-protocol, and cognitive radios, the wireless transceivers need to break through the traditional communication standard of the fixed pattern, such as central frequency and bandwidth, and build multi-mode wireless links to improve anti-interference ability, increase spectrum utilization, expand the communication capacity and quality of service (QoS) [6]. As microwave components including microwave filters are the key to constitute the radio interface of wireless equipment, reconfigurable microwave filter will have special significances in future wireless systems [7, 8]. In this paper, SIW and HMSIW loaded with CSRRs achieve forward electromagnetic wave transmission below the waveguide cutoff frequency due to evanescent wave amplification, and novel mechanical reconfigurable BPF was proposed. The filters were designed, fabricated and measured, and the attractive performances are validated theoretically and experimentally.

2. SIW/HMSIW BANDPASS FILTERS

Figure 1 shows the layout and photograph of the proposed BPF based on SIW/HMSIW loaded by coupled CSRRs. A pair of CSRRs is etched in the center of the top metal plane. The coupling effects of the two CSRRs are dominated by the electric coupling, and resonant frequency splitting can be occurred due to electric coupling of the two resonators, which is determined by the gap of the two CSRRs in Figure 1. To analyze the performances of the proposed BPF, Rogers RT/Duroid 5880 substrate with a thickness of 0.508 mm and a relative permittivity of 2.2 is used in our design.

The transmission responses for the filter are simulated and investigated by full-wave Electromagnetics (EM) Software, as shown in Figure 2. The measurement is accomplished with Agilent

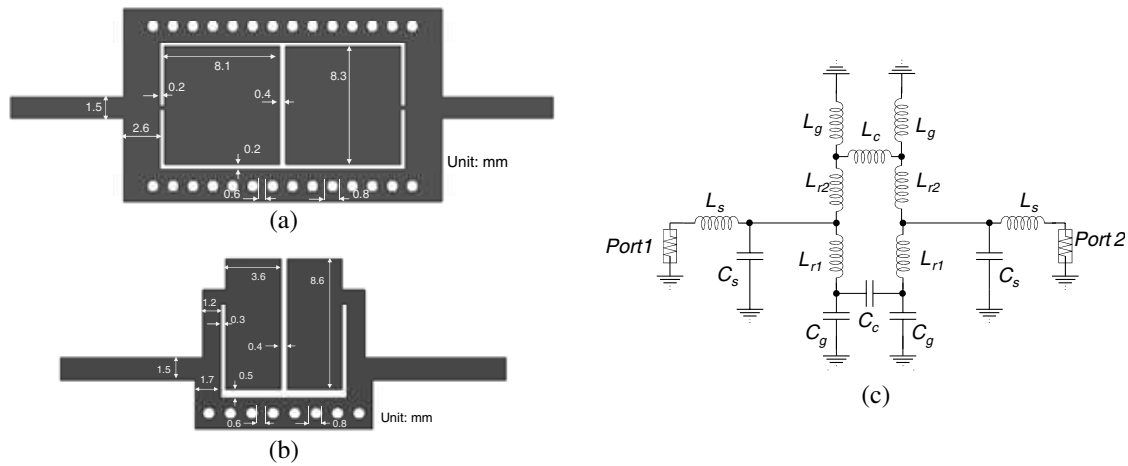


Figure 1: Layout and the geometry parameters of the SIW/HMSIW bandpass filter: (a) SIW, (b) HMSIW, (c) lumped equivalent circuit model.

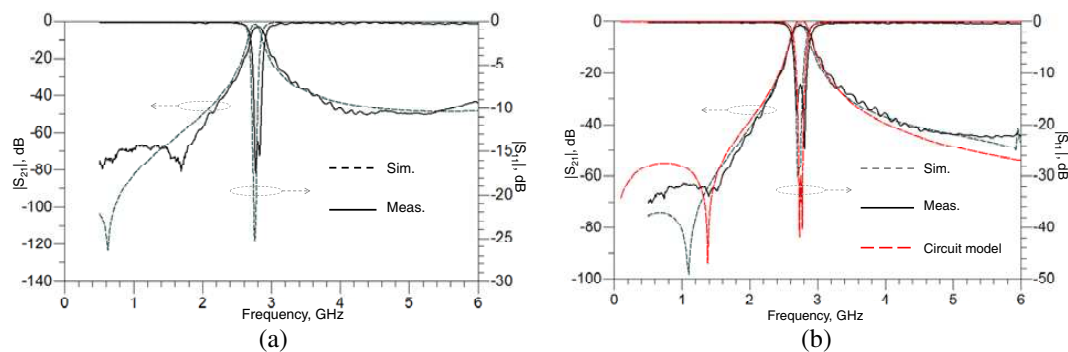


Figure 2: S -parameters of the proposed BPF with different gaps: (a) SIW, (b) HMSIW.

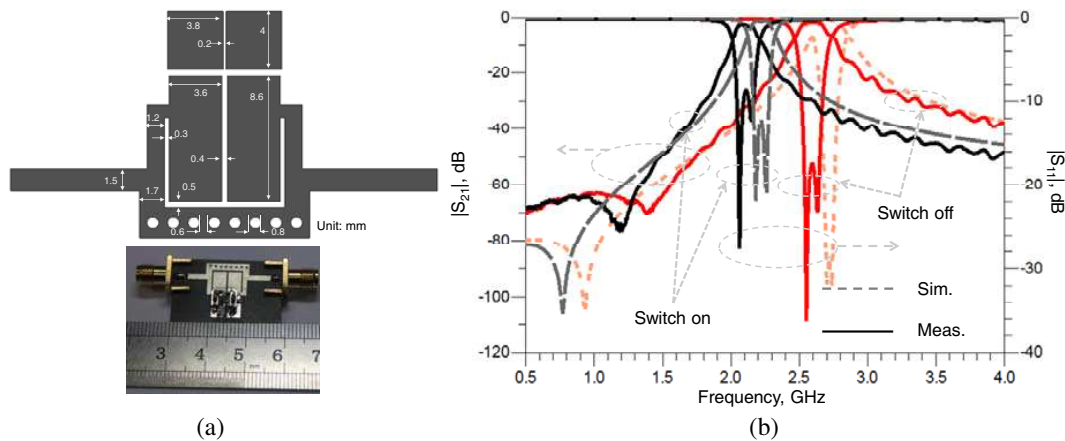


Figure 3: Layout and the frequency responses of the HMSIW mechanical reconfigurable bandpass filter: (a) layout and photograph, (b) frequency responses.

E5071C network analyzer. The SIW filter has a measured central frequency of 2.8 GHz and a -3 dB bandwidth of 165 MHz. The insertion loss is approximately 2.98 dB, which includes the extra loss caused by the subminiature A (SMA) connectors. Its return loss at center frequency is better than -15 dB, and the high-side stop-band rejection is better than -40 dB. The HMSIW filter has a measured central frequency of 2.76 GHz and a -3 dB bandwidth of 235 MHz. The insertion loss is approximately 1.32 dB, and the high-side stop-band rejection is better than -40 dB. By using the curve-fitting technology we have extracted the parameters $L_s = 5$ nH, $C_s = 0.45$ pF, $L_{r1} = 1.1$ pF,

$C_g = 1.31$ pF, $L_c = 15$ nH, $C_c = 0.095$ pF, $L_g = 0.5$ nH, and $L_{r2} = 0.82$ nH respectively from the equivalent circuit model network in Figure 1(c). It shows that the circuit model, EM simulated results and measured results match each other very well, therefore the equivalent circuit model is basically correct and is fully capable of explaining the frequency responses of the structure.

3. ONE-BIT MECHANICAL RECONFIGURABLE BANDPASS FILTER

By studying the equivalent circuit model in Figure 1(c), the passband can be adjusted by tuning the resonator capacitor C_g . To confirm and demonstrate the reconfigurable characteristics of the stop-band, two $3.8 \text{ mm} \times 4 \text{ mm}$ metal planes are used as the reconfigurable floating capacitors, as shown in Figure 3(a). The mechanical reconfigurable HMSIW BPF prototype with compact core size of $16 \text{ mm} \times 12 \text{ mm}$ was designed and fabricated. Figure 3(b) shows the measured s -parameters of the mechanical reconfigurable HMSIW BPF. The measured central frequencies were 2.1 GHz and 2.6 GHz, the fractional bandwidth were 7.3% and 7.6%, and the insertion loss were 2.5 dB and 1.5 dB, in switch on and off states, respectively.

4. CONCLUSIONS

Novel substrate integrated waveguide (SIW) and half mode substrate integrated waveguide (HMSIW) structures for bandpass filter and mechanical switchable bandpass filter applications are proposed in this paper. The SIW resonators are realized by etching the electrical coupled complementary resonators on the surface of waveguide, and the resonances are generated below the characteristic waveguide cut-off frequency. Lumped equivalent circuit analysis models are developed. The half mode configuration of the proposed SIW bandpass filter is open structure, and this kind of HMSIW filter is easy to load with the control elements. By using a floating capacitor with mechanical switches loaded on the HMSIW resonators, a 1-bit HMSIW switchable bandpass filter is demonstrated. The measured central frequency is 2.1 GHz and 2.6 GHz, the fractional bandwidth is 7.3% and 7.6%, and the insertion loss is 2.5 dB and 1.5 dB, at switch-on state and switch-off state, respectively.

ACKNOWLEDGMENT

This work is supported by the National Natural Science Foundation of China (NSFC) under Grant 60990320, 60990323, and the National 863 Project of China under Grant 2012AA012305.

REFERENCES

1. Zhang, Q. L., W.-Y. Yin, S. He, and L.-S. Wu, "Evanescent-mode substrate integrated waveguide (SIW) filters implemented with complementary split ring resonators," *Progress In Electromagnetics Research*, Vol. 111, 419–432, 2011.
2. Lin, S., S. Yang, A. E. Fathy, and A. Elsherbini, "Development of a novel UWB Vivaldi antenna array using SIW technology," *Progress In Electromagnetics Research*, Vol. 90, 369–384, 2009.
3. Song, Q., H. R. Cheng, X. H. Wang, L. Xu, X. Q. Chen, and X. W. Shi, "Novel wideband bandpass filter integrating HMSIW with DGS," *Journal of Electromagnetic Waves and Applications*, Vol. 23, Nos. 14–15, 2031–2040, 2009.
4. Shen, W., W.-Y. Yin, X.-W. Sun, and J.-F. Mao, "Compact coplanar waveguide-incorporated substrate integrated waveguide (SIW) filter," *Journal of Electromagnetic Waves and Applications*, Vol. 24, No. 7, 871–879, 2010.
5. Park, W. Y. and S. Lim, "Bandwidth tunable and compact band-pass filter (BPF) using complementary split ring resonators (CSRRL) on substrate integrated waveguide (SIW)," *Journal of Electromagnetic Waves and Applications*, Vol. 24, Nos. 17–18, 2407–2417, 2010.
6. Berezdivin, R., R. Breinig, and R. Topp, "Next-generation wireless communications concepts and technologies," *IEEE Communications Magazine*, Vol. 40, No. 3, 108–116, 2002.
7. Ishak, W. S. and K. W. Chang, "Tunable microwave resonators using magnetostatic wave in YIG films," *IEEE Transactions on Microwave Theory and Techniques*, Vol. 34, No. 12, 1383–1393, 1986.
8. Sekar, V., M. Armendariz, and K. Entesari, "A 1.2-1.6-GHz substrate-integrated-waveguide RF MEMS tunable filter," *IEEE Transactions on Microwave Theory and Techniques*, Vol. 59, No. 4, 866–876, 2011.

High Power Autonomous Pulse-train UWB Source

V. E. Fortov, Yu. I. Isaenkov, V. M. Mikhailov, E. V. Nesterov, V. E. Ostashev,
Yu. V. Semenov, and V. A. Stroganov

Joint Institute for High Temperatures of RAS (JIHT RAS), Russia

Abstract— The design and characteristics of powerful nanosecond UWB pulse source intended for study of particular electromagnetic compatibility problems are given. For excitation of UWB source we use high voltage drive-pulse generator based on resonance transformer. Power supply is a set of nickel metal hydride rechargeable batteries. Designed source of radiation is characterized by the following parameters: voltage output of the generator is approximately $U_G \approx 550$ kV, field range product ($FRP = E \times R$) equals to 300 kV (with reflector 670 kV approx.), effective radiated power (ERP) is approximately 3 GW (15 GW). Peak energy spectrum at the frequency of 0.3 GHz is 17 mJ/MHz. Pulse-repetition frequency is adjusted within 0 to 1 kHz range. Parabolic reflector is about $1.2 \times 1.2 \times 0.6$ m overall. The source as a whole is combined into monoblock of 1 m high and 0.24 m in diameter. Total weight of the source is 65 kg approximately.

1. INTRODUCTION

Nowadays, electronic devices have a deep impact upon human life; they monitor the sophisticated engineering procedures and lie at the heart of modern communications and management. Therefore, such system and devices must be very stable in operation, even under occasional or intentional electromagnetic interferences which can result in different system malfunctions.

Stability of operation of electronic systems is a subject of proper design and fabrication [1]. However, for its practical confirmation the verification nature test is necessary, which requires design of powerful electromagnetic interference systems.

There are some publications concerning existing and prospective generators of powerful electromagnetic pulses with FRP above 100 kV, in that number the works [2, 3]. In the paper [4], where a phased array was used as an emitting antenna, FRP value achieved 0.69 MV. In the report, we present results of design of compact autonomous mobile device including antenna made up of two dipoles working in synchronism with each other.

2. DEVICE DESCRIPTION

Power supply of all components of the generator is a set of 12 (twelve) LiFePo₄ 38120p, 3.2 V, 8 A · h rechargeable batteries. For excitation of antenna system made up of two Hertz dipoles a high-pressure hydrogen spark-gap switch with discharge voltage of ~ 550 kV is used. This voltage is generated by two-stage voltage converter.

The first stage is a classical push-pull DC-DC voltage converter 40 V/10 kV based on a pulse transformer with ferrite core. It is used for charging of two capacitive storages at the second stage of voltage conversion 10 kV/550 kV.

Every capacitive storage of the second stage of conversion is loaded into corresponding primary winding of two Tesla transformers with magnetic coupling coefficient equal $k = \frac{M}{\sqrt{L_1 L_2}} = 0.6$. The load for Tesla transformers is stray capacitance of dipoles.

For exact phasing of Tesla transformers operation the capacitive storages are switched by a single cell-type tube with operating voltage of 10 kV. Typical waveform of voltage on the capacitive storages of Tesla transformers in working conditions is shown in Fig. 1. Voltage pulse repetition rate is adjusted by variation of current-free interval set by controller of DC-DC converter.

Figure 2 shows waveforms of output voltages of Tesla transformers (curves 1 and 2) and differential voltage on the antenna section (curve 3). Secondary windings of the transformers are connected in opposition, so for output voltage equal 275 kV on the every winding the differential voltage is 550 kV.

Capacitive divider formed naturally by stray capacitances is responsible for steady voltage distribution over components of antenna part. Electric strength of emitting antenna is available by sulfur hexafluoride (SF₆ gas) at the pressure of 6 atm in the main section of the generator.

For pulse repetition frequency equal 400 Hz the emitter consumes power of 2.9 kW, that is about 7.2 J for one pulse. Energy delivered to the antenna is 2.7 J approximately, so the energy efficiency of pulsed excitation system is about $\sim 38\%$.

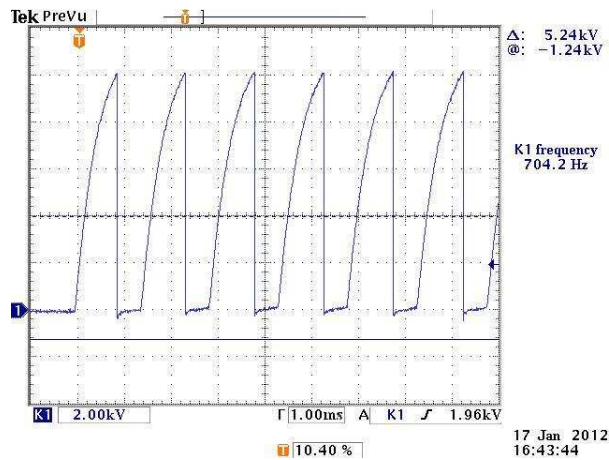


Figure 1: Voltage on the capacitive storages of Tesla transformer.

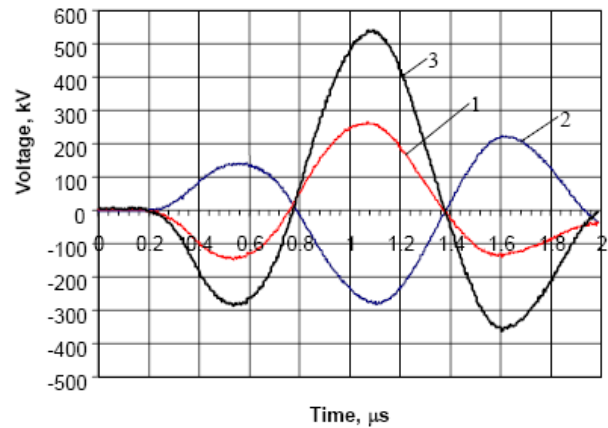


Figure 2: Output voltage of Tesla transformers and differential voltage on the antenna section.



Figure 3: UWB source at the stand for diagnostics of radiated pulsed power.

The general view of the generator under the measurement of parameters of radiated pulses is shown in Fig. 3.

3. MEASUREMENTS OF RADIATION PARAMETERS

Radiation parameters were measured in the shielded room 4.5 m high and 15×6 m in the base.

Pulsed electric field sensor was placed 10 m apart from the UWB source at the radiation axis. The source was properly positioned in the room to make possible recording of the direct radiated pulse during 5 ns.

Pulsed electric field sensor was made on the basis of strip line matched to the impedance of the sensor voltage recording path. Sensitivity of the probe is $0.7 \text{ V}/(\text{kV}/\text{m})$ approximately, rise-time of its transient response — 60 ps and allowable record time — about 5 ns. Pulsed voltage on the sensor was recorded by the digital oscilloscope TDS6604B (sampling 20 Gs/s).

Characteristic waveform of the radiated pulse given as a field range product is shown in Fig. 4. Frontal zone of radiated pulse follows direct radiation of the dipole. Peak value of this part of the waveform is $FRP \approx 0.3 \text{ MV}$, its length is about 0.8 ns at the half of the local peak voltage.

FRP parameter is determined by the maximum driving voltage on antenna. Indeed, if electric pulse excites long dipole then the electric field wave propagates through this dipole with speed c and induced current I . The length of the graded region of current wave is $c\tau$ and the current rate — I/τ . Under such conditions

$$FRP \approx 2 \times \frac{\mu_0(c\tau)}{4\pi} \dot{I} = \frac{\mu_0(c\tau)}{2\pi} \cdot \frac{I}{\tau} = 60I \approx 60U_{exc}/R_{DIP}, \quad (1)$$

that is, FRP of emitting dipole in the traveling wave mode is determined only by the amplitude of this wave (here $c \cdot \mu_0 = 120\pi$ — characteristic impedance of free space, U_{exc} — dipole driving voltage amplitude, R_{DIP} — dipole impedance).

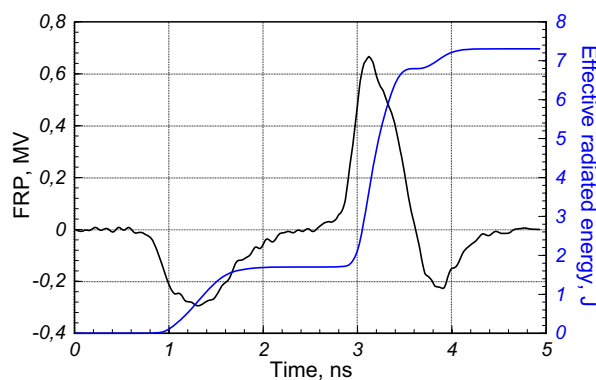


Figure 4: Waveform of electric field and effective energy of radiated pulse.

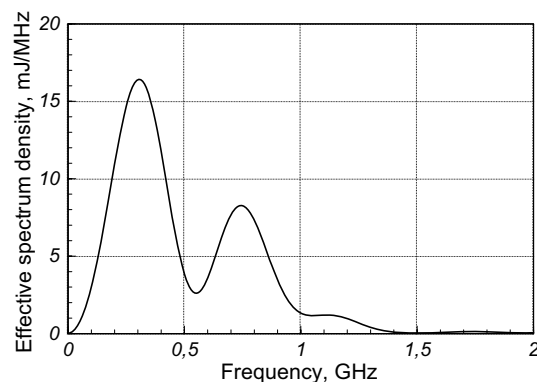


Figure 5: Energy spectrum of radiated pulse (effective value).

Since the emitting dipole driving voltage is $U_{exc} \approx 550$ kV, then for direct radiation of dipoles we have $FRP/U_{exc} \approx 0.55$. Therefore, the effective impedance of dipole antenna of the described UWB source is 110 Ohm approximately.

Amplitude of the signal reflected from the parabolic speculum is $FRP \approx 0.67$ MV and its length (≈ 0.5 ns) is shorter than that for direct pulse. Radiated pulse of such amplitude is characterized by effective power equal 15 GW.

Corresponding effective energy of radiated pulse is also shown in Fig. 4. Its maximum value is 7.5 J approximately. Excitation energy is about 2.7 J, consequently, antenna power gain equals $7.5/2.7 \approx 2.7$.

Energy spectrum of this radiated pulse is given in Fig. 5.

In its pattern the spectrum is a continuous ultra wideband (UWB) one [5]. Its peak value is equal to 17 mJ/MHz approximately at the frequency about 0.3 GHz. Spectrum distribution is a nonmonotonic function due to time shift of main components of the pulse.

4. CONCLUSIONS

Compact UWB source with the following parameters of radiated pulse is developed: $FRP \approx 0.67$ MV, effective radiated pulse power 15 GW, effective amplitude of pulse spectral density 17 mJ/MGHz.

UWB source works in a pulse-repetitive mode of operation.

Self-sufficient operation of the source makes it an efficient tool for simulation of powerful electromagnetic interference in electromagnetic compatibility problems.

REFERENCES

1. Williams, T. and K. Armstrong, *EMC for Systems and Installations*, © Reed Educational and Professional Publishing Ltd, 2000, ISBN 0-7506-4167-3.
2. Sarkar, P., B. Novac, I. Smith, R. Miller, R. Craven, and S. Braidwood, "A high repetition rate UWB source," *Proceedings of XI International Conference on Megagauss Magnetic Field Generation and Related Topics*, 324–327, London, UK, September 2006.
3. Novac, B. and I. Smith, "A 0.5 MV repetitive Tesla-based PFL system," *XIII International Conference on Megagauss Magnetic Field Generation and Related Topics*, Suzhou, China, July 2010.
4. Efremov, A. M., V. I. Koshelev, B. M. Kovalchuk, V. V. Plisko, and K. N. Soukhishin, "Powerful UWB sources with subnanosecond pulse length," *Prybory i tekhnika eksperimenta*, No. 1, 77–83, 2011 (in Russian).
5. Giri, D. V. and F. M. Tesche, "Classification of intentional electromagnetic environments (IEME)," *IEEE Transactions on Electromagnetic Compatibility*, Vol. 46, No. 3, 322–327, 2004.

Dependence of Avalanche Response Time on Photon Flux Incident on DDR Silicon IMPATT Devices

A. Acharyya and J. P. Banerjee

Institute of Radio Physics and Electronics
University of Calcutta, 92, APC Road, Kolkata 700009, India

Abstract— Effect of photo-irradiation on the avalanche response time of Millimeter-wave Double Drift Region (DDR) Silicon Impact Avalanche Transit Time (IMPATT) devices is investigated in this paper. A model to study the photo-irradiation effect on the DC and high-frequency properties of the mm-wave IMPATTs is developed by the authors based on which the simulation is carried out to calculate the avalanche response time of 94 GHz, 140 GHz, 220 GHz and 300 GHz DDR Silicon IMPATTs under two different optical illumination configurations (Top Mount (TM) and Flip Chip (FC)). It is interesting to observe that the DC and high-frequency parameters of the device are more sensitive to electron dominated photo current (TM structure) compared to the hole dominated photo current (FC structure). Results show that the avalanche response time of the device decreases due to optical illumination on both TM and FC structures and percentage of decrease in avalanche response time in TM structure is higher compared to FC structure. For example 7.57% and 3.14% decrease in avalanche response time is observed in TM and FC structure of 94 GHz IMPATT respectively for the incident photon flux density of $10^{26} \text{ m}^{-2} \text{ sec}^{-1}$ at 1000 nm wavelength near band gap absorption of Silicon.

1. INTRODUCTION

The photo irradiation on IMPATT devices leads to optical control of the high frequency properties of these devices. The optical control provides additional control over normal electronic control of the device and is of considerable research interest in view of its application in optoelectronic integrated circuits and phased array antennas for space based communication and imaging. Several optical control functions of the photo-irradiated device such as modulation of RF power, frequency tuning, injection locking have already been experimentally demonstrated [1–3]. The physical mechanism underlying these control functions is generation of photocurrent and consequent enhancement of leakage current in reverse biased device. The avalanche response time [4] of the charge carriers (electrons and holes) is related to the avalanche multiplication process and plays an important role in determining the high frequency performance of the IMPATT device. In this paper, the authors have made an attempt to investigate the effect of optical illumination on the avalanche response time of the charge carriers (electrons and holes) in millimeter-wave DDR Silicon IMPATT devices. A model to study the photo-irradiation effect on the DC and high-frequency properties of the mm-wave IMPATTs is developed based on which the simulation is carried out to calculate the avalanche response time of 94 GHz, 140 GHz, 220 GHz and 300 GHz IMPATTs under two different optical illumination configurations (Top Mount (TM) and Flip Chip (FC)). If τ_{An} and τ_{Ap} be the avalanche response times initiated by electrons and holes respectively, then these are expressed as [4],

$$\tau_{An} = \frac{1}{(v_{sn} + v_{sp})} \int_{-x_{A1}}^{x_{A2}} \exp \left[- \int_{-x_{A1}}^x (\alpha_n - \alpha_p) dx' \right] dx \quad \& \quad \tau_{Ap} = \tau_{An} \exp \left[\int_{-x_{A1}}^{x_{A2}} (\alpha_n - \alpha_p) dx \right] \quad (1)$$

where, $-x_{A1}$ & x_{A2} are the n -side and p -side avalanche layer edges. When avalanche process is initiated by a mixture of electrons and holes then the corresponding response time τ_A is given by [4],

$$\tau_A = \tau_{An} \left\{ (1 - k) + k \cdot \exp \left[- \int_{-x_{A1}}^{x_{A2}} (\alpha_n - \alpha_p) dx \right] \right\}^{-1} \quad (2)$$

where α_n and α_p are the ionization rates of electrons and holes respectively and $k = J_{ps}/J_s$ and $(1 - k) = J_{ns}/J_s$; where $J_s = J_{ps} + J_{ns}$ is the reverse saturation current of the device. Avalanche response times (τ_A) of the DDR IMPATTs based on Silicon can be calculated from Equation (2). Spatial variations of ionization rates of electrons (α_n) and holes (α_p) for each device are obtained from the output of the DC simulation program [5] and used to solve Equations (1) and (2).

2. PROPOSED MODEL FOR ANALYSIS OF IMPATT DEVICES UNDER OPTICAL ILLUMINATION

The optical energy can be fed to the conventional vertical structure of DDR IMPATTs by shining light on either p^+ -side (Top Mounted (TM)) or n^+ -side (Flip Chip (FC)) of the ring contact of mesa device through a controlled optical window [1–3] as shown in Figure 1. In this section, a relationship between incident photo flux density and the normalized difference of electron and hole current density at the depletion layer edges is established. This relation is incorporated in the simulation program to study the effect of optical illumination for different incident photo flux density on the DC and small-signal properties of vertically oriented DDR Silicon IMPATT devices for operation at different millimeter-wave frequencies. If P_{in} watts of optical power is incident on the device having effective device illumination area of A , then the photon flux density Φ_0 is given by,

$$\Phi_0 = P_{in} \frac{(1 - R(\lambda)) \lambda}{A h c} \quad (3)$$

The electron-hole pair generation rate due to optical illumination is given by,

$$G_L(x) = \Phi_0 \alpha(\lambda) \exp(-\alpha(\lambda)x) = P_{in} \frac{\alpha(\lambda)(1 - R(\lambda)) \lambda}{A h c} \exp(-\alpha(\lambda)x) \quad (4)$$

where, $\alpha(\lambda)$ and $R(\lambda)$ are the absorption coefficient (m^{-1}) and reflectance [$R = (n_2 - n_1)/(n_2 + n_1)$; $n_2 =$ refractive index of the semiconductor, $n_1 =$ refractive index of air] of the semiconductor material respectively at a wavelength of λ . The electron and hole multiplication factors at the n - & p -depletion layer edges are given by,

$$M_n = \frac{J_0}{J_{ns(Total)}} \quad \& \quad M_p = \frac{J_0}{J_{ps(Total)}} \quad (5)$$

where, $J_{ns/ps(Total)}$ is the total electron/hole reverse saturation current under optical illumination. Electron and hole reverse saturation currents can have two components. (a) Thermally generated saturation currents. (b) Optically generated saturation currents. Thus,

$$J_{ns(Total)} = J_{ns(Th)} + J_{ns(Opt)} \quad \& \quad J_{ps(Total)} = J_{ps(Th)} + J_{ps(Opt)} \quad (6)$$

The expression for thermally generated electron and hole reverse saturation currents are given by,

$$J_{ns(Th)} = \left[\frac{q D_n n_i^2}{L_n N_A} \right] \quad \& \quad J_{ps(Th)} = \left[\frac{q D_p n_i^2}{L_p N_D} \right] \quad (7)$$

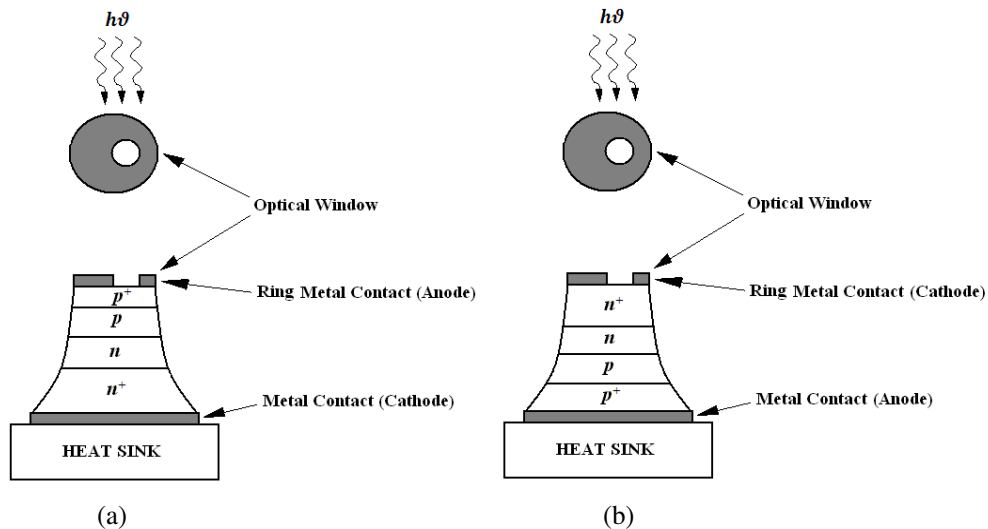


Figure 1: Schematic diagram of (a) Top Mounted (TM) and (b) Flip Chip (FC) vertical DDR IMPATT structures under optical-illumination.

Under dark condition (i.e., when $J_{ns(Opt)} = J_{ps(Opt)} = 0$) both M_n and M_p remain in the order of $\sim 10^6$ [3].

The drift component of the photocurrent density through the reverse-biased depletion layer is given by,

$$J_{(Opt_drift)} = -q \int_{-x_1}^{x_2} G_L(x) dx = qP_{in} \frac{(1 - R(\lambda)) \lambda}{Ahc} \{ \exp(\alpha(\lambda) x_1) - \exp(-\alpha(\lambda) x_2) \} \quad (8)$$

Due to very high conductivity, electric fields at the p^+ - and n^+ -layers are zero. Diffusion components of the photo current are generated within these undepleted p^+ - and n^+ -layers. Diffusion components of the photo current in both n^+ - and p^+ -layers separately can be determined by solving the one-dimensional diffusion equation with proper boundary conditions [6]. The electron and hole diffusion components of the photo current density in both p^+ - and n^+ -layers are given by,

$$J_{ns,ps(Opt_diff)} = qP_{in} \frac{(1 - R(\lambda)) \lambda}{Ahc} \left(\frac{\alpha(\lambda) L_{n,p}}{1 + \alpha(\lambda) L_{n,p}} \right) \exp(-\alpha(\lambda) x_{2,1}) \quad (9)$$

Total photocurrent density is the combination of drift and diffusion components; i.e.,

$$J_{ns,ps(Opt)} = J_{(Opt_drift)} + J_{ns,ps(Opt_diff)} \quad (10)$$

2.1. Top Mounted (TM) Structure

In Top Mounted (TM) structure the light is shined on the p^+ -side of the DDR IMPATT device. Thus the photocurrent density will be electron dominated in an illuminated TM structure. So the electron and hole multiplication factors at the n - & p -depletion layer edges in illuminated TM structure are given by,

$$M'_n = \frac{J_0}{J_{ns(Th)} + J_{ns(Opt)}} \quad \& \quad M_p = \frac{J_0}{J_{ps(Th)}} \quad (11)$$

In this case the value of M'_n is considerably reduced ($\ll 10^6$) while M_p remains unchanged ($\sim 10^6$). Thus the normalized current density boundary conditions at the depletion layer edges are modified to,

$$P(-x_1) = -1 \quad \& \quad P(x_2) = \left(1 - \frac{2}{M'_n} \right) \quad (12)$$

where M_p is very large ($\sim 10^6$) and M'_n is much smaller than M_p . The Equation (12) is used as one of the boundary conditions in the proposed model for simulating the DC and small-signal properties of the illuminated TM structure of DDR IMPATT device. For the illuminated TM structure of DDR IMPATT device the value of k in Equation (2) can be written as,

$$k = \frac{J_{ps(Th)}}{J_{ps(Th)} + J_{ns(Th)} + J_{ns(Opt)}} \quad (13)$$

2.2. Flip Chip (FC) Structure

In Flip Chip (FC) structure the light is shined on the n^+ -side of the DDR IMPATT device. Thus the photocurrent density will be hole dominated in an illuminated FC structure. So the electron and hole multiplication factors at the n - & p -depletion layer edges in illuminated FC structure are given by,

$$M_n = \frac{J_0}{J_{ns(Th)}} \quad \& \quad M'_p = \frac{J_0}{J_{ps(Th)} + J_{ps(Opt)}} \quad (14)$$

In this case the value of M'_p is considerably reduced ($\ll 10^6$) while M_n remains unchanged ($\sim 10^6$). Thus the normalized current density boundary conditions at the depletion layer edges are modified to,

$$P(-x_1) = \left(\frac{2}{M'_p} - 1 \right) \quad \& \quad P(x_2) = 1 \quad (15)$$

Table 1: Structural and doping parameters.

BASE MATERIAL	SERIAL NUMBER	f_d (GHz)	W_n (μm)	W_p (μm)	N_D ($\times 10^{23} \text{ m}^{-3}$)	N_A ($\times 10^{23} \text{ m}^{-3}$)	N_{Sub} ($\times 10^{26} \text{ m}^{-3}$)
Si	1	94	0.4000	0.3800	1.200	1.250	1.0
	2	140	0.2800	0.2450	1.800	2.100	1.0
	3	220	0.1800	0.1600	3.950	4.590	1.0
	4	300	0.1320	0.1120	6.000	7.300	1.0

where M_n is very large ($\sim 10^6$) and M'_p is much smaller than M_n . The Equation (15) is used as one of the boundary conditions in the proposed model for simulating the DC and small-signal properties of the illuminated FC structure of DDR IMPATT device. For the illuminated FC structure of DDR IMPATT device the value of k in Equation (2) can be written as,

$$k = \frac{J_{ps(Th)} + J_{ps(Opt)}}{J_{ps(Th)} + J_{ps(Opt)} + J_{ns(Th)}} \quad (16)$$

3. RESULTS AND DISCUSSION

The active layer widths and background doping concentrations have been designed from a simple transit time formula given by $W_{n,p} = 0.37v_{sn,sp}/f_d$; where $W_{n,p}$, $v_{sn,sp}$ and f_d are the total depletion layer width (n or p -side), saturation velocity of electrons/holes and design frequency respectively, so that the operating frequency of the devices remain nearly 94 GHz, 140 GHz, 220 GHz and 300 GHz. The design parameters of Double Drift Region (DDR) Silicon IMPATT devices are given in Table 1. Using a generalized computer method [5, 7] based on Gummel-Blue approach [8], the DC and small-signal properties of the devices are obtained.

Figure 2 shows the Variation of Breakdown Voltage and DC to RF Conversion Efficiency with Peak Optimum Frequency of mm-wave DDR Si IMPATTs under Dark ($\Phi_0 = 0$) and two Optical Illumination Configurations (TM & FC) for incident photon flux density of $\Phi_0 = 10^{26} \text{ m}^{-2} \text{ sec}^{-1}$ of 1000 nm wavelength. It can be observed from Figure 2 that both the breakdown voltage and efficiency of the device decreases due to the effect of optical illumination. Percentage of reduction in both these parameters is higher at higher frequencies for same incident photon flux density. It is interesting to observe that the reduction in breakdown voltage and efficiency of the device due to same degree of optical illumination (i.e., $\Phi_0 = 10^{26} \text{ m}^{-2} \text{ sec}^{-1}$ of 1000 nm wavelength) is higher in TM structure compared to the FC structure. The same nature can be observed from the Figure 3 in which the peak negative conductances and the RF power output densities (P_{RF}/A_j) are plotted against peak operating frequencies of DDR Si IMPATTs. Photon flux density of $10^{26} \text{ m}^{-2} \text{ sec}^{-1}$ of 1000 nm wavelength causes a decrease of the magnitude of peak negative conductance and the RF power output density by 8.6% and 9.6% respectively for 94 GHz FC Structured DDR IMPATT and a decrease by 13.1% and 18.5% for 94 GHz TM Structured DDR IMPATT respectively. Similarly the same photon flux density leads to a decrease of the magnitude of peak negative conductance and the RF power output density by 20.4% and 29.9% for 300 GHz FC Structured DDR IMPATT and a decrease by 30.5% and 45.0% for 300 GHz TM Structured DDR IMPATT respectively. Thus both the DC and small-signal parameters are more sensitive in electron dominated photo current (TM) compare to hole dominated photo current (FC). The cause of greater electron photo current sensitivity of Si IMPATTs is already explained in earlier paper [3].

Avalanche response time of DDR IMPATTs operating at 94 GHz, 140 GHz, 220 GHz and 300 GHz are calculated by using Equation (2) under dark and two different optical illumination configurations (TM and FC). Variation of avalanche response time with peak operating frequency of DDR Si IMPATTs is plotted in Figure 4. Avalanche response time of the device decreases significantly due to the effect of optical illumination. It can be noted from Figure 4 that the effect of electron dominated photo current (TM) on the avalanche response time of the device is more pronounced compared to hole dominated photo current (FC). For example 7.57% and 3.14% decrease in avalanche response time is observed in TM (electron dominated photo current) and FC (hole dominated photo current) structure of 94 GHz IMPATT respectively for the incident photon flux density of $10^{26} \text{ m}^{-2} \text{ sec}^{-1}$ at 1000 nm wavelength. Figure 5 shows the variation of avalanche response time of illuminated 94 GHz DDR Si IMPATT device with incident photon flux density ($\lambda = 1000 \text{ nm}$) under two Optical Illumination Configurations (TM & FC). So it can be concluded that the avalanche response time

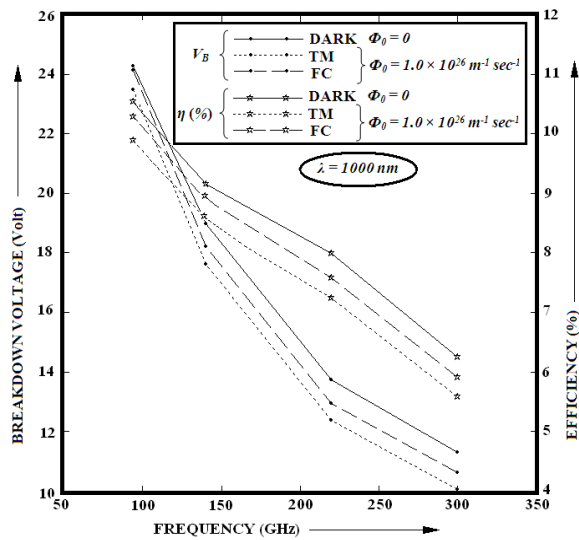


Figure 2: Variation of breakdown voltage and DC to RF conversion efficiency with peak optimum frequency of mm-wave DDR Si IMPATTs under dark and two optical illumination configurations (TM & FC).

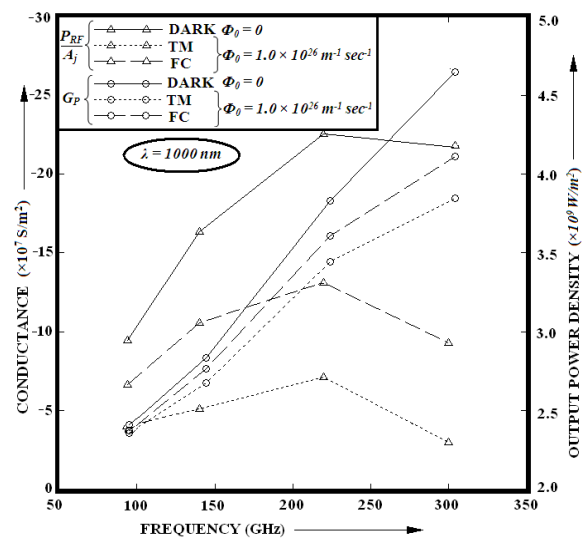


Figure 3: Variation of output power density and peak negative conductance with peak optimum frequency of mm-wave DDR Si IMPATTs under dark and two optical illumination configurations (TM & FC).

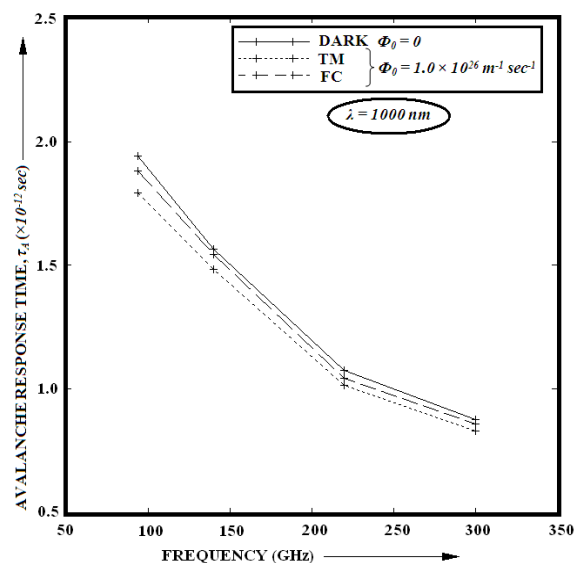


Figure 4: Variation of avalanche response time with peak optimum frequency of mm-wave DDR Si IMPATTs under dark and two optical illumination configurations (TM & FC).

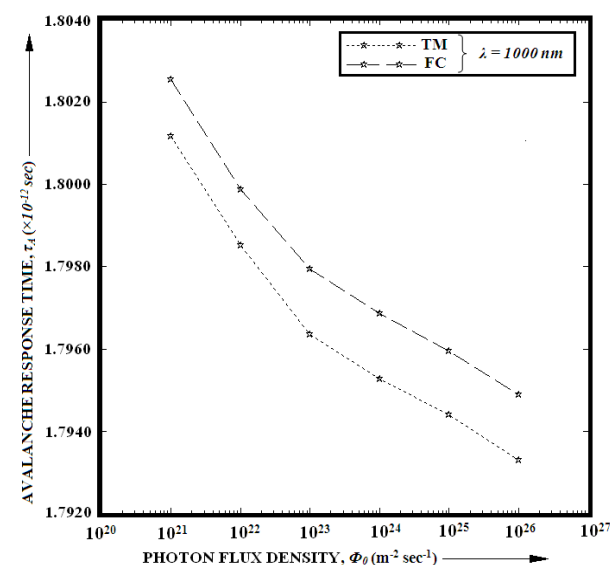


Figure 5: Variation of avalanche response time with incident photon flux density (λ = 1000 nm) of illuminated 94 GHz DDR Si IMPATT under two optical illumination configurations (TM & FC).

of the device decreases as more number of photons are incident of the active layer of the device. Figure 5 clearly shows that the reduction of avalanche response time greater when light is shined on the p^+ -side of the device (i.e., in TM structure) compared to when the light is shined on the n^+ -side of the device (i.e., in FC structure).

4. CONCLUSION

In this paper, the authors have made an attempt to investigate the effect of photo-irradiation on the avalanche response time of Millimeter-wave Double Drift Region (DDR) Silicon IMPATT devices. A model to analyze the effect of photo-irradiation on the DC and high-frequency properties of the mm-wave IMPATTs is developed based on which the simulation is carried out to calculate the avalanche

response time of 94 GHz, 140 GHz, 220 GHz and 300 GHz IMPATTs under two different optical illumination configurations (Top Mount (TM) and Flip Chip (FC)). It is interesting to observe that the DC and high-frequency parameters of the device are more sensitive to electron dominated photo current (TM structure) compared to the hole dominated photo current (FC structure). Results show that the avalanche response time of the device decreases due to optical illumination on both TM and FC structures. The percentage of decrease in avalanche response time in TM structure is higher compared to FC structure. For example 7.57% decrease in avalanche response time is observed in TM structure of 94 GHz IMPATT, whereas the same is only 3.14% in FC structure for the incident photon flux density of $10^{26} \text{ m}^{-2} \text{ sec}^{-1}$ at 1000 nm wavelength near band gap absorption of Silicon. Larger decrement of avalanche response time due to optical illumination in TM structure causes larger deviation of phase shift between RF voltage and terminal current of the device from 180° which is the ideal phase difference between current and voltage for maximum RF power output; this is the main cause of greater reduction in RF power output in TM structure compared to FC structure due to optical illumination which is clearly reflected in the simulation results.

REFERENCES

1. Vyas, H. P., R. J. Gutmann, and J. M. Borrego, "Leakage current enhancement in IMPATT oscillator by photo-excitation," *Electron. Lett.*, Vol. 13, 189–190, 1977.
2. Vyas, H. P., R. J. Gutmann, and J. M. Borrego, "Effect of hole versus electron photocurrent on microwave-optical interactions in impatt oscillators," *IEEE Transactions on Electron Devices*, Vol. 26, No. 3, 232–234, 1979.
3. Acharyya, A. and J. P. Banerjee, "A comparative study on the effect of optical illumination on $\text{Si}_{1-x}\text{Ge}_x$ and Si based DDR IMPATT diodes at W-band," *Iranian Journal of Electronics & Electrical Engineering*, Vol. 7, No. 3, 179–189, 2011.
4. Acharyya, A., S. Banerjee, and J. P. Banerjee, "Calculation of avalanche response time for determining the high frequency performance limitations of IMPATT devices," *Journal of Electron Devices*, Vol. 12, 756–760, 2012.
5. Roy, S. K., M. Sridharan, R. Ghosh, and B. B. Pal, "Computer method for the dc field and carrier current profiles in the IMPATT device starting from the field extremum in the depletion layer," *Proceedings of the 1st Conference on Numerical Analysis of Semiconductor Devices (NASECODE I)*, 266–274, Dublin, Ireland, 1979.
6. Sze, S. M. and K. K. Ng, *Physics of Semiconductor Devices*, Willy, India, 2010.
7. Roy, S. K., J. P. Banerjee, and S. P. Pati, "A computer analysis of the distribution of high frequency negative resistance in the depletion layer of IMPATT diodes," *Proceedings 4th Conf. on Numerical Analysis of Semiconductor Devices (NASECODE IV)*, 494–500, Dublin, Ireland, 1985.
8. Gummel, H. K. and J. L. Blue, "A small-signal theory of avalanche noise in IMPATT diodes," *IEEE Transactions on Electron Devices*, Vol. 14, No. 9, 569–580, 1967.

Universal Filters for Processing of NMR Signals

L. Fröhlich, J. Sedláček, M. Friedl, and R. Kadlec
 FEEC BUT, UTEE, Kolejní 2906/4, Brno 612 00, Czech Republic

Abstract— An analysis of the parameters and usage of universal filters in *NMR* area can be very interesting. In certain cases, there are situations when it is not possible to use standard filters, mainly because of requirements for tuning complete filter or using higher amount of transfer functions, which can be *LP*, *HP*, *BP*, *BR* but also *LPN* or *HPN* and *AP*. For this purpose, there can be used the universal filters which usually contain three and more *OAs*. One of these filter types are *Akerberg-Mossberg* or *Kerwin-Huelsman-Newcomb* circuits.

To be able to use their universality, it is necessary to realize suitable digital processing of their basic parameters of the set filter. These parameters are mainly resonant frequency, quality factor and transfer factor. For processing or tuning of filters it is possible to use digital potentiometers, digitally controlled switchers or other modern active blocks.

This article deals with the usage of these filters by control of their parameters with the help of microprocessor.

1. INTRODUCTION

There are many kinds of universal *ARC* filters and in most cases these filters can realize transfer function $H(s)$ in biquad form below:

$$H(s) = K \frac{N(s)}{D(s)} = K \frac{b_2 s^2 + b_1 s + b_0}{a_2 s^2 + a_1 s + a_0} = K \frac{s^2 + s\omega_z/Q_z + \omega_z^2}{s^2 + s\omega_0/Q_0 + \omega_0^2}. \quad (1)$$

One of the most used universal circuits in practice is *Akerberg-Mossberg*, *Kerwin-Huelsman-Newcomb*. The first two listed filters enable current realization of filters of type low-pass, high-pass, band-reject, band-pass, but also other transfer functions as low-pass or high-pass notch and all-pass. From transfer function (1), with the help of the software *SNAP* it is possible to derive the formulas for f_0 , f_N , Q , K_0 for both filters as we can see in next chapter. The tuning for these filters is realized by parallel change of elements R_1 and R_2 for tuning inside frequency decade and capacitors C_1 and C_2 for tuning between decades. Both filters are characterized by an independent setting of individual parameters and by usage of the band up to 10 MHz. Below stated filters and their qualities will be mainly compared with these filters, which already found their usage in practice.

2. PROPERTIES OF THESE FILTERS

Reported filters are showed in Fig. 1 and Fig. 2. With the help of special program it is possible to derive next formulas for both filters.

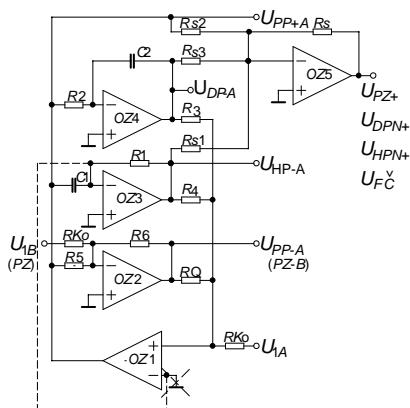


Figure 1: *A-M* modification block.

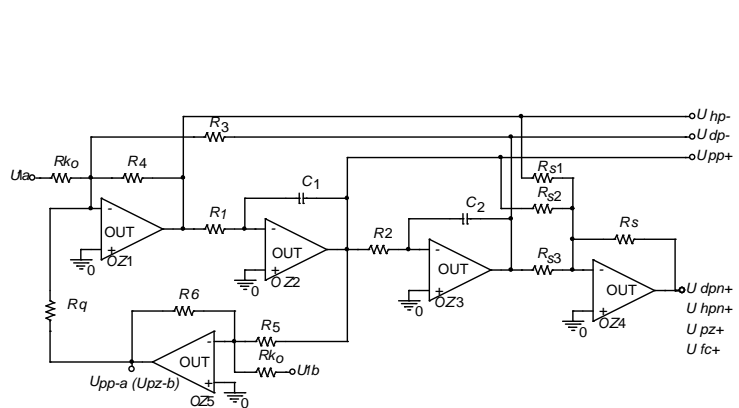


Figure 2: *K-H-N* universal block.

First, we will define the denominator $D(s)$ for both filters with 5OAs

$$D(s) = s^2 + s \frac{R_a}{R_Q R C} + \frac{1}{C^2 R^2}. \tag{2}$$

In case of use $K-H-N$ filter in variant without $OA5$ then we must define next formula with influence Q on K_0

$$D(s) = s^2 + s \frac{R_{Q1} (R_3 R_4 + R_3 R_{K0} + R_4 R_{K0})}{R_1 R_3 R_{K0} (R_{Q1} + R_{Q2}) C_1} + \frac{1}{C^2 R^2}. \tag{3}$$

In the case of optimized $A-M$ circuits are circuit elements chosen according equations (the same procedure is for $K-H-N$ circuit)

$$C_1 = C_2 = C, \quad R_1 = R_2 = R, \quad R_3 = R_4 = R_5 = R_6 = R_a. \tag{4}$$

Then we can determine Q -factor for both filters see Formula (5). For $K-H-N$ filter with 4OAs is Formula (6).

$$Q_{A-M(K-H-N)} = \frac{R_Q}{R_a}. \tag{5}$$

$$Q_{K-H-N} = \frac{R_{Q1} R_{Q2}}{R_a + 2R_{K0}}. \tag{6}$$

The numerators $N(s)$ from (1) are given different types of filter transfer functions of $K-H-N$ circuit as well as $A-M$ circuits then can be given by the same Formulas (7)–(11)

$$N_{LP}(s) = \omega_0^2, \tag{7}$$

$$N_{HP}(s) = -s^2, \tag{8}$$

$$N_{BP}(s) = s\omega_0, \tag{9}$$

$$N_{BH}(s) = R_s \left(s^2 \frac{R_s}{R_{s1}} + \frac{R_s \omega_z}{R_{s3}} \right), \tag{10}$$

$$N_{AP}(s) = R_s \left(s^2 \frac{1}{R_{s1}} - S \frac{\omega_0}{R_{s2}} + \frac{\omega_0^2}{R_{s3}} \right). \tag{11}$$

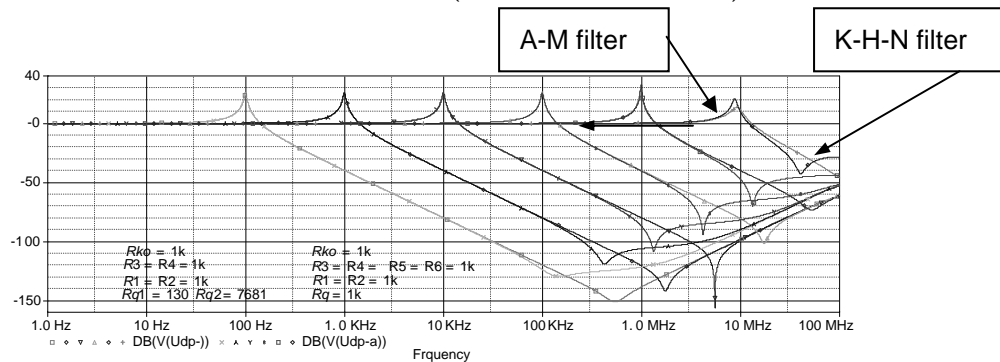


Figure 3: Comparison of $A-M$ and $K-H-N$ filters, low-pass $Q = 20$ and $K = 1$.

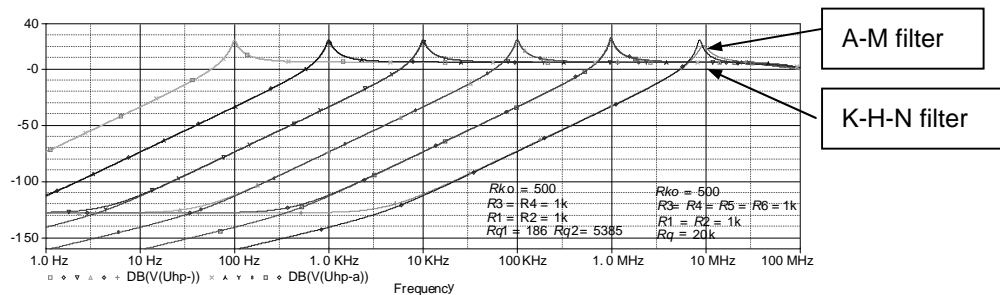


Figure 4: Comparison of $A-M$ and $K-H-N$ filters, high-pass $Q = 10$, $K = 6$.

When we look at the comparison of Q -factor in the Formulas (5), (6), we can say that the filter $A-M$ enables much easier setting of Q -factor than the filter $H-K-N$ (with only 4OAs). The second advantage of above presented modification of $A-M$ circuit is in wider and more accurate usable frequency range than $K-H-N$ filter. See the Figures 3 and 4.

Figures 5 and 6 present comparison of both filters with $Q = 10$ and using of ideal OA and real OA of type $CLC420$. It is obvious that the filter $A-M$ has smaller relative deviation then $K-H-N$ filter.

If we want to make use of digital tuning for this filter, we have to replace resistors R_1 and R_2 by the digital potentiometer, and capacitors C_1 and C_2 by the multiplexers. The multiplexers,

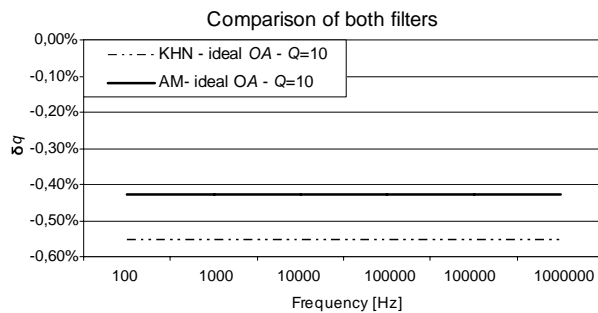


Figure 5: Comparison of both filters for ideal OA.

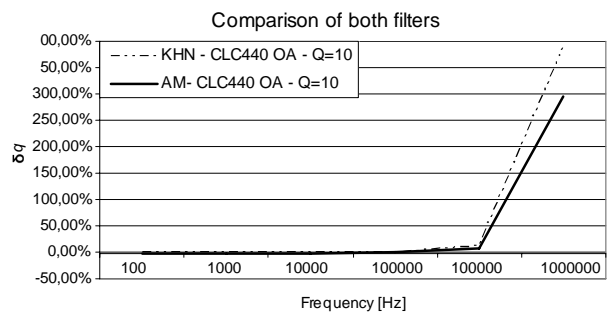


Figure 6: Comparison of both filters for real OA.

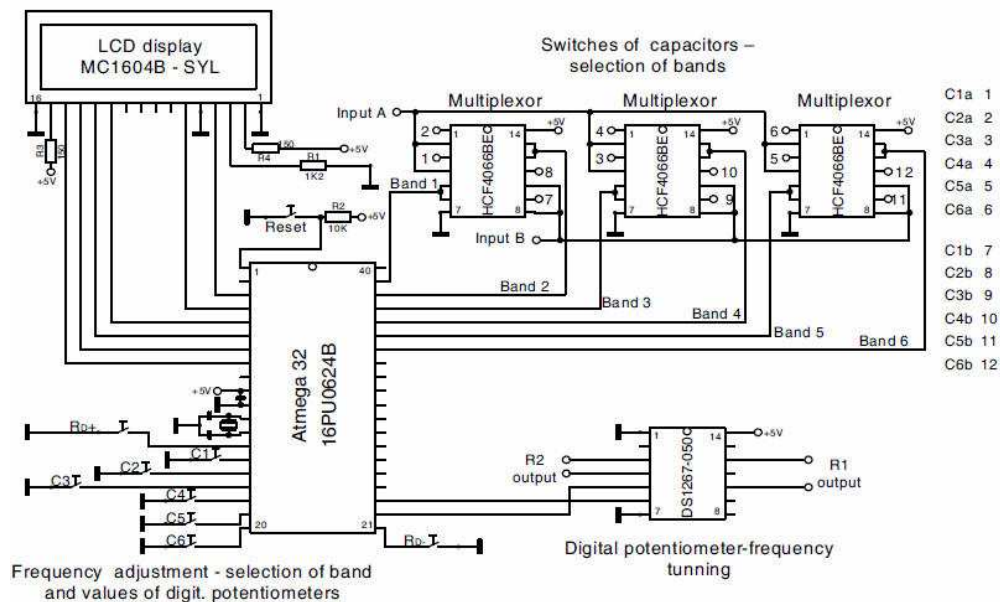


Figure 7: Main part of microprocessor control of the universal adaptive filter.

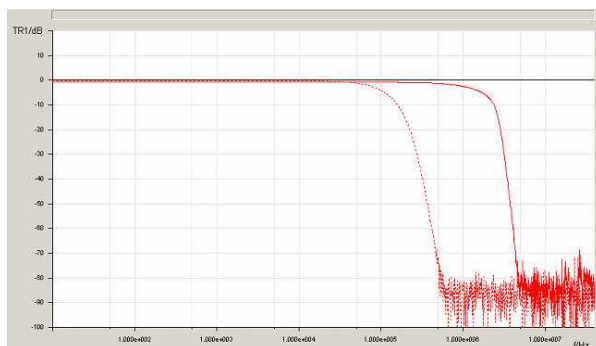


Figure 8: LP — Bessel 10. order, OPA656U.

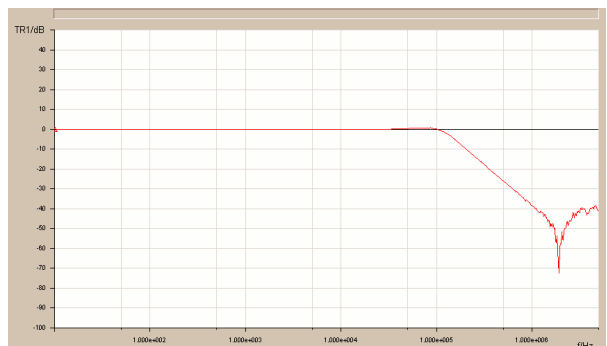
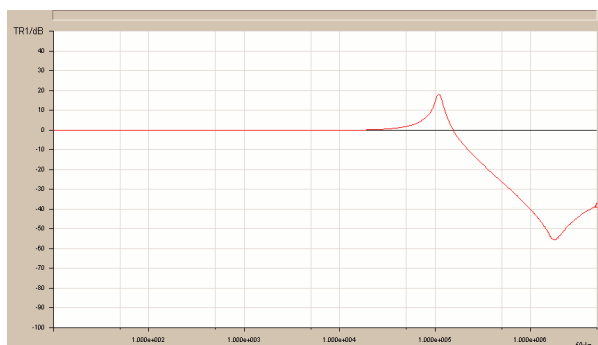
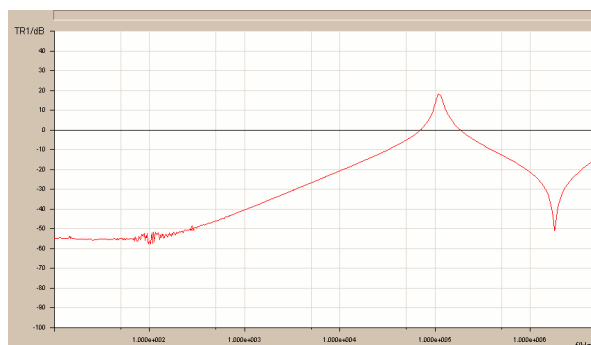


Figure 9: LP — 100 kHz, $Q = 1$, OPA656U.

Figure 10: LP — 100 kHz, $Q = 20$, *OPA656U*.Figure 11: BP — 100 kHz, $Q = 1$, *OPA656U*.

digital potentiometer and other electronic elements are tuned by the microprocessor *ATMEGA32*. Individual requirements from the user are set with the help of a keyboard and these commands are displayed on *LCD* display. The complex tuning can be seen on the Figure 7.

This universal biquad block is able to fulfil many special requirements on tuning of filter parameters or adaptive switchable filter options. The filter has a lot of output transfer functions which can be used in wide band from 10 Hz to 10 MHz with digital tuning of parameters Q -factor, transmission constant K_0 , frequency f_0 . The example of measurement of the low-pass of the *A-M* can be seen on the Figures 8–11.

3. CONCLUSIONS

This article presents some basic information about properties of modified *A-M* filter and *K-H-N* filter. These properties could be gained by the software *SNAP* which helped me with the creating of basic formulas of both filters. Other part compares these two types of filters in terms of individual simulations. By the help of these simulations, it was possible to create graphs which show relative deviation of the filters for resonant frequency f_0 and Q -factor. At the end, it can be said that *A-M* filter has better properties for both resonant frequency f_0 and Q -factor than *K-H-N*. *A-M* filter has much easier tuning Q -factor only with the help of resistor R_q . The whole design of filter was created for the frequency band from 10 Hz to 10 MHz using digital potentiometer. Switching of capacitors C_1 , C_2 and also choice of frequency decade was realized with the help of multiplexer. For the realization of the filter, *OAs CLC420* were used, it enables working on the resonant frequency around 1 MHz. Next increasing of the frequency leads to the deformation of the transfer functions. The following step will be creating of the filter enabling realization up to 10th orders with the use of *D/A* convertor.

ACKNOWLEDGMENT

The research described in the paper was financially supported by grant of Czech ministry of industry and trade No. FR-TI1/001, GACR 102/09/0314 and project of the BUT Grant Agency FEKT-S-11-15.

REFERENCES

1. Sedláček, J., K. Hájek, *Kmitočtové Filtry*, 1, vydání, Praha: BEN — Technická Literatura, 535, 2002, ISBN 80-7300-023-7.
2. Dostál, T., “Elektrické filtry,” Skripta FEI VUT, Brno, 1999.
3. Ghauri, M. S. and K. R. Laker, *Modern Filter Design*, Practice Hall, New Persey, 1981.
4. Chen, W. K., *The Circuits and Filters Handbook*, CRC Press, Florida, 2000.
5. Galiamichev, I. P., A. A. Lanne, V. Z. Lundin, and V. A. Petrakov, “The synthesis of active RC network,” 296, *Izdatel'stvo Sviaz'*, Moscow, Russia, 1975.
6. Frohlich, L., “Properties and comparison of akerberg-mossberg and kerwin-huelsman-newcomb filters,” *Student EEICT 2010*, 1–5, 2010, ISBN: 978-80-214-3870-5.

Design of an Effective Architecture for the Envelope Tracking Power Amplifier for LTE Applications

S. H. Kam¹, O. S. Kwon¹, and Y. H. Jeong^{1,2}

¹Department of Electrical Engineering

Pohang University of Science and Technology, Pohang, Gyeongbuk 790-784, Republic of Korea

²Department of Creative IT Excellence Engineering

Pohang University of Science and Technology, Pohang, Gyeongbuk 790-784, Republic of Korea

Abstract—This paper reports an effective architecture for the envelope tracking (ET) transmitter using an emitter follower. To achieve the stable circuit and high efficiency, an emitter follower which can sub for the role of the tantalum capacitor is used at the drain network. For verification, the proposed ET power amplifier (PA) is implemented with a 25 W class-AB PA and tested using continuous wave (CW) and LTE signals at 2.6 GHz. From the measured results for the LTE signal, the drain efficiency of 38.3% is achieved at an output power of 34 dBm, which is a 10 dB back-off region. After the digital predistortion (DPD) linearization, the proposed ET PA also shows the significant linearity improvement.

1. INTRODUCTION

As devices such as smart phones and tablet PCs come into wide use, modern wireless communication system requires high linearity and efficiency to use complex modulated signals such as worldwide interoperability for microwave access (WiMAX) and long term evolution (LTE) signals. For high linearity, recently, digital predistortion (DPD) technique has been widely investigated because of several merits of simple circuitry and excellent linearity improvement [1–4]. For high efficiency, various efficiency-boosting methods such as Doherty power amplifiers (PAs), switching PAs and envelope tracking (ET)/envelope elimination and restoration (EER) transmitter have received attention and developed [2–9].

Among them, ET transmitter is regarded as the promising solution because of its potential for high efficiency, which results from the fact that the PA can be operated under compression at nearly all power levels [7–9]. In the ET transmitter design process, however, the bias fluctuation effect at the drain network needs to be considered. Because nonlinear characteristics are not controlled by removing the tantalum capacitor at the drain.

In this paper, we propose an effective architecture for the ET transmitter using an emitter follower. By inserting an emitter follower which can sub for the role of the tantalum capacitor at the drain, the ET transmitter can be stable as well as achieves high efficiency performance. For experimental verification, the proposed ET PA has been implemented with a 25 W class-AB PA and tested using the LTE signal at 2.6 GHz. The measured results show clearly that the proposed ET PA has high efficiency performance and good digital predistortion (DPD) linearization performance.

2. ENVELOPE SIGNAL INJECTION CONSIDERATION

Figure 1(a) shows the drain network of the conventional PA. The tantalum capacitor is in charge of controlling the second harmonic and prevents that the PA has a severe memory effect creating

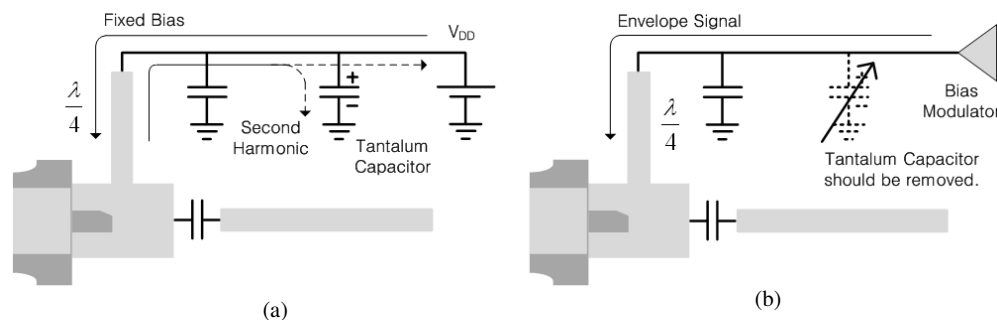


Figure 1: Drain network of (a) the conventional PA and (b) the ET transmitter.

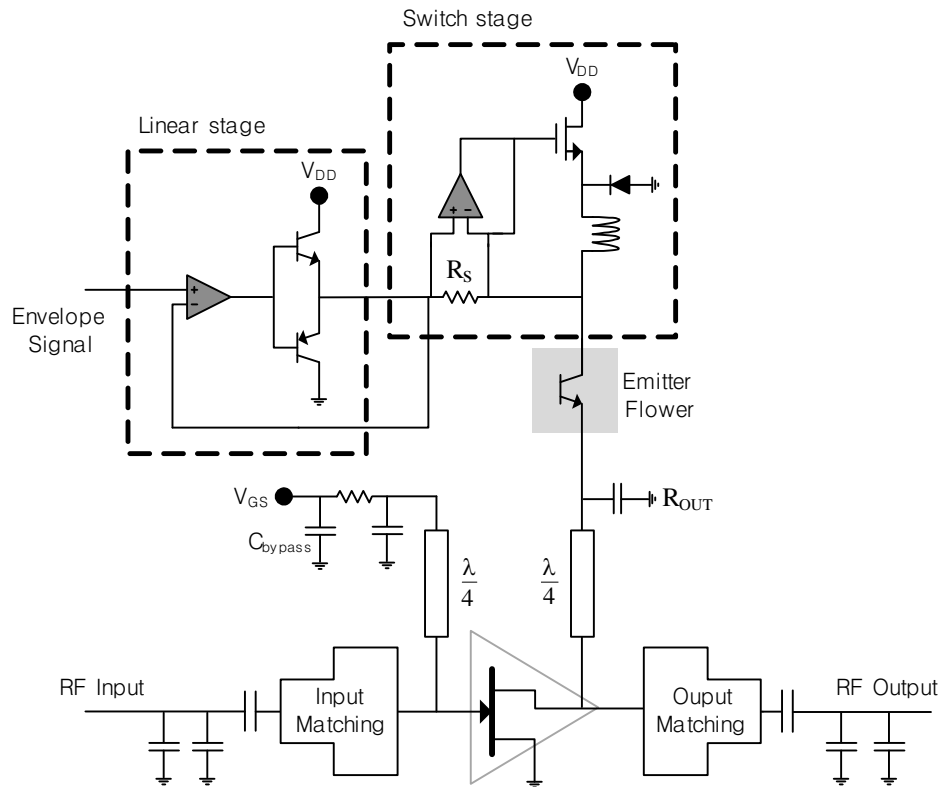


Figure 2: Schematic of the ET PA using an emitter follower.

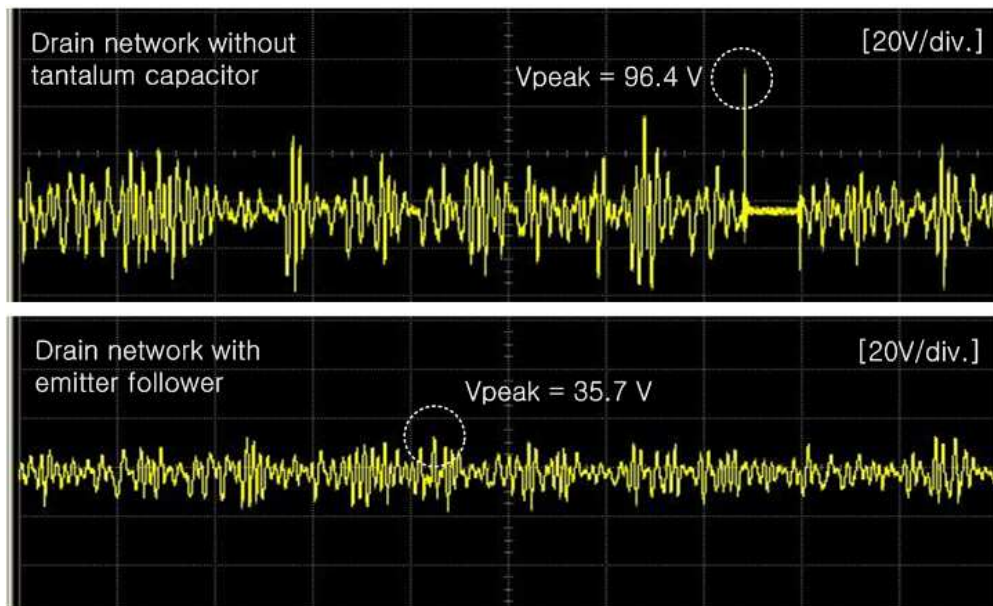


Figure 3: The bias fluctuation effect at drain network without tantalum capacitor and with emitter follower.

bias fluctuation. In the ET transmitter operation as shown in Fig. 1(b), the tantalum capacitor should be removed when the envelope signal from the bias modulator injected to the drain of the PA. Because the envelope signal should be amplified linearly and is related to linearity of the ET transmitter. But this operation causes the severe bias fluctuation so that whole ET system can be unstable. Therefore, we propose an effective architecture for the ET transmitter as shown in Fig. 2, to compensate above defect. By inserting an emitter follower which can sub for the role of the tantalum capacitor at the drain, a proper output impedance (R_{OUT}) can be generated according

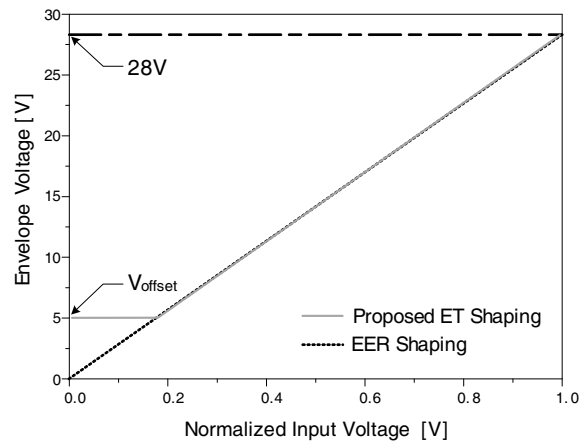


Figure 4: Proposed ET shaping function.

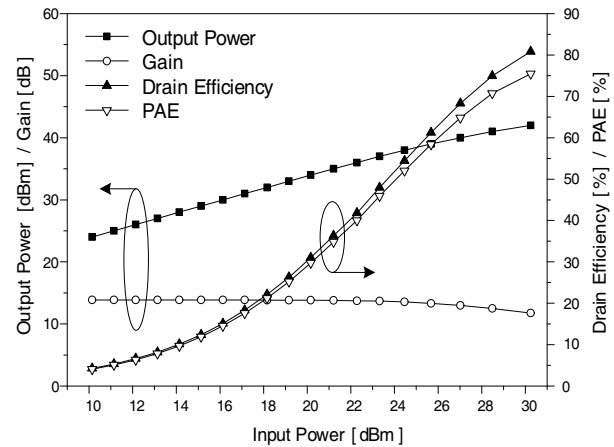


Figure 5: Measured results of the class-AB PA.

Table 1: Measured results summary of the main PA with and without proposed ET transmitter for a 3.5 GHz LTE signal at an average output power of 34 dBm (10 dB back-off).

Contents	Drain Efficiency [%]	PAE [%]	ACLR [dBc] $-/+5$ MHz
Class-AB	31.1	28.0	$-38.7/ -38.3$
Class-AB with ET	38.3	32.2	$-25.7/ -26.0$

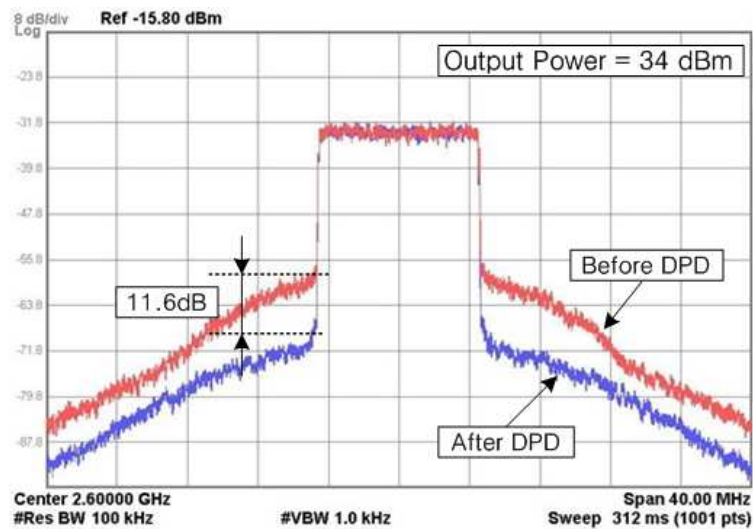


Figure 6: Measured PSDs of the class-AB PA with ET before and after DPD linearization.

to the envelope current, providing low R_{OUT} for an instantaneous envelope signal. Fig. 3 shows the bias fluctuation effect at the drain network. In the case of without tantalum capacitor, the drain bias (V_{DD}) is fluctuated, reaching to about 100 V which is the GaN's breakdown voltage. On the other hand, the case of with emitter follower shows that the drain bias fluctuation has suppressed effectively. Therefore, the stable circuit can be expected even if the tantalum capacitor is eliminated.

3. IMPLEMENTATION AND EXPERIMENTAL RESULTS

The ET transmitter has been built using the bias modulator and class-AB PA and tested using LTE signal with 10 MHz signal bandwidth and 9.4 dB PAPR. The PA has been implemented using Nitronex NPTB00025 GaN HEMT 25 W PEP at a V_{DD} of 28 V and a gate bias (V_{GS}) of -1.61 V ($I_{DQ} = 220$ mA) at 2.6 GHz. For interlock experiment, two E4438Cs of the Agilent have been used as master and slave units, respectively, for the modulation signal and envelope signal generators. The envelope shaping function is applied as shown in Fig. 4. To prevent gain compression and phase

distortion, we have added offset 5 V at low V_{DD} region. Except for low V_{DD} region, the shaping function is in accord with EER shaping for the linear AM-AM and AM-PM characteristics.

First, characteristics of the main PA were only measured to observe its own characteristics. Fig. 5 shows measured output power levels, power gain, drain efficiency, and power-added efficiency (PAE) according to input power levels for LTE signal. The measured results show a drain efficiency of 31.1% and a PAE of 28.0% with a power gain of 13.8 dB at an output power of 34 dBm, which is a 10 dB back-off region.

After using ET transmitter with emitter follower, the measured results are summarized in Table 1. At an output power of 34 dBm, a drain efficiency of 38.3% and a PAE of 32.2% are achieved. There are improvement of the drain efficiency of 7.2% and the PAE of 4.2% over the transmitter. For the linearity requirement, we have been employed the digital predistortion (DPD) technique. The AM-AM and AM-PM nonlinearities are characterized by the split augmented Hammerstein model [2]. The PD signal is generated by the Wiener predistorter of the direct learning architecture. Fig. 6 shows the measured power spectrum densities (PSDs) of the ET PA. This result shows that the ET PA after DPD linearization has excellent ACLR performance. Also, the linearity is improved without significantly decreasing efficiency.

4. CONCLUSIONS

We have proposed the effective architecture for the ET transmitter. By inserting an emitter follower which can sub for the role of the tantalum capacitor at the drain network, the memory effect, creating the bias fluctuation, can be significantly suppressed and whole circuit can be stable. To verify the proposed method, the class-AB PA is implemented with Nitronex NPTB00025 GaN HEMT 25 W PEP at 2.6 GHz. At an output power of 34 dBm which is a 10 dB back-off region, an efficiency of 38.3% is achieved using LTE signal with 10 MHz signal bandwidth and 9.4 dB PAPR. After the DPD linearization, an improved ACLR performance of over 11.6 dBc at ± 5 MHz offsets is obtained without decreasing efficiency.

ACKNOWLEDGMENT

This research was partially supported by the BK21 program, by the National Center for Nanomaterials Technology, by the World Class University program funded by the Ministry of Education, Science and Technology through the National Research Foundation of Korea (R31-10100), and by the MKE (The Ministry of Knowledge Economy), Korea, under the “IT Consilience Creative Program” support program supervised by the NIPA (National IT Industry Promotion Agency) (C1515-1121-0003).

REFERENCES

1. Liu, T., S. Boumaiza, and F. M. Ghannouchi, “Augmented hammerstein predistorter for linearization of broad-band wireless transmitters,” *IEEE Trans. Microwave Theory Tech.*, Vol. 54, No. 4, 1340–1349, 2006.
2. Lee, M.-W., Y.-S. Lee, S.-H. Kam, and Y.-H. Jeong, “A wideband digital presdistortion for highly linear and efficient GaN HEMT Doherty power amplifier,” *Microwave and Opt. Technol. Lett.*, Vol. 52, No. 2, 484–487, 2010.
3. Raab, F. H., P. Asbeck, S. Crpps, P. B. Kenington, Z. B. Popović, N. Potheary, J. F. Sevic, and N. O. Sokal, “Power amplifiers and transmitters for RF and microwave,” *IEEE Trans. Microwave Theory Tech.*, Vol. 50, No. 3, 814–826, 2002.
4. Cripps, S. C., *RF Power Amplifiers for Wireless Communications*, Artech House, Norwood, MA, 2006.
5. Kam, S.-H., M.-W. Lee, Y.-S. Lee, and Y.-H. Jeong, “A highly efficient and linear inverted Doherty power amplifier with unsymmetrical delay path,” *Microwave and Opt. Technol. Lett.*, Vol. 53, No. 6, 1302–1305, 2011.
6. Kam, S.-H., M.-W. Lee, and Y.-H. Jeong, “A high-efficiency inverse class-E power amplifier using double CRLH-TL for 3.5 GHz WiMAX applications,” *Proceedings of the Asia-Pacific Microwave Conference*, 279–282, Melbourne, Australia, December 2011.
7. Wang, F., D. Kimball, J. Popp, A. Yang, D. Y. C. Lie, P. Asbeck, and L. E. Larson, “An Improved power-added efficiency 19-dBm hybrid envelope elimination and restoration power amplifier for 802.11g WLAN applications,” *IEEE Trans. Microwav. Theory Tech.*, Vol. 54, No. 12, 4086–4099, 2006.

8. Kim, I., Y. Woo, J. Kim, J. Moon, J. Kim, and B. Kim, “High-efficiency hybrid EER transmitter using optimized power amplifier,” *IEEE Trans. Microwave Theory Tech.*, Vol. 56, No. 11, 2582–2593, 2008.
9. Jeong, J., D. F. Kimball, M. Kwak, C. Hsia, P. Draxler, and P. M. Asbeck, “Modeling and design of RF amplifiers for envelope tracking WCDMA base-station applications,” *IEEE Trans. Microwave Theory Tech.*, Vol. 57, No. 9, 2148–2159, 2009.

UWB Wilkinson Power Divider Using Tapered Transmission Lines

Faroq Razzaz, Majeed A. S. Alkanhal, and Abdel-Fattah Sheta

Department of Electrical Engineering, King Saud University

P. O. Box 800, Riyadh 11421, Kingdom of Saudi Arabia

Abstract— In this paper, an UWB Wilkinson power divider using tapered transmission lines is proposed. Using tapered transmission lines in microwave components results in reduction of the element length and therefore the overall component size while providing wider operational bandwidths. This power divider has superior performance in the UWB band (3.1 GHz–10.6 GHz) and is smaller in size as compared to traditional power dividers. The simulation and experimental results show good insertion loss which is approximately -3 dB, good return loss that is less than 11 dB for the input port over the entire UWB band and less than 16 dB for the other two ports. The power is divided equally between the output two ports and the isolation between the output ports is better than 11 dB.

1. INTRODUCTION

Power dividers are commonly used in microwave circuits such as in balanced mixers, phase shifters, amplifiers and antenna array feed networks. The Wilkinson power divider (WPD) is one of the most common components in microwave systems. The WPD can be matched at all three ports. It is lossless if the output ports are matched, reciprocal, and the output ports are largely isolated. Many designs and modifications were proposed to increase the bandwidth of the conventional Wilkinson power divider. The bandwidth of Wilkinson power divider can be increased using multisections [1], using open circuited stubs [2] or using tapered transmission lines [3]. Recently, ultra-wideband (UWB) communication systems have been introduced, and they require their own components that can operate over the UWB range (3.1–10.6 GHz). Many works had proposed to design UWB power dividers. A modified two-section UWB WPD with open circuited stub on each branch was proposed in [4]. Other UWB WPD was proposed in [5, 6] using open circuited radial stub on each branch. Also, an open circuited delta stub was proposed in [7]. In [8] a two section UWB WPD was designed using without stubs. UWB power dividers using tapered transmission lines were proposed in [9–11].

In this paper, an UWB Wilkinson power divider based on tapered transmission lines is proposed. The tapered transmission line is used to decrease the overall size and enhance the bandwidth of the power divider. This power divider is designed with only one isolation resistor for output ports. The simulation and measured results show good performance over the UWB range. Roger RT5880 substrate with relative permittivity of 2.2 and thickness of 0.508 mm has been used in the simulation and fabrication of this power divider.

2. DESIGN

Figure 1 shows the structure of the proposed UWB Wilkinson power divider. This power divider is based on the tapered transmission lines. To increase the bandwidth of the Wilkinson power divider a tapered transmission line has been integrated with another uniform transmission line section as shown in Figure 1.

The impedance of the tapered transmission line $Z(x)$ varies linearly from $Z(0) = Z_{01} = 2Z_0$ to $Z(L) = Z_{02}$, where L is the length of the tapered transmission line section as shown in Figure 2. The length of the tapered transmission line is less than quarter wavelength of the center frequency of the UWB spectrum which is 6.85 GHz. The second section is uniform transmission with characteristic impedance Z greater than Z_{02} . The even-odd mode analysis can be used to analyze the proposed power divider because it is symmetric in structure. The output ports are isolated and the isolation resistor is equal to $2Z_0$.

The characteristic impedance Z_0 is chosen to be 50Ω , the all other parameters can be determined and optimized with corresponding to this value and to the center frequency which is equal to 6.85 GHz. The line impedances $Z_{01} = 100 \Omega$, $Z_{02} = 65 \Omega$ and $Z = 75 \Omega$. The length of the tapered transmission line $L = \lambda/8$ and the electrical length of the uniform section is equal to 33° . The isolation resistor R is 100Ω .

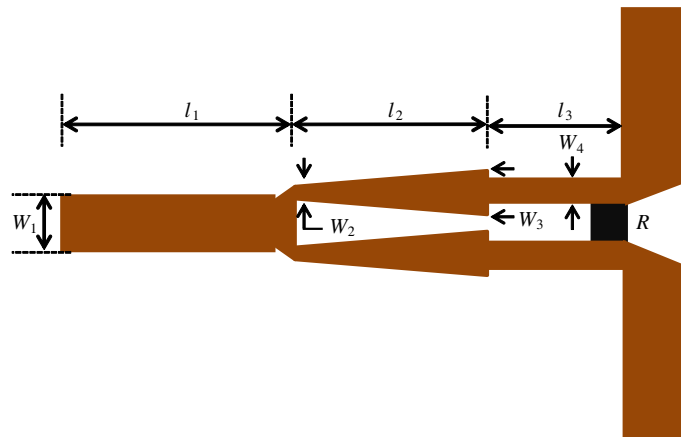


Figure 1: The structure of the proposed UWP power divider.

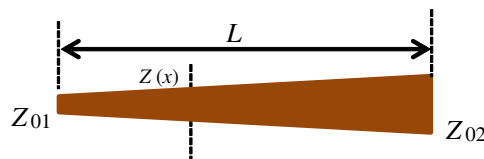


Figure 2: Linearly tapered transmission line section.

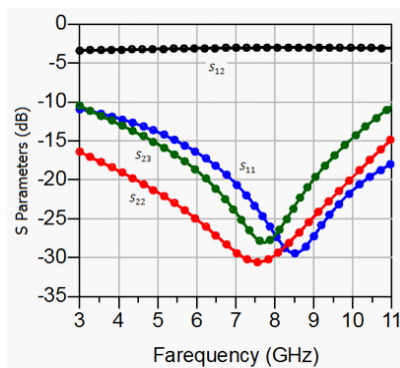
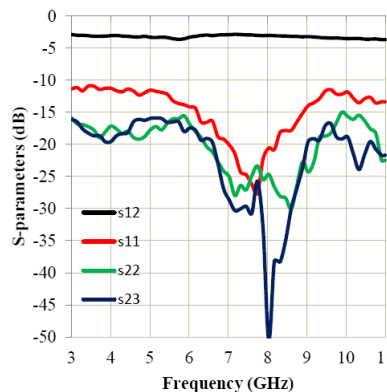
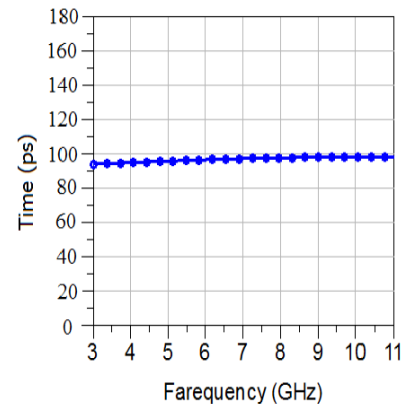

 Figure 3: Simulated S -parameters of the proposed UWB power divider.

 Figure 4: Measured S -parameters of the proposed UWB power divider.


Figure 5: Group delay of the proposed UWB power divider.

3. SIMULATION AND MEASUREMENT RESULTS

The designed power divider has been simulated using full-wave electromagnetic simulator software. Rogers RT5880 with a thickness of 0.508 mm, and a relative permittivity of 2.2 is used in this design. Table 1 contains the values of all optimized parameters of the designed UWB power divider. The overall size of the proposed UWB power divider is $15.51 \times 15.47 \text{ mm}^2$.

The performance of the designed circuit is shown in Figure 3. The simulation results show good insertion loss which is approximately -3 dB , good return loss that is less than 11 dB for the input port over the entire UWB band and less than 16 dB for the other two ports. The power is divided equally between the output two ports and the isolation between the output ports is better than 11 dB.

The measured results are shown in Figure 4. A good agreement with the simulated results is assumed. The measured results show good insertion loss which is approximately -3.6 dB , good return loss that is less than 11 dB for the input port over the entire UWB band and less than 15 dB for the other two ports. The power is divided equally between the output two ports and the

Table 1: Optimized parameters of the proposed UWB power divider.

Parameter	W_1	l_1	W_2	W_3	l_2	W_4	l_3
Value	1.54	6	0.43	1	4	0.78	3

isolation between the output ports is better than 15 dB. The group delay of the proposed UWB power divider is approximately flat and is less than 100 ps as shown in Figure 5.

4. CONCLUSIONS

A modified Wilkinson power divider using tapered transmission lines has been proposed for UWB applications. The designed power divider is compact and easy to fabricate. Quality better performance is obtained without using stubs and with only one isolation resistor. Good power dividing, matching, and isolations over the entire UWB spectrum range are obtained as demonstrated by simulation and experimental results.

ACKNOWLEDGMENT

This research is funded by The National Plan for Science & Technology, Kingdom of Saudi Arabia, under project No. 08-ADV210-2.

REFERENCES

1. Pazoki, R., M. R. Ghafouri Fard, and H. Ghafouri Fard, "A modification in the single-stage wilkinson power divider to obtain wider bandwidth," *Proc. Asia-Pacific Microw. Conf.*, 2325–2328, Dec. 2007.
2. Yi, K. and B. Kang, "Modified Wilkinson power divider for n th harmonic suppression," *IEEE Microw. Wireless Compon. Lett.*, Vol. 13, No. 5, 2003.
3. Womack, C. P., "The use of exponential transmission lines in microwave components," *IRE Trans. Microwave Theory and Techniques*, Vol. 10, 124–132, Mar. 1962.
4. Ou, X.-P. and Q.-X. Chu, "A modified two-section UWB Wilkinson power divider," *International Conference on Microwave and Millimeter Wave Technology, ICMMT 2008*, Vol. 3, 1258–1260, Apr. 21–24, 2008.
5. Ou, X.-P. and Q.-X. Chu, "A modified two-section UWB Wilkinson power divider," *International Conference on Microwave and Millimeter Wave Technology, ICMMT 2008*, Vol. 3, 1258–1260, Apr. 21–24, 2008.
6. Ahmed, O. and A. R. Sebak, "A modified Wilkinson power divider/combiner for ultrawide-band communications," *IEEE Antennas and Propagation Society International Symposium, APSURSI'09*, 1–4, Jun. 1–5, 2009.
7. Zhou, B., H. Wang, and W. Sheng, "A novel UWB Wilkinson power divider," *2010 2nd International Conference on Information Science and Engineering (ICISE)*, 1763–1765, Dec. 4–6, 2010.
8. Yang, L. and Q.-X. Chu, "Design of a compact UWB Wilkinson power divider," *International Conference on Microwave and Millimeter Wave Technology, ICMMT 2008*, Vol. 1, 360–362, Apr. 21–24, 2008.
9. Mencia-Oliva, B., A. M. Pelaez-Perez, P. Almorox-Gonzalez, and J. I. Alonso, "New technique for the design of ultra-broadband power dividers based on tapered lines," *IEEE MTT-S International Microwave Symposium Digest, MTT'09*, 493–496, Jun. 7–12, 2009.
10. Chiang, C.-T., "Ultra wideband power divider using tapered line," *Progress In Electromagnetic Research*, Vol. 106, 61–73, Jul. 2010.
11. Jia, Z., Q. Zhu, and F. Ao, "A 2-way broad-band microstrip matched power divider," *International Conference on Communications, Circuits and Systems Proceedings*, Vol. 4, 2592–2596, Jun. 25–28, 2006.

Nonreciprocal Magnetolectric Microwave Attenuator

D. V. Lavrentieva, M. I. Bichurin, and A. S. Tatarenko

Institute of Electronic and Information Systems, Novgorod State University
Veliky Novgorod 173003, Russia

Abstract— One of perspective directions of a solid-state electronic engineering is producing new devices on the basis of magnetolectric materials. Design and application of new nonreciprocal microstrip microwave attenuator are considered. Experimental results showed 38 dB attenuation at frequency range 5–10 GHz with applied electric field $E = 0\text{--}7\text{ kV/cm}$. The data obtained are in good agreement with theory. This technology can significantly reduce the cost of devices, and enhance speed of operation.

1. INTRODUCTION

The combination of magnetic and electrical properties, and properties caused by magnetolectric (ME) interaction in composite layered materials offers great features for the design of new microwave devices [1]. Microwave devices are designed on the basis of the various manifestations of the ME effect. Most strongly this effect is manifested in the form of microwave ME effect, which consists in a shift of the resonance line of FMR under the control of the electric field [2]. ME microwave attenuator is designed and researched. ME composite in this case acts as a resonator, which is a three-layer structure, based on single-crystal yttrium iron garnet (YIG) on a substrate of gadolinium gallium garnet (GGG) and a thin disk of magnesium niobate titanate (PMN-PT) [3].

2. DESIGN OF MICROWAVE MAGNETOELECTRIC ATTENUATOR

The base of the nonreciprocal magnetolectric microwave attenuator (Fig. 1) is a microstrip transmission line on alumina substrate ($\epsilon = 9.8$, thickness = 1 mm) and layered ferrite-piezoelectric resonator consisting of epitaxial single crystal (111) YIG films on GGG substrates and 0.44 mm thick (001) PMN-PT. Metal electrodes (200 nm in thickness of gold and 30 nm in thickness of chromium) were deposited on PMN-PT for electrical contacts and the crystal was initially poled in $E = 2\text{ kV/cm}$. A thin layer ($< 0.02\text{ mm}$) of an fast epoxy, ethylcyanoacrylate, was used to bond YIG to PMN-PT. Circular polarization of the magnetic field in volume of the ferrite-piezoelectric resonator results from using the microstrip stubs of $\lambda/8$ and $3\lambda/8$. Since the power absorption in ferromagnetic resonance occurs in a variable magnetic field with circular polarization and right direction of rotation relative to the direction of permanent magnetization M_0 , then the variable magnetic field in the ME cavity has a circular polarization with different directions of rotation of the polarization for different directions of propagation. Therefore, the energy losses are small at resonance for direct direction of electromagnetic wave propagation and large for converse one.

A bias field corresponding to FMR is applied to the resonator. Electrical tuning is realized with the application of a control voltage to electrodes leading to a shift of FMR line.

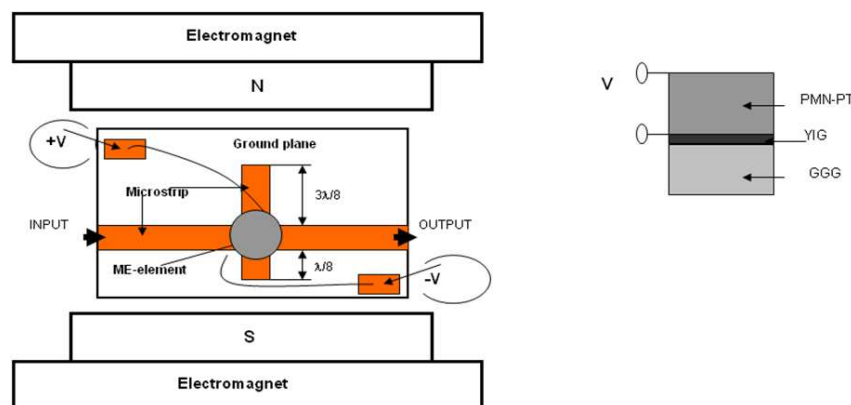


Figure 1: ME microwave attenuator.

3. THEORY AND EXPERIMENT

The ME resonator [3] is included as an absorbing inhomogeneity in a microstrip transmission line. Module coefficient of transmission is calculated by equation:

$$|T| = \frac{\sqrt{(1 - k^2 + \xi^2)^2 + (2k\xi)^2}}{(1 + k)^2 + \xi^2}; \quad (1)$$

$$L = 10 \cdot \lg \frac{1}{|T|^2}, \quad (2)$$

where k is coefficient of coupling; ξ is normalized detuning of a magnetic field from resonant magnitude.

For the analysis of work of the phase shifter expression for coupling coefficient of the ME resonator with a microstrip line is used. Coefficient of coupling of ME resonator with microstrip line is calculated by equation:

$$k = \frac{2V\chi_+''z_0\varepsilon}{\pi h^2\lambda_\nu Z} \left(\operatorname{arctg} \frac{Z}{z_0\sqrt{\varepsilon}} + \frac{1}{3} \operatorname{arctg} \frac{3Z}{z_0\sqrt{\varepsilon}} \right)^2; \quad (3)$$

$$\chi_+'' = \frac{8\pi M_0}{\Delta H}, \quad (4)$$

where V is volume of ME material; χ_+'' is an imaginary part of magnetic susceptibility tensor; z_0 is wave resistance of microstrip line; ε is relative dielectric permittivity; h is thickness of a substrate; λ_ν is wave length; Z is free space wave resistance. Normalized detuning of a magnetic field from resonant magnitude is calculated by equation:

$$\xi = \frac{H_r - H_0 + \Delta H_E}{\Delta H}, \quad (5)$$

where H_r is value of a resonant field for the given frequency; H_0 is constant biased magnetic field; ΔH is half-width of magnetic resonance; ΔH_E is increment of magnetic field under the action of an external electric field.

Microwave measurements were carried out using a vector network analyzer. A standard calibration procedure was performed before measurements. An input signal at 6500 MHz and power $P_{\text{in}} = 0.1$ mW was applied to the microstrip transducer. Low input power was chosen to prevent heating of the sample due to power absorption at FMR. Fig. 2 shows the attenuation dependence at the working frequency of the electric field E and an in-plane magnetic field H_0 for the forward direction of wave propagation.

Attenuation in the opposite direction due to the non-reciprocity device is about 40 dB, and remains virtually unchanged. Comparisons of the experimental data with theoretical calculations are made.

The insertion loss of attenuator is the sum of losses in the magnetolectric resonator (L_R), metal conductors (L_M), dielectric substrate (L_D), and due to nonideal coupling between the resonator and transmission lines (L_C):

$$L = L_R + L_D + L_M + L_C.$$

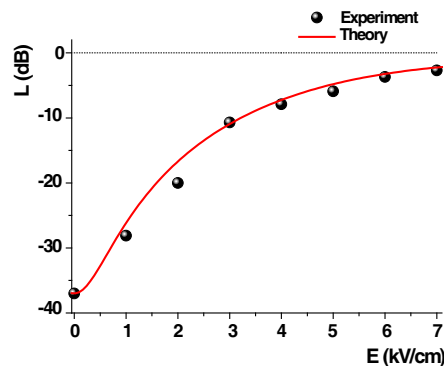


Figure 2: Comparison of experimental and theoretical data. Central frequency is 6500 MHz.

The estimated loss is compared with data in Fig. 2 and there is excellent agreement between the theory and experiment. The off-resonance insertion loss of the attenuator is the sum of losses in YIG and PMN-PT of about 1 dB, metal striplines (0.3 dB), dielectric ground plane (0.2 dB), and due to nonideal coupling between the resonator and transmission lines (0.5 dB) for a total of 2 dB.

4. CONCLUSION

We designed, fabricated and tested nonreciprocal microwave attenuator in a standard thin film passive technology. Experimental results showed 38 dB attenuation in the forward direction at frequency range 5–10 GHz with electric field $E = 0\text{--}7\text{ kV/cm}$. This technology can significantly reduce the cost of devices, and enhance speed of operation.

ACKNOWLEDGMENT

This work was supported by grants RFBR #11-02-00430-a.

REFERENCES

1. Bichurin, M. I., V. M. Petrov, R. V. Petrov, G. N. Kapralov, F. I. Bukashev, A. Yu. Smirnov, and A. S. Tatarenko, "Magnetolectric microwave devices," *Ferroelectrics*, Vol. 280, 213, 2002.
2. Bichurin, M. I., I. A. Kornev, V. M. Petrov, A. S. Tatarenko, Yu. V. Kiliba, and G. Srinivasan, "Theory of magnetolectric effects at microwave frequencies in a piezoelectric/magnetostrictive multilayer composite," *Phys. Rev. B*, Vol. 64, 094409, 2001.
3. Shastry, S., G. Srinivasan, M. I. Bichurin, V. M. Petrov, and A. S. Tatarenko, "Microwave magnetolectric effects in single crystal bilayers of yttrium iron garnet and lead magnesium niobate-lead titanate," *Phys. Rev. B*, Vol. 70, 064416, 2004.

A Peano Fractal-based Dual-mode Microstrip Bandpass Filters for Wireless Communication Systems

Jawad K. Ali, Hussam Alsaedi, Mohammed F. Hasan, and Hussain A. Hammam

Microwave Research Group, Department of Electrical Engineering
University of Technology, Baghdad, Iraq

Abstract— Peano fractal geometries are characterized by their high space filling properties. In this paper, a new compact dual-mode microstrip filter design, based on this fractal geometry, is presented as a candidate for use in modern wireless communication systems. A bandpass filter with a quasi-elliptic response has been designed based on the 2nd iteration Peano fractal curve at 2.45 GHz using a substrate of a relative dielectric constant of 9.6 and thickness of 0.508 mm. The resulting filter structure based on the second iteration Peano geometry leads to compact size dual-mode resonator with a side length of about $0.1\lambda_g$. This represents better miniaturization level compared with the other microstrip bandpass filters with structures based on other space-filling geometries and designed at the same frequency using the same substrate material specifications. Simulation and theoretical performance of the resulting filter structures have been carried out using method of moments (MoM) based electromagnetic simulator IE3D, from Zeland Software Inc.. The results also show that the proposed filter structure possesses good return loss and transmission responses besides the size reduction gained, making it suitable for use in a wide variety of wireless communication applications. Furthermore, the out-of-band response indicates that the proposed filter has less tendency to support higher harmonics.

1. INTRODUCTION

A wide variety of applications for fractal has been found in many areas of science and engineering, since the pioneer work of Mandelbrot [1]. An example of such area is fractal electrodynamics [2] in which fractal geometry is combined with electromagnetic theory for the purpose of investigating a new class of radiation, propagation, and scattering problems. One of the most promising areas of fractal electrodynamics research is its application to the antenna and microwave circuits design.

The application of fractal geometries in antenna and passive microwave circuit design has found continuing interest to meet the recent development in wireless communication systems that impose new challenges to design and produce high quality miniaturized components. These geometries have two common properties; space-filling and self-similarity. According to this property, fractal curves are characterized by a unique behavior that, after an infinite number of iterations, their length becomes infinite although the entire curve fits into the finite area. Space-filling property of fractal shapes has been successfully applied to the design of multi-band fractal antennas, while the space-filling property has been utilized to reduce the antenna size. This property can be exploited for the miniaturization of microstrip antennas, resonators, and filters. Due to the technology limitations, fractal curves are not physically realizable. Pre-fractals, fractal curves with finite order, are used instead [3].

However, most of the research efforts have been devoted to the antenna applications. Among the earliest predictions of the use of fractals in the design and fabrication of filters is that of Yordanov et al. [4]. Their predictions are based on their investigation of Cantor fractal geometry. Hilbert fractal curve has been used as a defected ground structure in the design of a microstrip lowpass filter operating at the L-band microwave frequency. Based on this fractal curve, compact high temperature superconductor microstrip bandpass resonator filters have been designed for wireless communication applications [5]. Sierpinski fractal geometry has been used in the implementation of a complementary split ring resonator [6]. Split ring geometry based on square Sierpinski fractal curves has been proposed to reduce resonant frequency of the structure and achieve improved frequency selectivity in the resonator performance. Koch fractal shape is applied to mm-wave microstrip bandpass filters integrated on a high-resistivity substrate [7]. Minkowski-like fractal geometries have been applied to the square ring resonator to design miniaturized dual-mode microstrip bandpass filters [8, 9]. The application of Hilbert fractal geometries to produce single-mode multi-resonator microstrip bandpass filters has been reported in [10]. Peano fractal geometry has been successfully used to design single-mode multi-resonator microstrip bandpass filters and open resonators with 2nd harmonic reduction [11–13]. Up to authors' knowledge, this fractal geometry has not been yet applied to design a dual-mode bandpass filter.

In this paper, dual-mode microstrip bandpass filter designs and has been presented for use in the modern compact communication systems. Based on the second iteration Peano fractal curve geometry, a microstrip bandpass filter has been designed at a frequency of 2.45 GHz. The resulting filter is expected to possess a considerable miniaturization owing to its remarkable space-filling property together with good transmission and return loss responses.

2. THE PEANO FRACTAL FILTER STRUCTURE

The Peano curve, proposed by Peano in 1890, was, in fact, the first set of space-filling curve [14]. One interesting feature of the Peano-curve algorithm is its relatively higher compression rate than the Hilbert-curve algorithm in filling a 2-D region, which suggests that the Peano resonator may resonate at a lower fundamental resonant frequency than a comparable Hilbert resonator of the same iteration order k . The Peano fractal curve, as shown in Figure 1, consists in a continuous line which connects the centers of a uniform background grid.

The fractal curve is fit in a square section of S as external side. By increasing the iteration level k of the curve, one reduces the elemental grid size as $S/(3^k - 1)$; the space between lines diminishes in the same proportion. For a Peano resonator, made of a thin conducting strip in the form of the Peano curve with side dimension S and order k , the length of each line segment d and the sum of all the line segments $L(k)$ are given by [11, 12]

$$L(k) = (3^k + 1) S \quad (1)$$

The main idea here is to increase the iteration of the Peano curve as much as possible in order to fit the resonator in the smallest area. However, it has been found that, when dealing with space-filling fractal shaped microstrip resonators, there is a tradeoff between miniaturization (curves with high k) and quality factor of the resonator. For a microstrip resonator, the width of the strip w and the spacing between the strips g are the parameters which actually define this tradeoff [11, 12]. Both dimensions (w and g) are connected with the external side S and iteration level k ($k \geq 2$) by:

$$S = 3^k(w + g) - g \quad (2)$$

From this equation, it is clear that trying to obtain higher levels of fractal iterations; this will lead to lower values of the microstrip width, thus increasing the dissipative losses with a corresponding degradation of the resonator quality factor. Hence, for these structures, the compromise between miniaturization and quality factor is simply defined by an adequate fractal iteration level. However, it has been concluded, in practice, that the number of generating iterations required to reap the benefits of miniaturization is only few before the additional complexities become indistinguishable [3].

The dimension of a fractal provides a description of how much a space it fills [14]. It is a measure of the prominence of the irregularities when viewed at very small scales. A dimension contains much information about the geometrical properties of a fractal. Because the total length of the conducting strip is larger than that of the same order Hilbert resonator, which is $(2^k + 1)S$, it would be expected that the Peano resonator resonates at a lower fundamental frequency than the same order Hilbert resonator [10].

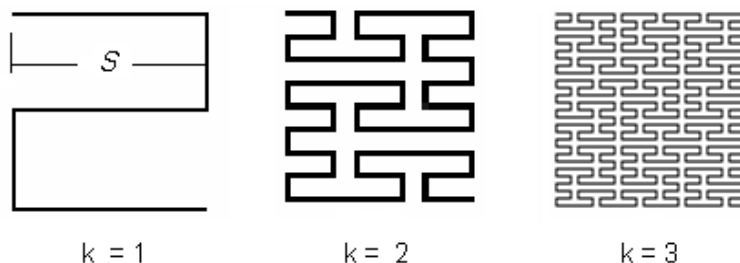


Figure 1: The first three iteration levels of the Peano fractal curve generation process.

3. THE PROPOSED FILTER MODELING

It is intended, in this work, to present a dual-mode microstrip bandpass filter with its resonator structure based on Peano fractal geometry after applying it on the conventional square ring resonator. In this context, the Peano fractal geometry has been successfully used to design single-mode microstrip bandpass filters [11, 12]. Up to authors' knowledge, this fractal geometry has not been yet applied to design a dual-mode bandpass filter. The application of the Peano fractal geometry on the square ring is shown in Figure 2.

At first, the square ring perimeter has been divided into four quarters, Figure 2(a), then replacing each of the four parts with the second iteration Peano structure. The resulting resonator, Figure 2(b), is composed of four Peano based structures. This resonator has been used to model a dual-mode microstrip bandpass filter. Owing to the space-filling property, the structure possesses, it is expected to gain a high miniaturization percent as compared with the conventional square ring resonator based bandpass filter. Figure 3 shows the layout of the resulting microstrip bandpass filter.

The filter is to be etched using a substrate with a relative dielectric constant of 9.6 and a thickness of 0.508 mm. The input/output feeds are with $50\ \Omega$ characteristic impedance with a transmission line width of about 0.5 mm. A small perturbation has been placed at a location midway of the resonator electrical length with respect of the feeds, to couple the two degenerate modes. The resonator is coupled to the input/output ports via two couplers. The coupler width is of about 0.2 mm, and the coupling gap between the resonator and the couplers is of about 0.5 mm. The resonator structure has an overall side length of 4.851 mm, $0.1\lambda_g$, and a conductor trace width of

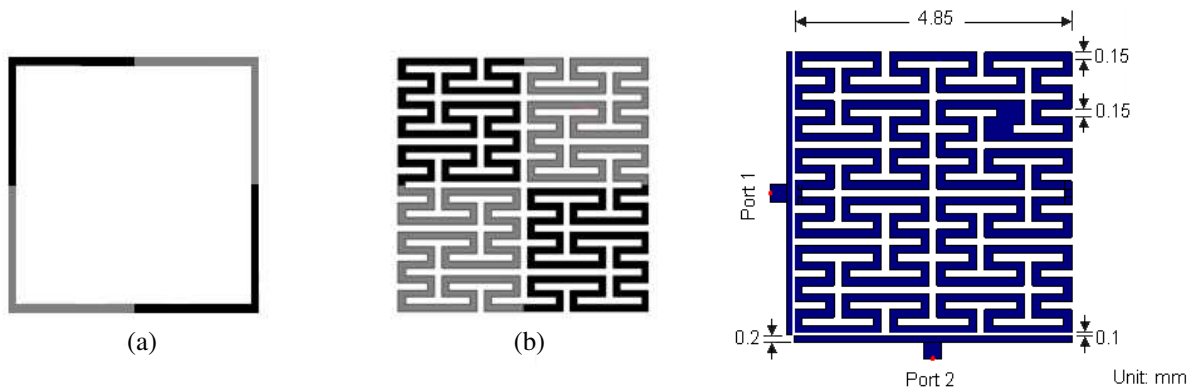


Figure 2: (a) The conventional square ring resonator with its perimeter divide into four quarters, and (b) the resulting resonator structure after each quarter in (a) being replaced with a Peano based second iteration structure shown in Figure 1(b).

Figure 3: The layout of the proposed fractal based dual-mode microstrip bandpass filter designed at 2.45 GHz.

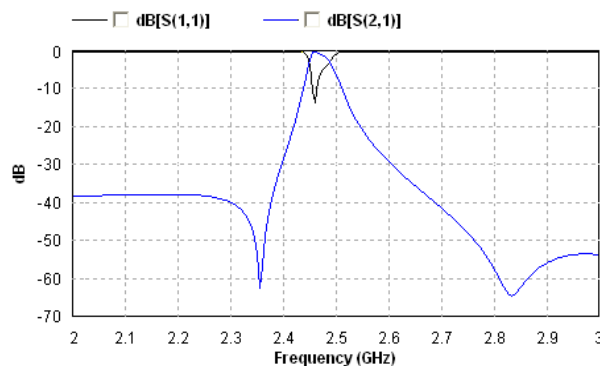


Figure 4: The return loss S_{11} and the transmission S_{21} responses of the Peano based dual-mode microstrip bandpass filter shown in Figure 3.

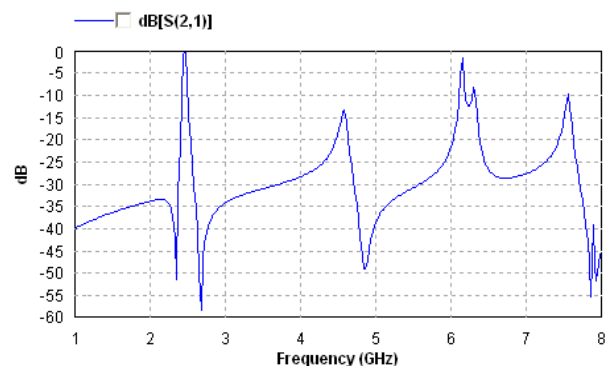


Figure 5: The out-of-band transmission S_{21} response of the Peano based resonator dual-mode bandpass filter shown in Figure 3.

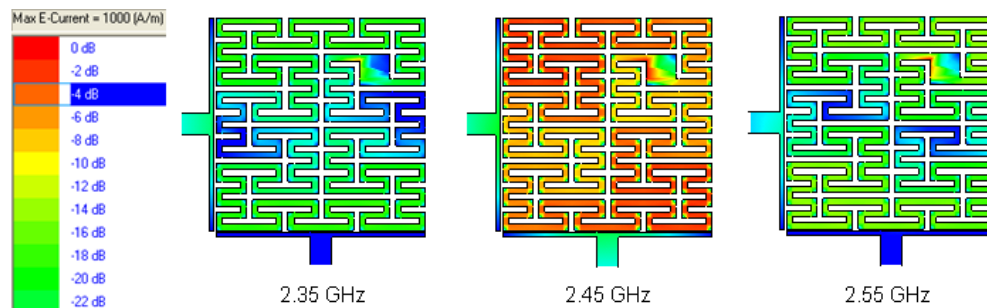


Figure 6: The surface current distribution on the Peano based resonator filter shown in Figure 3, at 2.45 GHz and two other frequencies below and beyond the design frequency.

0.15 mm to resonate at a design frequency of 2.45 GHz. This corresponds to a size reduction of about 84% as compared with the conventional dual-mode square ring resonator, since the resonant side length of the square ring dual-mode microstrip resonator is $0.5\lambda_g$ [15]; where λ_g is the guided wavelength, and it is given by:

$$\lambda_g = \frac{\lambda_0}{\sqrt{\epsilon_{eff}}} \quad (3)$$

where ϵ_{eff} is the effective dielectric constant, and can be calculated by empirical expressions reported in the literature [16].

However, most of the commercially available EM simulators can perform direct calculation of both λ_g and ϵ_{eff} , provided that substrate parameters and the operating frequency are known. For the present case, λ_g has been found to be 48.366 mm. The resulting side length of the modeled filter which is 4.85 mm is in very good agreement with what is predicted by Eqs. (1) and (3).

4. PERFORMANCE EVALUATION

The resulting dual-mode microstrip bandpass filter, with the layout shown in Figure 3, has been modeled at 2.45 GHz. The modeling and performance evaluation of the proposed filter structure have carried out using the commercially available IE3D EM simulator, from Zeland Software Inc. [17]. A suitable grid, in the EM solver, has to be chosen to make a good compromise between geometrical resolution and solution time. Figures 4 and 5 demonstrate the resulting performance curves after a slight tuning. Filter responses shown in Figure 4 imply symmetrical characteristics with sharper lower and higher cut-off passband, centered at a frequency of about 2.456 GHz. The resulting fractional bandwidth is of about 1.22%, as indicated in the in-band response shown in Figure 4.

Figure 5 shows the out-of-band responses of this filter throughout a swept frequency ranges from 1 to 6 GHz. The 3rd harmonic response appearing here is of little importance, since it is with a very narrow-band and with low value of transmission loss, while the 2nd harmonic response has considerably diminished.

Figure 6 shows the electric current density distribution on the surface of the modeled filter at three distinct frequencies; the design frequency, 2.45 GHz, and two other frequencies ± 100 MHz of the design frequency. It is clear that there are no currents flowing on the surface of the filter at 2.35 and 2.55 GHz, since these frequencies are out-of-band.

However, the current density on the surface of the filter at 2.45 GHz implies that the current with density will flow in the passband. On other hand, the degree of symmetry of the current densities throughout the entire filter surface is a measure of the filter response as depicted in Figure 4.

5. CONCLUSIONS

A new dual-mode microstrip bandpass filter design for use in modern compact wireless communication systems has been presented in this paper. The proposed filter structure has dual-mode microstrip resonator in the form of 2nd iteration Peano fractal curve. The space-filling property of the proposed fractal structure, results in a high degree of miniaturization of the dual-mode resonator. The fractal based resonator has been found to occupy an area of about $(0.1 \times 0.1) \lambda_g$ which represents a miniaturization percentage of about 84% as compared with conventional square ring resonator designed at the same frequency and using a substrate having the same parameters. The

resulting filter has reasonable passband performance besides the size reduction gained making it suitable for a wide variety of wireless communication applications. Furthermore, the out-of-band performance responses have shown that the proposed filter does not support the 2nd harmonic which conventionally accompanies the bandpass filter performance.

REFERENCES

1. Mandelbrot, B. B., *The Fractal Geometry of Nature*, W. H. Freeman and Company, New York, 1983.
2. Jaggard, D. L., “On fractal electrodynamics,” *Recent Advances in Electromagnetic Theory*, H. N. Kritikos and D. L. Jaggard, Eds., 183–224, Springer-Verlag, 1990.
3. Gianvittorio, J. P. and Y. Rahmat-Samii, “Fractal antennas: A novel miniaturization technique and applications,” *IEEE Ant. and Propag. Magazine*, Vol. 44, No. 1, 20–36, 2002.
4. Yordanov, O. I., I. Angelov, V. V. Konotop, and I. V. Yurkevich, “Prospects of fractal filters and reflectors,” *IEEE Seventh International Conference on Antenna and Propagation, ISCAP91*, York, UK, 1991.
5. Chen, J., Z. B. Weng, Y. C. Jiao, and F. S. Zhang, “Lowpass filter design of Hilbert curve ring defected ground structure,” *Progress In Electromagnetics Research*, Vol. 70, 269–280, 2007.
6. Crnojevic-Bengin, V., V. Radonic, and B. Jokanovic, “Complementary split ring resonators using square sierpinski fractal curves,” *Proceedings of the 36th European Microwave Conference*, 1333–1335, Manchester, UK, Sep. 2006.
7. Kim, I. K., N. Kingsley, M. A. Morton, S. Pinel, J. Papapolymerou, M. M. Tentzeris, J. Laskar, and J. G. Yook, “Koch fractal shape microstrip bandpass filters on high resistivity silicon for the suppression of the 2nd harmonic,” *Journal of the Korean Electromagnetic Engineering Society*, Vol. 6, No. 4, 1–10, Dec. 2006.
8. Ali, J. K., “A new miniaturized fractal bandpass filter based on dual-mode microstrip square ring resonator,” *Proceedings of the 5th International Multi-conference on Signals, Systems and Devices, IEEE SSD'08*, Amman, Jordan, Jul. 2008.
9. Ali, J. K. and N. N. Hussain, “An extra reduced size dual-mode bandpass filter for wireless communication systems,” *PIERS Proceedings*, 1467–1470, Suzhou, China, Sep. 12–16, 2011.
10. Barra, M., C. Collado, J. Mateu, and J. M. O’Callaghan, “Miniaturization of superconducting filters using hilbert fractal curves,” *IEEE Trans. Appl. Supercon.*, Vol. 15, No. 3, 3841–3846, 2005.
11. Ali, J. K. and Y. S. Miz’el, “A new miniature fractal-based bandpass filter design with 2nd harmonic suppression,” *Proceedings of 3rd IEEE International Symposium on Microwave, Antenna, Propagation and EMC Technologies for Wireless Communication, MAPE 2009*, Beijing, China, Sep. 2009.
12. Ali, J. K. and Y. S. Miz’el, “A new fractal microstrip bandpass filter design based on dual-mode square ring resonator for wireless communication systems,” *Iraqi Journal of Applied Physics, IJAP*, Vol. 5, No. 1, 7–12, 2009.
13. Ali, J. K. and H. Alsaedi, “Second harmonic reduction of miniaturized dual-mode microstrip bandpass filters using fractal shaped open stub resonators,” *PIERS Proceedings*, 1266–1269, Kuala Lumpur, Malaysia, Mar. 27–30, 2012.
14. Falconer, K., *Fractal Geometry; Mathematical Foundations and Applications*, 2nd Edition, John Wiley and Sons Ltd., Chichester, 2003.
15. Hong, J. S., *Microstrip Filters for RF/Microwave Applications*, 2nd Edition, John Wiley and Sons Inc. Publication, New Jersey, 2011.
16. Pozar, D. M., *Microwave Engineering*, 2nd Edition, John Wiley and Sons, 2003.
17. Zeland Software Inc., *IE3D User’s Manual*, May 2008.

Piezoelectric Multilayer Transformer

A. N. Soloviev, M. I. Bichuri, and D. V. Kovalenko
 Novgorod State University, Russia

Abstract— In the article the theoretical modeling of the Rozen piezoelectric transformer is described. The method of the operating frequency range and gain increasing is offered. The method is the configuration change of the exciter. It means that the exciter is fabricated as a multilayer structure with layers of different lengths. Correctness of the method is confirmed by obtained the gain frequency dependence.

1. INTRODUCTION

The implementations of piezoelectric transformers (PET) face some difficulties such as the narrow operating frequencies range, the varying transformation coefficient and efficiency in the range.

The operating frequencies range is the main parameter to increase the transformer efficiency. The transformation coefficient has a maximum value in the resonance region. Therefore it needs to find ways to expand the operating frequencies range. The purpose of this paper is to study the multilayer transformers that allow to increase the transformation coefficient and the operating frequency range of PET. The method considers the multilayer structure with layers of different lengths. For effectively increase of operating frequency range the several steps should be made such as analysis of the PET design, draft of the electrical equivalent circuit, definition and subsequent analysis of the expressions, mathematical modeling and computer simulating of the PET parameters. The transformation coefficient frequency dependences of the multilayer PETs with different numbers of layers have been obtained.

2. THEORETICAL MODELING

We consider the design of the Rosen transformer [2]. The main output parameters are the resonance frequency, the operating frequency range, the transformation coefficient, the efficiency and the power output.

Figure 1 shows the transformer design that is a cascade of two resonators. The first resonator is a multilayer structure with different lengths and thicknesses of the layers. The frequencies range and the resonant frequency strongly depend on the length of the piezoelectric element. The multilayer structure allows expanding the operating frequencies range. In this paper, we investigate the single-layer, three-layer and five-layer structures of the input section. The layers are connected parallel to the first resonator. It results to sum mechanical deformations of each layer. To perform the condition it is necessary that these vibrations must be in phase. The second resonator is a converter of these vibrations into an electrical signal due to the direct piezoelectric effect.

The PET electrical equivalent circuit was composed by electro-associations method [1]. After analyzing the circuit the calculated expressions of the equivalent circuit parameters were obtained [1].

The input (C_{31}) and output (C_{32}) capacitance are given by:

$$C_1 = \frac{\varepsilon_{33}^T \cdot (1 - k_{31}^2) \cdot b \cdot l_1}{a}, \quad (1)$$

$$C_2 = \frac{\varepsilon_{33}^T \cdot (1 - k_{33}^2) \cdot b \cdot a}{l_2}, \quad (2)$$

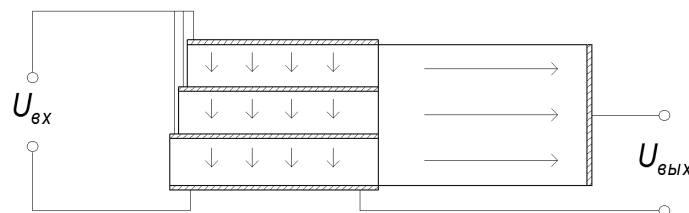


Figure 1: Design of the transformer with connection diagram of the circuit.

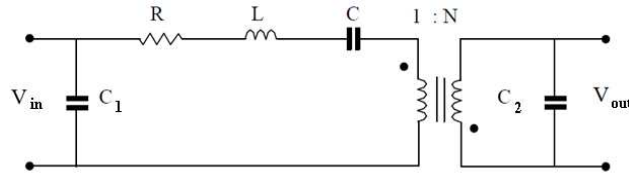


Figure 2: Simplified electrical equivalent circuit of PET.

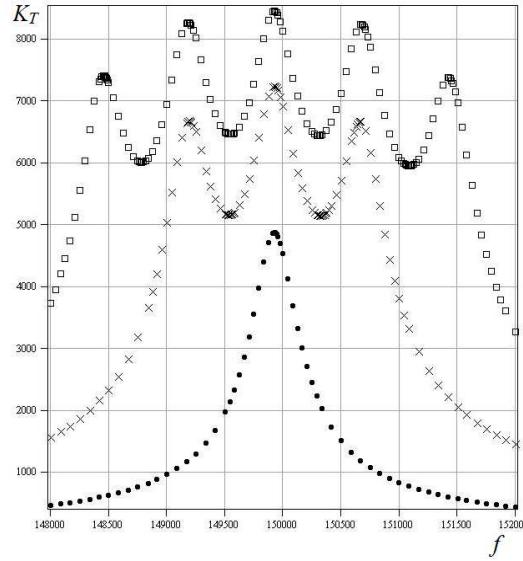


Figure 3: The transformation coefficient frequency dependences of single- and multilayer structures. Points mean the single-layer data, crosses mean the three-layer data, and squares mean the five-layer structure data.

where b and a are the transformer width and the transformer thickness, l_1 and l_2 are the first resonator and the second resonator lengths, respectively, ε_{33}^T is the dielectric permittivity of the material, k_{33} is the electromechanical coupling coefficient of longitudinal modes, k_{31} is the electromechanical coupling coefficient of transverse modes.

The mechanical part inductance (L) and the transfer ratio (N) have the form:

$$L = 4 \cdot a \cdot b \cdot l_1 \cdot \rho, \quad (3)$$

$$N = 2b \cdot d_{31} \cdot Y_1^E, \quad (4)$$

where ρ is the material density, d_{31} is the piezoelectric coefficient, Y_1^E is the elastic constant.

The mechanical part capacitance (C) is expressed by the equation:

$$C = \frac{l_1}{\pi^2 \cdot a \cdot b \cdot Y_1^E}. \quad (5)$$

The wave impedance (z_0) and the mechanical resistance (R) calculated as:

$$z_0 = a \cdot b \cdot \sqrt{\rho \cdot Y_1^E}, \quad (6)$$

$$R = \frac{2\pi \cdot z_0}{Q_M}, \quad (7)$$

where Q_M is the mechanical quality factor.

The longitudinal wave's resonance frequencies (f_p) have form:

$$f_p = \frac{n}{2 \cdot l_1} \cdot \sqrt{\frac{Y_1^E}{\rho}}, \quad (8)$$

where n is a integer of 1, 2, 3, ...

Table 1: Parameters of piezoelectric material.

$\rho, (\times 10^3) \text{ kg/m}^3$	d_{31}	d_{33}	Q_m	ε_{33}^T	ε_{31}^T	k_{31}	k_{33}
	$\times (10^{12}) \text{ C/N}$						
7.6	145	315	1200	1400	1100	0.33	0.68

Table 2: The calculation results of electrical equivalent circuit parameters.

z_0 (Ohm)	C_{31} (nF)	C_{32} (pF)	N	C (nF)	L (μH)	R (Ohm)
17.8	2.2	0.53	38	19	243	0.093

Table 3: The calculation results of transformer parameters.

Number of layers	Transformer parameters				
	f_p , (kHz)	Δf , (kHz)	$K_T, (U_{in} = 1 \text{ V})$	U_{out} , (kV)	η , %
1	150	0.7	4880	5	90
3	150	2.2	7200	7	90
5	150	3.6	8500	8.5	90

The operating frequencies range of the longitudinal modes is expressed by the equation [1]:

$$\Delta f = \frac{4}{\pi^2} \cdot \frac{k_{31}^2}{1 - k_{31}^2} \cdot f_p. \quad (9)$$

Transformation coefficient (K_T) and the efficiency (η) are calculated by the expressions:

$$K_T = \frac{\sqrt{m} A \cdot Q_M \cdot k_{33}^2 \cdot d_{31} \cdot l_1}{\pi^2 \cdot (1 - k_{33}^2) \cdot d_{33} \cdot a}, \quad (10)$$

$$\eta_m = \frac{2G_{33}}{2G_{33} + \pi^2}, \quad (11)$$

where m is the number of layers, d_{33} is the piezoelectric constant.

The piezoelectric transformer material was chosen as lead zirconate titanate with appropriate parameters shown in Table 1. The calculated results of the electrical equivalent circuit parameters are shown in Table 2, and the transformer parameters are shown in Table 3.

The samples have the dimensions such as the length of 10 mm, the width of 5 mm, and the thickness of 1 mm. The study showed that the parameters of the proposed transformer are 80% higher than the traditional piezoelectric transformer. In analyzing the dependences it was found that the transformation coefficient and the operating frequencies range increase with increasing number of layers. The operating frequencies range and the transformation coefficient for the single-layer structure were 0.7 kHz and 4800, respectively. The operating frequencies range and the transformation coefficient for the three-layer structure were 2.2 kHz and 7200, respectively. The operating frequencies range and the transformation coefficient for the five-layer structure were 3.6 kHz and 8500, respectively.

3. CONCLUSIONS

The results show the possibility of increasing the operating frequency range of more than 5 times, and the transformation coefficient of more than 80%. It was determined that the transformer efficiency of 90% didn't depend on the number of layers and had a constant value in the whole operating frequencies range. The use of a piezoelectric multilayer transformer allows to expand the frequency range and increase the transformation coefficient.

REFERENCES

1. Lavrinenko, V. V., "Piezoelectric transformers," *Energy*, 215, Moscow, 1975 (in Russian).
2. Yang, J. S., X. Zhang, and Y. Hu, "Analysis of rosen piezoelectric transformers with a varying cross-section," *IEEE Transactions on Ultrasonics, Ferroelectrics, and Frequency Control*, Vol. 55, No. 7, 1632–1639, 2008.

EMC Pre-compliance Test of RFIC and RF Systems Using a Laboratory GTEM Chamber

H. X. Araujo and L. C. Kretly
University of Campinas, Brazil

Abstract— In this work, the EMC — Electromagnetic Compatibility of RF systems is dealt with the use of techniques for low emission and susceptibility. In general, as the electronic device the major responsible of unintentional emissions and coupling, some specific pre-compliance setup tests were employed to analyze these detrimental effects to the system as a whole. A GTEM — Gigahertz Transverse Electromagnetic cell operating from 500 MHz–18 GHz was designed and built. Additional techniques were done to improve this chamber in terms of frequency range and cost effect. Simulated and experimental results are compared to validate the proposed EMC setup.

1. INTRODUCTION

Nowadays, the necessity to control the electromagnetic emissions and interference between circuits and electronic devices becomes a crucial point to assure its correct operation inside an electromagnetic environment [1]. Some approaches were designed to support the pre-compliance tests (EMC/EMI/EMS) setups, which are not designed to replace the well-known compliance equipments (anechoic chamber, stirring chamber, blue test chamber, etc.) but give a previously information about the device behavior. All of them have consolidated standards and regulations.

Based on the advantages in terms of frequency range, cost effect, and its versatility to realize both EMI/EMS a GTEM to operate from 500 MHz–18 GHz, with a test area of 10 cm × 10 cm × 10 cm, was designed and built [2]. Basically, the GTEM cell has an internal conductor called septum to carry the radiation over the DUT — device under test, in case of immunity test, or couple the interferences from the DUT, EMI test. Similar to a rectangular coaxial transmission line with outer conductors closed and joined together, the GTEM cell has tapered ends acting as transitions to adapt it to standard 50 Ω coaxial connectors [3]. The central conductor of the cell provides electromagnetic propagation in TEM mode. Therefore, the electromagnetic field is uniform only within a certain region of the chamber, normally in its middle, where the DUT should be located.

EMC problems associated to ICs are basically classified as intra-chip or externally-coupled [4]. When a circuit is interfered by the noise from another circuit on the same chip, an intra-chip problem is related. On the other hand, when the noise from an IC interferes with circuits or devices off the chip, it is called externally-coupled. Particularly, both of them can be analyzed with a GTEM cell.

2. GTEM PRE-COMPLIANCE TEST

The origin of the Gigahertz Transverse Electromagnetic chamber (GTEM) was based on the transverse electromagnetic chamber (TEM) which is basically a planar expanded transmission line operating in the TEM mode to simulate a free space planar wave [3]. This expanded waveguide with a flat and wide center conductor and coated by hybrid termination, which involves 50 Ω current termination and RF absorbers, is commonly used in analyses of devices that are physically small and compacts, especially electronic components, including antennas and mobile phones.

At low frequencies only the TEM mode propagates on the chamber. However, with the increase of the operational frequency, the TE and TM modes can be excited inside the chamber. The maximum frequency is calculated from the first lower resonant of the higher modes, which depends on the size and shape of the chamber.

The excitation section — APEX is the transition from the 50 Ω coaxial cable to the rectangular transmission line. It takes about 10% of the overall length of the cell with a front panel large enough to mount a *N* connector. To avoid reflections, the match between the connector and the center conductor should be carefully projected and implemented.

There are some known ways to build the APEX, such as casting the metal sheet or through the solder of two or more folded metallic sheet. Thus, the adopted strategy was split the APEX in two equal parts, and then weld them making it one, so RF shielding tests were exhaustively done, as can be seen in Fig. 1.

For a RF signal incident on one port, some fraction of the signal bounces back out of that port, some of it scatters and exits other ports (and is perhaps even amplified), and some of it disappears as heat or even electromagnetic radiation [5]. Therefore, to avoid reflections, the match between the connector and the center conductor should be carefully projected.

The measurements of electric and magnetic field inside and outside the chamber was done with near field probes, EE-6992 Electro-Metrics ball and loop respectively.

The ball probes are capable to realize cable and circuit measurements with a good accuracy in frequencies above 1 GHz. These probes can be easily implemented with coaxial cables and BNC connectors.

In the other hand, the magnetic loop has wide application, since fall of tension and current flux measurements in conductors and plans. Normally, these probes are shielded, otherwise they become sensitive for both magnetic and electric fields.

Another crucial point is the hybrid termination at the end of the chamber. To ensure the best accuracy of the chamber, the correct $50\ \Omega$ current termination and the RF absorbers should be carefully designed and implemented. The numerical simulation of a GTEM cell is an important tool to study and optimize such chamber. Simulation results in both frequency and time domain may be compared with values measured in real GTEM cells. As the chamber was designed to operate from 500 MHz to 18 GHz, the return loss for this range was simulated, as can be seen in Fig. 2(a). Comparing the results for the APEX/GTEM with and without septum, it can be observed the clear importance of the septum. Without septum (dash line) the return loss is almost zero along all the frequency range. Experimental measurements were also done to verify the real necessity to design correctly and carefully the APEX/GTEM. The measurements were done through the HP 8714ET RF Network Analyzer. Due to frequency range limitation, the return loss calculation was done from 0.5 GHz–3 GHz, and is shown in Fig. 2(b). As the implemented chamber is working correctly, EMI and EMS can be feasibly.



Figure 1: RF shielding test.

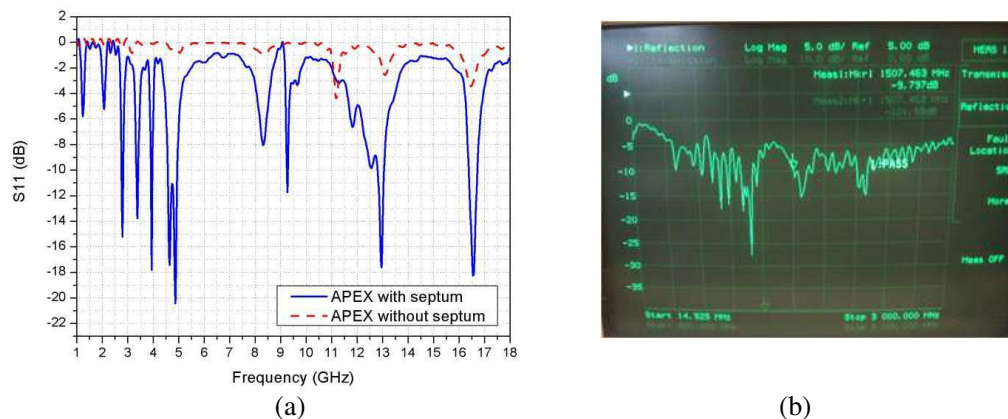


Figure 2: (a) S_{11} -parameter comparison between the APEX with and without septum; (b) S_{11} -parameter of the full GTEM.

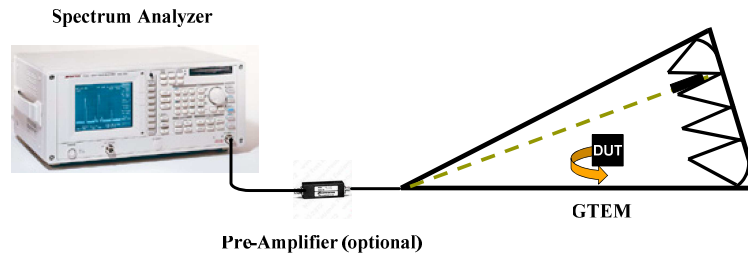


Figure 3: Setup configuration with GTEM chamber for EMI compliance test.



Figure 4: (a) EMI test — pulse identification at 2.29 GHz; (b) EMI test — pulse identification at 2.45 GHz.

3. EMI AND EMS TEST

The use of GTEM cells for emission test consists in the evaluation of the power magnitude that propagates on the TEM mode from the DUT, although the correct position of this power is unknown. Because it is a qualitative analysis, the study is done from the signal level along the frequency range. In this analysis, a spectrum analyzer is connected to the APEX of the chamber, so all the radiated signal emitted from the DUT can be monitored, Fig. 3. The device under test can be wireless or not, so that the power supply and control cables are connected to the DUT through a special shielded via with high frequency filters. As the GTEM works as a transmitter and a sensor, the use of antennas is not needed to measure the field strength from the DUT, which are captured by the septum. Therefore, the good accuracy is guarantee when the physical dimensions of the DUT are in accordance with the dimensions of the GTEM's test area.

The results of EMI obtained from the GTEM chamber can be easily correlated to the others pre-compliance setup tests. The correlation with a TEM cell, with the same test area, can be done trough the following expression:

$$\delta = \frac{V_{out,2}(f)}{V_{out,1}(f)} = \frac{h_1}{h_2} \quad (1)$$

where $V_{out,1}(f)$ is the voltage spectrum measured at the GTEM cell, with height h_1 from the bottom to the septum, and $V_{out,2}(f)$ the voltage spectrum measured at the TEM cell, with height h_2 from the bottom to the septum. The emission level shift between these two setups is given by:

$$V_{out,2}(f)|_{dB\mu V} = V_{out,1}(f)|_{dB\mu V} + 20 \log \left(\frac{h_1}{h_2} \right). \quad (2)$$

The correlation with the other setups like OATS — Open Area Test Site, Stirring Chamber e Anechoic is not straightforward, which demands the use of specific software.

The susceptibility tests are basically measurements that identify the DUT propensity to be interfered by radiation from other devices at the same environment, thus verifying the immunity of the device under test.

By definition, immunity is a relative measurement of a device capability to operate in the presence of interfering electromagnetic fields [6].

The EMS test is accomplished with a pulse generator coupled to the APEX of the GTEM, and the DUT allocated at the test area, where it will be exposed to a spherical electromagnetic field. Therefore, the performance of the DUT is monitored in function of the input power.

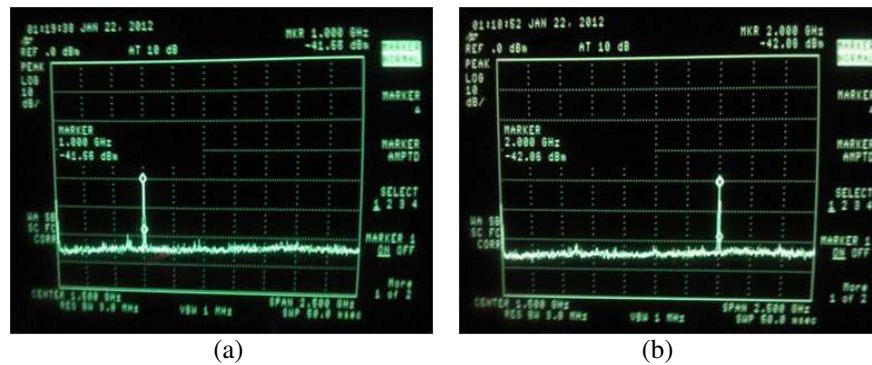


Figure 5: (a) EMS test — pulse identification at 1 GHz; (b) EMS test — pulse identification at 2 GHz.

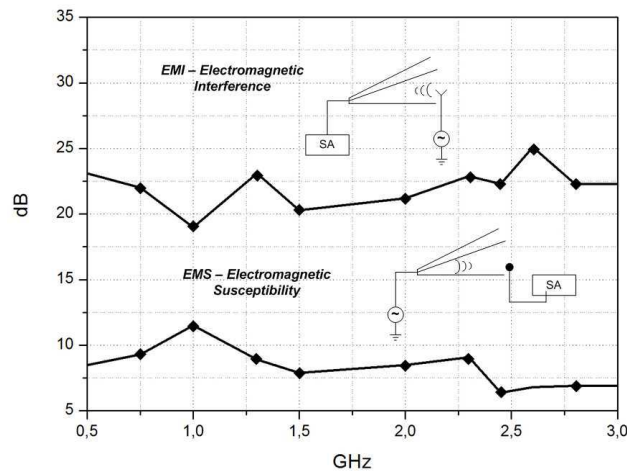


Figure 6: EMI/EMS tests with the laboratory grade GTEM chamber.

Due the aperture angle around 20° , the incident waves are slightly spherical, exposing the DUT to an almost planar wave. Thus, the comparison between the results for EMS tests obtained by the GTEM chamber with other compliance setups can be feasibly.

The EMI and EMS test were done with a HP 8714ET Network Analyzer. For the interference test, a quasi-yagi antenna was connected to the NA and then allocated inside the test area. The signal was monitored by a HP 8593E Spectrum Analyzer, connected to the APEX, and the tests were performed at the frequencies 0.5 GHz to 3 GHz. In Fig. 5 is shown the pulse identification at the frequencies 2.29 GHz and 2.45 GHz. On the other hand, for the EMS test the NA was connected to the APEX and an electric probe was placed at the test area. The pulses were also generated from 0.5 GHz to 3 GHz. In Fig. 6 is shown the pulse identification at the frequencies 1 GHz and 2 GHz. The EMI/EMS measurements are synthesized by Fig. 6.

4. CONCLUSIONS

Studies and researches around the electromagnetic compatibility have been a strongly grown during the last years. Therefore, some methodologies have been used and developed in prevention and for solving the problems related to interference and immunity.

Thus, in this work, it was shown the use of a laboratory grade GTEM chamber to perform EMI and EMS compliance tests of integrated circuits and electronic systems. The EMI/EMS test performed with a quasi-yagi antenna showed a good sensitivity of the implemented structure. Based on the obtained results and considering the power level, with the proposed GTEM chamber is possible to realize interference and immunity test of a wide variety of small and compact electronic devices.

ACKNOWLEDGMENT

The authors would like to thank FAPESP — São Paulo Research Foundation — for the partial financial support.

REFERENCES

1. Montrose M. I. and E. M. Nakauchi, *Testing for EMC Compliance*, Wiley Interscience, New York, 2004.
2. Araujo, H. X. and L. C. Kretly, “An EM simulation and design a GTEM chamber for EMC pre-compliance tests on electronic board and ICs in 500 MHz–18 GHz range,” *Momag 2010*, Vila Velha, Brazil, Aug. 2010.
3. Konigstein, D. and D. Hansen, “A new family of TEM-cells with enlarged bandwidth and optimized working volume,” *Proceedings of the 7th International Zurich Symposium on Electromagnetic Compatibility*, 127–130, Zurich, Mar. 1987.
4. Dhia, S. B., M. Ramdani, and E. Sicard, *Electromagnetic Compatibility of Integrated Circuits: Techniques for Low Emission and Susceptibility*, Springer, New York, 2006.
5. Yamashita, E. and K. Atsuki, “Strip line with rectangular outer conductor and three dielectric layers,” *IEEE Transactions on Microwave Theory and Techniques*, Vol. 18, No. 5, May 1970.
6. “Electromagnetic compatibility (EMC) — Part 4: Testing and measurement techniques — Section 3: Radiated, radio-frequency, electromagnetic field immunity test,” International Standard CEI/IEC 1000-4-3, Geneva, Feb. 1995.

Bayesian Estimation of Tumours in Breasts Using Microwave Imaging

E. Khosrowshahli¹ and A. Jeremić²

¹Department of Biomedical Engineering, McMaster University, Hamilton, ON, Canada

²Department of Electrical Engineering, McMaster University, Hamilton, ON, Canada

Abstract— According to Canadian Cancer Society, breast cancer is the most frequently diagnosed cancer in women. Our ability to potentially detect breast cancer in an early stage has potential of significantly decreasing mortality and hence is a very important issue in healthcare. Currently, mammography has been used widely for screening women over 50 who are statistically more vulnerable. However it suffers from some limitations such as false negative and positive results, using ionizing radiation and patient's discomfort. Microwave imaging has been introduced recently to overcome drawbacks of this method. In breast microwave imaging the imaging system consists of an array of antennas which can serve both as transmitting and receiving antennas. Therefore it is possible to illuminate object of interest (breast) from multiple directions thus obtaining a full three dimensional scan whose resolution depends only on the number of antennas. One of the most difficult parts when detecting potential tumours in breasts is presence of modelling noise due to large amount of scattering, which severely deteriorates performance of estimation and detection algorithms. In this paper, we propose a parametric 3D model of breast microwave propagation, i.e., signal measured on antennas with respect to tumours' and breast parameters including electromagnetic properties and geometry (our model includes multiple tumours with arbitrary shapes.) We illustrate the applicability of our results through numerical examples.

1. INTRODUCTION

According to Canadian Cancer Society, breast cancer is the most frequently diagnosed cancer in women with over 23,400 new cases expected in 2011 [1]. Due to the progressive nature of the disease early detection is extremely important and can significantly improve survival rates. Currently all of the clinical procedures are based on mammography which is routinely prescribed for older women who tend to be more susceptible to the disease [2]. Although mammography is extremely important diagnostic technique, it suffers from some limitations such as false negative and positive results, using ionizing radiation and patient's discomfort [2, 3]. The number of false positives is rather significant in the case of so called dense breasts in which healthy tissue may be mistaken for malignant and as a consequence unnecessary biopsies are prescribed. Furthermore, complicating the matter is the fact that mammography is a two-dimensional technique in which three-dimensional images are obtained through image reconstruction from 2D projections which can also lead to false positives.

Microwave imaging has been recently proposed as an additional medical imaging technique which can potentially overcome some of the shortcomings of the mammography. Essentially the technique is based on illuminating breast with electromagnetic-wave(s) in microwave range. From the physical point of view this can be represented as a wave propagation in medium (breast) that contains scatterers (both healthy and malignant tissue). Due to the fact that malignant tissue has larger conductivity the measurements obtained by receiving array of antennas will be different if the scatterers are present. Therefore once the wave propagates through the breast the received signal is analyzed in order to obtain permittivity map using appropriately selected image reconstruction technique [4]. Most of the image reconstruction techniques minimize a particular cost function (e.g., mean-square error). In most cases the number of unknowns (e.g., number of pixels in the map) is much larger than the number of available measurements which requires an additional constraint.

In this paper, we propose a simplified parametric inverse 3D model which enables us detection of tumour presence and estimation of its size and/or position. Most of the existing solutions [7] employ non-parametric image reconstruction techniques. We believe that accuracy can potentially be improved by considering parametric models. In general parametric models can increase modelling noise. However we believe that appropriately defined parametric model can be useful as long as an appropriate clinical decision can be made based on reduced number of parameters. To this purpose we first develop a three-dimensional finite element model of electromagnetic wave

propagation through the breast tissue. We define our model with respect to tumour size and location and assume that the permittivity of tumour can be modelled by Gaussian probability density function (pdf). We then derive probability density function of the measured data (power received by receiving antennas) and the corresponding likelihood function. We then maximize the likelihood with respect to the unknown parameters. The outline of the paper is as follows. In Section 2, we present computational models of electromagnetic wave propagation in breast when tumours are absent and present. In Section 3, we discuss how the aforementioned models were implemented using COMSOL. In Section 4, we present the statical models and present estimation algorithm. In Section 5, we present simulation results and discuss their potential use for inverse problems. Finally, Section 6 concludes the paper.

2. PHYSICAL MODEL

In this section, we develop mathematical model describing the measured signals. The imaging system consists of several antennas which can both serve as transmitting and receiving antennas. These antennas in principle can be distributed over the breast surface thus allowing for a three-dimensional scan whose resolution depends only on number of antennas. Obviously the number of antennas is determined by their size which may be constrained by technical requirements such as antenna-to-antenna noise (interference). Once the microwave is generated it propagates through the volume of the breast according to Maxwell's equations which in this particular case can be reduced to the phasor form since microwave antennas operate in a single-frequency mode.

It should be observed that any non-homogeneity in the object can be modelled as a scatterer and thus in the presence of multiple scatterers the resulting electromagnetic field becomes very complex superposition of reflected and refracted waves. Since malignant tissue has significantly larger permittivity than healthy tissue it can also be modelled as a scatterer (see Figure 1). The reflection/refraction from scatterers can then be modelled as described in Figure 2.

In the remainder of the paper we will assume that in the absence of cancer the scattering in the breast is due only to small non-homogeneities which will be included as the modelling noise. Of course if a particular patient is submitted to continuous monitoring in a regular intervals the previous images can be used a reference signal and thus "healthy scattering" can be properly recorded and modelled.

In the absence of scatterers the propagation can be described as:

$$\nabla^2 E + k^2 E = 0 \quad (1)$$

$$\nabla^2 H + k^2 H = 0 \quad (2)$$

where we implicitly assume that the medium (breast) is source-free, E and H are intensities of electric and magnetic fields respectively, $k = \omega\sqrt{\mu\epsilon}$ where ω is frequency, μ magnetic permittivity, and ϵ complex electric permittivity.

In this paper, we assume that the tumours can be modelled as spheres and therefore are uniquely defined by location vector and radius. In general, arbitrarily shaped tumours can be represented by spatial Fourier transform and corresponding spatial frequency amplitudes and phases. As we

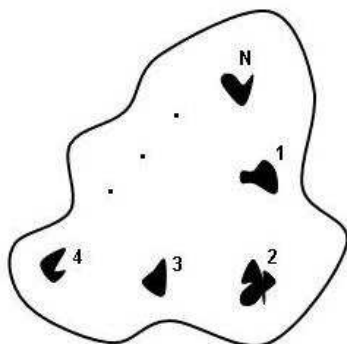


Figure 1: Medium with multiple scatterers.

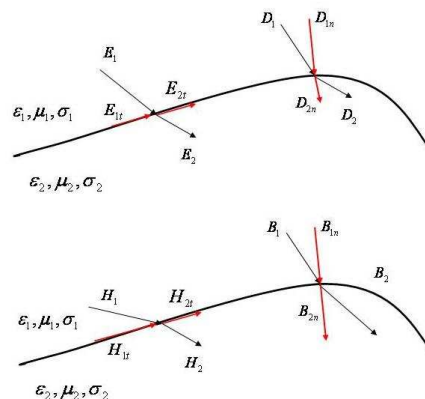


Figure 2: Boundary conditions.

stated before, the electromagnetic properties of the malignant tissue is significantly different than breast tissue and thus proper boundary conditions must be considered in order to ensure continuity (see Figure 2):

$$\vec{n} \times (\vec{E}_1 - \vec{E}_2) = 0 \quad (3)$$

$$\vec{n} \times (\vec{H}_1 - \vec{H}_2) = 0 \quad (4)$$

$$\vec{n} \times (\epsilon_1 \vec{E}_1 - \epsilon_2 \vec{E}_2) = 0 \quad (5)$$

$$\vec{n} \times (\mu_1 \vec{H}_1 - \mu_2 \vec{H}_2) = 0 \quad (6)$$

3. FINITE-ELEMENT MODEL

In order to solve the above equations we utilize finite-element method by developing three-dimensional model using RF module in COMSOL Multiphysics software. In this paper, we model the breast as a sphere with radius of 100 mm as shown in Figure 3. One antenna which acts as a transmitter is located on one side and nine receiving antennas are distributed on the other side of the sphere. These antennas are modelled as slim cubes which are centred on the surface of the sphere. Three boundary conditions are used to send waves in the medium. Electric field is applied to transmitter antenna. Perfect electric conductor boundary condition is applied to sides of antennas in order to guide wave through them, and scattering boundary condition is applied to the rest of surfaces to let waves propagate freely. Afterward, for different studies one or multiple tumours with arbitrary shapes can be modelled. In this study tumour is considered as a sphere inside the breast with an arbitrary size and in arbitrary position. Three different studies are done using this model: effect of tumour location, tumour size and tumour permittivity. As an example of wave propagation in simulation, in Figure 4, y -component of electric field is shown for the case of eccentric tumour. In this figure tumour is located between second and third plates, and scattering electric field is clearly seen around the tumour, and higher intensity of electric field immediately after the source is obvious.

4. STATISTICAL MODEL

We assume that the measured signal is given by average power and normalized to the transmitting antenna power. The measured signal when the tumour is absent \vec{y} is then given by

$$\vec{y} = \vec{f}_0 + \vec{e} \quad (7)$$

where \vec{f}_0 is model predicted vector of measurements (power) calculated using finite-element model and \vec{e} is the measurement/modelling noise.

In the presence of tumour the measured signal becomes

$$\vec{y} = \vec{f}(R_t, \vec{R}, \sigma, \epsilon_r) + \vec{e} \quad (8)$$

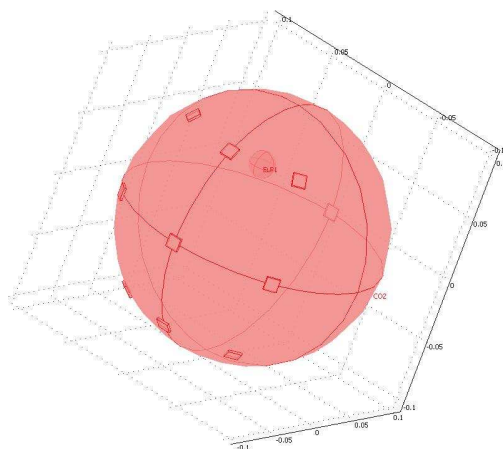


Figure 3: Geometry of the breast.

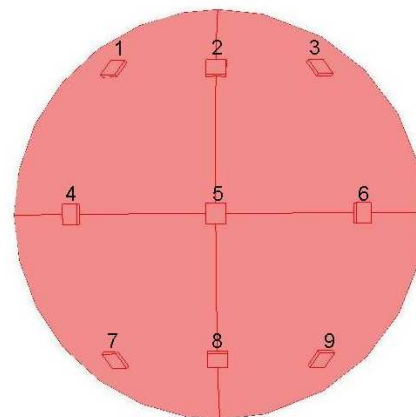


Figure 4: Antenna positions.

where R_t is the radius of tumour, \vec{R} is the position of tumour, σ and ϵ_r are conductivity and electric permittivities respectively. Note that in the above model we assumed a single tumour (scatterer) in order to simplify the computational cost but can be extended to account for multiple scatterers at the expense of computational time.

We assume that the conductivity and permittivity are given by Gaussian random variables with $\sigma = 4\text{S/m}$ and $\epsilon_r = 50$ means respectively and standard deviations of 10% of their nominal values [4]. The corresponding probability density function of the measured signal in the absence of tumours is multivariate Gaussian with mean \vec{y}_0 and covariance matrix $\sigma_e^2 I$ where we assumed that the measurement noise is uncorrelated in space and time. Note that the multiple measurements can be obtained in order to remove the measurement noise in statistically optimal way.

In presence of scattering the probability density function is given by

$$p_\sigma(\sigma) \cdot p_{\epsilon_r}(\epsilon_r) \cdot p(\vec{y}|\sigma, \epsilon_r, \vec{R}) \quad (9)$$

Note that for a particular patient conductivity and permittivity can be treated as deterministic variables. In this paper, we assume that sufficient set of previously measured properties is available and hence certain a priori knowledge on physiological values is available. The parameters can then be obtained by minimizing the cost function

$$c(\vec{R}_t, R, \sigma_r, \epsilon_r) = \log \left[p_{\sigma_r}(\sigma_r) \cdot p_{\epsilon_r}(\epsilon_r) \cdot p(\vec{y}|\mu_r, \epsilon_r, \vec{R}) \right] \quad (10)$$

which is commonly known as maximum a posteriori estimate of unknown parameters. Note that because of nonlinear dependence of measured signals on physical parameters the above estimations have to be performed using numerical optimization methods and Monte-Carlo simulations (in order to obtain posterior distribution).

5. NUMERICAL RESULTS

In order to evaluate the performance of our inverse model we simulate the measurement data using COMSOL and then add Gaussian noise in order to simulate measurement noise. In this preliminary approach we ignore several issues such as: skin reflection, calibration problems, antenna-to-antenna crosstalk, etc.

Although these issues are important our preliminary goal in this paper is to demonstrate ability of the model to accurately estimate tumour parameters using simulated data. The results of this analysis can then be useful in properly designing antennas for realistic measurements. We simulate measurement data for 100 patients for which the conductivity and permittivity are generated using aforementioned Gaussian distributions. For each of the patients we then generate posterior distribution $p(\vec{y}|\sigma, \epsilon_r, \vec{R}, R_t)$ in order to calculate the parameter estimates. In Figures 5 and 6, we illustrate posterior distribution for arbitrarily chosen antenna for two different tumour sizes.

In Figure 7, we show the y -component of the electric field in the presence of scatterer. As we can see the presence of tumour causes irregular patterns in the electric field which can be used for inverse modelling and consequently detection and estimation. In Figure 8, we show the mean-square error (MSE) for tumour size estimate as a function of tumour size. However, note that in reality the larger tumours have irregular (star-like patterns) and the effect of that was not included in this

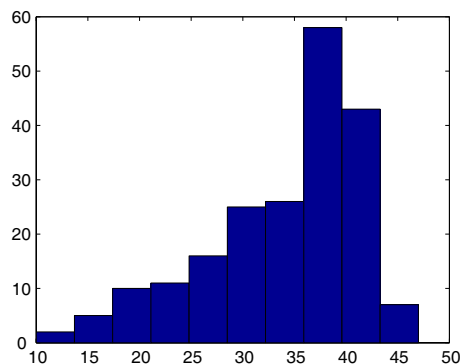


Figure 5: Posterior distribution for tumour in center size 1 cm.

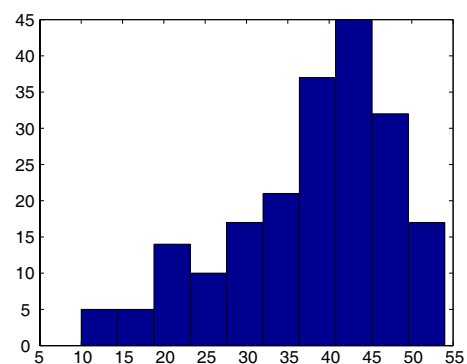


Figure 6: Posterior distribution for tumour in center size 2 cm.

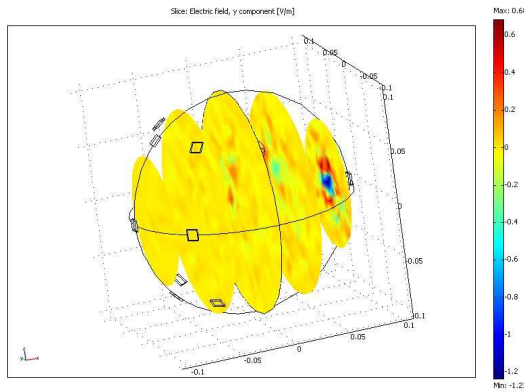


Figure 7: Electric field.

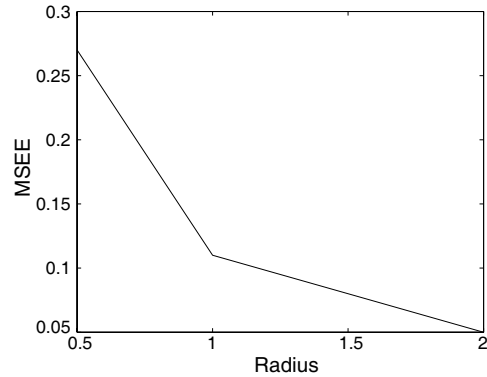


Figure 8: MSE of radius estimate as a function of tumour size.

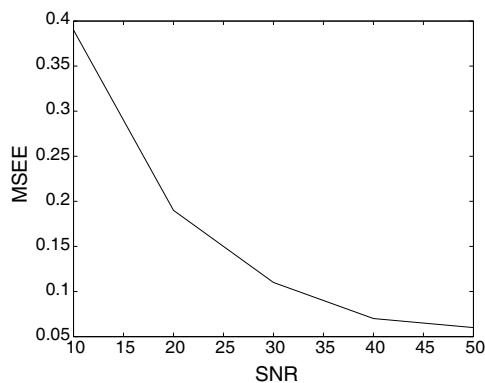


Figure 9: MSE of radius estimate.

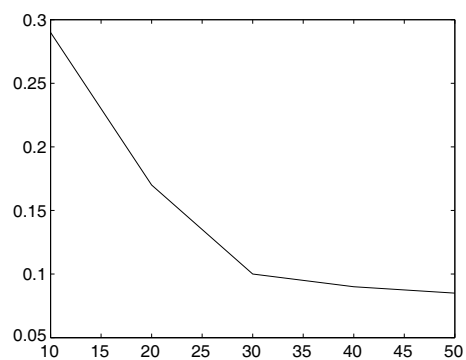


Figure 10: MSE of location estimate.

work. Consequently the actual estimation error may not decrease as rapidly as in our simulation results.

In Figures 9 and 10, we illustrate mean-square-error (MSE) estimates of tumour size and location as a function of signal-to-noise ratio (SNR).

6. CONCLUSION

In this paper, we proposed frequency domain parametric three-dimensional model of microwave propagation in breasts. The results presented in this paper suggest that it may be possible to obtain accurate estimates of tumour position and size using parametric model. Of course certain issues (e.g., skin reflection) have been disregarded and will be addressed in future work. Furthermore these results can be useful when designing antennas since these models can be used to determine the necessary power of the transmitted signal that is necessary in order to achieve certain estimation accuracy.

REFERENCES

1. Canadian Cancer Society, <http://www.cancer.ca/canada-wide/>.
2. Gemignani, M. L., "Breast cancer screening: Why, when, and how many?," *Clinical Obstetrics and Gynecology*, Vol. 54, No. 1, 125–132, 2011.
3. Tice, J. and K, Kerlikowske, "Screening and prevention of breast cancer in primary care," *Primary Care: Clinics in Office Practice*, Vol. 36, No. 3, 533–558, 2009.
4. Fear, E. C., "Enhancing breast tumor detection with near-field imaging," *IEEE Microwave Magazine*, Vol. 3, No. 1, 4846, 2002.
5. Cheng, D. K., *Field and Wave Electromagnetics*, Addison-Wesley Publishing Company, 1983.
6. Semenov, S., et al., "Microwave-tomographic imaging of the high dielectric-contrast objects using different image reconstruction approaches," *IEEE Transactions on Microwave Theory and Techniques*, Vol. 53, No. 7, 2284–2294, 2005.
7. Pastorino, M., "Stochastic optimization methods applied to microwave imaging: A review," *IEEE Transactions on Antennas and Propagation*, Vol. 55, No. 3, 538–548, 2007.

Design of High Isolation Electronically Switchable Bandpass Filter

Shih-Fong Chao and Ming-Wei Shih
National Kaohsiung Marine University, Taiwan

Abstract—In this paper, a simple method to design a high isolation electronically switchable bandpass filter is proposed. The circuit integrates a microwave switch and a microwave bandpass filter into a single circuit component. The uniform impedance resonator is loaded with a pin diode to change its resonant frequencies under different bias voltages. By loading the pin diode at different positions of the constituted resonators, the resonant frequencies can be misaligned over the band of interest to achieve a wideband isolation in the isolated state. In the thru state, the circuit shows a bandpass response with a measured insertion loss of 3 dB at the center frequency of 1 GHz, and the 3 dB fractional bandwidth is 8%. In the isolated state, the measured isolation is 51 dB at the center frequency and is higher than 30 dB from dc to 5 GHz. The paper proposed a simple and effective method to realized an electronically switchable bandpass filter with high isolation, and the circuit successfully increases the level of integration of the RF front end.

1. INTRODUCTION

A microwave switch is a essential component to control RF signal flow in the modern communication systems. Several literatures using passive FETs or pin diodes have been reported [1, 2]. However, these switches are wideband designs, implying that they can not provide adequate band selectivity for a system application. Therefore, a bandpass filter will be needed to cascade with a switch to reject out-of-band signals.

Recently, several methods were proposed to integrated the building blocks of the RF front into a multi-function circuit [3–6]. In [3], an SPDT bandpass filter-integrated switch that integrate an SPDT switch and a bandpass filter was proposed. Switchable dual-band bandpass filters that achieve independent switching control of band selection was proposed in [4, 5]. In [6], a balun-integrated bandpass switchplexer that integrates an SPDT switch, a diplexer, and a balun was demonstrated.

In this paper, a new method to design a high-isolation switchable bandpass filter is proposed. The pin diode loaded uniform resonator is used to realized the circuit instead of using stepped-impedance resonators. By connecting the pin diode at different locations of the uniform resonator, the resonant frequencies of the resonator can be controlled. Therefore, a high isolation can be obtained by interlacing the resonant frequencies over the band of interest in the isolated state.

2. CIRCUIT DESIGN

Figure 1 shows the structure of the diode-loaded uniform resonator and its equivalent circuit under different bias conditions. The θ_1 is the electrical length from the loading location to the open end, and θ_2 is the electrical length from the loading location to the other open end. When the diode is reversed biased (off-state), the resonator is loaded with a small capacitor. If the diode is forward biased (on-state), the resonator will be connected to ground via a small resistor R . Since the R is small, the diode could be considered as a short circuit to ground. Thus, the resonant frequencies are determined by two quarter-wavelength resonator with one end short to ground.

Figure 2 shows the circuit schematic of the proposed switchable bandpass filter. The circuit is composed by three diode-loaded hairpin resonators. In the thru state, the diodes are reversed biased, the first resonant frequency of each resonator is 1 GHz. The circuit was designed to have

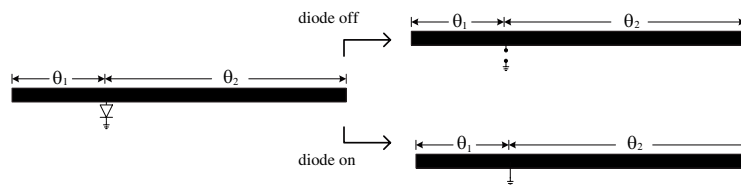


Figure 1: Photograph of the DPDT filter-integrated switch A.

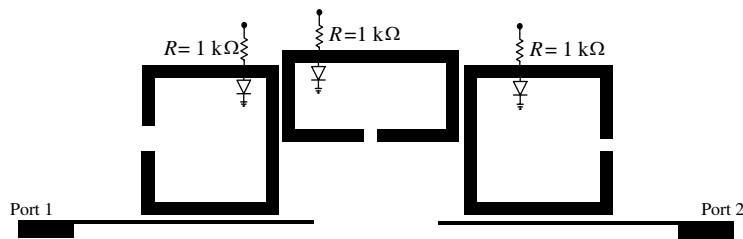


Figure 2: Circuit schematic of the proposed switchable bandpass filter.

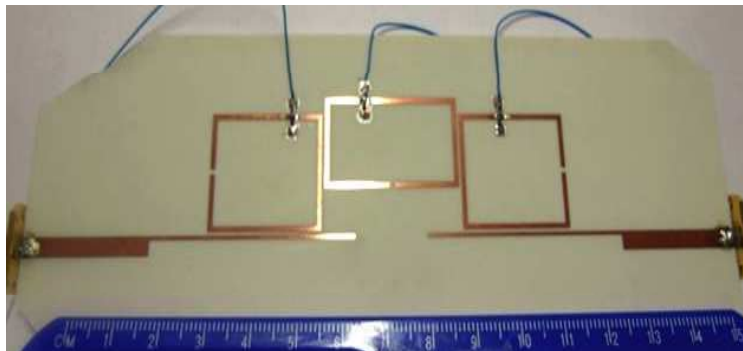


Figure 3: Photograph of the switchable bandpass filter.

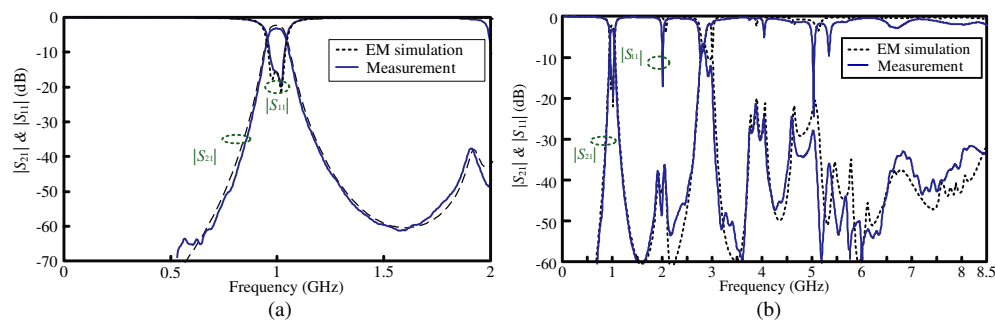


Figure 4: Simulation and measured results of the switchable bandpass filter in thru state. (a) Narrow band response. (b) Wideband response.

a 3rd-order Butterworth bandpass response at 1 GHz, and 3-dB fractional bandwidth $\Delta_{3\text{dB}}$ of 8%. The coupling coefficients and the external quality factor Q_{ext} can be obtained as

$$\begin{aligned}
 M_{12} &= \frac{\Delta_{3\text{dB}}}{\sqrt{g_1 g_2}} = M_{23} = 0.059 \\
 Q_{ei} &= \frac{g_0 g_1}{\Delta_{3\text{dB}}} = Q_{eo} = 10.9
 \end{aligned} \tag{1}$$

where M_{ij} represents the coupling coefficient between resonators i and j , g_n is the low-pass prototype parameter, and Q_{ei} and Q_{eo} are the external quality factors associated with the input and output couplings, respectively [7]. In the isolated state, the diodes are forward biased. By loading the diodes at different locations of the resonators, the resonant frequencies can be scattered over the band of interest. Thus, a high isolation could be obtained between the input and the output ports.

3. MEASUREMENT

The circuit is fabricated on the RO4003C substrate with $\epsilon_r = 3.58$, $h = 0.8$ mm, and $\tan \delta = 0.0015$. Fig. 3 is the photograph of the switchable bandpass filter. Fig. 4 shows the measured results when

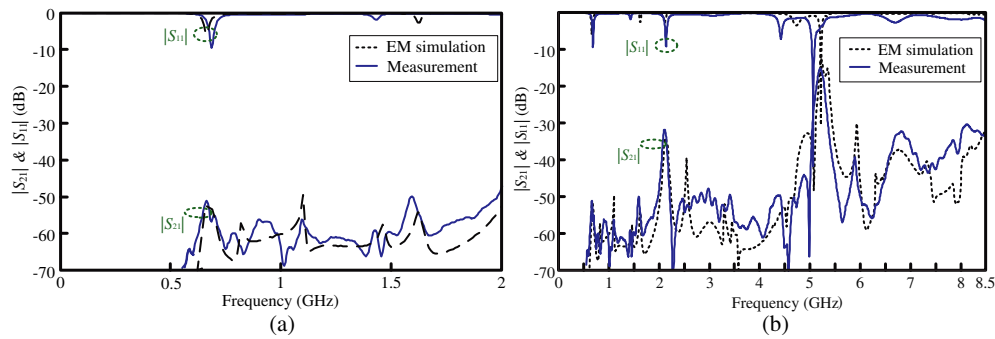


Figure 5: Simulation and measured results of the switchable bandpass filter in isolated state. (a) Narrow band response. (b) Wideband response.

the circuit is at thru state. It can be observed that a bandpass response with a passband insertion loss of 3.0 dB at center frequency of 1 GHz was measured, and the 3-dB bandwidth is 8.5%. The measured isolations of the circuit is shown in Fig. 5. The isolation is about 60 dB at the center frequency of 1 GHz and is better than 32 dB from dc to 5 GHz.

4. CONCLUSION

In this paper, a high isolation electronically switchable bandpass filter is designed and implemented. By loading the pin diode at different positions of the constituted resonators, the resonant frequencies can be misaligned to obtain an isolation in the isolated state. In the thru state, the circuit shows a bandpass response with a measured insertion loss of 3 dB at the center frequency of 1 GHz. In the isolated state, the measured isolation is 51 dB at the center frequency. The circuit successfully integrates a microwave switch and a bandpass filter into a single circuit and thus increases the level of integration of the RF front end.

ACKNOWLEDGMENT

The authors would like to thank Prof. Jui-Han Lu for the support of measurement equipments.

REFERENCES

1. Chao, S.-F., H. Wang, C.-Y. Su, and J. G. J. Chern, "A 50 to 94-GHz CMOS SPDT switch using traveling-wave concept," *IEEE Microw. Wireless Compon. Lett.*, Vol. 17, No. 2, 130–132, 2007.
2. Lai, R.-B., J.-J. Kuo, and H. Wang, "A 60–110 GHz transmission-line integrated spdt switch in 90 nm cmos technology," *IEEE Microw. Wireless Compon. Lett.*, Vol. 20, No. 2, 85–87, 2010.
3. Chao, S.-F., C.-H. Wu, Z.-M. Tsai, H. Wang, and C. H. Chen, "Electronically switchable bandpass filters using loaded stepped-impedance resonators," *IEEE Trans. Microw. Theory Tech.*, Vol. 54, No. 12, 4193–4201, 2006.
4. Dai, G. L. and M. Y. Xia, "Design of compact dual-band switchable bandpass filter," *Electronics Letters*, Vol. 45, No. 10, 506–507, 2009.
5. Deng, P.-H. and J.-H. Jheng, "A switched reconfigurable high-isolation dual-band bandpass filter," *IEEE Microw. Wireless Compon. Lett.*, Vol. 21, No. 2, 71–73, 2011.
6. Lin, Y.-S., P.-C. Wang, C.-W. You, and P.-Y. Chang, "New designs of bandpass diplexer and switchplexer based on parallel-coupled bandpass filters," *IEEE Trans. Microw. Theory Tech.*, Vol. 58, No. 12, 3417–3426, 2010.
7. Hong, J.-S. and M. J. Lancaster, *Microstrip Filter for RF/Microwave Applications*, K. Chang, Ed., Wiley, New York, 2001.

A Method of High Repetition Rate Femtosecond Optical Pulse Generation by Using Bi-stable Optical Micro-ring Resonators

Sanjeev Kumar Raghuwanshi, Ajay Kumar, and Santosh Kumar

Department of Electronics Engineering
Indian School of Mines, Dhanbad, Jharkhand 826004, India

Abstract— Generation of high repetition rate, short an optical pulse is an important topic of research at the present time. This is because in order to realize a high capacity optical communication system we need a combination of wavelength division multiplexing (WDM) and optical time division multiplexing (OTDM) techniques. In this paper, we propose a novel scheme of high repetition rate, femtoseconds optical pulse generation by using bi-stable optical micro ring resonator where it is possible to achieve a repetition rate of more than few hundred GHz.

1. INTRODUCTION

A combination of WDM and OTDM can result in a high capacity optical communication system within existing limitations. At present the electro-optic modulators can be operated at a rate of 40 Gb/s. To utilize this modulation rate, we must generate optical pulses having a repetition rate much greater than 40 GHz. Thus, to realize a high speed OTDM system, we need a high repetition rate, and short optical pulses. Various methods of optical pulse generation exist in the literature [1–3]. Some of the methods of optical pulse generation are mode locking of semiconductor lasers, harmonically mode locked fiber laser, soliton-assisted time lens compression, short pulse generation by interferometers, and repetition rate multiplication of a low rate pulse source. In this paper our attempts are to generate optical pulses having very high repetition rates.

2. PICOSECONDS PULSE GENERATION SCHEME

A schematic circuit diagram of the picoseconds optical pulse generator is shown in Fig. 1(a). Here, the output of a laser (LD) is phase modulated in an overdriven optical phase modulator (ODPM). The phase modulator can be fabricated on a LiNbO₃ substrate. There are five laser diodes. These five light-waves are combined in a (5 × 1) optical power combiner and at the output we get an optical pulse as shown in Fig. 1(b). This picoseconds pulse generation schemes may be found in greater detailed in Ref. [1]. It is apparent from Fig. 1(b) that higher the modulator drive frequency, the sharper is the pulse generated. It is shown in this paper that the pulse width decreases with the increase in drive frequency (f_m) and a pulse width of 1 ps can be obtained at a drive frequency of 40 GHz. For the case as shown in Fig. 1(a) one can get a value of repetition frequency of the pulse equal to $nf_m = 200$ GHz where $f_m = 40$ GHz. The frequency bandwidth of the pulse is equal to $4nf_m$. In this section, we have discussed one of the established schemes to generate the picoseconds pulse. In next section we will ride this high repetition picoseconds pulse on to the various types of the ring resonator to generate the femtosecond pulse.

3. BASIC INTEGRATED OPTICAL RING RESONATOR

In this section, we will apply the picoseconds optical pulse generated in Section 2 into a micro ring resonator as shown in Fig. 2(a). Let us start with the steady state input output relation of this micro ring-resonator [4, 5],

$$\begin{cases} A = (1 - \gamma)^{\frac{1}{2}} [A_0 \cos(\kappa l) - jB_0 \sin(\kappa l)] \\ B = (1 - \gamma)^{\frac{1}{2}} [-jA_0 \sin(\kappa l) + B_0 \cos(\kappa l)] \end{cases} \quad (1)$$

where κ , l , γ denotes the mode-coupling coefficient of the directional coupler, the coupling length, and the intensity insertion loss coefficient, respectively. When we denote the intensity attenuation coefficient of the waveguide as ρ , B_0 is expressed by $B_0 = B \exp(-\frac{\rho}{2}L - j\beta L)$. Where we also assumed that input/output and resonator waveguide has the same propagation constant β . Then we introduced new parameter x , y , and ϕ , defined by $x = (1 - \gamma)^{\frac{1}{2}} \exp(-\frac{\rho}{2}L)$, $y = \cos(\kappa l)$ and $\phi = \beta L$ respectively, where $\beta_0 = B \exp(-\frac{\rho}{2}L - j\beta L)$. Then after some manipulation of Eq. (1), the

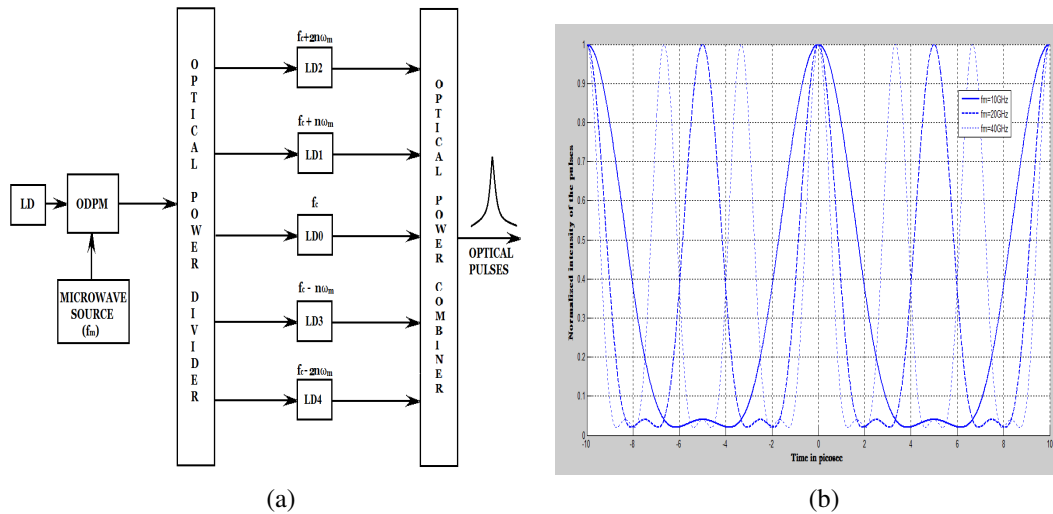


Figure 1: (a) Schematic optical circuit diagram of the Pulse generation LD laser diode, OPDM: overdriven optical phase modulator [1]. (b) Plot of the normalized intensity of the output light pulses as a function of time (t) using the modulator drive frequency (f_m) as a parameter for $n = 5$.

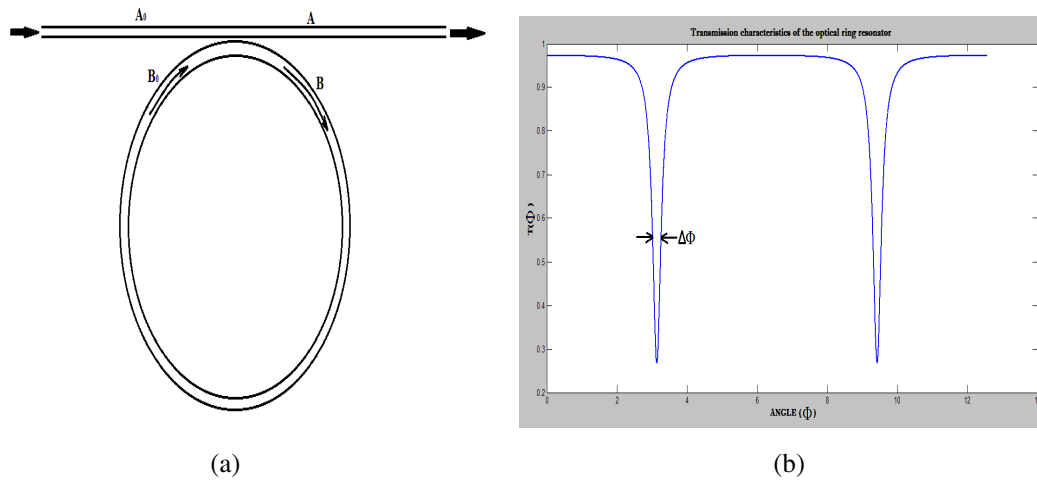


Figure 2: (a) Optical ring resonator. (b) Transmission characteristics of the optical Micro-ring resonator.

intensity transmittance of the optical micro ring resonator is obtained as

$$T(\phi) = \left| \frac{A}{A_0} \right|^2 = (1 - \gamma) \left[1 - \left| \frac{(1 - x^2)(1 - y^2)}{(1 - xy)^2 + 4xy \sin^2 \left(\frac{\phi}{2} \right)} \right| \right] \quad (2)$$

It is apparent that minimum and maximum values of $T(\phi)$ are $T(\phi = 0) = (1 - \gamma) \frac{(x-y)^2}{(1-xy)^2}$ and $T(\phi = \frac{\pi}{2}) = (1 - \gamma) \frac{(x+y)^2}{(1+xy)^2}$ respectively. Fig. 2(b) shows the transmission characteristics of the optical ring resonator as a function of ϕ . It is seen from these equation that $x = y \cong 1$ should be satisfied in order to maximize T_{\max} or minimizing of the T_{\min} as much as possible. Fig. 3 shows the output waveform computed from Eq. (2), when the input signal A_0 is assumed to be a picoseconds pulse generated by circuit shown in Fig. 1 at a drive frequency of 10, 20 and 40 GHz respectively. It is apparent from the Fig. 3, that there is pulse distortion at the peak of the input signal. In this case it seems that there is no further pulse compression effect whatsoever. However the pulse distortion is symmetric in this case.

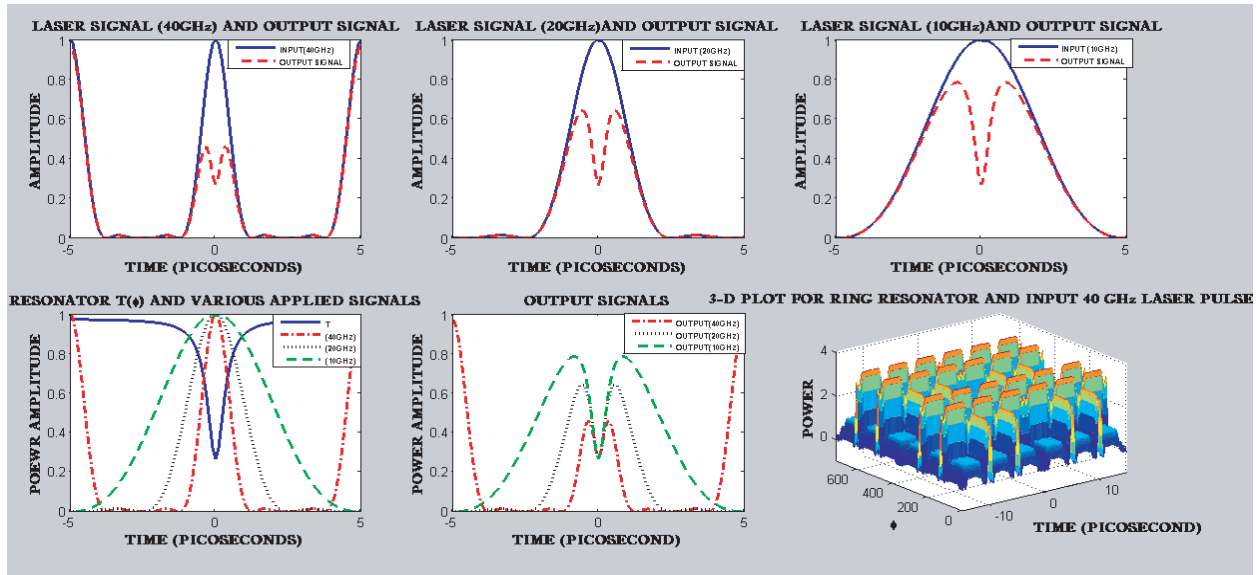


Figure 3: The output waveform for general micro ring resonator when laser signals of different frequencies are allowed to pass through the resonator.

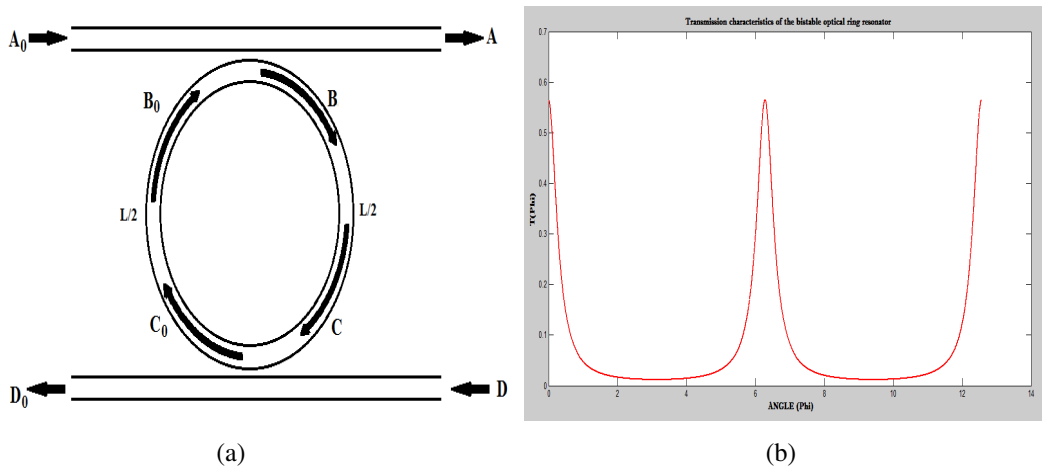


Figure 4: (a) Bi-stable ring resonator ($D = 0$). (b) The transmission characteristics curve for Bi-stable ring resonator.

4. INTEGRATED OPTICAL BI-STABLE MICRO RING RESONATOR

In this section, we change slightly in our micro ring resonator discussed previously into a bi-stable micro ring resonator structure as shown in Fig. 4(a). It proves to be a good technique to compress the optical pulse further. Apparently the steady state input output relation of this case are expressed by [4],

$$\begin{cases} A = (1 - \gamma)^{1/2} [A_0 \cos(kl) - jB_0 \sin(kl)] \\ B = (1 - \gamma)^{1/2} [-jA_0 \sin(kl) + B_0 \cos(kl)] \\ D_0 = (1 - \gamma)^{1/2} [D \cos(kl) - jC \sin(kl)] \\ C_0 = (1 - \gamma)^{1/2} [-jD \sin(kl) + C \cos(kl)] \end{cases} \quad (3)$$

where $C = B e^{(-\frac{\rho}{4}L - j\beta\frac{L}{2})}$ and $B_0 = C_0 e^{(-\frac{\rho}{4}L - j\beta\frac{L}{2})}$. After some algebraic manipulation for above Eq. (3) we get, where $x = \sqrt{(1 - \gamma)} e^{-\frac{\rho L}{4}}$, $y = \cos(kl)$ and $\phi = \beta L$,

$$T = \left| \frac{D_0}{A_0} \right| = (1 - \gamma) \frac{x^2(1 - y^2)^2}{(1 - x^2y^2)^2 + 4x^2y^2 \sin^2(\phi/2)} \quad (4)$$

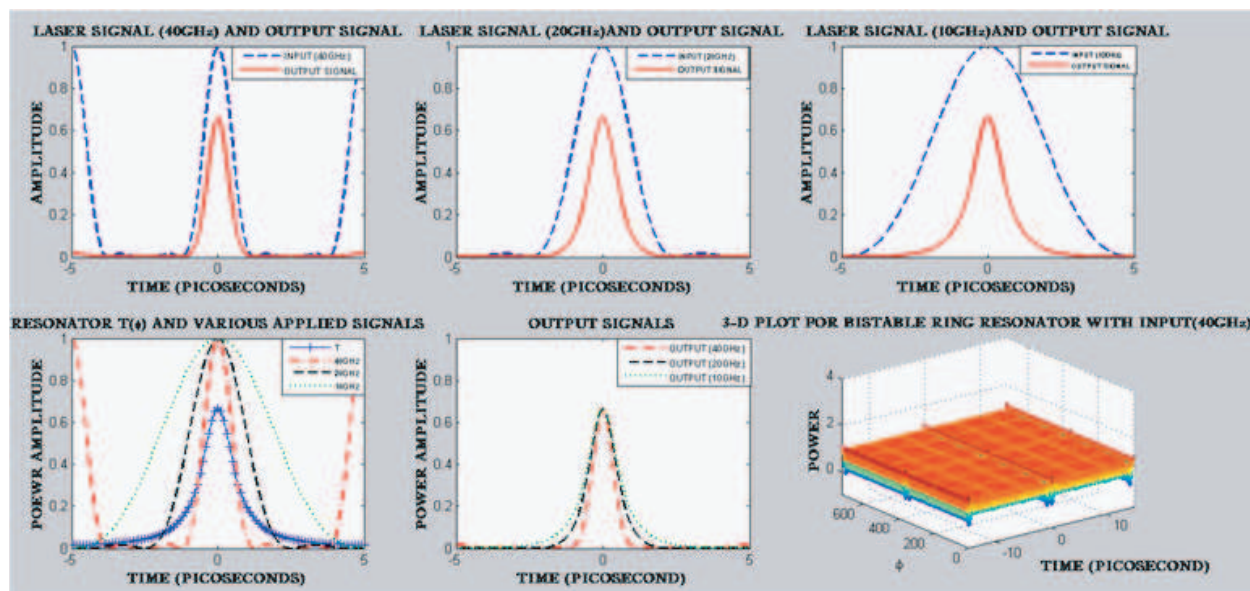


Figure 5: The output wave-form for Bi-stable micro-ring resonator when laser signals of different frequencies are allowed to pass through the resonator.

Fig. 4(b) shows the transmission characteristics curve of the optical bi-stable micro ring resonator as a function of angle ϕ . Fig. 5 shows the output waveform calculated from Eq. (4), when the input signal A_0 is assumed to be a picoseconds pulse generated by the circuit shown in Fig. 1(b) at a drive frequency of 10, 20 and 40 GHz respectively. Apparently in this case the pulse shape remains persevered in entire range of input signal. From the Fig. 5, it is also apparent that input signal (A_0) pulse width which is 1 ps at 40 GHz can be further compressed up to femtoseconds pulse width while it passing through Bi-stable micro ring resonator. The results may be further improved while replacing bi-stable micro-ring resonator discussed in this section with highly asymmetric mach-zehnder interferometer coupled micro-ring resonator [6].

5. CONCLUSION

In this paper, we have demonstrated a novel scheme of femtosecond optical pulse generation by using optical micro ring resonator. The repetition rate of the pulse can be tuned over a wide range. Two examples have been considered in the paper and shown that the pulse width decreases substantially without getting distortion when pulse passed through into our proposed bi-stable micro ring resonator.

REFERENCES

1. Das, S. and T. Chattopadhyay, "A method of tunable high repetition rate picosecond optical pulse generation using injection locking of laser diodes," *Appl. Physics B*, Vol. 83, 549–551, 2006.
2. Azafia, J., R. Slavik, P. Kockaert, L. R. Chen, and S. LaRochelle, "Generation of ultra-high repetition rate optical pulse bursts by means of fiber Bragg gratings operating in transmission," *Electronics Lett.*, Vol. 38, No. 24, 1555–1556, Nov. 21, 2002.
3. Chattopadhyay, T. and S. Das, "A novel scheme of optical pulse width compression using a feedback optical phase modulator," *Appl. Physics B: Laser and Optics*, Vol. 89, 9–13, Apr. 2007.
4. Okamoto, K., *Fundamentals of Optical Waveguides*, 1st Edition, Academic Press, USA, 2005.
5. Stokes, L. F., M. Chodorow, and H. J. Shaw, "All-single-mode fiber resonator," *Optics Letters*, Vol. 7, No. 6, 288–290, Jun. 1982.
6. Zhang, X.-Y., T. Zhang, X.-J. Xue, J.-L. Zhang, J. Hong, P.-Q. Wu, and Q.-Y. Chen, "Tunable optical ring resonator integrated with asymmetric mach-zehnder interferometer," *IEEE Journal of Light Wave Tech.*, Vol. 28, No. 17, 2512–2520, Sep. 2010.

Optimization of Phase Noise in a 2.3 ~ 3.5 GHz Voltage-controlled Oscillator Using the Impedance Locus

Kang-Chun Peng¹ and Tzyy-Sheng Horng²

¹Department of Computer and Communication Engineering
National Kaohsiung First University of Science and Technology, Taiwan, R.O.C.

²Department of Electrical Engineering
National Sun Yat-Sen University, Taiwan, R.O.C.

Abstract— This work develops a 2.3 ~ 3.5 GHz wideband voltage-controlled oscillator (VCO) using the impedance locus for both 802.11g and LTE-A applications. In this work, the operation bandwidth is expanded by using capacitor array. The phase noise performance is optimized by applying impedance locus design methodology. The analysis indicates that as the included angle approaches 90°, the VCO exhibits a better phase noise performance. To confirm the performance, a 2.3 ~ 3.5 GHz wideband VCO is designed and implemented with TSMC 0.18 μm CMOS technology. Measurements demonstrate that the wideband VCO design with phase noise optimization has a favorable phase noise and operation bandwidth performance. The phase noise is lower than -114 dBc/Hz at the 1 MHz offset frequencies over the 2.3 ~ 3.5 GHz operation range.

1. INTRODUCTION

The latest smart phones are required to support both LTE-A and IEEE 802.11g systems for increasing internet throughput. To cover the frequency bands of both LTE-A and IEEE 802.11g systems, the voltage-controlled oscillator (VCO) requires a fractional bandwidth of 42% to cover 2.3 ~ 3.5 GHz, where the lower frequency bands are achieved by using additional prescaler. The phase noise of the VCO should also be minimized since the LTE-A and IEEE 802.11g systems apply orthogonal frequency-division multiplexing (OFDM) technique to provide high spectral efficiency. Although the use of a phase-locked loop (PLL) can suppress the VCO phase noise inside the PLL bandwidth, which is usually under 100 kHz, the VCO phase noise outside the PLL bandwidth still considerably degrades the wireless system performance [1]. In particular, today's wideband wireless systems generally have a modulation bandwidth that exceeds several MHz and requires a much lower VCO phase noise. According to the well-known Leeson's model, the simplest way to improve the VCO phase noise is to increase the carrier output power. However, the overall power consumption increases with the carrier output power, and hence does not meet the need for low power consumption to maximize longer battery life [2, 3]. Another way to reduce the VCO phase noise is to increase the quality factor of the resonator. However, the VCO quality factor is typically below 20 under a standard CMOS process. To increase the VCO quality factor, special processes must be adopted, such as the use of bond-wires as inductors, micro electro mechanical systems (MEMS) or integrated passive devices (IPD) [4]. However, these special processes markedly increase the cost and die area. To solve these problems, this work develops a 2.3 ~ 3.5 GHz wideband VCO based on impedance locus theory.

2. IMPEDANCE LOCUS THEORY

Figure 1 shows the VCO equivalent model that was developed by Kurokawa [5]. The current, which flow into the active circuit, is given by

$$i_D = A \cos(\omega t + \phi), \quad (1)$$

Since the impedance of the active circuit varies with the amplitude of the current I_D , it is given by

$$-Z_D(A) = R_D(A) + jX_D(A). \quad (2)$$

The voltage drop across the active circuit can then be derived as

$$V_D(A) = -I_D Z_D(A) = AR_D(A) \cos(\omega t + \phi) + jAX_D(A) \cos(\omega t + \phi). \quad (3)$$

The impedance of the resonator can be derived as

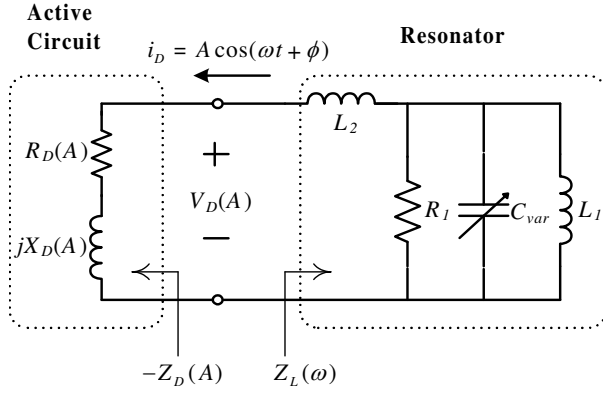
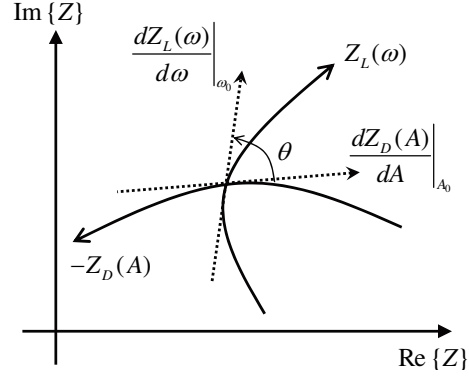


Figure 1: Equivalent model of a VCO.

Figure 2: Impedance loci in the Z -plane.

$$Z_L(\omega) = j\omega L_2 + \left(\frac{1}{R_1} + j\omega L_1 - j\frac{1}{\omega C_{var}} \right)^{-1} = R_L(\omega) + jX_L(\omega), \quad (4)$$

where

$$R_L(\omega) = \frac{\omega^2 L_1^2 R_1}{R_1^2 (1 - \omega^2 L_1 C_{var})^2 + (\omega L_1)^2}, \quad (5)$$

$$X_L(\omega) = \omega L_2 + \frac{\omega L_1 R_1^2 - \omega^3 R_1^2 L_1^2 C_{var}}{R_1^2 (1 - \omega^2 L_1 C_{var})^2 + (\omega L_1)^2}. \quad (6)$$

According to the Kirchhoff's voltage law (KVL), the equivalent model in Figure 1 should satisfy

$$[Z_L(\omega) - Z_D(A)] i_D = 0. \quad (7)$$

Kurokawa proved that, under this condition, the VCO oscillates stably at a frequency ω_0 with an amplitude A_0 if only if

$$\left. \frac{dR_D(A)}{dA} \right|_{A_0} \left. \frac{dX_L(\omega)}{d\omega} \right|_{\omega_0} - \left. \frac{dX_D(A)}{dA} \right|_{A_0} \left. \frac{dR_L(\omega)}{d\omega} \right|_{\omega_0} > 0. \quad (8)$$

To determine the physical meaning of Equation (8), Figure 2 depicts the impedance loci of $Z_D(A)$ and $Z_L(\omega)$ in the Z -plane. The arrowheads of the two loci indicate the increment of frequency ω and amplitude A , respectively. Two loci intersect at a frequency ω_0 with an amplitude A_0 . Equation (8) can then be re-derived as

$$\begin{aligned} & \left. \frac{dR_D(A)}{dA} \right|_{A_0} \left. \frac{dX_L(\omega)}{d\omega} \right|_{\omega_0} - \left. \frac{dX_D(A)}{dA} \right|_{A_0} \left. \frac{dR_L(\omega)}{d\omega} \right|_{\omega_0} \\ &= \left. \frac{dZ_D(A)}{dA} \right|_{A_0} \times \left. \frac{dR_L(\omega)}{d\omega} \right|_{\omega_0} = \left| \left. \frac{dZ_D(A)}{dA} \right|_{A_0} \right| \left| \left. \frac{dR_L(\omega)}{d\omega} \right|_{\omega_0} \right| \sin \theta > 0, \end{aligned} \quad (9)$$

where θ represents the included angle where the two impedance loci cross each other. Equation (9) indicates that the VCO oscillation is stable if only if $\sin \theta > 0$ and therefore $0 < \theta < 180^\circ$. To evaluate the VCO phase noise performance, Equation (7) is modified as

$$[Z_L(\omega) - Z_D(A)] i_D = e, \quad (10)$$

where e denotes the magnitude of the intrinsic white noise. The phase noise of the VCO can then be derived as

$$|\phi(\omega)|^2 = \frac{2|e|^2}{\omega^2 |A_0|^2} \cdot \frac{\omega^2 |Z'(\omega)|^2 + |A_0|^2 \left[\left(\left. \frac{dR_D(A)}{dA} \right|_{A_0} \right)^2 + \left(\left. \frac{dX_D(A)}{dA} \right|_{A_0} \right)^2 \right]}{\omega^2 |Z'(\omega)|^4 + |A_0|^2 \left| \left. \frac{dZ_D(A)}{dA} \right|_{A_0} \right|^2 \left| \left. \frac{dR_L(\omega)}{d\omega} \right|_{\omega_0} \right|^2 \sin^2 \theta}, \quad (11)$$

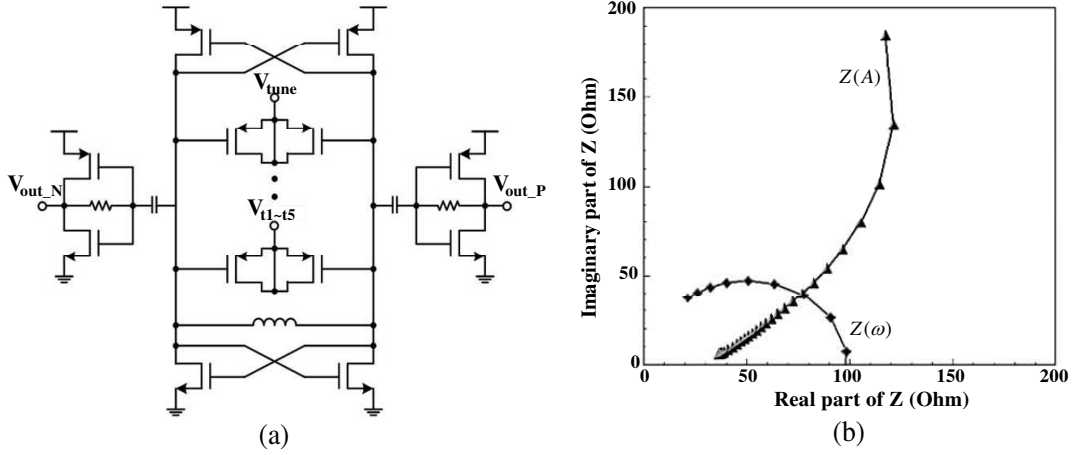


Figure 3: (a) Circuit design, and (b) impedance loci of the wideband VCO.

where

$$|Z'(\omega)|^2 = \left[\left(\frac{dR_L(\omega)}{d\omega} \right)^2 + \left(\frac{dX_L(\omega)}{d\omega} \right)^2 \right]_{|\omega_0} \quad (12)$$

3. CIRCUIT DESIGN

Generally, complementary cross-coupled VCOs exhibit a better balance between low phase noise and wide operating bandwidth than NMOS and PMOS cross-coupled VCOs. Therefore, the wideband VCO is designed with the complementary cross-coupled architecture that is presented in Figure 3(a). The wideband design considerations for the VCO tank demand the use of body-biased MOSFETs as varactors to provide a larger variation in capacitance than the one of conventional varactors. Hence, the operating bandwidth of the VCO is substantially increased. The phase noise performance of the VCO is optimized by applying impedance locus design methodology stated above. Figure 3(b) presents the simulated impedance loci of the wideband VCO, which are designed to have an included angle of approximately 90° , to optimize phase noise performance.

4. EXPERIMENTAL RESULTS

Figure 4 shows the implemented wideband VCO, which is fabricated using TSMC $0.18 \mu\text{m}$ CMOS technology and occupies an area of about $0.5 \times 0.8 \text{ mm}^2$. Figure 5 shows the measured output spectrum of the CMOS wideband VCO. The output power is about -7 dBm . The suppression of second harmonic and of third harmonic is approximately 35 dBc and 30 dBc , respectively. Figure 6(a) shows the measured operating range of CMOS wideband VCO. The implemented CMOS VCO can achieve a very wide operating range of $2.3 \sim 3.5 \text{ GHz}$, which is approximately 42% in fractional bandwidth. Figure 6(a) also shows that the variation of the output power is lower than 2 dB over the $2.3 \sim 3.5 \text{ GHz}$ operating range. Figure 6(b) shows the measured phase noise of the CMOS wideband VCO. The phase noise of the implemented VCO is measured as -96 dBc/Hz and -114 dBc/Hz at offset frequencies of 100 kHz and 1 MHz , respectively. To further evaluate the performance of the VCO, the figure of merit (FOM) and the figure of merit with the tuning range (FOMT) are used. The FOM is defined as

$$FOM = L(\Delta\omega) - 20 \log \left(\frac{\omega_0}{\Delta\omega} \right) + 10 \log \left(\frac{P_{diss}}{1 \text{ mW}} \right), \quad (13)$$

where $\Delta\omega$ denotes the offset frequency at which phase noise is evaluated, ω_0 denotes the fundamental frequency of the VCO, and P_{diss} denotes the power consumption. The FOMT is defined as

$$FOMT = FOM - 20 \log \left(\frac{FTR}{10} \right), \quad (14)$$

where FTR denotes the frequency tuning range as a percentage. These equations show that the FOM and FOMT of the CMOS wideband VCO are as low as -166 dBc/Hz and -178 dBc/Hz , respectively. Table 1 summarizes the performance of the CMOS wideband VCO. It can be found that the measured results are very consistent with the simulated results.

Table 1: Performance summary of the CMOS wideband VCO.

	Simulated	Measured
Supply voltage (V)	1.8	1.8
Power consumption (mW)	43	37
Operating range (MHz)	2365 ~ 3642	2306 ~ 3502
Sensitivity (MHz/V)	113	177
Output power (dBm)	3	7
Phase noise @ 1 MHz (dBc/Hz)	-113	-114
FoM (dBc/Hz)	-167	-166
FoMT (dBc/Hz)	-174	-178

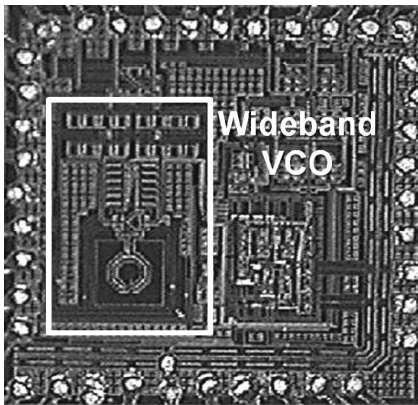


Figure 4: Implemented CMOS wideband VCO.

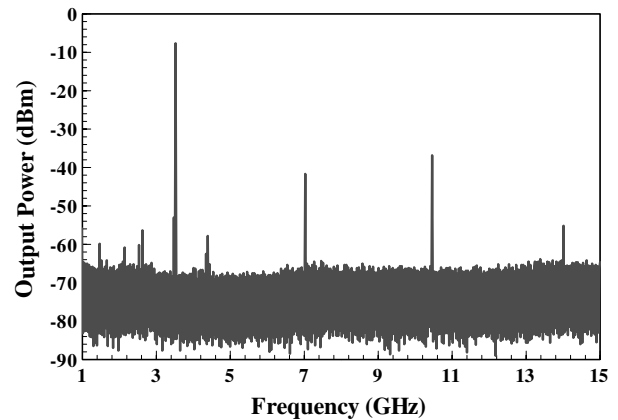


Figure 5: Measured output spectrum of the wideband VCO.

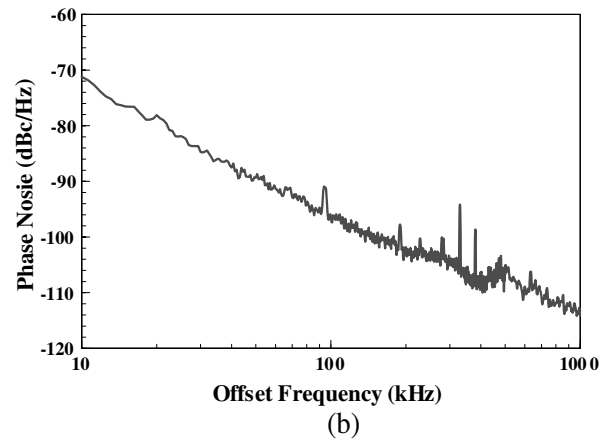
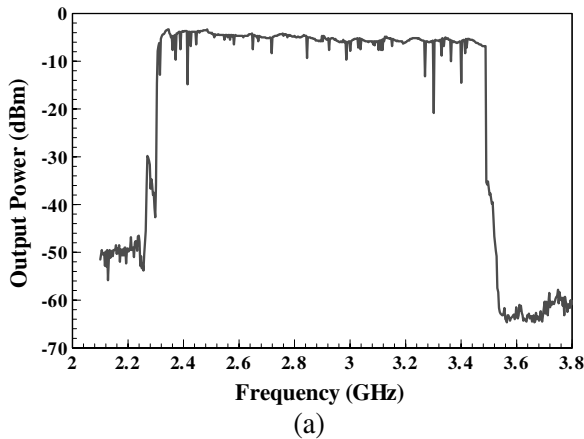


Figure 6: Measured (a) operating range and (b) phase noise of the CMOS wideband VCO.

5. CONCLUSIONS

This work presents a CMOS wideband VCO using the impedance locus for both 802.11g and LTE-A applications. The operating range and phase noise are optimized by applying capacitor array and impedance locus design methodology, respectively. Measurements demonstrate that the CMOS wideband VCO design with phase noise optimization has a favorable phase noise and operating bandwidth performance. The phase noise is lower than -114 dBc/Hz at the 1 MHz offset frequencies over the $2.3 \sim 3.5$ GHz operating range. The FoM and the FoMT are lower than -166 dBc/Hz and -178 dBc/Hz at the 1 MHz offset frequencies, respectively.

ACKNOWLEDGMENT

The authors would like to thank the National Science Council (NSC100-2221-E-327-040) for providing research funding.

REFERENCES

1. Hajimiri, A. and T. H. Lee, "Design issues in CMOS differential LC oscillators," *IEEE J. Solid-State Circuits*, Vol. 34, No. 5, 717–724, May 1999.
2. Hajimiri, A. and T. H. Lee, "Oscillator phase noise: A tutorial," *IEEE J. Solid-State Circuits*, Vol. 32, No. 3, 326–336, Mar. 2000.
3. Perrott, M. H., S. Pamarti, E. G. Hoffman, F. S. Lee, S. Mukherjee, C. Lee, V. Tsinker, S. Perumal, B. T. Soto, N. Arumugam, and B. W. Garlepp, "A low area, switched-resistor based fractional- N synthesizer applied to a MEMS-based programmable oscillator," *IEEE J. Solid-State Circuits*, Vol. 45, 2566–2581, Dec. 2010.
4. Kurokawa, L., "Injection-locking of solid state microwave oscillators," *Proc. IEEE*, Vol. 61, 1386–1409, Oct. 1973.
5. Esdale, D. J. and M. J. Howes, "A reflection coefficient approach to the design of one-port negative impedance oscillators," *IEEE Trans. Microwave Theory Tech.*, Vol. 29, 770–776, Aug. 1981.

New Measuring Instrument for the Characteristics of the Two-phase Flow of the Particulate Material Based on the Microwaves and Digital Processing of the Signals. Constructional Design Issues

V. F. Novikov

Novosibirsk State Technical University, Russia

Abstract— The discussion of the specific issues appeared for the first time while designing new measuring instrument for the characteristics of the two-phase flow of the particulate material moving inside the metal pipe line, started in [1], is continued. The measuring instrument is based on microwave (SHF) application and digital processing of the signals. A lot of attention is paid to the peculiarities of the design of the device for the input of the microwave energy to the pipe line by the connected waveguides with different cross sections.

1. INTRODUCTION

In [2] a scheme of the new measuring instrument for the characteristics of the two-phase flow of the particulate material moving inside the metal pipe line is described. The quantity of material in the flow, the range of velocities of the separate flow components, the discharge rate of the flow during any period like one minute, one hour, one working day, one month are simultaneously measured on-line. In [3, 4] are solved the problems of creating the theory of the measuring instrument. In [1] the discussion of the issues coming on for the first time when construction of such measuring instrument was started. It could be applied in transporting the milled coal — pulverized coal in metallurgy and power engineering. This problem in the sphere of pneumatic conveying of the particulate materials is the most complex and actual, especially when the conveying material is mordant (causing corrosion, like acids) and appeared in large quantities. The further discussion of these problems is suggested underneath.

2. THE INPUT OF THE MICROWAVE ENERGY TO THE PIPE LINE

2.1. The Peculiarities of the Input of Microwave Energy to the Metal Pipe Line

Figure 1 shows the simplified flow-diagram of the measuring instrument [2]. Microwave energy from the microwave generator (oscillator) is coming into the pipe line with the help of input device and is headed towards the output device. So the measured section of the pipe line is constantly examined with microwaves and this section serves not only for transporting the material, but also for transporting the microwave energy functioning as circular waveguide. The set of the microwaves could be either in phase with the flow set or oncoming.

The input and output devices for microwave energy into/out of pipe line are absolutely identical and represent the system of two wave guides connected on the narrow wall. The narrow wall in the connection area is fully taken out [3]. All the microwave generator energy is put in the pipe line through the system of connected wave guides and passing through the transporting material is output through the identical pipe line system.

Rectangular waveguide of the same sections are usually used in wave guide bridges. A significant part of the sources is devoted to the analyses and valuation of such schemes. In respect to the given issue bridges have some peculiarities. One of peculiar features is that for the effective launching of the circular guide it is technically reasonable to use rectangular waveguide as primary launching wave guide as shown in [3]. Therefore, the problem of transporting particulate material through the metal pipe line could be efficiently solved when applying the bridges based on connected wave guides with different sections.

Another characteristic property of the microwave energy input/output devices (into/out of pipe line) based on two interconnected wave guides is that it is necessary to introduce in their configuration the so-called “dielectric window”.

The movement of the material through the pipe line is provided by the excess air pressure. This is prerequisite for the introduction of “dielectric window” (Fig. 1) for the acoustical uncoupling of two wave guides. The isolator (dielectric) in “dielectric window” should be durable and must not contribute to friction electrification (static-charge accumulation of dielectric due to transporting material moving particles friction or encounter with it). Such properties are possessed by isolators

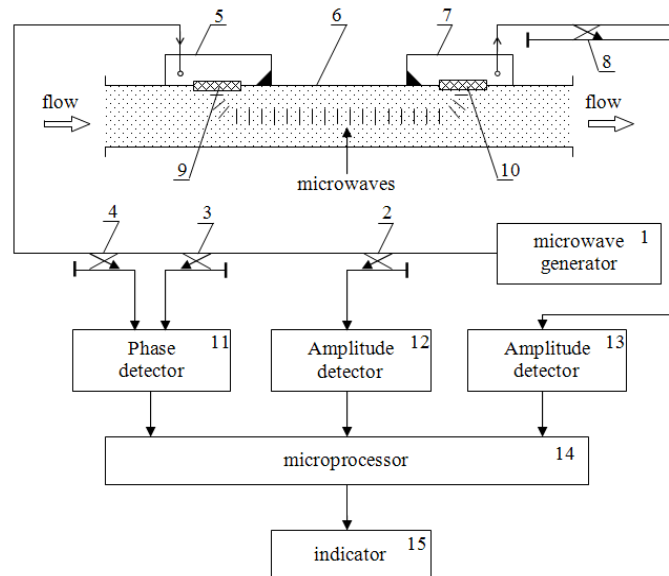


Figure 1. Scheme of the primary sensor.

from metal oxides, however they are marked by the high magnitude of the dielectric constant. That is why they influence significantly and variously the velocity H_{mn} mode waves, passing through the “dielectric window”, destroying the primary bridge setting-up.

Besides, the savor for the assessment of the possibilities for further reduction of the inner losses and directional selectivity building-up appears while designing the wave slot bridge hybrid for measuring instrument for the flow characteristics. The reduction of the inner losses is necessary for more effective adoption of the microwave generator capability. Directional selectivity building-up is essential for powering down the effect of the reflections (objectively existing inside the pipe line) from different material transporting duct elements (the duct transports microwave energy at the same time). In usual application, for example in antenna assemblies or transmitting equipment, the bridge is in such conditions when from its both sides the duct is almost coordinated. These issues are quite new and need additional study.

The work of the bridge on connected wave guides with equal or different sections is described using the picture of the connection area as a multimode waveguide. The width of each connected wave guide is chosen for the distribution of the wave H_{10} only in all the four bridge legs. The space in the connection area — slot creates an extended wave guide where waves H_{10}^s , H_{20}^s , H_{30}^s and waves of higher types could appear. The slot width d_s is chosen so that the first two waves could be distributed along the extended wave guide farther and all the rest die out quickly, creating the reluctance fields near the fringes.

Boundary data at the slot fringes are found by adding the waves H_{10}^s , H_{20}^s and H_{30}^s (waves of higher types are usually not considered). Adding the waves of different types in the slot port supports the separation of the input bridge legs. The separation of the output bridge legs is provided in the same way when the bridge transfers the power from one of input branches to one from the output branches.

It can be supposed that the calculation technique for the bridges on connected wave guides with the equal or different sections generally remains the same, because it is based on the multimode waveguide model.

The calculation task is to choose the slot width d_s and slot length l_s .

2.2. The Bridge on Connected Wave Guides with Equal Sections

The slot width. So that the wave H_{30}^s will not be distributed along the slot and die out quickly, the critical length $\lambda_{cr}^{H_{20}}$ for the given type of the waves should be a bit less than the working length λ_w and the critical length of the wave $\lambda_{cr}^{H_{30}}$ should be more than λ_0 . That conditions is met if:

$$\lambda_{cr}^{H_{30}} < \lambda_0 < \lambda_{cr}^{H_{20}}, \quad \lambda_{cr}^{H_{30}} = (2/3) d_s, \quad \lambda_{cr}^{H_{20}} = d_s \quad (1)$$

From (1) follows that the slot width d_s should meet the condition:

$$\lambda_0 < d_s < 1.5 \cdot \lambda_0 \quad (2)$$

For example, it is recommended to judge by the condition $d_s \approx (1.32 \div 1.38) \cdot \lambda_0$.

The slot length. The waves H_{10}^s and H_{20}^s move along the slot with different speeds: the distribution speed of the wave H_{10}^s is less than H_{20}^s distribution speed. That results in phase difference $\Delta\psi$ fields of the H_{10}^s and H_{20}^s waves by the end of the slot:

$$\Delta\psi = \frac{2\pi}{\Lambda_{10}^s} \cdot l_s - \frac{2\pi}{\Lambda_{20}^s} \cdot l_s \quad (3)$$

where $\Lambda_{10}^s, \Lambda_{20}^s$ — waves lengths in the wave guide in the slot area for H_{10}^s and H_{20}^s oscillations.

So the extended multimode waveguide stands for the device where the phase difference of the different types of waves is formed. Changing $\Delta\psi$ we can send the energy from branch 1 to branches 3 or 4. If we take $\Delta\psi = \pi$ the generator power from the branch l_s will go to the branch 4 — pipe line. The necessary slot length could be calculated from (3), taking $\Delta\psi = \pi$:

$$l_s = \frac{\lambda_0}{2} \cdot \frac{1}{\sqrt{1 - \left(\frac{\lambda_0}{2d_s}\right)^2} - \sqrt{1 - \left(\frac{\lambda_0}{d_s}\right)^2}} \quad (4)$$

2.3. The Bridge on the Wave Guides with Different Sections. Methods of Analysis

The above used results of the analysis of the multimode wave guide for the scheme of the bridge from two connected wave guides with the same sections can't be used in case when the bridge has wave guides with different sections. At the same time the strict analysis of the bridge on connected wave guides with different sections according to analytical methods is complicated by the fact that it is hard to design such solution of Maxwell equations, which will satisfy the boundary conditions on the inner side of both wave guides and will be continuous in all the interspace points including the points of the connection area. Approximate analytical method of solving the task for the system of connected wave guides with different sections is presented.

The method includes the solution of the Maxwell equations satisfying the boundary conditions on the inner sides of both wave guides and remaining continuous in all the interspace points excluding the points of the connection area.

The continuity of the field in the connection area, i.e., the requirement for the equal tangential components of phasors E and H on both sides of the connection panel, is replaced by the requirement of the equation of tangential components of only one field density phasor E or H and by the requirement of the both wave guides field interaction power (energy) will be equal to zero.

Then one should define the structure of the field separately for each wave guide excluding the connection area.

The constant of the two connected wave guides with different sections is presented as the constant in some equivalent wave guide with the rectangular cross-section, which width is an — where n -wave type index.

After defining the field structure on the inner side of each wave guide (excluding the connection area) the field for the formula tangential components in connection area is created. Here we must consider the fact that the connection area lines where the components of the field phasors E and H tangential to the connection area are extremely close to each other. This comes from the small size of the connection line in comparison with the circular waveguide diameter.

Using set of taken conditions the three formulas for calculation of waves $H_{10}^s, H_{20}^s, H_{30}^s$ are made and the width of the three equivalent rectangular wave guides a_1, a_2 and a_3 is found.

2.4. Consideration of the “Dielectric Window” Impact

“Dielectric window” is designed to be situated at the joint of the inner pipe line and rectangular wave guide surfaces along the whole slot length (Fig. 2). As the electric field component at the joint of two wave guides for the wave H_{20}^s equals to zero, so the “dielectric window” influences the interphasing of the waves H_{10}^s and H_{20}^s through the deceleration of the wave H_{10}^s .

Making allowance that the speed of the wave H_{20}^s is higher than the speed of the wave H_{10}^s it should be supposed that the introduction of the “dielectric window” into the slot will lead to some reduction of the slot length l_s .

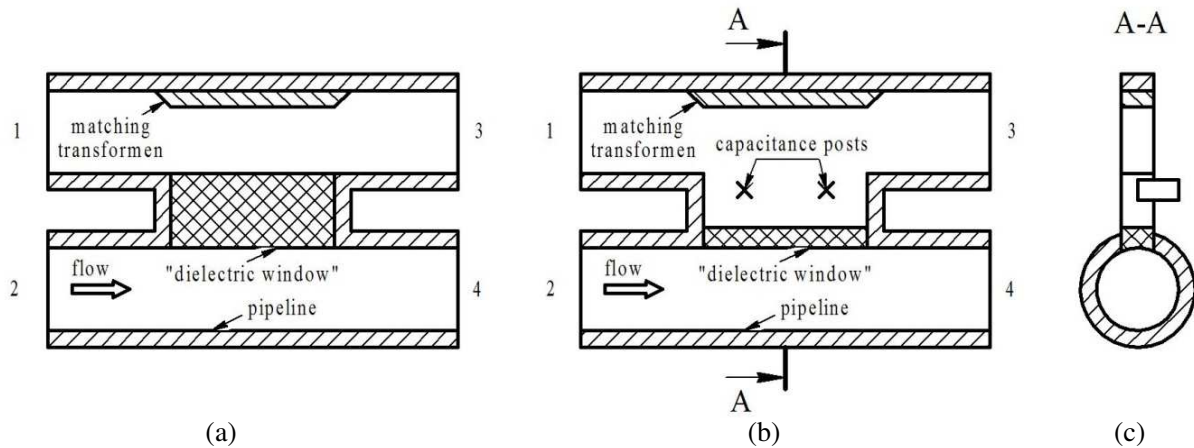


Figure 2.

Dielectric plate with the width d_{de} takes the relative volume k_V in the slot:

$$k_V = \frac{V_{de}}{V_s} = \frac{d_{de}}{a_1}. \quad (5)$$

where V_{de} , d_{de} — the volume and the thickness of the dielectric plate, V_s — the volume of the bridge slot, a_1 — the width of the equivalent wave guide for the wave H_{10}^s in the slot.

Then the relative dielectric transmissivity of the place occupied by the connecting device as the dielectric transmissivity of the mixture (cm) of the dielectric material ε_{cm} (dielectric plate plus air) will be equal to:

$$\varepsilon_{cm} = \varepsilon_{de} \cdot k_V + (1 - k_V) \cdot \varepsilon_0 \quad (6)$$

where ε_0 — the relative dielectric air transmissivity equals to one.

Taking into account (6) formula (4) for slot with “dielectric window” length l_s^{de} calculation will be:

$$l_s^{de} = \frac{\lambda_0}{2} \cdot \frac{1}{\sqrt{\varepsilon - \left(\frac{\lambda_0}{2a_1}\right)^2} - \sqrt{1 - \left(\frac{\lambda_0}{2a_2}\right)^2}} \quad (7)$$

Then it is necessary to constrict the wave guide complementarily as the incorporation of the dielectric “reams out” the wave guide. So the infeasibility condition of the wave H_{30}^s appearance in the slot will be as follows:

$$a_3 < 1.5 \cdot \frac{\lambda_0}{\sqrt{\varepsilon}} \quad (8)$$

With the caliber of ceramic plate $t = 1$ mm and its relevant dielectric transmissivity $\varepsilon_{de} = 10$ the dielectric transmissivity of the mixture ε_{cm} according to (6) will be 1.08. Inserting the obtained magnitude ε_{cm} into (7), (8), we realize that the ceramic plate mostly influences the choice of the slot length l_s .

2.5. Experiment

In the bridge on connected wave guides with different sections the circular waveguide is an industrial steel pipe line with the inner diameter ? 64 mm and with the caliber 6 mm, which was generated by the rectangular wave guide 61×10 mm². The caliber of the metal part of the “dielectric window” is 9 mm. The operating frequency is $f = 3000$ MHz.

At first teflon was used as dielectric material. The thickness of the teflon insert was $(9 + 6) = 15$ mm. The insert was placed in the middle of the slot between two wave guides (Fig. 2(a)). The bridge had quite satisfactory characteristics: direct losses (connectivity) ≈ 1 dB, crosscoupling isolation 2, 3 ≈ 18 dB. However, during the tests at CHP-plant it was found out that the flying past dust particles electrify teflon (friction electrification), sedimenting then on its surface or simply cutting into it.

Dielectric characteristics of the window “reel” during the running, the same is happening with the measurement inaccuracy of the quantity of the substance in the output flow.

Then the thick teflon insert was replaced by the thin' plate of superhard ceramics of the SHF range: $\epsilon' = 8.2$, $\text{tg} = 2 \cdot 10^{-4}$. The thin plate should be faced towards the flow (Fig. 2(b)). In such case the plate turns out to be shifted against the middle of the slot. Phasing adjustment of the bridge is broken: the direct losses are increasing, crosscoupling isolations are derating. These disadvantages, connected to the previous design of the "dielectric window", are smoothed, if the capacitance post tuners are introduced in the start and in the end of the slot. It is possible to improve the direct losses up to ≈ 1.5 dB and the isolation t to ≈ 26 dB.

3. CONCLUSIONS

1. When we design new measuring instrument based on microwave application and digital processing of the signals for the characteristics of the flow of the particulate material, we deal with the task of the most effective input of the microwave energy to the metal pipeline — circular wave guide. In such case the wave guide bridges on connected wave guides with equal sections are usually used. But in this case it is more appropriate to use bridges on connected wave guides with different sections.

2. The results of the analysis, which is based on the multimode wave guide model application, for the bridges on connected wave guides with different sections can't be directly applied for the bridges on connected wave guides with different sections. It is due to the specific structure of the field in the connection area at the boundary of two wave guides with different sections, where boundary condition (equitation of tangential components of fields on each side of the boundary line) is not achieved. If this fact is not taken into account, that could result in some mistakes, for example, when estimating the slot length.

3. The computer electrodynamic modeling and full-scale test show that the Modal A. I. method, presented in [5], can be used for calculating the main slot characteristics (l_s and d_s) for the bridge on connected wave guides with different sections.

4. The computer electrodynamic modeling shows and full-scale test sustains the opportunity for improvement of directivity of the bridge on connected wave guides with different sections using the capacitance element. It is particularly important for designing new measuring instrument for the characteristics of the flow of the particulate material.

ACKNOWLEDGMENT

The article partially presents the results of the work done under the Government contract of Ministry of Education and Science of the Russian Federation from June, 8, 2011, No. 16.516.11.6092.

REFERENCES

1. Novikov, V. F. and Y. M. Sidorkin, "Measuring instrument for the characteristics of the flow of the particulate material pneumatically transported inside the metal pipe line," Patent for Invention No. 339914 — G01F1/74 — Filed in State Inventions Register of Russian Federation, Bulletin No. 33, Nov. 27, 2008.
2. Novikov, V. F., "Measuring instrument for the characteristics of the two-phase flow of the particulate material. Theoretics (Part 1)," *Legal and Applied Metrology*, No. 6, 2–9, 2009.
3. Novikov, V. F., "Measuring instrument for the characteristics of the two-phase flow of the particulate material. Theoretics (Part 2)," *Legal and Applied Metrology*, No. 6, 13–19, 2009.
4. Novikov, V. F., "Measuring instrument for the characteristics of the two-phase flow of the particulate material. Constructional design issues (Part 1)," *Legal and Applied Metrology*, No. 4, 10–14, 2010.
5. Model, A. M., *SHF Filters in Radio Systems*, M-SVYAZ, 1967.

A SiGe Voltage-controlled Oscillator for 4G LTE Applications

J.-M. Wu¹, S. Chou², and Z.-C. Hong¹

¹Department of Electronic Engineering, National Kaohsiung Normal University, Taiwan

²T&C Technologies Inc., Taiwan

Abstract— A voltage-controlled oscillator (VCO) for fourth generation (4G) long term evolution (LTE) applications is designed and implemented using a standard 0.35- μm SiGe BiCMOS foundry process in this paper. A crucial goal for the design is to achieve low phase noise required in 4G LTE systems under a low supply voltage. The presented VCO design is based on a NMOS-only cross-coupled pair with an integrated LC tank. An on-chip inductance is used in place of a tail current transistor in a conventional NMOS-only cross-coupled oscillator, which can reduce the supply voltage of the VCO. A phase noise is inversely proportional to the ratio of Q factor to inductance in a tank. Therefore, the tank with high ratio of Q factor to inductance is adopted for low phase noise. A supply voltage of 1 V is used with a power consumption of 5 mW. Measurements of the VCO are made, revealing that the frequency tuning range is 5.4%; the output power is -0.9 dBm; the second harmonic suppression is -29 dBc, and the phase noise is -116 dBc/Hz at a 1 MHz offset.

1. INTRODUCTION

Long term evolution (LTE) systems with orthogonal frequency division multiplexing (OFDM) techniques are growing into one solution to fourth generation (4G) wireless systems due to the advantages of high spectrum efficient and low susceptibility to the multipath fading. A voltage-controlled oscillator (VCO) that is an essential component in a phase-locked loop (PLL) is required low phase noise for 4G LTE systems when a low supply voltage is applied. Proposed techniques to design a low phase noise VCO with a low supply voltage include: 1) using an inductor instead of the tail current source [1, 2], 2) removing the tail current source [3], 3) use of a resonant tunneling diode [4], 4) use of a switched resonator [5], 5) subthreshold scheme [6], 6) transformer feedback scheme [7], and 7) body bias scheme [8].

In this paper, a low phase noise cross-coupled VCO is designed under a low supply voltage. The VCO adopts an inductor to replace the tail current source in conventional cross-coupled oscillators [1, 2]. The transistor in a tail current source is absent so the supply voltage of the VCO can be reduced. It can be particularly noticed that high ratio of Q factor to inductance in a tank network is used to improve the phase noise of the VCO [3]. The VCO is implemented using the TSMC 0.35- μm SiGe BiCMOS foundry process.

2. CIRCUIT DESIGN

Figure 1 shows the circuit schematic of the VCO for 4G LTE applications [2]. The VCO design is based on a NMOS-only cross-coupled pair with an integrated LC tank. The NMOS transistor M is used as an active component for providing the power of oscillation. The passive tank network that is composed of the inductance L_1 , the capacitance C_1 , and the capacitance of a varactor C_2 is employed to select the frequency of oscillation. By referring to the derivation with half-circuit model of the VCO in [2], the oscillation frequency f_0 can be expressed as

$$f_0 = \frac{1}{2\pi} \sqrt{\frac{1}{L_1} \left(\frac{1}{C_1} + \frac{2}{C_2} \right)}. \quad (1)$$

As a matter of fact, the most important parameter to evaluate the performance of a VCO is a phase noise. The single sideband noise spectral density can be expressed in terms of the average power dissipated in the resistance and the Q factor in a tank [9]. From the derivation with the definition of Q factor in [3], the single sideband noise spectral density $\mathcal{L}\{\Delta\omega\}$ of the VCO can be approximated as

$$\begin{aligned} \mathcal{L}\{\Delta\omega\} &\approx 10 \log \left[\frac{FkT\omega^3}{A^2} L_1 Q \left(\frac{\omega_0}{Q\Delta\omega} \right)^2 \right] \\ &\alpha 10 \log \left(\frac{1}{Q/L_1} \right) \end{aligned} \quad (2)$$

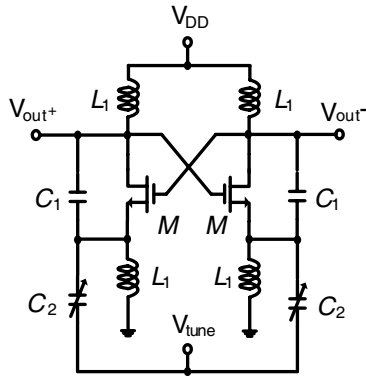


Figure 1: Circuit schematic of the VCO.

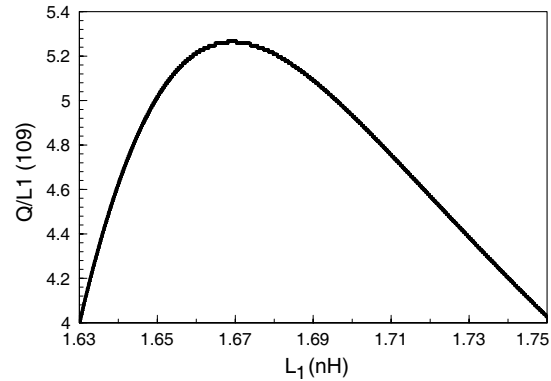
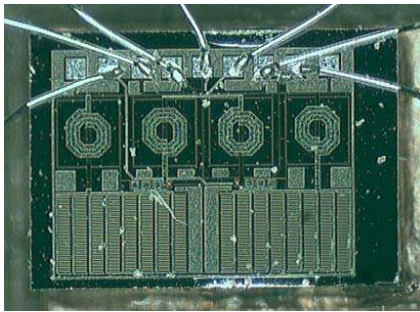
Figure 2: The simulated ratio of Q to L_1 within range of L_1 values from 1.63 to 1.75 nH.

Figure 3: Chip micrograph of the implemented VCO RFIC.

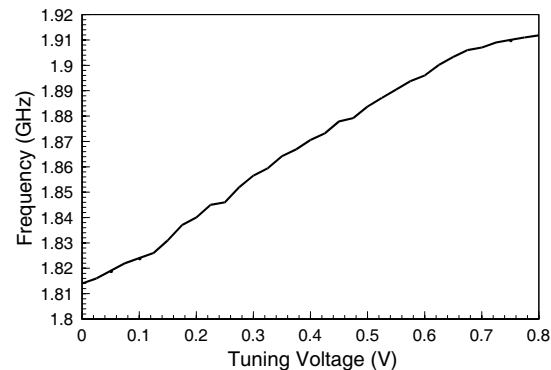


Figure 4: Measured tuning frequency of the VCO.

where F is the device excess noise number; $k = 1.380 \times 10^{-23}$ J/K is the Boltzmann's constant; T is the absolute temperature; ω is the angular frequency; A is the oscillation amplitude; ω_0 is the angular frequency of oscillation, $\Delta\omega$ is the angular frequency offset from the carrier. Notice that (2) clearly indicates that the phase noise of a VCO is inversely proportional to the Q/L_1 . The phase noise, then, can be reduced by increasing the Q/L_1 value. Figure 2 shows the simulated Q/L_1 within range of L_1 values from 163 to 1.75 nH. The simulation results are generated by Agilent Advanced Design System (ADS). As shown in Figure 2, the Q/L_1 has a maximum of 5.27×10^9 when the L_1 is 1.67 nH. Therefore, the L_1 value in this design is set to 1.67 nH to obtain the lowest phase noise for the VCO.

In order to maintain the oscillation of a VCO, the transconductance of cross-coupled transistors plays an important role in a VCO design. The transconductance of cross-coupled transistors is denoted by gm . According to the small-signal analysis in [2], the gm can be formulated in terms of the parasitic resistance R_1 of the on-chip inductor and the C_1/C_2 in a tank. That is

$$gm = \frac{1}{R_1} \left[1 + \frac{4(C_1/C_2)^2}{1 + 2(C_1/C_2)} \right]. \quad (3)$$

Since the gm is directly proportional to the power consumption of a VCO, the small ratio of C_1 to C_2 enables a VCO to save its power consumption. However, reducing the C_1/C_2 value causes the degradation of the phase noise [2]. This clearly shows that the power consumption and phase noise is a trade-off in the VCO design. The ratio of C_1 to C_2 is from 0.37 to 0.46 in this design.

3. IMPLEMENTATION AND MEASUREMENT

The VCO for 4G LTE applications is designed and implemented using TSMC 0.35- μ m SiGe BiCMOS foundry process. The chip, shown in a microphotograph in Figure 3 has an area of 1.037 mm \times 1.38 mm including the pads. The NMOS transistor, octagonal spiral inductor, metal-insulator-metal (MIM) capacitor and junction varactor with specific value are used in the 0.35- μ m

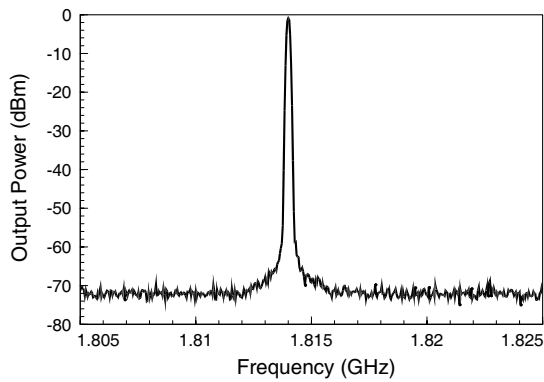


Figure 5: Measured output spectrum of the VCO.

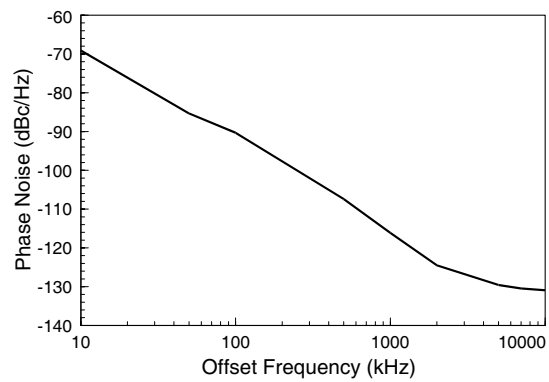


Figure 6: Measured phase noise of the VCO.

SiGe BiCMOS standard process. The VCO RFIC was mounted and bounded on an FR4 printed circuit board for testing. An R&S FSV signal analyzer is used to test all of the RF parameters of the VCO. A supply voltage of 1 V is used with a power consumption of 5 mW.

Figure 4 plots the measured tuning frequency for the VCO within the tuning voltage from 0 to 0.8 V. This clearly shows that the operating range of the VCO is from 1.814 to 1.912 GHz, revealing that the frequency tuning range is 5.4%. Note that within this frequency range the tuning curve is linear. According to the measurements in Figure 4, the applied range of the VCO includes the LTE Band 35 that covers from 185 to 191 GHz. Figure 4 also indicates that the tuning sensitivity of the VCO is 122.5 MHz/V. Figure 5 shows that the measured output spectrum of the VCO when a controlled voltage is 0 V. Figure 5 indicates that the output power of the VCO is -0.9 dBm. The second harmonic suppression is -29 dBc. Figure 6 presents the measured phase noise of the VCO. One can see that the phase noise of the VCO is -116 dBc/Hz at a 1 MHz offset.

4. CONCLUSIONS

A low phase noise VCO with low supply voltage for 4G LTE applications has been designed and implemented by use of the TSMC $0.35\text{-}\mu\text{m}$ SiGe BiCMOS process. The measured results demonstrate that the VCO achieves the phase noise of -116 dBc/Hz at a 1 MHz offset when the supply voltage of 1 V is applied.

ACKNOWLEDGMENT

This research was supported by the R.O.C. (Taiwan) National Science Council under Grant 100-2221-E-017-016. The authors wish to thank the R.O.C. (Taiwan) National Chip Implementation Center for providing the TSMC $0.35\text{-}\mu\text{m}$ SiGe BiCMOS foundry service.

REFERENCES

1. Troedsson, N. and H. Sjoland, "An ultra low voltage 2.4 GHz CMOS VCO," *Proceedings of IEEE Radio and Wireless Conference*, 205–208, Boston, Massachusetts, US, Aug. 2002.
2. Hsieh, H.-H. and L.-H. Lu, "A high-performance CMOS voltage-controlled oscillator for ultra-low-voltage operations," *IEEE Trans. Microw. Theory Tech.*, Vol. 55, No. 3, 467–473, 2007.
3. Park, D. and S. Cho, "A power-optimized CMOS LC VCO with wide tuning range in 0.5-V supply," *Proceedings of IEEE International Symposium on Circuits and Systems*, 3233–3236, Island of Kos, Greece, May 2006.
4. Choi, S., Y. Jeong, and K. Yang, "Low DC-power Ku-band RTD VCO based on an InP monolithic RTD/HBT technology," *IEEE MTT-S International Microwave Symposium Digest*, 1361–1364, Long Beach, California, US, Jun. 2005.
5. Mukhopadhyay, R., C.-H. Lee, and J. Laskar, "A $580\text{-}\mu\text{W}$ 1.8–6 GHz multiband switched-resonator SiGe VCO with 0.3-V supply voltage," *IEEE Microw. Wirel. Compon. Lett.*, Vol. 17, No. 11, 793–795, 2007.
6. Lee, H. and S. Mohammadi, "A subthreshold low phase noise CMOS LC VCO for ultra low power applications," *IEEE Microw. Wirel. Compon. Lett.*, Vol. 17, No. 11, 796–798, 2007.
7. Hsieh, C.-K., K.-Y. Kao, and K.-Y. Lin, "An ultra-low-power CMOS complementary VCO using three-coil transformer feedback," *IEEE Radio Frequency Integrated Circuits Symposium Digest*, 91–94, Boston, Massachusetts, US, Jun. 2009.

8. Sun, P., G. Wang, W. Woods, H. Wang, and Y. J. Yu, “An adaptive body-bias low voltage low power LC VCO,” *Proceedings of IEEE International Symposium on Circuits and Systems*, 1121–1124, Paris, France, May–Jun. 2010.
9. Hajimiri, A. and T. H. Lee, “A general theory of phase noise in electrical oscillators,” *IEEE J. Solid-State Circuit*, Vol. 33, No. 2, 179–194, 1998.

Planar Heterojunction Diode for Millimeter Waves Detection

A. Sužiedėlis¹, S. Ašmontas¹, A. J. Kundrotas¹, J. Gradauskas¹,
A. Čerškus¹, V. Nargelienė¹, and T. Anbineris²

¹Center for Physical Sciences and Technology, Savanorių Ave. 231, Vilnius LT-02300, Lithuania

²Elmika Ltd., Naugarduko St. 41, Vilnius LT-03227, Lithuania

Abstract— Search for new concepts of detection of electromagnetic radiation in the terahertz frequencies motivates one to approach to this spectrum range from both the microwaves and the infrared. In this paper, we present the results of investigation of the detection of microwave and infrared radiation when the diode is biased by DC voltage, expecting more explicit clarification of the nature of detected voltage of the diode. First experimental results of investigation of both MW and IR radiation detection using planar GaAs/Al_xGa_{1-x}As small area heterojunction structure of the same planar design having various values of AlAs mole fraction x are presented in this paper as well.

1. INTRODUCTION

Search for new concepts of detection of electromagnetic radiation in the terahertz frequencies motivates one to approach to this spectrum range from both the microwaves and the infrared. Previous experimental results have shown possibility to detect microwave (MW) [1] and infrared (IR) [2] radiation with GaAs/AlGaAs heterojunctions. Detectors of different design were used to detect the both types of radiation: the point contact diodes for microwaves and square mesas of GaAs/AlGaAs heterojunction for infrared radiation. Highest sensitivity of the MW and IR detectors was achieved for different values of AlAs mole fraction x in the Al_xGa_{1-x}As compound semiconductor: $x = 0.3$ was optimal for the MWs, and $x = 0.2$ was most favourable for the IR. The point contact design of the microwave diode is inadequate for high frequency application. Therefore, planar diodes with small area GaAs/Al_{0.3}Ga_{0.7}As heterojunction were investigated both in microwaves and infrared [3]. High voltage sensitivity in microwaves and high operational speed in infrared were appropriate features of the planar diodes. However, origination of the detected voltage over the contacts of the planar heterojunction diode under microwave and infrared radiation is revealed insufficiently up to now. Therefore, in this paper we present the results of investigation of the detection of microwave and infrared radiation when the diode is biased by DC voltage, expecting more explicit clarification of the nature of detected voltage of the diode. First experimental results of investigation of both MW and IR radiation detection using planar GaAs/Al_xGa_{1-x}As small area heterojunction structure of the same planar design having various values of AlAs mole fraction x are presented in this paper as well.

2. SAMPLES AND EXPERIMENTAL TECHNIQUE

Molecular beam epitaxy grown structures were used for the planar diodes fabrication. The *i*-GaAs buffer layer was grown onto semiinsulating GaAs substrate. Then the series of semiconductor layers were grown having following thickness t : n^+ -GaAs, $t = 300$ nm, n -GaAs, $t = 300$ nm, n -Al_xGa_{1-x}As, $t = 300$ nm, and upper contact layer that consists of n^+ -Al_xGa_{1-x}As and n^+ -GaAs layers, each of $t = 100$ nm thickness. The single photon counting photoluminescence method was used to control AlAs mole fraction x in the MBE grown semiconductor layers. The fabrication procedure of the planar diode is described in [3]. Clystron generator operating in K_a frequency range and traveling-wave tube generator operating in W frequency range were used as the sources of MW radiation. As a source of IR radiation, a passively Q -switched CO₂ laser producing smooth 200 ns pulses at 9.29 μm wavelength in a single transverse mode was used.

3. RESULTS AND DISCUSSION

Polarity of the detected voltage of the planar heterojunction diode corresponded to the sign of asymmetry of I-V characteristic of the diode both in microwaves and infrared. Moreover, the value of voltage sensitivity of the diodes correlated with the quantity of the asymmetry of I-V characteristics. In case of MW diodes that operation is based on carrier heating phenomena by electric field in Ohmic junctions the voltage sensitivity of the diode can be expressed as: $S = \Delta R/2U$, where ΔR is electrical resistance difference of the diode at negative and positive polarity of the applied

voltage U [4]. Detection properties as well as I-V characteristics of MW diodes with different electrical resistance were investigated. The dependences of their asymmetry of I-V characteristics and voltage sensitivity in K_a frequency range on power are presented in Fig. 1. It is worth to note that voltage sensitivity dependence is on MW power in a waveguide, while the asymmetry of I-V characteristics dependence on electrical power absorbed by the diode. However qualitative agreement between both these dependences is obvious. Therefore, we can conclude that microwave current rectification is responsible for the MW signals detection in the planar heterojunction diode.

In case of asymmetry of I-V characteristic the detected voltage of the MW diode should depend on external voltage bias. Fig. 2 depicts the dependence of detected voltage on the bias measured in the K_a frequency range. This dependence also can be explained on the basis of the dependence of asymmetry of I-V characteristics on the working point position in the I-V characteristic. Fig. 3 shows the dependence of asymmetry of an I-V characteristic on applied voltage, when the diode is biased negatively, positively, and unbiased. The presented results coincide with the dependence presented in Fig. 2, however qualitatively only. Therefore, additional mechanism should be involved in explanation of the detected voltage in the heterojunction diode. In case of hot carrier diode the dependence of detected voltage on external electrical bias was explained through the field dependence of electron mobility [5].

Hot carrier phenomena are employed for the detection of IR radiation. That is why the planar heterojunction diodes were used in infrared experiments. Photoresponse of the diode was observed under CO_2 laser radiation, and the polarity of the detected voltage was the same as in case of

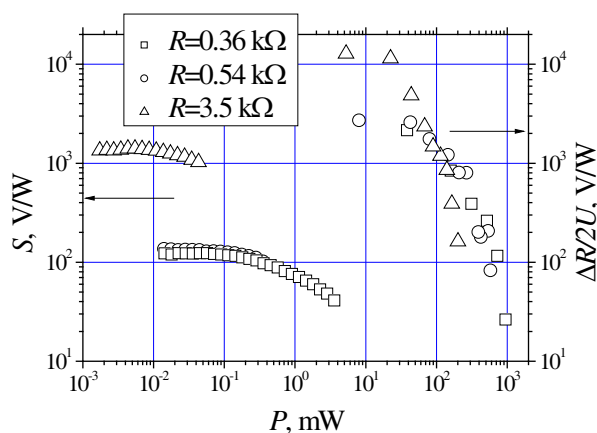


Figure 1: The power dependences of asymmetry of I-V characteristics and voltage sensitivity of the planar diodes.

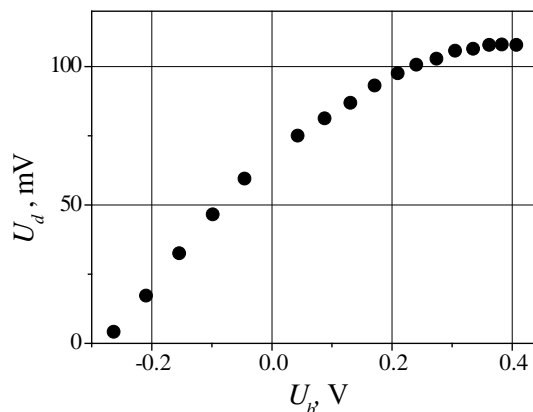


Figure 2: The dependences of detected voltage on DC electrical bias of the MW diode measured at $f = 26$ GHz frequency.

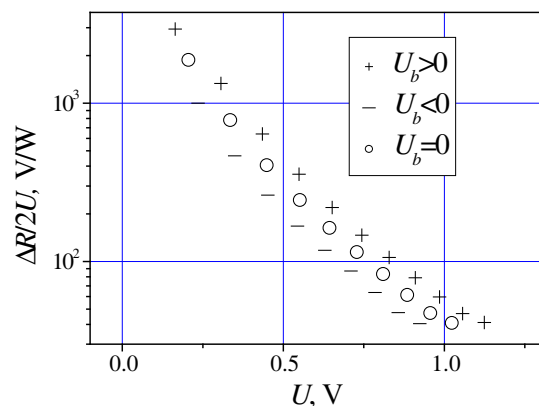


Figure 3: The dependences of asymmetry of I-V characteristics on applied voltage when the diode is biased positively, negatively and unbiased.

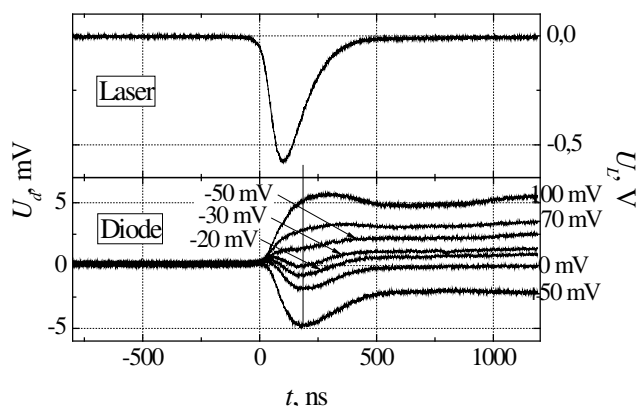


Figure 4: Photoresponse signal shape induced by CO_2 laser pulse in planar heterojunction diode.

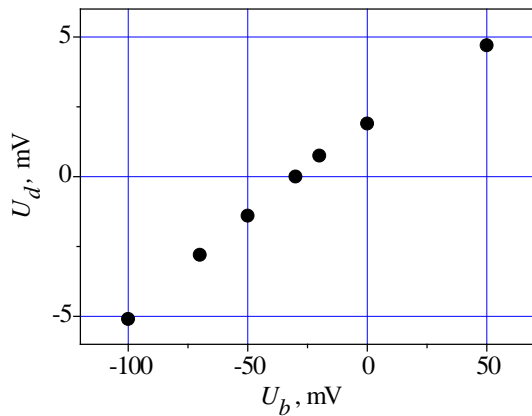


Figure 5: The dependence of photovoltage on the bias voltage.

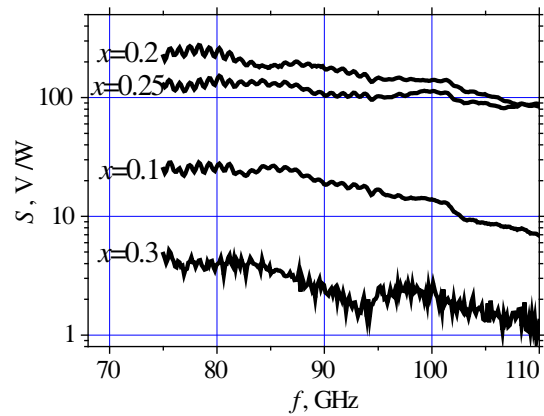


Figure 6: Frequency dependence of voltage sensitivity of planar GaAs/Al_xGa_{1-x}As heterojunction diode.

microwaves. Temporal profiles of the laser pulse and photoresponse signal are shown in Fig. 4. The photoresponse signals for various electrical bias voltages are presented in Fig. 4 as well. The photoresponse of the diode cannot be explained by current rectification in this case. The voltage over the ends of the diode under IR radiation arises due to charge carrier heating by laser radiation. The details of the influence of external electrical bias voltage on the photoresponse can be seen in Fig. 5, where the dependence of photovoltage on the bias voltage is presented. When the forward bias voltage is applied to the diode the photovoltage increases. The photoresponse of the biased diode consists of two parts: fast and slow. The fast part of the photovoltage is due to the charge carrier heating, while the slow one is related with crystal lattice heating by laser radiation. When the bias voltage is applied in backward direction the photovoltage decreases, then changes its polarity. The same as in case of the forward bias voltage, the photoresponse consists of fast and slow parts. The dependence of the photosignal on bias voltage can be explained by energy barrier change in the heterojunction under influence of the external voltage bias. The value of the photoresponse of the planar heterojunction diode is lower than the photodetector on the basis of compensated germanium that operates at liquid nitrogen temperature (see Fig. 4), the heterojunction diode operates at room temperature. The presence of slow part in the photoresponse of the biased heterojunction diode does not require fast indication technique for the detection of short laser pulses.

Finally, we present experimental results of microwave detection using planar GaAs/Al_xGa_{1-x}As small area heterojunction structure having various values of AlAs mole fraction x . Frequency dependence of voltage sensitivity $S = U_d/P$ (U_d is the detected voltage, P denotes microwave power in a waveguide) of the planar diode in W frequency range is presented in Fig. 6. Maximum sensitivity is achieved for the heterojunction diodes with $x = 0.2$, while the diodes with $x = 0.25$ exhibit flatter frequency dependence. Further increase of x causes drastic decrease of the sensitivity.

4. CONCLUSIONS

Planar diode with small area GaAs/AlGaAs heterojunction may be used for the detection of both microwave and infrared radiation and MW current rectification and carrier heating phenomena are responsible for arising of voltage response under microwave radiation. The photoresponse of the diode under IR radiation is due to carrier and crystal lattice heating by the IR laser.

ACKNOWLEDGMENT

This work in part was supported by Agency for Science, Innovation and Technology (grant No. 31V-32) in the frame of High Technology Development Programme for 2011-2013. Authors are thankful to Angelé Steikūnienė and Gytis Steikūnas for sample preparation.

REFERENCES

1. Ašmontas, S., J. Gradauskas, J. Kundrotas, A. Sužiedėlis, A. Šilėnas, and G. Valušis, "New aspects of microwave detection in GaAs/AlGaAs heterojunctions," *Proceedings of 24th Int. Conf.*

- on Physics of Semiconductors 24ICPS'98*, Jerusalem, Israel, Aug. 3–9, 1998 (D. Gershoni, Ed., CD-ROM (1193.pdf), *World Scientific*, 1999).
2. Ašmontas, S., J. Gradauskas, D. Seliuta, and E. Širmulis, “Photoelectrical properties of nonuniform semiconductor under infrared laser radiation,” *Proceedings of SPIE*, Vol. 4423, 18–27, 2001.
 3. Gradauskas, J., A. Sužiedėlis, S. Ašmontas, E. Širmulis, V. Kazlauskaitė, A. Lucun, and M. Vingelis, “Sensitive planar semiconductor detector from microwave to infrared applications,” *IEEE Sensors Journal*, Vol. 10, No. 3, 662–667, 2010.
 4. Ašmontas, S. and A. Sužiedėlis, “New microwave detector,” *Int. Journ. Infr. Millimeter Waves*, Vol. 15, No. 3, 525–538, 1994.
 5. Ašmontas, S., *Electrogradient Phenomena in Semiconductors*, Mokslas, Vilnius, 1984.

Plasma Relativistic Microwave Amplifier

P. S. Strelkov, E. I. Ivanov, and D. V. Shumeiko

Prohorov General Physics Institute, Vavilova 38, Moscow, Russia

Abstract— The use of plasma in microwave electronics to create microwave devices with a wide band of frequencies. We created the plasma relativistic microwave amplifier with the band of changing frequency from 2.4 to 3.1 GHz, with output power of 60–90 MW, effective microwave pulse duration of the 300 ns, efficiency 6–10%, with amplifying coefficient more than 30 dB, with signal-noise ratio at 22–25 dB.

1. INTRODUCTION

The mechanism of amplifying of the microwave signal in the plasma relativistic microwave amplifier is similar to the mechanism of amplifying of the electromagnetic wave in the ordinary microwave traveling-wave tube. The amplifying comes when the electrons beam velocity is nearly equal to the phase velocity of the electromagnetic wave. In order to slow down the wave, in vacuum microwave electronics they put a spiral in cylindrical waveguide or use metal ripple waveguide. The dispersion of this slowing structure determines the frequency band in which the effective amplifying is possible. To amplify the entering signal in some other frequency band, one should work out another amplifier with a new slowing structure. The dispersion of waves in plasma waveguide is determined by the diameters of smooth metal waveguide, electron beam, plasma and plasma density [1]. During the experiment, the plasma density may change very fast in usual time of 100 mcs. That's why plasma relativistic microwave amplifier affords to change one frequency band of the amplified signal to another without changing the construction of the device.

The main difficulty of creating a powerful microwave amplifier (with an amplifying coefficient of 30 dB) is the drop-out of the self-excitation. The vacuum relativistic microwave electronics uses here the several sections managed to excite in them different modes with the frequency fixed. That's why these amplifiers have very narrow amplifying frequency band. To extract the self excitation, the plasma relativistic microwave amplifier uses microwave absorbent [2] similarly to the non-relativistic microwave amplifiers, because the frequency band of absorption of such absorbents is high. Still, this method is not sufficient. To reduce the positive feedback we use the mechanism of the resonance of the fast cyclotron wave of the electron beam and plasma wave reflected from the output radiating device [3, 4]. The experiments brought another way of reducing of generation. It turned out that, having the high input signal, which makes the output signal near to nonlinear regime the level of the generation near the main frequency reduces dramatically [5]. Previously, we examined the amplification process at two frequencies, and suggested that the enhancement occurs at any frequency within this frequency range. The purpose of this paper is the experimental proof of this assumption.

2. EXPERIMENTAL SETUP

The experiments were carried out at the setup that was described in detail in [2, 5]. The schematic of the plasma relativistic amplifier is shown in Fig. 1.

Circular metal waveguide 1 is placed in a uniform magnetic field of 4.5 kG. Annular plasma 2 is produced by ionizing xenon at a pressure of 1.5×10^{-4} Torr with an auxiliary electron beam over a time of 100 mcs, and then annular REB 3 is injected into the plasma. The plasma density

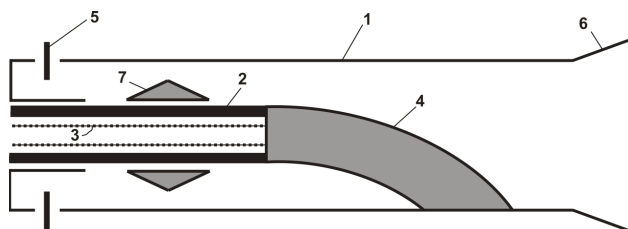


Figure 1: Schematic of the plasma relativistic microwave amplifier: (1) circular metal waveguide, (2) annular plasma, (3) REB, (4) collector, (5) amplifier input, (6) horn, and (7) microwave absorbent.

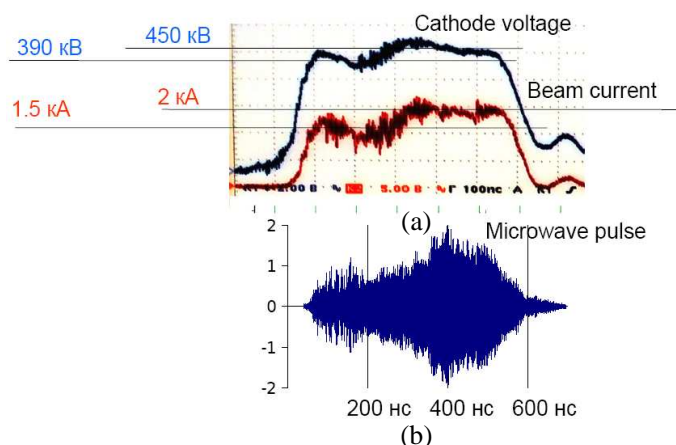


Figure 2: (a) Waveforms of the beam current and the voltage at the accelerator cathode and (b) time dependence of the output microwave electric field.

can be varied by varying the current of the auxiliary beam at a constant Xe pressure. The REB parameters are as follows: the electron energy is 450 keV, the beam current is 2 kA, and the current pulse duration is 500 ns. The REB electrons fall onto collector 4. This collector also serves to convert the plasma wave mode into the TEM mode of the coaxial vacuum waveguide and then into the H_{11} mode of the cylindrical vacuum waveguide [2]. The input signal is supplied to the plasma waveguide from one of the four magnetrons by using rod antenna 5. Each magnetron operates at its own frequency: 2.4, 2.71, 2.83, or 3.1 GHz. The power of the input signal is about 50 kW, and the duration of the microwave pulse is 5 μ s. The REB accelerator is switched on 200–500 ns after the start of the magnetron. The input radiation passes through the plasma waveguide and is amplified in the plasma-beam system. After the plasma wave is converted into the vacuum mode H_{11} in mode transformer 4, the amplified radiation is emitted from horn 6 into free space, the electric field at the axis of the output microwave beam being directed vertically. Microwave generation is suppressed due to the normal Doppler effect [3, 4], as well as by placing microwave absorbent 7 in the plasma waveguide. The output radiation is received by a 2 cm long rod antenna placed vertically on the axis of the microwave beam at a distance of 70 cm from the horn. The antenna signal is transmitted through a 60 dB attenuator to a Tektronix TDS7404 oscilloscope with a bandwidth of up to 4 GHz. The total energy of the output microwave pulse is recorded by a 50 cm diameter calorimeter placed at a distance of 35 cm from the horn. Fig. 2 shows the waveform of the accelerator cathode voltage, which determines the electron energy, as well as the time dependences of the REB current and output microwave electric field.

Note that the electron energy and current of the REB in the time interval 50–250 ns (390 keV and 1.5 kA, respectively) differ from those in the time interval 250–450 ns (450 keV and 2 kA). This is why the amplitude of the microwave signal in the first half of the pulse differs from that in the second half. When the REB is injected into a low density plasma, the amplitude of the microwave signal in the first half of the pulse is higher than that in the second half. However, after optimizing the parameters of the system (the plasma density and plasma length), the maximum microwave power is achieved in the second half of the REB current pulse, because the REB power is maximum at the end of the pulse. A specific feature of the present experiments is that we could perform them at four different frequencies of the input signal during the same working day. This allowed us to study the amplifier operation at different frequencies under the same external conditions.

3. PARAMETERS OF MICROWAVE PULSES AT FOUR FIXED FREQUENCIES OF 2.4, 2.7, 2.83, AND 3.1 GHz

For the above REB parameters, plasma waveguide length of 94 cm, and magnetic field of 4.5 kG, 60 to 90 MW microwave pulses were obtained at frequencies of 2.4, 2.71, 2.83, and 3.1 GHz. The output microwave pulse for the frequency 2.83 GHz and results of its analysis are presented in Fig. 3.

The input microwave power is about 50 kW. The maximum amplification at each particular frequency can be achieved by varying only one parameter, namely, the plasma density. Panel (a) in Figs. 3 shows the time dependence of the electric field $E(t)$ of the output microwave radiation. The

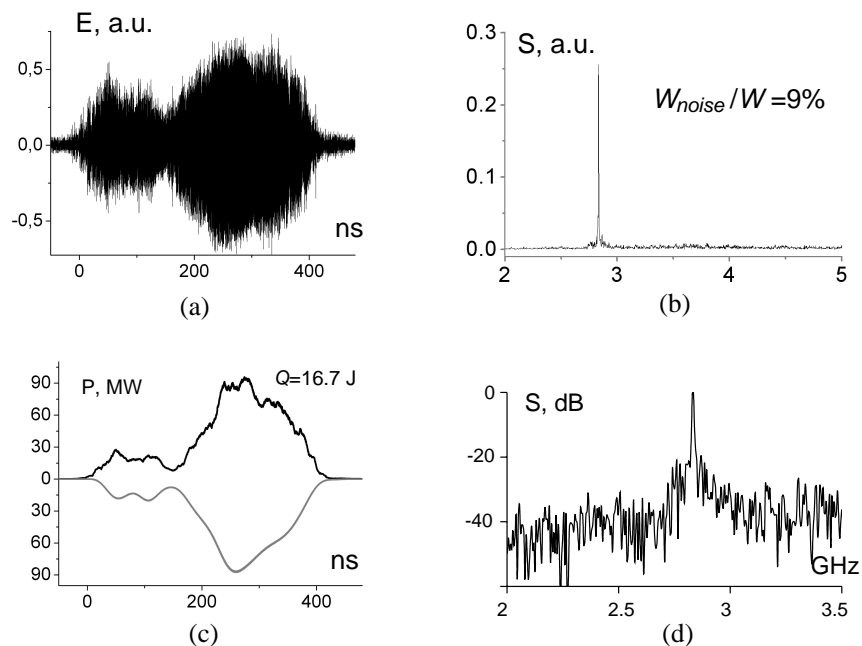


Figure 3: (a) Time dependence of the microwave electric field, (b) spectrum of the electric field $E(t)$ in the time interval of 500 ns, (c) time dependence of the microwave power $P(t)$ (the upper curve) and time dependence of the microwave power at the input signal frequency (the lower curve), and (d) spectrum of $E(t)$ in the time interval 240–440 ns, plotted on a logarithmic scale. The input frequency is 2.83 GHz, and the plasma density is equal to 10^{12} cm^{-3} approximately.

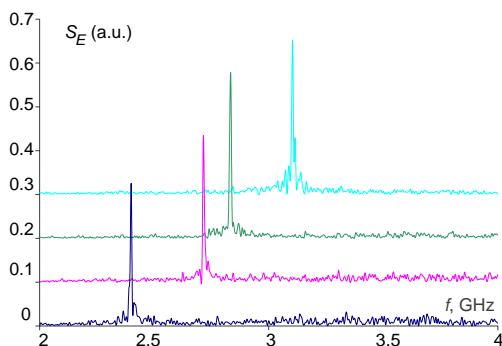


Figure 4: The spectra of output radiation at four frequencies of the input signals.

other plots in Fig. 3 were obtained by processing the waveforms presented in Panel (a). Panel (b) in this figure shows the spectrum of the output signal recorded over the time interval of 500 ns. The spectrum consists of a line at the frequency of the input signal and the noise spectrum (mainly at frequencies exceeding the input frequency). The spectral amplitude S at the input frequency is proportional to the electric field of the output microwave radiation at this frequency, averaged over the time interval of 500 ns. This spectrum allows us to estimate the ratio of the noise energy to the total microwave energy in the time interval 0–500 ns. This ratio is shown in Panel (b). The squared electric field dependence on time is shown in Panel (c) — the upper curve. The squared electric field is averaged over the time interval of 10 ns. The calorimetric measurement of the total microwave energy made it possible to plot the time dependence of the microwave power $P(t)$ in absolute units instead of the dependence in arbitrary units. The maximum power was equal 95 MW. Here, we assumed that the directional pattern of the output microwave radiation was constant and the square of the electric field at the axis of the microwave beam was proportional to the total microwave power. Earlier [2], it was shown that the distribution of the electric field across the microwave beam was close to that of the H_{11} mode at frequencies of 2 and 3.2 GHz. The lower curve in Fig. 3(c), shows the time dependence $P(t)$ in the frequency range of 15 MHz with respect to the input signal frequency. It can be seen that the maximum power at the frequency of the

input signal is 90 MW. In Panel (d) of Fig. 3, the spectrum is plotted on a logarithmic scale, which makes it possible to estimate the signal to noise ratio, which is more than 20 dB.

The similar microwave pulses were obtained for another three frequencies. The output microwave spectra for the input frequencies of 2.4, 2.71, 2.83, and 3.1 GHz are presented in Fig. 4. Selection of the optimal values of the plasma density for each frequency yielded the value of the total microwave pulse energy of 15–17 J at all frequencies and maximum output power 60–90 MW. Indirect methods proved that the amplifier operates with the same efficiency at any frequency in the range of 2.4 to 3.1 GHz.

REFERENCES

1. Kuzelev, M. V., A. A. Rukhadze, and P. S. Strelkov, *Plasma Relativistic Microwave Electronics*, Mosk. Gos. Tekhn. Univ. im. N.E. Bauman, Moscow, Russian, 2002.
2. Bogdankevich, I. L., I. E. Ivanov, O. T. Loza, et al., “Relativistic plasma microwave amplifier tunable within 2–3 GHz frequency band,” *Tech. Phys. Lett.*, Vol. 33, 480, 2007.
3. Strelkov, P. S., A. V. Ponomarev, and I. L. Bogdankevich, “Normal doppler effect in experiments on the interaction of relativistic electron beams with plasma: Plasma relativistic microwave amplifier,” *Plasma Phys. Rep.*, Vol. 33, 329, 2007.
4. Bogdankevich, I. L., I. E. Ivanov, and P. S. Strelkov, “Experimental study and numerical simulations of a plasma relativistic microwave amplifier,” *Plasma Phys. Rep.*, Vol. 36, 762, 2010.
5. Ivanov, E. I., P. S. Strelkov, and D. V. Shumeiko, “Radiation spectrum of a relativistic plasma microwave amplifier,” *J. Comm. Technol. Electron.*, Vol. 54, 1035, 2009.

SOI CMOS Miniaturized Tunable Bandpass Filter with Two Transmission Zeros for High Power Applications

Do-Kyung Im, Donggu Im, and Kwyro Lee

Department of EE, Korea Advanced Institute of Science and Technology, Daejeon, Korea

Abstract—This paper presents a capacitor loaded tunable bandpass chip filter using planar multiple split ring resonators (MSRRs) with two transmission zeros. To obtain high selectivity and minimize the chip size, asymmetric feed lines are adopted to make a pair of transmission zeros located on each side of passband. Compared with conventional filters using cross-coupling or source-load coupling techniques, the proposed filter uses only two resonators to achieve high selectivity through a pair of transmission zeros. This saves chip area by removing an additional resonator for transmission zeros. In order to optimize selectivity and sensitivity (insertion loss) of the filter, the effect of the position of asymmetric feed line on transmission zeros and insertion loss is analyzed. The digitally programmable 1 bit capacitor composed of metal-insulator-metal (MIM) capacitor and stacked-FETs is loaded at outer rings of MSRRs to tune passband frequency and handle high power signal up to +30 dBm. By turning on or off the gate of the transistors, the passband frequency can be shifted from 4 GHz to 5 GHz. The proposed on-chip filter is implemented in 0.18- μm SOI CMOS technology that makes it possible to integrate high-Q passive devices and stacked-FETs. The designed filter shows miniaturized size of only $4\text{ mm} \times 2\text{ mm}$ (i.e., $0.177\lambda_g \times 0.088\lambda_g$), where λ_g denotes the guided wave length of the $50\ \Omega$ microstrip line at center frequency. The measured insertion loss (S_{21}) is about 5.1 dB and 6.9 dB at 5.4 GHz and 4.5 GHz, respectively. The designed filter shows out-of-band rejection greater than 20 dB at 500 MHz offset from center frequency.

1. INTRODUCTION

Various radio access technologies (RATs) have been developed to meet different needs, ranging from personal area networks (PANs, like Bluetooth), wireless local area network (WLANs, like IEEE 802.11 b/g), wireless metropolitan area networks (WMANs, like Mobile WiMAX/IEEE 802.16e) to well-known cellular services like GSM/EDGE, W-CDMA, or CDMA2K. As a result, there is great interest in the implementation of multi-mode (MM), multi-band (MB), and multi-standard (MS) radio to cover any communication channels. This has resulted in the efforts towards software-defined radios (SDRs).

Although RF transceiver and baseband integrated circuits (ICs) are towards SDRs because their reconfigurability and software programmability drastically decrease the hardware complexity for MM/MB/MS radio, many external front-end modules (FEMs) such as power amplifiers (PAs), RF switches, and SAW filters/duplexer filters are still used at corresponding frequency bands. Especially, in case of SAW filter or FBAR filter, although they provide excellent out-of-band rejection characteristic and low insertion loss, very small tuning range with a few percent limits their use for SDRs. In order to achieve wide tuning range, most of published works use of transmission line (TL) filters [1, 2]. There are two major design challenges in designing tunable TL filters for high power applications. One is the miniaturization of the required filter size, the other is the implementation of highly linear electronically tunable device handling high power signal from PA. Traditionally, to vary the center frequency of the filter, ferro-electrical varactors, diode varactors, and micro-electro-mechanical system (MEMS) switched capacitors are used. Although these special technologies satisfy the requirement of power handling capability and linearity, they are not compatible with silicon-based process technologies. In addition, these require the tuning/switching voltage in the range of 25 V, which of course is unsuitable for battery-driven handsets.

In this paper, highly miniaturized planar bandpass filter adopting multiple split ring resonators (MSRRs) and asymmetric feed line technique is designed with high frequency selectivity. By integrating miniaturized MSRRs and highly linear SOI-CMOS switched capacitors on the same die, fully integrated planar on-chip tunable filter is firstly proposed for high power applications.

2. DESIGN OF PLANAR TUNABLE FILTER

Figure 1 shows proposed highly miniaturized planar bandpass filter using two MSRRs with asymmetric feed lines. The input and output feed lines divide input and output MSRRs into two sections of l_1 and l_2 , respectively, where the total length $l_1 + l_2$ is equal to λ_{go} (the guided wavelength at

fundamental-mode frequency). The coupling capacitance between two MSRRs is expressed by the C_s and the C_L denotes loading capacitance. The signals at the input and output feed points are in phase when the structure is resonant at its fundamental-mode frequency. As well known, the coupled resonators with asymmetric feeding points create two more transmission zeros [3]. In Fig. 1, the first zero occurs at the frequency when the length of arm (l_1) of the input resonator approaches a quarter-wavelength and the other occurs at the frequency when the length of arm (l_2) is near a quarter-wavelength.

To find the frequency of two transmission zeros, the equation for the insertion loss of proposed structure at these frequencies are derived by establishing the ABCD matrices for the upper and the lower signal paths when the length of l_1 and l_2 is a quarter-wavelength. The ABCD matrices for the upper and lower signal paths are expressed as

$$\begin{aligned} \begin{pmatrix} A_{up} & B_{up} \\ C_{up} & D_{up} \end{pmatrix} &= M_1 \times M_2 \times M_3 \quad \text{and} \quad \begin{pmatrix} A_{low} & B_{low} \\ C_{low} & D_{low} \end{pmatrix} = M_3 \times M_2 \times M_1 \quad (1) \\ M_1 &= \begin{pmatrix} \frac{\frac{1}{\omega C_L} \cos \theta_1 - Z_0 \sin \theta_1}{\frac{1}{\omega C_L} - Z_0 \sin \theta_1} & j \frac{\frac{1}{\omega C_L} Z_0 \sin \theta_1}{\frac{1}{\omega C_L} - Z_0 \sin \theta_1} \\ j \frac{\frac{1}{\omega C_L} Y_0 \sin \theta_1}{\frac{1}{\omega C_L} - Z_0 \sin \theta_1} & \frac{\frac{1}{\omega C_L} \cos \theta_1 - Z_0 \sin \theta_1}{\frac{1}{\omega C_L} - Z_0 \sin \theta_1} \end{pmatrix} \\ M_2 &= \begin{pmatrix} 1 & \frac{1}{j\omega C_s} \\ 0 & 1 \end{pmatrix} \\ M_3 &= \begin{pmatrix} \frac{\frac{1}{\omega C_L} \cos \theta_2 - Z_0 \sin \theta_2}{\frac{1}{\omega C_L} - Z_0 \sin \theta_2} & j \frac{\frac{1}{\omega C_L} Z_0 \sin \theta_2}{\frac{1}{\omega C_L} - Z_0 \sin \theta_2} \\ j \frac{\frac{1}{\omega C_L} Y_0 \sin \theta_2}{\frac{1}{\omega C_L} - Z_0 \sin \theta_2} & \frac{\frac{1}{\omega C_L} \cos \theta_1 - Z_0 \sin \theta_2}{\frac{1}{\omega C_L} - Z_0 \sin \theta_2} \end{pmatrix} \end{aligned}$$

where M_1 is the ABCD matrix of transmission line ($\theta_1 = \beta_1 l_1$) with loading capacitance (C_L), M_2 is the ABCD matrix of coupling capacitance between two MSRRs, and M_3 is the ABCD matrix of transmission line ($\theta_2 = \beta_2 l_2$) with loading capacitance (C_L), ω is the angular frequency, and Z_0 (Y_0) is the characteristic impedance (admittance). From (1), the ABCD matrices for the upper

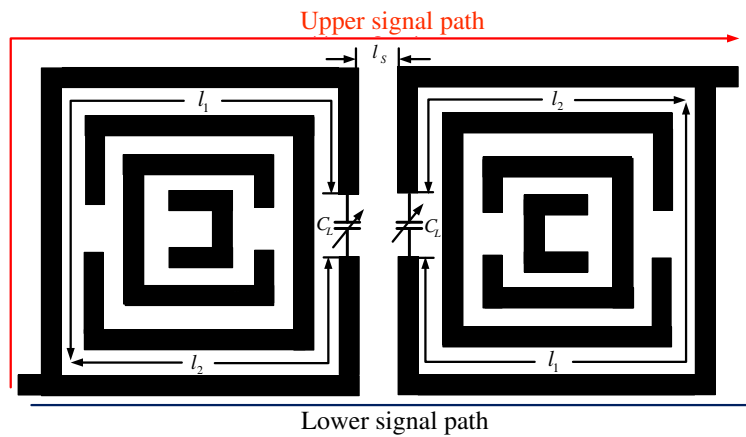


Figure 1: Proposed planar tunable bandpass filter adopting miniaturized split ring resonators (MSRRs) and asymmetric feed line technique. The SOI-CMOS switched capacitor composed of metal-insulator-metal (MIM) capacitor and stacked-FETs is loaded at outer rings of MSRRs to tune passband frequency.

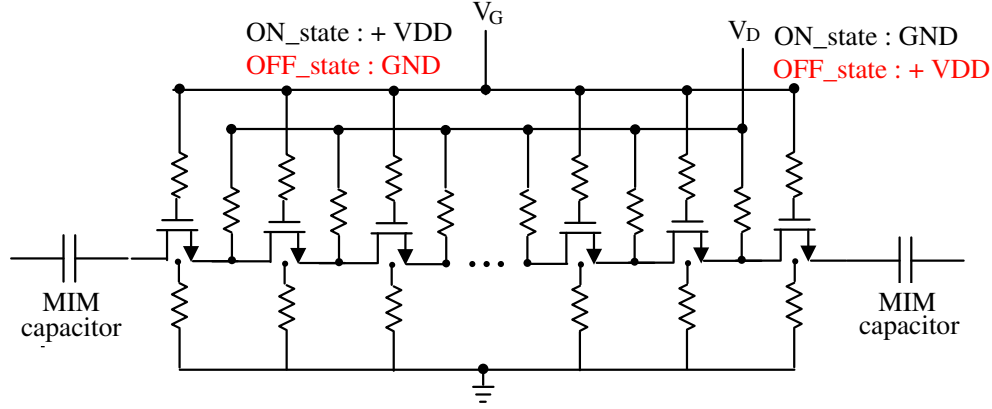


Figure 2: 1-bit digitally programmable capacitor inside of proposed tunable filter to tune passband frequency while handling high power signal from PA.

and lower signal paths are calculated as

$$\begin{aligned}
 A_{low}(D_{up}) &= \frac{\frac{1}{\omega^2 C_L^2} \cos \theta - \frac{1}{\omega C_L} Z_0 \sin \theta + Z_0^2 \sin \theta_1 \sin \theta_2 + \frac{1}{\omega^3 C_L C_S} Y_0 \cos \theta_1 \sin \theta_2 - \frac{1}{\omega^2 C_L C_S} \sin \theta_1 \sin \theta_2}{\left(\frac{1}{\omega C_L} - Z_0 \sin \theta_1\right) - \left(\frac{1}{\omega C_L} - Z_0 \sin \theta_2\right)} \\
 B_{low}(B_{up}) &= j \frac{\frac{1}{\omega^2 C_L^2} Z_0 \sin \theta - \frac{1}{\omega^2 C_L C_S} Z_0 \sin \theta + \frac{1}{\omega^3 C_L C_S} \cos \theta_1 \cos \theta_2 - \left(\frac{2}{\omega C_L} + \frac{1}{\omega C_S}\right) Z_0^2 \sin \theta_1 \sin \theta_2}{\left(\frac{1}{\omega C_L} - Z_0 \sin \theta_1\right) - \left(\frac{1}{\omega C_L} - Z_0 \sin \theta_2\right)} \\
 D_{low}(A_{up}) &= \frac{\frac{1}{\omega^2 C_L^2} \cos \theta - \frac{1}{\omega C_L} Z_0 \sin \theta + Z_0^2 \sin \theta_1 \sin \theta_2 + \frac{1}{\omega^3 C_L C_S} Y_0 \cos \theta_1 \sin \theta_2 - \frac{1}{\omega^2 C_L C_S} \sin \theta_1 \sin \theta_2}{\left(\frac{1}{\omega C_L} - Z_0 \sin \theta_1\right) - \left(\frac{1}{\omega C_L} - Z_0 \sin \theta_2\right)} \\
 C_{low}(C_{up}) &= j \frac{\left(\frac{1}{\omega C_L}\right)^2 Y_0 \sin \theta + \left(\frac{1}{\omega C_L}\right)^2 \frac{1}{\omega C_S} Y_0^2 \sin \theta_1 \sin \theta_2 - \frac{2}{\omega C_L} \sin \theta_1 \sin \theta_2}{\left(\frac{1}{\omega C_L} - Z_0 \sin \theta_1\right) - \left(\frac{1}{\omega C_L} - Z_0 \sin \theta_2\right)} \quad (2)
 \end{aligned}$$

where θ is the sum of θ_1 and θ_2 . The insertion loss (S_{21}) of proposed filter be calculated using parameter conversion from ABCD parameters and is expressed as

$$S_{21} = \frac{4B_{low}Y_0}{B_{low}^2 Y_0^2 + 2B_{low}(A_{low} + D_{low})Y_0 + (A_{low} + D_{low})^2 - 4(B_{low}C_{low} - A_{low}D_{low})}. \quad (3)$$

Since the S_{21} becomes close to zero at frequencies of transmission zeros, the position of two transmission zeros can be found by setting the numerator of (3) (i.e., B_{low}) equal to zero. In addition, we know that the position of two transmission zeros can be moved by changing the position of feed points, because this changes the θ_1 and θ_2 in the B_{low} .

It is important to find optimum point where the tunable capacitor is loaded to minimize the degradation of insertion loss and out-of-band rejection performances in the MSRR. The experimental results of [4] show that the highest size reduction of split ring resonator (SRR) is achieved when capacitors are loaded at the outer ring's split region. Therefore, in this design, 1-bit SOI-CMOS digitally programmable capacitor of Fig. 2 is loaded at outer rings of MSRRs to tune passband frequency. To handle high power signal up to +30 dBm from PA, stacked-FETs, where a very high voltage swing is evenly distributed across each transistor in a chain through a capacitive voltage divider, is adopted. In addition, in order to increase power handling capability of off-state FETs, the gate is reverse-biased by applying the positive (+VDD) voltage to the drain and the source with respect to the gate and the body with ground potential.

3. EXPERIMENT RESULTS

The proposed planar tunable bandpass filter has been implemented in a 0.18 μm PDSOI-CMOS process technology. Fig. 3 shows the chip photograph of the filter. To tune passband frequencies from 5.4 GHz to 4 GHz, the l_1 , l_2 , and l_s are set equal to 2.8 mm, 4.8 mm, and 5 μm , respectively, in Fig. 1. The designed filter shows miniaturized size of only 4 mm \times 2 mm (i.e., $0.177\lambda_g \times 0.088\lambda_g$), where λ_g denotes the guided wave length of the 50 Ω microstrip line at center frequency.

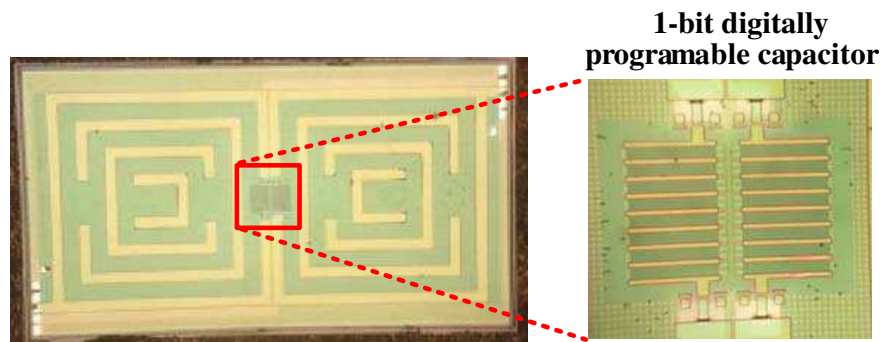


Figure 3: Chip photograph of proposed planar tunable filter.

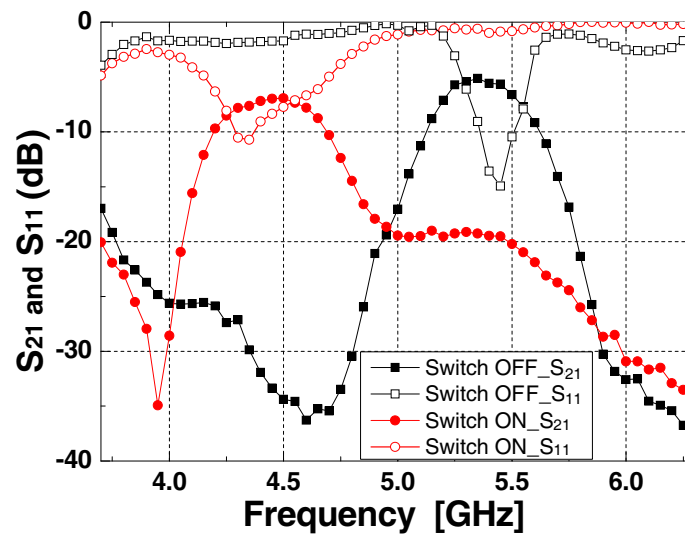


Figure 4: Measured S_{21} and S_{11} of the planar tunable filter by on/off control of 1-bit digitally programmable capacitor.

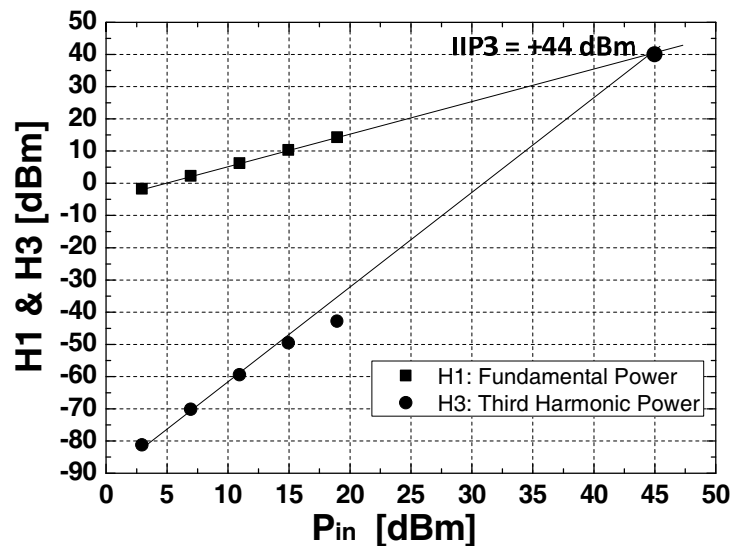


Figure 5: Measured third-order input-referred intercept point (IIP3) of proposed tunable planar filter.

The measured frequency tuning range of the planar tunable filter is from 5.4 GHz to 4.5 GHz as shown in Fig. 4. The measured insertion loss (S_{21}) is about 5.1 dB and 6.9 dB at 5.4 GHz and 4.5 GHz, respectively, and the measured input reflection coefficient (S_{11}) is less than -10 dB. As

predicted, the proposed planar tunable filter shows a pair of transmission zeros located on each side of passband. Despite using only two resonators, high frequency selectivity is achieved owing to a pair of transmission zeros. The designed filter shows out-of-band rejection greater than 20 dB at 500 MHz offset from center frequency. Two tone measurements for intermodulation distortion are performed over 5.4 GHz passband frequency. In case of power handling capability and harmonic distortions, this passband frequency is the worst case due to off-state MOSFETs. Tone spacing used in the linearity measurement is 50 MHz. As shown in Fig. 5, the third-order input-referred intercept point (IIP3) of +44 dBm is obtained. As a result, the proposed planar tunable filter is expected to work as a passive component introducing no extra non-linearity.

4. CONCLUSIONS

In this paper, highly miniaturized planar bandpass filter adopting multiple split ring resonators (MSRRs) and asymmetric feed line technique is designed with high frequency selectivity. By integrating miniaturized MSRRs and highly linear SOI-CMOS switched capacitors on the same die, fully integrated planar on-chip tunable filter is firstly proposed for high power applications.

ACKNOWLEDGMENT

This work was supported by the National Research Foundation of Korea (NRF) grant funded by the Korea government (MEST). The chip fabrication was supported by National NanoFab Center (NNFC), Daejeon, Korea.

REFERENCES

1. Entesari, K. and G. M. Rebeiz, "A differential 4-bit 6.5–10-GHz RF MEMS tunable filter," *IEEE Trans. on Microwave Theory and Techniques*, Vol. 53, No. 3, 1103–1110, Mar. 2005.
2. Nath, J., et al., "An electronically tunable microstrip bandpass filter using thin-film Barium-Strontium-Titanate varactors," *IEEE Trans. on Microwave Theory and Techniques*, Vol. 53, No. 9, 2707–2712, 2005.
3. Lee, S.-Y. and C.-M. Tsai, "New cross-coupled filter design using improved hairpin resonator," *IEEE Trans. Microwave Theory Tech.*, Vol. 48, 2482–2490, Dec. 2000.
4. Aydin, K. and E. Ozbay, "Capacitor-loaded split ring resonators as tunable metamaterial components," *Journal of Applied Physics*, Vol. 101, No. 2, 024911, 2007.

Variability of GPS-derived Zenith Tropospheric Delay and Some Result of Its Assimilation into Numeric Atmosphere Model

O. G. Khutorova, G. M. Teptin, V. E. Khutorov, V. V. Kalinnikov, and T. R. Kurbangaliev
Kazan Federal University, Russia

Abstract— The total zenith tropospheric delay (ZTD) is an important parameter of the atmosphere and directly or indirectly reflects the weather processes and variations. This paper presents a hardware and software complex for continuous measurements and prediction of atmospheric thermodynamics and radiowaves refraction index. The main part is a network of ground-based spatially separated GPS-GLONASS receivers, which allows the remote sensing zenith tropospheric delay. GPS-Derived Zenith Tropospheric Delay shows the day to day variation and mesoscale spatial and temporal variability. Comparison with the numerical weather reanalysis fields and solar photometer measurements showed agreement with the relative deviation of less than 10%. Hardware-software complex includes the numerical model of the atmosphere on a computational cluster. A variational assimilation system was used to examine the comparative impact of including satellite derived total zenith tropospheric delay from GPS and GLONASS ground observations. Preliminary results show that the initial field of radiowaves refraction index was improved by assimilating the satellite derived ZTD.

1. INTRODUCTION

Numerical weather prediction is an initial and boundary value problem; the more accurate initial conditions could result in the improvement of forecast skill. Over the past decades, considerable progress has been made in satellite navigation systems monitoring technology, which is significantly increasing the atmospheric information. In the ionospheric investigation the method may be considered as a global tool for radiosounding [1–3]. It is shown that a network of ground receivers GPS — a tool for studying the troposphere with high temporal resolution [3, 4]. Due to the strong spatial inhomogeneity and temporal variability of atmospheric density, especially for water vapor, accurate modeling of path delay in GPS signals is necessary in high-accuracy positioning and meteorological applications (climatology and weather forecasting).

2. RADIOWAVES ZENITH TROPOSPHERIC DELAY AND ITS MONITORING

This paper presents hardware-software complex for continuous measurements and prediction of atmospheric thermodynamics. The main part of the hardware-software complex is a network of ground-based spatially separated GPS-GLONASS receivers. The network of seven GPS-GLONASS receivers arranged to distance from 3 to 35 kilometers in Kazan city (56°N, 49°E) gives a good possibility of the atmosphere remote sensing [7, 8].

All existing theories accept the refraction index as key parameter determining features of distribution of radiowaves in the atmosphere. GPS signals are significantly influenced by the atmosphere, especially the ionosphere and troposphere, along their path from the satellite to the GPS antenna. Dependence of the refraction index of air on height above a terrestrial surface causes a curvature of the radiowaves trajectory. Fluctuations of parameters of the electromagnetic waves extending in an atmosphere are connected to various atmospheric processes. The equation for a parameter of refraction looks like [1, 3]

$$N = 77.6 \frac{P_d}{T} + 72 \frac{e}{T} + 3.75 \cdot 10^5 \frac{e}{T^2}. \quad (1)$$

Here, T is the absolute air temperature, p is the dry-air pressure, and l is the water-vapor pressure.

The resulted factor of refraction of radiowaves in plasma for high frequencies is defined as [1]:

$$N = -\gamma \cdot N_e \cdot f^{-2} \quad (2)$$

Here $\gamma = 40.4$ if electronic concentration N_e is expressed in m^{-3} , and frequency f — in Hz. An additional way of radio waves from the satellite to the antenna associated with refraction in the atmosphere [1, 5]:

$$L_i^j = I_i^j + \Delta L_i^j = 10^{-6} \int_s N(s) ds \quad (3)$$

The integral is taken along the line radio paths from the satellite to the antenna.

The atmosphere is illuminated with 1.6 and 1.2 GHz (L_1 and L_2) signals transmitted by the GNSS satellites. Phases of signals from a ten or so of these satellites can be simultaneously observed with mm precision during all weather conditions, using several receivers. Ground-based receivers measure the received radio signal parameters (group and phase path from the satellite to the receiver, the Doppler shift of carrier frequency, etc.). Observing from sea level, the lower and upper atmosphere induce GPS signal phase path delays of several meters or more. The distance to the satellite receiver can be measured as follows:

$$L_i^j = \rho_i^j + I_i^j + \Delta L_i^j + \varepsilon_i^j \quad (4)$$

where the indices i and j — number and the satellite receiver, respectively, ρ — the true distance between the satellite and the receiver (calculated from the known coordinates of the antenna and satellite ephemeris data [1], we use final precise satellite orbits [6] to calculate satellite-antenna distance.); I and ΔL — ionospheric and tropospheric delays the signal; ε — measurement errors, including errors due to receiver and satellite clock bias.

At use of the multifrequency equipment, probably to compensate errors of measurement of the pseudo distance, caused by an ionosphere I , using the dependence of these errors on frequency bearing. The geometrical distance differs from the actual ray path in troposphere is called slant tropospheric delay. Tropospheric delay consists of a hydrostatic component depending on air pressure and temperature, and a wet delay depending on water vapor pressure and temperature. The tropospheric delay in zenith direction called zenith tropospheric delay (ZTD) The total zenith tropospheric delay (ZTD) is an important parameter of the atmosphere and directly or indirectly reflects the weather processes and variations.

Carrier phases are the primary and most important type of observation for high-precision parameter estimation. The original carrier phases are not used for filtering because these measurements are corrupted by receiver and satellite clock errors. Instead, double differences are used. Ionospheric refraction causes range delays that may be corrected for by receiving two carrier frequencies simultaneously to correct for the dispersive characteristics of the ionosphere. The system of equations constructed based on measurements collected at each interval of fifteen minutes from all the satellites simultaneously, solved by the method of least squares. Phase ambiguities are estimated as unknown. For the residual variance of the differences we have are these fifteen-minute estimates. The resulting estimates of ZTD , we smoothed them using a Kalman filter.

GNSS-derived ZTD have been validated against NCEP-NCAR NCEP/NCAR reanalysis data [5]. Comparing the results with remote sensing data of weather stations, radiosonde and reanalysis showed good agreement (Table 1).

GNSS-derived zenith tropospheric delay shows the day to day variation and mesoscale spatial and temporal variability [7]. The most changeable part of the ZTD is zenith wet delay, caused by the integral water vapor (IWV) [3]. We estimate IWV using GNSS-derived ZTD and ground measurement air pressure and temperature. The Saastamoinen model is used when computing the zenith hydrostatic delay [3]. The consistency between GNSS-derived IWV and NCEP-NCAR reanalysis data shows and a standard deviation of about $2 \text{ kg}\cdot\text{m}^{-2}$ IWV. The example of comparison is shown in Figure 1.

It is noted that when comparing the integral water vapor of satellite navigation system with numerical weather fields, differences arise relating to model overestimations for hydrostatic delay. The average bias of ZTD estimates increase with the growth of cloudiness. ZTD bias reaches about 7 mm, which causes the overestimation of integral water vapor from 0.98 to $1.18 \text{ kg}/\text{m}^2$. So, it is appropriate to assimilate into numerical weather model field evaluation of the initial tropospheric delay, and not integral water vapor content.

Table 1: Verification of GNSS-derived ZTD versus reanalysis-derived ZTD .

season	mean residual (m)	standard deviation (M)	correlation coefficient
winter	0.006	0.011	0.82 ± 0.09
spring	0.013	0.009	0.94 ± 0.03
summer	-0.022	0.027	0.73 ± 0.13
fall	-0.014	0.013	0.86 ± 0.07

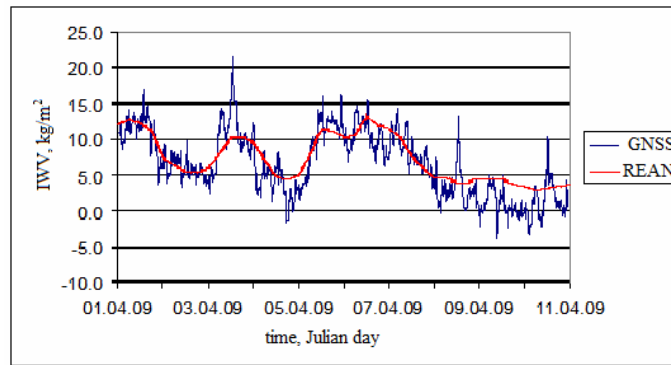


Figure 1: GNSS-derived I WV versus NCEP-NCAR reanalysis derived I WV. Kazan, 1–11.04.2009.

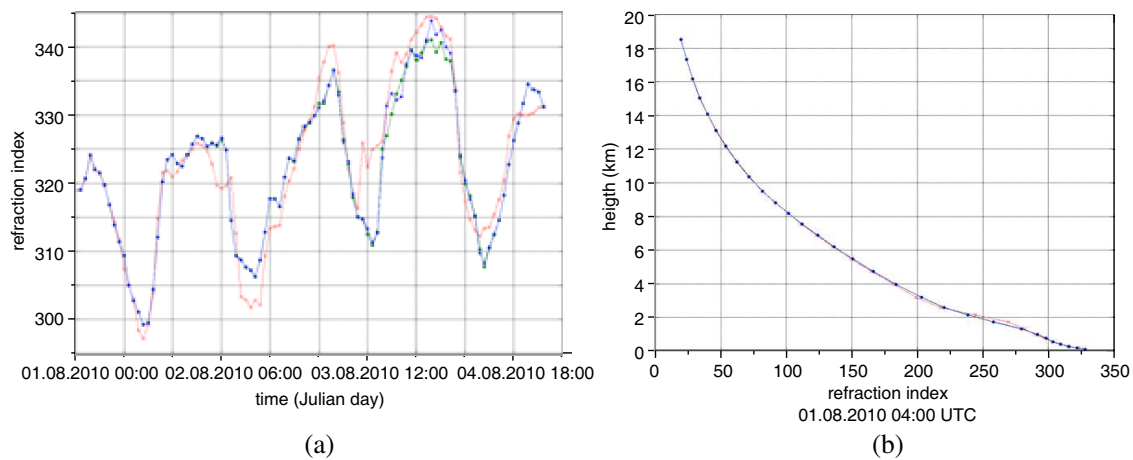


Figure 2: Comparison of radiowaves (a) refraction index time and (b) vertical structure. (red — prediction without ZTD assimilation, green — control, blue — prediction with ZTD assimilation).

3. NUMERICAL SIMULATION RESULTS

Hardware-software complex includes the numerical model of the atmosphere on a computational cluster. WRF-model is used for prediction of 3d structure of troposphere meteo parameters and radio waves refraction index [8]. The Advanced Research WRF model version 3.1 and its three-dimensional variational data assimilation system (3D-Var) were used [10]. The domain configuration included a domain of 5 km horizontal resolutions. The grids extended vertically to 50 hPa and were resolved by 31 unevenly spaced levels with the nest resolution in the boundary layer. The initial and boundary conditions and surface temperature data were from the National Centers for Environmental Prediction Global Forecast System (GFS) with spatial and temporal resolutions of $1^\circ \times 1^\circ$ and 6 h, respectively. A variational assimilation system was used to examine the comparative impact of including satellite derived total zenith tropospheric delay from GPS and GLONASS ground observations.

Preliminary results show that the initial field of wind and temperature was improved by assimilating the satellite derived ZTD. Figure 2 shows the time and vertical structure of radiowave refraction index forecast for August 1–4, 2010.

It indicates that the all has been well predicted with ZTD assimilation against without. The standard deviation with assimilation tropospheric delay is decreased up to 6 times. For vertical structure prediction is very similar to control data with and without assimilation too.

4. CONCLUSION

We have presented some experimental results of zenith tropospheric delay and integral water vapour variations measurement. A variational assimilation system was used to examine the comparative impact of including satellite derived total zenith tropospheric delay from GPS and GLONASS ground observations. Preliminary results show that the initial field of wind, temperature and

radiowaves refraction index was improved by assimilating the satellite derived ZTD.

ACKNOWLEDGMENT

This work was supported by the Russian Federal Program “Research and scientific-pedagogical cadres of Innovative Russia”.

REFERENCES

1. Yakovlev, O. I., *Space Radio Science*, Taylor and Francis, London, 2003.
2. Kunitsyn, V. E. and E. D. Tereshchenko, *Ionospheric Tomography*, Springer-Verlag, Berlin, 2003.
3. Hofmann-Wellenhof, B., H. Lichtenegger, and J. Collins, *Global Positioning System. Theory and Practice*, Springer-Verlag, Wien, New York, 1994.
4. Davies, O. T. and C. N. Mitchell, “Application of GPS phase delay measurements in radio science and atmospheric studies,” *IEEE Proc. Microw. Antennas Propag.*, Vol. 151, No. 1, 1–6, 2004.
5. NCEP/NCAR Reanalysis, Model Description, http://dss.ucar.edu/pub/reanalysis/rean_model.html.
6. The International GNSS Service, <http://igsb.jpl.nasa.gov/>.
7. Khutorova, O. G., G. M. Teptin, A. A. Vasil’ev, V. E. Khutorov, and A. P. Shlychkov, “Passive sounding of the radiowaves refraction index structure in the troposphere by the set of satellite navigation system receivers in Kazan city,” *Radiophysics and Quantum Electronics*, Vol. 54, No. 1, 1–8, 2011.
8. Teptin, G. M., O. G. Khutorova, D. P. Zinin, and V. E. Khutorov, “Study of mesoscale irregularities of the refraction coefficient of radiowaves in the troposphere by the methods of numerical simulation,” *Radiophysics and Quantum Electronics*, Vol. 53, No. 1, 1–12, 2010.
9. Khutorova, O. G., A. A. Vasil’ev, and V. E. Khutorov, “On prospects of investigation of the inhomogeneous troposphere structure using the set of GPS-GLONASS receivers,” *Atmos. Ocean. Opt.*, Vol. 23, No. 6, 510–514, 2010.
10. Huang, X. Y., Q. Xiao, D. M. Barker, et al., “Four-dimensional variational data assimilation for WRF: Formulation and preliminary results,” *Mon. Wea. Rev.*, Vol. 137, 299–314, 2009.

Horizontal Structural Functions in Troposphere for Radio Waves Refractivity Index by Use of Ground Set of GPS-GLONASS Receivers

V. E. Khutorov, A. A. Jurravlev, and G. M. Teptin
Kazan Federal University, Russia

Abstract— In this paper we show results of troposphere fluctuation analysis and its influence on radiowaves refractive index variations. For comparison of inhomogeneous impurities structure we used electromagnetic waves refraction index data which don't depend on impurity but depend on atmospheric parameters only. Our main object of investigation is a mesoscale process in troposphere. We can estimate space structure of atmospheric parameters, using the data from network based on Global Navigation Satellite System receivers. We used structure function to estimate characteristics of impurities and refraction index fluctuation. Function shows the contribution of the processes of the defined scale in the total variance of the fluctuations. The received structure functions demonstrate increasing with distance between stations. The results show a significant effect on electromagnetic wave refraction index caused by the mesoscale troposphere process.

1. INTRODUCTION

Investigation of inhomogeneities and their connection with the movement of air masses in the atmosphere is one of the most difficult modern scientific problems. So far is slightly investigated their influence, in the radar measurements and satellite navigation. Our main object of investigation is a mesoscale process in troposphere and their influence on radio waves. These processes have size from 1 km up to 1000 km and time scale about few hours. Mesoscale processes are less investigated than smaller or larger processes. One of main reason is that, this task requires system with good temporal and spatial resolution. At present, with the modern development Global Navigation Satellite System (GNSS) there is opportunity to use their signals for remote sensing of the troposphere. Using the data from network based on Global Navigation System receivers, we can estimate space structure of atmospheric parameters, and calculate influence of mesoscale processes and other irregularities on the propagation of radio waves in the troposphere.

In this paper we show results of troposphere fluctuation analysis and its influence on radio waves refractive index variations. For comparison of inhomogeneous impurities structure we used electromagnetic waves refraction index data which don't depend on impurity but depend on atmospheric parameters only.

2. MEASUREMENT METHODS

Since the route between the satellite and receiver radio waves are affected by the atmosphere, the radio signal comes on the receiver with delay. If we calculated its spatial and temporal variations, we can estimate the quantitative characteristics of the atmospheric processes [1, 2].

The distance between satellite and receiver measured by carrier phase can be represented as the sum of the true distance between satellite and receiver, ionosphere and troposphere delays of the signal, measured errors, including errors due receiver and satellite clock drift. Atmospheric correction, which characterizes the delay of radio waves as compared to propagation in vacuum, is defined as the integral of the refractive index of the path passed by radio wave in the atmosphere [1–3].

Main parameter in remote sensing of troposphere is zenith troposphere delay (ZTD), equal to the difference of the optical and geometric path signals of satellite navigation systems in a neutral atmosphere in the zenith direction. ZTD is measured in units of length.

Investigation of the effect of inhomogeneities on radio waves propagation of are most commonly used two methods — the method of spectral and structural features. When measuring the spectra should be borne in mind that the measured signal is a superposition of the inhomogeneities influence in absolutely all sizes, and the use of structural features in the measured signal is not taken into account the influence of inhomogeneities in less than a certain size. For satellite radio paths — most suitable ground-based receiver is the second method — the structure functions. Structure function is a basic characteristic of process with random increments. Physically, structure function

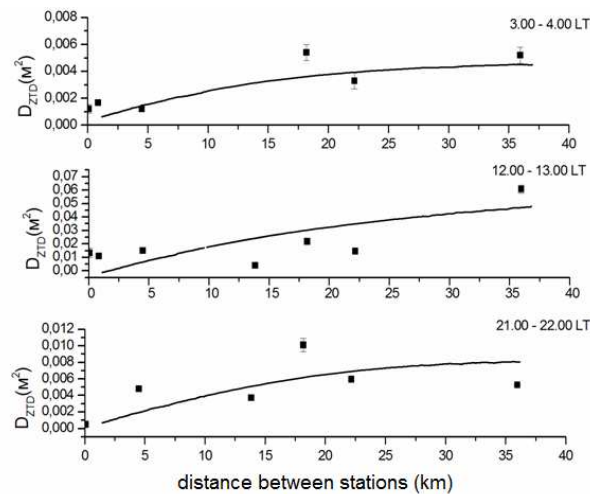


Figure 1: Structure functions of radio signals zenith tropospheric delay measured by August 23, 2009, by a network of GNSS receivers in the range of scales 0.85–35 km, for different times of day and it's approximated by a power function.

is a square of fluctuation of the investigated parameter. Function shows the contribution of the processes of the defined scale in the total variance of the fluctuations [4].

We calculate the structure function of zenith troposphere delay GNSS signal and refractive index of the decimeter radio waves, depending on the horizontal distance r between the station of the network GPS-GLONASS.

$$\begin{aligned} D_n(r) &= \langle (N(0) - N(r))^2 \rangle \\ D_q(r) &= \langle (ZTD(0) - ZTD(r))^2 \rangle \end{aligned} \quad (1)$$

The first term in parentheses corresponds to the reference point with the conventional receiver coordinate (0), and the second — to a point at distance r from the reference point. The angle brackets denote averaging over time. The physical meaning of the structure function is the mean square fluctuation in the value of the study of the spatial scales of processes with stationary increments. As indicator of mesoscale processes influence, structure function should have a power-law behavior [3]. For calculation structure functions were used estimates of the difference zenith troposphere delay and the refractive index of radio waves on two spaced points received for 10 seconds, which are averaged over a period of at least 1 hour.

For estimation value of error technique, described above is a specific experiment. We evaluated the estimation variance of the difference in the ZTD horizontal receiving antenna spacing of 12 m to 26 m. This approach allowed us to estimate the accuracy of our method. After measuring the structure function of troposphere delay for a low base, we have determined that the accuracy of the structure function is equal to 0.002 m^2 .

3. EXPERIMENT WITH NETWORK OF GNSS RECEIVERS

For analysis two independent networks of stations were used. The first network of automated stations measure main meteorological parameters. They are located in various sites within urban territory and spaced on distance from 0.9 up to 5.3 km from each other. The second network of GPS-GLONASS collects the data about spatial structure of electromagnetic waves refraction index. They are also located in various sites of city and spaced on distance from 0.83 up to 35 km from each other. Using data from each network we calculated spatial structure of refractivity index.

To assess the influence of the daily dynamics of mesoscale inhomogeneities on of GNSS radio signals troposphere delay, an experiment was performed with a network of GNSS receivers separated by distances of 1 to 35 km. In Figure 2 shows example plots of structure functions calculated from experimental data.

As expected, the structure functions increase with increasing distance between the points of measurement. That is, contribution of inhomogeneities in troposphere delay increases with the size of the inhomogeneities. It is seen that in a 35 km scale structure function shows a significant

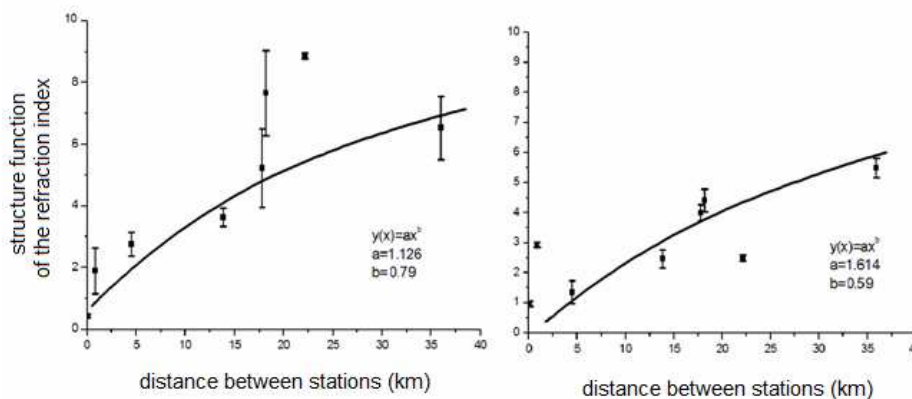


Figure 2: Structural functions of radio waves refraction index measured by the network of GNSS receivers on the range of scales 0.85–35 km at different altitudes and its approximated by a power function.

variation depending on time of day. For the base in 21–35 km in the daytime its value reaches values $0.06\text{--}0.07\text{ m}^2$ in the morning and evening, 0.007 m^2 . This behavior of the structure function means, that during the day increases the variance of the index of refraction of radio waves in the horizontal direction of the scale of the order of tens of kilometers.

For comprising with data from monitoring station, calculation of structure function of the refraction index was made. Evaluation was performed on the surface of the Earth (at the height of the antenna) and at altitudes of 160 m, 450 m, 800 m, 1400 m, 3 km, 5 km, 8 km and 10 km relative to the surface of the Earth. In Figure 2 shows example plots of structure functions and their approximations for the study of several heights. Based on these results we can note a number of general laws.

First, there is a substantial increase in the horizontal structure function of the index of refraction of radio waves with an increase in the scale of the inhomogeneities, with increasing distance between the receiving points of radio signals. That is, inhomogeneities contribute to the dispersion of the refractive index increases with the size of the inhomogeneities at all levels of high-rise [5, 6].

Secondly, the value of the structure functions were approximated by power functions with an exponent equal to 0.69–0.82 and structural constant 1.2–1.7, largest structural feature of the structure constant level of 0.82 and 1.72 was obtained for the surface layer. The received structure functions demonstrate increasing with distance between stations.

4. CONCLUSIONS

It is shown that remote sensing signals, of GLONASS and GPS satellites passed through troposphere, measured by a network of receivers, allows us to study the quantitative characteristics of inhomogeneities of the refractive index dm radio waves at different heights of the troposphere, in particular, the horizontal structure functions of the index of refraction and troposphere delay of signals, including their diurnal variations. Comparison of results obtained in the data of independent ground-based measurements of the structural function of the refraction index and high-altitude radiosonde measurements showed good agreement. The results obtained in this paper do not contradict the previously known publications [4–7].

REFERENCES

1. Hofmann-Wellenhof, B., H. Lichtenegger, and J. Collins, *Global Positioning System. Theory and Practice*, Springer-Verlag, Wien, New York, 1994.
2. Flores, A., J. V.-G. de Arellano, L. P. Gradinarsky, and A. Rius, "Tomography of lower troposphere using small dense network of GPS receivers," *IEEE Transactions on Geoscience and Remote Sensing*, Vol. 39, No. 2, 439, 2001.
3. Davies, O. T., C. N. Mitchell, P. S. J. Spenser, and P. A. Watsons, "Application of GPS phase delay measurements in radio science and atmospheric science," *International Conference on Antennas and Propagation*, No. 480, 288, 2001.
4. Vennebusch, M. and S. Schön, "Power-law behaviour of GPS phase observations reflecting atmospheric turbulence," *Geophysical Research Abstracts*, Vol. 13, 40–46, 2011.

5. Khutorova, O. G., G. M. Teptin, A. M. Maksimov, V. E. Khutorov, and A. A. Vasiliyev, “Investigations of space temporal structure for atmospheric inhomogenities over Tatarstan,” *Environ. Radioecol. Appl. Ecol.*, Vol. 13, No. 3, 20–24, 2007.
6. Khutorov, V. E., “Estimation of macroturbulence influence on the radiowaves propogation in the troposphere and ionosphere usig GPS-GLONASS,” *Environ. Radioecol. Appl. Ecol.*, Vol. 14, No. 2, 20–23, 2008.
7. Khutorov, V. E. and O. G. Khutorova, “Macroturbulence influence on radiowaves propogation in the troposphere with use GPS-GLONASS radiosignals,” *Environ. Radioecol. Appl. Ecol.*, Vol. 15, No. 1–2, 21–24, 2008.
8. Khutorov, V. E., “About minimal value of structural function for tropospheric radio waves delay,” *Environ. Radioecol. Appl. Ecol.*, Vol. 17, No. 2, 24–27, 2011.

Remote Sensing for Estimating Cultivated and Arable Land Areas on Slopes

Y. Fernandez-Ordoñez¹, J. Soria-Ruiz², and M. Mauricio Vázquez-Rivera²

¹Colegio de Postgraduados, Mexico

²Geomatics Lab., National Institute of Research for Forestry Agriculture and Livestock (INIFAP)
Toluca, Mexico

Abstract— Planning and strategies of government subsidized programs for agriculture require accurate information about extents and classification of arable land for crop production. In Mexico 20% of arable land is on slopes and ravines, and cultivated extents vary from one agricultural cycle to the next one due to local practices and other factors. There is a problem posed for government decision makers to obtain accurate estimations of cultivated extents and arable land on a yearly basis. Surface values provided by photographic interpretations or by the producers themselves are inaccurate estimations. To increase accuracy a topographical survey of each parcel and current field data would be required for each agricultural cycle, a practical impossibility. Remote sensing (RS) technologies offer an alternative to timely estimate surfaces for decision making at different scales — local, regional or higher — to support planning and management of government programs. In some places RS based methodologies already provide information about seeded crops, advance estimated yields and accurate arable surfaces. These methodologies are well adapted to relatively flat and large areas. Sloped surface estimation directly from an optical satellite image introduces inaccuracies since the calculated values correspond to a planar view of the terrain. An adjustment method to control slope effects based on regression estimates and adjustment factors according to a slope classification is proposed. This work reports on a pilot study realized on an area located in Central Mexico which covers approximately 25 km². Plots with slope intervals of 0–9%; 9.1–19%; 19.1–29%; 29.1–39% and > 39%, which were classified as simple or complex were considered. The plot areas were calculated by triangulation from polar coordinates using one or several points within each polygon on the images. The accuracy of the measurements was verified with topographical instruments on the field. Comparisons were made between remote sensing results and from field surveying data. The study concludes on the advantages and applicability of the method using images from SPOT and Ikonos sensors.

1. INTRODUCTION

Planning and implementation of government subsidized programs for agriculture require accurate information about extents and classification of land for crop production. In Mexico information about the extent of agricultural land is routinely collected. According to the latest official statistics approximately a total of 29 million hectares are cultivated, of which an estimated 20% is arable and is located on slopes and ravines [1]. Accurate data about arable areas is required by government for different purposes, a main one being annual funding programs for farmers in order to improve yield or for the recent initiatives towards the sustainable modernization of traditional agriculture [2]. The official estimates of arable extents are not close to reality because on the one hand, they are often based on farmer survey reports on the size of their plot, and on the other hand, when the estimates rely on photographic or satellite image interpretations flat surfaces are being assumed. Besides there is a notorious yearly land use change from agricultural to urban coverage and from *ejidos* to private property that is not totally quantified. *Ejido* is a communal agricultural and farm land of a village, which is usually assigned to its inhabitants in small parcels, which are used under the federally supported system of communal land tenure, programs and incentives. In recent years the *ejido* type of land has been given private property status which makes estimation of surfaces occupied by agricultural crops more difficult since owners are not required to provide information on cultivated surfaces.

A substantial accuracy increase of estimated arable extents would require topographical surveys of parcels, a prohibitively expensive solution. The use of optical remote sensing — the current available know-how and technology in this country — seems to be an intermediate alternative solution. Remote sensing based methodologies are already in use for obtaining detailed information about crop surfaces, types of seeded crops as well as estimated yields at different geographic scales [3]. A methodology is needed which provides accurate results with acceptable cost/benefit characteristics and which takes into account the non-planar characteristics of the terrain. Such a methodology is presented in the following section.

2. METHODOLOGY FOR ESTIMATING CULTIVATED AND ARABLE LAND AREAS ON SLOPES

Remote sensing techniques using optical satellite images may be used for estimations of parceled extents used for agricultural cultivation over relatively flat areas. However the direct estimation of surfaces from a satellite image will introduce inaccuracies for sloped surfaces, especially those with small and irregular plots. The calculated values would correspond to a planar view if information is extracted from each pixel without consideration terrain slope. Therefore in order to obtain more accurate values an adjustment technique to control these effects is needed and its applicability needs to be evaluated. This work applied and evaluated a methodology for estimation of cultivated/arable plot areas through a calculation technique based on triangulation from polar coordinates, using one or several points within each polygon on the images. The remote sensing area estimations were obtained from high and medium resolution satellite images: multispectral Ikonos and panchromatic and multispectral Spot 5 respectively, and from a digital orthophoto. The satellite images were selected because they are readily available within research and government institutions where this approach could be used.

The methodology applied two levels of geometric correction. In the first level the images were rectified without considering the elevation of the terrain. In the second level the images were orthorectified using data from a digital elevation model. 29 cuts of parcels with five levels of slope degree intervals were made and the surfaces were estimated through supervised classification of panchromatic and multispectral Spot and multispectral Ikonos imaging. The accuracy of these estimates was compared against measurements taken from field surveys in the pilot parcels. The pilot assay was carried out over the study area and the results were compared with those obtained on the field through topographical surveying methods.

The study area covers approximately 25 km² and is located in the Santa María Jajalpa *ejido*, in the Tenango municipality in the State of Mexico, within central Mexico. The zone where the study area lies is characterized by generally practicing non irrigated agriculture and by small and irregular parcel plots. There is also a spatio-temporal variation in the seeded crops for any agricultural cycle. In the methodology, shown schematically in Figure 1, pilot plots with slope intervals of 0–9%; 9.1–19%; 19.1–29%; 29.1–39% and > 39% were selected, their characteristics verified with topographical instruments. Then plot areas were calculated by triangulation from polar coordinates using one or

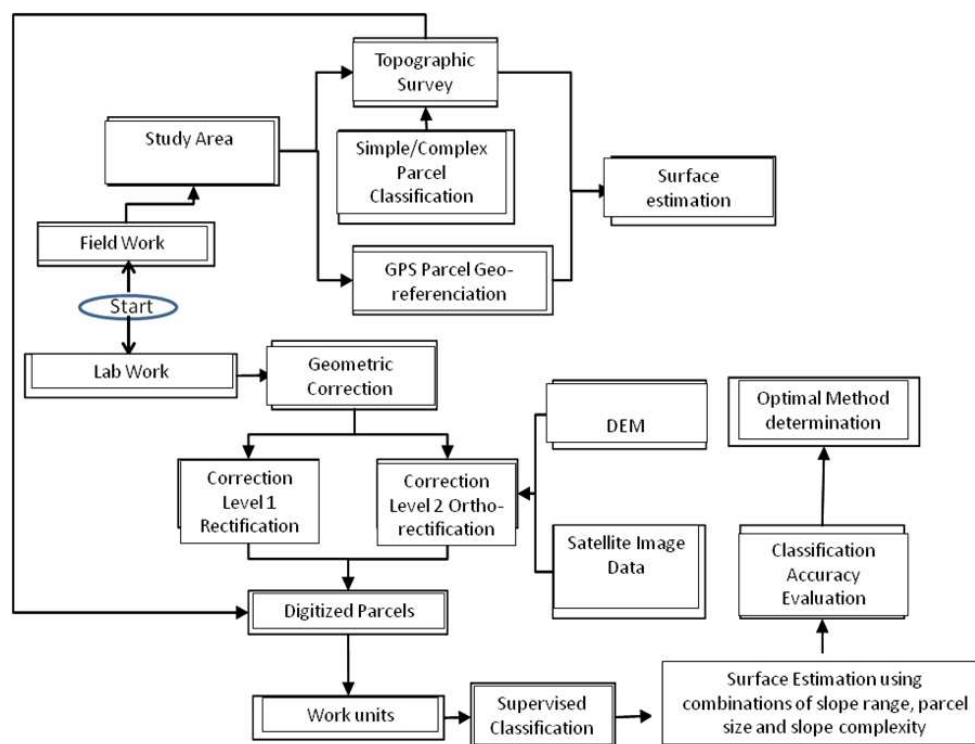


Figure 1: Methodological scheme for estimating cultivated surfaces on sloped terrain from satellite images.

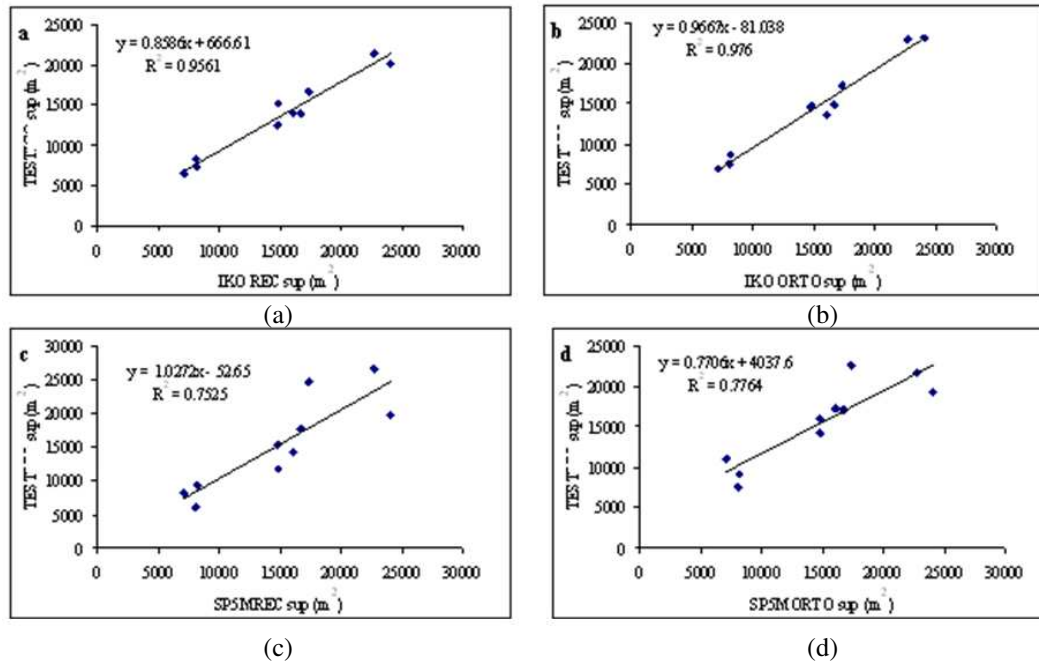


Figure 2: Regression models for data analyses of parcels with complex slope: (a) rectified Ikonos; (b) ortho-rectified Ikonos; (c) rectified Spot 5 and (d) ortho-rectified Spot 5.

several points within each polygon. Plot parcels were further classified as simple or complex, these last ones showing an undulated relief pattern. The technique for the estimation of plot surface involved regression estimates and adjustment factors.

Comparisons were made between remote sensing results and from field surveying data, namely, from test values and treatment values; these showed that 87% of the calculated surfaces using Ikonos images and 37% of those calculated from Spot 5 images were underestimated. In some cases there were overestimations. In a global analysis the estimated surfaces from remote sensing procedures were correlated with the surfaces resulting from the topological survey, a better adjustment was obtained with a quadratic model with correlation coefficients of 0.9481 for the ortho rectified Ikonos case, while the quadratic model adjustment for the multispectral Spot 5 image presented a correlation coefficient of 0.752 in Figure 2. More details about the field work and verifications are reported in [4].

3. CONCLUSIONS

This study showed that terrain slope hampers obtaining accurate values for cultivated surfaces from remote sensed images, especially if medium or low resolution images are used. The lower spatial resolution of the multispectral Spot 5 image did not support reliable results for the relatively small sized parcels which dominate the study area. The largest inaccuracies corresponded to parcels grouped according to the complexity criterion, showing that higher slope values together with pronounced roughness or undulation of the terrain will induce errors if surface estimations are obtained solely from satellite image processing. The results show that starting at 9% slope values important errors appear. The highest accuracy was obtained using elevation data in the orthorectification of the images, which clearly depends on the digital elevation model used. The surface estimates from the higher resolution Ikonos image are closer to the ones obtained through topographic surveying.

ACKNOWLEDGMENT

The first author acknowledges the support of Colegio de Postgraduados-Campus Montecillo, Research Line No. 9 Applied Geomatics to the Study and Management of Natural Resources and Agronomical Systems, for the preparation of this paper.

REFERENCES

1. De las Salas, G., *Suelos y Ecosistemas Forestales con Énfasis en América Tropical*, Instituto Interamericano de Cooperación para la Agricultura (IICA), San José, Costa Rica, 1987 (in

- Spanish).
2. SAGARPA, “The sustainable modernization of traditional agriculture masagro project,” Bulletin No. 0112012, Mexico, March 2012 (in Spanish).
 3. GEOSS, *Best Practices for Crop Area Estimation with Remote Sensing*, J. Gallego, M. Craig, J. Michaelsen, B. Bossyns, Eds., Ispra, June 5–6, 2008.
 4. Vázquez-Rivera, M., “Determinación de superficies cultivadas en terrenos de ladera a partir de imágenes de satélite y ortofotos digitales,” Master of Science Thesis, Colegio de Postgraduados, July 2008 (in Spanish).

Extraction of Laver Cultivation Area Using SAR Dual Polarization Data

Mitsunobu Sugimoto and Kazuo Ouchi

Department of Computer Science, School of Electrical and Computer Engineering
National Defense Academy, 1-10-20 Hashirimizu, Yokosuka, Kanagawa 239-8686, Japan

Abstract— In this study, we examine the techniques of extracting laver cultivation area using various parameters that can be calculated by synthetic aperture radar (SAR) dual polarization data, in order to detect the target area more effectively and decide suitable methods within the limitation of available polarization. Eigenvalue analysis and coherence analysis are one of the methods that can effectively utilize dual polarization data. Comparison was made using parameters derived from those methods, and experimental results showed that the parameters utilizing dual polarization data showed better performance than single polarization data.

1. INTRODUCTION

In Japan and other Asian countries, laver cultivation has been an important marine industry in coastal areas as well as fishery because laver (*Porphyra*) is nutrient-rich food and has been used in many Asian cuisines. However, laver cultivation is vulnerable to natural disasters such as typhoons and tsunamis. If those disasters hit laver cultivation area, laver cultivation structures would be devastated and scattered around the coast. This will affect not only owners of the laver cultivation structures but also the free passage of ships around the area. Therefore, monitoring laver cultivation area is important.

Synthetic aperture radar (SAR) has been proven to be one of the most useful sensors and therefore used in a variety of areas because of its all-weather and day-and-night observation capabilities with high resolution. While most of the traditional SAR systems were operated on single polarization mode, recent technological advancements allowed us to develop and operate SAR systems with multi polarization observation capability. Multi polarization data have shown the potential to increase further the ability of extracting physical quantities of the scattering targets. While quad polarization data have several advantages, they are relatively few compared with single or dual polarization data because of the operational costs and system constraints of full polarization SAR systems. Although there are many platforms that can be operated on quad polarization mode, they are more often to be operated on single or dual polarization mode instead, because of those reasons. There is a certain trade-off between data availability and multi polarization. Therefore, we focused on *HH-VV* dual polarization data as a good compromise between single and quad polarization data.

2. LAVER CULTIVATION AND SAR RESPONSE

In our test site of laver cultivation in Tokyo Bay, every year starting from October, cultivation nets are placed at approximately 10–20 cm below the sea surface with supporting floats with laver spores attached to the nets, grow during winter, and the grown laver is harvested in next April. Through this process, the nets are sometimes placed above the sea surface to promote photosynthesis. When the nets are placed underwater, the areas become effectively shallow water, and small-scale waves, that are the principal scatterers, are damped, resulting in reduced radar backscatter. Therefore, the cultivation area should have smoother sea surface compared with the area without laver cultivation nets (background area), and this difference in roughness can appear in acquired SAR data. For example, if the surface of cultivation area is smooth enough, the surface looks as specular surface for SAR, and backscattering from such surface is very small and close to the system noise level. Polarimetric entropy derived from eigenvalue analysis [1] should be high and coherence [2, 3] between *HH* and *VV* should be low in such area because the backscattering is close to the system noise.

3. ANALYTICAL METHOD

Entropy/alpha decomposition [1] was originally proposed for quad-polarization data, but modified and applied to dual-polarization data later [4, 5]. The entropy/alpha decomposition for dual-

polarization data can be expressed as follows:

$$\langle [C_{coh}] \rangle = [U] \begin{bmatrix} \lambda_1 & 0 \\ 0 & \lambda_2 \end{bmatrix} [U]^*{}^T = \lambda_1 \mathbf{u}_1 \mathbf{u}_1^{*T} + \lambda_2 \mathbf{u}_2 \mathbf{u}_2^{*T} \quad (1)$$

$$[U] = \begin{bmatrix} U_{11} & U_{12} \\ U_{21} & U_{22} \end{bmatrix} = [\mathbf{u}_1 \quad \mathbf{u}_2] \quad (2)$$

$$\mathbf{u}_i = [\cos \alpha_i \quad \sin \alpha_i e^{j\delta_i}]^T \quad (3)$$

where $\langle [C_{coh}] \rangle$ is averaged coherency matrix, $\lambda_1 \geq \lambda_2$ are eigenvalues, and $[U]$ is orthogonal unitary matrix. $*$ and T denote complex conjugate and transpose respectively. Entropy H and scattering angle $\bar{\alpha}$ and can be expressed as

$$H = -P_1 \log_2 P_1 - P_2 \log_2 P_2 \quad (4)$$

$$\bar{\alpha} = P_1 \cos^{-1}(|U_{11}|) + P_2 \cos^{-1}(|U_{12}|) \quad (5)$$

where

$$P_i = \frac{\lambda_i}{\lambda_1 + \lambda_2}. \quad (6)$$

The coherence between HH and VV polarization is described as follows:

$$\gamma_{coh} = \frac{|\langle S_{HH} S_{VV}^* \rangle|}{\sqrt{\langle S_{HH} S_{HH}^* \rangle \langle S_{VV} S_{VV}^* \rangle}}. \quad (7)$$

where S_{HH} and S_{VV} are complex scattering components of the corresponding polarization combination. In coherence analysis, the phase difference between the two components is also an important factor.

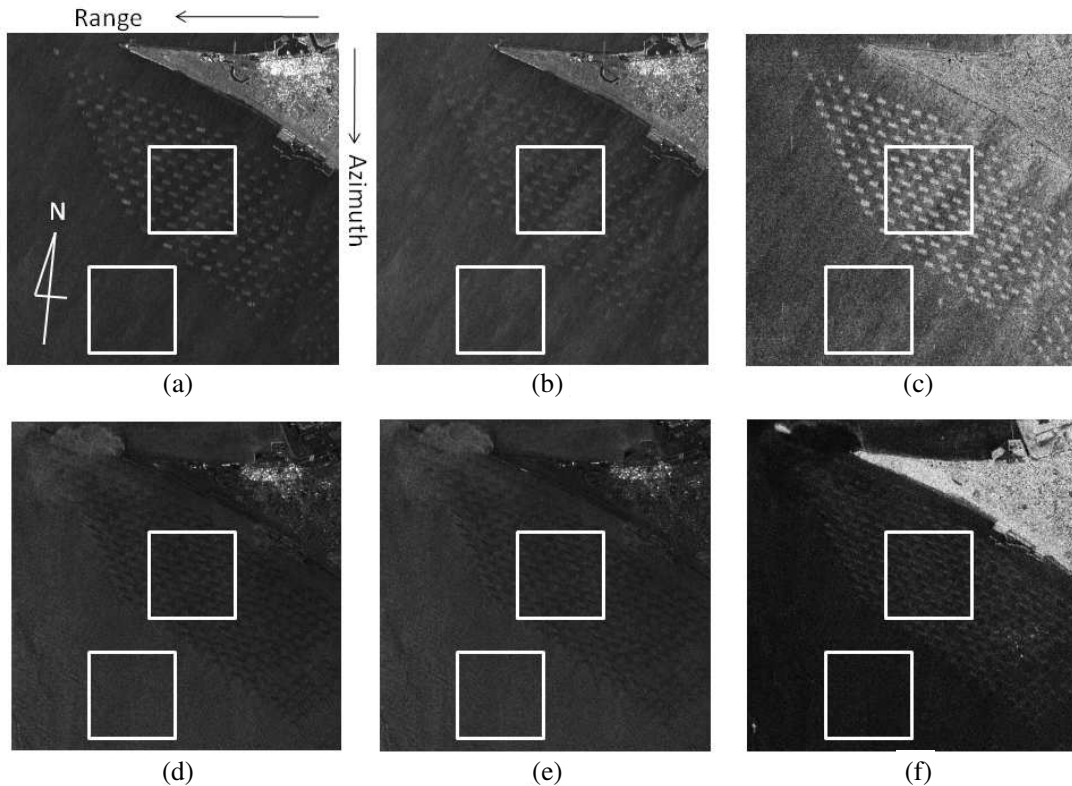


Figure 1: TerraSAR-X images of Futtsu Horn laver cultivation area in Tokyo Bay, Japan. The data were acquired on October 20, 2011 (upper row (a), (b), and (c)) and December 26, 2008 (lower row (d), (e), and (f)), respectively. (a) (d): HH polarization image, (b) (e): VV polarization image, (c): coherence image, (f): dual entropy image.

In order to assess contrast between the areas with and without cultivation nets, the following criterion, mean contrast, was defined. The mean contrast is expressed as

$$C_{mean} = \left| \frac{\langle A_{cultivation} \rangle - \langle A_{background} \rangle}{\langle A_{cultivation} \rangle + \langle A_{background} \rangle} \right| \quad (8)$$

where $\langle A_{cultivation} \rangle$ represents a mean value of pixels in laver cultivation area, $\langle A_{background} \rangle$ stands for a mean value of pixels in background area.

The process of extracting the cultivation area is as follows. First, median filtering is applied to image data of cultivation area to reduce the noise effect. Then, a binary image is created by applying thresholding and morphological filtering to the filtered image. Based on the binary image, cultivation area is extracted, and the criterion is applied to the extracted cultivation area and background area in each parameter image.

4. EXPERIMENTAL RESULTS AND DISCUSSIONS

Figure 1 shows images of Futtsu Horn laver cultivation area ($139^{\circ}48'E, 35^{\circ}17'N$) in Tokyo Bay, Japan. The data were acquired on October 20, 2011 and December 26, 2008 respectively by TerraSAR-X dual-polarization mode (HH and VV). The net and background areas used in the comparison are marked as rectangles in Fig. 1. In Figs. 1(a) and (b), the amplitude of the net areas are higher than background area. Thus, it can be assumed that the nets were above the sea surface. On the other hand, in Figs. 1(d) and (e), the amplitudes of the net areas are lower than the background area. Thus, the nets seem to have been placed underwater. Table 1 shows contrast between laver cultivation area and background area. In 2011 data, coherence showed highest contrast compared with other parameters, and that was dual entropy in 2008 data. Increased contrast can be seen by comparing the right images (coherence and dual entropy images) with the corresponding left and middle images in Fig. 1. These results could be comparable to previously suggested polarimetric entropy based methods which require full polarization data [6, 7].

In order to assess the usefulness of dual polarization data further, additional experiments were performed using ALOS-PALSAR quad polarization data. The quad polarization data used here were acquired on November 24, 2008 (ALPSRP150972900-P1.1). Table 2 shows contrast comparison between cultivation area and background area in ALOS-PALSAR data. Dual polarization analyses

Table 1: Contrast between laver cultivation area and background area in Fig. 1.

Parameter	Mean contrast	
	2011/10/20	2008/12/26
HH	0.1414	0.2587
VV	0.0529	0.2412
$HH + VV$	0.0013	0.2536
$HH - VV$	0.3273	0.2439
Entropy	0.2531	0.4645
Scattering angle	0.3479	0.0081
Coherence	0.6740	0.0311
Phase Difference	0.2257	0.0078

Table 2: Contrast comparison between laver cultivation area and background area in ALOS-PALSAR data.

Polarization	Parameter	Mean contrast
Single	HH	0.1582
	VV	0.1470
	HV	0.0025
Dual	$HH + VV$	0.1629
	$HH - VV$	0.0043
	Entropy (dual)	0.2323
	Alpha angle (dual)	0.2101
	Coherence	0.0477
Quad	Phase difference	0.1581
	Entropy	0.2164
	Alpha angle	0.2087
	Anisotropy	0.0059
	P_s	0.3178
	P_d	0.0815
	P_v	0.0018
	P_c	0.0100
	P_s (rotation)	0.3098
	P_d (rotation)	0.0585
P_v (rotation)	0.0026	
P_c (rotation)	0.0131	

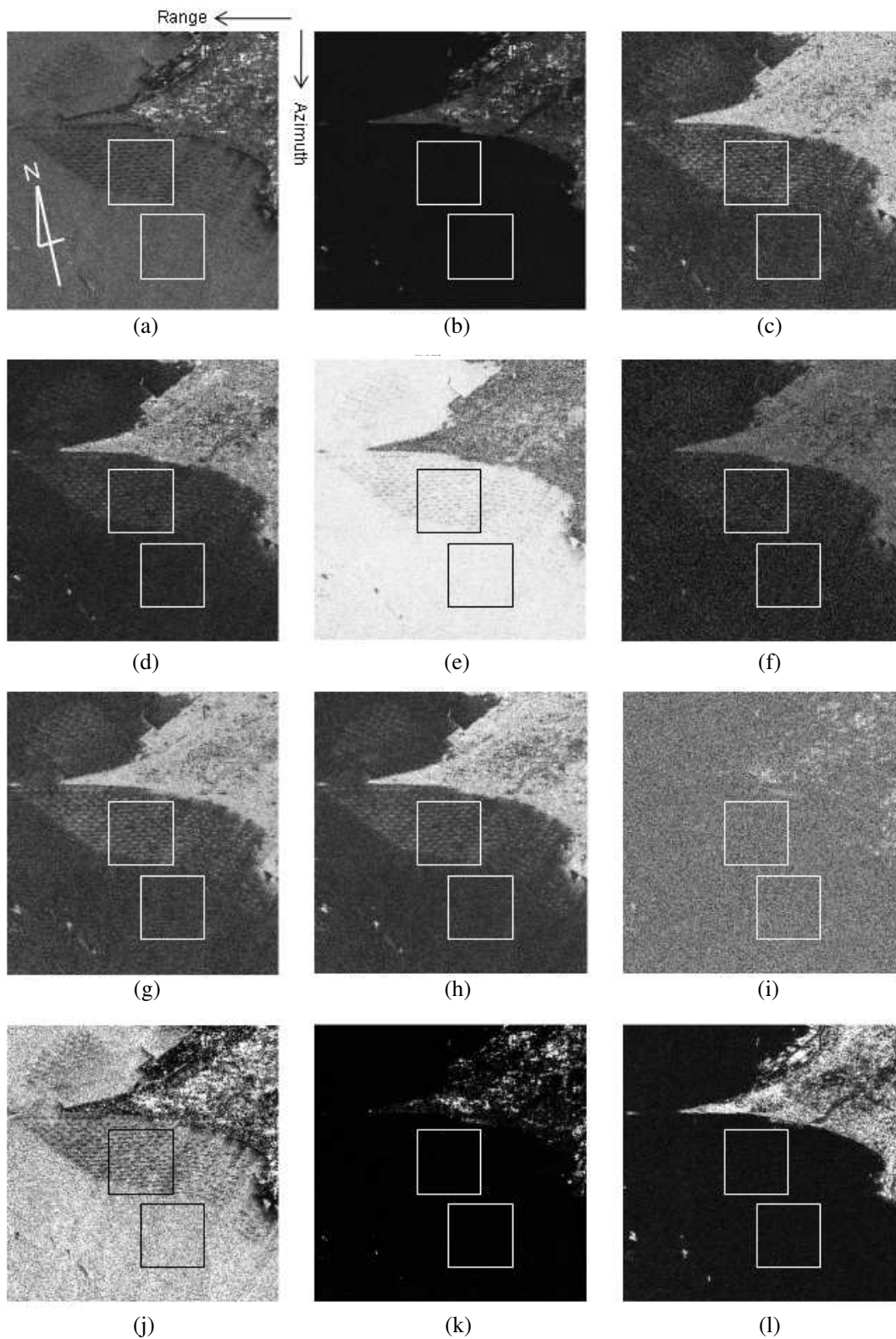


Figure 2: Contrast comparison between laver cultivation area and background area in ALOS-PALSAR data (only selected parameters are shown). (a) $HH + VV$ image $C_{mean} = 0.1629$. (b) $HH - VV$ image $C_{mean} = 0.0043$. (c) Entropy image (dual) $C_{mean} = 0.2323$. (d) Alpha angle image (dual) $C_{mean} = 0.2101$. (e) Coherence image $C_{mean} = 0.0477$. (f) Phase difference image $C_{mean} = 0.1581$. (g) Entropy image (quad) $C_{mean} = 0.2164$. (h) Alpha angle image (quad) $C_{mean} = 0.2087$. (i) Anisotropy image $C_{mean} = 0.0059$. (j) P_s image $C_{mean} = 0.3178$. (k) P_d image $C_{mean} = 0.0815$. (l) P_v image $C_{mean} = 0.0018$.

were made using only HH and VV polarization data among quad polarization data. Fig. 2 shows selected parameter images made from ALOS-PALSAR dual (HH and VV only) and quad (HH , HV/VH , and VV) polarization data. The net and background areas used in the comparison are marked as rectangles in Fig. 2. Among the parameters derived from dual polarization data, entropy showed highest contrast, which is higher than using each individual polarization amplitude. It also should be emphasized that entropy from dual polarization data showed as high contrast as entropy from quad polarization data. Among all the parameters analyzed in this comparison, P_s (surface scattering) from the four-component scattering power decomposition (4-CSPD) using quad polarization data showed highest contrast. Results from 4-CSPD with rotation were also analyzed but the difference was not significant.

5. CONCLUSION

In this study, we extracted laver cultivation area and evaluated contrasts between laver cultivation area and background area using various parameters derived from multi polarization data, for the purpose of extracting the target area more effectively and deciding suitable methods within the limitation of available polarization. We showed that parameters from dual polarization data performs better than single polarization data. This study could also be applied to detect polluted area caused by tanker accident or offshore-oil disaster since spilled oil on the sea has similar physical characteristics to laver cultivation area.

ACKNOWLEDGMENT

Authors should like to thank JAXA for providing ALOS-PALSAR data and PASCO Co. Japan for providing TerraSAR-X data used in this study.

REFERENCES

1. Cloude, S. R. and E. Pottier, "An entropy based classification scheme for land applications of polarimetric SAR," *IEEE Trans. Geosci. Remote Sens.*, Vol. 35, No. 1, 68–78, Jan. 1997.
2. Wang, H., M. Iwakiri, and K. Ouchi, "Some potential information in airborne single-pass Pol-InSAR data over land and sea," *Progress In Electromagnetics Research Symposium Abstracts*, Hangzhou, China, Mar. 24–28, 2008.
3. Velotto, D., M. Migliaccio, F. Nunziata, and S. Lehner, "Dual-polarized TerraSAR-X data for oil-spill observation," *IEEE Trans. Geosci. Remote Sens.*, Vol. 49, No. 12, 4751–4762, Dec. 2011.
4. Cloude, S., "The dual polarization entropy/alpha decomposition: A pulsar case study," *Proc. PolinSAR*, Frascati, Italy, Jan. 2007.
5. Shan, Z., C. Wang, H. Zhang, and J. Chen, " H - α decomposition and alternative parameters for dual polarization SAR data," *PIERS Proceedings*, 1386–1390, Suzhou, China, Sep. 12–16, 2011.
6. Won, E. S. and K. Ouchi, "A novel method to estimate underwater marine cultivation area by using SAR polarimetric entropy," *Proc. IGARSS*, 2097–2100, Vancouver, Canada, Jul. 2011.
7. Yang, C. S. and K. Ouchi, "Monitoring of marine laver cultivation using two ALOS-PALSAR PLR acquisition mode data," *Proc. APSAR*, Seoul, South Korea, Sep. 2011.

Half Loop Antenna with Ultra-wide Bandwidth

Tae-Hwan Jeong and Jong-Myung Woo

Department of Radio Science and Engineering, Chungnam National University
99 Daehak-ro, Yuseong-gu, Daejeon 306-764, Korea

Abstract— This paper proposes an ultra-wideband half loop antenna for aircraft. The basic structure of the proposed antenna is a loop antenna applied self-complementary structure to obtain ultra-wide band. The ultra-wide band loop antenna is changed into a half loop structure on the ground plane by using image effect. This change reduces the size of the loop antenna in half and the half loop antenna can be installed on metallic surface of aircraft. To minimize wind load for the half loop antenna on aircraft, the height of the antenna is reduced from 0.155λ to 0.11λ where λ is free space wavelength at 0.3 GHz. The overall size of the designed antenna is $315\text{ mm} \times 295\text{ mm} \times 110\text{ mm}$ ($0.315\lambda \times 0.295\lambda \times 0.11\lambda$). The measured -10 dB bandwidth is $100:1$ (0.3–30 GHz). It shows extremely ultra-wide bandwidth. The radiation pattern in xy -plane shows monopolelike radiation pattern and the gain is higher than 0 dBi in the measured frequency 0.3–18 GHz. The proposed half loop antenna was simulated with an unmanned aerial vehicle (UAV) to verify the radiation pattern. The antenna was installed on the fuselage of UAV. As a result of the simulation, the radiation pattern on UAV was similar to that of the half loop antenna.

1. INTRODUCTION

Recently, broadband antennas are required for Ultra-WideBand (UWB) communications systems and broadband radar systems. In addition, an Unmanned Aerial Vehicles (UAV) are being equipped with several communications systems, a lots of antennas are required. However, it is difficult to install a large number of antennas in the limited space on small UAV and the ability of the flight is influenced by many antennas mounted on an UAV. Therefore, one ultra-wide band antenna is desirable for combine a lot of antennas and low-profile antenna is suitable for reduced the wind load.

Ultra-wideband antennas have been reported. The inverted-hat antenna [1] with $40:1$ bandwidth has been proposed. It is not, however, matched with $50\ \Omega$ in the entire operating band. If this antenna matched with $50\ \text{ohm}$, the -10 dB bandwidth would be reduced. The tactical broadband omnidirectional antenna [2] with $9.1:1$ (100 MHz–915 MHz) bandwidth has been proposed. It has a low-frequency and high frequency mode. The low-frequency mode operates at 100 MHz–500 MHz and the high-frequency mode operates at 415–915 MHz. This antenna should be chosen for only one mode of use. Moreover, it's difficult to make antennas of a low-frequency mode.

Previously we reported ultra-wideband loop antenna [3] and half loop antenna [4]. The half loop antenna had the height of 165 mm. In this paper, we design a low-profile half loop antenna. The structure of the half loop antenna is changed to reduce the antenna height for mounting on UAV. The low-profile antenna on UAV is simulated to verify radiation patterns.

2. LOW-PROFILE HALF LOOP ANTENNA

The ultra-wideband loop antenna applied self-complementary structure [3] is not appropriate to install on UAVs because it has 3-dimentional structure. Also if the antenna is close to the UAV's metal surface, the performance of the antenna is degraded. Therefore, the ultra-wideband loop antenna was changed to the half loop antenna [4].

Figure 1 shows the geometry and return loss of the half loop antenna. As shown in Figure 1(a), the antenna is designed on ground plane of $1000\text{ mm} \times 1000\text{ mm}$ ($1\lambda \times 1\lambda$). The size of the antenna is $183\text{ mm} \times 160\text{ mm} \times 165\text{ mm}$ ($0.183\lambda \times 0.16\lambda \times 0.165\lambda$). This antenna has high height (165 mm) for UAV antenna applications. The -10 bandwidth of the antenna was measured as $49.3:1$ (0.3–14.8 GHz) as shown in Figure 1(b). The designed antenna has ultra-wide bandwidth and monopolelike radiation pattern in the xy -plane but the height of the antenna should be reduced for aircraft antennas. Therefore, we designed a low-profile half loop antenna as depicted in Figure 2.

The designed half loop antenna with low-profile characteristics has the size of $315\text{ mm} \times 295\text{ mm} \times 110\text{ mm}$ ($0.315\lambda \times 0.295\lambda \times 0.11\lambda$). The height of the antenna was reduced from 165 mm (Figure 1(a)) to 55 mm. However, the width and length of the antenna was lengthened for the lowest frequency (0.3 GHz) impedance matching. Simulated and measured return loss is represented in Figure 2(b).

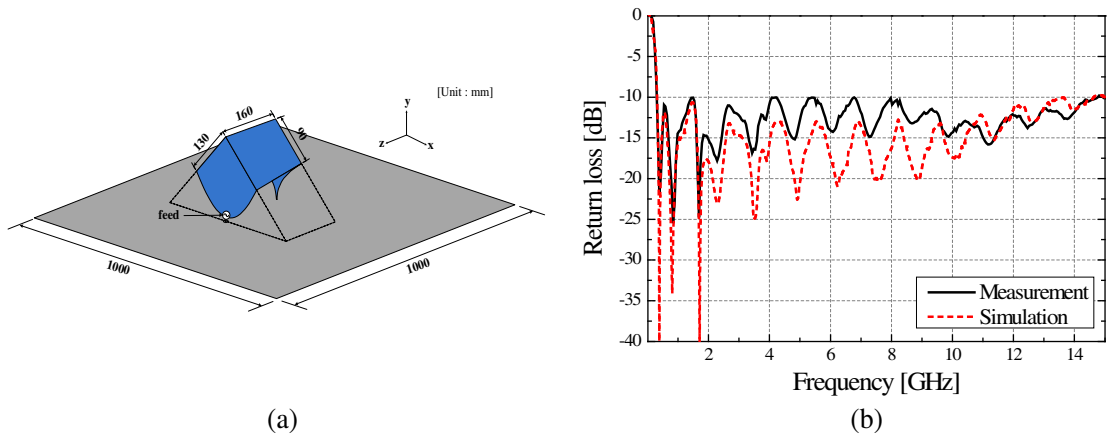


Figure 1: Geometry and return loss of half loop antenna. (a) Geometry. (b) Return loss.

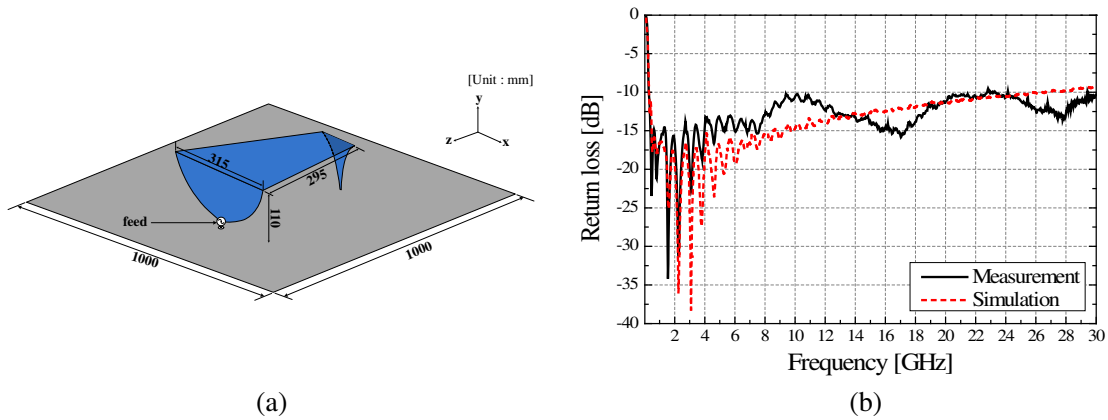


Figure 2: Geometry and return loss of low-profile loop antenna. (a) Geometry. (b) Return loss.

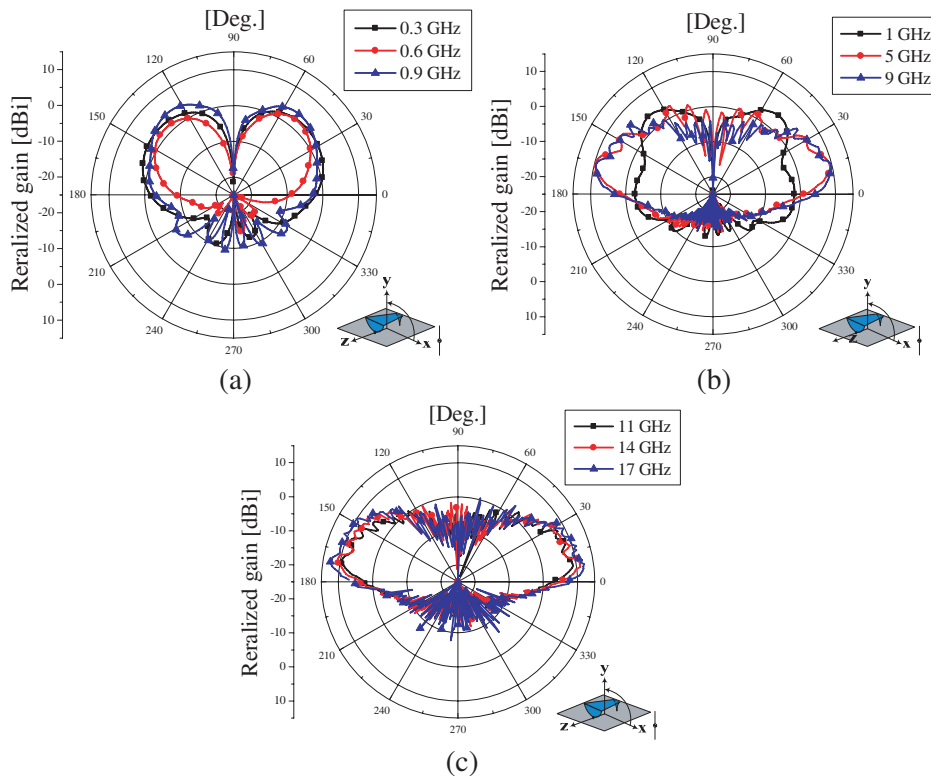


Figure 3: Radiation pattern in xy -plane of low-profile half-loop antenna (measurement).

Measured -10 dB bandwidth is $100 : 1$ (0.3–30 GHz). The bandwidth is wider than that of the half loop antenna. This is because the low-profile half loop antenna has wider width. It is possible to make tapered curve for high frequency (16–30 GHz) impedance matching.

Figure 3 shows radiation pattern of the low-profile half loop antenna in the xy -plane. The radiation pattern was measured for several frequencies. All radiation patterns showed monopole-like pattern. This pattern would be useful for communication link between an UAV and a ground station.

3. LOW-PROFILE HALF LOOP MOUNTED ON ANTENNA

To verify radiation characteristics of the low-profile half loop antenna mounted on UAV, the antenna was installed on UAV and was simulated. The simulation was performed with CST Microwave studio. Figure 3 shows geometry of the low-profile half loop antenna installed on UAV. For simulation

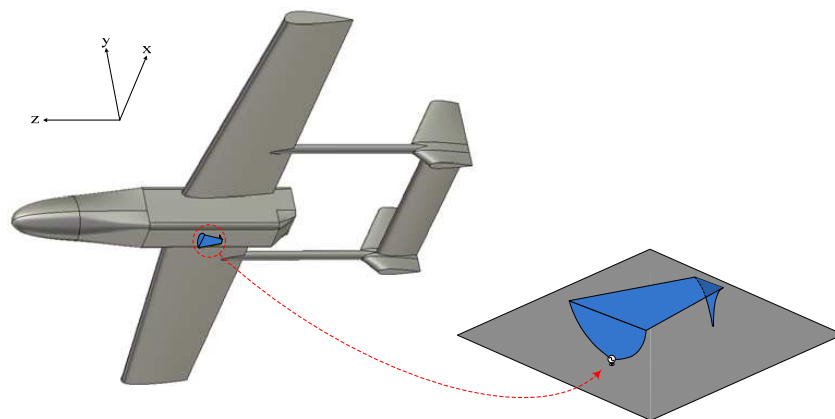


Figure 4: Geometry of the low-profile half loop antenna installed on UAV.

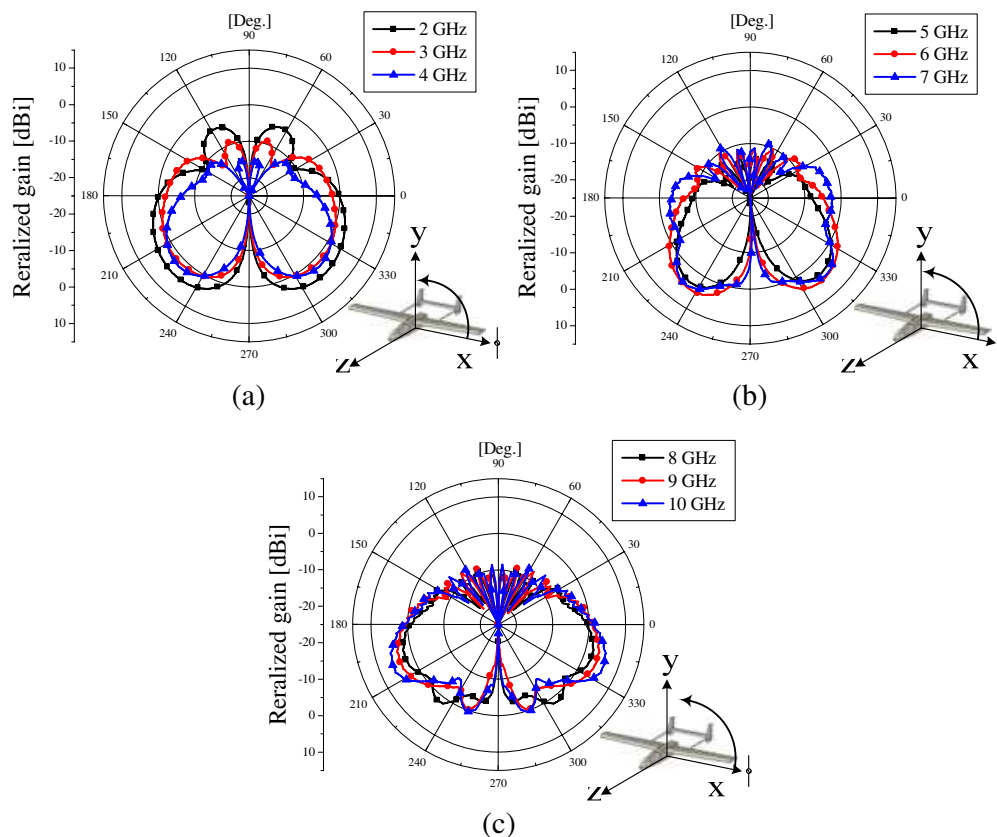


Figure 5: Radiation pattern of low-profile half loop antenna installed on UAV (Simulation).

speed, 1/7 scaled UAV model was used. Therefore the size of the antenna was reduced. Frequency was increased by 7 times.

In Figure 4, the xy -plane radiation pattern of low-profile antenna is showed in several frequencies. The radiation pattern shows monopole-like radiation pattern in xy -plane, and the radiation characteristics of the antenna were maintained in installation for an UAV. Accordingly, the low-profile half loop antenna is confirmed to be suitable for an UAV.

4. CONCLUSIONS

In this paper, the low-profile half loop antenna was proposed for mounted on an UAV. The proposed antenna is a combination of a wavelength loop antenna and the self-complementary principle. In addition, because the low-profile is a favorable condition for mounting on the UAV, the structure of the antenna changed from a half loop antenna form to low-profile half loop antenna with decreasing its height up to 55 mm. The measured -10 dB bandwidth is 100 : 1 (0.3–31 GHz) and the xy -plane radiation pattern shows monopole-like radiation pattern. Also, the simulation results are the same characteristics of it. Therefore, it is suitable to be mounted on an UAV.

REFERENCES

1. Zhao, J., T. Peng, and C. C. Chen, and J. L. Volakis, “Low-profile ultra-wideband inverted-hat monopole antenna for 50 MHz–2 GHz operation,” *Electron. Lett.*, Vol. 45, No. 3, 142–144, Jan. 29, 2009.
2. Palud, S., F. Colombel, M. Himdi, and C. Le Meins, “A tactical broadband omnidirectional antenna,” *Asia-Pacific Microwave Conference*, Hong Kong, China, Dec. 2008.
3. Yoon, M.-H, Y.-I. Shin, H.-K. Ryu, and J.-M. Woo, “Ultra-wideband loop antenna,” *Electronics Letters*, Vol. 46, No. 18, 1249–1251, Sep. 2010.
4. Shin, Y.-I. and J.-M. Woo, “Design of loop antenna for ultra wide bandwidth,” *Proceedings of International Symposium on Microwave and Optical Technology*, Prague, Czech Republic, Jun. 2011.

Wideband Linear Antenna with H-shaped Parasitic Element

R. Suzuki¹, H. Morishita¹, and F. Sakuma²

¹Department of Electrical and Electronic Engineering, National Defense Academy, Japan

²Sakuma Antenna Co., Ltd., Japan

Abstract— Many types of linear antennas are widely used in the mobile communication, because they have a simple and light structures. Sleeve antennas, which are one of linear antennas, have a possibility of wider bandwidth. In this paper, a new type of sleeve antennas is proposed and its characteristic are analyzed.

1. INTRODUCTION

It has already been analyzed that the broadband characteristic can be acquired by loading the X-shaped liner parasitic element on the outside surface of semi-rigid coaxial cable. Moreover, it has been analyzed that a wider bandwidth is obtained by changing the X-shaped liner parasitic element into the H-shaped plate parasitic element, and miniaturization of the parasitic element is also realized by bending H-shaped plate. In this paper, the antenna characteristics are analyzed, when a plate element is loaded at the tip of the straight liner radiating element of the antenna with the H-shaped parasitic element.

2. ANTENNA AND SUBSTRATE STRUCTURE

The model of the X-shaped antenna is shown in Fig. 1. The model of the H-shaped antenna is shown in Fig. 2. The model of H-shaped bending antenna, which miniaturization is realized by bending H-shaped plate, is shown in Fig. 3. The model of the proposal antenna is shown in Fig. 4. In Figs. 3 and 4, the above figures are seen from the top and the following figures are seen from the front. Then, in Fig. 4, the width of the plate element loaded at the tip of the straight liner radiating element is set to the parameter a , and length is set to the parameter b . The thickness of all elements is 0.1 mm.

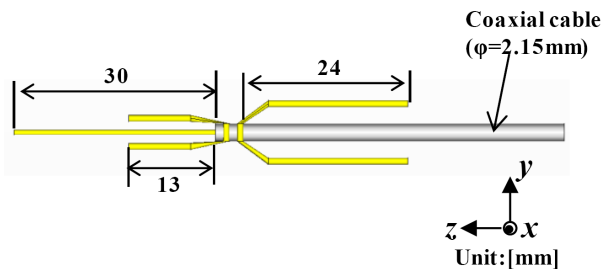


Figure 1: X-shaped antenna.

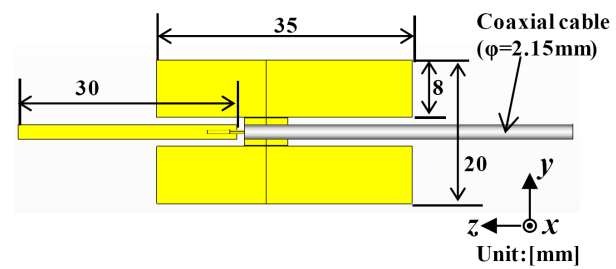


Figure 2: H-shaped antenna.

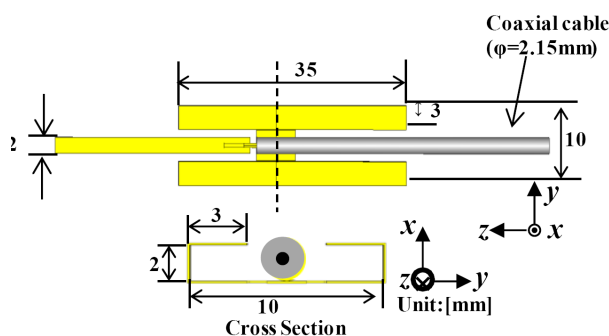


Figure 3: H-shaped bending antenna.

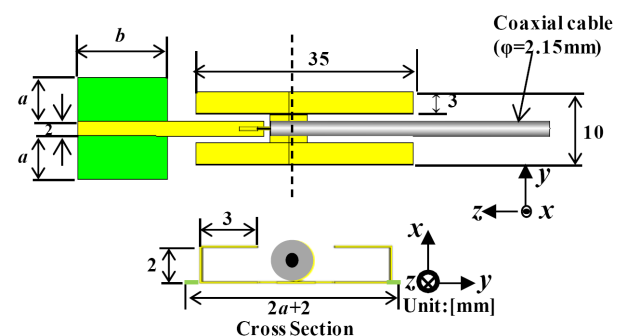


Figure 4: Proposal antenna.

3. ANALYTICAL RESULT

At first, the VSWR characteristics of X-shaped antenna are shown in Fig. 5. The bandwidth (VSWR is less than 3) is from 3.3 GHz to 6.3 GHz and the relative bandwidth is approximately 62.5%. The radiation patterns are almost the same as those of dipole antennas. The VSWR characteristics of H-shaped antenna are shown in Fig. 6. The bandwidth (VSWR is less than 3) is from 2.7 GHz to 6.4 GHz and the relative bandwidth is approximately 78%. The characteristics of H-shaped antenna and H-shaped bending antenna are almost the same. Next, the VSWR characteristics of the proposal antenna are shown in Fig. 7, when the parameter b is fixed to 1 mm and the parameter a is changed from 1 mm to 10 mm. It is found that it is possible to lower the minimum resonant frequency, where the VSWR is less than 3 by the parameter a . The lowest resonant frequency is obtained when the parameter a is 6 mm. Next, the VSWR characteristics are shown in Fig. 8 when the parameter a is fixed to 6 mm and the parameter b is changed from 5 mm to 16 mm. It is considered that the parameter b decides the highest resonant frequency of the bandwidth and it is also found that the wider bandwidth can be obtained. The optimal value of the parameter b is set to 14.5 mm. The model of the parameter $a = 6$ mm and the parameter $b = 14.5$ mm, is used as the proposal antenna, and the comparison of the VSWR between the proposal antenna and the H-shaped bending antenna is shown in Fig. 9. The H-shaped bending

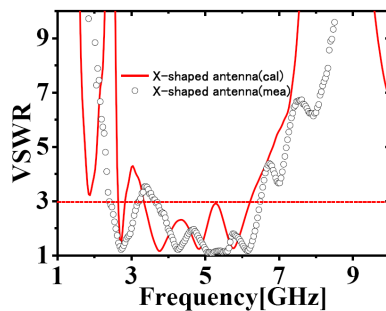


Figure 5: X-shaped antenna.

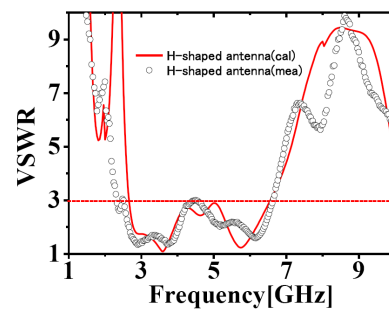


Figure 6: H-shaped antenna.

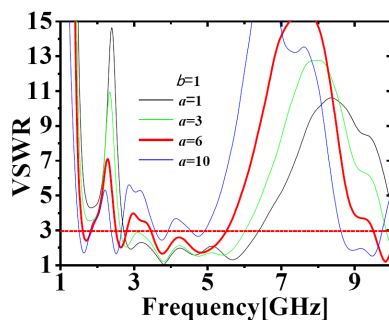
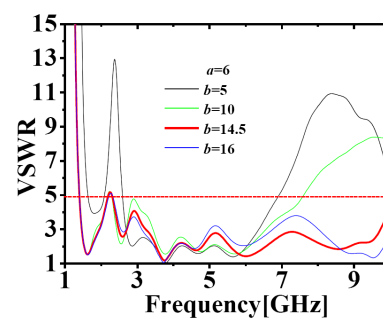
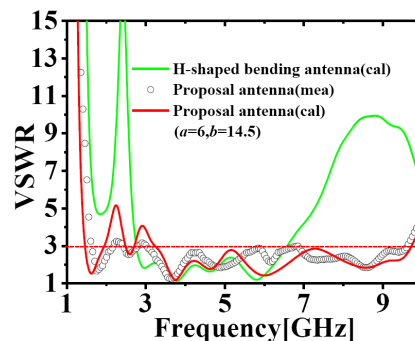
Figure 7: The VSWR characteristic for length a .Figure 8: The VSWR characteristic for length b .

Figure 9: The VSWR characteristic of proposal antenna.

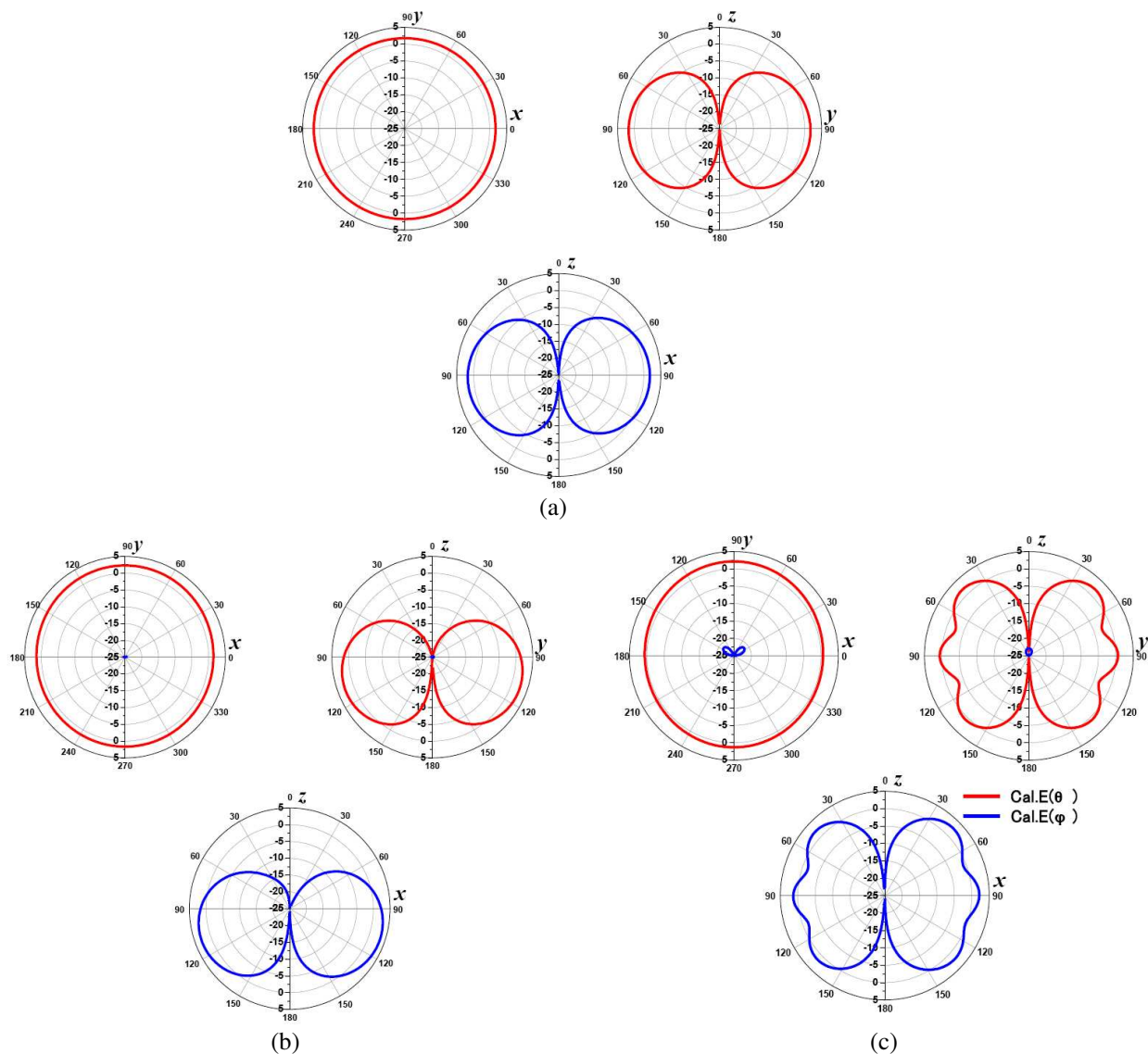


Figure 10: Radiation pattern.

antenna covers the bandwidth from 2.7 GHz to 6.4 GHz, where the VSWR is less than 3, and the relative bandwidth is approximately 78%. On the other hand, the proposal antenna can cover the bandwidth from 3.0 GHz to 9.6 GHz, where the VSWR is less than 3. It is confirmed that that the relative bandwidth becomes wider up to about 105%. Finally, the simulation result of the radiation pattern of the proposal antenna is shown in Fig. 10. The radiation patterns at 1.6 GHz, 3.7 GHz and 6.0 GHz are shown. The radiation pattern of the xy -plane can be regarded as an omnidirectional pattern, yz -plane and xz -plane can be regarded as the character 8, respectively, the gain is 2.0 dBi.

4. CONCLUSIONS

This paper has examined the fundamental characteristics of the proposal antenna, which loads the plate element at the tip of the straight line radiating element of the H-shaped bending antenna. It has been confirmed that these loaded elements, width a and length b , determine the operation bandwidth and the wider bandwidth is achieved by adding these elements to the conventional H-shaped bending antenna. Moreover, about radiation pattern, there are respectively sufficient antenna gains. As a next study, we will analyze the operating principle in detail.

REFERENCES

1. Johnson, R. C., *Antenna Engineering Handbook*, 1993.

Reduction of Cross Polarization in Circularly Polarized Broadband Waveguide Antenna Using an L-shaped Probe

S. Yamaura and T. Fukusako

Computer Science & Electrical Engineering

Graduate School of Science & Technology, Kumamoto University, Japan

Abstract— This paper presents a circularly polarized broadband waveguide antenna with low cross polarization. The center frequency is chosen to be close to the middle value of the cutoff frequency between that of the dominant mode (TE_{10}/TE_{01}) and the second higher-order mode (TE_{20}/TE_{02}). The cross polarization gets worse at a higher frequency which is close to the cutoff frequency of the TE_{20}/TE_{02} . For avoiding this effect, four thin metal poles ($2\text{ mm} \times 2\text{ mm} \times 52\text{ mm}$) are installed at the inside corners of the waveguide. The cross polarization becomes lower in the wide azimuth rang. As a result, circular polarization with low cross polarization over a wide azimuth range is also achieved even in the higher frequency.

1. INTRODUCTION

Recently, circular polarization have been extensively studied and received much advantage such as reduction of multipath fading, avoidance of the clutter effect in RADAR and no need of antenna alignment [1–3]. And, it received attention due to alluring applications in satellite, RADARs, GPS and Wireless LAN.

Broadband circularly polarized antenna using a waveguide of square aperture and an L-shaped probe is presented in [4]. Numerous wideband circularly polarized antennas using an L-shaped probe are proposed [5–7]. Inserting the poles ($8\text{ mm} \times 8\text{ mm} \times 5\text{ mm}$) at the inside corners of the waveguide weaken the effect of the higher order mode of TM_{11} which prevent the good broadband axial ratio (AR) characteristics [4]. The antenna has a simple waveguide structure and has a 3-dB bandwidth in AR of approximately 50%.

In this paper, the center frequency is changed to be close to the middle value of the cutoff frequency between that of the dominant mode (TE_{10}/TE_{01}) and the second higher-order mode (TE_{20}/TE_{02}) for bandwidth enhancement. In addition, four thin poles ($2\text{ mm} \times 2\text{ mm} \times 52\text{ mm}$) are inserted at the inside corner of the waveguide to reduce cross polarization. These effects in proposed antenna are verified through simulation. The simulation results of this paper were obtained using Ansoft HFSS 10.1 which employs finite element method.

2. ANTENNA STRUCTURE

Figure 1 shows the proposed circularly polarized antenna which has a waveguide structure with the L-shaped probe. The cross section of the waveguide is chosen as $25\text{ mm} \times 25\text{ mm}$ in order to set the cutoff frequency at 6.0 GHz. The L-probe is placed perpendicular to the direction of the propagation wave and at a distance of an effective quarter wavelength from the closed back side wall. The waveguide has a square cross section to degenerate TE_{10} and TE_{01} components of circular polarization. To generate circular polarization, a phase difference of 90 degree is given through the length of vertical probe is chosen about $\lambda/4$ mm. The L-probe has two arms with diameter of 0.8 mm and 2.0 mm for vertical and horizontal part. The variation in diameter of the horizontal part is possible to control the amplitude ratio characteristics. Therefore the characteristics are optimized by choosing the diameter as 2.0 mm.

The antenna is redesigned with a modified center frequency at 8.6 GHz for considering frequency at the center between the cutoff frequency of the TE_{10}/TE_{01} and the TE_{20}/TE_{02} . Therefore, the distance between the probe and the closed backside wall is chosen as 12 mm corresponding to $\lambda_g/4$ at 8.6 GHz. Note that the electric field of TM_{11} mode directs propagation direction. It deteriorates the AR characteristics beyond the cutoff frequency of TM_{11} because of the asymmetrical distribution. However, the large degradation is improved by choosing the optimized waveguide length from $l = 48\text{ mm}$ (λ_g) to $l = 52\text{ mm}$ due to electric field of the mode has constant cycle length at each frequency. In addition, four thin poles ($2\text{ mm} \times 2\text{ mm} \times 52\text{ mm}$) are inserted at the inside corners of the waveguide. It decreases of the cross polarization over the wide azimuth range because the poles reduce a concentration of electric field at the corners.

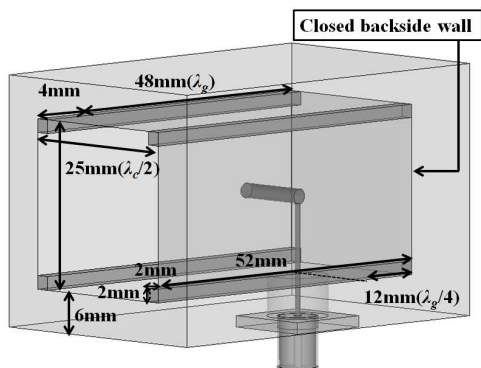


Figure 1: Proposed antenna.

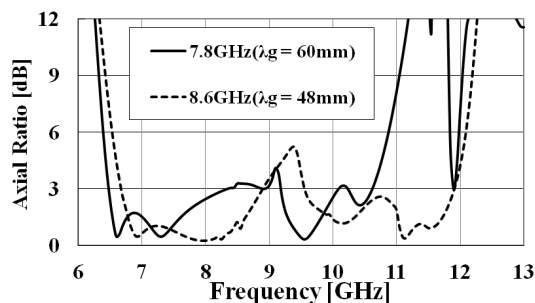


Figure 2: Reconfiguration of center frequency.

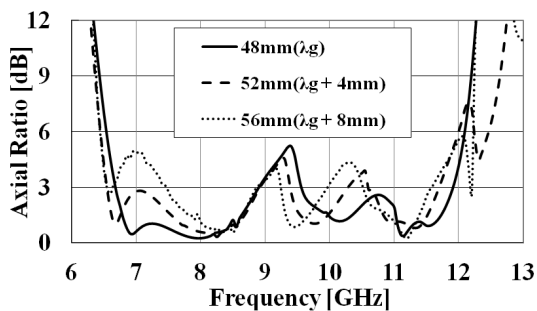


Figure 3: Extension of waveguide length.

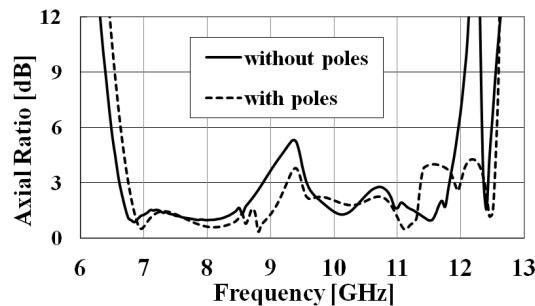
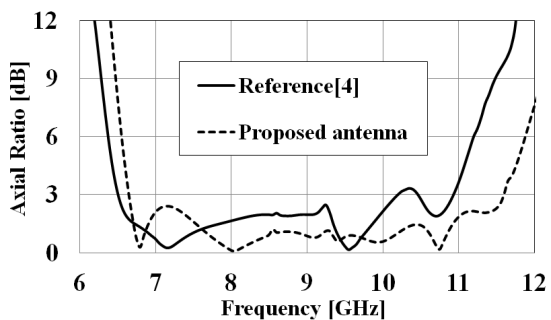
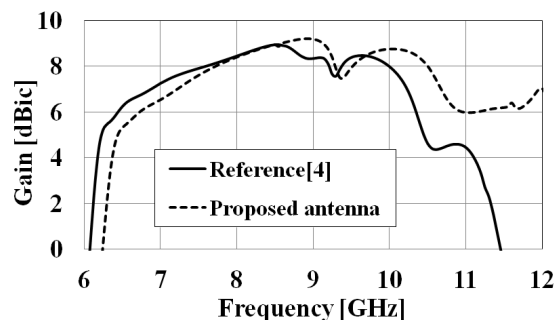


Figure 4: Effect of poles (2 mm × 2 mm × 48 mm).

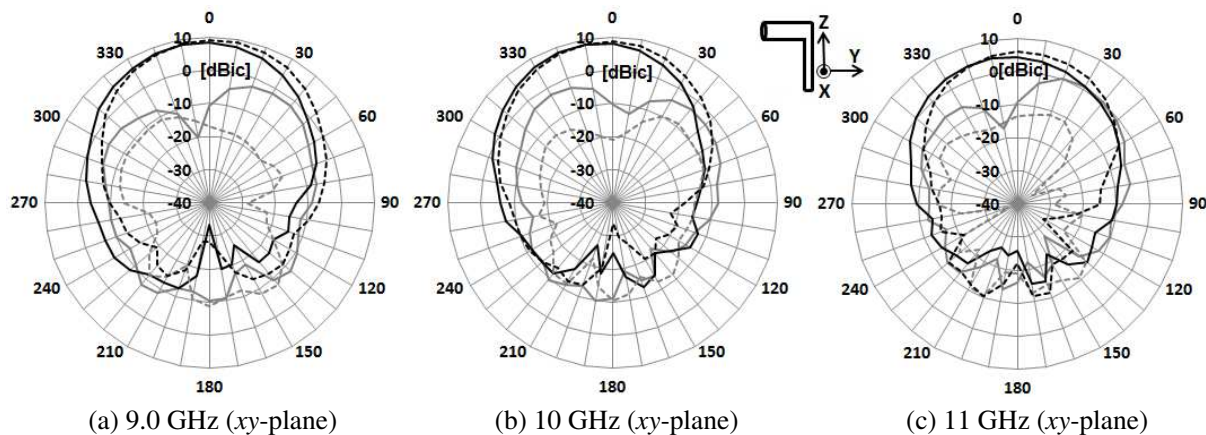


(a) AR characteristics



(b) Gain characteristics

Figure 5: Comparison of previous antenna and proposed antenna.



(a) 9.0 GHz (xy-plane)

(b) 10 GHz (xy-plane)

(c) 11 GHz (xy-plane)

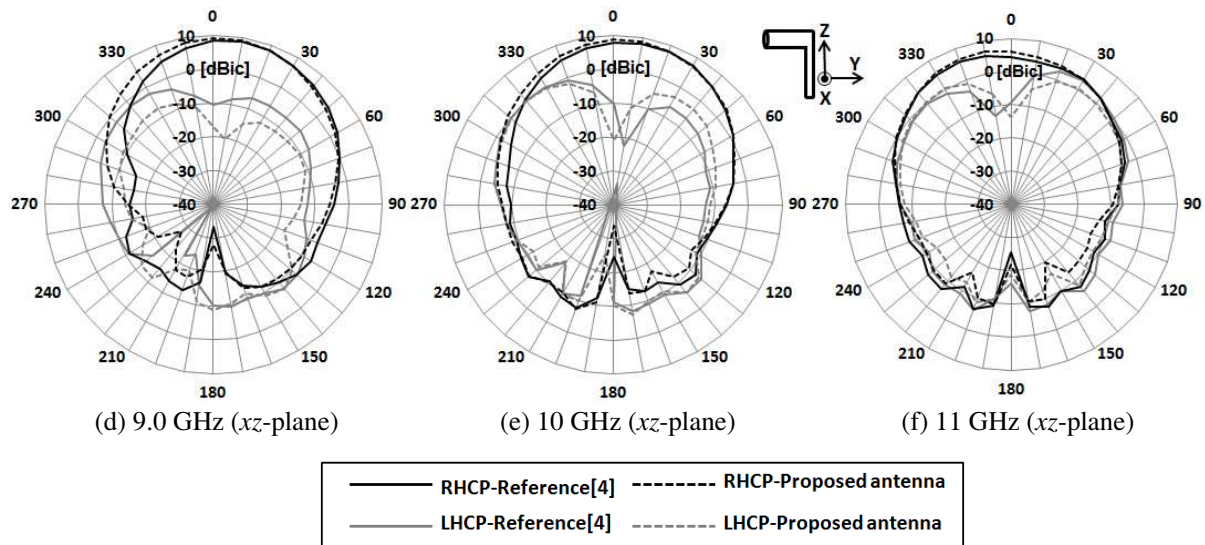


Figure 6: Radiation patterns.

3. RESULTS

Simulation results are discussed in this section. In the first place, the good AR characteristics are obtained over higher frequency by changing the cutoff frequency from 7.8 GHz ($\lambda_g = 60$ mm) to 8.6 GHz ($\lambda_g = 48$ mm) shown in Fig. 2. Secondly, extension of waveguide length improves the AR characteristics around 9.4 GHz which higher order mode (TM_{11}) generates strongly. Variation in AR characteristics with waveguide length l is presented in Fig. 3. Next, the effectiveness of thin poles ($2\text{ mm} \times 2\text{ mm} \times 48\text{ mm}$) on AR characteristics is shown in Fig. 4. Notable improvement of AR characteristics is achieved about 9.4 GHz.

Characteristics of the proposed antenna is compared with previous antenna [4] shown in Fig. 5. The 3-dB AR bandwidth is expanded to 54.0% (6.66–11.59 GHz) from 49.4% in the $+x$ direction, while the antenna gain maintains around 7 dBic high gain up to higher frequency than previous antenna. Radiation patterns in the x - y and the x - z plane at high frequency (9.0, 10 and 11 GHz) are presented in Fig. 6. It is found that cross polarization (LHCP) is reduced over the wide azimuth range by the inserted thin poles.

4. CONCLUSIONS

A broadband circularly polarized waveguide antenna with an L-shaped probe showing lower cross polarization has been presented in this paper. It is realized that reconfiguration of the center frequency causes lower AR characteristics over higher frequency. In addition, it is demonstrated that the extension of waveguide length l causes the effect to generate good circular polarization. And, reduction of cross polarization is achieved by inserting the thin poles at the inside corners of the waveguide. The proposed antenna could attain a simulated 10-dB S_{11} bandwidth of 51.6% and 3-dB AR bandwidth of 54.0%.

This antenna could be used in high speed communication such as UWB hand-band (from 7.25–10.25 GHz) for large information handling capacity in a broadband characteristic. Also, application as RADARs with high resolution is expected.

REFERENCES

1. Hung, K. F. and Y. C. Lin, "Novel broadband circularly polarized cavity-backed aperture antenna with traveling wave excitation," *IEEE Trans. Antennas and Propagation*, Vol. 598, No. 1, 35–42, Jan. 2010.
2. Pourahmadazar, J., C. Ghobadi, J. Nourinia, N. Felegari, and H. Shirzad, "Broadband CPW-fed circularly polarized square slot antenna with inverted-L strips for UWB application," *IEEE Antennas and Wireless Propagation Letters*, Vol. 10, 369–372, Apr. 2011.
3. Mao, S. G., J. C. Yeh, and S. L. Chen, "Ultrawideband circularly polarized spiral antenna using integrated balun with application to time-domain target detection," *IEEE Trans. Antennas and Propagation*, Vol. 57, No. 7, 1914–1920, Jul. 2009.

4. Yamaura, S. and T. Fukusako, “Bandwidth enhancement of circularly polarized waveguide antenna using L-shaped probe,” *ISAP 2011*, FrA4-6, Juju, Korea, Oct. 2011.
5. Fukusako, T. and L. Shafai, “Design of broadband circularly polarized horn antenna using an L-shaped probe,” *IEEE AP-S international Symposium*, 3161–3164, 2006.
6. Yang, S. S., A. A. Kishk, and K. F. Lee, “Wideband circularly polarized antenna with L-shaped slot,” *IEEE Trans. Antennas and Propagation*, Vol. 56, No. 6, 1780–1783, Jun. 2008.
7. Joseph, R., S. Nakao, and T. Fukusako, “Broadband square slot antenna for circular polarization with separated L-probes and stubs in the slot,” *IEICE Trans. Commun.*, Vol. E94-B, No. 3, 951–959, Apr. 2011.

Design of Ultra-wideband MIMO Antenna for Mobile Handset Applications

Hong-Kyun Ryu and Jong-Myung Woo

Department of Radio Science and Engineering, Chungnam National University
99 Daehak-ro, Yuseong-gu, Daejeon 306-764, Korea

Abstract— This paper presents an ultra-wideband MIMO antenna covering WCDMA, WLAN, WiMax and UWB bands for mobile handset applications. The designed ultra-wideband antenna is consisted of a folded monopole antenna coupled with inverted-L element and meander lines. An open stub is inserted in the folded monopole to block 5 GHz WLAN band which interferes to UWB band. The proposed antennas are symmetrically placed on top part of the mobile handset ground for MIMO antenna technology. Meander lines are positioned between two antennas for improving the isolation in operation bands. The size of the designed MIMO antenna is 55 mm × 13.5 mm. The -10 dB bandwidth was measured as 1.85–11.9 GHz without the rejected band (5.15–5.85 GHz). The isolation between two antennas is higher than 17.2 dB. Average gain and total efficiency are 4.96 dBi and 91.4% respectively. Due to the compact size and ultra-wide bandwidth, the proposed antenna is a good candidate for a mobile handset antenna that has a limited space available.

1. INTRODUCTION

Recently, multiple-input multiple-output (MIMO) antenna technology is becoming very popular in wireless communication systems because this technology can significantly improve data transmission speed and channel capacity [1]. The technology has been adopted in several wireless communication systems and a compact wideband MIMO antenna is needed for mobile device applications. Various multi-band MIMO antennas have been proposed for mobile device applications. A quad-band MIMO antenna with a three-dimensional structure has been reported [2]. This antenna covers the WLAN and WiMAX bands. A modified monopole antenna with a parasitic element was developed for dual-band MIMO antenna applications [3]. This antenna covers various communication bands except the UWB band. A UWB-MIMO antenna presented in [4] has large size. It is difficult to apply to modern mobile handsets. This antenna covers only the UWB band and does not block the WLAN (5.15–5.85 GHz) band.

This paper presents a compact MIMO antenna for mobile device applications. The proposed antenna covers several communication systems such as WCDMA (1.92–2.17 GHz), WiMAX (2.3 GHz, 2.5 GHz), WLAN (2.4 GHz), and UWB (3.1–10.6 GHz) bands. The designed antenna consists of a printed folded monopole antenna coupled with a parasitic inverted-L element [5]. To block the WLAN (5.15–5.85 GHz) band that interferes with the UWB band, an open stub is inserted in the folded monopole antenna. The size of the antenna is changed to cover the WCDMA band. In the proposed antenna system, antennas are symmetrically arrayed on the top part of the mobile phone substrate to obtain good isolation performance. In addition, parasitic meander lines are printed between the arrayed antennas to improve the isolation. The next section describes the proposed antenna in detail.

2. ULTRA-WIDEBAND ANTENNA WITH BAND-REJECTED OPERATION

Figure 1 shows the structure of the wideband folded monopole antenna coupled with a parasitic inverted-L element [6]. FR-4 ($\epsilon_r = 4.4$) with a thickness of 0.8 mm is used as the substrate.

The ground plane size is determined to be 120 mm (0.9 λ) × 40 mm (0.3 λ). The antenna is fed by a semi-rigid coaxial cable. The frequency range of the UWB system (3.1 ~ 10.6 GHz) causes interference to the WLAN (5.15 ~ 5.85 GHz) band. To obtain characteristics of band-rejected effect, the open stub is inserted in the printed folded monopole. The rejected band is controlled by parameters that are the width and length (L) of the open stub. The optimized values for width and length of open stub are chosen as 0.6 mm and 7.9 mm which are, respectively 0.14 λ of 5.5 GHz. The size of the antenna is 12.75 mm (1 λ /10) × 12 mm (1 λ /11).

Figure 2(a) shows the simulated and measured return losses of the band-rejected antenna compared to a return loss of the no band-rejected antenna. Good agreement was observed between the simulation and the measurement. The measured -10 dB bandwidth is 2.27–10.6 GHz (4.7 : 1)

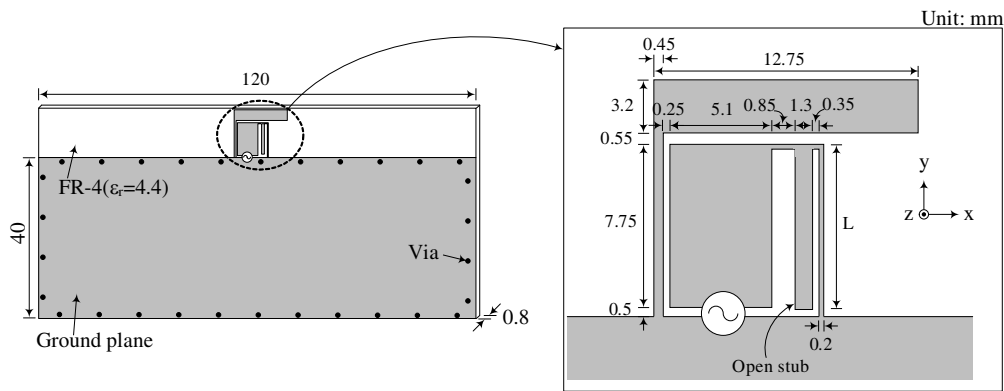


Figure 1: Structure of ultra-wideband antenna with band-rejected operation.

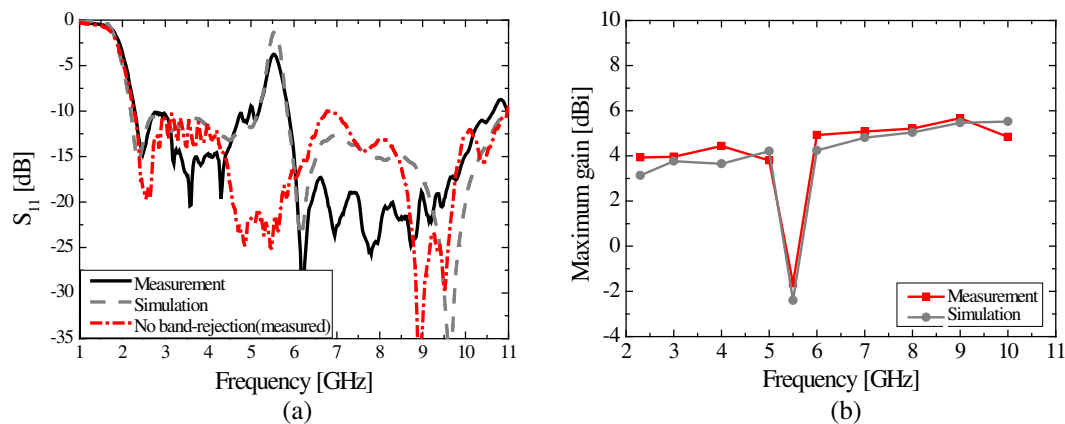


Figure 2: Return loss and maximum gain. (a) Return loss. (b) Gain.

including rejected band and the bandwidth of the band-reject is 700 MHz (5.15–5.85 GHz). It is observed that the antenna has band-rejection characteristic at WLAN frequency band compared with the measured result of nonopen stub antenna. Except for WLAN (5.15–5.85 GHz) system, it covers WiMAX, Bluetooth, and UWB system bandwidths. Figure 2(b) shows the simulated and measured maximum gain in the operating band. In the band-rejected band of 5.6 GHz, antenna gain is -1.65 dBi. This antenna can reject the WLAN band. The maximum gain increases with the frequency except for the rejection band because the electrical size of the antenna increases.

3. ULTRA-WIDEBAND MIMO ANTENNA

For a good diversity performance, MIMO antenna should have high isolation characteristics between antennas in a mobile handset. Several antenna placements were simulated for a high isolation performance. Figure 3 shows S_{21} by antenna placement on mobile handset ground plane. The proposed MIMO antenna is printed on the top part of a mobile phone ground plane. The size of the ground plane is $55 \text{ mm} \times 86.5 \text{ mm}$, and FR-4 ($\epsilon_r = 4.4$, thickness = 0.8 mm) is used as the substrate. The size of the antenna (Figure 1) is changed from $12.75 \times 12 \text{ mm}^2$ to $16.5 \times 13.5 \text{ mm}^2$ to cover WCDMA band (1.92–2.17 GHz). Two antenna placements are compared. The designed antennas are symmetrically placed on the top part of the ground plane in antenna placement 1 whereas the antennas are asymmetrically positioned in antenna placement 2. As shown in Figure 3, S_{21} of antenna placement 2 is lower than that of antenna placement 1. This is because the end of the inverted-L element has strong electric field. Therefore, to achieve further high isolation performance, the antennas are symmetrically placed as shown in Figure 4(a).

As shown in Figure 4(a), the ends of arrayed inverted-L elements have opposite direction for improving isolation. Figure 4(b) is simulated S -parameter. The -10 dB bandwidth is 1.969–11.66 GHz (5.92:1) except rejected band which is 5.07–5.88 GHz. This MIMO antenna can cover WiMAX (2.3 GHz, 2.5 GHz), WLAN (2.4 GHz), and UWB (3.1–10.6 GHz) bands. Also WCDMA (1.92–2.17 GHz) band is partly covered. The S_{21} is simulated below -11.56 dB in 1.965–10.4 GHz.

The S_{21} was improved when compared with antenna placement 2 for around 2 GHz from -9.5 dB to -11.56 dB. The left and right side antennas in Figure 4(a) have same radiation characteristics because of symmetrical position.

Thus, Figure 5 shows simulated maximum gain and radiation patterns in several frequencies (1.92, 4, 5.6, 7, 10 GHz) for the left side antenna. The maximum gain is higher than 3.8 dBi except for 5.6 GHz. The maximum gain of rejected band at 5.6 GHz is -4.53 dBi. The radiation level of 5.6 GHz is low due to rejected band operation. The radiation pattern at 10 GHz showed harmonic pattern. The other radiation patterns are nearly omni-directional. The simulated antenna did not

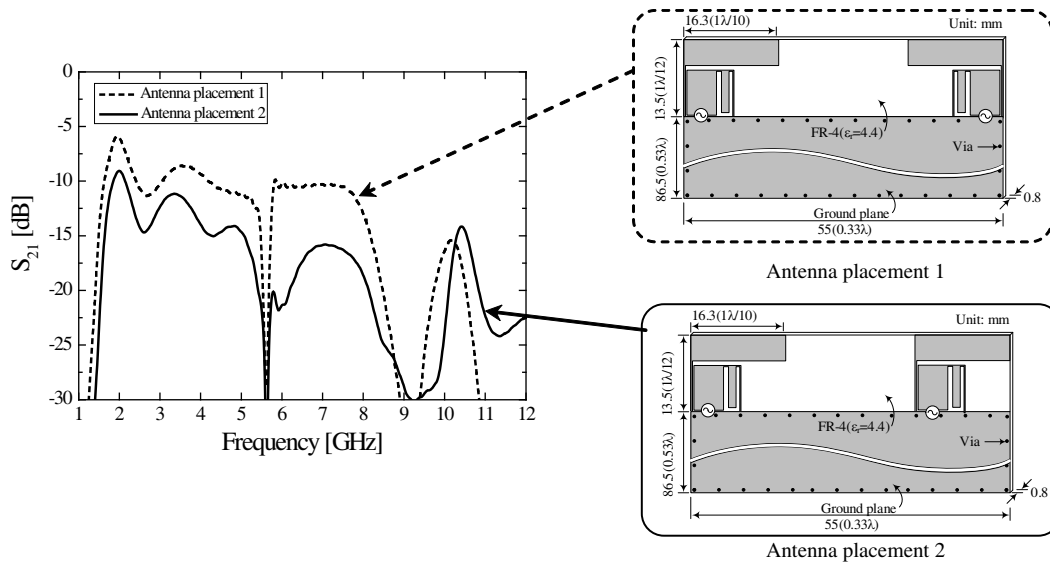


Figure 3: S_{21} by antenna placement on mobile handset ground plane.

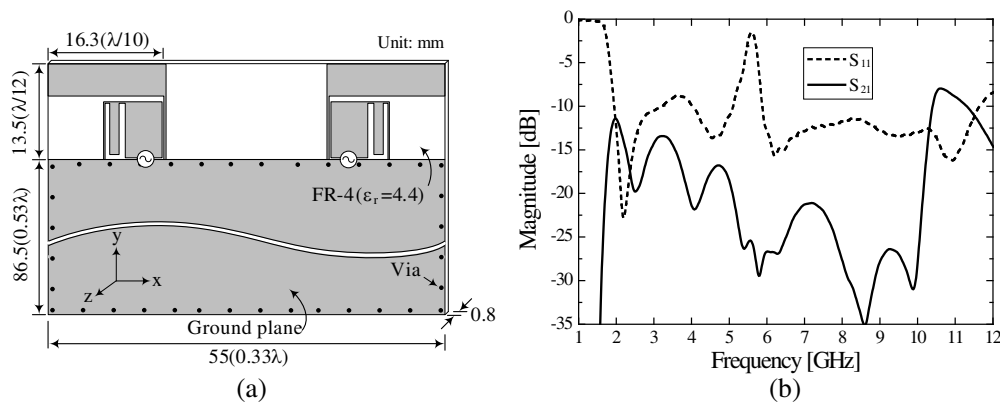
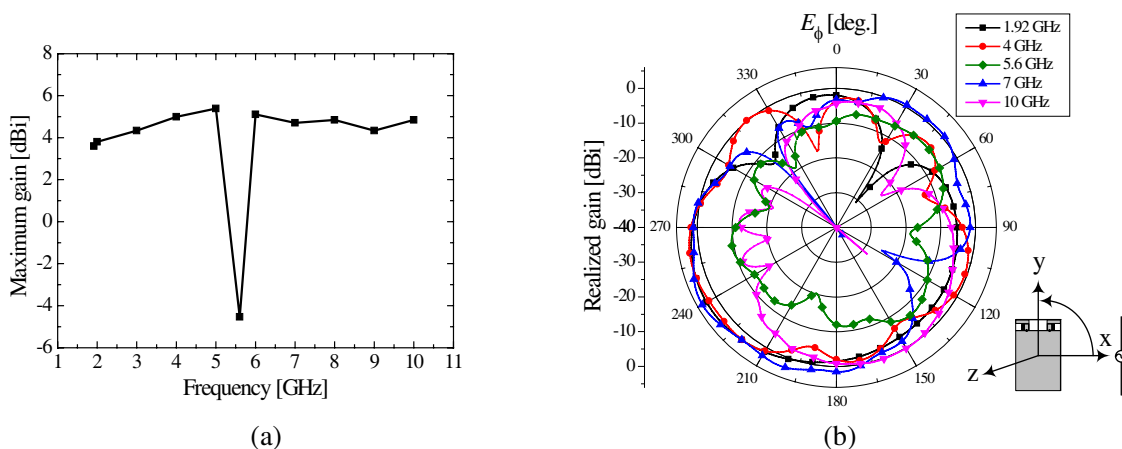


Figure 4: Structure and S -parameter of the proposed MIMO antenna. (a) Structure. (b) S -parameter.



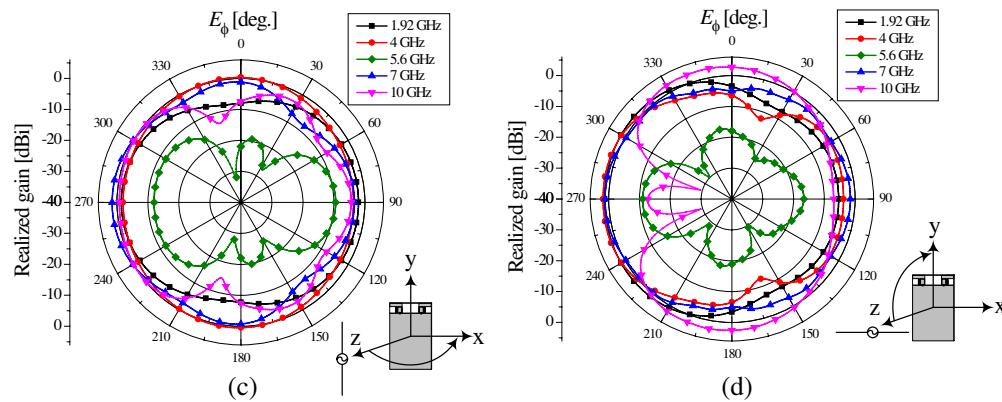


Figure 5: Maximum gain and radiation patterns. (a) Maximum gain. (b) E_ϕ in the xy plane. (c) E_ϕ in the xz plane. (d) E_ϕ in the yz plane.

cover WCDMA band perfectly and the isolation performance is not enough for MIMO antenna.

To improve the isolation in operation bands and to broaden the -10 dB bandwidth meander lines are positioned between two antennas. The -10 dB bandwidth was measured as 1.85–11.9 GHz without the rejected band (5.15 ~ 5.85 GHz). The isolation between two antennas is higher than 17.2 dB. The average gain and total efficiency are 4.96 dBi and 91.4% respectively.

4. CONCLUSIONS

This paper designed an ultra-wideband MIMO antenna with WLAN band rejected operation for 1.92–10.6 GHz band. The size of the ultra-wideband antenna with band-rejected operation was changed to cover WCDMA band and two designed antennas were placed on top part of the mobile handset ground plane for MIMO antenna system. For good isolation characteristics, several antenna placements were simulated and symmetrically antenna placement was determined. To improve the isolation in operation bands and to broaden the -10 dB bandwidth, meander lines are positioned between two antennas. The designed ultra-wideband MIMO antenna showed good radiation and isolation performance. Due to the compact size and ultra-wide bandwidth, the proposed antenna would be useful for MIMO antenna in mobile handset applications.

REFERENCES

1. Foschini, G. J., "On limits of wireless communications in a fading environment when using multiple antennas," *Wireless Personal Commun.*, Vol. 6, No. 3, 311–355, 1998.
2. Bhatti, R. A., J.-H. Choi, and S.-O. Park, "Quad-band MIMO antenna array for portable wireless communication terminals," *IEEE Antennas and Wireless Propag. Lett.*, Vol. 8, 129–132, 2009.
3. Chu, Q. X. and J. F. Chu, "A compact wider dual-band MIMO antenna array for mobile phone," *Proc. IEEE Wireless Information Technology and Systems Conf.*, 1–4, Honolulu, HI, Aug. 2010.
4. Najam, A. I., Y. Duroc, and S. Tedjni, "UWB-MIMO antenna with novel stub structure," *Progress In Electromagnetics Research C*, Vol. 19, 245–257, 2011.
5. Kim, K.-B., H.-K. Ryu, and J.-M. Woo, "Compact wideband folded monopole antenna coupled with parasitic inverted-L element for laptop computer applications," *Electron Lett.*, Vol. 47, No. 5, 301–303, Mar. 2011.
6. Kim, K.-B. and J.-M. Woo, "Wideband printed type folded monopole antenna coupled with a parasitic inverted-L element," *Proceedings of International Symposium on Microwave and Optical Technology*, Prague, Czech, Jun. 2011.

Circularly Polarized Leaky Wave Antenna Using Composite Right/left-handed Transmission Line

M. Ishii and T. Fukusako

Computer Science & Electrical Engineering
Graduate School of Science and Technology, Kumamoto University, Japan

Abstract— This paper demonstrates the generation of circular polarization (CP) from the composite right/left handed transmission line (CRLH-TL). The CP generation is obtained by selecting a suitable position of the CRLH-TL between both edges of the ground. As a result, a CP with a measured bandwidth of 21.8% for an axial ratio (AR) of < 3 dB in the boresight direction is obtained. Using the behavior in both the left-handed and right-handed frequency regions, a scanning angle of the main beam of approximately 30° can be obtained by varying the frequency between 2.58 GHz and 2.99 GHz.

1. INTRODUCTION

The leaky wave antenna (LWA) that uses a composite right/left-handed transmission line (CRLH-TL) has been investigated by numerous researchers [1–4]. The radiation in the right-handed frequency with parallel phase and group velocities is directed in the forward propagating direction. However, the radiation in the left-handed frequency with anti-parallel phase and group velocities is directed in the backward propagating direction. Therefore, backward-to-endfire frequency scanning (BEFS) is available by sweeping the frequency between the left- and right-handed frequencies. Although BEFS behavior can be applied to radars and sensors, most of the conventional LWAs with a CRLH-TL are linearly polarized. An LWA that can generate CP has recently been presented in [5]. This structure has two LWAs and a phase shifter for generating two orthogonal polarizations that are 90° out of phase.

Based on the above considerations, we herein present a single-element circularly polarized LWA having a CRLH-TL structure. One key to generating CP is the L-shaped structure of a stub and the inter-digit structure of a unit cell, both of which should be designed considering the dispersion characteristics around the frequency and the 90° phase difference between E_x and E_y . Another key is to control the ratio of $|E_x|$ and $|E_y|$ by choosing a suitable position of the LWA element transmission line between the two edges of the ground plane so as to effectively take advantage of the effect of radiation from the edges. As such, in the present study, the axial ratio (AR) characteristics are presented, a brief explanation of the physical behavior is presented, and the dependence of the radiation pattern on frequency is discussed.

2. ANTENNA STRUCTURE

The structure of a unit cell of the proposed antenna is shown in Fig. 1(a). The unit cell is composed of a ground plane, a dielectric, a feeding microstrip line, fingers (a coupled inter-digit structure), and an inductive parallel stub with a shorted termination through a via ($\phi = 0.5$ mm) to the ground plane. Fig. 1(b) shows the comb-shaped LWA of eight unit cells used in this study. A

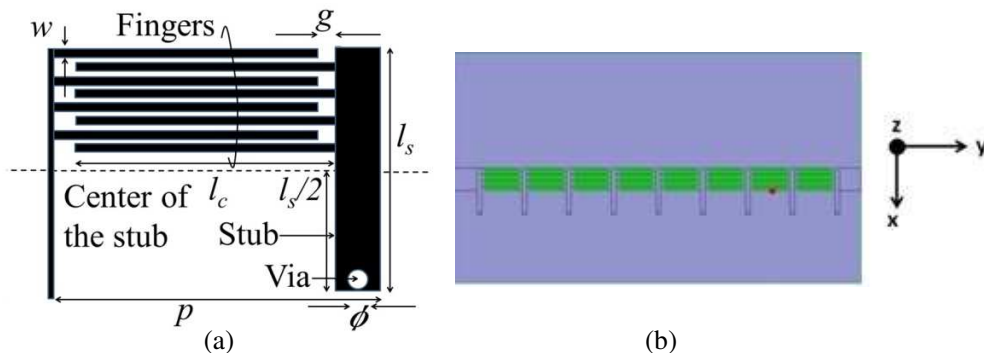


Figure 1: (a) Structure of the unit cell. (b) Basic structure of the comb-shaped LWA using a CRLH-TL.

Taconnic substrate of TLY-5 CH/CH with a dielectric constant of 2.2, a loss tangent of 0.001, and a thickness of 1.6 mm was used for the present structure, which had a ground with dimension of $97.4 \text{ mm} \times 50 \text{ mm} \times 0.035 \text{ mm}$. And the unit cell has finger length l_c and stub length l_s , both of which have been optimized as 9 mm and 10.1 mm, respectively, considering both the 90° phase difference. The gap g between the stub and the fingers is also optimized as 0.8 mm, where the width w of a finger has been chosen as 0.35 mm. Furthermore, the intervals between the fingers are 0.3 mm.

The TL element of the LWA is initially placed on the ground plane so that the center position of the stub is located at the center of the ground plane in the x direction.

3. DESIGN AND SIMULATION RESULTS

To understand the dispersion characteristics and also for parametric studies, the simulations were conducted by HFSS 13.0. In this section, the dispersion characteristics for a unit cell are first discussed. The effect of the position on the ground plane is discussed.

3.1. Dispersion Characteristics

The dispersion characteristics of the unit cell which have narrow bandwidth is shown in Fig. 2. Considering that βp should be lower than that of the free space for a leaky wave to occur, the frequency for left-handed behavior is from 2.18 GHz to 2.71 GHz. Similarly, the frequency for right-handed behavior is from 2.76 GHz to 4.24 GHz. Therefore, a band gap from 2.71 to 2.76 GHz is allowed to exist for generating CP.

3.2. Parametric Study on the Position on the Ground Plane

The length of the fingers and stubs are 9 mm and 10.1 mm, respectively. The AR characteristics of the proposed LWA are observed when the element position is shifted by 8 mm in the $+x$ direction. As shown in Fig. 4, a bandwidth of 32.7% for an AR of $< 3 \text{ dB}$ is obtained when the LWA element is shifted. The bandwidth of the AR is widened by changing the shift distance. This is because

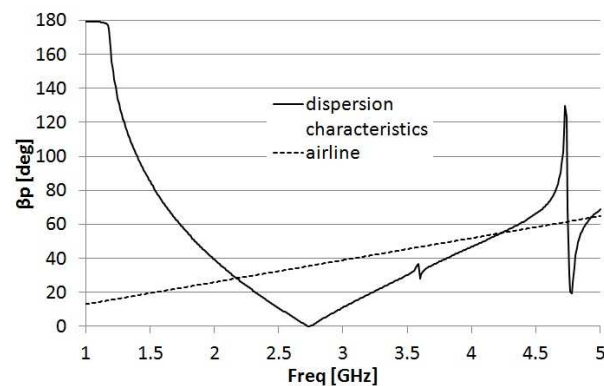


Figure 2: Dispersion characteristics of the unit cell.

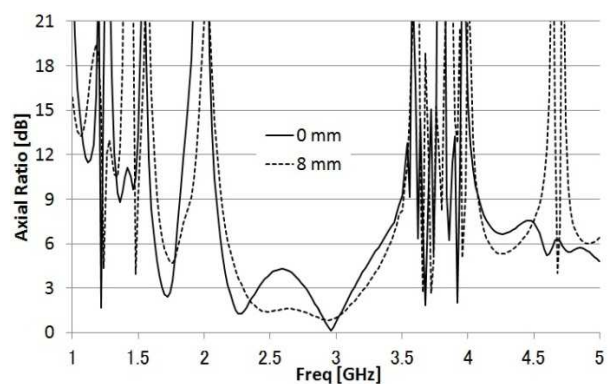


Figure 3: Variation in AR while shifting the LWA element in the x direction from the initial position.

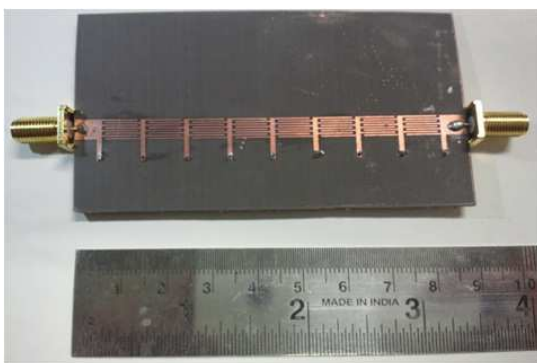


Figure 4: Fabricated antenna.

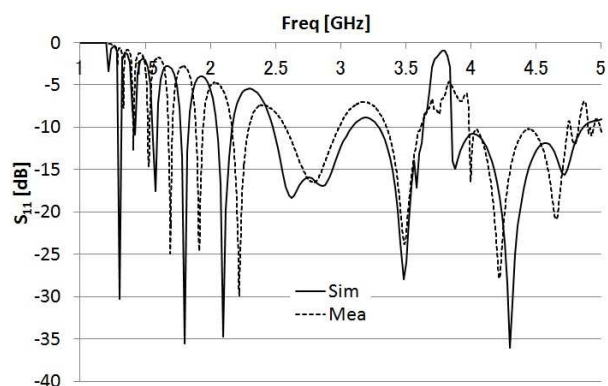


Figure 5: S_{11} for the simulation and the measurement.

of the electric field changes in both x and y directions, E_x and E_y . The radiation from the edge of the ground plane affects E_y when the ground plane is shifted by 8 mm. As a result, the shift to $+x$ results in nearly equal values of E_x and E_y , which results in the generation of CP. In order to generate CP, a phase difference of 90° is also required. In this structure, the phase difference is caused by the current on the fingers and stub. Therefore, such an L-shaped structure generates a phase difference by traveling-wave-like excitation. A CP antenna based on a similar principle is discussed in [6].

4. EXPERIMENTAL RESULTS

The proposed antenna design with $l_s = 10.1$ mm, $l_c = 9$ mm, and a shift of element by 8 mm was fabricated and measured. The fabricated antenna is shown in Fig. 4. Fig. 5 shows both the simulated and measured S_{11} characteristics. The slight disagreement in the characteristics is due to fabrication errors around the fingers and the stubs. However, right/left handed regions are covered with the enough S_{11} . In this structure, $S_{11} (< -10$ dB) was obtained since the number of unit cell is 8, which is very much lesser than infinite, and calculated process of bloch impedance doesn't consider the amplitude of the circuit. Fig. 6 shows the AR characteristics in the $+z$ direction. A 3-dB AR band is observed for bore-sight direction ($+z$) around the band gap frequency. These figures reveal the good agreement between simulated and measured result with sufficient cross-polarization discrimination (XPD) of more than 15 dB for an AR of 3 dB.

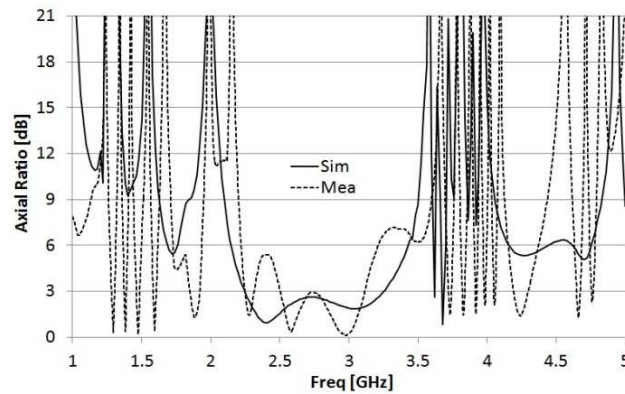


Figure 6: AR for the simulation and the measurement.

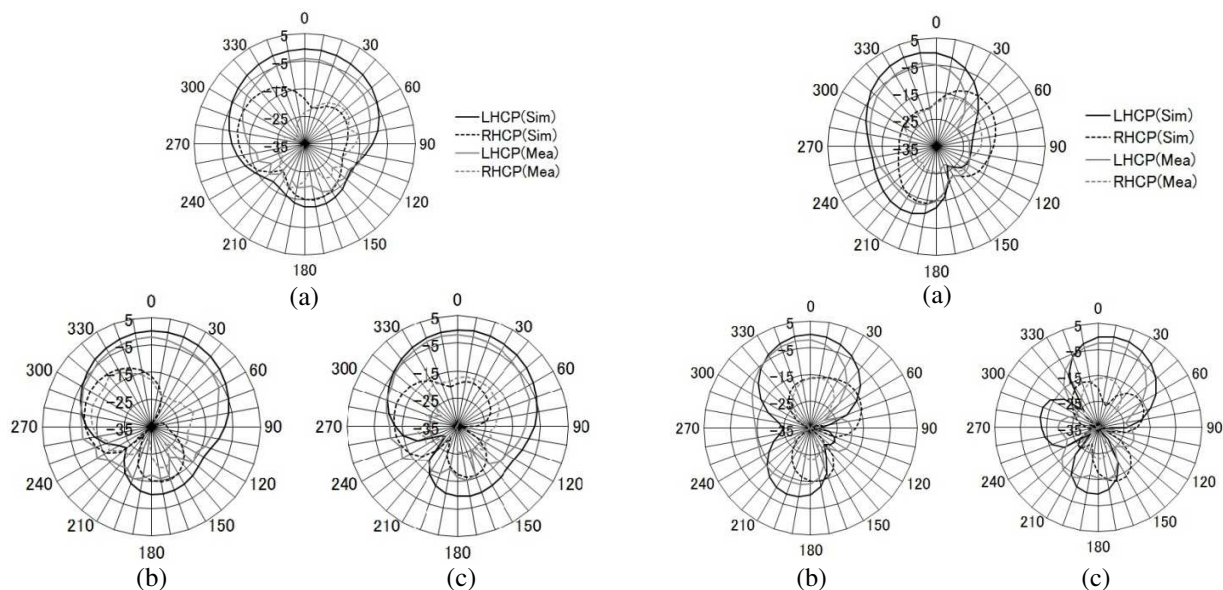


Figure 7: Simulated and measured radiation patterns on the z - x plane at (a) 2.58 GHz, (b) 2.74 GHz, (c) 2.99 GHz. The units of the radial axes are dBic.

Figure 8: Simulated and measured radiation patterns on the y - z plane at (a) 2.58 GHz, (b) 2.74 GHz, (c) 2.99 GHz. The units of the radial axes are dBic.

Figures 7 and 8 show the radiation pattern on the z - x and y - z planes, respectively, at (a) 2.58 GHz (left-handed region), (b) 2.74 GHz (band gap region), and (c) 2.99 GHz (right-handed region). However, no scanning in the z - x plane is observed. As a result, a CP scanning of 30° is obtained by varying the frequency between 2.58 GHz and 2.99 GHz. The antenna gain is approximately 1 dBic. However, the antenna gain improves as the number of unit cell increases.

5. CONCLUSION

We have presented a circularly polarized LWA with a CRLH-TL structure. The CP radiation was obtained by the 90° of phase difference caused by the L-shaped structure consisted of the stub and the fingers and by the nearly equal amplitude occurred in E_x and E_y . The proposed LWA covers right/left handed frequency bands which are needed for scanning. Therefore, it is applicable to radars and sensors using CP.

REFERENCES

1. Kang, M., C. Caloz, and T. Itoh, "Miniaturized MIM CRLH transmission line structure and application to backfire-to-endfire leaky wave antenna," *IEEE Antennas and Propagation Society International Symposium*, Vol. 1, 827–830, 2004.
2. Heshemi, M. R. and T. Itoh, "Dispersion engineered metamaterial-based transmission line for conformal surface application," *2008 IEEE MTT-S International Microwave Symposium Digest*, 331–334, 2008.
3. Liu, L., C. Caloz, and T. Itoh, "Dominant mode (DM) leaky wave antenna with backfire-to-endfire scanning capability," *Electron. Lett.*, Vol. 38, No. 23, 1414–1416, 2002.
4. Caloz, C. and T. Itoh, "Novel microwave devices and structures based on the transmission line approach of meta-materials," *2003 IEEE MTT-S International Microwave Symposium Digest*, Vol. 1, 195–198, 2003.
5. Heshemi, M. R. and T. Itoh, "Circularly polarized composite right/left-handed leaky wave antenna," *2010 IEEE International Conference Wireless Information Technology and System (ICWITS)*, 1–4, 2010.
6. Joseph, R., S. Nakao, and T. Fukusako, "Broadband square slot antenna for circular polarization with separated L-probes and stubs in the slot," *IEICE Trans. Communication*, Vol. E94-B, No. 04, 951–959, 2011.

Dielectric Rod Antenna Array with SIW Feed Network for Radar Imaging System

Robab Kazemi and Ramezan Ali Sadeghzadeh

K. N. Toosi University of Technology, Tehran 1431714191, Iran

Abstract— An array is designed to be used in UWB imaging systems. The antenna is an eight-element dielectric rod array covering 8–12 GHz frequency range and has the ability to send short electromagnetic pulses in a directional manner with low distortion and low loss. The array antenna performance is further improved by the inclusion of a low-loss SIW feed network and wide-band input matching through optimized GCPW transition. The array is optimized to have a compact size and almost constant radiation pattern with frequency. Measured results are successfully confirmed with simulation; it has a broadband performance at 8–12 GHz, with 14.5 ± 2 dB gain, -14 dB SLL, and better than 27 dB front-to-back ratio. Meanwhile, the antenna provides a symmetric radiation pattern with relatively low cross polarization of better than -19 dB and occupies $10 \text{ cm} \times 9 \text{ cm}$.

The antenna is geared towards imaging with high resolution. Reflections of a target are measured for the developed array and compared to the previously-fabricated antenna. Strong reflected pulse and high resolution image are recorded by new antenna, demonstrating the potential of this feature for microwave imaging systems.

1. INTRODUCTION

Ultra wideband imaging approaches are a topic of growing interest. It is of particular interest to the military, law enforcement, and rescue/search departments [1]. One approach to microwave imaging is radar-based, which operates by sending a short-term pulse towards the object of interest using one or many antennas. The reflections are measured and used to create an image related to the differences in dielectric properties of the structure. In order to reliably sense the reflections from the object located in an area, a high quality antennas are required to send and receive UWB pulses with low distortion and high efficiency [2]. Additionally, the transmitting and receiving antennas have to be compact and lightweight for portability and to be compatible with prototype imaging systems.

The antenna radiation pattern needs to be accounted for — since significant image distortion might be seen due to the radiation pattern angle dependence. Numerous antenna designs for radar-based ultra wideband (UWB) imaging have been reported [2–4]. Vivaldi antennas are used because of their favorable characteristics for imaging, and specifically they have relatively simple structure, light weight, small lateral dimensions, wide band, and high efficiency. However, the directivity of Vivaldi antenna is relatively low. Recently, some improvement methods have been proposed, such as array technique, but high loss of the feeding system is a big problem in array configuration [5, 6].

In this paper, we have developed a dielectric rod antenna array using low-loss SIW power divider and relatively thick substrate to increase imaging efficiency. The configuration of the array was optimized to work at 8–12 GHz with small size and low loss, while providing reasonable imaging capabilities with an acceptable number of measurement locations. This paper is organized as follows: Section 2 introduces the single element Vivaldi antenna design and its feeding structure. Section 3 will focus on the implementation of the array and its radiation characteristics. In Section 4, the experimental results of our developed array in an imaging system will be presented with emphasis on the image resolution, and compared with a previously-fabricated antenna. The conclusion will be given in Section 5.

2. SINGLE ELEMENT VIVALDI ANTENNA DESIGN

An antipodal Vivaldi antenna to use in array configuration was designed to operate over 8–12 GHz frequency range. It is fed by a grounded coplanar waveguide (GCPW) line through a SIW structure as shown in Fig. 1. The top and bottom layers show the exponential taper profile which is defined

Table 1: Parameters of Vivaldi antenna.

Parameter	W_s (mm)	W_1 (mm)	L_{ant} (mm)	L_{tap} (mm)	d_y (mm)	r
Value	11.65	2.185	15.5	4.5	1	0.4

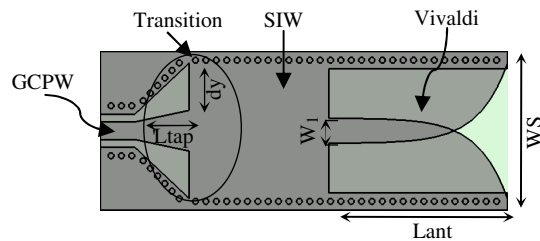


Figure 1: Sketch of antipodal Vivaldi antenna.

in (1).

$$\begin{aligned}
 y &= Ae^{rx} + B \\
 A &= \frac{W_S + W_1}{2} \cdot (e^{r \cdot L_{ant}} - 1)^{-1} \\
 B &= -\frac{W_S + W_1 e^{r \cdot L_{ant}}}{2} \cdot (e^{r \cdot L_{ant}} - 1)^{-1}
 \end{aligned} \tag{1}$$

where r is the taper rate and other parameters are indicated in Fig. 1.

In this design, we used a relatively thick substrate to lower the conductor loss of the SIW structure. However, for this thick substrate, 50Ω microstrip feed line will be very wide and would excite higher order modes with the potential to radiate [5]. The antenna is fed through GCPW line followed by a gradual transition from GCPW to SIW. Along this wideband transition, the slot width increases linearly (triangular shape) to convert the arbitrary impedance of SIW to 50Ω input impedance. In our implementation, Vivaldi antenna and SIW feed are realized on RO4003c substrate with a thickness of $t = 1.524$ mm. For a compact size and wide band operation with low return loss, the antenna parameters are optimized and summarized in Table 1.

3. ARRAY CONFIGURATION

In an array design, typical requirements include low return loss and minimum structure insertion loss to achieve high radiation efficiency. The array gain and radiation pattern are functions of the elements' spacing and differential phase between its elements. Using element spacing beyond one wavelength would generate grating lobes in addition to increasing the antenna size. Meanwhile, the directivity is a function of element spacing and it has a maximum around 0.9λ . Dielectric Rod Antennas (DRAs), however, could be designed with even relatively close spacing for a compact overall size due to their high decoupling efficiency without significant gain drop.

One problem, however, in implementing DRA arrays is the difficulty of designing an efficient feed network with a high packing density. Another requirement for array design is the antenna to be as much as simple, and small as possible. We utilize a low loss eight-way splitter that was thoroughly optimized using CST Microwave Studio. This splitter was designed using SIW guides that has 0.4λ (12.1 mm) width for single mode operation at X-band, and provided over 4 GHz operating band with less than 1.1 dB insertion loss. The structure of the feed network and its measured characteristics are presented in Fig. 2. As can be seen, this feed network covers over 40% bandwidth, and has better than 10 dB return loss and a good power division at the desired frequency range, with less than $\pm 4^\circ$ and ± 0.9 dB phase and amplitude imbalance, respectively.

Requirements for imaging antenna include wide band operation, minimal dispersion, frequency independent radiation pattern, compact size and low loss. A prototype eight-element DRA was built by inserting a concentric two-layer rod at the end of each Vivaldi antenna element as shown in Fig. 3(a). By adding the rods, the mutual coupling effects are significantly reduced, especially around the lower end of the frequency band. The measured radiation characteristics of the array are shown in Figs. 3(b)–(d). Well-formed beams are generally obtained and the patterns are very similar across the band. The 3-dB beamwidth in the E -plane is 13° , SLL is less than -14 dB and

front-to-back ratio is better than 27 dB. The gain of 14.5 ± 2 dB is obtained across the frequency band. Meanwhile, the antenna provides a symmetric radiation pattern with relatively low cross polarization of better than -19 dB, as shown in Fig. 3(e). The array antenna is extremely compact and its whole size is $10 \text{ cm} \times 9 \text{ cm}$ including the rods.

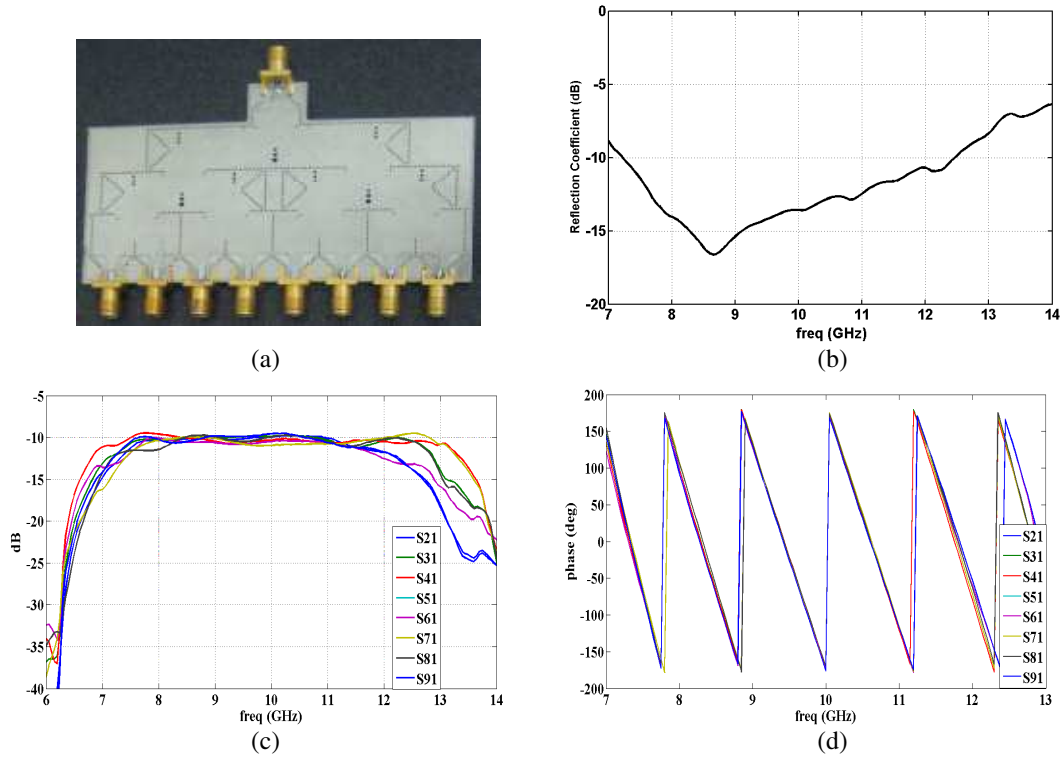
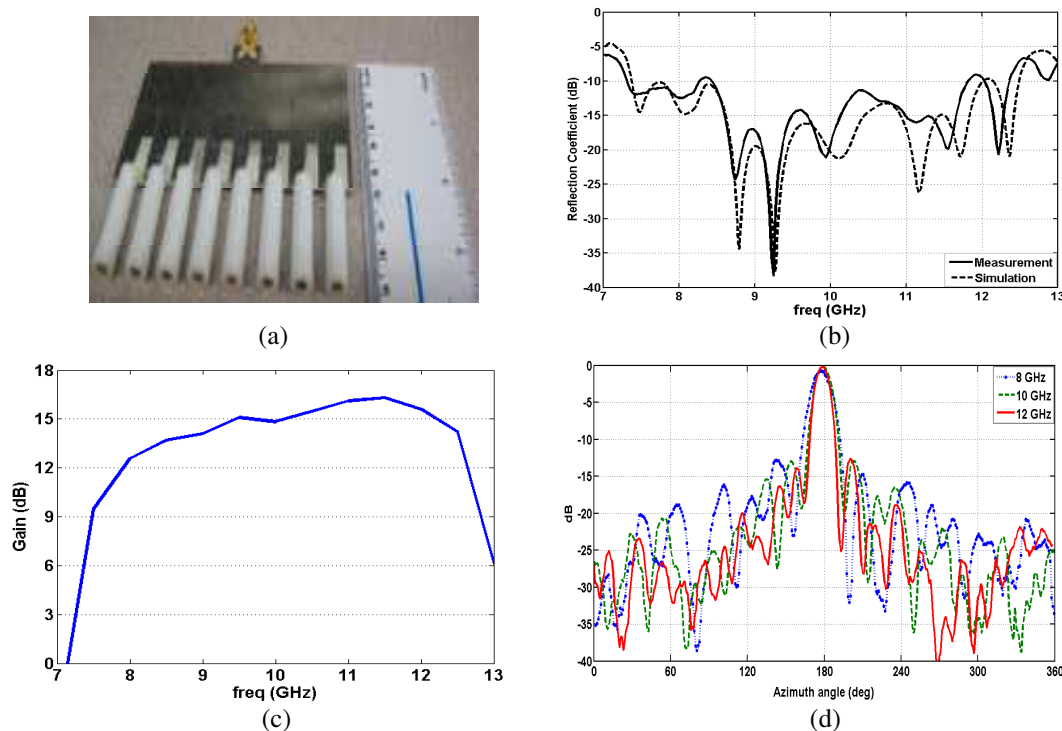


Figure 2: (a) Manufactured wideband SIW 1×8 power divider; (b) Measured input reflection coefficient; (c) Amplitude and (d) phase of output signals at X-band.



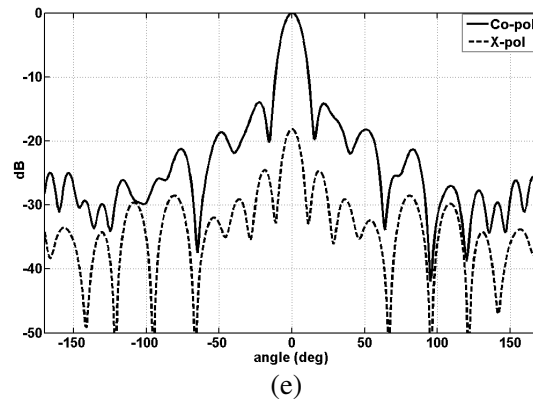


Figure 3: (a) Fabricated array structure; (b) Measured and simulated return loss; (c) Measured Gain; (d) Measured radiation patterns; (e) E -plane and cross-polarization radiation patterns.

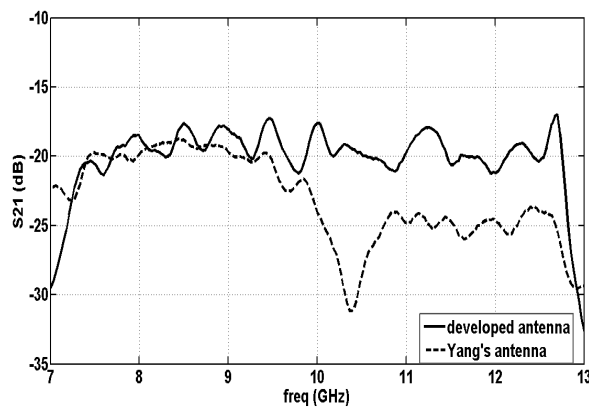


Figure 4: Transmission coefficient (S_{21}) obtained with two antennas facing each other with 150 mm separation.

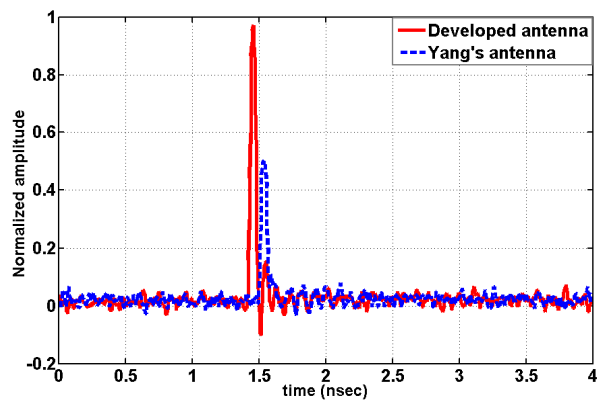


Figure 5: Received signal for two antennas.

4. EVALUATION METHODS

From a detection perspective, an antenna with higher S_{21} will receive more reflected energy from a target placed in front of the antenna. Fig. 4 presents the measured transmission coefficient (S_{21}) for our developed antenna and a previously-fabricated antenna [3] facing an UWB horn and separated 150 mm. It is observed that for the new proposed antenna S_{21} magnitude is improved, especially at the high frequency range. This improvement is due to the use of a relatively thick substrate for lowering conductor loss and low-loss SIW feed network. The old array was fabricated using Wilkinson divider which is lossy. Similar behavior has been observed at separation distance between 50 to 300 mm and therefore it is concluded that there is no direct dependence on the separation distance.

Next, reflections from a target placed at 1.5 m in front of the antenna's aperture are measured and compared to the old antenna. The array received signal is down-converted through I/Q demodulation, and then routed to the oscilloscope. Fig. 5 presents the measured received pulses for both antennas. The strong pulse of new antenna confirms the performance improvement due to low-loss feed network.

Since the ultimate purpose of this antenna is for imaging, its performance is evaluated as a receiver antenna in an imaging system and compared with old antenna. An experiment was conducted to test the developed antenna performance. An UWB standard horn with 1–18 GHz range is used as a transmitting antenna and the developed array is for receiving. The antennas are aligned with the target. The antenna scans the target each 3 cm. The reference location is defined 40 cm between the transmitter and receiver. The target responses at 8 locations are received. The reflections are used to create an image related to the differences in dielectric properties of the structure.

Figure 6(a) shows the image of the target for our antenna and Fig. 6(b) shows the image for the

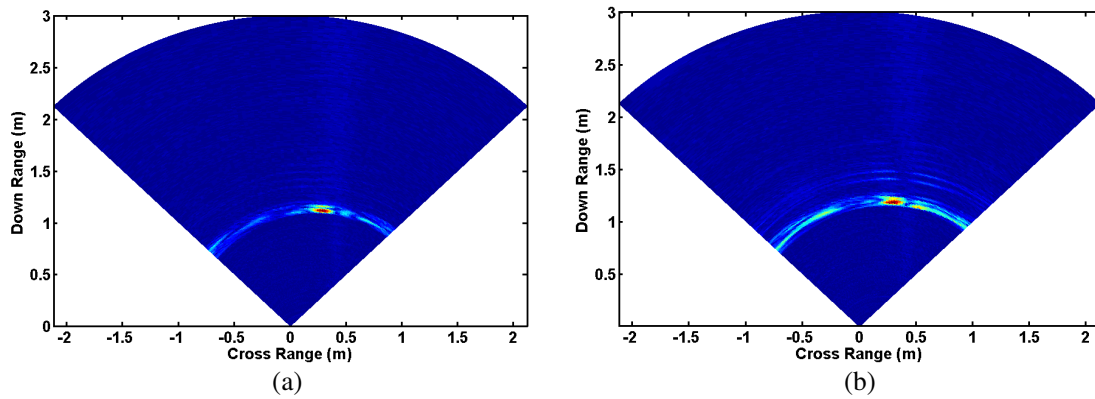


Figure 6: (a) New developed antenna's image; (b) Old antenna's image.

old antenna for comparison. The strongest response spot at the middle bottom of the image is a result of the direct reflection of the target. There is no side image for new antenna.

5. CONCLUSION

In this paper, the directivity of a dielectric rod antenna array is improved by using a low-loss SIW feed network. Moreover, for this application, the efficiency is improved since conductor loss is lower due to using relatively thick substrate. The array produces a high gain while keeping S_{11} below -10 dB at 8–12 GHz frequency band. The effect of this low-loss feed is also noticed in S_{21} since the transmitted energy between two antennas is significantly higher. Additionally, it is demonstrated that the antenna increases the reflected energy from an object placed in front of the antenna, consequently a high-resolution image is obtained when used in an imaging system. From a detection point of view, this is an advantage.

REFERENCES

1. Fontana, R. J., "Recent system applications of short-pulse ultra-wideband (UWB) technology," *IEEE Trans. Microw. Theory Tech.*, Vol. 52, No. 9, 2087–2104, Sep. 2004.
2. Bourqui, J., M. Okoniewski, and E. C. Fear, "Balanced antipodal Vivaldi antenna with dielectric director for near-field microwave imaging," *IEEE Trans. Ant. Propag.*, Vol. 58, No. 7, 2318–2326, Jul. 2010.
3. Yang, Y. and A. E. Fathy, "Development and implementation of a real-time see-through-wall radar system based on FPGA," *IEEE Trans. Geoscience and Remote Sensing*, Vol. 47, No. 5, 1270–1280, May 2009.
4. Li, X., S. Hagness, M. Choi, and D. van der Weide, "Numerical and experimental investigation of an ultrawideband ridged pyramidal horn antenna with curved launching plane for pulse radiation," *IEEE Ant. Wirel. Propag. Lett.*, Vol. 2, 259–262, 2003.
5. Yang, Y., C. Zhang, S. Lin, and A. Fathy, "Development of an ultra wideband Vivaldi antenna array," *IEEE Ant. Propag. Soc. Int. Symp.*, Vol. 1A, 606–609, 2005.
6. Hao, Z., W. Hong, H. Li, H. Zhang, and K. Wu, "Multiway broadband substrate integrated waveguide (SIW) power divider," *IEEE Ant. Propag. Soc. Int. Symp.*, Vol. 1A, 639–642, 2005.

Designing Transformation-based Metamaterials for Numerical Modeling of Low Frequency Electromagnetic Scattering

Ozlem Ozgun¹ and Mustafa Kuzuoglu²

¹Department of Electrical and Electronics Engineering
TED University, Ankara, Turkey

²Department of Electrical and Electronics Engineering
Middle East Technical University, Ankara, Turkey

Abstract— This paper presents coordinate transformation techniques for solving low-frequency electromagnetic boundary value problems involving electrically-small geometrical features. The major motivation is to eliminate the need for fine mesh and to allow uniform and easy-to-generate meshes by placing transformation media into the computational domain. A salutary feature of the proposed methods is the capability to handle arbitrarily-shaped geometries by using a ‘single’ mesh and by changing only the constitutive parameters inside the metamaterial layer. Several numerical simulations are illustrated in the context of finite element solution of electromagnetic scattering problems.

1. INTRODUCTION

Electromagnetic wave scattering from electrically-small (i.e., dimensions are small compared to the wavelength) objects or features has always been of interest in various fields of science and engineering for more than a century. However, in such problems, numerical solution techniques suffer from some difficulties due to the necessity to capture the small scale effects on the large scale with adequate numerical precision. For instance, if an electrically-small object is located in a medium together with other large scale objects, the mesh must be refined over the object, leading in turn to a large number of unknowns. Practical applications may include the modeling of a small antenna mounted on a large platform, or simulating thin interconnect structures in integrated circuits. Such problems also complicate the process of mesh generation because of the mesh refinement, and often introduce ill-conditioned matrix systems because of poor mesh quality. This, in turn, makes it difficult to extract an accurate solution of such problems in a numerically efficient manner.

In this paper, efficient numerical modeling of electromagnetic low-frequency problems is achieved by means of specially-designed transformation-based metamaterials in the context of finite methods (such as finite element or finite difference methods). The transformation-based metamaterials, in general, depend on the duality relationship between the coordinate transformation and the material parameters, in conjunction with the form invariance property of Maxwell’s equations under coordinate transformations [1–7]. That is, Maxwell’s equations keep their form the same in the modified coordinate system, but the original material parameters are replaced by anisotropic parameters to mimic the field behavior resulting from the coordinate transformation. The principal idea in the proposed techniques is to modify the computational domain and to suitably place transformation-based metamaterial structures within the modified domain, and hence, to devise efficient simulation tools employing uniform and easy-to-generate meshes and less number of unknowns. The proposed techniques are illustrated via several finite element simulations.

2. DUALITY BETWEEN COORDINATE TRANSFORMATION AND MATERIAL PARAMETERS

Let $\vec{r} \rightarrow \tilde{\vec{r}} = T(\vec{r})$ be a general coordinate transformation, where \vec{r} and $\tilde{\vec{r}}$ are the coordinates in the original and transformed domain, respectively. Instead of dealing with the field formulations within the modified domain, the original medium is replaced by an anisotropic medium so that transformed fields satisfy the original forms of Maxwell’s equations. This property is known as the form-invariance property of Maxwell’s equations under coordinate transformations. The constitutive tensors of the anisotropic medium are obtained by [2]

$$\tilde{\bar{\epsilon}} = \epsilon \bar{\bar{\Lambda}} \quad \text{and} \quad \tilde{\bar{\mu}} = \mu \bar{\bar{\Lambda}}, \quad \text{where} \quad \bar{\bar{\Lambda}} = \left(\det \bar{\bar{J}} \right) \left(\bar{\bar{J}}^T \cdot \bar{\bar{J}} \right)^{-1} \quad (1)$$

Here, ε and μ are the permittivity and permeability of the original medium, respectively, and $\bar{\bar{J}}$ is the Jacobian tensor that is $\bar{\bar{J}} = \partial(\tilde{x}, \tilde{y}, \tilde{z})/\partial(x, y, z)$ in Cartesian coordinates.

Original fields in transformed coordinates, $\vec{E}(\vec{r})$, and transformed fields in original coordinates, $\tilde{\vec{E}}(\vec{r})$, are interdependent. Namely, that the original fields within the transformed space can be recovered by using the fields within the anisotropic material by using the following relation [2]:

$$\vec{E}(\vec{r}) \rightarrow \tilde{\vec{E}}(\vec{r}) = \bar{\bar{J}}^T \cdot \vec{E}(\vec{r}) \quad \text{and} \quad \vec{H}(\vec{r}) \rightarrow \tilde{\vec{H}}(\vec{r}) = \bar{\bar{J}}^T \cdot \vec{H}(\vec{r}) \quad (2)$$

3. SCATTERING FROM ELECTRICALLY-SMALL OBJECTS

We consider a scattering problem where four electrically-small objects are illuminated by a plane-wave (see Fig. 1). Numerical solution of this problem is challenging, because a large number of unknowns must be introduced within the computational domain that is not occupied by the object. The reason of this requirement is twofold: (i) The mesh must be refined around the object to accurately estimate field variation with adequate numerical precision; (ii) Mesh truncation boundaries (such as perfectly matched layer) must be located sufficiently far away from the object to reduce spurious reflections. The equivalent problem transforms the original problem into a relatively high-frequency problem, and employs a more convenient and uniform mesh generation scheme with less number of unknowns. The “equivalence” here means that both problems result in identical field values in their common free-space regions, and the fields inside the anisotropic layer are related to the original near-fields at the close vicinity of the object through the field equivalence in (2). A salutary feature of the equivalent problem is that the *same* mesh can be used for any arbitrarily-shaped object by simply changing the constitutive parameters of the anisotropic layer with respect to the geometry of the object.

In designing the metamaterial region, each point P inside Ω_M is mapped to \tilde{P} inside the transformed region $\tilde{\Omega} = \Omega \cup \Omega_M$, by using the following coordinate transformation $T: \Omega_M \rightarrow \tilde{\Omega}$:

$$\vec{r} \rightarrow \tilde{\vec{r}} = T(\vec{r}) = K(\vec{r} - \vec{r}_b) + \vec{r}_c \quad \text{where} \quad K = \|\vec{r}_a - \vec{r}_c\| / \|\vec{r}_a - \vec{r}_b\| \quad (3)$$

Here, \vec{r}_a , \vec{r}_b and \vec{r}_c are the position vectors of the corresponding points. The unit vector \hat{a} is emanated from a point inside the innermost domain (such as the center-of-mass point) in the direction of the point P.

The technique is simulated by the finite element method, and illustrated in Fig. 2. In this example, assuming TM_z case, a plane wave whose angle of incidence is 90° with respect to the x -axis is incident to four circular conducting objects, each of which has a radius of $\lambda/20$ ($\lambda = 1$ m).

4. SCATTERING FROM OBJECTS COATED BY ELECTRICALLY-THIN DIELECTRIC LAYERS

This section considers the scattering problem involving an object coated by electrically-thin dielectric layers. It is evident that smaller-sized elements must be chosen inside the dielectric layers for

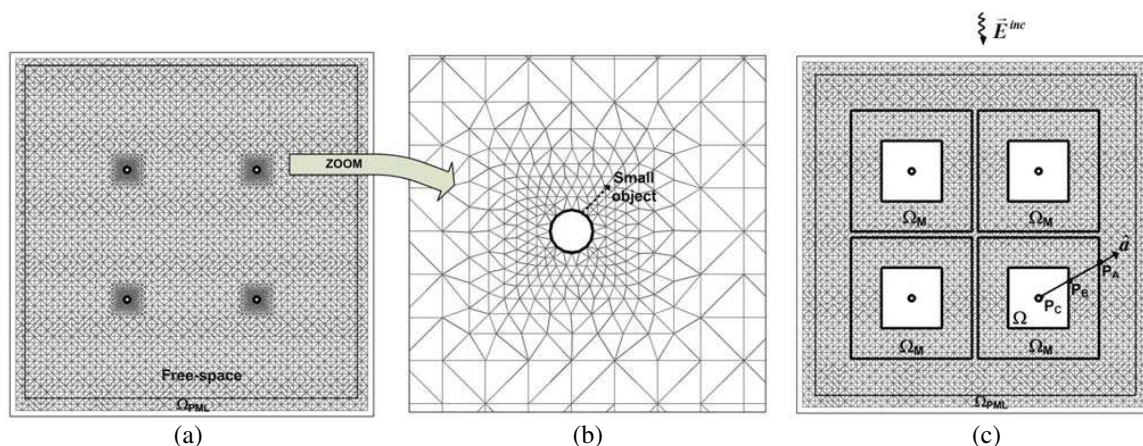


Figure 1: Scattering from four electrically-small objects: (a) Original problem with refined mesh. (b) Zoom-in of mesh refinement. (c) Equivalent problem with anisotropic metamaterial layers and uniform mesh [Ω_M : metamaterial layer, Ω_{PML} : perfectly matched layer].

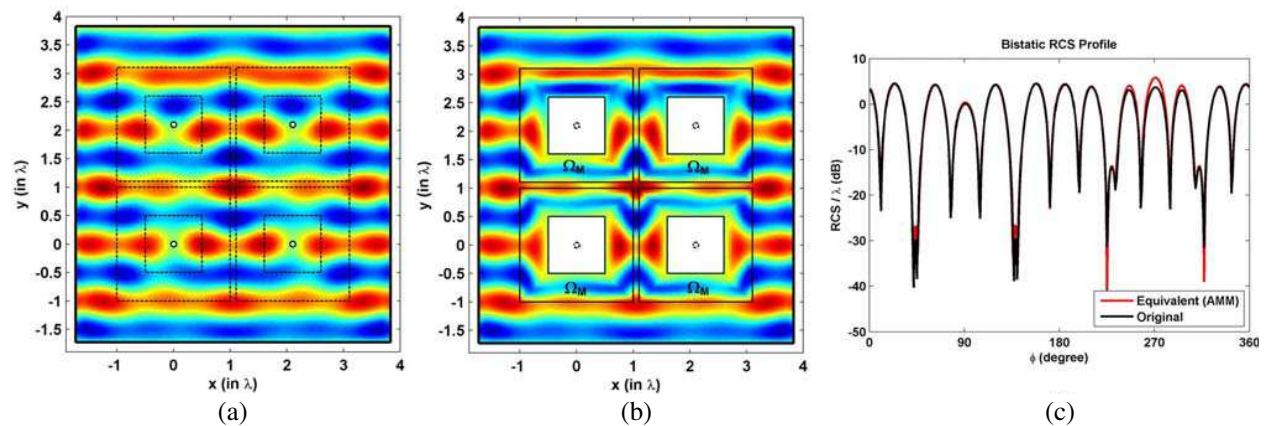


Figure 2: Finite element simulation of scattering from four electrically-small objects: (a) Scattered electric field map in original problem. (b) Scattered electric field map in equivalent problem. (c) Bistatic RCS profile.

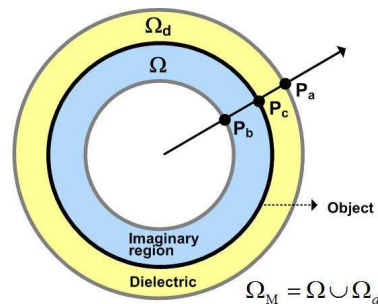


Figure 3: Metamaterial layer design for scattering from an object coated by a dielectric layer.

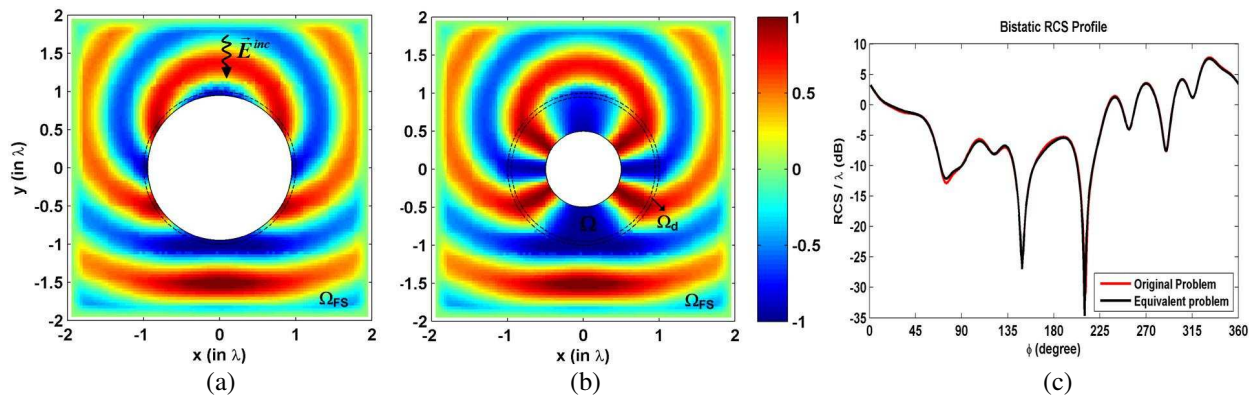


Figure 4: Finite element simulation of scattering from an object coated by an electrically-thin dielectric layer: (a) Scattered electric field map in original problem. (b) Scattered electric field map in equivalent problem. (c) Bistatic RCS profile.

good numerical precision. However, by means of the proposed coordinate transformation technique, it is possible to employ an easy-to-generate mesh without mesh refinement (see Fig. 3). In the design of the metamaterial, the region $\Omega_M = \Omega \cup \Omega_d$ is mapped to the region $\tilde{\Omega} = \Omega_d$, by using (3). This transformation expands the fields inside the thin dielectric layer to the metamaterial region. The finite element simulations are demonstrated in Fig. 4, where a circular object of diameter 2λ is coated by a thin dielectric layer of thickness $\lambda/20$ and dielectric constant 4.

5. CONCLUSIONS

We have proposed new techniques for numerical solution of low-frequency electromagnetic boundary value problems by placing anisotropic metamaterial regions, whose parameters are obtained by the coordinate transformation, within the computational domain to alleviate certain numerical

difficulties. We have observed, through numerical results, that theoretical predictions are in good agreement with the numerical simulations.

REFERENCES

1. Bateman, H., “The transformation of the electro-dynamical equations,” *Proc. London Math. Soc.*, Vol. 8, 223–264, 1910.
2. Lindell, I. V., *Methods for Electromagnetic Field Analysis*, Oxford University Press, 1992.
3. Pendry, J. B., D. Schurig, and D. R. Smith, “Controlling electromagnetic fields,” *Science*, Vol. 312, 1780–1782, 2006.
4. Ozgun, O. and M. Kuzuoglu, “Electromagnetic metamorphosis: Reshaping scatterers via conformal anisotropic metamaterial coatings,” *Microwave Opt. Technol. Lett.*, Vol. 49, No. 10, 2386–2392, 2007.
5. Ozgun, O. and M. Kuzuoglu, “Utilization of anisotropic metamaterial layers in waveguide miniaturization and transitions,” *IEEE Microwave and Wireless Components Letters*, Vol. 17, No. 11, 754–756, 2007.
6. Ozgun, O. and M. Kuzuoglu, “Efficient finite element solution of low-frequency scattering problems via anisotropic metamaterial layers,” *Microwave Opt. Technol. Lett.*, Vol. 50, No. 3, 639–646, 2008.
7. Ozgun, O. and M. Kuzuoglu, “Form-invariance of Maxwell’s equations in coordinate transformations: Metamaterials and numerical models,” *Metamaterials: Classes, Properties and Applications*, Chapter 3, Nova Science, 2010.

A Genetic Algorithm Enhanced by SVM and DPE

Zhi Zheng and Xing Chen

College of Electronics and Information Engineering, Sichuan University, Chengdu 610064, China

Abstract— The Genetic Algorithm (GA) is a popular global optimizer. But in many applications, an optimization process of the GA is very computational cost due to the large quantity of the fitness function evaluations. This paper explores reducing the GA’s computation burden by using approximate function with the Support Vector Machine (SVM) to replace some exact fitness function evaluations and the Dynamic Parameter Encoding (DPE) to compress the solution space adaptively. Numerical results are presented on a series of benchmark functions, and show that in comparison with the traditional GA, the proposed GA enhanced by SVM and DPE is able to reduce the quantity of exact fitness function evaluations more than 55%, or even more than 80% while retains the basic robust search capability.

1. INTRODUCTION

The Genetic Algorithm has achieved great successes in many applications as a global optimizer. But the GA optimization process is usually time-consuming because the fitness function evaluation is a heavy burden, such as the computation of full-wave simulation [1] in antenna design optimization, and it is common that the fitness function evaluations are invoked hundreds or even thousands times before an acceptable solution is found. A promising approach to solve this problem is the application of the approximate function evaluation based on learning machine, such as the Artificial Neural Network [2], the Support Vector Machine [3] and so on, where the computational time of the approximate function evaluation can be considered negligible in comparison with that of exact function evaluation.

In these years the application of approximate function evaluation has been extensively exploited in literatures [4–7]. Duo to the limited number and poor distribution of training data, the high dimensionality of input space and the complication of the object function, it is very difficult for learning machine to obtain a well global approximation of the exact fitness function which means one can get a false optimum (false optimum for exact fitness function but real optimum for approximate function). Many methods have been proposed to tackle this problem, but few of them are directly connected with the accuracy of the approximation function which is the basic cause leading to this problem.

In this work, a method which has a close connection with the accuracy of the approximate function is proposed with SVM as learning machine to replace some exact fitness function evaluations. And in order to improve the efficiency further, DPE [8] is used to compress the solution space adaptively.

2. A BRIEF INTRODUCTION OF SVM AND DPE

2.1. SVM

The SVM algorithm is a nonlinear generalization of the Generalized Portrait algorithm developed in Russia in the 1960s. It is firmly grounded in the framework of statistical learning theory which characterizes it the properties to generalize to unseen data [3].

Loosely speaking, like other learning machines, SVM can “learn” the relationship between the independent and dependent variables of the training data generated by an unknown function and construct an approximate function to describe the relationship.

2.2. DPE

The DPE can alter the mapping from gene to real value adaptively by using convergence statistics derived from the GA population [8]. As shown in Figure 1, each generation the DPE algorithm counts the population over the three overlapping target intervals. If the population counts for any one of them exceeds a given trigger threshold then the search interval is changed from current search interval to the corresponding target interval

DPE works as follows, shorter code length and smaller population size lead to a fast convergence, then the mapping from genes to real values is changed, and another convergence comes, one time after another until a satisfying result got.

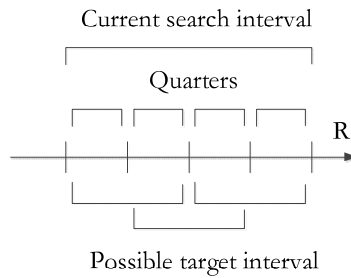


Figure 1: Intervals in DPE.

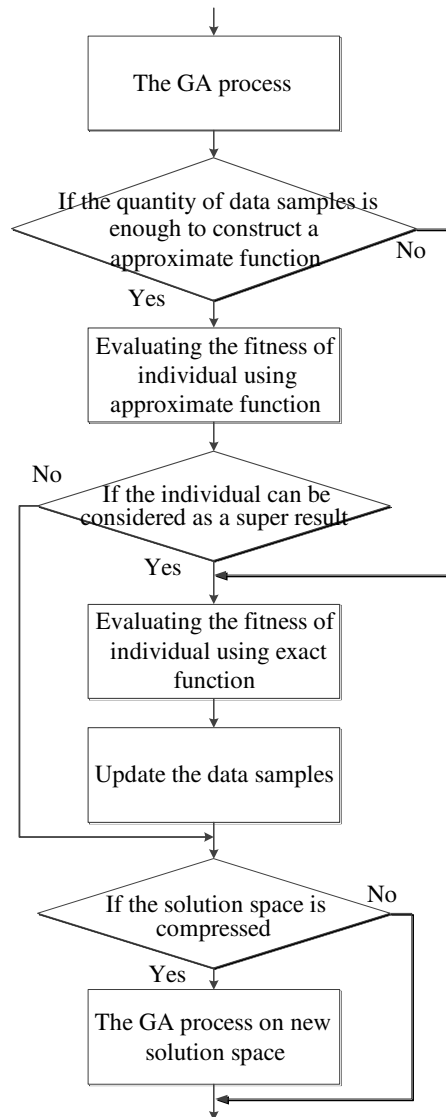


Figure 2: The main procedure of the proposed GA.

3. THE PROPOSED GA

As mentioned above, in order to avoid a false optimum, the approximate function evaluations are usually used together with the exact function evaluations. There are generally two approaches. One is individual-based which means in a population whose size is M , N ($N \leq M$) individuals are reevaluated by exact function evaluation (all individuals are firstly evaluated by approximate function evaluation). The other is generation-based which means in every M generations, all individuals in N ($N \leq M$) generations are reevaluated by exact function evaluation.

As we have known, the super results play an important role in the GA optimization process while other individuals have little effect on the convergence. So it will work well that only the individual which is considered as a super result (fitness ranking by approximate function evaluation) will be reevaluated by exact function evaluation. We can see it is essentially an individual-based method.

The individual whose fitness A evaluated by approximate function satisfies the inequality (1) will be considered as a super result

$$A + \alpha \cdot error \geq B \quad (1)$$

where B is the fitness value of the individual who is the top $a\%$ of the last generation ranking by the fitness, $error$ is the average of the prediction error in last generation. Notice that the prediction error can be evaluated only when it is considered as a super result so one can know its exact fitness value and α is a coefficient.

We can see from inequality (1) that the proposed method is closely associated with the accuracy of the approximate model. If the performance of model is unsatisfying, then $error$ is large, so more individuals will be regarded as super results to avoid that the real super result is missed. It coincides with the situation that when approximate model performs bad, more exact function evaluations are needed to avoid a false optimum. If the approximate model works well, $error$ is small, then less individuals are needed to be reevaluated using exact function to reduce the computational cost as much as possible.

The DPE algorithm here is a little different from its original format but the basic method is not changed. The normal length of gene and size of population is adopted to avoid the constraint of gene so the method can be applied on other algorithms without the gene. And the following results show the changed form can still work well.

The main procedure of proposed GA is shown in Figure 2. At the beginning of the GA optimization, the individuals evaluated using exact fitness function are kept as data samples to train the SVM. During the whole process, the individuals evaluated using exact fitness function are kept and every time the SVM is re-trained by newest data so the constructed approximate function can perform better.

4. EMPIRICAL RESULTS

Some benchmark functions are utilized to verify the performance of the proposed GA. In this work we set $a = 10$ and $\alpha = 1.2$. And the parameters of GA are set as follow: population size 100, crossover probability 0.8, mutation probability 0.05 and using the test function as the objective function. The convergence curves of best fitness are showed below. Every result is averaged over 20 time runs.

We can see from Figure 3 to Figure 6 that the proposed GA enhanced by SVM and DPE can find better solutions with less quantity of exact function evaluations. And the GA enhanced by either DPE or SVM also works better than the traditional GA. The further comparison is listed in Table 1. To get the results which have nearly the same fitness with each other, the computation cost saved by the proposed GA is about 55% for 10D Griewangk's function and 88%, 86% and 83% for 10D Sphere function, 10D Ackley function and 10D Rastrigin function respectively.

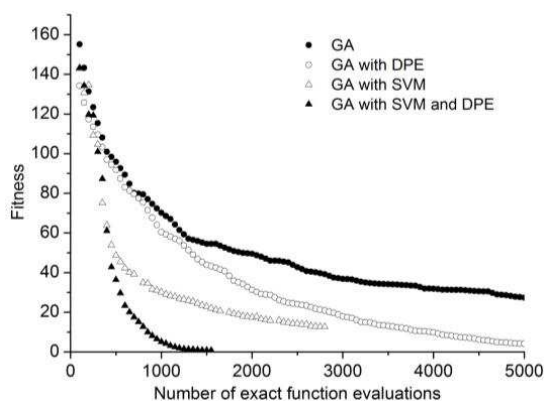


Figure 3: 10D Sphere test function: Fitness of best individual for different methods.

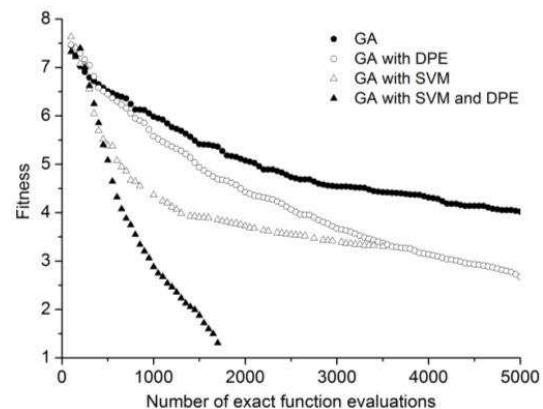


Figure 4: 10D Ackley test function: Fitness of best individual for different methods.

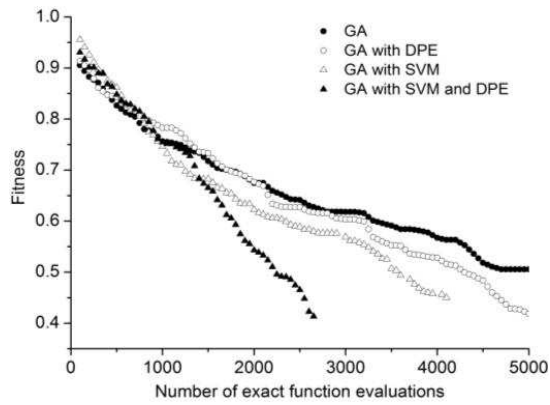


Figure 5: 10D Griewangk's test function: Fitness of best individual for different methods.

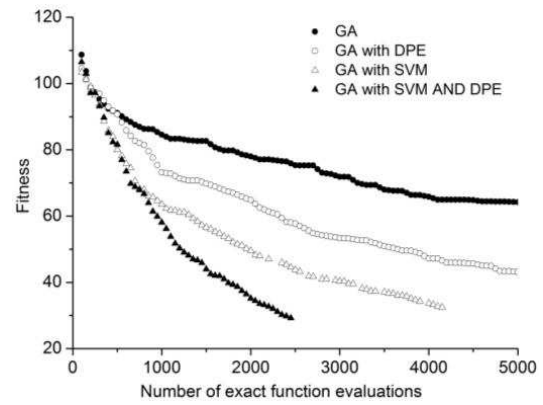


Figure 6: 10D Rastrigin test function: Fitness of best individual for different methods.

Table 1: The comparison of the proposed GA and the traditional GA.

Test function	Traditional GA		Proposed GA	
	Average best fitness	Number of exact function evaluations	Average best fitness	Number of exact function evaluations
10D Sphere	27.4	5000	23.3	600
10D Ackley	4.0	5000	3.9	700
10D Griewangk's	0.5	5000	0.5	2250
10D Rastrigin	64.2	5000	64.0	850

5. CONCLUSION

In this article, a GA with SVM to reduce the computational burden and DPE to compress the solution space for greater efficiency is presented. The method used in this work is close related with the accuracy of the approximate function. Results shows, it can save more than 55% computational time.

REFERENCES

1. Craeye, C., A. G. Tijhuis, and D. H. Schaubert, "An efficient MoM formulation for finite-by-infinite arrays of two-dimensional antennas arranged in a three-dimensional structure," *IEEE Trans. on Antennas and Propag.*, Vol. 52, 271–281, 2004.
2. Hassoun, M. H., *Fundamentals of Artificial Neural Networks*, Prentice Hall of India, New Delhi, 1999.
3. Gunn, S. R., "Support vector machines for classification and regression," *Technical Report*, 6459, 1998.
4. Jin, Y., "A comprehensive survey of fitness approximation in evolutionary computation," *Soft comput.*, Vol. 9, No. 1, 3–12, 2005.
5. Jin, Y. and B. Sendhoff, "Fitness approximation in evolutionary computation: A survey," *Proc. Genetic Evol. Comput. Conf.*, 1105–1112, 2002.
6. Ong, Y. S., P. B. Nair, and A. J. Keane. "Evolutionary optimization of computationally expensive problems via surrogate modeling," *AIAA Journal*, 2003.
7. Oduguwa, V. and R. Roy. "Multiobjective optimization of rolling rod product design using meta-modeling approach," *Genetic and Evolutionary Computation Conference*, 1164–1171, New York, 2002.
8. Schraudolph, N. N. and R. K. Belwe. "Dynamic parameter encoding for genetic algorithms," *Machine Learning*, Vol. 9, 9–21, 1992.

Image Restoration of the Objects with Superresolution on the Basis of Spline — Interpolation

B. A. Lagovsky

Moscow State Institute of Radio Engineering and Automation (Technical University), Russia

Abstract— A new method of digital signal processing, which allows to obtain an image of the object with superresolution presented and validated. The method is based on an approximate numerical solution of Fredholm integral equation of convolution type. Solution is found in the form of a set of discrete points with different amplitudes of the emitted signal, combined into one image using spline interpolation. The maximum effective angular resolution found during the numerical experiments on the mathematical model for different objects.

1. INTRODUCTION

The most important modern trend to improve surveillance and goniometric systems is obtaining images of objects with the highest possible angular superresolution.

The inverse problem of reconstruction the angular distribution of the amplitude of the signal source is investigated. A new method of digital processing of measuring data, which allows to restore the image of objects with superresolution substantiated.

The method is based on the representation of the source in the form of sample values in a number of equally spaced points and carrying-out the spline interpolation. The proposed signal processing allows, increasing the required angular resolution, to approach to the limit of superresolution for each problem. Use of the method is effective in reconstruction images of objects in different ranges of electromagnetic waves, when the identification of objects, in the hydro- and radiolocation, navigation.

2. PROBLEM STATEMENT

Denote the angular distribution of the amplitude of the emitted source (or reflected by) the signal — $I(\alpha)$, the angular dependence of the signal envelope — $U(\alpha)$, radiation pattern — $f(\alpha)$. Then:

$$U(\alpha) = \int_{\Omega} f(\alpha - \phi)I(\phi)d\phi, \quad (1)$$

where Ω — the angular location of the source region.

The problem is to reconstruct the distribution of the amplitude $I(\alpha)$ with the greatest possible accuracy and the highest possible angular resolution, based on the analysis of $U(\alpha)$ and $f(\alpha)$. The problem under consideration belongs to a class of inverse problems. Attempts to increase the angular resolution compared to the classical value of

$$\delta\theta \cong \lambda/D, \quad (2)$$

where D — the size of the aperture, λ — wavelength of the radiation, by solving the Equation (1) lead to the appearance instabilities in the solutions [1, 2].

It is well known that a significant improvement in stability and quality of the solutions can be achieved by using a priori information about the source $I(\alpha)$.

Let a priori or from the analysis of measuring data is known that the zone of the location of the source signal is limited by a certain angular region — Ω . The approximate solution will be constructed by selecting initially values of $I(\alpha)$ in a number of discrete points $\alpha_j \in \Omega$, $j = 1 \dots M$, covering the whole area Ω .

Next, we represent the solution in the form of spline interpolation on these points:

$$I(\alpha) \cong \sum_{j=1}^M S_j(J, \alpha), \quad (3)$$

where S_j — polynomial describing the solution on the interval $[\alpha_j; \alpha_{j+1}]$ and $S_j = 0$ outside it, J — vector of values of the amplitudes of the signal source at selected points with coordinates $J_j = I(\alpha_j)$.

The problem thus reduces to choosing M — the number of restore points, searching the values of $I(\alpha_j)$ at these points and the coefficients of the splines on each interval $[\alpha_j; \alpha_{j+1}]$. The number of points M determines the required resolution.

We introduce the notation: B_j — vectors of coefficients of polynomials S_j . Vectors B_j form a rectangular matrix B . Posed problem of reconstructing the distribution of the amplitude $I(\alpha)$, thus reduced to search the optimum in a certain sense the coefficients of the matrix B .

3. MAIN RESULTS

In a typical problem of constructing the interpolation functions the values of the function itself in a number of discrete points are given. Is required to find the coefficients of the splines. The values $I(\alpha_j)$ in the present problem of finding an approximate solution (1) are not given and worked out together with the values the coefficients of splines.

Using (1, 3):

$$U(\alpha) \cong \sum_{j=1}^M \int_{\Omega} f(\alpha - \phi) S_j(J, \phi) d\phi = \sum_{j=1}^M \tilde{S}_j(J, \alpha), \quad (4)$$

where \tilde{S}_j — integral transformations of splines.

To construct a solution based on (4) values α are chosen, belonging to a certain angular region Ψ , where the signal to noise ratio greater than the minimum acceptable. Usually, Ψ exceeds the location of the source region Ω . It is easy to show that the stability of the solutions of the inverse problem increases with the increasing Ψ .

Functions \tilde{S}_j are defined in Ψ and form nonorthogonal system in it. Since the functions S_j , and, consequently \tilde{S}_j , are completely determined by the matrix B , the inverse problem is parameterized.

Thus, for a given M the approximate solution of the inverse problem reduces to searching the matrix of coefficients B on the basis of the analysis (4).

To construct the solution initially selected the desired resolution, which sets the required number of points M . Further, the solution (4) can be realized in two ways.

First, the traditional way for the problems of this kind is to find a splines coefficients that minimize the standard deviation of the right-hand side of (4) and the values of the received signal $U(\alpha)$ in the sector Ψ .

The second way — replacing the continuous distribution $U(\alpha)$ by a set of discrete values of the signal $V_m = U(\alpha_m)$, $m = 1, 2, \dots, M$ in points covering the whole angular region Ψ . Further in this way, the matrix of coefficients B is calculated, providing the fulfillment strict Equality (4) at these points.

The second way does not guarantee a minimum standard deviation, but it is more stable with respect to the random components in the investigated signal. In addition, the processing of signal in this case is much higher.

Both ways of solving the inverse problem leads to finding solutions of systems of linear algebraic equations.

In the first way, the first M equations of the system are obtained by differentiation:

$$\int_{\Psi} (U(\alpha) - \tilde{S}_j(J, \alpha)) \frac{\partial}{\partial J_m} \tilde{S}_j(J, \alpha) d\alpha = 0, \quad m, j = 1, 2, \dots, M. \quad (5)$$

In the second way, the first M equations are a sampling signal values:

$$U(\alpha_m) = \sum_{j=1}^M \int_{\Omega} f(\alpha_m - \phi) S_j(J, \phi) d\phi, \quad m, j = 1, 2, \dots, M \quad (6)$$

Most widespread type of spline interpolation is to construct cubic function on each interval $[\alpha_n, \alpha_{n+1}]$, $n = 1, 2 \dots M$. On the whole interval, it is piecewise continuous with their first and second derivatives. The coefficients of splines are evaluated from the spline conditions join of solutions of adjacent splines of the nodal points.

These conditions allow us to make $3M$ equations. As a result, we obtain a system of $4M$ equations. The resulting system is a complete system of equations for the values of the function $I(\alpha)$ at the points α_j and the coefficients of all splines.

When using other types of splines conditions of joining of solutions of adjacent splines also allow to get together with (5), (6) a complete system of equations for the coefficients of splines.

Systems of linear equations that need to be solved to determine the coefficients of the splines at given values of J , a well-conditioned. It allows to obtain the coefficients of polynomials with high accuracy. As a result, even with a large number of equations, calculation scheme does not lose stability. Stability of the solutions in these cases completely determined by stability of systems of equations for J_j based on (4).

In an iterative search for the approximate solution of (1) the number of points M consistently increased until it is still possible to obtain stable adequate solutions.

Thus, the proposed method and algorithms based on it make allow to approach to the limit effective angular resolution for each problem to be solved.

4. SIMULATION RESULTS

Quantitative characteristics of superresolution were investigated on a mathematical model. Considered radiation pattern formed by the antenna array with uniform current distribution on the radiators. Dimensions of the antenna array are equal to $30\lambda \times 30\lambda$. First, the characteristics of the object were specified in the form of distribution $I(\alpha)$. Next, the received signal measurement system $U(a)$ was calculated. In the next stage of modeling the inverse problem is solved, i.e., the restoration of the distribution of $I(\alpha)$ by solving the resulting system of linear algebraic Equations (5), (6).

The inverse problem was solved with ever higher resolution, ie sequential increase in the number of points M in (4).

The effectiveness of different types of interpolation was investigated on the model. There are many ways interpolation of functions. Here are some of them.

The easiest and quickest way of interpolation is linear spline. The accuracy of interpolation with linear splines is not very high; in addition, they do not provide the continuity of the derivatives. They should be used for initial estimates of the angular distribution of the amplitude of the signal source.

Their use also is effective in finding the location of discrete sources. In addition, in some cases, a piecewise linear approximation of the function may be preferable to the approximation of higher order. For example, a linear spline preserves the monotonicity given set of points.

Other types of splines interpolation is carried out a bit slower than linear, but the quality of signal restoration is much higher. Using various methods of splines interpolation, for example, Bessel for a smooth signal restoration, or Akima splines to minimize false oscillations we can qualitatively and quickly restore the amplitude distribution $I(\alpha)$ of different types [3, 4].

Figure 1 shows the results of reconstruction of source of signals in the form of two sharp peaks with different amplitudes. Showing: dashed curve — analyzed the received signal $U(\alpha)$, fat dashed curve — the signal source $I(\alpha)$, broken line — reconstructed source on the basis of linear interpolation, fat curve — reconstructed source on the basis of the cubic of interpolation, $\theta_{0,5}$ — the beamwidth.

The quality of source reconstruction of signals should be regarded as a good. The angular resolution exceeds the Rayleigh criterion in 4–5 times. Source positions of the two maxima are found exactly, almost without moving from their true position.

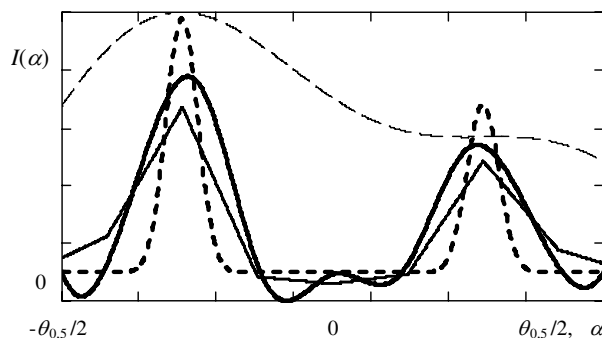


Figure 1: The results of reconstruction of the source image.

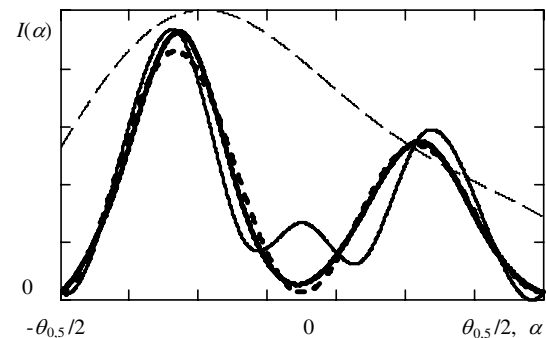


Figure 2: The example of reconstruction.

The results confirm the well-known lack of cubic splines. They begin to oscillate around the point, significantly different from their neighbors. On the segments adjacent to the ejection, the spline deviates noticeably from the interpolated function due to the influence of the ejection. In such a cases, preferable to use Akima spline — a special type of cubic spline that minimizes false oscillations and resistant to outliers. Only data from the next neighbor points is used to determine the coefficients of the interpolation polynomial. There is no need to solve large equation systems and therefore this interpolation method is computationally very efficient [3]. The monotonicity of the specified data points is not necessarily retained by the resulting interpolation function. By additional constraints on the estimated derivatives a monotonicity preserving interpolation function can be constructed [4].

Figure 2 shows the results of source reconstruction of signals in the form of a smooth curve with two maxima. The dashed curve — $U(\alpha)$, thick dashed line — the source of the signal $I(\alpha)$, solid curve — the reconstructed source based on parabolic interpolation, fat curve — source reconstructed by Akima spline.

The distribution of the amplitude of the source of the main peak using a parabolic interpolation was found with high accuracy. The position of the second peak was found with a little mistake. In the area bordering with splashes of functions false oscillations arose.

Using Akima splines allowed almost perfectly restore the image of the object.

5. CONCLUSIONS

Investigation results show that the proposed method of digital signal processing allows to reconstruct images of objects with superresolution with little distortion. The main advantages of spline interpolation are the stability of the obtained solutions and the low labour-intensiveness. Using the suggested algorithms in the design of new systems allows to simplify the technical solutions and to reduce their cost.

The achieved resolution exceeded the Rayleigh criterion in 4–7 times, which coincides with the results obtained by other algebraic methods [5, 6].

REFERENCES

1. Engl, H. W., M. Hanke, and A. Neubauer, *Regularization of Inverse Problems*, Kluwer Academic Publishing, Dordrecht, 2000.
2. Quinquis, A., E. Radoi, and F.-C. Totir, “Some radar imagery results using superresolution techniques,” *IEEE Trans. Antennas and Propagation*, Vol. 52. No. 5, 1230–1244, 2004.
3. Akima, H., “A new method of interpolation and smooth curve fitting based on local procedures,” *J. ACM*, Vol. 17, No. 4, 589–602, 1970.
4. Hyman, J., “Accurate monotonicity preserving cubic interpolation,” *SIAM J. Sci. Stat. Comput.*, Vol. 4, No. 4, 645–654, 1983.
5. Lagovsky, B. A., “High performance angular resolution algorithm for radar systems,” *PIERS Proceedings*, 1637–1641, Moscow, Russia, Aug. 18–21, 2009.
6. Lagovsky, B. A., “Algorithm for the determination of targets coordinates in structure of the multiple targets with the increased effective resolution,” *PIERS Proceedings*, 1642–1645, Moscow, Russia, Aug. 18–21, 2009.

Superresolution: Simultaneous Orthogonalization of Function Systems Describing the Received Signal and its Source

B. A. Lagovsky

Moscow State Institute of Radio Engineering and Automation (Technical University), Russia

Abstract— This paper describes how the quality of image reconstruction signal source can be improved by increasing the stability of the inverse problem. Increased stability is ensured by the simultaneous representation of the solution and the investigated signal in the form of interconnected series.

1. INTRODUCTION

We investigate one of the most important ways to improve a broad class of devices and systems of different physical nature: improving the quality of work by increasing the angular resolution on the basis of new methods and algorithms for signal processing. Used methods and algorithms for digital signal processing, called algebraic, allow to reconstruct the image of objects with superresolution. Their work is based on the carrying out the parameterization of inverse problems and reducing them to ill-conditioned systems of linear algebraic equations.

2. PROBLEM STATEMENT

Suppose that the object of investigation with finite angular size is located in a scan sector. Directional pattern $f(\alpha)$ and the angular dependence of the envelope of the output signal $U(\alpha)$, obtained by scanning the sector for one of the angular coordinates, are given.

The received signal associated with the radiation source by means of integral transform:

$$U(\alpha) = \int_{\Omega} f(\alpha - \phi)I(\phi)d\phi, \quad (1)$$

where Ω — the space angle in which the source is located. Based on analysis of the signal $U(\alpha)$ is required to find the angular distribution of the amplitude of the reflected (or emitted) by the object signal $I(\alpha)$ with the largest possible angular resolution and accuracy. The problem reduces to an approximate solution of (1) — the linear Fredholm integral equation of the first kind of convolution type [1, 2].

Since the required solution $I(\alpha)$ can always be represented as an expansion in the complete orthonormal function system $g_m(\alpha)$ in Ω :

$$I(\alpha) = \sum_{m=1}^{\infty} b_m g_m(\alpha), \quad (2)$$

then the received signal can be written as a superposition of functions $\chi_m(\alpha)$, are the images of $g_m(\alpha)$:

$$\chi_m(\alpha) = \int_{\Omega} f(\alpha - \phi)g_m(\phi)d\phi, \quad U(\alpha) = \sum_{m=1}^{\infty} b_m \chi_m(\alpha) \quad (3)$$

To construct an approximate numerical solution the decomposition of a finite function system when N functions $g_m(\alpha)$ is used. The expansion coefficients b_m can be found by minimizing the standard deviation δ^2 of the finite sum in the form (3) from the $U(\alpha)$ in the scan sector Θ , i.e., by solving the system of equations:

$$\int_{\Theta} U(\alpha)\chi_j(\alpha)d\alpha = \sum_{m=1}^N b_m \int_{\Theta} \chi_j(\alpha)\chi_m(\alpha)d\alpha \quad j = 1, 2, \dots, N \quad (4)$$

In matrix notation by typing:

$$V_j = \int_{\Theta} U(\alpha)\chi_j(\alpha)d\alpha \quad G_{j,m} = \int_{\Theta} \chi_j(\alpha)\chi_m(\alpha)d\alpha \quad (5)$$

we obtain a system of equations for the unknown vector B :

$$V = GB \quad (6)$$

The principal feature of the systems of Equations (5), (6) is their ill-conditioning, which is a consequence of attempts to solve the inverse problem. Even small perturbation by the standards of direct problems of the received signal due to the presence of noise can significantly change the obtained solutions.

Increased stability of solutions can be achieved if the functions $\chi_m(\alpha)$ are orthogonal in the sector Θ . In this case, only the main diagonal elements of the matrix G are nonzero.

The coefficients b_m are arrived directly at a solution of each of Equation (4), but not for solving ill-conditioned systems (5), (6):

$$\int_{\Theta} U(\alpha)\chi_m(\alpha)d\alpha = b_m \int_{\Theta} \chi_m(\alpha)^2 d\alpha \quad m = 1, 2, \dots, N \quad (7)$$

In the role of orthogonal functions $\chi_m(\alpha)$ can act eigen function (1). However, their numerical search even in the case of a degenerate kernel is reduced to solving ill-conditioned problems, and hence to the appearance of instabilities. Construction of an orthogonal function system in sector Θ can be done on the basis of the process of Gram-Schmidt orthogonalization of $\chi_m(\alpha)$. In this case, however, the resulting functions are the images of non-orthogonal functions in sector Ω , and hence the source $I(\alpha)$ is represented as a superposition of non-orthogonal functions, which reduces the quality of the solutions.

The problem arises of choosing an orthonormal function system $\tilde{g}_m(\alpha)$ in Ω , images of which $\tilde{\chi}_m(\alpha)$ are orthogonal in Θ .

3. MAIN RESULTS

To build such a system first, we introduce in Ω an orthonormal function system $\tilde{g}_m(\alpha)$, $m = 1, 2, \dots, N$. On this basis, in accordance with (3) we obtain a nonorthogonal function system $\chi_m(\alpha)$ in Θ . Next, we arrange a matrix of scalar products:

$$S_{m,n} = (\chi_m, \chi_n) = \int_{\Theta} \chi_m(\phi)\chi_n(\phi)d\phi \quad (8)$$

and transform it to a diagonal form, for example, by transforming

$$S = T^T S T, \quad (9)$$

where the columns of the matrix T — eigenvectors of S , T^T — transposed matrix. Also in order to reduce the matrix S to the diagonal form well-known numerical algorithms can be used.

Using the found matrix T , we get a new function system $\tilde{\chi}_m(\alpha)$:

$$\tilde{\chi}_m(\alpha) = \sum_{j=1}^N T_{j,m} \chi_j(\alpha), \quad m = 1, 2, \dots, N. \quad (10)$$

The system (10) is orthogonal in the area Θ , that is easily verified by direct computation of scalar products:

$$(\tilde{\chi}_m, \tilde{\chi}_n) = \sum_{j,i=1}^N T_{j,m} T_{i,n} \int_{\Theta} \chi_j(\phi)\chi_i(\phi)d\phi = \sum_{j,i=1}^N T_{j,m} T_{i,n} S_{j,i} = \bar{S}_{m,n}, \quad (11)$$

where $S_{m,n}$ — diagonal matrix elements (9).

So we find the function system $\tilde{g}_m(\alpha)$ that generates the resulting orthogonal system (10):

$$\tilde{\chi}_m(\alpha) = \int_{\Omega} f(\alpha - \phi) \tilde{g}_m(\phi) d\phi, \quad m = 1, 2, \dots, N. \quad (12)$$

From (10):

$$\tilde{\chi}_m(\alpha) = \sum_{j=1}^N T_{m,j} \int_{\Omega} f(\alpha - \phi) g_j(\phi) d\phi = \int_{\Omega} f(\alpha - \phi) \left(\sum_{j=1}^N T_{m,j} g_j(\phi) \right) d\phi \quad (13)$$

Comparing (12) and (13), we obtain:

$$\tilde{g}_m(\alpha) = \sum_{j=1}^N T_{m,j} g_j(\alpha) \quad (14)$$

Therefore, the desired function system is a superposition of the original functions $g_m(\alpha)$. Moreover, it is formed by the same linear transformation (10) as the system $\tilde{\chi}_m(\alpha)$.

The obtained system (14) is orthogonal in the location of the source area Ω .

Indeed, since the functions $g_m(\alpha)$ are orthogonal and eigenvectors of S , that form a matrix T , are orthogonal too, we obtain:

$$\int_{\Omega} \tilde{g}_m(\phi) \tilde{g}_n(\phi) d\phi = \sum_{j,i=1}^N T_{m,j} T_{n,i} \int_{\Omega} g_j(\phi) g_i(\phi) d\phi = \begin{cases} 0, & m \neq n \\ \lambda_m, & m = n \end{cases}, \quad \lambda_m = \sum_{j=1}^N T_{m,j}^2, \quad (15)$$

Thus, based on a given of N orthogonal in Ω functions $g_m(\alpha)$ we constructed a new orthogonal in the same range function system $\tilde{g}_m(\alpha)$. It generates an system of functions $\tilde{\chi}_m(\alpha)$ orthogonal in Θ . The resulting system (14) and initial system (10) allow us simultaneously to present the required solution, and analyzed signal $U(\alpha)$ in the form of expansions in orthogonal functions, which simplifies the analysis of the problem and its numerical solution.

As a result, representing the received signal in the form:

$$U(\alpha) \cong \sum_{m=1}^N C_m \tilde{\chi}_m(\alpha) \quad (16)$$

we find the coefficients of the expansion:

$$C_m = \frac{1}{P_m} \int_{\Theta} U(\alpha) \tilde{\chi}_m(\alpha) d\alpha, \quad P_m = \int_{\Theta} \tilde{\chi}_m(\alpha)^2 d\alpha \quad (17)$$

The received signal, using (1), (14), (16), also can be written as:

$$U(\alpha) = \int_{\Theta} f(\alpha - \phi) I(\phi) d\phi \cong \sum_{m=1}^N C_m \tilde{\chi}_m(\alpha) = \int_{\Theta} f(\alpha - \phi) \left(\sum_{m=1}^N C_m \tilde{g}_m(\phi) \right) d\phi \quad (18)$$

Equating the integrands in (18), we obtain an approximate solution to the inverse problem as an expansion in a finite function system introduced by (14) or by the original system $g_m(\alpha)$:

$$I(\alpha) \cong \sum_{m=1}^N C_m \tilde{g}_m(\alpha) \quad I(\alpha) = \sum_{j=1}^N b_j g_j(\alpha), \quad b_j = \sum_{m=1}^N C_m T_{m,j} \quad (19)$$

The open question is the choice of the initial function system $g_m(\alpha)$. At the same stability of algorithms based on various $g_m(\alpha)$ the degree of conformity the obtained approximate solutions to the true depends on the chosen function system.

The choice of the $g_m(\alpha)$ should be based on a priori, and also detected in the signal processing new information about the solution. Such information can be, in particular, the size and location of source localization, monotonicity, smoothness, continuity of the angular distribution of the amplitude of the emitted signal, the presence of regions with a discrete distributions, the dynamic range of intensity changes, restrictions on the gradient, and other characteristics.

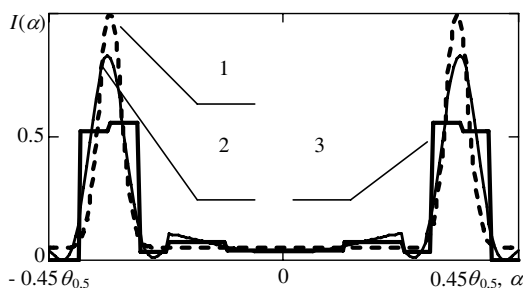


Figure 1: Restoration of the angular distribution of the amplitude of the reflected signal.

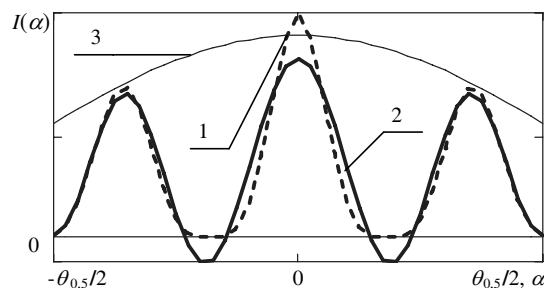


Figure 2: Restored images of the three sources not resolved in the ordinary observation.

4. SIMULATION RESULTS

Quantitative characteristics of increasing angular resolution and its boundaries were studied on a mathematical model.

Figure 1 shows an example of a source image reconstruction with large gradients of the angular distribution of the signal amplitude, and localization of small areas comparable to the width of the beam.

The sources of this type can be conveniently represented as a superposition of wavelets. Wavelets can simultaneously describe the general form of the source and its local features up to the gaps that can not be detected by, for example, the Fourier transform. Showing: 1 — the true distribution, 2 — the distribution, obtained by using MHAT-wavelets, 3 — distribution obtained by using Haar wavelets.

Signal processing has improved the stability of the solutions in comparison with (5), (6) and increase the effective angular resolution is 3 times as compared to the Rayleigh criterion. The quality of the reconstructed image was good.

The effective resolution can be increased (in 5–7 times), but the image quality deteriorates.

The value of the achieved degree of superresolution is limited by the signal-to-noise ratio.

The developed algorithms allow to restore the image at a lower signal-to-noise ratio than many of the known methods by increasing the stability of the solutions — at 15–20 dB, and sometimes at 12–13 dB.

The use of smooth functions effective to represent the solutions with a priori information about the continuous distribution of the emitted signal amplitude with a relatively small gradient.

One option is the use of Fourier series. Figure 2 shows the solution of this problem. We set out results when using the first 5 functions of the chosen function system. By rational choice of the functions the approximate solution was close to true. Effective resolution exceeded the Rayleigh criterion in more than three times.

Showing: 1 — the true intensity distribution of the source, 2 — approximate solution using 5 functions, 3 — investigated received signal.

5. CONCLUSIONS

The use of orthogonal function systems $\tilde{g}_m(\alpha)$ and $\tilde{\chi}_m(\alpha)$ allowed us to obtain more effective solution with high quality image reconstruction of objects than when solving the inverse problem with the help of other algebraic methods [3, 4]. Image signal sources can be restored with an angular resolution in 2–5 times higher than Rayleigh criterion. The relatively small amount of computation allows the processing of signals in a time comparable with the time of observation of the object, i.e., in real time mode.

REFERENCES

1. Park, S. C., M. K. Park, and M. G. Kang, "Super-resolution image reconstruction: A technical overview," *IEEE Signal Processing Magazine*, Vol. 20, No. 3, 21–36, 2003.
2. Aubert, G. and P. Kornprobst, *Mathematical Problems in Image Processing*, Springer Science, New York, 2006.
3. Lagovsky, B. A., "High performance angular resolution algorithm for radar systems," *PIERS Proceedings*, 1637–1641, Moscow, Russia, Aug. 18–21, 2009.
4. Lagovsky, B. A., "Algorithm for the determination of targets coordinates in structure of the multiple targets with the increased effective resolution," *PIERS Proceedings*, 1642–1645, Moscow, Russia, Aug. 18–21, 2009.

Cellular Communication by Magnetic Scalar Waves

Konstantin Meyl

Faculty of Computer and Electrical Engineering, Furtwangen University, Germany

Abstract— The DNA generates a longitudinal wave which propagates within the magnetic field vector. Computed frequencies from DNA structure agree with bio photon radiation frequencies as predicted. Optimization of efficiency is done by minimizing the conduction losses which leads to the double helix structure of DNA. The vortex model of the magnetic scalar wave not only covers the many observed structures within the nucleus but also introduces the reader to the hyperboloid channels in the matrix as two cells are then found to communicate with each other. Physical results were revealed in 1990 which form the theoretical basis of the essential component of a potential vortex scalar wave. An extended field theory approach has been known since 2009 following the discovery of magnetic monopoles. For the first time magnetic scalar wave theory best explains the physical basis of life not only from the biological discipline of science understanding only. And for the first time this interdisciplinary theory and provides a new understanding of cellular functions that are explained such theory depicting the complex relationships of nature. The characteristics of the potential vortex are decisive. Now using the concentration effect, my theory provides a cellular miniaturization view down to a few nanometers. This theory for the first time allows a better understanding of the outrageously high information density in the nucleus. Magnetic scalar wave theory explains how the dual base pair-stored information of the genetic code is formed. The process of converting electrical modulation into “piggyback” information that transfers or is send from the cell nucleus to another cell is a revolutionary theory. Information transferred at the receiving end during the reverse process takes place involving a change in the physical and chemical cellular structure. The energy required to power the chemical process, is now understood by the extended field theory to come from the magnetic scalar wave itself.

This article has been removed from the website on February 1, 2013, because it has been found that its contents have been published in other journals [1,2] and violate self-plagiarism and copyright infringement rules of PIERS Proceedings.

[1] Meyl, K., “Task of the introns, cell communication explained by field physics,” *Journal of Cell Communication and Signaling*, Vol. 6, No. 1, 53–58, 2012.

[2] Meyl, K., “DNA and cell resonance: Magnetic waves enable cell communication,” *DNA and Cell Biology*, Vol. 31, No. 4, 422–426, 2012.

The Theoretical Rationale of the Existence of Electric and Magnetic Fields Spreading Instantaneously

A. Chubykalo, A. Espinoza, and R. Ivanov

Unidad Académica de Física, Universidad Autónoma de Zacatecas, A. P. C-580, Zacatecas, México

Abstract— In this note, we show that the use of the Helmholtz vector decomposition theorem leads to the theoretical rationale of the existence of solenoidal electric and magnetic fields which can spread instantaneously.

In the comparatively recent experimental work [1] it was shown that the standard retardation condition does not take into account the complex structure of the whole electromagnetic field in the near zone. In the experiment described in [1] this unusual conclusion was obtained: the bound magnetic field in the near zone spreads with the velocity $v \gg c$, i.e., practically instantaneously. Is it possible to explain this surprising result within the framework of classical electrodynamics? In the modern literature many publications dedicated to the problem of instantaneous action at a distance (IAAD) just in classical electrodynamics do not exist. But among the few works devoted to this topic, from our point of view the most important from them are the following [2–8].

In the present work, we try to explain the result obtained in [1] taking advantage of the results of [2]. In this work the authors of [2] applied Helmholtz theorem to the vector fields in the Maxwell equations

$$\left. \begin{aligned} \nabla \cdot \mathbf{E} &= 4\pi\rho \\ \nabla \times \mathbf{E} &= -\frac{1}{c} \frac{\partial \mathbf{B}}{\partial t} \\ \nabla \cdot \mathbf{B} &= 0 \\ \nabla \times \mathbf{B} &= \frac{1}{c} \frac{\partial \mathbf{E}}{\partial t} + \frac{4\pi}{c} \mathbf{j} \end{aligned} \right\}, \quad (1)$$

(let us remind ourselves that Helmholtz vector decomposition theorem reads as follows¹: *If the divergence $D(\mathbf{r})$ and curl $\mathbf{C}(\mathbf{r})$ of a vector function $\mathbf{F}(\mathbf{r})$ are specified, and if they both go to zero faster than $1/r^2$ as $r \rightarrow \infty$, and if $\mathbf{F}(\mathbf{r})$ itself tends to zero as $r \rightarrow \infty$, then $\mathbf{F}(\mathbf{r})$ is uniquely given by*

$$\mathbf{F} = -\nabla U + \nabla \times \mathbf{W}, \quad (H)$$

where

$$U(\mathbf{r}) = \frac{1}{4\pi} \iiint_{\text{All space}} \frac{D(\mathbf{r}')}{|\mathbf{r}-\mathbf{r}'|} d^3\mathbf{r}', \quad (H1)$$

and

$$\mathbf{W}(\mathbf{r}) = \frac{1}{4\pi} \iiint_{\text{All space}} \frac{\mathbf{C}(\mathbf{r}')}{|\mathbf{r}-\mathbf{r}'|} d^3\mathbf{r}', \quad (H2)$$

where the vector $-\nabla U$ is the irrotational component of \mathbf{F} and the vector $\nabla \times \mathbf{W}$ is the solenoidal one). As the result in [2] it was obtained that

$$\left. \begin{aligned} \mathbf{E} &= \mathbf{E}_i + \mathbf{E}_s \\ \mathbf{B} &= \mathbf{B}_i + \mathbf{B}_s \\ \mathbf{j} &= \mathbf{j}_i + \mathbf{j}_s \end{aligned} \right\}, \quad (2)$$

where indexes “ i ” and “ s ” signify irrotational (curl-less) and solenoidal (divergence-less) components of the vectors, respectively, and, for example,

$$\mathbf{j}_i = -\frac{1}{4\pi} \nabla \iiint_{\text{All space}} \frac{\nabla' \cdot \mathbf{j}(\mathbf{r}', t)}{|\mathbf{r}-\mathbf{r}'|} d^3\mathbf{r}' \quad (3a)$$

¹See, e.g., §1.16, p. 92 in [9]

and

$$\mathbf{j}_s = \frac{1}{4\pi} \nabla \times \iiint_{\text{All space}} \frac{\nabla' \times \mathbf{j}(\mathbf{r}', t)}{|\mathbf{r} - \mathbf{r}'|} d^3\mathbf{r}'. \quad (3b)$$

It was also obtained that for the irrotational components from (1) and (2)

$$\left. \begin{aligned} \nabla \cdot \mathbf{E}_i &= 4\pi\rho \\ \frac{\partial \mathbf{E}_i}{\partial t} &= -4\pi\mathbf{j}_i \end{aligned} \right\}, \quad (4)$$

$$\left. \begin{aligned} \nabla \cdot \mathbf{B}_i &= 0 \\ \frac{\partial \mathbf{B}_i}{\partial t} &= 0 \end{aligned} \right\}, \quad (5)$$

and for the solenoidal components from (1) and (2)

$$\left. \begin{aligned} \nabla \times \mathbf{E}_s &= -\frac{1}{c} \frac{\partial \mathbf{B}_s}{\partial t} \\ \nabla \times \mathbf{B}_s &= \frac{1}{c} \frac{\partial \mathbf{E}_s}{\partial t} + \frac{4\pi}{c} \mathbf{j}_s \end{aligned} \right\}. \quad (6)$$

From Eq. (5) it is clear that $\mathbf{B}_i = 0$, and from Eq. (4) one can deduce that the irrotational part of the electric field is not associated with any magnetic field. But then combining Eq. (6) one can obtain wave equations for \mathbf{E}_s and \mathbf{B}_s

$$\nabla^2 \mathbf{E}_s - \frac{1}{c^2} \frac{\partial^2 \mathbf{E}_s}{\partial t^2} = \frac{4\pi}{c^2} \frac{\partial \mathbf{j}_s}{\partial t}, \quad (7)$$

$$\nabla^2 \mathbf{B}_s - \frac{1}{c^2} \frac{\partial^2 \mathbf{B}_s}{\partial t^2} = -\frac{4\pi}{c} \nabla \times \mathbf{j}_s. \quad (8)$$

From the first equation of Eq. (4), one can deduce that \mathbf{E}_i can propagate instantaneously only (i.e., with infinity velocity), whereas solutions of Eqs. (7) and (8) for \mathbf{E}_s and \mathbf{B}_s can characterize waves spreading with the finite velocity c . Nevertheless, wave solutions do not comprise *all* possible solutions of Eqs. (7) and (8) or solutions of the equivalent system (6).

Indeed, as it was shown in [2]

$$\mathbf{B}_s = \nabla \times \mathbf{A}_s \quad \text{and} \quad \mathbf{E}_s = -\frac{1}{c} \frac{\partial \mathbf{A}_s}{\partial t}, \quad (9)$$

where \mathbf{A}_s is the solenoidal component of the magnetic vector-potential \mathbf{A} , and \mathbf{A}_s satisfies the equation

$$\nabla^2 \mathbf{A}_s - \frac{1}{c^2} \frac{\partial^2 \mathbf{A}_s}{\partial t^2} = -\frac{4\pi}{c} \mathbf{j}_s. \quad (10)$$

Let us seek for *such* solution $\mathbf{A}_{s(inst)}$ of this equation which gives us

$$\frac{\partial^2 \mathbf{A}_{s(inst)}}{\partial t^2} = 0. \quad (11)$$

It means that this solution of (10) is also the solution of the equation

$$\nabla^2 \mathbf{A}_{s(inst)} = -\frac{4\pi}{c} \mathbf{j}_s, \quad (12)$$

and this in turn means that $\mathbf{A}_{s(inst)}$ is an instantaneous field although it is the solution of Eq. (10). In this case fields $\mathbf{E}_{s(inst)}$ and $\mathbf{B}_{s(inst)}$ obtained from Eq. (9) give us the equations

$$\nabla^2 \mathbf{E}_{s(inst)} = \frac{4\pi}{c^2} \frac{\partial \mathbf{j}_s}{\partial t}, \quad (13)$$

and

$$\nabla^2 \mathbf{B}_{s(inst)} = -\frac{4\pi}{c} \nabla \times \mathbf{j}_s, \quad (14)$$

that means instantaneous action for the fields $\mathbf{E}_{s(inst)}$ and $\mathbf{B}_{s(inst)}$.

This case ($\frac{\partial^2 \mathbf{A}_{s(inst)}}{\partial t^2} = 0$), considering the second equation of (9), corresponds to

$$\frac{\partial \mathbf{E}_{s(inst)}}{\partial t} = 0, \quad (15)$$

accordingly Eq. (6) convert themselves into

$$\left. \begin{aligned} \nabla \times \mathbf{E}_{s(inst)} &= -\frac{1}{c} \frac{\partial \mathbf{B}_{s(inst)}}{\partial t} \\ \nabla \times \mathbf{B}_{s(inst)} &= \frac{4\pi}{c} \mathbf{j}_s \end{aligned} \right\}. \quad (16)$$

So $\mathbf{B}_{s(inst)}$ as well as \mathbf{j}_s are linear functions with respect to time. In other words, the case $\frac{\partial^2 \mathbf{A}_{s(inst)}}{\partial t^2} = 0$ means that

$$\mathbf{A}_{s(inst)}(\mathbf{r}, t) = \mathbf{A}_{s0}(\mathbf{r}) + t\mathbf{A}_{s1}(\mathbf{r}), \quad (17)$$

$$\mathbf{E}_{s(inst)} = -\frac{1}{c} \mathbf{A}_{s1}(\mathbf{r}), \quad (18)$$

$$\mathbf{B}_{s(inst)} = \nabla \times \mathbf{A}_{s0}(\mathbf{r}) + t\nabla \times \mathbf{A}_{s1}(\mathbf{r}), \quad (19)$$

$$\mathbf{j}_s = -\frac{c}{4\pi} \nabla^2 \mathbf{A}_{s0}(\mathbf{r}) - \frac{c}{4\pi} t \nabla^2 \mathbf{A}_{s1}(\mathbf{r}). \quad (20)$$

So one can infer that instantaneous field $\mathbf{A}_{s(inst)}$ generates instantaneous fields $\mathbf{E}_{s(inst)}$ and $\mathbf{B}_{s(inst)}$, and the current \mathbf{j}_s generating the field $\mathbf{A}_{s(inst)}$ must be linear functions with respect to time.

It is obvious that our field $\mathbf{B}_{s(inst)}$ can play the role of the *bound magnetic field in the near zone spreading with the infinite velocity (i.e., instantaneously)* that has been observed in [1]. The authors of the paper [1] obtained experimentally the propagation speed of bound magnetic field. The measurements consisted of measuring the dependence of the propagation time between emitting multisection loop antenna and receiving multisection loop antenna, on the distance between them. The authors conclude that experimental data do not support the validity of the standard retardation constraint $v = c$, generally accepted in respect to bound fields. In contrast, in the paper [1] one can see nearly perfect coincidence between experimental data and theoretical prediction when the retardation parameter v for bound fields highly exceeds the velocity of light, i.e., $v > 10c$. Thus it can be considered that the existence of superluminal (de facto instantaneous) bound magnetic field generated by the current linearly dependent on time, recently experimentally demonstrated in [1], now is theoretically substantiated.

REFERENCES

1. Kholmetskii, A., O. Missevitch, R. Smirnov-Rueda, R. Ivanov, and A. Chubykalo, "Experimental test on the applicability of the standard retardation condition to bound magnetic fields," *Journal of Applied Physics*, Vol. 101, 023532-1-11, 2007, doi:10.1063/1.2409771.
2. Chubykalo, A., A. Espinoza, and R. Alvarado-Flores, "Electromagnetic potentials without gauge transformation," *Physica Scripta*, Vol. 84, 015009-1-6, 2011, doi:10.1088/0031-8949/84/01/015009, (see also Corrigendum for the article *Phys. Scr.*, Vol. 84, 015009, doi:10.1088/0031-8949/84/6/069502).
3. Hill, R. N., "Instantaneous action-at-a-distance in classical relativistic mechanics," *J. Math. Phys.*, Vol. 8, 201–220, 1967, doi:10.1063/1.170518.
4. Hirondel, D., "Free-particle-like formulation of Newtonian instantaneous action-at-a-distance electrodynamics," *J. Math. Phys.*, Vol. 15, 1689–1697, 1974, doi: 10.1063/1.170518.
5. Hoil, F. and J. Narlikar, "Cosmology and action-at-a-distance electrodynamics," *Rev. Mod. Phys.*, Vol. 67, 113–155, 1995.
6. Vilecco, R., "Instantaneous action-at-a-distance representation of field theories," *Phys. Rev. E*, Vol. 48, 4008–4026, 1993.
7. Chubykalo, A. and S. Vlaev, "Necessity of simultaneous co-existence of instantaneous and retarded interactions in classical electrodynamics," *Int. J. Mod. Phys. A*, Vol. 14, 3789–3798, 1999, DOI: 10.1142/S0217751X99001755.

8. Heras, J., “A formal interpretation of the displacement current and the instantaneous formulation of Maxwell’s equations,” *Am. J. Phys.*, Vol. 79, 409, 2011.
9. Arfken, G. B. and H. J. Weber, *Mathematical Methods for Physicists*, Academic, New York, 1995.

A Local Ether Lens Path Integral Model of Electromagnetic Wave Reception by Wires

M. J. Underhill

Underhill Research Ltd., UK

Abstract— At present there is no *direct* theory of reception of radiation by a thin wire antenna such as a simple half-wave dipole. The capture aperture of a wire dipole is much larger than the physical area of the wire. The explanation is that the local ether formed around the wire acts as a lens to focus the incoming radiation on to the wire. The lens is formed by EM coupling which appears to be inversely proportional to the square root of frequency. The profile of the lens is assumed to be determined by a summation of all possible coupling paths, similar to the formation of the Feynman Path Integral in quantum theory. Here we investigate the power flow path trajectories taken by the radiation in the near field local ether focussing region. We find a transcendental differential equation for partially refracted radiation trajectories starting just outside the edge of the capture area with the assumption of a defined radial refractive index profile. This equation appears not to be analytically soluble. But stepped ‘projectile’ and heuristic solutions can be found numerically. Examples are given for the sets of trajectories well above and well below a critical frequency at which the EM coupling limit distance is approximately equal to the half-width of the capture aperture.

1. INTRODUCTION

The objective is a *direct* theory of reception including the power flow lines of the radiation for a thin wire antenna such as a simple half-wave dipole. Rivni and Papas [1] have considered Poynting Vector power flow lines qualitatively in some interesting special cases, but not in the specific case of reception by a wire dipole. They conclude that power flow-line equations are not easily soluble, but nonetheless present some useful qualitative solutions.

At present there is no *direct* theory of reception to be found in the literature. Thus the question of power flow lines for reception by antennas appears never to have been addressed before. The question to be answered is how does the incoming power from a given capture become focussed on to the much smaller surface area of the antenna wire?

The generally accepted *indirect* theory of reception is based on the ‘theory of reciprocity’. This states that the radiation patterns of any antenna are the same for transmission and reception. The transmit pattern can be computed directly on the classical assumption that the conductor currents are the source of radiation from a wire antenna. A small current element is found to have the classical toroidal ‘doughnut’ shaped radiation pattern. The pattern of a half-wave dipole is computed by applying array theory to combine the current elements of the dipole antenna. As a consequence the doughnut pattern of a half pattern is slightly flattened as compared with a small dipole or a single current element. The indirect theory then uses reciprocity to state that the pattern, aperture shape in any direction, and therefore the ‘directivity’ of an antenna is the same for transmission as for reception. (The directivity is the same as the gain of an antenna, if the antenna is 100% efficient).

By applying antenna array aperture theory to the dipole doughnut pattern, we find that the maximum receive ‘capture’ aperture area of a dipole is an ellipse with major axis of about $\lambda/2$ at right angles to the dipole wire and a minor axis of about $\lambda/4$ along the wire. Note that the dipole capture area is many times the physical area of the dipole wire. The inescapable conclusion is that the presence of the dipole has modified the properties (ϵ , μ , impedance, and refractive index η) of the local space surrounding the dipole at least out to a distance comparable with the half-major axis. This modification of space is the ‘local ether’ [2]. It then follows that the local ether effectively is a lens that focuses incoming radiation from an area equal to the antenna aperture onto the wire of the dipole. The problem then is to find the local refractive index profile and the power flow lines of the incoming energy captured by the antenna. Here we consider power flow-lines as ‘missile trajectories’ and also ‘heuristic’ solutions are obtained. The heuristic solutions are obtained by dividing the trajectory into two parts for which analytic solutions can be obtained. The two parts are then joined heuristically to obtain the best fit with the assumed EM physics. Energy conservation and power continuity are essential assumptions.

In principle the refractive index profile may then be obtained. If this is known already for example from real measurements or some assumed but calibrated EM physics the parameters of the heuristic equations can be adjusted for the best fit.

The method has been implemented in an analytic Mathcad simulation. This is a direct simulation that does not require any matrix inversion. It is not a finite element method. The complexity of representation may therefore be increased to any desired level without excessive simulation times being required.

2. POWER-FLOW TRAJECTORY EQUATIONS

Figure 1 shows a set of paths on a central cross-section of space heuristically derived from the ‘uniform distribution’ assumption that the uniform incoming energy density finally approaches the wire with uniform angular intensity. Only the energy within the boundaries of the antenna aperture on the left is focussed onto and collected by the wire antenna at 0.0 on the right. This is an assumption that may not be exactly true in practice but without some assumption on the final approach angle of the energy there is not enough information for a solution set of trajectories to be obtained. The problem would then be ‘under-defined’.

Figure 2 shows the geometry for a single trajectory. The distance along the trajectory is s . The radial distance from the final focal point is r . The angle of the radius to the horizontal is θ_1 . The angle between s and r at any point is θ_2 . The angle between the trajectory and the horizontal is the difference $\theta_1 - \theta_2$.

3. THE LOCAL ETHER REFRACTIVE INDEX PROFILE

The wire dipole antenna modifies the effective refractive index of the space surrounding the antenna. A ‘local ether’ is formed. The refractive index $\eta(r)$ is assumed to be circularly symmetrical about the wire and in general to increase towards the wire, but with no mathematical singularity assumed at the centre of the wire. The singularity is removed by assuming the index profile is defined by the (newly discovered) laws of EM coupling [2]. The profile is taken to be the same as the EM energy surrounding a Goubau single wire transmission line, shown in Figure 2(a) of reference [2]. Two cases for $\eta(r)$ are considered. These are where the flat highly coupled central region is respectively (a) much smaller, and (b) significantly larger, than the width of the dipole capture area.

Ideally the refractive index $\eta(r)$ should be taken to be a radially symmetric function given by an evanescent wave profile of the type shown in Equation (1) of reference [1]:

$$\eta(r) = \eta(0) \left(1 - e^{-\kappa_n / (\sqrt{f} \times r^n)} \right) \quad (1)$$

where n is best taken to be $n = 1$ in this case. However up to $n = 3$ could be more representative if and when measurements of the actual profiles can be obtained directly.

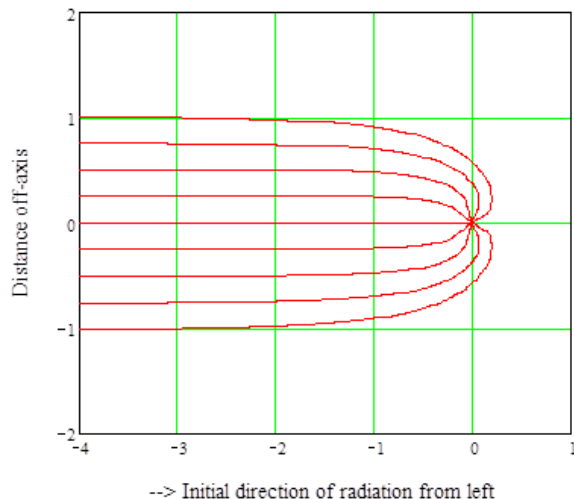


Figure 1: Power flow trajectories from aperture left to all angles on a wire dipole at 0.0 on right.

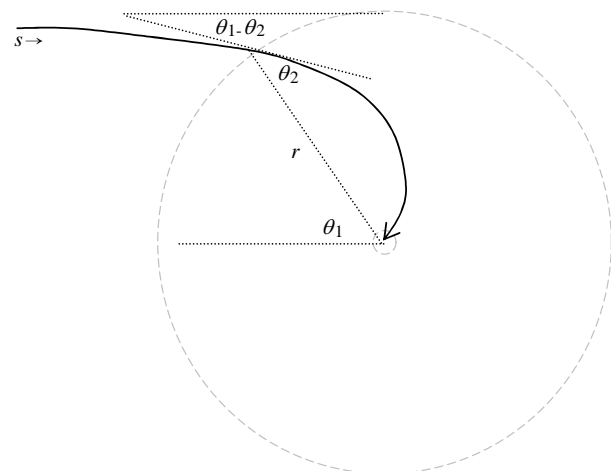


Figure 2: Geometry of a power flow trajectory from aperture left to a wire dipole on right.

Actually the local refractive index profile cannot be obtained from the trajectory equations without knowledge of the EM velocity along the trajectory. It may be that the radial velocity differs substantially from the circumferential velocity. Further measurements need to be made confirming whatever physics assumptions are valid in this case. At present there is no known way of determining the exact trajectory paths by measurements of sufficient accuracy to be of use.

4. EM COUPLING AND THE FEYNMAN PATH INTEGRAL

The refractive index profile of Equation (1) has been derived from the assumption of the existence of ‘EM coupling’ [3]. The EM coupling between two points in space is actually a Feynman ‘path integral’ as used in Quantum Theory. The Feynman path integral is explained in terms of probabilities of each path that a particle could possibly take but still to take another path. In this case the probability values are changed into EM coupling factor values. Equation (1) can be said to be the outcome of a Feynman path integral process applied to the EM coupling.

The EM coupling for wire elements is given by the evanescent wave profile solutions given in Equation (1), has also been shown to be inversely proportional to the square root of frequency [2]. This implies two types of path profile solutions, above and below a transition frequency of about 20 MHz. At high frequencies (THz) we find that energy is scattered or reflected from the local ether out to a distance of several wavelengths.

5. POWER FLOW TRAJECTORY EQUATIONS

We find a transcendental differential equation for partially refracted radiation trajectories starting just outside the edge of the capture area with the assumption of a defined radial refractive index profile, and with the variables as shown in Figure 2. Also we use s as a convenient parameter that is approximately equal to the distance along the trajectory. And y_0 is the initial vertical height of the trajectory.

$$d\theta_2/ds = y_0 \sin \theta_1 + \eta(r) \cos \theta_2 \quad \text{where} \quad x = r \cos \theta_1 \quad \text{and} \quad y = r \sin \theta_1 \quad (2)$$

It appears that this equation does not have a simple analytic solution. In principle it can be solved as a trajectory equation as if of a missile being fired from left to right in Figures 1 and 2. But this trajectory equation is still problematical. The ‘uniform distribution’ assumption above is not sufficient to yield a simple analytic solution. We find that it is not possible to define the start of the trajectory precisely without a trial solution followed by iteration to reduce the final trajectory angle error to the expected value.

Approximate solutions can be obtained by splitting the trajectory into two parts modelling the start and finish respectively. The two parts are then joined together seamlessly by a weighting function which is the m th root of some combination of the n th powers of the two terms. This can be seen in the left-hand centre equation in Figure 3. The parameters of the weighting function are chosen by trial and error (heuristically) to fit best with what can be deduced or measured with respect to the expected trajectories. These parameters have been varied to obtain the different plots shown in Figures 1, 3, and 5.

Figure 3 is the key part of the Mathcad worksheet that has been used to plot all the trajectories in Figures 1, 4, and 5. Variable $a1$ represents steps along the trajectory distance s . It is a parameter chosen for mathematical convenience, which means that the step size varies by a small amount

$a1 := 0...500$	$a2 := 0, 1...8$	$x1(a1) := \frac{a1}{50}$	$y0 := .5$	$y1(a2) := \frac{1}{24}y0 \cdot a2$
$x2(a1) := 0.2 + 1.2 \cdot \left[\frac{x1(a1)^2}{(y0)^2 + x1(a1)^2} \right]^4$		$\theta1(a1, a2) := \frac{4.5y1(a2)}{y0} \cdot \text{acos}(1 x2(a1))$		
$Y(a1, a2) := (.2 + 0.5x1(a1)) \cdot \sin(\theta1(a1, a2))$		$X(a1, a2) := -[(.2 + 0.5x1(a1)) \cdot \cos(\theta1(a1, a2))]$		

Figure 3: Mathcad worksheet equations for generating trial EM wave energy path trajectories as in Figures 1, 4 and 5.

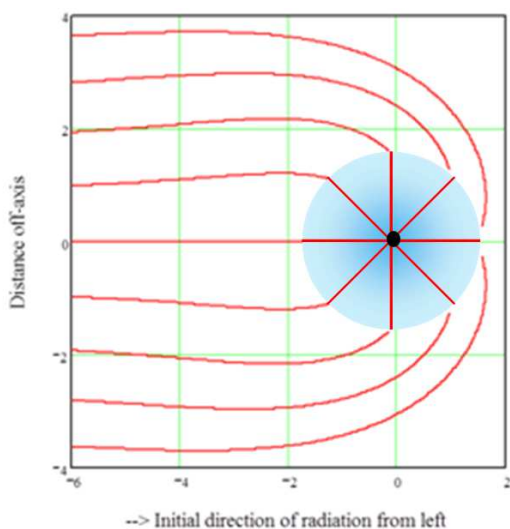


Figure 4: Power flow trajectories from aperture left to all angles on a wire dipole at 0.0 on right. Shaded blue lens region is finite but less than the capture aperture size for a frequency below about 90 MHz.

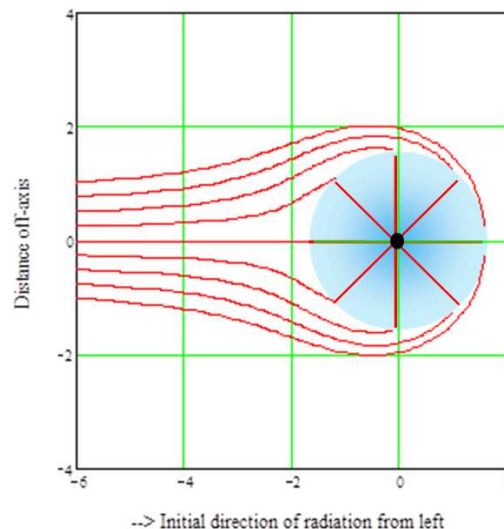


Figure 5: Shaded blue lens region is finite and larger than less than the capture aperture size, as is the case above about 90 MHz.

when the path is significantly curved. The variable $a2$ is the number of trajectories available on one diagram. $x1(a1)$ and $y1(a1)$ are the horizontal and vertical distances from the wire at the origin for the two parts of the trajectory considered separately. $x2(a1)$ is the weighting function with selectable parameters. $\theta_1(a2)$ is the angle θ_1 as in Figure 2. $X(a1, a2)$ and $Y(a1, a2)$ are the coordinates of the computed trajectories.

6. EFFECT OF FREQUENCY DEPENDENT ELECTROMAGNETIC COUPLING

The local ether lens that focuses the incoming radiation on to the wire is a region of local space that is highly coupled to itself and the wire. But this electromagnetic (EM) coupling is found to be inversely proportional to the square root of frequency [2]. It means that at a frequency of about 90 MHz the region of coupled space surrounding the wire is comparable in dimension to the capture aperture of the wire dipole. In the highly coupled region the power flow lines can be assumed to be essentially radial as shown in the central blue region of Figures 4 and 5. For simplicity the transitions have been shown as being abrupt at an assumed sharp boundary. In all these cases the Mathcad equation parameters have been adjusted to provide realistic solutions.

7. CONCLUSION

This is a first attempt at representing the focussing process of a wire dipole. At present not enough is known or has been measured for this newly elucidated mechanism. Approximate trajectories have been presented which satisfy the constraints of well known capture aperture area of a dipole and the assumption that the local ether lens is the region of high EM self-coupling. And the size of this is the (Goubau) EM coupling distance [2]. Further measurements and more exact solutions to the trajectory equations are needed to refine the heuristic power flow trajectories that have so far been obtained.

REFERENCES

1. Rivni, A. A. and C. H. Papas, "Power flow structures in two dimensional electromagnetic fields," *Progress In Electromagnetics Research*, Vol. 29, 261–294, 2000.
2. Underhill, M. J., "A physical model of electro-magnetism for a theory of everything," *PIERS Online*, Vol. 7, No. 2, 196–200, 2011.
3. Underhill, M. J., "The phase noise spectrum and structure of photons?," *Proc. 16th EFTF-2010*, 8 Pages, Noordwijk, Netherlands, April 13–16, 2010.

Antenna Pattern Formation in the Near Field Local Ether

Michael J. Underhill

Underhill Research Ltd., Lingfield, UK

Abstract—A radial trajectory method is proposed for finding the transmission *and* reception power flow lines of multi-element antennas such as the Yagi or phased array. In the antenna pattern formation region the radial trajectories are assumed to be cones of constant solid angle. In the local ether region inside this region the power transmitted from each element is radiated initially with the radiation pattern of that element. Thereafter in the pattern formation region the power along the radial trajectories varies progressively to form the antenna pattern. The assumption is that the power on each radial trajectory either radiates power to or receives power from adjacent trajectories so that total radiated antenna power is conserved exactly at all distances from the antenna. The transfer of power is assumed to occur exponentially with distance. The exponential is assumed to be defined by the EM coupling distance, which is found to vary inversely as the square root of the frequency. The radial line concept can be used in reverse for antenna pattern formation on reception. For reception the trajectories should represent focussing by the near-field ether of incoming plane waves on to the elements of the antenna [1]. Reception and transmission can conveniently be regarded as separate processes occurring in the same region. The pattern formation region is where the coupling of the antenna elements modifies the ‘local ether refractive index’. The power flow line trajectories for transmission and reception are very different but ‘reciprocity’ always applies.

1. INTRODUCTION

The pattern of a multi-element Yagi or phased array antenna is formed in space in a region at some distance away from the antenna. Initially the power from each radiating element in the array is radiated with angular intensity (power per unit solid angle) as dictated by the element pattern. In the absence of any dissipation the total power of all the elements remains the same as the far-field antenna pattern is progressively formed. This power/energy conservation is required by the Laws of Physics. But it raises a number of questions to be answered:

(a) How is the radiating energy from omnidirectional array elements diverted from the null directions and focussed into the lobe directions?

(b) At what distance is the antenna pattern of an array actually formed?

(c) For a directional antenna the sum of the momentum from each radiating element is not the same as the overall momentum of the radiation as seen in the far-field. There is a backward force on the antenna, but what are the lines of force for this? Is the antenna actually pushing against the ether or is it purely back pressure from the radiation?

(d) Is there any variation in the velocity of power flow in the near field local ether? Does it deviate slightly from the velocity c_{EM} in free space? Is this of secondary concern?

There is little to be found in the literature to answer these questions. The following method for addressing the above problems is derived from previous publications by the author [1–5].

2. METHOD

For an array antenna in effect the pattern is defined by the *potential distribution* in space established by the currents in each element. This essentially classical definition is retained here as an axiom. The three element end-fire (Yagi) array is taken as an illustrative example of array behaviour in the following.

The radiated power starts out uniformly from each wire element. This can be defined as a radially directed bi-vector current with polarisation vector component in the direction of the current in the wire element [2]. The power density S of the radiation at any point is the local vector potential Φ times the radial current density I_r . We thus have $S = \Phi \cdot I_r$. This is an alternative (more logical?) definition of the Poynting vector $S = E \times H$. Thus

$$S = \Phi \cdot I_r \quad \text{is equivalent to the Poynting Vector :} \quad S = E \times H \quad (1)$$

The radiated power has a momentum density M given by $M = S/c_{em}$ where c_{em} is the EM wave velocity in free space. The wave momentum is radiated initially in all directions in accordance with the the circular pattern of the dipole elements assumed in the array.

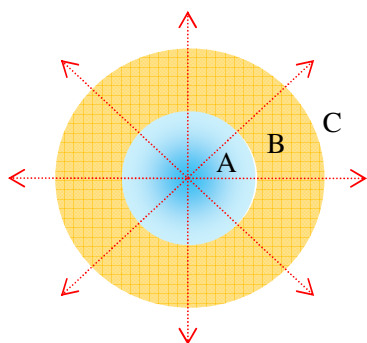


Figure 1: Antenna Process Regions for antenna at centre: A, the shaded blue local ether lens region in which element patterns hold; brown shell, region B, is the array pattern formation region; and C, is the far-field region where array pattern is fully formed.

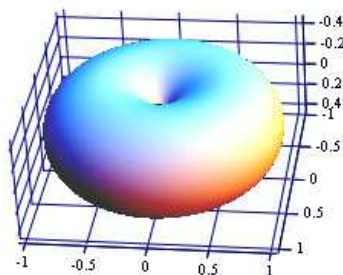


Figure 2: Pattern of vertical half wave dipole elements.

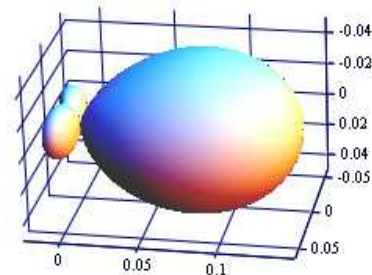


Figure 3: Pattern of optimal three dipole element end-fire (Yagi) array with maximum gain/directivity.

The combined potential distribution of the array elements steers and redirects the power flow momentum from the elements eventually to create the far-field pattern. To do this the potential exerts sideways forces on the momentum flow lines. These become curved in the same way as is described in reference [1].

But an alternative way of describing the formation of the antenna pattern is used here. It is a remapping of the conical constant power lines into radial lines along which the power increases or decreases. Straight flow lines are defined that radiate from one point near whatever can be considered as the centre of the antenna. The position does not have to be precise. All the element power is assumed to start from the centre in this case with the element pattern that is common to all elements. For convenience the radiated power intensity is defined in terms of solid angle subtended at the central point. In this way the inverse square law spreading function is factored out. The pattern is formed by the progressive lateral transfer of power from one (conical) flow line to another over a finite distance in the pattern formation region shown in Figure 1.

In Figure 1 the element pattern, for example as shown in Figure 2, holds in the central blue 'local ether lens' [1], region A. The array pattern, as for example shown in Figure 3, is formed in the brown spherical shell region B. Anywhere in the free space region C the array pattern holds.

Figures 4 to 6 show the progressive transfer from the element pattern in red through half formed patterns in brown to the final array patterns in blue. Figures 4 and 5 show the pattern evolution respectively for the H -plane and E -plane patterns. Figure 6 shows progressive formation of H -plane patterns deliberately separated by partially scaling with distance.

3. PATTERN FORMATION PROFILE

Power either increases or decreases along each conical flow line by lateral transfer of power between adjacent lines. The main processes are refraction, partial reflection and scattering of power flow by the local ether. Scattering causes progressive decrease of power density in the power flow direction, while retaining strict power and energy conservation. Any mapping of power flow lines can always be defined in terms of these processes.

At any point on an individual power flow line we can determine whether the line is progressively radiating or receiving power by comparing *external* vector potential Φ_e and the *internal* vector potential Φ_i at that point. The internal vector potential is directly proportional to the displacement current in the direction of power flow. The constant of proportionality is $Z_0/2\pi = 60$ ohms. The external vector potential is the coherent combination of all the potential contributions from all the elements in the array. It is the external vector potential that creates the final far-field pattern from the combined radiated power from all the array elements.

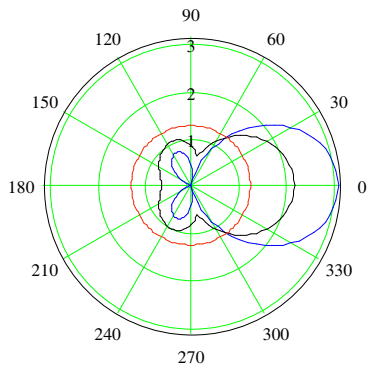


Figure 4: H -plane antenna patterns in at three distances from the centre of the three element antenna. Red centre pattern is the dipole element pattern. Outside blue pattern is the fully formed three element (yagi) array pattern. Intermediate brown pattern is a half formed array pattern in the pattern formation region.

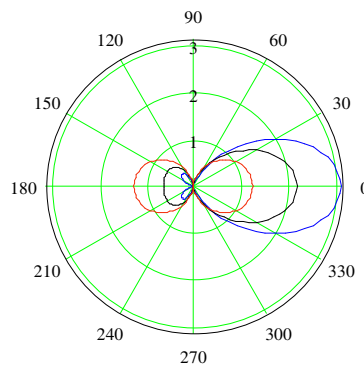


Figure 5: E -plane patterns for the three element antenna, but otherwise as for Figure 4.

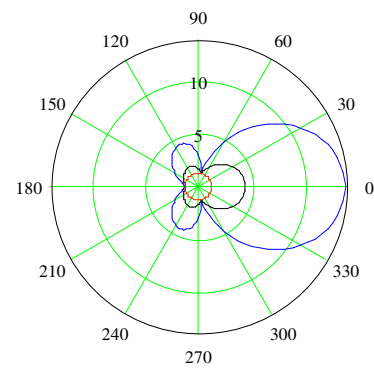


Figure 6: Progressive formation of patterns but with sizes scaled to be outside the central region.

The conditions for radiation or reception of power along a radial power flow line are:

$$\Phi_e = \Phi_i \text{ for no radiation or reception and constant power along line} \quad (2)$$

$$\Phi_e < \Phi_i \text{ for radiation and progressive decrease of power along line to a non-zero value} \quad (3)$$

$$\Phi_e > \Phi_i \text{ for reception and progressive increase of power along line to a maximum value} \quad (4)$$

$$\Phi_e = -\Phi_i \text{ for radiation and progressive decrease of power along line to a null value of zero} \quad (5)$$

We assume that the profile of the progressive transformation $F(r)$ from one the element pattern to the far-field pattern is symmetrically exponential going at the two sides of the pattern formation and focussing region. The transcendental function selected to represent the processes in this region is the ‘hyperbolic tangent’ function, \tanh . The recommended and simplest mathematical representation for this is

$$\tanh x = (e^{2x} - 1) / (e^{2x} + 1) \quad (6)$$

This is what has been used for the Mathcad implementations of the plots in this paper.

The boundary conditions that have to be satisfied for each flow line are that for a given direction they start with a value given by the element pattern and finish with the value given by the array pattern. Selecting some representative points from the patterns given in Figures 2 to 6, and applying the \tanh function to the step differences we obtain the plots shown in Figures 7 and 8. Three parameters, a , b , c and d were inserted in Equation (6) as shown in Equation (7):

$$F(x) = a + b \left(e^{2d(x-c)} - 1 \right) / \left(e^{2d(x-c)} + 1 \right) \quad (7)$$

where a is the initial y value, b is the step up, or step down if negative, c is the positive distance to the half-way point of the \tanh curve, which is the centre of the pattern formation region, and d is inversely proportional to the square root of frequency and sets the length of the pattern formation region.

4. RECEPTION

For reception of signals the pattern formation region becomes the first focusing region for the antenna. The physical explanation is, that the impedance and refractive index properties of space in this region are altered by the external effects of the EM coupling between the antenna elements. Note that this coupling, and hence also the local ether profile, remains the same whatever the field strength or power of is being transmitted or received. It truly is a modification of the local ether

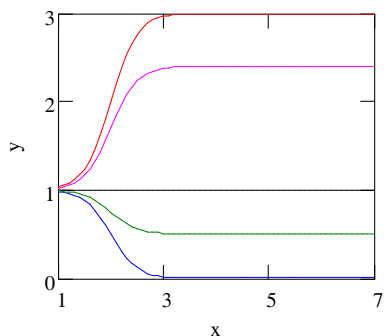


Figure 7: Enhancement or reduction of angle intensity y (power per solid angle) with distance x away from the antenna centre for different angles to antenna boresight; red at top is in the boresight direction; next to top magenta line is for the 3 dB down on boresight directions; central brown line is where the angle intensity is unchanged; next down green line is a reduction of angle intensity by 6 dB; bottom blue line is for the direction of a perfect null.

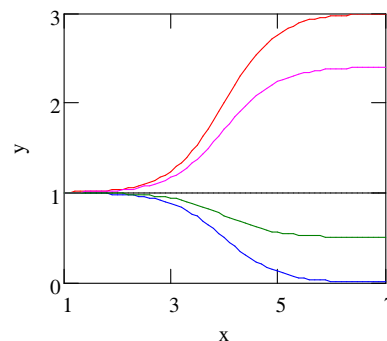


Figure 8: Is the same as for Figure 7, but at a quarter of the frequency. The x scale remains in units of absolute length and is not scaled relative to the wavelength. The length of the pattern formation region is thus increased in this case by $\sqrt{4} = 2$ times, and *not* by 4 times.

that surrounds the antenna. In the central lens region the local ether is also modified as noted in reference [1].

5. CONCLUSION

A new explanation of how array antenna patterns are formed in the ‘local ether’ near-field space surrounding an antenna has been put forward. The antenna pattern is defined by the potential distribution established by the currents in each element. In essence this is the same as the classical view of pattern formation. The radiated power starts out uniformly from each wire element and is then progressively increase or decrease by transfer of energy laterally between adjacent power flow lines in a ‘pattern formation’ shell region of finite thickness surrounding the central ‘element lens’ region. The transfer profile with distance is governed by the (newly discovered [2]) electromagnetic coupling that defines the local ether around any antenna.

For an array antenna two process regions have been defined. The central (usually spherical) region is where the element radiation patterns are considered to hold. The (spherical) shell that surrounds this is the array pattern formation region. Outside this the far-field array pattern is considered to be fully formed.

The hyperbolic tangent function with four adjustable parameters has been found to be a good representation of the variation of power along the power flow (conical) lines. One parameter is set according to the inverse of the square root of frequency. The other parameters depend mainly on the physical size of the antenna.

This new description of how a pattern is formed preserves energy/power conservation at every point in the pattern formation region. It analyses and explains in detail why global energy conservation can safely be applied in antenna pattern formation. Thus it confirms that the directivity of an antenna can always be computed from its measured antenna pattern.

REFERENCES

1. Underhill, M. J., “A local ether lens path integral model of electromagnetic wave reception by wires,” To be presented at *PIERS Proceedings*, Moscow, Russia, August 19–23, 2012.
2. Underhill, M. J., “A physical model of electro-magnetism for a theory of everything,” *PIERS Online*, Vol. 7, No. 2, 196–200, 2011.
3. Underhill, M. J., “The phase noise spectrum and structure of photons?,” *Proc. 16th EFTF-2010*, 8 pages, Noordwijk, Netherlands, April 13–16, 2010.
4. Underhill, M. J., “Maxwell’s transfer functions,” *PIERS Proceedings*, 1766–1770, Kuala Lumpur, Malaysia, March 27–30, 2012.
5. Underhill, M. J., “Novel analytic EM modelling of antennas and fields,” *PIERS Proceedings*, 1771–1775, Kuala Lumpur, Malaysia, March 27–30, 2012.

Calculation of an Equivalent Electrical Conductivity Tensor for Multidirectional Carbon Fiber Reinforced Materials

N. Athanasopoulos and V. Kostopoulos

Department of Mechanical Engineering and Aeronautics
University of Patras, Greece

Abstract— The ability of carbon fibers to conduct electric current can be used in a plethora of applications. Carbon fiber reinforced plastics (CFRPs) can be divided into unidirectional and multidirectional laminates. The electric conductivity of the unidirectional laminates presents strong electric anisotropy and can be expressed by a symmetric, second order tensor. There is no point in studying the electrical conductivity of CFRPs ignoring the microstructure of the material. In order to consider a multi-layered material homogenous, it is of paramount importance that we examine the intralaminar and interlaminar areas.

Using the continuity equation, it can be proved that the electric conductivity of the multidirectional laminates can also be expressed by a second order tensor (equivalent tensor). Therefore, the electrical conductivity tensor of the CF preform can be calculated for any stacking sequence assuming that the material is homogenous and that the plies' thickness is negligible in comparison to the other dimensions. The equivalent tensor can be imported into the elliptic partial differential equation which is the governing equation for steady current in anisotropic media. Consequently, the electric field and the current density can be calculated by solving the aforementioned elliptic PDE.

The validity of the equivalent tensor was confirmed by measuring the electrical resistivity of the multidirectional laminates media for various multidirectional laminates (stacking sequences). For a second confirmation the coupled thermo-electric problem was solved numerically using as input material the calculated equivalent tensor. The calculated temperature field for each multidirectional laminate was confirmed experimentally via a thermal camera.

1. INTRODUCTION

The electric conductivity (EC) of unidirectional CFRP laminates has been thoroughly studied and is dependant upon the fibre conductivity, fiber direction [1], fiber volume fraction [2] as well as the temperature [3, 4] and the plies' thickness [5]. In real structures, CFRPs consist of multidirectional layers. The determination of the electric conductivity of the anisotropic multilayered material is the most crucial factor for the calculation of the electric potential field, electric field and the current density. Certain factors that are crucial as far as the electric field distribution is concerned, are the following: the fibre volume fraction, as well as the material imperfections at a scale of micrometers. All the above affect the electric field distribution at the microscopic level, resulting in an obvious disturbance at the macroscopic level. In this study, we assume that the material used is homogenous and anisotropic, hence it approximates the ideal anisotropic material. Also, the layers' thickness is negligible compared to the other dimensions (no electric potential gradient through the layers' thickness) and that the layers are in perfect contact with each other. This can be achieved under certain conditions of temperature and pressure during the manufacturing stages of the CFRP laminate.

Using optical microscopy, the intralaminar and interlaminar regions of the multi-layered CFRP material can be examined and therefore we can decide whether the material's EC can be described by the suggested equivalent second order tensor.

2. MATHEMATICAL PROOF OF THE EQUIVALENT TENSOR

The authors have verified the EC of any dry CF multidirectional layered material can be expressed by a second order tensor, which is derived from each layer's tensor [6]. Assuming that the body is thin (2D space), the EC tensor can be determined very simply by using the continuity equation for anisotropic continuum media. The EC tensor that describes the new equivalent multilayered material is composed of the EC tensors that describe each CF layer, separately. As it is well known, the following equation, Equation (1) expresses the current conservation in a closed surface S for the anisotropic body. Integrated Equation (1) over a control volume and using the Divergence theorem:

$$\iiint_V (\nabla \cdot \mathbf{J}) dV = \iint_S \mathbf{J} \cdot d\mathbf{S} \quad (1)$$

The total current that passes through the surface S_L (total cross section area) is equal to the sum of the electric current that passes the cross section of each layer of the surface S_n , Fig. 1(a), where \mathbf{n} is the outward unit normal vector of the surfaces S_L and S_n . Hence, the integral of the dot product of the current density and the surface of the cross section expressed by Equation (2).

$$\begin{aligned} I_L &= \sum_{i=1}^N I_i \Leftrightarrow \iint_{S_L} \mathbf{J}_L \cdot \mathbf{n} dS_L = \sum_{n=1}^N \iint_{S_n} \mathbf{J}_n \cdot \mathbf{n} dS_n \Leftrightarrow \iint_{S_L} (J_{L1}i + J_{L2}j) \cdot \mathbf{n} dS_L \\ &= \sum_{n=1}^N \iint_{S_n} (J_{n1}i + J_{n2}j) \cdot \mathbf{n} dS_n \end{aligned} \quad (2)$$

where J_{L1} is the current density that crosses the representative volume in the direction x_1 , and J_{L2} is the current density that crosses the representative volume in the direction x_2 .

Integrated Equation (2) over the thickness (H) and the width (W) from $-W/2$ to $W/2$ of the representative volume and dividing by the total surface ($S_{L1} = HW$) the current density at direction x_1 is given by Equation (3).

$$|J_{L1}| = \sigma_{11}^L E_1 + \sigma_{12}^L E_2 = \sum_{n=1}^N \frac{S_n}{S_{L1}} (\sigma_{11}^n E_1 + \sigma_{12}^n E_2) \quad (3)$$

where $S_n = h_n W$ is the cross section surface of each layer. Following the same procedure and integrating over the other side of the representative volume (from $-W/2$ to $W/2$) then it is concluded that the current density at direction x_2 is given by Equation (4).

$$|J_{L2}| = \sigma_{21}^L E_1 + \sigma_{22}^L E_2 = \sum_{n=1}^N \frac{S_n}{S_{L2}} (\sigma_{21}^n E_1 + \sigma_{22}^n E_2) \quad (4)$$

The total current density (\mathbf{J}_L) is equal to $\mathbf{J}_L = J_{L1}\mathbf{i} + J_{L2}\mathbf{j}$. Based on Equation (3) and Equation (4) the final expression of the equivalent EC tensor (σ_L) for the multidirectional laminate can be expressed by Equation (5).

$$\sigma_L = \begin{bmatrix} \sigma_{11}^L & \sigma_{12}^L \\ \sigma_{21}^L & \sigma_{22}^L \end{bmatrix} = \frac{1}{S_T} \begin{bmatrix} \sum_{n=1}^N S_n \sigma_{11}^n & \sum_{n=1}^N S_n \sigma_{12}^n \\ \sum_{n=1}^N S_n \sigma_{21}^n & \sum_{n=1}^N S_n \sigma_{22}^n \end{bmatrix} = \frac{1}{S_L} \sum_{n=1}^N S_n \sigma_L \quad (5)$$

By combining layers of different direction, a new material is produced whose electric conductivity depends on its layers' electric conductivity. Fig. 2(b) demonstrates each layer's EC tensor ellipse (black line) for 0° fiber directions and (red line) for 30° fiber direction as well as the final material's EC tensor ellipse (blue line) for stacking sequence (0/30/30/0). The eigenvalues as well as the eigenvectors can be calculated as known. The equivalent EC tensor is valid only if the CFRP layers are in perfect contact and the fiber volume fraction is high enough. The fiber volume fraction of the laminate must be uniform at the intralaminar and interlaminar areas (detailed microscope images, Fig. 1(a)). This uniformity can only be achieved by applying a specific temperature and pressure profile during the CFRP's manufacturing stages, which will cause the rich-in-resin layer to be diminished.

3. ELECTRIC POTENTIAL FIELD (3D TO 2D SPACE PROBLEM)

As far as a multilayered material is concerned and taking into account the second assumption (no electric potential gradient through the thickness), the electric field distribution is a 3D space problem. However, in the case where the plies' thickness is small relatively to the other dimensions the problem can be deduced to the 2D space, neglecting the plies' thickness and the electrical gradient through the thickness of the material. We studied the electric field distribution in multilayered materials of circular geometry by applying potential difference between the two concentric circles of Fig. 2 (using Dirichlet boundary conditions). The results were compared to the respective analytical 2D space problem solution. Two layers with EC tensors of σ_{45} and σ_{-45} respectively,

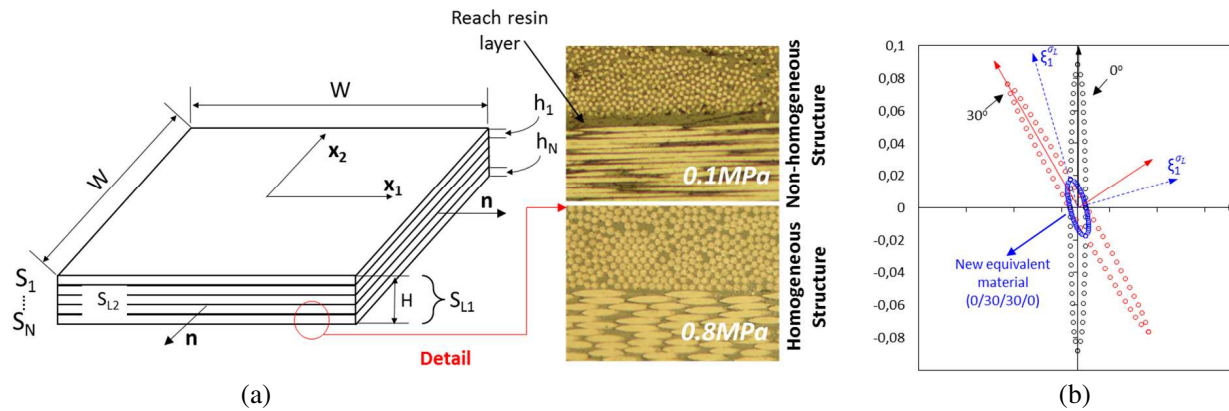


Figure 1: (a) Elementary volume of the multidirectional laminates and the microstructure of the material for two different pressure levels at manufacturing stage of the material, (b) eigenvalues and eigenvectors for each CFRP layer and the new multidirectional CFRP material.

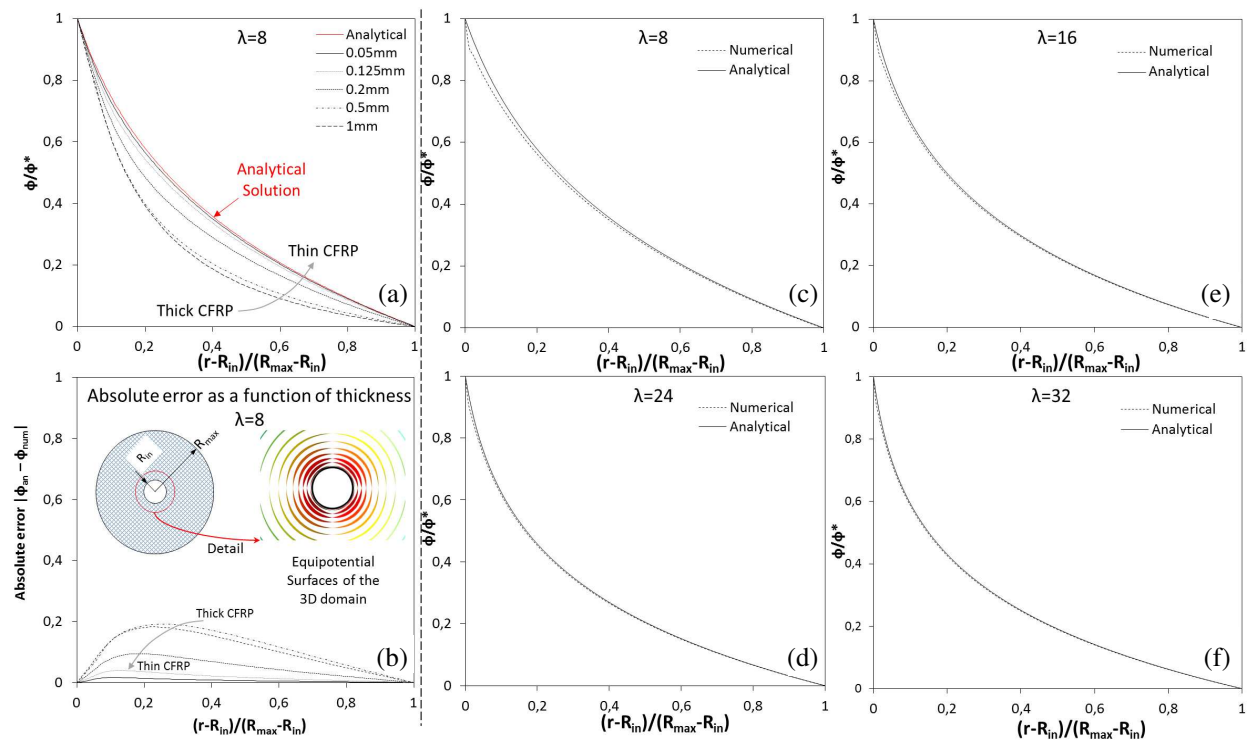


Figure 2: (a) Dimensionless electric potential field for circular domains as a function of layers thickness, (b) absolute error between the numerical solution (3D space) and the (2D space) analytical solution, (c), (d), (e), (f) comparison between numerical and analytical solutions as a function of ratio $\lambda = R_{max}/R_{in}$ for layer thickness $h = 0.05$ mm.

produce a new multidirectional material of $(\pm 45^\circ)$ with EC tensor of $\sigma_{\pm 45}$. Considering that the new material $\sigma_{\pm 45}$ can be expressed by a scalar quantity and not a tensor, we can calculate the electric potential field distribution in polar coordinates using the Equation (6).

$$\phi(r) = \phi_o \ln \left(\frac{r/R_{max}}{R_{in}/R_{max}} \right) \quad (6)$$

The previously mentioned analytical solution is compared to the respective numerical solution in 3D space, for various thickness layers and various ratios ($\lambda = R_{max}/R_{in}$) where (λ) is the external to internal radius of the domain.

Figure 2(a) demonstrates the electric potential field distribution as a function of the radius (r),

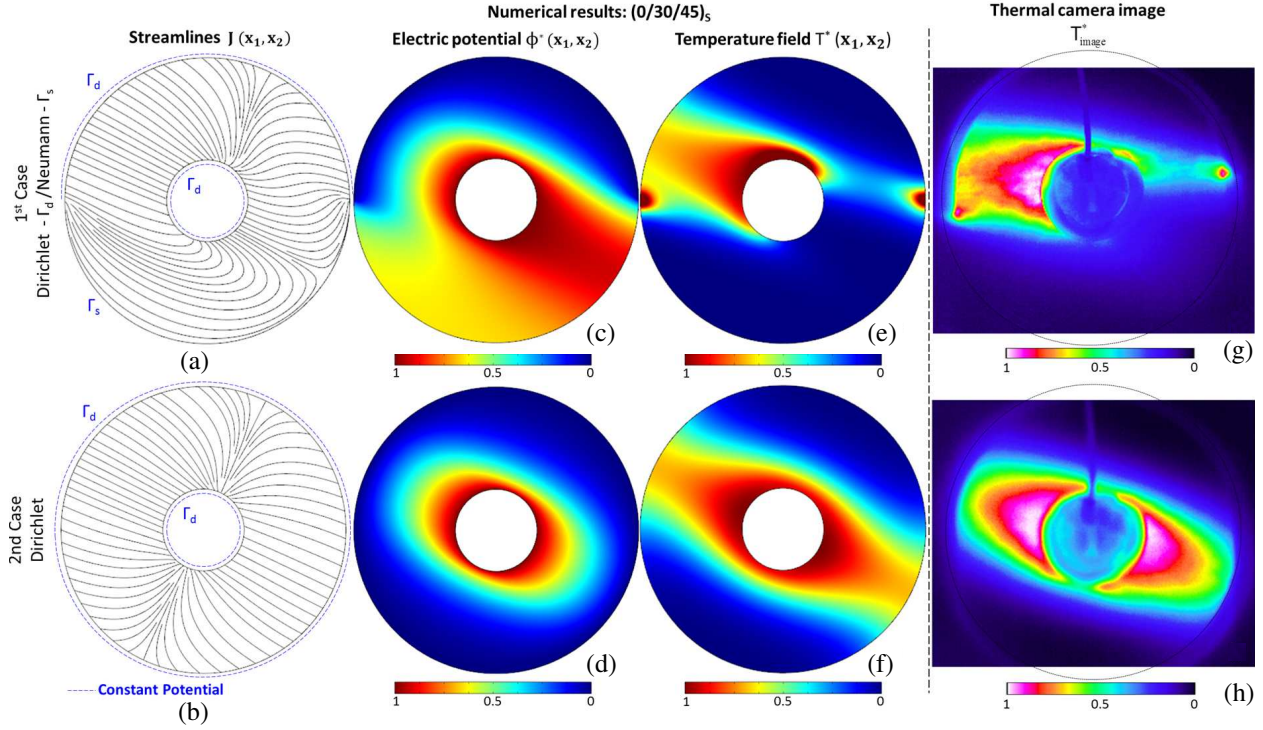


Figure 3: Numerical results and thermal camera images for two circular multidirectional CFRPs using the equivalent EC tensor ($R_{\max}/R_{\text{in}} = 4.5$, $R_{\max} = 157.5$ mm, $H = 0.726$ mm, $h = 0.121$ mm). (a), (b) current density, (c), (d) electric potential field (e), (f) calculated temperature field, (g), (h) measured temperature field.

for a ratio of $\lambda = 8$ and for various ply thicknesses. It can be observed that as the thickness reduces, the numerical solution at the middle of the laminates approximates the analytical solution. It is obvious in Fig. 2(b) that the error between the two curves for an internal radius (R_{in}) tends to zero for high ratios ($\mu = R_{\max}/h$ where (μ) is the external radius to the layer thickness).

Final, Figs. 2(c), (d), (e), and (f) demonstrate the electric potential in dimensionless form, as a function of radius (r) for layer thickness $h = 0.05$ mm and $\lambda = 8, 16, 24, 32$ ratios. These diagrams depict the electric potential at the region where maximum deviation from the analytical solution can be observed. The curves coincide for ratios $\lambda > 8$. Therefore Equation (5) is valid when the layer thickness is small and it is safe to say that the error tends to zero.

4. VALIDATION OF THE EC TENSOR VIA THE JOULE EFFECT

The electric potential field in anisotropic homogeneous media can be expressed by an elliptic partial differential equation, Equation (7). The symmetry of the EC tensor is a consequence of the symmetry of the kinetic coefficients (Onsager theorem [7]). Since the EC tensor is symmetric ($\sigma_{12} = \sigma_{21}$), the electric potential field satisfies the following simplified elliptic PDE.

$$\nabla \cdot (\boldsymbol{\sigma}_L \nabla \phi) = 0 \Leftrightarrow \sigma_{11} \frac{\partial^2 \phi}{\partial x_1^2} + 2\sigma_{12} \frac{\partial^2 \phi}{\partial x_1 \partial x_2} + \sigma_{22} \frac{\partial^2 \phi}{\partial x_2^2} = 0 \quad (7)$$

where ($\boldsymbol{\sigma}_L$) is the EC tensor and (ϕ) is the electric potential field. In the present work, the thermoelectric effect is considered negligible. Using this assumption, the relation between the current density (\mathbf{J}) and the electric field for a homogeneous anisotropic conductor is expressed by Equation (8).

$$\mathbf{J} = \boldsymbol{\sigma}_L (\mathbf{E} - \mathbf{a} \nabla T) \stackrel{a \nabla T = 0}{\Rightarrow} \mathbf{J} = \boldsymbol{\sigma}_L \mathbf{E} = \boldsymbol{\sigma}_L (-\nabla \phi) \quad (8)$$

The boundary conditions for the following problem are described by a first kind boundary condition (Dirichlet boundary condition) at the Γ_d regions and by second kind boundary conditions (Neumann boundary condition) at the Γ_s .

The indirect method for the validation of the tensor involved the use of a thermal camera. We studied a circular domain with a symmetric stacking sequence $(0/30/45)_s$ and ratio ($\lambda =$

$R_{\max}/R_{\min} = 4.5$) using different boundary conditions (two cases, Figs. 3(a) and (b)). The electric potential difference was applied at the edges of the circular domain. Then, certain numerical models were developed in order to solve the electrical problem of an anisotropic continuum body as well as to find the electric field distribution and the current density. Since the thermoelectric effect has been omitted, then the generated heat per unit time and volume is the dot product of the electric field and the current density. The dot product in a known domain Ω , with given boundary conditions, changes according to the EC tensor of the layered medium. Different stacking sequences lead to different equivalent EC tensors. Thus, the resulting generated heat in the known domain is also different.

Considering an elementary volume, the heat transfer energy equation of an anisotropic porous medium is given by Equation (9) [8].

$$((1 - \varphi)(\rho c)_f + \varphi(\rho c)_m) \frac{\partial T}{\partial t} = \nabla \cdot (\mathbf{k} \nabla T) + \mathbf{J} \cdot \mathbf{E} - \dot{Q}_{\text{losses}} \quad (9)$$

where (\mathbf{k}) is the thermal conductivity tensor and $(1 - \varphi)$ is the fraction that is occupied by fibers, (φ) is the fraction that is occupied by matrix material, $(\dot{Q}_{\text{losses}})$ is the energy losses through convection, $(\rho c)_f$ and $(\rho c)_m$ denote the product of the density and specific heat capacity of the carbon fibers and the matrix material respectively.

The measured temperature field Figs. 3(g) and (h) of each case was compared to the respective numerically calculated, Figs. 3(e) and (f). For confrontation, the results will be presented in dimensionless form. More precisely, the electric potential field and the temperature field are presented in dimensionless form, following the expression $\phi^* = \phi/\phi_{\max}$ and $T^* = (T - T_{\text{env}})/(T_{\max} - T_{\text{env}})$ respectively, Fig. 3.

5. CONCLUSIONS

The electric conductivity tensor of a multidirectional CFRP material can be expressed by a symmetric second order tensor which derives from the combination of each layer's electrical conductivity tensor, Equation (6). The above is valid in the case where the material is homogenous and the plies' thickness is negligible compared to the body's other dimensions. If the applied pressure level is satisfactory during the material's manufacturing stages, the material could be assumed homogenous and anisotropic. Applying electrical potential at the specimen's inner and outer radius the temperature of the medium increase due to the Joule effect. The temperature field of the multilayered medium depends on the EC tensor (stacking sequence of the CFRP) and the boundary conditions. The calculated temperature field is in excellent agreement with the temperature measurements using the thermal camera.

REFERENCES

1. Greenwood, J. H., S. Lebedat, and J. Bernasconi, "The anisotropic electrical resistivity of a carbon fibre reinforced plastic disc and its use as a transducer," *J. Phys. E: Sci. Instruments*, Vol. 8, 369–370, 1975.
2. Weber, M. and M. R. Kamal, "Estimation of the volume resistivity of electrically conductive composites," *Polym. Compos.*, Vol. 8, No. 6, 711–725, 1997.
3. Athanasopoulos, N., D. Sikoutris, T. Panidis, and V. Kostopoulos, "Numerical investigation and experimental verification of the Joule heating effect of polyacrylonitrile-based carbon fiber tows under high vacuum conditions," *J. Compos. Mater.*, 2011, DOI: 10.1177/0021998311430159.
4. Takahashi, K. and H. T. Hahn, "Investigation of temperature dependency of electrical resistance changes for structural management of graphite/ polymer composite," *J. Compos. Mater.*, Vol. 45, No. 25, 2603–2611, 2011.
5. Athanasopoulos, N. and V. Kostopoulos, "Prediction and experimental validation of the electrical conductivity of dry carbon fibre unidirectional layers," *Composites Part B: Engineering*, Vol. 40, 1578–1587, 2011.
6. Athanasopoulos, N. and V. Kostopoulos, "Resistive heating of multi-directional and unidirectional dry carbon fibre preforms," *Compos. Sci. Technol.*, Apr. 18, 2012, DOI: 10.1016/j.compscitech.
7. Landau, L. D. and E. M. Lifshitz, *Steady Current, Electrodynamics of Continuous Media*, 2nd Edition, Vol. 8, 86–104, Pergamon Press, Oxford, 2009.

8. Nield, D. A. and A. Bejan, *Heat Transfer through a Porous Medium, Convection in Porous Media*, 2nd Edition, 27–28, Springer, 2006.

Spherical Wave Representation of the Dyadic Green's Function for a Spherical Impedance Boss at the Edge of a Perfectly Conducting Wedge

B. Ghassemiparvin and A. Altintas

Electrical and Electronics Engineering Department, Bilkent University, Turkey

Abstract— In this work, canonical problem of a scatterer at the edge of a wedge is considered and eigenfunction solution is developed. Initially, a dyadic Green's function for a spherical impedance boss at the edge of a perfect electrically conducting (PEC) wedge is obtained. Since scattering from objects at the edge is of interest, a three-dimensional Green's function is formulated in terms of spherical vector wave functions. First, an incomplete dyadic Green's function is expanded in terms of solenoidal vector wave functions with unknown coefficients, which is not valid in the source region. Unknown coefficients are calculated by utilizing the Green's second identity and orthogonality of the vector wave functions. Then, the solution is completed by adding general source correction term. Resulting Green's function is decomposed into two parts. First part is the dyadic Green's function of the wedge in the absence of the sphere and the second part represents the effects of the spherical boss and the interaction between the wedge and the scatterer. In contrast to cylindrical vector wave function expansions and asymptotic solutions which fail to converge in the paraxial region, proposed solution exhibits good convergence everywhere in space. Using the developed Green's function scattered field patterns are obtained for several impedance values and results are compared with those of a PEC spherical boss. Effects of the incident angle and surface impedance of the boss on the scattering pattern are also examined.

1. INTRODUCTION

In modeling radar targets and developing propagation models for wireless networks structures on wedges are often involved. Analytical treatment of such canonical structures will provide accurate and fast simulations and a physical insight of the problem. In this work, we present an eigenfunction solution for an impedance spherical boss placed at the edge of perfect electrically conducting (PEC) wedge which provides a basis to analyze impedance scatteres at the edge.

Configurations consisting of wedge structures are treated extensively in literature. A Geometrical Theory of Diffraction (GTD) based solution for scattering from cylinder-tipped wedge is first presented in [1], then numerical results in the shadow boundaries are improved by introducing higher order terms [2]. Also in [3], Green's function based on eigenfunction expansion is for cylinder-tipped wedge with a sectoral or annular groove. In addition, scattering from corrugated, grooved and cavity backed wedge are considered in [4] and [5] where hybrid methods using Uniform Theory of Diffraction, Method of Moments and Finite Element Method are employed. Nevertheless, published works mostly refer to configurations which conform to cylindrical coordinates and do not mention the scattering from structures at the edge.

Procedure followed here is an extension of that outlined in [6] where Dyadic Green's function is developed for spherical PEC boss at the edge. Due to three-dimensional geometry of the problem, spherical vector wave functions are utilized. This approach is convenient for accurate field calculation in the paraxial region where the scatterer is located.

2. FORMULATION

Geometry of the problem is shown in Fig. 1. A PEC wedge with exterior angle γ is considered which extends infinitely in the z direction. One side of the wedge lies on the xz plane. A spherical impedance boss with radius a is centered at the edge of the PEC wedge. $\bar{R} = r\hat{r}$ and $\bar{R}' = r'\hat{r}'$ are two position vectors denoting the observation and the source locations, respectively. S_w and S_B denotes the surface of the wedge and the boss, respectively. Σ is an imaginary spherical surface which extends to infinity. These surfaces enclose the volume V . \hat{n} is the unit normal vector directed in the volume V . Throughout the paper $e^{j\omega t}$ time convention is assumed and suppressed.

The electric field due to the volume current density, \bar{J}_v , which is confined to volume V_j , can be written in the form of

$$\bar{E}(\bar{R}) = j\omega\mu_0 \int_{V_j} \bar{J}_v(\bar{R}') \cdot \bar{\Gamma}_{WB}(\bar{R}, \bar{R}') dv' \quad (1)$$

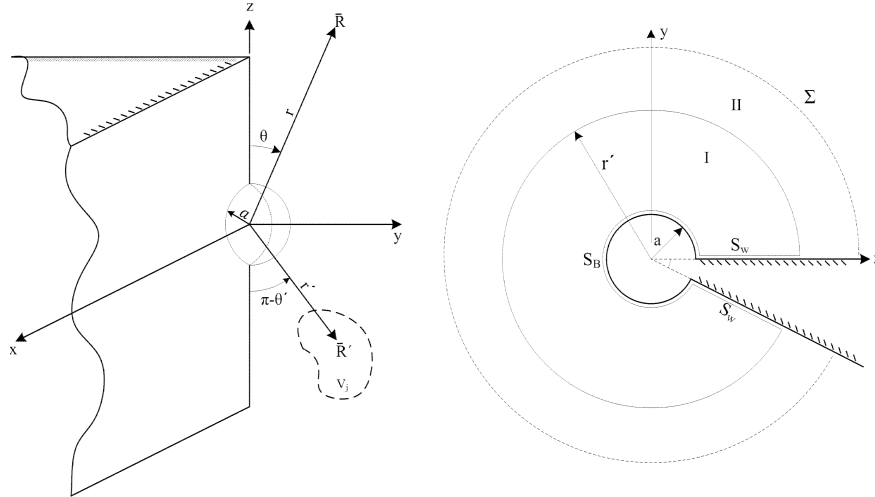


Figure 1: Geometry of the problem.

where $\bar{\bar{\Gamma}}_{WB}(\bar{R}, \bar{R}')$ is the dyadic Green's function for the PEC wedge and boss. For the isotropic, homogeneous medium in V , k_0 and Z_0 are the wave number and characteristic impedance of free space, respectively.

Dyadic Green's function satisfies the following differential equation

$$\nabla \times \nabla \times \bar{\bar{\Gamma}}_{WB}(\bar{R}, \bar{R}') - k_0^2 \bar{\bar{\Gamma}}_{WB}(\bar{R}, \bar{R}') = \bar{\bar{I}} \delta(\bar{R} - \bar{R}') \quad (2)$$

where $\bar{\bar{I}}$ is the unit dyad and $\delta(\bar{R} - \bar{R}')$ is the Dirac delta function. In addition to (2), $\bar{\bar{\Gamma}}_{WB}(\bar{R}, \bar{R}')$ satisfies the following boundary condition at S_w

$$\hat{n} \times \bar{\bar{\Gamma}}_{WB}(\bar{R}, \bar{R}') = 0 \quad (3)$$

and also satisfies the impedance boundary condition at surface of the boss, S_B , $\hat{n} \times \hat{n} \times \bar{E}(\bar{R}) = -\eta \hat{n} \times \bar{H}(\bar{R})$ which can be written in terms of dyadic Green's function as follows:

$$\hat{n} \times \hat{n} \times \bar{\bar{\Gamma}}_{WB}(\bar{R}, \bar{R}') = \kappa \hat{n} \times \nabla \times \bar{\bar{\Gamma}}_{WB}(\bar{R}, \bar{R}') \quad (4)$$

where $\kappa = \frac{\eta}{jk_0 Z_0}$ and η is the surface impedance of the boss. $\bar{\bar{\Gamma}}_{WB}$ also satisfies the Meixner edge condition and the radiation condition.

To construct the dyadic Green's function, first an incomplete dyadic Green's function is expanded in terms of solenoidal spherical vector wave functions, which is valid for $\bar{R} \neq \bar{R}'$, then the solution is completed by adding a source correction term introduced in [7].

Volume V is divided into two regions which is separated by the sphere of radius r' . To simplify the derivation, vector Green's function is defined as follows

$$\bar{G}(\bar{R}, \bar{R}') = \bar{\bar{\Gamma}}(\bar{R}, \bar{R}') \cdot \hat{u} \quad (5)$$

where \hat{u} is a unit vector in an arbitrary direction. Vector Green's function can be expanded in terms of spherical vector wave functions which are presented in [8].

$$\bar{G}^I = \sum_q a_q(\bar{R}') \bar{M}_{eq}^{(IM)}(k_0 \bar{R}) + b_q(\bar{R}') \bar{N}_{oq}^{(IN)}(k_0 \bar{R}) \quad (6)$$

$$\bar{G}^{II} = \sum_q c_q(\bar{R}') \bar{M}_{eq}^{(4)}(k_0 \bar{R}) + d_q(\bar{R}') \bar{N}_{oq}^{(4)}(k_0 \bar{R}) \quad (7)$$

where \bar{G}^I and \bar{G}^{II} are the Green's function in the region I and region II , respectively. q is the compact summation index representing m, n . Since \bar{G}^I satisfies the impedance boundary condition, vector wave functions are modified as follows:

$$\bar{M}_{e\mu n}^{(IM),(4)}(k_0 \bar{R}) = k_0 z_{\mu+n}^{(IM),(4)}(k_0 r) \bar{m}_{e\mu n}(\theta, \phi) \quad (8)$$

$$\bar{N}_{o\mu n}^{(IN),(4)}(k_0 \bar{R}) = \frac{1}{r} z_{\mu+n}^{(IN),(4)}(k_0 r) \bar{l}_{o\mu n}(\theta, \phi) + \frac{1}{r} \frac{d}{dr} \left[r z_{\mu+n}^{(IN),(4)}(k_0 r) \right] \bar{n}_{o\mu n}(\theta, \phi) \quad (9)$$

where

$$z_{\mu+n}^{(4)}(k_0 r) = h_{\mu+n}^{(2)}(k_0 r) \quad (10)$$

$$z_{\mu+n}^{(IM)} = j_{\mu+n}(k_0 r) - \frac{k_0 \kappa j'_{\mu+n}(k_0 a) + \left(\frac{\kappa}{a} - 1\right) j_{\mu+n}(k_0 a)}{k_0 \kappa h_{\mu+n}^{(2)'}(k_0 a) + \left(\frac{\kappa}{a} - 1\right) h_{\mu+n}^{(2)}(k_0 a)} h_{\mu+n}^{(2)}(k_0 r) \quad (11)$$

$$z_{\mu+n}^{(IN)} = j_{\mu+n}(k_0 r) - \frac{k_0 j'_{\mu+n}(k_0 a) + \left(\frac{1}{a} + k_0^2 \kappa\right) j_{\mu+n}(k_0 a)}{k_0 h_{\mu+n}^{(2)'}(k_0 a) + \left(\frac{1}{a} + k_0^2 \kappa\right) h_{\mu+n}^{(2)}(k_0 a)} h_{\mu+n}^{(2)}(k_0 r) \quad (12)$$

$\bar{m}_{e\mu n}$ and $\bar{n}_{o\mu n}$ are auxiliary vector wave functions which are defined in [8]. To satisfy the boundary conditions on S_w , \bar{M} and \bar{N} functions are chosen as even and odd, respectively. Additionally, $\mu = \frac{m\pi}{\gamma}$ are the eigenvalues defined by the exterior angle of the PEC wedge. The primes in the Equation (12) denote derivatives of the functions with respect to their argument.

To solve for the unknown coefficients, Green's second identity is applied in the volume V_1 and V_2 and orthogonality of the vector wave functions over spherical surfaces is used. Consequently, the coefficients are calculated as,

$$a_q(\bar{R}') = \frac{j\pi}{2k_0} \frac{1}{Q_{\mu n}(\mu+n)(\mu+n+1)} \bar{M}_{eq}^{(4)}(k_0 \bar{R}') \cdot \hat{u} \quad (13)$$

$$b_q(\bar{R}') = \frac{j\pi}{2k_0} \frac{1}{Q_{\mu n}(\mu+n)(\mu+n+1)} \bar{N}_{oq}^{(4)}(k_0 \bar{R}') \cdot \hat{u} \quad (14)$$

$$c_q(\bar{R}') = \frac{j\pi}{2k_0} \frac{1}{Q_{\mu n}(\mu+n)(\mu+n+1)} \bar{M}_{eq}^{(IM)}(k_0 \bar{R}') \cdot \hat{u} \quad (15)$$

$$d_q(\bar{R}') = \frac{j\pi}{2k_0} \frac{1}{Q_{\mu n}(\mu+n)(\mu+n+1)} \bar{N}_{oq}^{(IN)}(k_0 \bar{R}') \cdot \hat{u} \quad (16)$$

where

$$Q_{\mu n} = \frac{\epsilon_m \pi \gamma n!}{2(2\mu + 2n + 1) \Gamma(2\mu + n + 1)} \quad (17)$$

$$\epsilon_m = \begin{cases} 2 & m = 0 \\ 1 & m \neq 0. \end{cases} \quad (18)$$

By comparing the Equations (6) and (7) with Equation (5) and adding the source correction term, one could obtain the dyadic Green's function as

$$\bar{\Gamma}_{WB}(\bar{R}, \bar{R}') = \frac{\hat{r}\hat{r}}{k_0^2} \delta(\bar{R} - \bar{R}') + \frac{j\pi}{2k_0} \begin{cases} \sum_{m=0}^{\infty} \sum_{n=0}^{\infty} \frac{\bar{M}_{e\mu n}^{(4)}(k_0 \bar{R}) \bar{M}_{e\mu n}^{(IM)}(k_0 \bar{R}') + \bar{N}_{o\mu n}^{(4)}(k_0 \bar{R}) \bar{N}_{o\mu n}^{(IN)}(k_0 \bar{R}')}{Q_{\mu n}(\mu+n)(\mu+n+1)} & r \geq r' \\ \sum_{m=0}^{\infty} \sum_{n=0}^{\infty} \frac{\bar{M}_{e\mu n}^{(IM)}(k_0 \bar{R}) \bar{M}_{e\mu n}^{(4)}(k_0 \bar{R}') + \bar{N}_{o\mu n}^{(IN)}(k_0 \bar{R}) \bar{N}_{o\mu n}^{(4)}(k_0 \bar{R}')}{Q_{\mu n}(\mu+n)(\mu+n+1)} & r \leq r'. \end{cases} \quad (19)$$

Using the explicit equations for $\bar{M}^{(IM)}$ and $\bar{N}^{(IN)}$, one could obtain

$$\bar{\Gamma}_{WB}(\bar{R}, \bar{R}') = \bar{\Gamma}_B(\bar{R}, \bar{R}') + \bar{\Gamma}_W(\bar{R}, \bar{R}') \quad (20)$$

where $\bar{\Gamma}_W(\bar{R}, \bar{R}')$ is the dyadic Green's function for the PEC wedge defined in the [8]. $\bar{\Gamma}_B(\bar{R}, \bar{R}')$ includes the terms added due to the presence of the spherical scatterer which represents the scattering from the sphere and its interaction with the wedge.

$$\bar{\Gamma}_B(\bar{R}, \bar{R}') = \sum_{m=0}^{\infty} \sum_{n=0}^{\infty} \frac{\alpha_{\mu n}(k_0 a) \bar{M}_{e\mu n}^{(4)}(k_0 \bar{R}') \bar{M}_{e\mu n}^{(4)}(k_0 \bar{R}) + \beta_{\mu n}(k_0 a) \bar{N}_{o\mu n}^{(4)}(k_0 \bar{R}) \bar{N}_{o\mu n}^{(4)}(k_0 \bar{R}')}{Q_{\mu n}(\mu+n)(\mu+n+1)} \quad r \begin{matrix} \geq \\ \leq \end{matrix} r' \quad (21)$$

where

$$\alpha_{\mu n}(k_0 a) = -\frac{k_0 \kappa j'_{\mu+n}(k_0 a) + \left(\frac{\kappa}{a} - 1\right) j_{\mu+n}(k_0 a)}{k_0 \kappa h_{\mu+n}^{(2)'}(k_0 a) + \left(\frac{\kappa}{a} - 1\right) h_{\mu+n}^{(2)}(k_0 a)} \quad (22)$$

$$\beta_{\mu n}(k_0 a) = -\frac{k_0 j'_{\mu+n}(k_0 a) + \left(\frac{1}{a} + k_0^2 \kappa\right) j_{\mu+n}(k_0 a)}{k_0 h_{\mu+n}^{(2)'}(k_0 a) + \left(\frac{1}{a} + k_0^2 \kappa\right) h_{\mu+n}^{(2)}(k_0 a)}. \quad (23)$$

For the limiting case of PEC scatterer, $\eta = 0$, $\bar{\Gamma}_B$ reduces to the dyadic Green's function for a PEC boss which is presented in [6].

3. NUMERICAL RESULTS

In this section, dyadic Green's function given by (21) alongside with (22) and (23) is used to investigate the effect of the spherical boss on the scattering of the PEC wedge. The field scattered from the impedance boss is defined as follows:

$$\bar{E}^s(\bar{R}) = j k_0 Z_0 \int_{V_j} \bar{\Gamma}_B(\bar{R}, \bar{R}') \cdot \bar{J}_V(\bar{R}') dv'. \quad (24)$$

A point source is assumed at $\bar{R}_0 = r_0 \hat{r}_0$ which is in the far zone of the sphere.

$$\bar{J}_V(\bar{R}') = \delta(\bar{R}' - \bar{R}_0) \bar{p}_e \quad (25)$$

where \bar{p}_e is an electric dipole moment which is determined by the angular unit vectors $\hat{\theta}$ and $\hat{\phi}$. In the following examples, a sphere of radius 0.25λ is centered at the edge of a half plane. Origin of the coordinate system is chosen as the center of the sphere.

In Figs. 2 and 3, monostatic scattered field is plotted for normalized surface impedance values of $\eta_s = \eta/Z_0 = 0, 1.5, 3$. Scattered field is calculated with elevation angle fixed at a value θ_0 , and ϕ is varied from 0 to 360° . $E_{\theta\theta}$ represents the scattered electric field in $\hat{\theta}$ direction when the incident field is in $\hat{\theta}$ direction and $E_{\phi\phi}$ represents the scattered electric field in $\hat{\phi}$ direction when incident field is in $\hat{\phi}$ direction.

In Fig. 2, incident and scattered fields are in the paraxial region, hence the scattered field is high due to the edge excited guided waves. In this region field pattern varies as $\cos^2(\frac{\phi}{2})$ and $\sin^2(\frac{\phi}{2})$ for $E_{\theta\theta}$ and $E_{\phi\phi}$, respectively which indicates that $n = 0, m = 1$ mode is dominant.

As the incident field moves away from the paraxial region (Fig. 3), higher order modes are excited. In addition, field intensity drops significantly due to the weakened edge guidance. The amount of decrease in the field amplitude is observed to be more for the PEC scatterer.

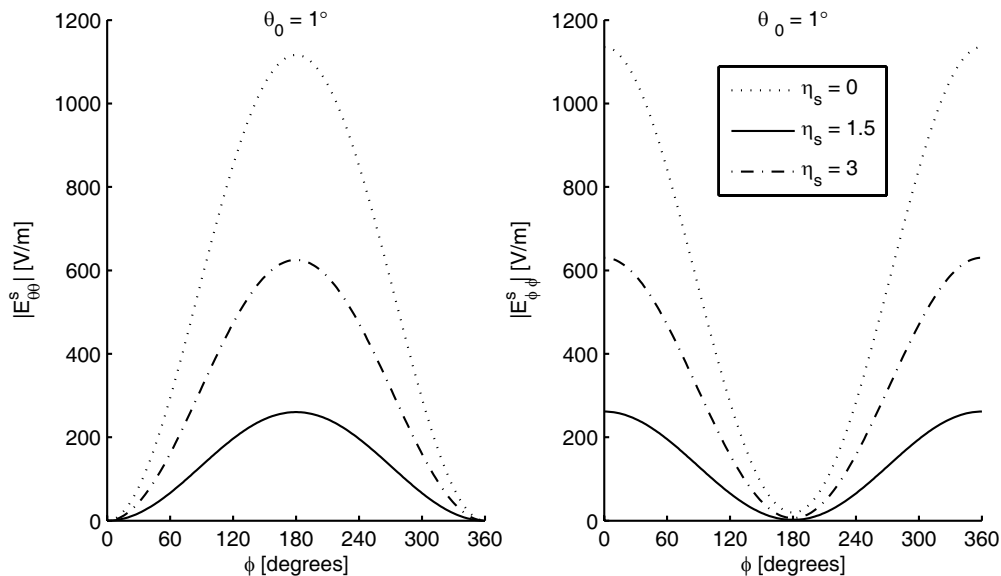


Figure 2: Monostatic scattered field for the spherical boss at the edge. The incident angle $\theta_0 = 1^\circ$, $a = 0.25\lambda$.

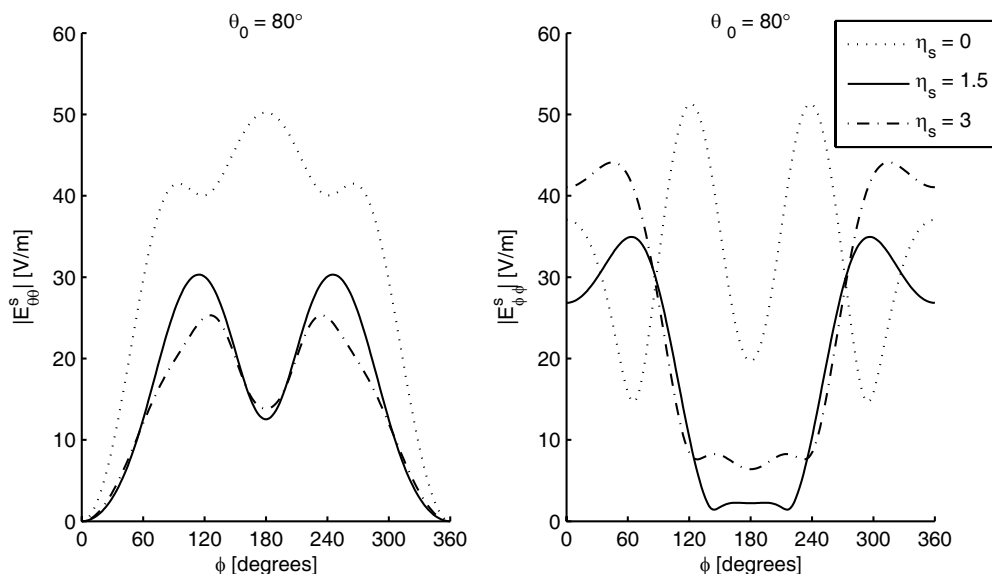


Figure 3: Monostatic scattered field for the spherical boss at the edge. The incident angle $\theta_0 = 80^\circ$, $a = 0.25\lambda$.

4. CONCLUSION

We have developed a dyadic Green's function for an impedance boss at the edge based on the spherical vector wave function expansion that gives accurate results everywhere in space. In the limiting case of $\eta = 0$, dyadic Green's function expression reduces to the one for the PEC boss. Numerical results are obtained for impedance scatterer and compared with the PEC scatterer. This study could set a benchmark for numerical solvers and lead to an extension for the current high-frequency approaches.

REFERENCES

1. Keller, J. B., "How dark is the shadow of a round ended screen?," *J. Appl. Phys.*, Vol. 30, 1452–1454, 1959.
2. Kouyoumjian, R. G. and W. D. Burnside, "The diffraction of a cylinder tipped half-plane," *IEEE Trans. Antennas Propag.*, Vol. 18, No. 3, 424–426, 1970.
3. Polycarpou, A. C. and M. A. Christou, "Full-wave scattering from a grooved cylinder-tipped conducting wedge," *IEEE Trans. Antennas Propag.*, Vol. 59, No. 7, 2732–2735, 2011.
4. Pelosi, G., R. Coccioli, G. Manara, and A. Monorchio, "Scattering from a wedge with cavity backed apertures in its faces and related configurations: TE case," *IEE Proc. Microw. Antennas Propag.*, Vol. 142, No. 2, 183–188, 1995.
5. Borgioli, A., R. Coccioli, G. Pelosi, and J. L. Volakis, "Electromagnetic scattering from a corrugated wedge," *IEEE Trans. Antennas Propag.*, Vol. 45, No. 8, 1265–1269, 1997.
6. Buyukdura, O. M., "Radiation from sources and scatterers near the edge of a perfectly conducting wedge," Ph.D. Dissertation, The Ohio State University, 1984.
7. Pathak, P. H., "On the eigenfunction expansion of electromagnetic dyadic Green's functions," *IEEE Trans. Antennas Propag.*, Vol. 31, No. 6, 12–22, 1983.
8. Buyukdura, O. M., S. D. Goad, and R. G. Kouyoumjian, "A spherical wave representation of the dyadic Green's function for a wedge," *IEEE Trans. Antennas Propag.*, Vol. 44, No. 1, 12–22, 1996.

Electromagnetic Sources and Observers in Motion VII — Medium Support for a New Relativity Theory

S. E. Wright

Moor Lane Laboratory, ECASS Technologies Ltd, Kirkburton, Huddersfield, HD8 0QS, UK

Abstract— This is the first of two papers to be presented at the Moscow Symposium, and the seventh paper in the series of electromagnetic (EM) sources and observers in motion. Two given in Xian China, two in Cambridge USA and two in Marrakesh Morocco, over the last two years. The Moscow paper deals with the existence of the propagation medium (ether) and its support for a new relativity theory. This theory, derived directly from Lorentz’s medium based motional transform (LT), removes non causality apparent in Einstein’s relativity, clarifying our understanding of the universe. Einstein believed there was no propagation medium (ether), predicting an irrational (non causal) wave theory, but then used a medium in his field equations predicting causal observations. A new medium based theory indicates that Einstein’s ether-less relativity is in error and his medium based Special Relativity (SR) incomplete. It describes an improved theory that agrees with the measured predictions of SR, but predicts additional measured observations that SR cannot predict, and identifies aspects of SR that cannot be measured. Historically, Lorentz was the first to predict the measured effects of electromagnetic (EM) systems in motion. Einstein was the first to solve the EM wave equation (partially), based on Lorentz’s medium based transform, predicting the same motional properties as Lorentz. Therefore, Einstein’s SR has a medium based causal aspect that predicts many of today’s measured observations, and an ether-less, non causal aspect, which cannot. A New Relativity (NR) theory extends the LT, distinguishing between measured source and observer motional properties and between different motional reference frames. This allows a new set of problems to be solved that cannot be accounted for using Einstein’s ether-less SR. Restoring the medium removes the discontinuity between classical and modern physics. The medium’s existence provides a common link between electrical and gravitational fields, accelerating frames and perhaps to the unification theory of the universe.

1. INTRODUCTION

Viewing the sky at night, it is difficult to imagine that the universe is not continuous and absolute, i.e., it is not one piece of spatial fabric. Einstein concluded just that, implying that space is a patch-work of autonomous regions of relativity. He believed there was no medium and no absolute time and space. Einstein based his belief mainly on his interpretation of the undetectable motion on Earth as it moves through space, as measured by the Michelson and Morley Experiment (MMX) [1]. Also, that source and observer Doppler [2] effects (observed source changing frequencies through motion) are identical. Although these results appeared initially not to be predicted by classical wave theory, it is shown conclusively that they are based on a propagation medium and are both supported by the medium based wave equation.

Convinced of his ether-less relativity, Einstein decided that only relative motion between spaceships was meaningful, coining the misnomer term ‘relativity’. Ships could travel notionally at any velocity, without being able to resolve their speed, providing there was no relative velocity between them. With relative motion, either ship could be considered to be moving with their astronauts ageing less than the other ship. Incredibly, both situations were considered possible, even at the same time, which is impossible in the real world. It was claimed that the situation could not be resolved until one of the ships changed speed or direction. But what would have been the situation immediately before the ships changed course? What would have happened if the ships never change course? These questions can only be satisfactorily answered if the medium exists and all motions are considered relative to the propagation medium.

Because it seemed to work, relativists over the last 100 years have been convinced that Einstein’s ether-less relativity made sense, when in fact it is non causal (cannot be measured). The main problem is that electromagnetic (EM) waves (light) are supposed to propagate without a propagation medium (ether), which by definition is a contradiction and in reality physically impossible. In the absence of all gravitational matter, fields and particles, a vacuum is not empty space. It has a defined and measureable medium, (permeability $\mu = 1.25 \times 10^{-6} \text{ N/A}^2$ and permittivity

*Corresponding author: Selwyn E. Wright (selwyn.wright@ntlworld.com).

$\epsilon = 8.85 \times 10^{-12}$ F/m). With well established properties it is pointless to deny the medium's existence. The medium determines the wave characteristics, including the wave propagation speed. EM waves are no exception; their electrical medium properties are finite giving a finite speed of light. If there was no medium the propagation speed in space would be infinite, which is not the case.

It appears that all electrical fields use the same medium to transmit their steady state values and disturbances. It seems that unsteady electrical fields create EM waves, steady difference electric fields create gravity, and net gravity fields through the universe create a residual inertial field (Higgs [3]). Field disturbances can be represented by waves or non massive particles: light waves as photons, gravity waves as gravitons and Higgs field disturbances by bosons, they all appear to be electrical, Wright [4]. This includes Einstein's Special Relativity (SR) [5] involving light, and General Relativity (GR) [6] concerning gravity.

2. NEW RELATIVITY

There is ample evidence to support the propagation medium, but no evidence to support its non existence. To extend and solve the electromagnetic motional wave equation it is important to establish the credibility of the medium's existence. To do so, it should be recognised that without a medium, there is no known way of transmitting EM waves, solving the wave equation, predicting events, maintaining continuity of time and space, and no way of creating inertia. Further, without a propagation medium time has no direction, one cannot distinguish between which system is moving, the source or observer, which system is ageing least, or identify the optical paths — they are indeterminate. Simultaneity (equal propagation times upstream and down) and reciprocity (interchanging the observer and source makes no difference optically), cannot be supported by the medium based Maxwell's Equations (ME's) [7], or the medium based Lorentz transform [8]. These insurmountable problems could have been avoided by simply accepting the medium's presence.

Thus all wave theories should have a medium, to be rational. Without a medium, they cannot be a solution of the wave equation, or predict causal events. The medium is not a mathematical artefact that can be removed as Einstein believed. The medium is needed to support the field that supports the waves that illuminates the observed events. This medium's presence should not have been doubted over a century ago, there was considerable evidence then to support the medium. There is no justification now to reject it, and there has never been substantial evidence to support Einstein's ether-less relativity. All motional effects, both classical and relativistic, are shown to be caused by motion relative to the medium, as Lorentz predicted, and not relative to other systems, as Einstein claimed.

This motion relative to the medium is easily verified, either by inspection of Einstein's field equations that use Lorentz's medium based transform. Or absolutely derived directly from the medium based classical wave equation, using Lorentz's time rate and structural contraction through motion. Either way, Einstein's measured SR observations are predicted using a medium, whereas Einstein's ether-less concept of relativity is false and his ether-less predictions not measurable. Relativists claim that no medium exists or indeed is required. They interpret Minkowski's [9] rectangular axes space-time four vector analysis as requiring no medium. However, this is not possible, the vertical and horizontal axes of space-time still require Lorentz's rectangular axes transform, representing time and space respectively. Normalised against the speed of light, the velocity becomes a 45 degree gradient. This is just a mathematical convenience of representing time and space, there is *no mechanism to remove the medium*.

On Earth, most motional effects, without involving particle accelerators, are predicted solely by the medium based classical wave theory. At Earth speeds and field strengths, relativistic and gravitational contributions, unless integrated over long periods of time are very small compared to the dominant classical instantaneous motional effect. Confusion in relativity also occurs through there being two types of reference frames. Einstein believed EM waves were some how different from classical ones. It was acknowledged that the medium existed for stationary EM systems, but suddenly disappeared when the systems were set in motion. This inconsistency was suggested by Einstein's ether-less invariant inertial frame, where the mechanics and physics are invariant.

However, this frame, not recognising the medium's existence, is incapable of predicting observations. The measured situation is described by Lorentz's variant optical frame containing the additional effect of the medium and its waves, which make the judgment of observations possible. Although the propagation speed and observations are invariant within the moving frame, the propagation time asymmetry (PTA) for all waves travelling around a moving system, including

EM waves, always become asymmetric, revealing the system's motion. This PTA, which is absent in Einstein's inertial frame, is a classical, and causal prediction, passing through into Lorentz's medium based motional transform, completely negating Einstein's ether-less concept of relativity. Thus all sources, including classical and EM, behave similarly, to make waves they both require a propagation medium.

Further, ether-less relativity cannot distinguish between various types of frame motion. One is where systems move with respect to the medium, causing a measured propagation time difference between source and observer motion. The other is where there is no motion between the medium and the frame, as in distinguishing between propagation in the medium at rest in space, moving with the Earth (Earth centred) and moving with the Sun and Solar System (heliocentric). These frames are implemented without authority (cause), they can only be explained if the medium exists, is generally at rest, moves with the Earth and finally with the Solar System. The medium motion and motion relative to the medium cannot be support by Einstein's ether-less concept of relativity. Thus Einstein's claims: i) only relative motion between systems can be detected, ii) distinction cannot be made between reference frames moving at various constant speeds and iii) the medium is redundant, which we have accepted on faith, are all non causal (false). Einstein's inertial frame, responsible for these beliefs, is inappropriate to predict measured SR observations; it is the medium based optical frame that correctly predicts them.

Einstein's ether-less SR predicts no absolute time and space, and time travel, both of which are non causal (impossible). In the New Relativity (NR), it is possible (causal) to travel visually to the past, but not to interfere or change it, as it has already happened. It is not possible to visually travel to the future as it has not yet occurred. Neither is it possible to materially (physically) travel into the future or past. But it is possible to slow one's time down through material transport, by physically moving at a high speed or visiting a gravitational body. However, this is not reversible time travel, it is just relatively changing the rate of ageing between systems. Accepting the reality of the propagation medium, and presuming that the speed of light cannot be exceeded, $M = v/c < 1$, where M is the system speed ' v ' compared to the light speed ' c ' in the medium. It appears that the speed can be exceeded across frames, $M^* > 1$, where $M^* = M/\alpha$. The speed and distance capability is much greater across the hybrid frame by α^{-1} , where α is the Lorentzian contraction factor. Distance is measured in the stationary propagation medium and the slower time in the moving system frame. As $M \rightarrow 1$, $\alpha \rightarrow 0$ and $M^* \rightarrow \infty$, allowing the hybrid speed of light to exceeding the speed of light in the medium, resulting in huge distances to be achieved in space travel in a human life.

Ignoring the medium's existence has led to confusion in the basic understanding of EM wave theory. It has led to the discontinuity between classical and modern physics. It has not helped in the unification of EM and gravitational fields, and the ultimate unification theory of the universe. Basic optics tells us that all fundamental wave concepts, such as Huygens's [10] wave theory, ME's and LT are medium based. They are meaningless without their propagation medium to propagate their steady fields and disturbances. Again, all motional effects are with respect to the medium, not through relative motion between systems. This includes the propagation speed, which also propagates relative to the medium. It is not generally understood that the speed of light is invariant only because time rate and systems shrink through motion relative to the medium, by exactly the same ratio, maintaining its propagation speed in the moving frame. Although the mechanics (first postulate) and the speed of light (second postulate) are invariant in Einstein's inertial frame, the PTA in a moving optical frame is asymmetrical and variant. Therefore, in the New Relativity (NR), a third postulate is required, stating that the PTA and its variance exist in an optical frame moving relative to the medium.

Finally, the ether-less predictions were supported by Born [11]. He adopted Minkowsky's oblique transform axes representation, rather than the rectangular axes used in the Lorentz transform. However, these simulations based on no medium, cannot be a solution of the wave equation; they are non causal and cannot be measured. A causal EM motional analysis (EMMA) by Wright [6, 31] based on the medium, has been developed that extends the medium based Lorentzian transform to include both source and observer motion. It distinguishes between measured motional differences using individual pairs of time and space scales representing source, observer and medium, rather than the two unspecified pairs in the incomplete SR. This extension predicts the measured observations that Einstein's medium based SR predicts. However, it predicts additional measured properties that SR cannot predict, such as the different properties that sources and observers have when in motion. It also provides overwhelming evidence that Einstein's non measureable ether-less

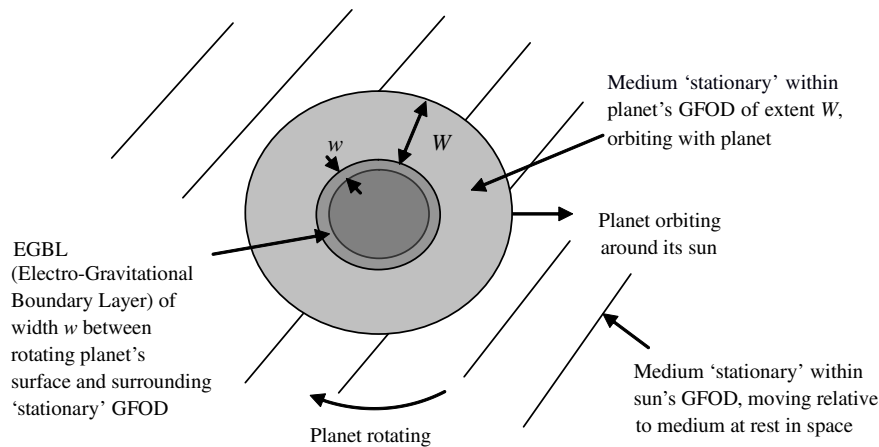


Figure 1: Medium profile around a rotating and orbiting planet, according to Michelson and Morley, Sagnac, Michelson and Gale, Penzias and Wilson, Hafele and Keating, Saburi et al., Reasenburg et al., COBE and GPS.

aspects are purely speculative.

3. MOVING MEDIUM

A mass-less vacuum devoid of all gravitational matter, fields and particles has an electrical medium with finite properties. Considerable data provides indisputable proof of this medium's presence. It can be shown that Bradley's forward aberration angle [12], is caused through the Earth and telescope (observer) orbiting around the Sun, moving laterally to the light from a distant star propagating in the medium at 'rest' in space. Whereas, in Global Positioning Systems, (GPS) [13] a backward displacement angle is formed through satellite (source) motion in the 'stationary' medium surrounding the Earth. The signal propagates between the satellite and Earth station, which rotate laterally to this signal propagating in the 'stationary' medium, resulting in a displacement error of 30 m at UK latitudes, Wright [4]. These two examples clearly distinguish between source and observer motion relative to the medium, which Einstein's ether-less SR cannot distinguish between. An opportunity to confirm the existence of the medium went without fanfare when Hafele and Keating [14], using atomic clocks, measured symmetrical time slowing through motion relative to the Earth's position, not the Earth's rotation where asymmetric time slowing is measured. Flying at 10 km above the Earth, in the medium surrounding and orbiting with the Earth, the symmetrical time slowing confirmed that the medium at this altitude is 'stationary', not rotating with the Earth.

Saburi et al. [15] also demonstrated the existence of the propagation medium. Here measurements in satellite communication across the Pacific demonstrated longitudinal propagation time asymmetry (PTA) of 300 ns (100 m), in and against the direction of the geostationary satellite rotating with the Earth. This is relative to the 'stationary' medium surrounding and orbiting with the Earth, the asymmetry again confirming the medium's presence. This medium orbiting with the Earth, is in turn shown to move relative to the 'stationary' medium surrounding the Sun and Solar System, moving through the universe. This has been confirmed through symmetrical signals, in each direction, between Mars and Earth in the Mars-Viking Lander project by Reasenburg et al. [16]. If the medium did not move with the Solar System, but was stationary in space, there would be huge asymmetries in communication time in and against the direction of the Sun and Solar System moving ($M = v/c = 10^{-2}$) through the universe. These examples demonstrate absolutely the medium's existence. The above data indicates that the medium is attracted to and surrounds large gravitational bodies to an extent ' W '. This extent appears to be controlled by the planet's gravitational field of dominance (GFOD) in the presence of the Sun's gravitational field of influence.

The medium moving with the planet is illustrated in Figure 1. In the Earth's case, the effective boundary appears to be approximately $W = 50$ Earth radii. Of course the boundary will be graded, not abrupt. Whereas, the MMX [1] and Sagnac [17, 18] showed that the medium on the Earth's surface, rotates with the Earth, probably through gravitational attraction of the massive atmosphere. Further, Michelson and Gale [19] showed that surface medium rotated relative to the stationary medium surrounding the Earth. Therefore, the Earth's rotation relative to the

surrounding medium creates a medium velocity electro-gravitational boundary layer (EGBL) of extent ‘ w ’ above its surface. The extent of this boundary layer is less than 10 km, according to Hafele and Keating. The medium surrounding the planet then orbits with the planet through the medium ‘stationary’ around its sun’s GFOD and solar system.

This model is supported by the latest results from NASA’s Gravitation Probe B [20]. In the absence of gravitational matter, the medium in the universe appears to be stationary, on average, providing a universal reference for motion. The cosmic microwave background (CMB), discovered by Penzias and Wilson [21], is shown to be EM radiation, propagating uniformly in all directions, throughout the universe, relative to the medium basically at rest in space. The stationary medium away from gravitational bodies has also been confirmed through the Cosmic Background Explorer COBE [22]. Here the CMB energy collection increases with motion relative to the stationary medium, similar to trawling fish nets catch more fish than stationary ones. What is surprising, with all the evidence available, even in Einstein’s time, is that *Einstein did not realise that his measured predictions were not based on an ether-less universe, but based on the existence of a propagation medium.*

4. CONCLUSION

There is an abundance of data confirming the propagation medium’s existence. Not accepting the medium’s presence, one cannot comprehend that the medium is generally at rest in space, attracted to and moves with massive gravitational bodies and forms medium velocity gradients (boundary layers) on their rotating surfaces. This NR model is extensively supported by: Galileo [23], Huygens, Bradley, Fresnel [24], Stokes [25], Fizeau [26], Maxwell, MMX, Lorentz, Sagnac, Schwarzschild [27], Saburi et al., Reasenberg et al., GPS, COBE, Kramer et al. [28] and Gravity Probe B, to name but a few medium based theories, experiments and observations. Restoring the medium restores causality and legitimately explains all data wrongly considered to support an ether-less SR. It is easy to verify the medium’s presence, whereas removing it causes erroneous results. It appears that all fields, electric, gravitational and inertial require the same well defined and established EM medium to propagate their fields and disturbances, Wright [32]. It is remarkable that irrational arguments for an ether-less universe have been supported, without proof, for over 100 years by relativists believing that they could see merit in an ether-less non causal cosmos. Further details can be found in the six peer reviewed papers given during this last two years at the Progress in Electromagnetic Research Symposiums (PIERS), and the two papers presented in Moscow this year, are listed at the end of the References.

REFERENCES

1. Michelson, A. A. and E. W. Morley, “On the relative motion of the Earth and the luminiferous ether,” *American Journal of Science*, Vol. 34, No. 203, 333–345, 1887.
2. Doppler, C., “On the coloured light of the binary refracted stars and other celestial bodies — Attempt of a more general theory including Bradley’s theorem as an integral,” *Monograph*, 1842.
3. Higgs, P. W., “Broken symmetries, massless particles and gauge fields,” *Phys. Lett.*, Vol. 12, 132, 1964.
4. Wright, S. E., *Problems with Einstein’s Relativity*, Trafford Publishing, 2010.
5. Einstein, A., “On the electrodynamics of moving bodies,” *Annalen der Physik*, Vol. 17, 891–921, 1905.
6. Einstein, A., “Die feldgleichungen der gravitation (The field equations of gravitation),” *Königlich Preussische Akademie der Wissenschaften*, 844–847, 1915.
7. Maxwell, J. C., “A dynamical theory of the electromagnetic field,” *Philosophical Transactions of the Royal Society of London*, Vol. 155, 459–512, 1865.
8. Lorentz, H. A., “Simplified theory of electrical and optical phenomena in moving systems,” *Proc. Acad. Science Amsterdam*, Vol. 1, 427–442, 1899.
9. Minkowski, H., *Raum und Zeit*, 1908.
10. Huygens, C., *Traité de la Lumière*, Pieter van der Aa, Leiden, Netherlands, 1690.
11. Born, M., *Einstein’s Theory of Relativity*, Dover, New York, 1924, Latest Revision, 1965.
12. Bradley, J., *Third Astronomer Royal*, Reprint from the *Philosophical Transactions of Stellar Aberration: On the Motion of the Fixed Stars*, 1725.
13. GPS, Logsdon, T., *The NAVSTAR Global Positioning System (GPS)*, Van Nostrand Reinhold, 1992.

14. Hafele, J. and R. Keating, “Around the world atomic clocks. Predicted relativistic time gains,” *Science*, Vol. 177, No. 4044, 166–168, 1972.
15. Saburi, Y., M. Yamamoto, and K. Harada, “High precision time comparison via satellite and observed discrepancy of synchronization,” *IEEE Transactions*, Vol. 25, 473–477, 1976.
16. Reasenberg, R. D., I. I. Shapiro, P. E. MacNeil, R. B. Goldstein, J. C. Breiden-thal, J. P. Brenkle, D. L. Cain, T. M. Kaufman, T. A. Komarek, and A. I. Zygielbaum, “Viking relativitve experiment — Verification of signal retardation by solar gravity,” *Astrophysical Journal*, Vol. 234, L219–L221, 1979.
17. Sagnac, G., “L’éther lumineux démontré par l’effet du vent relatif d’éther dans un interféromètre en rotation uniforme,” *Comptes Rendus*, Vol. 157, 708–710, 1913.
18. Sagnac, G., “Sur la preuve de la réalité de l’éther lumineux par l’expérience de l’interférographe tournant,” *Comptes Rendus*, Vol. 157, 1410–141, 1913.
19. Michelson, A. A. and H. G. Gale, “The effect of the Earth’s rotation on the velocity of light,” *The Astrophysical Journal*, Vol. 61, 140–145, 1925.
20. Gravity Probe B, <http://www.npr.org/2011/05/06/136057344/proof-that-einstein-got-it-right?> and <http://www.sciencedaily.com/releases/2011/05/110504150655.htm>, 2011.
21. Penzias, A. A. and R. W. Wilson, “A measurement of the flux density at 4080 Mc/s,” *Astrophysical Journal Letters*, Vol. 142, 1149–1154, 1965.
22. Cosmic Background Explore, NASA Goddard Space Flight Center, 1992.
23. Galileo, G., *Dialogue Concerning the Two Chief World Systems*, Using the Example of a Ship Travelling at Constant Velocity, 1632.
24. Fresnel, A., “Lettre d’Augustin Fresnel a Francios Arago sur l’influence du mouvement terrestre dans quelque phenomenes d’optique,” *Annales de Chimie el de Physique*, Vol. 9, 57–66, 1818.
25. Stokes, G. G., “On the aberration of light,” *Philosophical Magazine*, Vol. 27, 9–15, 1845.
26. Fizeau M. H., “Sur les hypothèses relatives à l’éther lumineux,” *Comptes Rendus*, Vol. 33, 349–355, 1851; *Ann. De Chim. Et de Phys.*, Vol. 57, 385–404, 1859.
27. Schwarzschild, K., “Über das gravitationsfeld eines massenpunktes nach der Einstein’schen theorie,” *Sitzungsberichte der Königlich Preussischen Akademie der Wissenschaften*, Vol. 1, 189–196, 1915.
28. Kramer, M., I. H. Stairs, R. N. Manchester, M. A. Mc Laughlin, A. G. Lyne, R. D. Ferdman, M. Burgay, D. R. Lorimer, A. Possentti, N. D. Amico, J. M. Sarkissian, G. B. Hobbs, J. E. Reynolds, P. C. C. Freire, and F. Camilo, “Tests of general relativity from timing the double pulsar,” 2006.
29. Wright, S. E., “Electromagnetic sources and observers in motion I — Evidence supporting the EM propagation medium for the transmission of light,” *PIERS Proceedings*, 71–76, Xi’an, China, Mar. 22–26, 2010.
30. Wright, S. E., “Electromagnetic sources and observers in motion II — Einstein’s ether-less relativity versus lorentz’s medium based theory,” *PIERS Proceedings*, 77–81, Xi’an, China, Mar. 22–26, 2010.
31. Wright, S. E., “Electromagnetic sources and observers in motion III — Derivation and solution of the electromagnetic motional wave equation,” *PIERS Proceedings*, 1151–1155, Cambridge, USA, Jul. 5–8, 2010.
32. Wright, S. E., “Electromagnetic sources and observers in motion IV — The nature of gravity and its effect on the propagation medium,” *PIERS Proceedings*, 1156–1161, Cambridge, USA, Jul. 5–8, 2010.
33. Wright, S. E., “Electromagnetic sources and observers in motion V — A revised theory of relativity,” *PIERS Proceedings*, 367–372, Marrakech, Morocco, Mar. 20–23, 2011.
34. Wright, S. E., “Electromagnetic sources and observers in motion VI — New motional optics,” *PIERS Proceedings*, 362–366, Marrakech, Morocco, Mar. 20–23, 2011.
35. Wright, S. E., “Electromagnetic sources and observers in motion VII — Medium support for a new relativity theory,” *PIERS Proceedings*, Moscow, Russia, Aug. 19–23, 2012.
36. Wright, S. E., “Electromagnetic sources and observers in motion VIII — New relativity theory establishes Einstein’s ether-less aspect of relativity as irrational,” *PIERS Proceedings*, Moscow, Russia, Aug. 19–23, 2012.

Electromagnetic Sources and Observers in Motion VIII — New Relativity Theory Establishes Einstein’s Ether-less Aspect of Relativity as Irrational

S. E. Wright

Moor Lane Laboratory, ECASS Technologies Ltd, Kirkburton, Huddersfield, HD8 0QS, UK

Abstract— This is the second paper to be presented to the symposium in Moscow, and the eighth paper in the series of EM sources and observers in motion. The first paper at this symposium considers the existence of the propagation medium (ether) and its support for a new relativity theory. This paper establishes Einstein’s ether-less aspect of relativity as non causal (cannot be measured). The medium based Lorentz Transform (LT), is the fundamental motional transform. It predicts the complete motional effect, including the classical wave propagation time asymmetry (PTA) surrounding a system moving relative to the medium. And the additional relativistic time rate and system contraction (LC) through high speed motion, again with respect to the medium, (notionally $LT = PTA + LC$). PTA can exist without LC, but LC cannot exist without PTA. Thus all sources, including classical and EM, behave similarly, to make waves they both require a propagation medium. The classical PTA is therefore a vital part of any causal wave theory, which Einstein’s ether-less relativity cannot predict. Lorentz’s theory is causal (the cause must always occur before the effect (event)), it is a solution of the wave equation predicting measured events. Both PTA and LC are a result of motion relative to the medium, as Lorentz predicted. However, Einstein’s ether-less aspect of Special Relativity (SR), cannot support the fundamental medium based PTA. His belief in relative motion and his omission of the PTA is not supported by the medium based LT. Einstein’s ether-less aspect is therefore irrational, it predicts his ether-less properties, such as time travel and no absolute time and space, neither of which can be measured. These ether-less non measureable predictions are based on Einstein’s invariant inertial frame, which without the medium cannot anticipate PTA. The measured predictions, are based on Lorentz’s moving optical frame, which describes waves and systems moving with respect to the medium. The measured SR predictions are therefore medium based, in conflict with and discrediting Einstein’s own ether-less predictions. To complete the process, distinction is made in the New Relativity (NR) between source and observer motion time and space scales allowing their flight paths to be plotted on the same space-time diagram for the first time. In brief: SR is inconsistent, incomplete and its ether-less interpretation fallacious.

1. INTRODUCTION

Relativists, not aware of the measured predictions of the medium based NR, are unable to arrive at comprehensive conclusions. An abundance of data confirms that all fields require a medium to make their wave equation causal. Motion relative to the medium can be readily demonstrated either through classical PTA or relativistic medium based LC measurements. Also, gravity attracts and compresses the medium (space-time distortion), according to the Schwarzschild [1] metric. At satellite and Earth rotational speeds ($M = v/c \approx 10^{-5}$), the relativistic LC effect is $M^{-1} \approx 10^5$ smaller than the classical PTA effect. Therefore, apart from Lorentz’s gradual time slowing through satellite motion, the dominant instantaneous displacement error in GPS [2] and satellite communications (Saburi et al. [3]), is the medium based classical Sagnac [4, 5] (PTA) effect. Here, PTA is caused through satellite and Earth’s rotation relative to the ‘stationary’ medium surrounding and orbiting with the Earth. Further, Special Relativity [6] (SR) is incomplete, it cannot distinguish between moving Earth centred and Heliocentric Solar System reference frames, or solve the general wave equation for both source and observer motion. To distinguish between these measured differences, the medium’s presence has to be accepted; Einstein’s concept of relative motion rejected and the medium based Lorentz Transform [7] (LT) extended. To make the distinction, three pairs of time and space scales are required, instead of the two non defined pair used in SR. The medium based NR provides a link between LT, SR, General Relativity [8] (GR), accelerating frames and the Equivalence Principle. It removes the non causal predictions, removing the mystical aurora surrounding relativity. NR establishes reality from non real situations, restores the connection between classical and modern physics and provides a possible link to the theory of everything. Lorentz is

*Corresponding author: Selwyn E. Wright (selwyn.wright@ntlworld.com).

fundamental, Einstein’s ether-less SR is a misinterpretation of Lorentz and NR is an extension of Lorentz’s motional theory.

2. NEW SPACE-TIME DIAGRAM

The space-time diagram for arbitrary motion is illustrated in Figure 1. It is supported by the complete solution of the motional wave equation for arbitrary sources and observers in motion, relative to the propagation medium, described briefly below and in detail in an EM motional analysis (EMMA), Wright [9].

To completely define the radiation process, distinction has to be made between source and observer time and space, relative to the medium time and space. Three time and space scale pairs are therefore essential and specified (source, observer and medium). Whereas only two unspecified scale pairs are used in Einstein’s incomplete SR, where there is no distinction made between source and observer motion. The vertical and horizontal axes in Figure 1 represent absolute time t_p and space x_p , in the medium, respectively. Corresponding times, between the source emission event time τ_s and observer reception event time τ_o curves are connected by propagation light paths. These paths represent light moving forward with time, from source to observer, going from left to right in the direction of the arrows, whose gradient is $1/c$ (45° if x_p is in light years). The segment of integrated or accumulative observed event time τ_o , in terms of the integrated source event time τ_s , for arbitrary source and observer flight paths through the universe are given by Equation (1), from Equation (22) in reference [9].

$$\tau_o = \int [\varepsilon_s \alpha_s^{-1} \varepsilon_o^{-1} \alpha_o]_{t_p} d\tau_s, \quad t_o = \tau_o + R_o/c, \quad R_o = \alpha_o R_p \quad (1)$$

This equation gives, for the first time, the complete time transform. It is plural/poly chromatic giving both red and blue shifting simultaneously for sources and observers in motion. The observed event time depends on the initial propagation distance R_p in the medium, and on how the individual motional operators ε_o^{-1} , α_o , ε_s , and α_s^{-1} change with time during the source and observer journeys through space. At any source emission time t_s and corresponding observer reception instant, t_o , the instantaneous time transform is given by:

$$K = t_o/t_s = \varepsilon_s \alpha_s^{-1} \varepsilon_o^{-1} \alpha_o \quad (2)$$

The kinematic or relativistic omni-directional time change operators $\alpha_s^{-1} \alpha_o$, given by $\alpha_s = (1 - M_s^2)^{1/2}$ and $\alpha_o = (1 - M_o^2)^{1/2}$, result in instantaneous Lorentzian time slowing at the moving source (emission time). And an effective time quickening of the surroundings at the moving observer (reception time), R_o/c later, their time values are accumulative. The classical directional Doppler factors $\varepsilon_s \varepsilon_o^{-1}$, are given by $\varepsilon_s = 1 - M_s \cos \sigma_s$ and $\varepsilon_o = 1 - M_o \cos \sigma_o$, where $M_s = s/c$ & $M_o = o/c$, and s and o are the source and observer velocities respectively, compared to the speed of light c . σ_s and σ_o are the source and observer angles made with a line joining the emission and the reception positions. The Doppler factors effectively compress or expand time and space

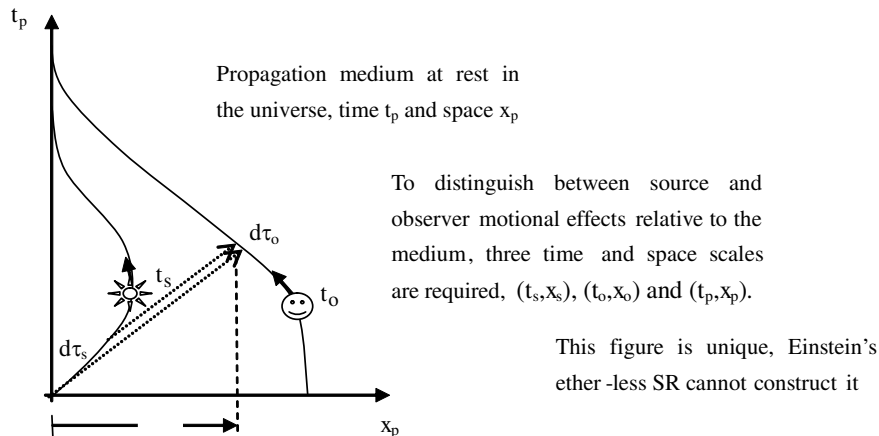


Figure 1: Relationship between source time t_s and observer time t_o for a given arbitrary motion relative to a stationary propagation medium of time t_p .

momentarily, depending on whether the systems are approaching (M positive for source, M negative for observer) and vice versa for receding systems. In a closed loop (flight path) the compression and expansion of the Doppler factors around the loop integrate to zero, they cancel.

In this theory, time changes instantly at the source emission and the later observer reception times, according to their speeds in the medium at that instant, not according to relative motion between systems, as Einstein thought. This allows for the first time both source and observer flight paths to be plotted on the same Minkowski space-time diagram. Interchanging the source and observer for the same flight paths can give entirely different observations, confirming Einstein's concept of relativity is inappropriate. Further applications of Figure 1 can be found in reference [10].

3. MAIN CONCEPTS

The main concepts of the New Relativity (NR) theory are summarized below:

3.1. Medium Required

A propagation medium (ether) is essential to transmit fields, including electric, gravitational and an inertial field. The medium determines the wave propagation speed for their disturbances i.e., photons, gravitons and bosons respectively. The measured medium properties are finite giving a finite propagation speed, no medium would give infinite speed. Without a medium there is no wave equation solution resulting in non causal predictions.

3.2. Common Link

The medium is the common link between system motion, accelerating frames, gravity and inertia. The medium fills the space part of space-time, referred to in gravitational theories, and space-time distortion around bodies is the compression of the medium's space and time rate, by gravity.

3.3. Vacuum Medium

Extensive data shows that the mass-less medium (vacuum), having no atomic structure, behaves as a fluid, which is attracted to and moves with large gravitational bodies. If the body rotates and there is a gravitational atmosphere, the medium close to the body's surface will rotate.

3.4. Motional Effects

All observations and measurements, including classical and relativistic, (time slowing, systems contraction, propagation time asymmetry (PTA) and invariant speed of light) are caused through motion with respect to the medium, as Lorentz predicted, not through relative motion between systems, as Einstein believed.

3.5. Causal Wave Theories

All rational wave theories are shown to be medium based, including the EM wave equation, Maxwell's equations, Lorentz transform and Relativistic addition of velocities. The speed of light is invariant only because its time rate and systems shrink through motion relative to the medium, by exactly the same ratio, maintaining its propagation speed in the moving frame.

3.6. Space-time

Minkowski's [11] rectangular axes four vector space-time analysis is medium based. The vertical and horizontal axes of the space-time diagram use Lorentz's rectangular axes medium based transform, representing time and space. There is no mechanism to remove the medium. Born's [12] oblique transform axes are a simulation, they are not a solution of the wave equation, they are non causal.

3.7. Two Types of Frames

There are two types of reference frames: Einstein's ether-less invariant inertial frame, where the mechanics and physics are invariant, which is not capable of making observations. And a variant optical frame containing the medium and its waves, which facilitates judgment of observations.

3.8. Two Types of Motion

There are two types of frame motion. One is where systems move with respect to the medium, causing a measured wave propagation time difference between source and observer motion. The other is where there is no motion between the frame and medium, as in distinguishing between the medium at rest in space, moving with the Earth (Earth centred) and moving with the Sun and Solar System (heliocentric). Recognising the presence of the medium allows these motional distinctions to be made.

3.9. Lorentz Fundamental

The Lorentz Transform (LT) is based on the propagation medium. It predicts the general solution of the motional wave equation. Its motional effects are therefore predictable (causal), represented by $LT = PTA + LC$. It includes the essential classical wave propagation time asymmetry (PTA), and an additional modifying Lorentzian time rate and system contraction (LC) at high speed. At Earth speeds, LC is dominated by PTA.

3.10. Einstein's Ether-less SR

Einstein assumed there was no medium needed to propagate light (observed events) through space. Without its medium, the EM wave equation cannot be solved, without its solution measured events cannot be predicted. This theory, without a medium, cannot support the basic PTA. It lacks the fundamental requirement of radiating systems, it is non causal.

3.11. Einstein's False Predictions

Einstein's ether-less claims are: i) only relative motion between systems can be detected, ii) distinction cannot be made between reference frames moving at various constant speeds, iii) the medium is redundant, iv) material time travel is possible and v) there is no absolute time and space, they are all non causal (false). Einstein's inertial frame, responsible for these beliefs, is inappropriate to predict measured SR observations. It is the medium based optical frame that correctly predicts the events.

3.12. Measured Predictions

Einstein's field equations use the medium based LT. Its solution of the EM wave equation is therefore causal, predicting measured observations. The same predictions can be obtained directly from the classical wave equation, modified by the LC. Therefore, Einstein's measured predictions are medium based.

3.13. Incomplete Theory

Einstein's medium based theory is not complete, it does not distinguish between measured source and observer motional differences. A general EM motional analysis (EMMA) determines source and observer motional effects relative to the medium, using three sets of time and space scales, rather than the two used in SR.

3.14.

It is not possible to materially *time travel*. Causally it is possible to visually visit the past, but not to interact with it. However, it is not possible to visit the future, it is non causal, it has not yet happened. Finally, the speed of light can be exceeded across *hybrid reference frames*, allowing huge distances in space travel to be achieved, without exceeding the speed of light in the medium.

4. CONCLUSIONS

Short. This New Relativity Theory (NR) is an extension of Lorentz's medium based motional theory. The theory is an improved version of Einstein's Special Relativity (SR). It predicts the same measured predictions as SR, but based on a propagation medium. It also predicts other measured observations that SR cannot predict, and shows that all other ether-less SR predictions are false (non measurable). In brief:

- Extensive data supports the propagation medium (ether).
- All motional effects and measured predictions are medium based.
- Einstein's ether-less (non causal) SR predictions are fallacious.
- Einstein's measured (causal) SR predictions are medium based.
- SR cannot distinguish between source and observer motion.
- A new medium based general theory 'EMMA' is developed.

Extended. Einstein's medium based SR, which predicts many of today's measured observations, is founded on Lorentz's medium based motional theory, although Einstein gave no credit to Lorentz. Einstein's ether-less aspects of SR (simultaneity, optical reciprocity, no absolute time and space, and time travel), are a mathematical simulation equivalent to an oblique time and space axes transform. This model, which attempts to remove the effect of the propagation medium by using a medium (circular argument), does not represent reality. It is not a solution of the wave

equation, it is non causal and not supported by the medium based rectangular axes Lorentz transform. To restore reality and propagation with respect to the medium, the oblique transform axes are returned back to their original rectangular Lorentzian positions. This breaks the propagation time symmetry, removes the unnatural simulated concepts of simultaneity (simultaneous propagation times upstream and down), and reciprocity (interchanging source and observer does not affect observations) and restores the variant propagation time asymmetry (PTA) measured in the moving frame. Thus, there are two aspects of SR; an ether-less non causal simulated aspect that is not reality, and a medium based aspect that is.

There is no basis for the ether-less SR, apart from attempting to satisfy the Michelson and Morley experiment null result (MMX) [13], which was misinterpreted to support an ether-less universe. It is now accounted for quite naturally through the propagation medium being at rest on the Earth's surface. The ether-less non causal aspect of SR cannot be measured, those who claim they have measured it have usually measured motional aspects of the medium based LT. Although Einstein denied the medium's existence and creatively described elaborate details of an ether-less SR, these details have never been measured. Einstein actually used a propagation medium in his motional electrodynamics, rendering his own ether-less SR model as untenable. Einstein's space in his space-time, used to measure distance in his SR and space compression in his General Relativity (GR), are in fact the same space, but filled with the propagation medium, used by Lorentz. Also it is the same medium used in accelerating frames, linking these concepts together. NR does nothing remarkable, it simply restores the rationality of EM theory by re-establishing the medium. This makes it possible to distinguish between source and observer motion and between Earth centred and heliocentric moving medium reference frames, which in turn restores the connection between classical and modern physics, removing the inconsistency in SR.

NR predicts the measured aspects of SR and additional measured properties created by distinguishing between source and observer motion with respect to the medium. NR is in agreement with transverse Doppler, changes in time, space, mass, momentum and Einstein's famous energy equation. Also, it is in agreement with Schrödinger's [14] wave equation, Relativistic Quantum Mechanics (RQM), which is Lorentz invariant, the theories of Dirac [15], Quantum Electro Dynamics (QED) and the Standard Model (SM) in particle physics. Einstein's GR which results through expressing the LT in terms of Minkowski's space-time four-vector analysis and his gravitational theory, which form the basis of astrophysics and cosmology. They are all based on the same medium. It can be shown that the medium supports the Schwarzschild metric and event horizon. Assuming the medium to be homogeneous and isotropic, the Robertson [16]-Walker [17] metric in cosmology is obtained, and through the Friedmann metric [18], the Hubble constant [19].

It is believed that it has been shown beyond doubt that the EM medium exists, and that it is false to believe that steady fields and their disturbances can propagate through space without it. Without the medium none of the motional effects discussed in this paper could occur. There is no need to remove the propagation medium as Einstein attempted to do, the universe works extremely well with it.

REFERENCES

1. Schwarzschild, K., "Über das Gravitationsfeld eines Massenpunktes nach der Einstein'schen Theorie," *Sitzungsberichte der Königlich Preussischen Akademie der Wissenschaften*, Vol. 1, 189–196, 1915.
2. Logsdon, T., *The NAVSTAR Global Positioning System*, GPS, Van Nostrand Reinhold, 1992.
3. Saburi, Y., M. Yamamoto, and K. Harada, "High precision time comparison via satellite and observed discrepancy of synchronization," *IEEE Transactions on Instrumentation and Measurement*, Vol. 25, 473–477, 1976.
4. Sagnac, G., "L'éther lumineux démontré par l'effet du vent relatif d'éther dans un interféromètre en rotation uniforme," *Comptes Rendus*, Vol. 157, 708–710, 1913.
5. Sagnac, G., "Sur la preuve de la réalité de l'éther lumineux par l'expérience de l'interférographe tournant," *Comptes Rendus*, Vol. 157, 1410–1411, 1913.
6. Einstein, A., "On the electrodynamics of moving bodies," *Annalen der Physik*, Vol. 17, 891–921, 1905.
7. Lorentz, H. A., "Simplified theory of electrical and optical phenomena in moving systems," *Proc. Acad. Science Amsterdam*, Vol. 1, 427–442, 1899.
8. Einstein, A., "Die feldgleichungen der gravitation (the field equations of gravitation)," 844–847, *Königlich Preussische Akademie der Wissenschaften*, 1915.

9. Wright, S. E., “Electromagnetic sources and observers in motion III — Derivation and solution of the electromagnetic motional wave equation,” *PIERS Proceedings*, 1151–1155, Cambridge, USA, July 5–8, 2010.
10. Wright, S. E., “Electromagnetic sources and observers in motion VI — New motional optics,” *PIERS Proceedings*, 367–372, Marrakech, Morocco, Mar. 20–23, 2011.
11. Minkowski, H., *Raum und Zeit*, 1908.
12. Born, M., *Einstein’s Theory of Relativity*, Dover, New York, 1924; Latest Revision 1965.
13. Michelson, A. A. and E. W. Morley, “On the relative motion of the Earth and the luminiferous ether,” *American Journal of Science*, Vol. 34, No. 203, 333–345, 1887.
14. Schrödinger, E. R. J. A., “Annalen der Physik,” *Quantisierung als Eigenwertproblem*, 1927.
15. Dirac, P., “The quantum theory of the electron,” *Proceedings of the Royal Society of London. Series A*, Vol. 117, No. 778, 610–624, 1928.
16. Robertson, H. P., “Kinematics and world structure,” *Astrophysical Journal*, Vol. 83, 257, 1936.
17. Walker, A. G., “On Milne’s theory of world-structure,” *Proceedings of the London Mathematical Society. Series 2*, Vol. 42, 90–127, 1937.
18. Friedmann, A., “Über die Möglichkeit einer Welt mit konstanter negativer Krümmung des Raumes,” *Zeitschrift für Physik A*, Vol. 21, 326–332, 1924.
19. Hubble, E., “A relation between distance and radial velocity among extra-galactic nebulae,” *PNAS*, Vol. 15 No. 3, 168–173, 1929.

Design of Stripline Structure for Electromagnetic Characterization at Microwave Frequency

Ellen Yoshie Sudo Lutfi^{1,2}, Anderson Kenji Hirata²,
Alberto José de Faro Orlando¹, and Antonio Carlos da Cunha Migliano^{1,2}

¹Aerospace Technological Institute (ITA), CTA, Brazil

²Institute of Advanced Studies (IEAv), CTA, Brazil

Abstract— A comprehensive approach to the design of a stripline for EMC testing is given in this paper. The authors attention has been focused on the design items that are most crucial by the achievement of satisfactory value of the VSWR and impedance. The characteristic impedance of the stripline test section should be smoothly matched with the feed and terminations points in order to minimize the standing waves. Thereby, the most critical parameters that directly determine the physical design of the stripline are impedance matching at the feed port (S_{11} parameter) and transmission between two ports (S_{21} parameter). An analysis can be performed for the stripline configuration using a vector network analyzer. A measurement of the reflection from transmission through a material along with knowledge of its physical dimensions provides the information to characterize electromagnetic waves at microwave frequencies range.

1. INTRODUCTION

Typical striplines are constructed to have an impedance of either $50\ \Omega$ or $90\ \Omega$. The ratio between the width of the active conductor and the height of the active conductor and the height of the active conductor above the ground plane determines the characteristic impedance. The design given in this paper is focused on the $50\ \Omega$ stripline.

Today in communication systems the use of magnetic and dielectric materials exceeds the usual fields of application (randomes, antennae, microwave circuits, ...). New components are developed to meet the demand of leading areas. This is the case for materials absorbing the electromagnetic energy, which are used for microwave electromagnetic compatibility (EMC). A vector analyzer is a versatile measurement system, which comprises of a two or four channels for microwave receiver designed to process the magnitude and phase of transmitted and reflected waves of the network. It directly displays the S -parameters of passive and active networks at the desired frequency range. With advancement of technology, VNA are available now with full range of parameters to be measured like S -parameters in magnitude (dB)/phase form, real/imaginary form, as well as in the linear form, VSWR, Group delay, impedance, etc.. When dealing with vector measurement quantities, such as complex reflection and transmission coefficients (i.e., S -parameters) in RF and microwave metrology, several important factors need to be considered such as the expression form of the complex quantities (either in the real and imaginary components or magnitude and phase components) and correlation between these components [1].

Earlier the magnitude and phase form of complex S -parameter was selected as the measurand. The uncertainties in the magnitude and phase form of the VNA measurements have been studied and reported earlier [2]. The mathematical model for determining the measurement uncertainty depends on the type of measurand. The studies showed an ambiguity in the phase measurement, where phase depends highly on the structure and application of device under test (DUT) as well as the operating frequency. To avoid the problems during the statistical analysis of complex quantities in the magnitude/phase form, the real and imaginary form has been chosen to analyze the complex quantities. In this form, the real and imaginary components of complex S -parameter are correlated, so their covariance also contributes to the uncertainty.

2. THEORY

2.1. Stripline Design

A stripline consists of upper and down grounding plates, and the central conductor. Between the grounding plates and the central conductor is air or dielectric materials.

The fundamental propagation mode for a stripline is TEM. For the TEM wave propagation in a stripline, the phase velocity is:

$$v_p = \frac{c}{\sqrt{\epsilon_r}} \quad (1)$$

where ε_r is the dielectric constant of the filling medium and c is the speed of light.

If the central conductor is narrow, the interference between the fields at the two edges cannot be neglected. We may take the central conductor as a cylinder by introducing equivalent diameter as shown in the equation above:

$$d = \frac{\omega}{2} \left\{ 1 + \frac{t}{\omega} \left[1 + \ln \frac{4\pi\omega}{t} + 0.51\pi \left(\frac{t}{\omega} \right)^2 \right] \right\} \quad (2)$$

where the characteristic impedance can be calculated using the following equation:

$$Z_0 = \frac{60}{\sqrt{\varepsilon_r}} \ln \left(\frac{4b}{\pi d} \right) (\Omega) \quad (3)$$

2.2. The Stripline for Material Characterization

Open structures can radiate and have a complicated field structure. Measuring the permittivity of lossy materials, circuit boards, thin films, and substrates nondestructively is frequently of interest [4].

When the dielectric is solid (as opposed to being air), as is usually the case, the speed at which the wave travels along the transmission line (velocity of propagation) is reduced, as is the wavelength [6, 7]. The actual stripline wavelength (λ) is equal to the free space wavelength (λ_0) divided by the square root of the relative permittivity (ε_r):

$$\lambda = \frac{\lambda_0}{\sqrt{\varepsilon_r}} \quad (4)$$

To emphasize the importance of the dielectric constant to the physical size of stripline, the table below shows five frequencies and their wavelengths in air and in two types of dielectrics [5].

The Table 1 shows how the dielectric constant of the measured material increases, the required size of the stripline components may be reduced [8–10]. Because the dielectric constant controls the wavelengths in the stripline circuit, it is a critical property in all applications; however, the thickness of the dielectric is often of equal importance. The characteristic impedance (Z_0) — a fundamental design parameter for all stripline circuits — depends on the dielectric constant [11–13], the width and thickness of the conductor, and the thickness of the dielectric layers.

This structure of the stripline with two ground planes as shown in Figure 1 has a much higher quality factor than the microstrip line. Also, this stripline structure is very useful for broadband

Table 1: Wavelength versus frequency at different materials.

Frequency (GHz)	λ_0 (air) in inch	$\lambda(\varepsilon_r = 5)$ in inch	$\lambda(\varepsilon_r = 9)$ in inch
0.50	23.60	10.5	7.87
1.00	11.80	5.27	3.93
3.00	3.93	1.75	1.31
5.00	2.36	0.99	0.79
12.00	0.98	0.44	0.33



Figure 1: Stripline structure cross-section connected with a vector network analyzer.

circuits, since it can be modeled by assuming TEM propagation and using a standard lossy transmission line model [14]; the transmission line can be characterized by a characteristic impedance Z_0 and a complex propagation constant $\gamma = a + j\beta$. Using this model the properties can be found by time or frequency domain measurements [15, 16]. This stripline technique depends on the fact that the conductor loss and the dielectric loss vary differently with frequency in order to separate the loss terms from the total attenuation.

A cross section of the stripline configuration is shown in Figure 1. It depicts a narrow, flat strip of perfect conductor sandwiched between two outer layers. The outer surfaces of the dielectric sheets are faced with perfect conductor. The circuit metallization is located in the middle of the layers. Metallic plates are located at the top and bottom of the structure, resulting in a stripline structure.

3. RESULTS

Relative complex permittivity (permittivity) of printed circuit (PC) board and substrate material is a critical parameter that affects circuit performance.

Characterizing this parameter at RF is becoming more important because of increased clock frequencies used in today's high speed computers. In addition, performance of dielectric materials at RF is equally important for wireless communication circuits and components. The goal was to perform a physical design of stripline according to the ISO standard [3] by which the improvements of S_{11} and S_{21} parameters were achieved by an application of the experience from numerical simulations.

The calibration of the cables assures a perfect matching with 50 Ohms in the frequency of 0 GHz until 12 GHz. The results of VSWR show dimensional resonance in frequency range, according Figure 4 and Figure 5. According to the results the work area changes a lot in the frequency range,

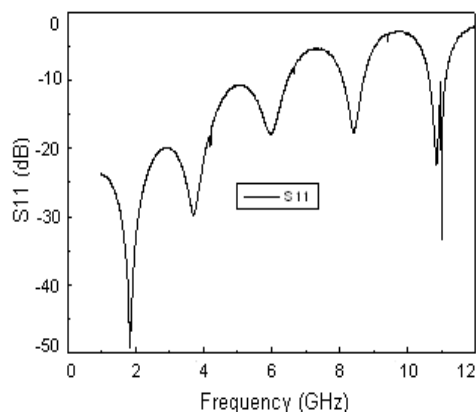


Figure 2: Reflection coefficient as a function of frequency.

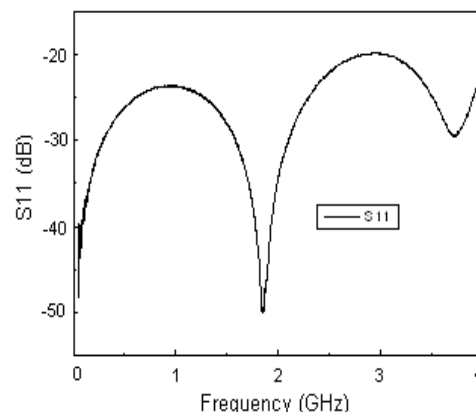


Figure 3: Reflection coefficient as a function of frequency.

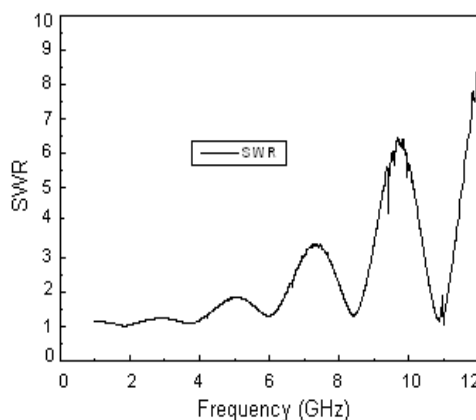


Figure 4: VSWR as a function of frequency.

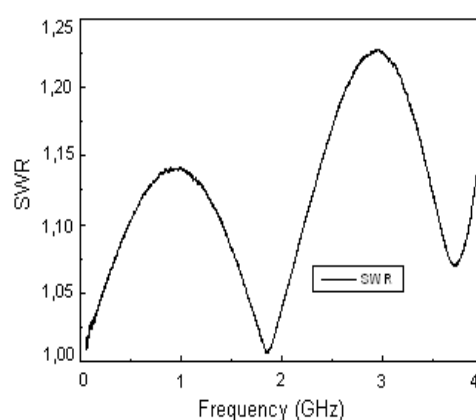


Figure 5: VSWR as a function of frequency.

according to Figure 2 and Figure 3. The electromagnetic sensitivity is related with low reflection smaller than -10 dB and transmission near than 0 dB.

4. CONCLUSION

The goal of this paper was to provide with the comprehensive design study of stripline with focus on the achievement of satisfactory level of the VSWR and reflection coefficient at the extended frequency range from 0 GHz to 12 GHz. The VSWR of stripline model was lower than by the commercial equipment in the upper frequency range from 1 GHz to 4 GHz.

ACKNOWLEDGMENT

The authors wish to thank the laboratory of electromagnetic systems at Advanced Study Institute for infrastructure offered. And, they wish to thank Microwave Department at Aerospace Technological Institute for the realization of this work.

REFERENCES

1. Ridler, N. M. and M. J. Salter, "An approach to the treatment of uncertainty in complex S -parameter measurements," *Metrologia*, Vol. 39, 295–302, 2002.
2. "EA guidelines on the evaluation of vector network analyzers (VNA)," Publication Reference EA-10/12, European Cooperation for Accreditation, May 2000.
3. ISO 11452-5, "Road vehicles — Component test methods for electrical disturbances from narrowband radiated electromagnetic energy — Part 5: Stripline," Geneva, 2002.
4. Baker-Jarvis, J. and P. Kabos, "Nonequilibrium electromagnetics: Local and macroscopic fields using statistical mechanics," *Phys. Rev. E*, Vol. 70, 036615-1–13, 2004.
5. Thomas, S. L., *Microwave Measurements and Techniques*, Artech House, Dedham, Massachusetts, 1976.
6. Jastrzebski, Z. D., "The nature and properties of engineering materials," 2nd Edition, SI Version, John Wiley and Sons, New York, 1977.
7. Cole, K. S. and R. H. Cole, "Dispersion and absorption in dielectrics; I. Alternating current characteristics," *Journal of Chemical Physics*, Vol. 9, 341–351, 1941.
8. Afsar, M. N., J. Birch, and R. Clarke, "The measurement of properties of materials," *Proc. J. IEEE*, 183–199, 1986.
9. Saed, M. A., S. M. Riad, and A. Elshabini-Riad, "Wide-band measurement of the complex permittivity of dielectric materials using a wide-band cavity," *IEEE Transactions on Instrumentation and Measurement*, Vol. 38, No. 2, Apr. 1989.
10. Fidanboyly, K. M., S. M. Riad, and A. Elshabini-Riad, "An enhanced time-domain approach for dielectric characterization using stripline geometry," *IEEE Transactions on Instrumentation and Measurement*, Vol. 41, No. 1, Feb. 1992.
11. Gunston, M. A. R., *Microwave Transmission Line Impedance Data*, Noble Publishing Corporation, Atlanta, 1997.
12. Cohn, S. B., "Characterization impedance of the shielded-strip transmission line," *Trans. IRE*, Vol. 2, No. 2, 52–57, Jul. 1954.
13. Pease, R. L., "Characteristic impedance of strip transmission lines with rectangular inner conductors in the low impedance region," Tufts College Interim Report No. 2 on Contract No. AF 19(604)-575, Jan. 12, 1954.
14. Gupta, K. C., et al., *Microstrip Lines and Slotlines*, Artech House Inc., 1996.
15. Shaarawi, A. M., "Dielectric characterization using time domain techniques," M.S. Thesis, Virginia Polytechnic Institute & State University, Jun. 1984.
16. Cole, R. H., "Evaluation of dielectric behaviour by time domain spectroscopy. II. Complex permittivity," *J. Phy. Chem.*, Vol. 79, No. 14, 1469–1474, 1975.

Experimental Evidence for the Magneto-kinematic Effect

Vladimir Leus¹ and Stephen Taylor²

¹Sobolev Institute of Mathematics, Novosibirsk 630090, Russia

²Department of Electrical Engineering and Electronics
University of Liverpool, Liverpool L69 3GJ, UK

Abstract— The movement of a magnetic field together with its source (a moving permanent magnet) has been a controversial topic in the scientific literature for decades. In essence the debate hinges upon whether a permanent magnetic field exhibits wave like motion or whether it moves as a body. The following question arises: is the induced *emf* measured purely a consequence of electrodynamics or is the *emf* kinematically induced? Such a magneto-kinematic effect has been previously observed and reported by two Russian researchers N. Zajev and A. Dokuchajev as early as in 1958 (published in 1964) for the case of a rotating coil energised by a direct current. In this paper, we present further evidence confirming this effect for a different experimental arrangement: that of a rotating magnetic circuit and a magnetized sphere moving through the conducting loop. The magnetic circuit used comprised a permanent ring magnet and a soft iron yoke rotating together. Two types of magnetic ring were considered: a dipole and quadrupole. In each case the resulting induced *emf* was quantifiably explicable in terms of the Zajev-Dokuchajev (Z-D) effect: the moving of the magnetic field with the rotating magnet. We also present a novel method for measurement of the induced *emf* in a stationary conducting loop in the case of rectilinear motion of a permanent magnetic dipole through the loop. In each case the motion of the magnetic field are detected by measuring the *emf* induced in a stationary conductor. A new method of calculation is presented which is applicable to a range of generic problems dealing with moving sources of magnetic flux.

1. INTRODUCTION

In the laboratory reference frame with coordinates x, y, z a point charge q moves with velocity \mathbf{v} or a permanent bar magnet moves with velocity \mathbf{V} (Figure 1). In contemporary physics the prevailing view about the interaction between charge and magnet is as follows. ‘*If a charge q moves in a magnetic field \mathbf{B} with velocity \mathbf{v} , it will be subject to magnetic force $q\mathbf{v} \times \mathbf{B}$, where it is not influential whether the source of \mathbf{B} is in motion or not with respect to charge and/or to observer: what it is important in order to calculate the force is the temporal evolution of \mathbf{B} . Only for the determination of latter is it meaningful to consider the motion of field source*’ [1, p. 115]. In the famous textbook by Richard Feynman et al we read: ‘*... it makes no sense to say something like: when I move a magnet, it takes its field with it, so the lines of \mathbf{B} are also moved*’ [2, p. 10–13]. Moreover: ‘*no meaning can be attached to any motion of field lines*’ [3, p. 227]; *motion (rotation in this case) of the source of the magnetic field does not affect any physical process*’ [4, p. 338]. Thus physicists admit the Lorentz force $F_L = q\mathbf{v} \times \mathbf{B}$, and but some reject the idea of a converse Lorentz force: $F_L = q\mathbf{B} \times \mathbf{V}$.

However it is accepted that the field of a permanent magnet is a material object having mass, energy and momentum [5, p. 900]. When a permanent magnet moves in the laboratory at a constant velocity \mathbf{V} , its field also is transferred in the laboratory with the same velocity \mathbf{V} . Macroscopic mechanics knows two types of motion: wave like and body like, where the term ‘body’ can mean gaseous, liquid or solid. Most researchers believe that the field of permanent magnet exhibits wave like motion. In the case of a permanent magnet the question arises as to the nature of the field movement.

In the case of a rotating permanent magnet the phenomenon of unipolar induction occurs. A unipolar generator with a cylindrical bar magnet rotating about its axis (Figure 2) was used by M. Faraday in 1831, and since then the question as to where the seat of *emf* is situated has been discussed [6]. Nobel prize winner I. E. Tamm holds the induced *emf* to be located inside the magnet itself (segment AB) due to redistribution of charges in the conductor moving through the stable magnetic field [7, p. 541-3]. Another Nobel laureate L. D. Landau, in contrast, believes the *emf* is situated in the external wires (segment ACB) due to magnetic field rotating as a body [8, p. 220]. Such questions in natural science are best solved by experiment.

The first successful experiment was performed by two Russian engineers N. E. Zajev and A. I. Dok-uchajev. In 1949 Zajev took out a patent for the new type of unipolar generator using a

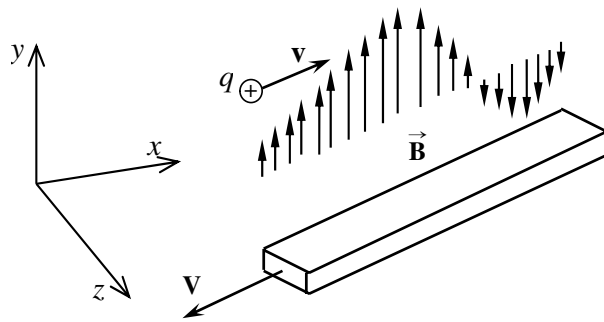


Figure 1: Kinematic interaction between point charge q and a permanent magnet.

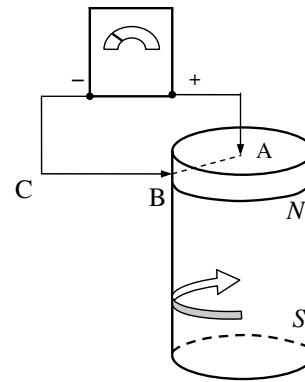


Figure 2: Rotating cylindrical bar magnet shows the phenomenon of unipolar induction.

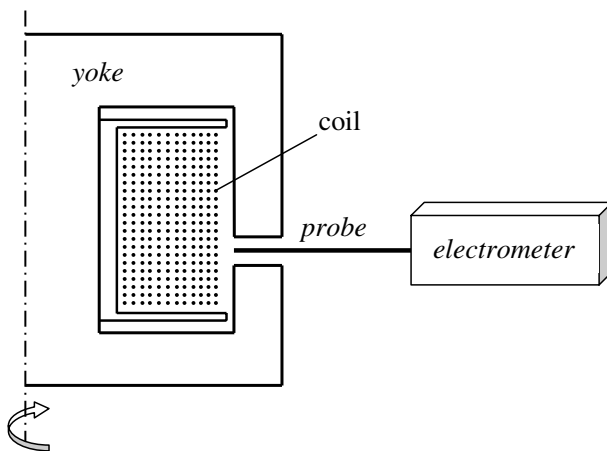


Figure 3: The experiment of Zajev and Dokuchajev (1958).

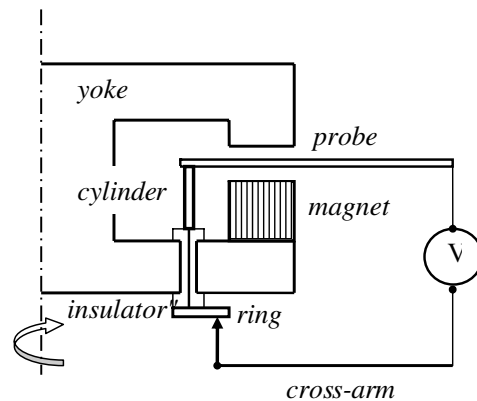


Figure 4: Rotating magnetic circuit provided by a permanent magnet and yoke.

coil as the source of the magnetic field and a torus-like yoke (Figure 3). In 1958 Zajev and Docuchajev undertook an attempt to elucidate the seat of emf in this unipolar generator. For this purpose they used a string electrometer (*CT2M*), with a probe placed through a circular slot made in the outer wall of the yoke. The winding of the electromagnet was powered through sliding contacts by 120 V DC and rotated together with the yoke at a constant speed $n = 940$ rev/min. From the electrometer measurement, the potential values in millivolts were computed as: 108.6, 106.4, 116.2, 98.0. After each successive measurement the probe was earthed, i.e., reset to zero, and then the measurement was repeated. The measurement with a voltmeter gave an average value of 110 mV. Changing the direction of rotation changed the sign of the measured potential. The authors drew the conclusion: ‘the magnetic field lines rotate together with the electromagnet’ [9].

In our recent papers the same effect was observed for both uniform and non-uniform magnetic fields provided by permanent magnets for the cases of rotating and rectilinear motion [10, 11]. Our experiments provide further evidence of the magneto-kinematic phenomenon observed by Zajev-Dokuchajev.

2. ROTATION OF A RING MAGNET

This experimental approach adopted was reported earlier [12] and a schematic diagram of the apparatus used is shown in Figure 4. A small permanent ring bipolar magnet with a torus yoke were housed in a plastic holder, and the assembly was attached to the shaft of an electromotor with n variable in the range to 3000 rev/min. Such geometry minimises leakage flux and confines almost all magnetic field to the narrow circular slot. Connection to the brass probe was made through an embedded copper cylinder rotating with the plastic magnet holder to form the first sliding contact as shown in Figure 4. The copper cylinder was connected to a brass ring by means of two perpendicular copper wire legs going through opposing orifices in the bottom disk of the yoke. A

brass cross-arm has one end resting on the brass ring to provide the second sliding contact. A digital millivoltmeter was connected between cross-arm and probe to measure any induced voltage.

The magnetic flux density in the slot was measured using a Gaussmeter to be $B \cong 0.2 \text{ T}$, whereas in the orifice through the bottom disk it was very low ($B_{\text{orifice}} < 0.0003 \text{ T}$). The induced electromotive force (is $emf = (\pi/30)lrBn = kn$, where r is middle radius of the magnetic ring. For $l = 10 \text{ mm}$, $r = 51 \text{ mm}$, so k was calculated as $k \cong 0.00535$ for an emf in mV. As the magnet and yoke rotate, a voltage was measured across the stationary probe as shown in Figure 5. The magnitude of the measured voltage was proportional to the speed of the rotation of magnet with an accuracy of $\approx 2\%$. Changing the orientation of the magnet from North pole face to South pole face adjacent to the yoke, altered the sign of measured voltage from positive to negative in accordance with Fleming's right hand rule.

3. ROTATION OF A NON-UNIFORM MAGNETIC FIELD

In the following experiment a ring magnet of the same dimensions as above, but with a quadrupole field (N-S pole on each face) was used in place of the bipolar magnet previously described. On the contact probe a wire loop was mounted through an insulator as shown in Figure 6.

In this case therefore there are two independent measurement circuits and one space-variable magnetic flux common for both circuits. At the working frequency used here (50 Hz) the capacitive coupling between the measurement circuits is negligible.

Figure 7 shows the measured emf recorded on a double-beam oscilloscope as the magnet rotates. The upper trace (approximately rectangular pulses) shows the induced voltage in the probe circuit. It is of a similar order to the value measured in Section 3 but in this case the measured values alternate positively and negatively in sympathy with the alternating $\mathbf{B}(\varphi)$, where φ is phase angle on the quadrupole magnet. The lower trace in Figure 7 shows the induced voltage in the wire loop. Significantly there are the essentially different shapes of the both signals and a phase difference of $\pi/2$ between the maximum value of the measured emf F in the upper and lower oscilloscope traces with the peak value in the lower coinciding with the zero value in the upper trace. The $\pi/2$ phase shift was consistently observed for varying loop widths and for different frequencies (speeds of rotation). This phase shift cannot be explained if the magnetic field is considered to be immobile but is readily explained by the rotation of the magnetic field with the magnet.

The total electromotive force induced in the loop is the difference between the emfs due to Z-D effect in the upper and lower sides of the loop: $emf = emf_u - emf_l$. Both have the same kinematic origin, but are induced in opposite directions in the circuit. So this value is proportional to the divided difference for the function $\mathbf{B}(\varphi)$, which explains why the result looks as input-output of a differential network. When one copper leg connecting the cylinder and ring was disconnected, the result is as shown in Figure 7. The $\pi/2$ phase shift persists when voltage measurement is made using the opposite connecting leg only.

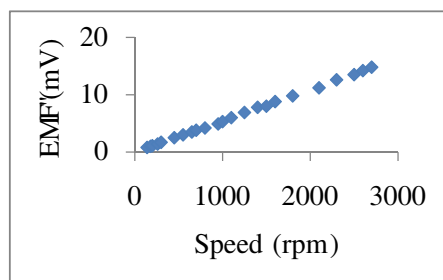


Figure 5: Experimental curve showing the dependence of induced EMF on speed of rotation of the magnetic circuit.

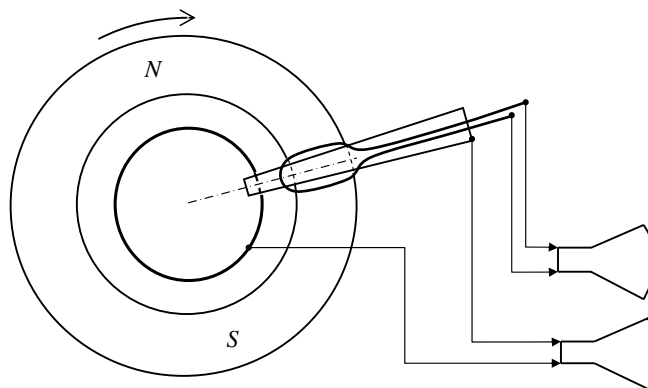


Figure 6: Experimental arrangement used for the case of non uniform magnetic field.

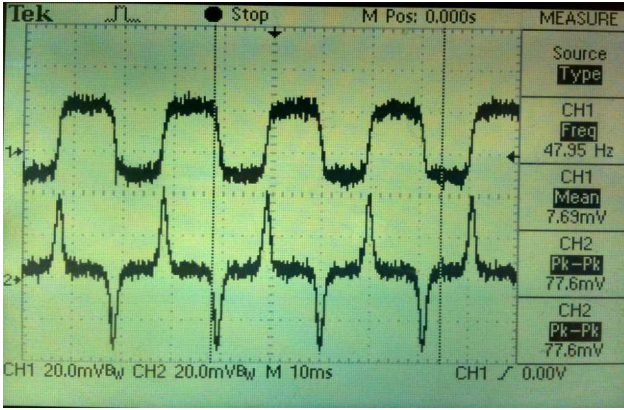


Figure 7: Resulting waveforms in the case of the non uniform field experiment.

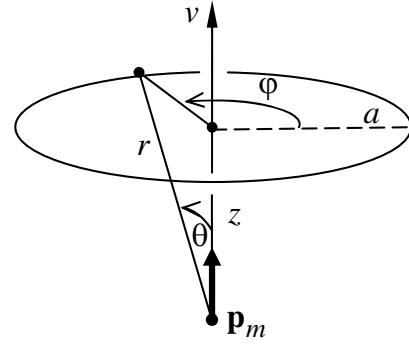


Figure 8: A single circular conducting loop in relation to the moving magnetic dipole.

4. MAGNETIC DIPOLE MOVING THROUGH A CIRCULAR LOOP

The field of a magnetic dipole may be expressed through simple elementary functions [13, p. 183]. Let \mathbf{p}_m be the magnetic moment of dipole, and (r, θ, φ) be the system of spherical coordinates with polar axis directed along the vector \mathbf{p}_m . In this case the components of the magnetic flux density (SI-units) are:

$$\begin{aligned} B_r &= \frac{\mu\mu_0 p_m}{2\pi} \cdot \frac{\cos \theta}{r^3} = p \frac{\cos \theta}{r^3} \\ B_\theta &= \frac{\mu\mu_0 p_m}{4\pi} \cdot \frac{\sin \theta}{r^3} = \frac{p \sin \theta}{2 r^3} \\ B_\varphi &= 0 \end{aligned} \quad (1)$$

If a magnetic dipole goes through centre of a circular conducting loop of radius a (Figure 8), the motional emf is induced. Let the magnetic moment and velocity are perpendicular to the loop plane. The motional emf in the loop may be readily calculated due to the magneto-kinematic effect.

At a point on the circular conductor loop the component of a vector \mathbf{B} , parallel to the plane of the loop, is given by:

$$B_a^{\parallel} = B_r^{\parallel} - B_\theta^{\parallel} = \frac{p}{2} \cdot \frac{2 \cos \theta \sin \theta + \sin \theta \cos \theta}{r^3} = \frac{3p}{2} \cdot \frac{\sin \theta \cos \theta}{r^3} = \frac{3p}{2} \cdot \frac{a/r \cdot z/r}{r^3} = \frac{3paz}{2r^5}.$$

The electromotive force induced in every small part dl of the wire due to Z-D effect is $dE(z) = B_a^{\parallel} \cdot v \cdot dl$, so the full emf may be expressed as:

$$E(z) = B_a^{\parallel} \cdot 2\pi a \cdot v = \frac{3p\pi a^2 v z}{(a^2 + z^2)^{5/2}}. \quad (2)$$

The function $E(z)$ has zero-value in the origin of coordinate system ($z = 0$) and it tends to zero when $|z|$ increases to infinity. The derivative of this function over z is

$$\frac{dE}{dz} = 3p\pi a^2 v \cdot \frac{d}{dz} \left[\frac{z}{(a^2 + z^2)^{5/2}} \right] = 3p\pi a^2 v \frac{a^2 - 4z^2}{(a^2 + z^2)^{7/2}}.$$

The numerator becomes zero at the two points: $z_{1,2} = \pm a/2$, at these points the induced emf reaches its maximum values:

$$E_v^{\max} = E(\pm a/2) = \pm \frac{48\pi p v}{25\sqrt{5}a^2} \cong \pm 2.7 \frac{p v}{a^2}.$$

For the experiment we used a $NdFeB$ sphere of diameter $d = 25.4$ mm, with a uniform magnetization \mathbf{M} parallel to any axis. Outside this sphere there is field of the magnetic dipole with



Figure 9: Assembly of wooden/plastic casing holding the magnetised sphere.

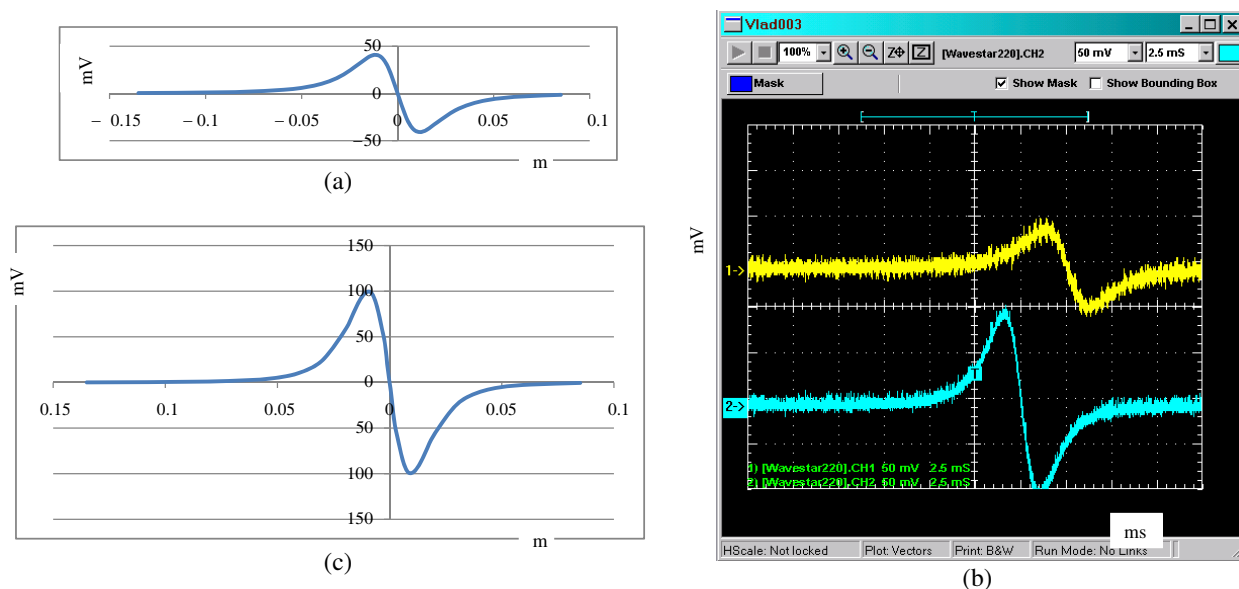


Figure 10: Comparison of (a) and (c) theoretically calculated and (b) experimentally measured signals in the case of a “longitudinally” moving magnetic dipole. In cases (a) and (c) the y -axis is millivolts and the x -axis is distance in metres.

magnetic moment $\mathbf{p}_m = \frac{\pi d^3}{6} \mathbf{M}$, $p_m \approx 6.0 \text{ A} \cdot \text{m}^2$. This sphere was set into a plastic casing with \mathbf{p}_m orientated along. It was drop for six metre high free fall in the guiding pipe through a circular conducting loop of radius $a = 19 \text{ mm}$ so that \mathbf{p}_m remain in parallel with velocity, which reaches 10.5 m/sec . Figure 10(c) shows a graph of emf (2) versus distance with the corresponding experimentally obtained trace on the oscilloscope curve number 2 (lower) shown in Figure 10(b).

It is patently that the signal from the passing sphere due to depend on the loop’s shape. For a rectangular loop $2l$ long and $2b$ width Z-D effect gives the emf

$$E_l = pvb \cdot \frac{(2l^3 + 3lb^2)z + 3lz^3}{(z^2 + b^2)^2 (z^2 + y^2 + b^2)^{3/2}}. \quad (3)$$

The graph shown in Figure 10(a) pertains to rectangular loop half a metre long and 42 m width formed by straight wires. It was calculated according to (3) for velocity $v = 10.5 \text{ m/sec}$. Curve number 1 (upper) in Figure 10(b) was obtained from the oscilloscope. It is clear that agreement between calculated and experimental lines is excellent and well within the limits of experimental uncertainty.

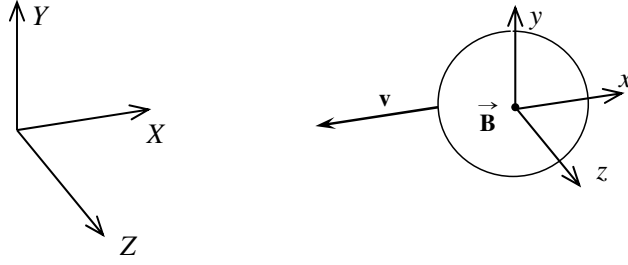


Figure 11: Moving field with relation to laboratory reference frame.

5. Z-D EFFECT VERSUS THE WAVE EQUATION

Let (x, y, z) be Cartesian coordinates in their own frame of reference, where a magnetised sphere is at rest. The components B_x, B_y, B_z of the vector \mathbf{B} , given by (1) are

$$B_x = 3p \frac{xz}{r^5}, \quad B_y = 3p \frac{yz}{r^5}, \quad B_z = p \frac{2z^2 - x^2 - y^2}{r^5}.$$

Let the sphere move relative to the laboratory reference frame with coordinates X, Y, Z along the X axis at a constant velocity \mathbf{v} (Figure 11). Eliminating the constant factor p which is dependent upon magnetisation etc:

$$B_X = 3 \frac{(X - vt)Z}{r^5}, \quad B_Y = 3 \frac{YZ}{r^5}, \quad B_Z = \frac{2Z^2 - (X - vt)^2 - Y^2}{r^5}, \quad (4)$$

where $\mathbf{r} = (X - vt, Y, Z)$. The corresponding electric field $\mathbf{E} = \mathbf{B} \times \mathbf{v}$ of kinematic origin has the following components:

$$E_X = 0, \quad E_Y = v \frac{2Z^2 - (X - vt)^2 - Y^2}{r^5}, \quad E_Z = -3v \frac{YZ}{r^5}. \quad (5)$$

The converse Lorentz force $q\mathbf{B} \times \mathbf{v}$ exerted on a charge q fixed in a point (X, Y, Z) of the laboratory reference frame. This force is variable in time although the magnetic field is stationary in its source. So there is an implicit dependence originating from mechanical transfer, this is in contrast to electromagnetic waves, in which case the dependence on time is explicit.

Using the partial derivatives of the magnetic components (4) in the laboratory system

$$\frac{\partial B_X}{\partial X}, \quad \frac{\partial B_X}{\partial Y}, \quad \frac{\partial B_X}{\partial Z}, \quad \frac{\partial B_Y}{\partial X}, \quad \frac{\partial B_Y}{\partial Y}, \quad \frac{\partial B_Y}{\partial Z}, \quad \frac{\partial B_Z}{\partial X}, \quad \frac{\partial B_Z}{\partial Y}, \quad \frac{\partial B_Z}{\partial Z},$$

we have

$$\begin{aligned} \operatorname{div} \mathbf{B} &= \frac{\partial B_X}{\partial X} + \frac{\partial B_Y}{\partial Y} + \frac{\partial B_Z}{\partial Z} = 0; \\ \operatorname{curl} \mathbf{B} &= \left(\frac{\partial B_Z}{\partial Y} - \frac{\partial B_Y}{\partial Z}, \frac{\partial B_X}{\partial Z} - \frac{\partial B_Z}{\partial X}, \frac{\partial B_Y}{\partial X} - \frac{\partial B_X}{\partial Y} \right) = (0, 0, 0) \end{aligned}$$

The partial derivatives of the magnetic components (4) over time are

$$\begin{aligned} \frac{\partial B_X}{\partial t} &= -3vZ \frac{Y^2 + Z^2 - 4(X - vt)^2}{r^7}, \quad \frac{\partial B_Y}{\partial t} = 15v \frac{(X - vt)YZ}{r^7}, \\ \frac{\partial B_Z}{\partial t} &= 3v(X - vt) \frac{4Z^2 - (X - vt)^2 - Y^2}{r^7}. \end{aligned}$$

Using the partial derivatives of the induced electric components (5), we obtain

$$\operatorname{div} \mathbf{E} = \frac{\partial E_X}{\partial X} + \frac{\partial E_Y}{\partial Y} + \frac{\partial E_Z}{\partial Z} = 0;$$

and

$$\begin{aligned} \text{curl}\mathbf{E} &= \left(\frac{\partial E_Z}{\partial Y} - \frac{\partial E_Y}{\partial Z}, -\frac{\partial E_Z}{\partial X}, \frac{\partial E_Y}{\partial X} \right) \\ &= \left(-3vZ \frac{4(X-vt)^2 - Y^2 - Z^2}{r^7}, -15v \frac{(X-vt)YZ}{r^7}, -3v(X-vt) \frac{4Z^2 - (X-vt)^2 - Y^2}{r^7} \right). \end{aligned}$$

The partial derivatives of the electric components (5) over time are

$$\frac{\partial E_X}{\partial t} = 0, \quad \frac{\partial E_Y}{\partial t} = -3v^2(X-vt) \frac{4Z^2 - (X-vt)^2 - Y^2}{r^7}, \quad \frac{\partial E_Z}{\partial t} = -15v^2 \frac{(X-vt)YZ}{r^7}.$$

In comparison we find that $\text{curl}\mathbf{E} = -\partial\mathbf{B}/\partial t$ in accordance with Faraday's law. However $\text{curl}\mathbf{B} \neq \frac{1}{c^2}\partial\mathbf{E}/\partial t$ in contradiction with the Ampere-Maxwell law. It is necessary therefore to consider whether the wave equation applies in this case. The second partial derivative of the magnetic field vector (4) and electric field vector (5) give the following equalities: $\nabla^2\mathbf{B} \equiv 0$; $\nabla^2\mathbf{E} \equiv 0$. The second partial derivative

$$\frac{\partial^2 B_Y}{\partial t^2} = \frac{\partial}{\partial t} \left(15v \frac{(X-vt)YZ}{r^7} \right) = 15v^2 YZ \frac{6(X-vt)^2 - Y^2 - Z^2}{r^9}$$

is not identical to zero, and so the wave equation

$$\nabla^2\mathbf{B} - \frac{1}{v^2} \frac{\partial^2\mathbf{B}}{\partial t^2} = 0$$

is not satisfied by magnetic vector \mathbf{B} of a moving magnetized sphere. By analogy, the second time derivative is

$$\frac{\partial^2 E_Z}{\partial t^2} = -15YZv^2 \frac{\partial}{\partial t} \frac{(X-vt)}{r^7} = -15YZv^3 \frac{6(X-vt)^2 - Y^2 - Z^2}{r^9} \neq 0,$$

and the wave equation $\nabla^2\mathbf{E} - \frac{1}{v^2} \frac{\partial^2\mathbf{E}}{\partial t^2} = 0$ is also not possible. Thus, the field of a moving permanent magnet is not a wave; it is moving together with its source in a body-like fashion.

6. DISCUSSION AND CONCLUSIONS

The field of a permanent magnet is magneto-static. The movement of the magnetic source causes the the Z-D effect which we term magneto-kinematic. The Lorentz transformation for electromagnetic fields has been established for over a century, however, the results of magneto-kinematic experiments allow the application of the Lorentz transformation in a way that has not been previously considered. Recently some authors have commented that implementation of the Lorentz transformation can lead to some unusual features: Bogach (1996) in the case of magnetic source rotation [14] and Alemanov (2002) for translational motion of the source [15]. As evident above, a magneto-static field does not meet the requirement for wave motion and moves like a body synchronously with its source. Nevertheless, the magnetic field satisfies Faraday's law just like any electromagnetic wave. Stokes' theorem may be applied leading to the flux rule, which relates the magnetic flux through a surface area with the *emf* induced in the boundary path:

$$emf = \oint_C \mathbf{E} \cdot d\mathbf{l} = -\frac{d\Phi}{dt}.$$

The flux rule is suitable and widely applicable in electrodynamics, however it is not always applicable in the case of certain kinematic phenomena. In these cases the details of the kinematic process play a significant role, while the transition from a differential form $\text{curl}\mathbf{E}$ to integral *emf* removes all details of the inductive process. In contrast, the magneto-kinematic approach allows the local representation of an *emf* induced in any part of a conductor. The above experiment with a rotating quadrupole magnet illustrates this deficiency, whereas the result is readily explained from the magneto-kinematic (Z-D) point of view. The suitability of the magneto-kinematic approach

suggests that it may be used to advantage in other calculations involving electric and magnetic field motion and in other experimental scenarios.

The question arises as to the relativistic case, that is, how the moving magnetic field interacts with a stationary charge q . In this case the force is equal to $\gamma q[\mathbf{B} \times \mathbf{V}]$, whereas the Lorentz force is $\mathbf{F}_L = q[\mathbf{v} \times \mathbf{B}]$. There is no discrepancy with the relativistic factor gamma, since the Lorentz transform for the transverse component of a force is $\mathbf{F}'_{\perp} = \mathbf{F}_{\perp}/\gamma$ [16, p. 237]. Hence, the Lorentz force is nothing more than the Z-D force viewed from the proper inertial system of a permanent magnet.

The experiments described above clearly show the existence of two diverse types of induction: $\text{curl}\mathbf{E} = -\frac{\partial\mathbf{B}}{\partial t}$, and $\mathbf{E} = \mathbf{v} \times \mathbf{B}$. The first one pertains solely to electromagnetic waves, but the second is a purely kinematical entity. Faraday experimented with the magneto-kinematical effect when he moved a permanent magnet near to a closed circuit containing galvanometer [17, p. 27]. Griffiths commented: ‘*There are really two totally different mechanisms . . . and to identify them both as “Faraday’s law” is a little like saying that because identical twins look alike we ought to call them by the same name*’ [18, p. 303]. The terms “motional *emf*” and “transformer *emf*” are often mixed indiscriminately (via the flux rule applied outside its validated range) and a shift in mindset to more precise thinking would be helpful. A similar opinion is expressed in [19]: ‘*We are not implying that Faraday’s law should be revised, but we do want to set the stage for careful rethinking regarding the meaning and application of each term of the law as it appears in traditional introductory [electrodynamics] courses*’. Unfortunately, others propose to conflate the two different phenomena into a single equation [20].

In 1831 Faraday reported the following series of 3 types of experiments:

- 1) He pulled a loop of wire to the right through a magnetic field. A current flowed in the loop.
- 2) He moved the magnet to the left, holding the loop still. Again, a current flowed in the loop.
- 3) With both the loop and the magnet at rest, he changed the strength of the field (he used an electromagnet, and varied the current in the coil). Once again, current flowed in the loop.

Griffiths comments: ‘*I shall reserve the term “Faraday’s law” for electric fields induced by changing magnetic fields, and I do not regard Experiment 1 as an instance of Faraday’s law*’ [18, p. 301–303]. This is true, but it is not the whole story. In the same way experiment 2, although explicable using the flux rule, is also not an instance of Faraday’s law. This is the main result of our work in Section 5 which, it is hoped, will focus the attention of researchers to this important and fundamental aspect of electromagnetism.

REFERENCES

1. Mencherini, L., “Relativistic interpretation of Kennard’s (1912 and 1917) and Müller’s (1979) experiments on the unipolar induction phenomenon,” *Speculations in Science and Technology*, Vol. 16, No. 4, 114–121, 2011.
2. Feynman, R. P., R. B. Leighton, and M. Sands, *The Feynman Lecture on Physics*, Vol. 2, Addison-Wesley, 1989.
3. Duffin, W. J., *Electricity and Magnetism*, 3rd Edition, Longmans Green, London, 1980.
4. Panovsky, W. and M. Phillips, *Classical Electricity and Magnetism*, Addison-Wesley, Cambridge, 1975.
5. Giancoli, D. C., *Physics for Scientist and Engineers*, 3rd Edition, Pearson Education Inc., New Jersey, US, 2005.
6. Whittaker, E. T., *A History of the Theories of Aether and Electricity*, Longmans Green, London, 1910.
7. Tamm, I. E., *Osnovy Teorii Elektrichestva — Fundamentals of the Electricity Theory*, 9th Edition, Nauka, Moscow, 1976 (in Russian).
8. Landau, L. D. and E. M. Lifshitz, *Electrodynamics of Continuous Media*, 2nd Edition, Pergamon, Oxford, 1981.
9. Zajev, N. E. and V. I. Dokuchajev, “About the behaviour of force lines of the field of a rotating magnet,” *Electrotehnika — Electrical Engineering*, No. 11, 64, 1964 (in Russian).
10. Leus, V. and S. Taylor, “On the motion of the field of a permanent magnet,” *Eur. J. Phys.*, Vol. 32, No. 5, 1179–1192, 2011.
11. Taylor, S. and V. Leus, “The magnetokinematic effect for the case of rectilinear motion,” *Eur. J. Phys.*, Vol. 33, No. 4, 837–852, 2012.

12. Leus, V. A. and V. N. Zatolokin, “The magnetokinematical effect,” *International Journal of Electrical Engineering Education*, Vol. 43, No. 4, 245–251, 2006.
13. Jackson, J. D., *Classical Electrodynamics*, 3rd Edition, John Wiley, New York, 1998.
14. Bogach, V. A., “Hypothesis of existence of a static electromagnetic field and its properties,” Preprint 13-96-463, JINR, Dubna, Russia, 1996 (in Russian).
15. Alemanov, S. B., “Non-solenoidal vorticity field,” <http://n-t.ru/tp/ng/evnp.htm>, 2002 (in Russian).
16. French, A. P., *Special Relativity*, Nelson and Sons, UK, 1968.
17. Tricker, R. A. R., *The Contribution of Faraday and Maxwell to Electrical Science*, Pergamon, Oxford, 1966.
18. Griffiths, D. J., *Introduction to Electrodynamics*, 3rd Edition, Pearson, San Francisco, 2008.
19. Zuza, K., J. Guisasola, M. Michelini, and L. Santi, “Rethinking Farady’s law for teaching motional electromotive force,” *Eur. J. Phys.*, Vol. 33, No. 2, 397–406, 2012.
20. Benedetto, E., M. Capriolo, A. Feoli, and D. Tucci, “A little help for a better understanding and application of Faraday’s law,” *Eur. J. Phys.*, Vol. 33, No. 3, L15–L20, 2012.

Investigation of Resonance Interactions of Microwaves with 3D Magnetic Nanocomposites Using the Probabilistic Model

G. S. Makeeva¹, O. A. Golovanov¹, and A. B. Rinkevich²

¹Penza State University, Russia

²Institute of Metal Physics, Ural Division of Russian Academy of Science, Russia

Abstract— A probabilistic approach to model the resonance interactions of electromagnetic waves (EMWs) with 3D magnetic opal nanocomposites has been developed. We consider the value of the ferromagnetic resonance (FMR) magnetic field H_r of magnetic nanoparticles as a random quantity having a normal distribution because the FMR fields are determined by the internal magnetic field depending on the shape of particles. The numerical approach is based on the decomposition of domain of the 3D magnetic nanocomposite into autonomous blocks with Floquet channels. We find the expectation values of the components of the effective permeability tensor as a function of DC magnetic field. The influence of the damping parameter of magnetic nanoparticles and the standard deviation of the random quantity H_r are analyzed at a frequency 26 GHz. The agreement of numerical results with the measured values FMR results shows the robustness of the developed probabilistic algorithm.

1. INTRODUCTION

The 3D magnetic opal-based nanocomposites, consisting of close packed SiO₂ spheres, where voids between the spheres are filled by a magnetic material, show interesting magnetic properties and unique microwave behavior [1]. The electromagnetic properties of such nanocomposites can be tuned by external bias magnetic field with potential applications for future microwave devices such as attenuators, filters, circulators, phase shifters, absorbers.

The ferrite nanoparticles are embedded into the inter-sphere voids via chemical precipitation procedure [1]. Typically, the real ferrite filling the octahedral voids between the opal sub-micron spheres in the periodic matrix of magnetic nanocomposite has a random distribution of shape and size of nanoparticles [1]. From the TEM microscopy data, the size of particles varies from 5 to 60 nm and the particles can form of aggregates in which the individual particles are located very close to one another at the distances of few nanometers and even less.

The FMR in the 3D magnetic nanocomposites is especially interesting for the possible applications. The resonance phenomena in 3D opal nanocomposites were studied in [1] via investigations of the frequency and magnetic field dependences of the transmission and reflection coefficients at millimeter waveband. Under the FMR conditions the variations of microwave signal transmitted through or reflected from the surface of samples of the opal nanocomposites containing the particles of ferrites were mostly due to changes in the surface impedance and absorption of EMWs. It was shown [1] that under the FMR conditions the amplitudes of transmitted EMWs sharply decrease.

The FMR is determined by the physical parameters of the ferromagnetic material, namely, the saturation magnetization, the anisotropy coefficient, the damping parameter and the shape of magnetic nanoparticles [2]. The susceptibility, the magnetization and the FMR frequency depend also on the size of magnetic nanoparticles if the nanoparticles are so small that they exhibit superparamagnetic behavior [3]. With diminishing of size of nanoparticle the surface effects become increasingly important, affecting primarily the anisotropy coefficient and the damping parameter [3–5]. Besides intrinsic damping, depending on the selected material, there is also damping due to surface effects [3, 6], which increases with diminishing of size and interparticle interactions [7]. The effective anisotropy coefficient also incorporates various contributions, such as the intrinsic surface and shape anisotropy [3–5], inversely depending on the size of particle and important at diameters below a few hundred nanometers.

That's why in contrast to our previous works [8,9] a probabilistic approach for developing mathematical models of resonance interaction of EMWs with the 3D magnetic nanocomposites is proposed. In goal to analyze the effective parameters of 3D magnetic opal nanocomposites and to investigate properties of magnetic nanoparticles the probabilistic models taking into account the difference of shape, size and orientation of nanoparticles and interparticle interactions are developed in this paper.

2. DETERMINISTIC ELECTRODYNAMIC MODEL

The rigorous mathematical model is based on the solution of the Maxwell's equations with electrodynamic boundary conditions, complemented by the Landau-Lifshitz equation, without any simplification of the equations and boundary conditions:

$$\begin{aligned}
 \operatorname{curl} \vec{H} &= i\omega \varepsilon_0 \varepsilon \vec{E}, \\
 \operatorname{curl} \vec{E} &= -i\omega \vec{M} - i\omega \mu_0 \vec{H}; \\
 -(\omega_r + i\omega) \vec{M} + \omega_r \chi_0 \vec{H} - \gamma \vec{M}_0 \times \vec{H} - \gamma \vec{M}_0 \times \vec{H}_q - \gamma \vec{M} \times \vec{H}_0; \\
 \operatorname{curl} \vec{M} &= \vec{F}; \\
 \operatorname{curl} \vec{F} &= -q^{-1} \vec{H}_q,
 \end{aligned} \tag{1}$$

where \mathbf{E} and \mathbf{H} are the EM fields, \mathbf{M} is the magnetization of the magnetic component of nanocomposite, \mathbf{H}_q is the effective exchange field, γ is the gyromagnetic ratio, $\omega_r = \alpha\gamma H_0$ is the relaxation frequency, χ_0 is the susceptibility, $q = 2A/\mu_0 M_0$ is the exchange constant; \mathbf{H}_0 and \mathbf{M}_0 are the external DC magnetic field and the saturation magnetization; ε_0 and μ_0 are the electric and magnetic constants.

The numerical approach is based on the decomposition into autonomous blocks with virtual Floquet channels (FAB) [10]. The domain of the 3D opal-based magnetic nanocomposite is divided into FAB (Fig. 1(a)), containing the SiO₂ nanospheres and the magnetic nanoparticles, filling the octahedral void regions of the opal structure (Fig. 1(b)). For the calculations we consider the elementary cell of the periodic 3D-nanostructure as FAB (Fig. 1(c)). In contrast to our previous work [9], in the model we take into account several (number N from 1 to 5) ferromagnetic nanospheres filling the void regions (Fig. 1(b)) in each cell (FAB).

The deterministic electrodynamic model was created in the following way. At each case we propose that number N of ferromagnetic nanoparticle with a spherical geometry embedded into an every intersphere opal void is different but the diameter d of the magnetic nanospheres was set for the constant value of the filling factor of the magnetic component in the opal voids in all cases. The cell is described by its FAB conductivity matrix \mathbf{Y} [10], taking into account electrodynamic boundary conditions, the number N and the shape of magnetic nanoparticles.

The electromagnetic wave (fields \mathbf{E} , \mathbf{H} ; frequency ω) propagating in the 3D periodic nanostructure along axis ζ (Fig. 1) is a superposition of inhomogeneous plane EMWs having fields $\mathbf{E}_n(\xi, \eta)$ $\mathbf{H}_n(\xi, \eta)$ and propagation constants [11]:

$$\Gamma_n = \nu + \frac{2\pi n}{\Lambda}, \quad n = 0, \pm 1, \pm 2, \dots, \pm\infty, \tag{2}$$

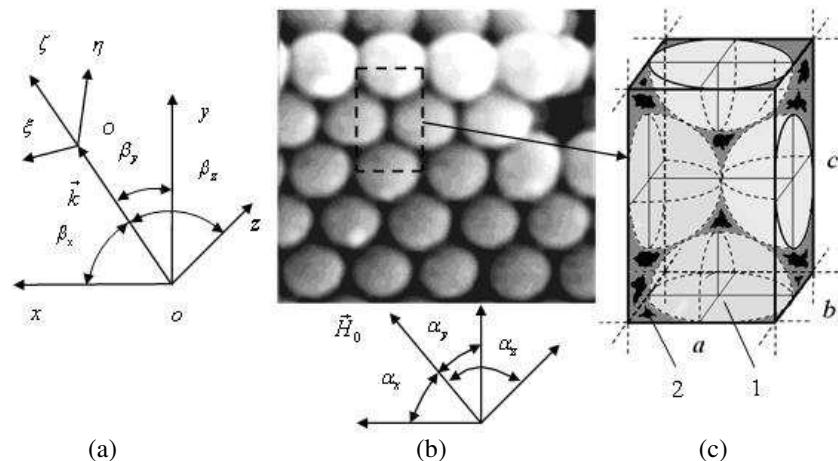


Figure 1: Model of 3D opal-based magnetic nanocomposite: (a) direction of propagating EMW of wave vector \mathbf{k} ; (b) periodic 3D-nanostructure and orientation of the DC magnetic field \mathbf{H}_0 ; (c) model of a cell of autonomous blocks with Floquet channels (FAB): 1 — SiO₂ nanospheres; 2 — region, filled by magnetic nanoparticles.

where $\Gamma_0 = \nu$ is the unknown propagation constant of the fundamental wave ($n = 0$); and Λ is the cell periodicity along the direction of propagation of EMW.

For the 3D magnetic opal nanocomposite we introduce the effective permeability tensor with components μ^Σ , μ_a^Σ , μ_z^Σ , and the effective permittivity ε^Σ . The components μ^Σ , μ_a^Σ of the effective permeability tensor and the effective permittivity ε^Σ can be determined by solving the system:

$$\Gamma_\Sigma^+ = \omega \sqrt{\varepsilon_0 \mu_0 \varepsilon^\Sigma (\mu^\Sigma + \mu_a^\Sigma)}, \quad (3)$$

$$\Gamma_\Sigma^- = \omega \sqrt{\varepsilon_0 \mu_0 \varepsilon^\Sigma (\mu^\Sigma - \mu_a^\Sigma)}, \quad (4)$$

$$\Gamma_\parallel^\Sigma = \omega \sqrt{\varepsilon_0 \mu_0 \varepsilon^\Sigma \mu_z^\Sigma}, \quad (5)$$

$$\Gamma_\perp^\Sigma = \omega \sqrt{\varepsilon_0 \varepsilon^\Sigma \mu_0 \frac{(\mu^\Sigma)^2 - (\mu_a^\Sigma)^2}{\mu^\Sigma}}, \quad (6)$$

where Γ_Σ^+ , Γ_Σ^- are the propagation constants of clockwise and counterclockwise polarized EMWs ($\mathbf{H}_0 = H_0 \mathbf{z}$); Γ_\parallel^Σ , Γ_\perp^Σ are the propagation constants of the ordinary and extraordinary modes ($\mathbf{H}_0 = H_0 \mathbf{x}$) in the gyromagnetic medium [12]. The propagation constants Γ_0 of the fundamental modes propagating along direction \mathbf{z} in a periodic 3D nanostructure (Fig. 1) for transverse $\mathbf{H}_0 = H_0 \mathbf{x}$ and longitudinal $\mathbf{H}_0 = H_0 \mathbf{z}$ orientations of the DC magnetic field \mathbf{H}_0 was obtained from the characteristic equation [9]:

$$\Delta(\Gamma_n) = |Y_{AA} - H^{-1} \cdot Y_{BA} + Y_{AB} \cdot H - H^{-1} \cdot Y_{BB} \cdot H| = 0, \quad (7)$$

where Γ_n are the unknown complex wave numbers; $\Delta(\Gamma_n)$ is the determinant of matrix; Y_{AA} , Y_{AB} , Y_{BA} , Y_{BB} are the blocks of conductivity matrix \mathbf{Y} , the indices A are for $\alpha = 1, 2, 3$; and B for $\alpha = 4, 5, 6$; H is a diagonal matrix having diagonal elements $q_{i(lj)} = -i\delta_{lj}\Gamma_n a \cos \beta_i$, where β_i are angles between the wave vector \mathbf{k} and the x , y , z axes.

Substituting the computed values of the propagation constants into (3)–(6) and solving the system of equations, the complex diagonal μ^Σ and off-diagonal μ_a^Σ components of the effective permeability tensor and the effective permittivity ε^Σ of 3D opal magnetic nanocomposite, were calculated at microwaves.

The following parameters were used in the calculations: the radius of the SiO_2 nanospheres was set $r = 100$ nm, $\varepsilon_r = 4.6 - i4 \cdot 10^{-4}$; and for magnetic nanoparticles $\text{Ni}_{0.7}\text{Zn}_{0.3}\text{Fe}_2\text{O}_4$ with saturation magnetization $4\pi M_s = 5$ kG, exchange constant $A = 2.2 \cdot 10^{-9}$ Oe cm², damping parameter $\alpha = 0.08$, $\varepsilon_r = 9.5 - i0.3$.

The real part $\text{Re}\mu^\Sigma$ of the diagonal μ^Σ component of the effective permeability tensor of the 3D opal magnetic nanocomposite, depending on the relative value of DC magnetic field $H_0^{rel} = (H_0 - H_r)/H_r$, where H_r is ferromagnetic resonance field (FMR), at the frequency of $f = 26$ GHz ($H_r = 9.18$ Oe) was calculated for different magnetic nanoparticle numbers $N = 1, 3, 4, 5$, having diameters $d = 50, 35, 31, 29$ nm, correspondingly. The results are shown in Figs. 2, 3. At each case (curves 1–4) the diameter d depends on the number N of magnetic nanospheres because the value of the filling factor of the magnetic component is kept constant.

As it follows from the results of modeling (Fig. 2 curves 1–4) the effective permeability increase upon reducing the diameter d ($d = 50, 35, 31, 29$ nm, $N = 1, 3, 4, 5$ correspondently) of the magnetic nanoparticles.

Figure 3 compares the results of calculation and the experimentally measured data from Ref. [1] at $f = 26$ GHz of the real and imaginary parts of the complex diagonal μ^Σ and off-diagonal μ_a^Σ components of the effective permeability tensor of the 3D opal magnetic nanocomposite depending on the relative value of DC magnetic field $H_0^{rel} = (H_0 - H_r)/H_r$.

From the comparison with the experiment [1] it follows that the agreement with the measured values is very good if the number of ferromagnetic nanospheres filling of the void regions in the opal matrix in each cell (FAB) $N = 5$, having diameter of $d = 29$ nm is assumed in the model. The effective permittivity ε^Σ of 3D opal magnetic nanocomposite is $\varepsilon^\Sigma = 4.87 - i0.03$.

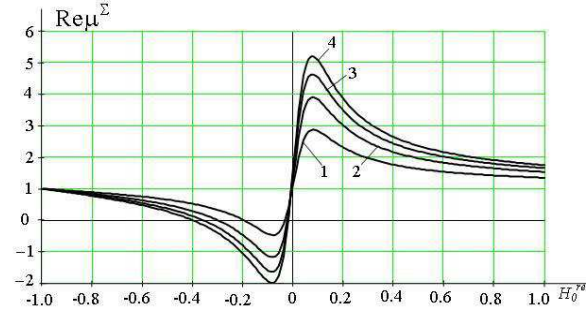


Figure 2: The real part $\text{Re}\mu^\Sigma$ of the diagonal μ^Σ component of the effective permeability tensor, depending on the relative value of DC magnetic field $H_0^{\text{rel}} = (H_0 - H_r)/H_r$ for the 3D opal magnetic nanocomposite. $f = 26$ GHz; curve 1 — $N = 1$, $d = 50$ nm; curve 2 — $N = 3$, $d = 35$ nm; curve 3 — $N = 4$, $d = 31$ nm; curve 4 — $N = 5$, $d = 29$ nm.

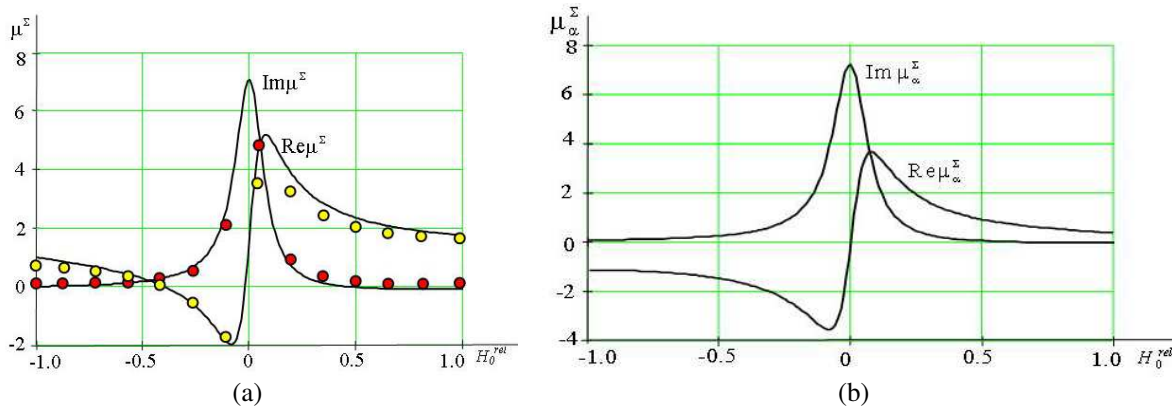


Figure 3: Calculated (a) real and (b) imaginary parts of the diagonal μ^Σ and off-diagonal μ_α^Σ components of the effective permeability tensor of the 3D opal magnetic nanocomposite (magnetic nanoparticles $\text{Ni}_{0.7}\text{Zn}_{0.3}\text{Fe}_2\text{O}_4$) vs. the relative DC magnetic field $H_0^{\text{rel}} = (H_0 - H_r)/H_r$ at $f = 26$ GHz; $N = 5$, $d = 29$ nm.

3. PROBABILISTIC MODEL AND RESULTS

From the measurements of the FMR response of opal nanocomposites [1] the FMR peak shape and the large value of the FMR linewidth are determined both by the random distribution of shape and size of magnetic nanoparticles and by the random spatial distribution of its aggregates. The probabilistic model of FMR in the 3D magnetic opal-based nanocomposite is developed in the following way. We consider that the value of the FMR magnetic field H_r of nanoparticles is a random quantity (because the FMR eigenfrequencies of nanoparticles, determined by the internal magnetic field, depends on the shape [12]). We propose that the random quantity H_r (the FMR magnetic field H_r of magnetic nanoparticle in an elementary cell of the periodic 3D nanostructure has a normal distribution law [13]:

$$f(H_r) = \frac{1}{\sigma\sqrt{2\pi}} \exp\left(-\frac{(H_r - H_r^0)^2}{2\sigma^2}\right), \quad (8)$$

where $f(H_r)$ is the probability density, H_r^0 is the expectation value of the random quantity H_r , σ is the standard deviation. A random-number generator was used to simulate the random quantity H_r with the normal distribution (8). For determining the random functions we use the distribution of H_r from the simulation.

Using the deterministic electrodynamic model, described above, the complex diagonal μ^Σ and off-diagonal μ_α^Σ components of the effective permeability tensor and the effective permittivity ε^Σ of the 3D magnetic opal- nanocomposite were calculated. At second stage, the random functions $\mu^\Sigma(H_r)$, $\mu_\alpha^\Sigma(H_r)$, depending on the random quantity H_r , were obtained by using the probabilistic simulation model. Then the expectation values of random quantities μ^Σ , μ_α^Σ were obtained.

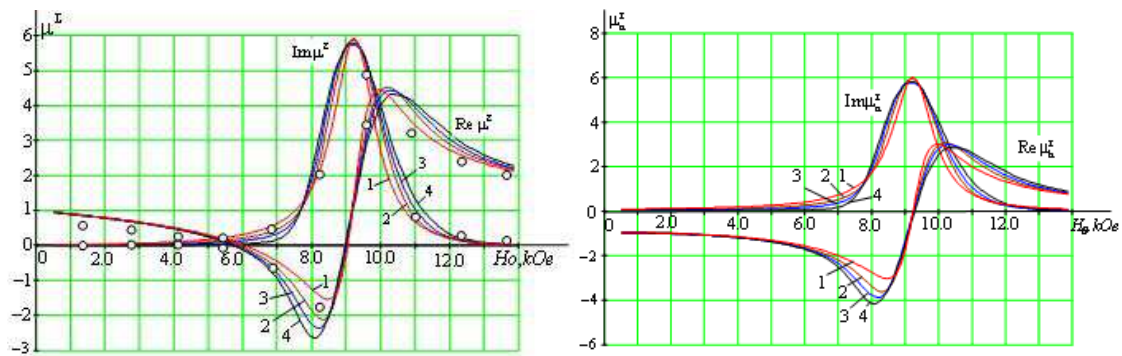


Figure 4: Calculated bias field dependence of the real and imaginary parts of the diagonal μ^Σ and off-diagonal μ_a^Σ components of the effective permeability tensor of 3D magnetic opal nanocomposite. $N = 4$, $d = 31$ nm, $f = 26$ GHz; curve 1 — $\alpha = 0.08$, $H_r^0 = 9,180$ Oe, $\sigma = 0$; curve 2 — $\alpha = 0.05$, $H_r^0 = 9,230$ Oe, $\sigma = 535$ Oe; curve 3 — $\alpha = 0.03$, $H_r^0 = 9,250$ Oe, $\sigma = 722$ Oe; curve 4 — $\alpha = 0.006$, $H_r^0 = 9,270$ Oe, $\sigma = 895$ Oe. Circles mark experimentally measured data from [1].

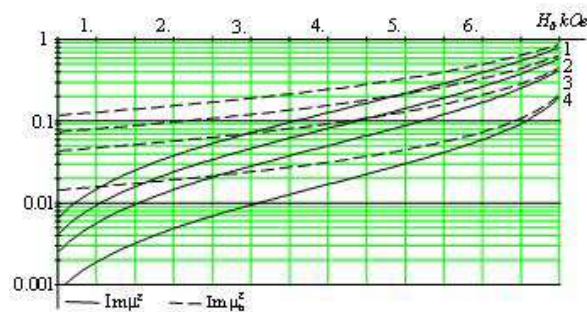


Figure 5: Calculated bias field dependence of magnetic losses of 3D magnetic opal nanocomposites. $N = 4$, $d = 31$ nm, $f = 26$ GHz; curve 1 — $\alpha = 0.08$, $H_r^0 = 9,180$ Oe, $\sigma = 0$; curve 2 — $\alpha = 0.05$, $H_r^0 = 9,230$ Oe, $\sigma = 535$ Oe; curve 3 — $\alpha = 0.03$, $H_r^0 = 9,250$ Oe, $\sigma = 722$ Oe; curve 4 — $\alpha = 0.006$, $H_r^0 = 9,270$ Oe, $\sigma = 895$ Oe.

Using the numerical algorithm, outlined above, the expectation values [7] of random quantities $\text{Re}\mu^\Sigma$, $\text{Im}\mu^\Sigma$, $\text{Re}\mu_a^\Sigma$, $\text{Im}\mu_a^\Sigma$ (the real and imaginary parts of complex diagonal μ^Σ and off-diagonal μ_a^Σ components of the effective permeability tensor of the 3D opal nanocomposites) depending on DC magnetic field, H_0 , were obtained at a frequency $f = 26$ GHz for different values of the damping parameter α of magnetic nanoparticles and the standard deviation σ of random quantity H_r of the FMR resonance field. The results are shown in Fig. 4 (curve 1–4) for particle number $N = 4$ (diameter $d = 31$ nm). The other parameters used in the calculations are the same as in Fig. 2).

Using the probabilistic algorithm, the influence of the damping parameter α of magnetic nanoparticles and the standard deviation σ of H_r of the FMR resonance field of the nanoparticles on the magnetic losses of the $\text{Ni}_{0.7}\text{Zn}_{0.3}\text{Fe}_2\text{O}_4$ infiltrated opal nanocomposites as a function of DC magnetic field were analyzed at a frequency of $f = 26$ GHz. The main results of modeling for $\alpha = 0.08$, 0.05, 0.03, 0.006 and $\sigma = 0$, 535 Oe, 722 Oe, 895 Oe, correspondently) are shown in Fig. 5 (curve 1–4).

4. CONCLUSIONS

The numerical technique using the developed probabilistic algorithm shows an agreement with recent experimental data of waveguide measurements [1] on ferrite opal nanocomposites and opens new possibilities for computer analysis of the resonance interactions of EMWs with 3D magnetic opal nanocomposites at microwaves.

REFERENCES

1. Ustinov, V. V., A. B. Rinkevich, D. V. Perov, M. I. Samoilovich, and S. M. Klescheva, "Anomalous magnetic antiresonance and resonance in ferrite nanoparticles embedded in opal matrix,"

- Journal of Magnetism and Magnetic Materials*, Vol. 324, 78–82, 2012.
2. Lax, B. and K. J. Button, *Microwave Ferrites and Ferrimagnetics*, McGraw-Hill, New York, 1962.
 3. Dormann, J. L., D. Fiorani, and E. Tronc, “Magnetic relaxation in fine particle systems,” *Adv. Chem. Phys.*, Vol. 98, 283–494, 1997.
 4. Kodama, R. H., “Magnetic nanoparticles,” *J. Magn. Magn. Mater.*, Vol. 200, 359–372, 1999.
 5. Batlle, X. and A. Labarta, “Finite-size effects in fine particles: Magnetic and transport properties,” *J. Phys. D: Appl. Phys.*, Vol. 35, R15–R42, 2002.
 6. Coffey, W. T., D. S. F. Crothers, J. L. Dormann, Y. P. Kalmykov, E. C. Kennedy, and W. Wernsdorfer, “Thermally activated relaxation time of a single domain ferromagnetic particle subjected to a uniform field at an oblique angle to the easy axis: Comparison with experimental observations,” *Phys. Rev. Lett.*, Vol. 80, 5655–5658, 1998.
 7. Dormann, J. L., F. D’Orazio, F. Lucari, E. Tronc, P. Prene, J. P. Jolivet, D. Fiorani, R. Cherkaoui, and M. Nogues, “Thermal variation of the relaxation time of the magnetic moment of γ -Fe₂O₃ nanoparticles with interparticle interactions of various strengths,” *Phys. Rev. B*, Vol. 53, 14291–14297, 1996.
 8. Pardavi-Horvath, M., G. S. Makeeva, and O. A. Golovanov, “Electrodynamic model for low loss microwave nanocomposite magnets using autonomous blocks with Floquet channels,” *J. App. Phys.*, Vol. 105, 07C104, 2009.
 9. Pardavi-Horvath, M., G. S. Makeeva, and O. A. Golovanov, “Interactions of electromagnetic waves with 3D opal-based magnetophotonic crystals at microwave frequencies,” *IEEE Transaction on Magnetics*, Vol. 47, No. 2, 341–344, Feb. 2011.
 10. Golovanov, O. A. and G. S. Makeeva, “The method of autonomous blocks with magnetic nano-inclusions and floquet channels applied for simulation of magnetic nanostructures with allowance for the exchange and boundary conditions,” *Journal of Communications Technology and Electronics*, Vol. 54, 1345–1352, 2009 (*Radiotekhnika i Elektronika*, Vol. 54, No. 12, 1421–1428, 2009).
 11. Nikol’skii, V. V., *Electrodynamics and Propagation of Radiowaves*, Nauka, Moscow, 1978 (in Russian).
 12. Gurevich, A. G. and G. A. Melkov, *Magnetization Oscillations and Waves*, CRC Press, New York, 1996.
 13. Ventzel, E. S., *Probability Theory*, Vysshaya Shkola, Moscow, 2001.

Spin and Electric Polarization Waves in Dielectric Systems of Different Dimensions

P. A. Andreev¹ and L. S. Kuzmenkov²

¹Department of General Physics, Physics Faculty, Moscow State University, Russian Federation

²Department of Theoretical Physics, Physics Faculty, Moscow State University, Russian Federation

Abstract— We study quantum dispersion properties of spin waves and waves of electrical polarization in systems of neutral particles. We pay attention for one-, two-, and three-dimensional dielectric systems. We consider spinning particles in the presence of an external uniform constant magnetic field, and electrically polarized particles are regarded in the presence of an external uniform constant electrical field.

Electric dipole moment and magnetic dipole moment has different nature. It leads to the difference in the dispersion properties of collective excitations. We can watch properties of dipole moments in systems of neutral particles there the Coulomb interaction does not overshadow the dynamical picture.

For collective excitation studying we use the method of many-particle quantum hydrodynamic. Quantum hydrodynamic equations are derived from many-particle Schrodinger equation, so, quantum hydrodynamic equations are deduced from first principles of quantum mechanics. For electrically polarized dielectrics a quantum hydrodynamic equations consist of four tensor equations, these are continuity equation, Euler equation, equation of polarization evolution and equation of polarization current evolution. For magnetized dielectrics a quantum hydrodynamic equations consist of three tensor equations, these are continuity equation, Euler equation and magnetic moment evolution equation (a generalization of Bloch equation).

We brief discuss the evident form of Hamiltonians for spin-spin interaction and electric dipole-dipole interaction. We present Hamiltonians corresponding to the Maxwell equation.

As the result we present the dispersion dependencies for dipole waves in one-, two-, and three-dimensional dielectric systems *and* compare dispersion dependencies for the spin waves and the waves of electric dipole moment.

1. INTRODUCTION

In recent years an interest in dynamical properties of both electrically and magnetically polarized dielectrics and semiconductors has been growing especially to low-dimensional [1, 2]. In this report we present a dispersion of eigenwaves for described systems and make comparison of properties for magnetization (spin) waves and electrically polarization waves. To study dispersion properties we have used method of many-particle quantum hydrodynamics [2–5], which was for the first time suggested in Ref. [6].

2. MODEL

We develop our model using many-particle Schrodinger equation. The last one contains a term describing dipole-dipole interaction H_{dd} . If we consider particles having electric dipole moment when Schrodinger equation has form

$$i\hbar\partial_t\psi(R, t) = \left(\sum_i \left(\frac{1}{2m_i} \hat{\mathbf{p}}_i^2 - d_i^\alpha E_{i,ext}^\alpha \right) - \frac{1}{2} \sum_{i,j \neq i} \left(d_i^\alpha d_j^\beta \cdot \partial_i^\alpha \partial_i^\beta \frac{1}{r_{ij}} \right) \right). \quad (1)$$

Usually an energy of interaction for the electric dipoles is considered in the form

$$H_{dd,ij} = \frac{\delta^{\alpha\beta} - 3r^\alpha r^\beta / r^2}{r^3} d_i^\alpha d_j^\beta, \quad (2)$$

but we use another formula

$$H_{dd,ij} = -\partial_i^\alpha \partial_i^\beta \frac{1}{r} \cdot d_i^\alpha d_j^\beta. \quad (3)$$

To describe the difference between (2) and (3) we present well-known identity

$$-\partial^\alpha \partial^\beta \frac{1}{r} = \frac{\delta^{\alpha\beta} - 3r^\alpha r^\beta / r^2}{r^3} + \frac{4\pi}{3} \delta^{\alpha\beta} \delta(\mathbf{r}). \quad (4)$$

We have chosen Hamiltonian (3) for next reason. Equations for description of collective motions appearing from Equation (1) must corresponds to the Maxwell equations. Using Hamiltonian (3) we find

$$\nabla \mathbf{E}(\mathbf{r}, t) = -4\pi \nabla \mathbf{P}(\mathbf{r}, t), \quad (5)$$

and

$$\nabla \times \mathbf{E} = 0. \quad (6)$$

In last formula we do not obtain contribution of magnetic field because we use non-relativistic model. If we use Hamiltonian (2) we will receive

$$\nabla \mathbf{E}(\mathbf{r}, t) = \frac{8\pi}{3} \nabla \mathbf{P}(\mathbf{r}, t), \quad (7)$$

instead of (5).

Now, let us to consider Hamiltonian for spin-spin interaction. Schrodinger equation for neutral spinning particles is

$$i\hbar \partial_t \psi_s(R, t) = \left(\left(\sum_i \left(\frac{p_i^2}{2m_i} - \gamma_i \hat{s}_i^\alpha B_{i(ext)}^\alpha \right) - \frac{1}{2} \sum_{i,j \neq i} \gamma_i \gamma_j G_{ij,M}^{\alpha\beta} \hat{s}_i^\alpha \hat{s}_j^\beta \right) \psi \right)_s (R, t). \quad (8)$$

where the last term describes spin-spin interaction and evident form of Green function of spin-spin interaction is $G_{ij,M}^{\alpha\beta} = 4\pi \delta_{\alpha\beta} \delta(\mathbf{r}_{ij}) + \nabla_i^\alpha \nabla_i^\beta (1/r_{ij})$, spin matrixes \hat{s}_i^α satisfy to the commutation relations

$$[\hat{s}_i^\alpha, \hat{s}_j^\beta] = i \delta_{ij} \varepsilon^{\alpha\beta\gamma} \hat{s}_i^\gamma.$$

Notice that an energy of spin-spin interaction contains additional term in comparison with the energy of interaction between electric dipoles. It also differs from the formula presented in Ref. [7]. Electric and magnetic dipoles have different nature and magnetic field \mathbf{B} caused by magnetic dipoles satisfies to another pair of Maxwell equations

$$div \mathbf{B} = 0, \quad (9)$$

and

$$\nabla \times \mathbf{B} = 4\pi \nabla \times \mathbf{M}. \quad (10)$$

For the first time it was shown in Ref. [4].

The first pair of a set of quantum hydrodynamic equations are continuity equation

$$\partial_t n + \partial^\alpha (n \cdot v^\alpha) = 0, \quad (11)$$

and momentum balance equation

$$\begin{aligned} mn(\partial_t + \mathbf{v} \cdot \nabla) v^\alpha + \partial_\beta p^{\alpha\beta} - \frac{\hbar^2}{4m} \partial^\alpha \Delta n + \frac{\hbar^2}{4m} \partial^\beta \left(\frac{\partial^\alpha n \cdot \partial^\beta n}{n} \right) \\ = P^\beta \partial^\alpha \left(E_{ext}^\beta(\mathbf{r}, t) + \int d\mathbf{r}' G_D^{\beta\gamma}(\mathbf{r}, \mathbf{r}') P^\gamma(\mathbf{r}', t) \right). \end{aligned} \quad (12)$$

These equations are written for electric polarized particles. They have the same form for the system of spinning particles, but in right hand side of Equation (12) we have to write magnetization \mathbf{M} and magnetic field \mathbf{B}_{ext} instead of polarization \mathbf{P} and electric field \mathbf{E}_{ext} , and we also must change $G_D^{\gamma\delta}$ on $G_M^{\gamma\delta}$. Integral term in right-hand side of Equation (12) might be considered as electric field (magnetic field for spinning particles) caused by polarization (magnetization). This electric (magnetic) field must satisfy to Equations (5) and (6) ((9) and (10)).

Studying of dynamic of electrically polarized (spinning) particles requires to find equation of temporal evolution of polarization \mathbf{P} (magnetization \mathbf{M}). Equations for polarization and magnetization differ from each other. Let us present equations for polarization evolution

$$\partial_t P^\alpha + \partial^\beta R^{\alpha\beta} = 0, \quad (13)$$

where $R^{\alpha\beta}(\mathbf{r}, t)$ is the current of polarization, in addition we include equation describing evolution of current of polarization $R^{\alpha\beta}(\mathbf{r}, t)$

$$\begin{aligned} & \partial_t R^{\alpha\beta} + \partial^\gamma \left(R^{\alpha\beta} v^\gamma + R^{\alpha\gamma} v^\beta - P^\alpha v^\beta v^\gamma \right) - \frac{\hbar^2}{4m^2} \partial_\beta \Delta P^\alpha + \frac{\hbar^2}{8m^2} \partial^\gamma \left(\frac{\partial_\beta P^\alpha \partial_\gamma n}{n} + \frac{\partial_\gamma P^\alpha \partial_\beta n}{n} \right) \\ & = \frac{\sigma}{m} \frac{P^\alpha P^\gamma}{n} \partial^\beta \left(E_{ext}^\gamma(\mathbf{r}, t) + \int d\mathbf{r}' G_D^{\gamma\delta}(\mathbf{r}, \mathbf{r}') P^\delta(\mathbf{r}', t) \right). \end{aligned} \quad (14)$$

The last one is interesting because it involve influence of interaction on polarization dynamic. Magnetization evolution is described by the following equation

$$\partial_t M^\alpha + \partial^\beta (M^\alpha v^\beta) = \frac{\gamma}{\hbar} \varepsilon^{\alpha\beta\gamma} M^\beta \left(B_{ext}^\gamma(\mathbf{r}, t) + \int d\mathbf{r}' G_M^{\gamma\delta}(\mathbf{r}, \mathbf{r}') M^\delta(\mathbf{r}', t) \right), \quad (15)$$

To find dispersion dependencies of wave we must consider dynamic of small perturbations. For this purpose we should put following formulas into Equations (11), (12) and (13), (14) or (15)

$$\begin{aligned} n &= n_0 + \delta n, \quad v^\alpha = 0 + v^\alpha, \quad \text{and} \\ P^\alpha &= P_0^\alpha + \delta P^\alpha, \quad R^{\alpha\beta} = 0 + \delta R^{\alpha\beta} \quad \text{or} \quad M^\alpha = M_0^\alpha + \delta M^\alpha. \end{aligned} \quad (16)$$

The dispersion dependence $\omega(k)$ for waves of electrical polarization in three dimensional sample appears as

$$\omega = \sqrt{\frac{4\pi\sigma}{mn_0}} P_0 k_z. \quad (17)$$

If we derive a solution for eigenwaves in a 2D system the dispersion equation has a form of

$$\omega = \sqrt{\frac{2\pi\sigma}{mn_0} \int_{kr_0}^{\infty} d\xi \frac{J_0(\xi)}{\xi^2}} P_0 k^{3/2}. \quad (18)$$

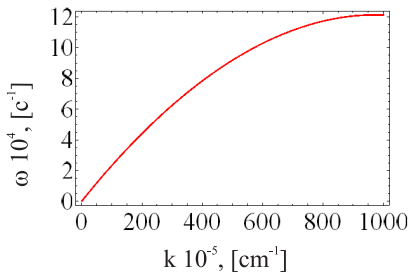


Figure 1: The figure shows the dispersion characteristic of the 2D quantum atomic polarization wave frequency $\omega(k)$ versus the wave vector k , which is described by the Equation (18). The atomic radius r_0 is supposed to be 0.1 nm. Equilibrium polarization has form $P_0 = \kappa E_0$. Static electric permeability κ is defined by the equation $\kappa = n_0 p_0^2 / (3k_B T)$. p_0 — is a dipole moment of an atom, T — temperature of the medium, k_B — Boltzmann constant. System parameters are assumed to be as follows: $n_0 = 10^8 \text{ cm}^{-2}$, $p_0 = 3 \cdot 10^{-20} \text{ C m}$, $T = 100 \text{ K}$, $E_0 = 3 \cdot 10^4 \text{ V/m}$, $m = 10^{-23} \text{ g}$.

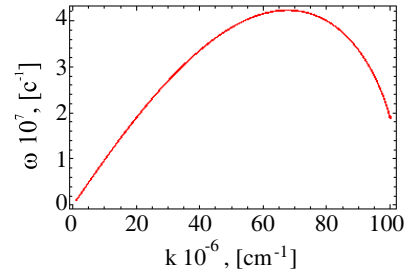


Figure 2: The dependence of frequency ω on the wave vector k is displayed for the case of single dimension polarization mode which dispersion characteristic is defined by the Equation (19). System parameters are analogous to the presented at ... to Fig. 1, but here we have deal with one dimensional concentration its value to be $n_0 = 10^4 \text{ cm}^{-1}$.

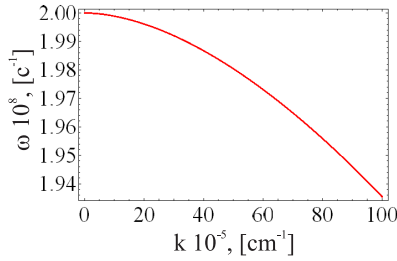


Figure 3: The figure shows the dispersion characteristic of the 2D quantum atomic magnetization wave frequency $\omega(k)$ versus the wave vector k , which is described by the Equation (21). Magnetic field \mathbf{B}_0 is taken equal to $10^3 G$. System parameters are the magnetic susceptibility $\kappa = 10^{-6}$ and the atomic radius $r_0 = 0.1$ nm.

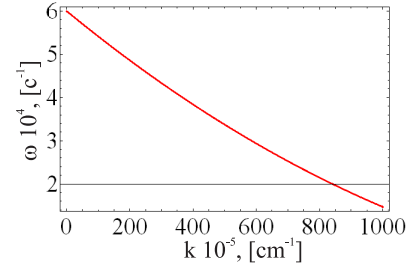


Figure 4: The figure shows the dispersion characteristic of the 2D quantum atomic magnetization wave frequency $\omega(k)$ versus the wave vector k , which is described by the Equation (22). Magnetic field \mathbf{B}_0 is taken equal to $10^3 G$. System parameters are the magnetic susceptibility $\kappa = 10^{-6}$ and the atomic radius $r_0 = 0.1$ nm.

where k is the module of wave vector, J_0 is a Bessel function of the zero order, r_0 is a radius of a molecule. The dispersion dependence (18) is presented on Fig. 4.

In 1D case $\omega(k)$ occurs as

$$\omega = \sqrt{\frac{2\sigma}{mn_0} \int_{kr_0}^{\infty} d\xi \frac{\cos(\xi)}{\xi^3} P_0 k^2}, \quad (19)$$

Dispersion dependence for wave of polarization in one dimensional case (19) is presented on Fig. 2.

Now, let us to present dispersion dependencies for spin (magnetic moment) waves in dielectrics. We start with a solution for three dimensional system of particles. It has form of

$$\omega = \frac{1}{\sqrt{\mu}} \frac{2\gamma}{\hbar} B_0 \quad (20)$$

where μ is the magnetic permeability.

Dispersion dependencies in one-dimensional and two-dimensional cases can not be presented in elementary functions therefore we present theirs at Figs. 3 and 4. Theirs analytic form to be

$$\omega = \frac{2\gamma}{\hbar} M_0 \int_{kr_0}^{\infty} d\xi \frac{J_0(\xi)}{\xi^2} \cdot k \quad (21)$$

in two dimensional case, and

$$\omega = \frac{2\gamma}{\hbar} M_0 \int_{kr_0}^{\infty} d\xi \frac{\cos(\xi)}{\xi^3} \cdot k^2 \quad (22)$$

in one dimensional case.

Due to the fact that we consider paramagnetic dielectrics we can write $\mathbf{M}_0 = \kappa/(1 + 4\pi\kappa) \cdot \mathbf{B}_0$, where κ is the magnetic susceptibility and we take it equal to 10^{-6} .

Notice that frequencies of one-dimensional and two-dimensional spin waves are proportional to an integral. Whereas frequencies of waves of electric polarization are proportional to the square root of the integral. As a conclusion, in this paper we point out differences in properties of wave of electric and magnetic dipole moments. This notice very important because it is widely used a treating of electric and magnetic dipole moments in the same way and using for its description the same models [8, 9].

REFERENCES

1. Li, Q., E. H. Hwang, and S. Das Sarma, "Collective modes of monolayer, bilayer, and multilayer fermionic dipolar liquid," *Phys. Rev. B*, Vol. 82, 235126(11), 2011.
2. Andreev, P. A., L. S. Kuzmenkov, and M. I. Trukhanova, "Quantum hydrodynamics approach to the formation of waves in polarized two-dimensional systems of charged and neutral particles," *Phys. Rev. B*, Vol. 84, 245401(13), 2011.

3. Marklund, M. and G. Brodin, “Dynamics of spin-1/2 quantum plasmas,” *Phys. Rev. Lett.*, Vol. 98, 025001(4), 2007.
4. Kuz'menkov, L. S., S. G. Maksimov, and V. V. Fedoseev, “Microscopic quantum hydrodynamics of systems of fermions: Part 1,” *Theoretical and Mathematical Physics*, Vol. 126, 110–120, 2001.
5. Shukla, P. K. and B. Eliasson, “Nonlinear collective interactions in quantum plasmas with degenerate electron fluids,” *Rev. Mod. Phys.*, Vol. 83, 885–906, 2011.
6. Kuz'menkov, L. S. and S. G. Maksimov, “Quantum hydrodynamics of particle systems with coulomb interaction and quantum bohm potential,” *Theoretical and Mathematical Physics*, Vol. 118, 227–240, 1999.
7. Berestetskii, V. B., E. M. Lifshitz, L. P. Pitaevskii, *Quantum Electrodynamics*, 2nd Edition, Vol. 4, Butterworth-Heinemann, 1982.
8. Lahaye, T., C. Menotti, L. Santos, M. Lewenstein, and T. Pfau, “The physics of dipolar bosonic quantum gases,” *Rep. Prog. Phys.*, Vol. 72, 126401(41), 2009.
9. Yi, S. and L. You, “Probing dipolar effects with condensate shape oscillation,” *Phys. Rev. A*, Vol. 66, 013607(4), 2002.

Shear Vibrations of Magnetostrictive-piezoelectric Film Structure

K. V. Lavrentjeva, V. M. Petrov, and R. V. Petrov

Institute of Electronic and Information Systems, Novgorod State University
Veliky Novgorod 173003, Russia

Abstract— This article discusses magnetoelectric effect at shear modes in a magnetostrictive-piezoelectric film on a substrate in electromechanical resonance (EMR) region. The expression for magnetoelectric voltage coefficient is obtained using material parameters of composite components. Theoretical estimates are obtained for the bilayer of lead zirconate titanate (PZT) and nickel ferrite (NFO) on SrTiO₃ substrate.

1. INTRODUCTION

The magnetoelectric (ME) effect in composites is caused by mechanically coupled magnetostrictive and piezoelectric subsystems in a material and consists in inducing the electric polarization in an applied magnetic field, or vice versa inducing the magnetization in an applied electric field. Because the ME effect in composites is due to mechanically coupled piezoelectric and magnetostrictive subsystems, it sharply increases in the vicinity of the electromechanical resonance frequency [1, 2].

Expression for ME coefficient is obtained using the simultaneous solution of electrostatic, magnetostatic and elastodynamic equations. The ME voltage coefficient α_E defined as the ratio of induced electric field E and applied magnetic field H is estimated from known material parameters (piezoelectric coupling, magnetostriction, elastic constants, etc.) of composite components.

2. THEORY

Mechanical oscillations of a ME composite can be induced either by alternating magnetic or electric fields. If the length of the electromagnetic wave exceeds the spatial size of the composite by some orders of magnitude, then it is possible to neglect gradients of the electric and magnetic fields within the sample volume. Therefore, based on elastodynamics and electrostatics, the equations of medium motion are governed by

$$\rho_p \frac{\partial^2 u_1}{\partial t^2} = \frac{\partial T_{p5}}{\partial z}, \quad (1)$$

where U_i is the displacement vector component, ρ_p is the mass density of piezoelectric, V is the ferroelectric volume fraction, ${}^p\rho$ and ${}^m\rho$, ${}^pT_{ij}$ and ${}^mT_{ij}$ are the densities and stress tensor components of ferroelectric and ferromagnet, correspondingly.

Similar equations of media shear motion can be written for magnetostrictive phases and substrate. To solve these equations for displacement component, one should use the appropriate boundary conditions for stress and strain components on interfaces. Substituting the found solutions into the open circuit condition enables one to obtain the expression for ME voltage coefficient.

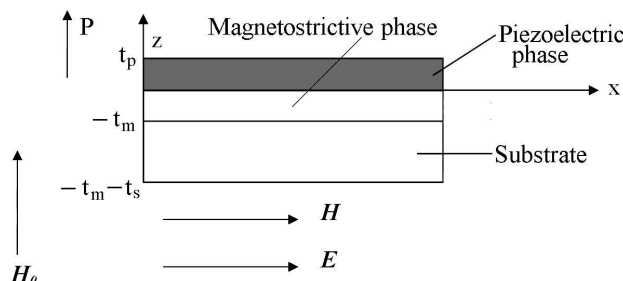


Figure 1: Bilayer of piezoelectric and ferrite in the x - z plane on the substrate. The poling electric field E_0 is along z direction and ac electric field E is along x . The bias magnetic field H_0 and the alternating magnetic field H are along z and x , respectively.

Expressions for the strain in the ferromagnetic layers S_{mi} , the strain in the ferroelectric layers S_{pi} , and strain in the substrate S_{si} have the form:

$$\begin{cases} S_{p5} = d_{15}E_1 + s_{p44}T_{p5}(z) \\ S_{5m} = q_{15}H_1 + s_{m44}T_{m5}(z) \\ S_{s5} = s_{s44}T_{s5}(z) \end{cases} \quad (2)$$

where T_{pi} is the stress and s_{pii} is the compliance of the ferroelectric at constant electric field, T_{mi} is the stress and s_{mii} is the compliance of the ferromagnetic at constant magnetic field, d_{ij} is the piezoelectric coefficient of the ferroelectric, q_{ij} is the piezomagnetic coefficient of ferromagnetic, E_1 and H_1 are electric and magnetic fields.

Electric displacements D for the piezoelectric phases is given by

$$D_p(z) = d_{15}T_{p5}(z) + \varepsilon_{33}E_1 \quad (3)$$

where ε_{33} is the relevant component of the electrical permittivity.

For determining the ME voltage coefficient, we use the open circuit condition:

$$\int_0^{t_p} D_p(z)dz = 0 \quad (4)$$

Substituting expression (3) into Equation (4) and solving Equation (4) for E_1 enables finding the expression for the ME voltage coefficient $\alpha = \frac{E_1}{H_1}$

$$\alpha = \frac{k_p d_{15} q_{15} [(-1 + Q_4)Q_2 - Q_4 + 1]}{\left[\left\{ (2s_{m44}k_p Q_4 + s_{p44}k_p t_p k_m Q_3)Q_2 + (-s_{p44}k_m Q_3 + k_p^2 t_p s_{m44} Q_4)Q_1 - 2s_{m44}k_p Q_4 \right\} K^2 - s_{p44}k_p t_p k_m Q_2 Q_3 - k_p^2 t_p s_{m44} Q_1 Q_4 \right] \varepsilon_{33}} \quad (5)$$

where

$$Q_1 = \sin(k_p t_p), \quad Q_2 = \cos(k_p t_p), \quad Q_3 = \sin(k_m t_m), \quad Q_4 = \cos(k_m t_m). \\ k_m = \omega \sqrt{\rho_m s_{m44}}, \quad k_p = \omega \sqrt{\rho_p s_{p44}}, \quad k_s = \omega \sqrt{\rho_s s_{s44}}$$

ω is the circular frequency, ${}^p\rho$, ${}^m\rho$ and ${}^s\rho$ are the piezoelectric, piezomagnetic and substrate densities.

Material parameters used for numerical estimations are listed in Table 1.

As an example, Fig. 2 shows a resonances peak at shear modes in free standing bilayer of lead zirconate titanate (PZT) and nickel ferrite NiFe_2O_3 . The maximum value of the ME coefficient (20 V/(cm Oe)) is observed at frequency of about 0.8 GHz.

Placing the magnetostrictive-piezoelectric film on a substrate is expected to lead to two significant effects: a decrease in the EMR frequency due to clamping and a fine structure in the ME voltage versus frequency spectrum. Fig. 3 shows a family of equally spaced peaks that are linear combinations of the modes corresponding to the substrate and bilayer structure.

The frequency separation between two consecutive peaks is determined primarily by the substrate thickness. The envelope of the fine structure shows a maximum at 0.3 GHz. This maximum is due to EMR in ME bilayer. Peak value of ME voltage coefficient (2.2 V/cm Oe) is a factor of about ten smaller than for free standing bilayer.

Table 1: Material parameters — compliance coefficient s , piezomagnetic coupling q , piezoelectric coefficient d , permeability ε , and density ρ for lead zirconate titanate (PZT), nickel ferrite NiFe_2O_3 (NFO) and strontium titanate (SrTiO_3).

Material	s_{44} (10^{-12} m ² /N)	q_{15} (10^{-12} m/A)	d_{15} (10^{-12} m/V)	$\varepsilon_{33}/\varepsilon_0$	ρ (10^3 kg/m ³)
PZT	34		-350	1750	7.5
NFO	12.6	-560			5.37
SrTiO ₃	4				7.75

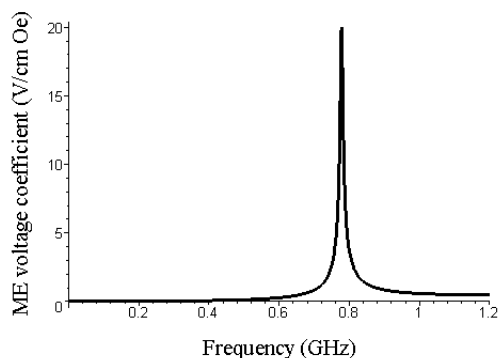


Figure 2: Frequency dependence of ME voltage coefficient for a free bilayer structure of PZT of thickness 300 nm and NFO of thickness 2 μm and without substrate.

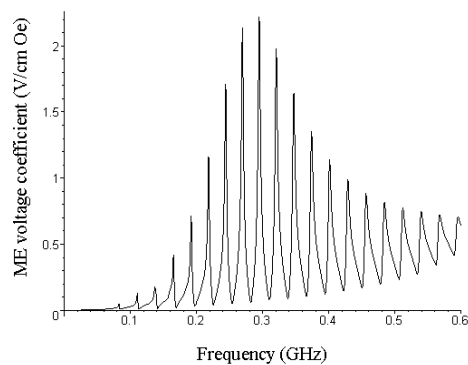


Figure 3: Frequency dependence of ME voltage coefficient for bilayer of 300 nm thick PZT and 2 μm thick NFO on 100 μm thick SrTiO_3 substrate.

3. CONCLUSION

A theory has been described for ME interactions at shear modes in a magnetostrictive-piezoelectric film on a substrate in EMR region. For a NFO-PZT structure on SrTiO_3 substrate, the strength of ME interactions is weaker than for thick film bilayers due to the strong clamping effects of the substrate. For increasing substrate thickness in a bilayer, the ME coefficient drops rapidly and the EMR frequency decreases. For a magnetostrictive-piezoelectric film on a substrate, the ME voltage versus frequency profile shows a fine structure consisting of equally spaced peaks. The distance between the peaks is a function of the substrate thickness.

The obtained phenomenon is of importance for the realization of multifunctional ME sensors/transducers operating at microwave frequencies.

REFERENCES

1. Nan, C.-W., M. I. Bichurin, S. Dong, D. Viehland, and G. Srinivasan, *J. Appl. Phys.*, Vol. 103, 031101, 2008.
2. Bichurin, M. I., D. A. Filipov, V. M. Petrov, V. M. Laletsin, N. Paddubnaya, and G. Srinivasan, *Phys. Rev. B*, Vol. 68, 132408, 2003.

Impact of Temperature on the Electromagnetic Susceptibility of Operational Amplifiers

R. Fernández-García and I. Gil

Department of Electronic Engineering
Universitat Politècnica de Catalunya, Colom 1, Terrassa 08222, Spain

Abstract— In this paper, the impact of temperature on the electromagnetic susceptibility of operational amplifiers at different frequencies is presented. The IEC 62132-4 direct power injection standard has been used with several commercial operational amplifiers in a printed circuit board specifically fabricated. The results show that the susceptibility of the operational amplifier is reduced with the temperature.

1. INTRODUCTION

Over recent years, due to the increasing demand for wireless operation electronic devices, a severe and complex electromagnetic pollution environment has been created. Therefore, the susceptibility to Radiofrequency Interference (RFI) has become a more important constraint for integrated circuit designers, particularly for analogue integrated circuits (ICs), which are the most sensitive circuits to RFI [1]. In order to characterize the IC susceptibility different standards have been proposed and the IEC 62132-4 Direct Power Injection (DPI) is one of the most extensively used [2]. In this work, the IEC 62132-4 standard has been used in order to characterize the most widely known analog device, the operational amplifier (OpAmp). In this case, unlike others works, where the operational amplifier susceptibility is evaluated [3, 4], the temperature has been taking into account. The impact of the temperature can be critical in a lot of safety application, i.e., automotive, where the electronic equipments located near the engine should resist, under normal operation conditions, temperatures about 100°C.

2. EXPERIMENTAL

Figure 1(a) shows the experimental fabricated PCB. The PCB dimensions are $8 \times 8 \text{ cm}^2$ and as it can be observed a symmetrical microstrip layout with same electrical length traces and characteristic impedance, $Z_0 = 50 \Omega$, has been used. With this layout, all the injection ports present identical behavior. In order to investigate the operational amplifier susceptibility, a follower topology has been selected, as a worst EMI case [3]. Moreover, all the devices under test are mounted on a DIP-8 package in combination with an 8 pin dual in line IC socket. The prototype has been fabricated on the commercial *Rogers RO3010* substrate (dielectric constant $\epsilon_r = 10.2$, thickness $h = 1.27 \text{ mm}$, $\tan \delta = 0.0023$) in order to have high performance above 1 GHz.

The susceptibility to electromagnetic interference has been evaluated under the standard IEC 62132-4 DPI [2] which is a very popular and efficient method to apply a conducted interference disturbance to a component. Fig. 1(b) describes the DPI setup. It consists of a RF signal generator

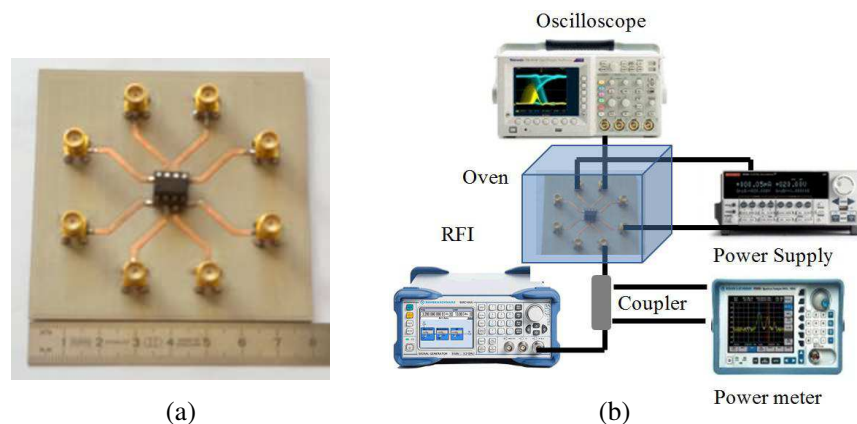


Figure 1: (a) PCB specifically designed for this experiment. (b) Experimental setup.

(providing the RFI disturbance) directly connected to a directional coupler in order to measure the actual level of power injected into the DUT with a power meter. A power supply provides the DC voltage to the integrated circuit and an oscilloscope is used to measure the OpAmps offset voltage due to RFI. Notice that the PCB is located in an oven in order to control the temperature of the devices under test. The RF interference has been swept from 10 MHz to 1 GHz with a input power forward level up to 10 dBm, at three temperatures: 25°C, 50°C and 75°C. The experiments have been performed for two types of operational amplifiers, the well-known LM741 operational amplifier and the TL081, which is wide bandwidth JFET input operational amplifier.

3. RESULTS

Figure 2 shows the frequency dependency of the offset voltage when a power level of 0 dBm is injected into the operational amplifier non-inverter input at room temperature (25°C). The results are shown for two different integrated circuits, LM741 and TL081. It is observed that the offset voltage of LM741 reach a value about 300 mV, meanwhile the TL081 reach a voltage offset below 40 mV.

In order to evaluate the impact of the temperature, both operational amplifiers have been subjected at different temperatures. The results are shown in Fig. 3. It both cases the offset voltage is reduced when the temperature is increased. For instance, for a RFI interference of 100 MHz the offset voltage drops from 360 mV at 25°C to 328 mV at 75°C for the LM741, which represents a reduction 8.9%. At the same frequency, the reduction of TL081 offset voltage drops from 22.3 mV to 13.8 mV, which corresponds to a 38% offset voltage reduction.

Notice that, although the absolute offset voltage reduction is higher in case of LM741, the relative reduction is lower than in case of TL081 due to the high offset voltage at room temperature. Fig. 4 details the offset voltage temperature dependence in case of 100 MHz RFI with three different RFI power levels, -20 dBm, -10 dBm and 0 dBm for LM741 and -10 dBm, 0 dBm and 10 dBm for TL081.

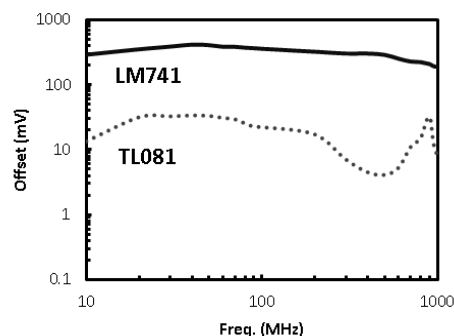


Figure 2: Operational amplifier offset voltage when a RFI interference of 0 dBm is injected at the inverter input at room temperature.

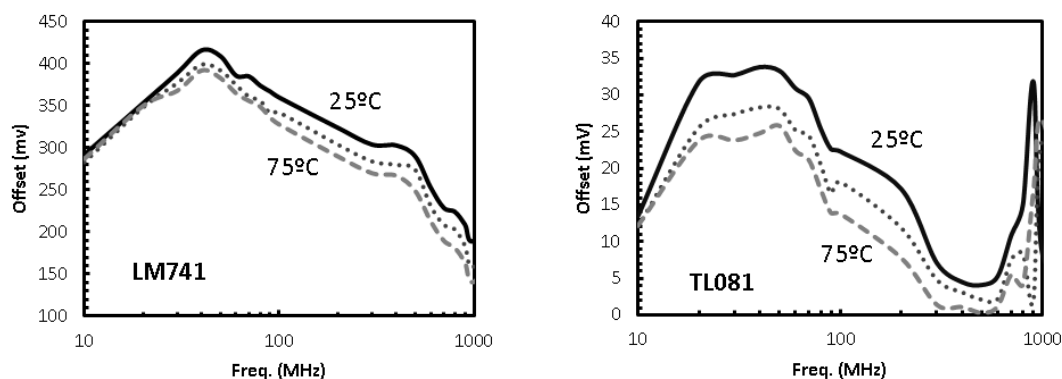


Figure 3: Operational amplifier offset voltage when a RFI interference of 0 dBm is injected at the inverter input ($f = 100$ MHz). The results are shown for three temperatures: 25°C, 50°C and 75°C.

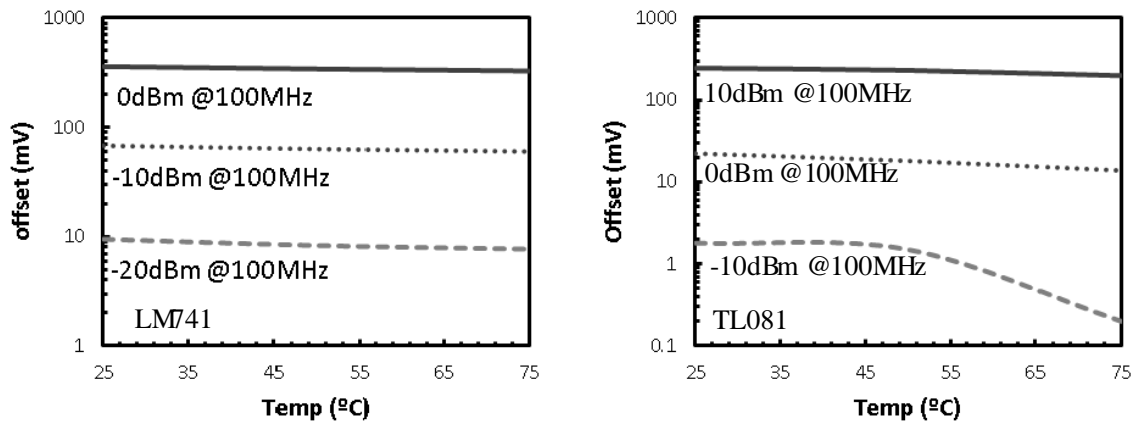


Figure 4: Operational amplifier offset voltage temperature dependence. The results are show for three different RFI power injection levels.

As in Fig. 2, the offset voltage of LM741 is about one order of magnitude worse than TL081. In order to achieve similar offset voltage in both integrated circuits, the power injection level of TL081 should be increased 10 dBm. The experimental results of Fig. 4 confirm the voltage reduction trend when the temperature is increased. A deeply investigation should be done in order to explain the physical reason of this behavior. However, one brief explanation can be the improvement of the non-linearity behavior of the transistor at high temperatures.

4. CONCLUSIONS

In this paper, the impact of temperature on the electromagnetic susceptibility performance of operational amplifiers has been experimentally evaluated. Specifically, the offset voltage of the operational amplifiers in a follower topology has been evaluated when a conducted RF interference from 10 MHz to 1 GHz is introduced into the non-inverter input at different temperatures. The experiments have been developed in two different commercial devices, the LM741 and the TL081. The results show that in both cases the offset voltage is reduced when the temperature is increased. Although a deeply investigation should be done in order to know the physical reason of this offset reduction, the improvement of the non-linearity performance of transistor could be a reason.

ACKNOWLEDGMENT

This work has been supported by the Spain-MINECO under Project TEC2010-18550 and AGAUR 2009 SGR 1425.

REFERENCES

1. Ramdani, M., E. Sicard, A. Boyer, S. Ben Dhia, J. J. Whalen, T. H. Hubing, M. Coenen, and O. Wada, "The electromagnetic compatibility of integrated circuits-past, present and future," *IEEE Transactions on Electromagnetic Compatibility*, Vol. 51, 78–100, Feb. 2009.
2. EN IEC 62134-4, "Integrated circuits — Measurement of electromagnetic immunity, 150 kHz to 1 GHz — Part 4: Direct RF power injection method," 2006.
3. Richelli, A., "Measurements of EMI susceptibility in ultra-low-voltage OpAmps," *Proc. of the EMC Compo.*, 13–17, Dubrovnik, Croatia, Nov. 2011.
4. Gago, J., J. Balcells, D. González, M. Lamich, J. Mon, and A. Santolaria, "EMI susceptibility model of signal conditioning circuits based on operational amplifiers," *IEEE Transactions on Electromagnetic Compatibility*, Vol. 49, 849–859, Nov. 2007.

Control of Coherence and Polarization of an Electromagnetic Beam by Means of Liquid Crystal Spatial Light Modulators

C. Rickenstorff, E. Flores-Cruz, and A. S. Ostrovsky

Facultad de Ciencias Físico Matemáticas

Benemérita Universidad Autónoma de Puebla, Puebla 72000, México

Abstract— An experimental method for modulating the coherence and polarization of the electromagnetic beam by means of 90°-twist liquid-crystal spatial light modulators (LC-SLMs) is proposed. In the present technique, the statistical properties of light are controlled through computer generated random signals applied to a pair of 90°-twist LC-SLMs arranged in an interferometric setup. Experimental results obtained using Holoeye LC2002 modulators show the efficiency of the proposed method.

1. INTRODUCTION

Since the mid-1980's the nematic liquid-crystal spatial light modulators LC-SLMs have been used for amplitude or phase modulation of the optical field in many applications such as optical data processing, adaptive optics, real time holography, etc.. Recently, with the development of the vector coherence theory it has been shown that the LC-SLM is also able to modulate the coherence and polarization of the electromagnetic field [1–3]. However, the reported techniques lack experimental results and presuppose the use of 0°-twist LC-SLMs that are extremely expensive [4]. Here we propose an alternative technique for modulating the coherence and polarization of light which uses more economic 90°-twist LC-SLM working in phase mode. In order to obtain the desired result, two orthogonal 90°-twist LC-SLMs displaying a special random signal are placed at both arms of a Mach-Zehnder interferometer. The efficiency of the proposed technique is demonstrated with experimental results using the Holoeye LC2002 modulators.

2. BACKGROUND

According to Wolf, the degree of coherence and polarization of an electromagnetic field characterized by the 2×2 cross spectral density matrix $\mathbf{W}(\mathbf{x}_1, \mathbf{x}_2)$ are defined as [1]

$$\mu(\mathbf{x}_1, \mathbf{x}_2) = \frac{\text{Tr}\mathbf{W}(\mathbf{x}_1, \mathbf{x}_2)}{[\text{Tr}\mathbf{W}(\mathbf{x}_1, \mathbf{x}_1)\text{Tr}\mathbf{W}(\mathbf{x}_2, \mathbf{x}_2)]^{1/2}}, \quad (1)$$

$$P(\mathbf{x}) = \left(1 - \frac{4\text{Det}\mathbf{W}(\mathbf{x}, \mathbf{x})}{[\text{Tr}\mathbf{W}(\mathbf{x}, \mathbf{x})]^2}\right)^{1/2}, \quad (2)$$

respectively, where Tr is the trace and Det is the determinant. When the optical field given by $\mathbf{W}(\mathbf{x}_1, \mathbf{x}_2)$ traverses a screen with random transmittance described by the Jones matrix $\mathbf{T}(\mathbf{x})$, the transmitted cross-spectral density matrix is calculated with the formula

$$\mathbf{W}'(\mathbf{x}_1, \mathbf{x}_2) = \langle \mathbf{T}^t(\mathbf{x}_1)\mathbf{W}(\mathbf{x}_1, \mathbf{x}_2)\mathbf{T}(\mathbf{x}_2) \rangle, \quad (3)$$

where the dagger denotes Hermitian conjugate and the angle brackets stand for the ensemble average. From Eqs. (1)–(3), one concludes that the degrees of coherence and polarization are modified during the transmission through the random screen. Particularly, if the elements of $\mathbf{T}(\mathbf{x})$ are pure phase terms there are no energy losses in the modulated light.

3. PROPOSED TECHNIQUE

The system for modulating the coherence and polarization of the electromagnetic field is shown in Fig. 1. In the setup, the orthogonal field components of the primary source are separated by the polarizing beam splitter PBS1 and modulated by the 90°-twist LC-SLM placed in each arm of a Mach-Zehnder interferometer. Afterwards, the modulated field components are joined by the polarizing beam splitter PBS2 forming the secondary source.

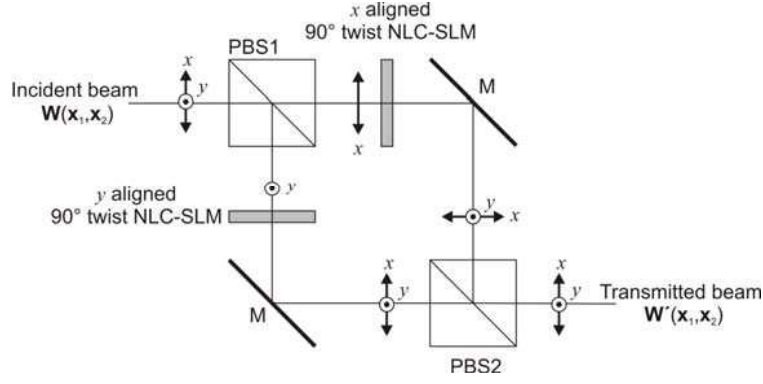


Figure 1: Technique for generating the partially coherent and partially polarized source: PBS1, PBS2, polarizing beam splitters; M, mirror. The bold-faced arrows denote polarization directions.

The arrangement of Fig. 1 fulfills the conditions established by Lu and Saleh [5] and thus each 90°-twist LC-SLM performs pure phase modulation of the incident field. Disregarding negligible changes due to transmission in free space, the system of Fig. 1 is described by the Jones matrix

$$\mathbf{T}(\mathbf{x}) = \exp(-i\varphi_0) \begin{pmatrix} 0 & \exp[-i\varphi_2(\mathbf{x})] \\ \exp[-i\varphi_1(\mathbf{x})] & 0 \end{pmatrix}, \quad (4)$$

where φ_0 is a constant and $\varphi_{1(2)}(\mathbf{x})$ are zero mean random variables having Gaussian probability density

$$p[\varphi_{1(2)}(\mathbf{x})] = \frac{1}{\sqrt{2\pi}\sigma_\varphi} \exp\left[-\frac{\varphi_{1(2)}^2(\mathbf{x})}{2\sigma_\varphi^2}\right], \quad (5)$$

with variance $\langle\varphi^2(\mathbf{x})\rangle = \sigma_\varphi^2$ and cross correlation defined at two different points

$$\langle\varphi_{1(2)}(\mathbf{x}_1)\varphi_{1(2)}(\mathbf{x}_2)\rangle = \sigma_\varphi^2 \exp\left[-\frac{\xi^2}{2\alpha_\varphi^2}\right], \quad (6)$$

where $\xi = |\mathbf{x}_1 - \mathbf{x}_2|$ and α_φ is a positive constant related to the correlation width of $\varphi(\mathbf{x})$.

As the incident field it is chosen a linearly polarized Gaussian beam characterized by the cross spectral density matrix

$$\mathbf{W}(\mathbf{x}_1, \mathbf{x}_2) = E_0^2 \exp\left(-\frac{\mathbf{x}_1^2 + \mathbf{x}_2^2}{4\varepsilon^2}\right) \begin{pmatrix} \cos^2\theta & \cos\theta\sin\theta \\ \cos\theta\sin\theta & \sin^2\theta \end{pmatrix}, \quad (7)$$

where E_0 is the value of power spectrum at the origin of the source plane, ε is the effective (rms) size of the source, and θ is the direction of polarization with respect to x axis. As seen from Eqs. (1) and (2), the beam described in Eq. (7) is completely coherent, $\mu(\mathbf{x}_1, \mathbf{x}_2) = 1$ and completely polarized, $P(\mathbf{x}) = 1$, respectively. On substituting Eqs. (4) and (7) into Eq. (3), one finds that the modulated secondary source has the cross spectral density matrix

$$\mathbf{W}'(\mathbf{x}_1, \mathbf{x}_2) = E_0^2 \exp\left(-\frac{\mathbf{x}_1^2 + \mathbf{x}_2^2}{4\varepsilon^2}\right) \begin{pmatrix} \sin^2\theta \langle\exp\{-i[\varphi_1(\mathbf{x}_2) - \varphi_1(\mathbf{x}_1)]\}\rangle & \cos\theta\sin\theta \langle\exp\{-i[\varphi_2(\mathbf{x}_2) - \varphi_1(\mathbf{x}_1)]\}\rangle \\ \cos\theta\sin\theta \langle\exp\{-i[\varphi_1(\mathbf{x}_2) - \varphi_2(\mathbf{x}_1)]\}\rangle & \cos^2\theta \langle\exp\{-i[\varphi_2(\mathbf{x}_2) - \varphi_2(\mathbf{x}_1)]\}\rangle \end{pmatrix}. \quad (8)$$

Based on the properties of function $\varphi(\mathbf{x})$ it can be shown [3] that

$$\langle\exp\{i[\varphi_{1(2)}(\mathbf{x}_2) \pm \varphi_{2(1)}(\mathbf{x}_1)]\}\rangle = \exp(-\sigma_\varphi^2), \quad (9)$$

$$\langle\exp\{+i[\varphi(\mathbf{x}_2) \pm \varphi(\mathbf{x}_1)]\}\rangle = \langle\exp\{-i[\varphi(\mathbf{x}_2) \pm \varphi(\mathbf{x}_1)]\}\rangle = \exp\left\{-\sigma_\varphi^2 \left[1 \pm \exp\left(\frac{\xi^2}{2\alpha_\varphi^2}\right)\right]\right\}. \quad (10)$$

In addition, to simplify the subsequent analysis, we assume that variance σ_φ of the control signal is large enough to accept the following approximations [1]

$$\exp(-\sigma_\varphi^2) \approx 0, \quad (11)$$

$$\exp\left\{-\sigma_\varphi^2\left[1 - \exp\left(\frac{\xi^2}{2\alpha_\varphi^2}\right)\right]\right\} \approx \exp\left(-\frac{\xi^2}{2\eta_\varphi^2}\right), \quad (12)$$

where $\eta_\varphi = \alpha_\varphi/\sigma_\varphi$. Finally, the transmitted cross spectral density matrix given by Eq. (8) has the form

$$\mathbf{W}'(\mathbf{x}_1, \mathbf{x}_2) = E_0^2 \exp\left(-\frac{\mathbf{x}_1^2 + \mathbf{x}_2^2}{4\varepsilon^2}\right) \exp\left(-\frac{\xi^2}{2\eta_\varphi^2}\right) \begin{pmatrix} \sin^2\theta & 0 \\ 0 & \cos^2\theta \end{pmatrix}, \quad (13)$$

and, using Eqs. (1) and (2), it is found that

$$\mu'(\xi) = \exp\left(-\frac{\xi^2}{2\eta_\varphi^2}\right), \quad (14)$$

$$P'(\mathbf{x}) = |\cos 2\theta|. \quad (15)$$

As can be seen from Eq. (15), the output degree of polarization depends only on the angle of input polarization and varies from 0 to 1. Meanwhile, for a fixed angle θ of the primary source, the degree of coherence (14) is controlled with the proper choice of the computational variable η_φ of the modulation signal $\varphi(\mathbf{x})$.

4. EXPERIMENTS AND RESULTS

The arrangement for generating and characterizing the secondary source is shown in Fig. 2. In the experimental setup, the second Mach-Zehnder interferometer with the translating pinholes reproduces the Young experiment [6] used for measuring the elements of matrix $\mathbf{W}(\mathbf{x}_1, \mathbf{x}_2)$. In our case, the elements of matrix (13) are determined through the interference of x and y components of the modulated beam selected by polarizers P_1 and P_2 . Finally, observing the visibility of the fringes at the exit of the beam splitter BS, the elements of the cross spectral density matrix are determined and substituted in Eqs. (1) and (2).

As the primary source it was used a linearly polarized He-Ne laser (Spectra-Physics model 117A, $\lambda = 633$ nm, 4.5 mW) whose polarization angle θ was controlled by means of a rotary stage. As the 90°-twist LC-SLM we used the Holoeye LC2002 model with resolution of 800×600 pixels ($32 \mu\text{m}$ square in size) and 256 grey level signal display. The control of the LC-SLMs was realized independently by two computers generating the random signals with the required Gaussian statistics.

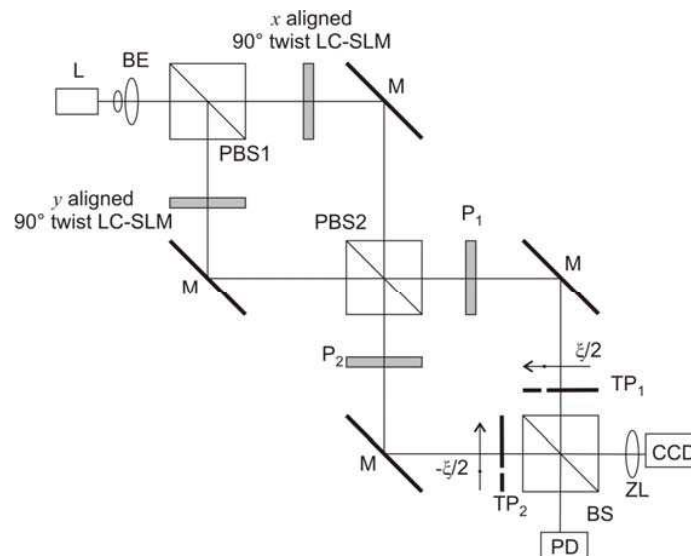


Figure 2: Experimental setup: L, laser; BE, beam expander; ZL, zoom-lens; PD, photodiode; BS, beam splitter; TP, translating pinhole; P_1 , P_2 , polarizers. Other notations are the same as in Fig. 1.

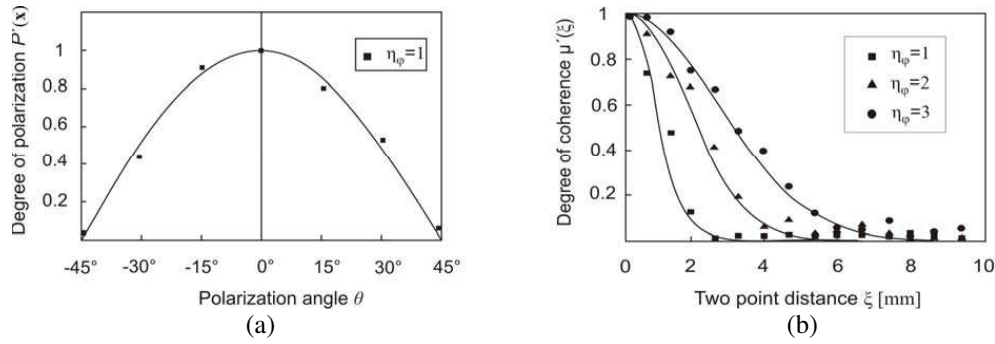


Figure 3: (a) Measurements of polarization degree for $\eta_\varphi \approx 1$. (b) Measurements of the degree of coherence for $\theta = \pi/4$ and different values of parameter η_φ .

We realized two sets of experiments. In the first one the degree of polarization was determined for different values of the input polarization angle θ , the position $\xi = 0$ and the value $\eta_\varphi \approx 1$ of the control signal. In the second experiment we measured the degree of coherence for $\theta = \pi/4$ and different positions ξ of pinholes, varying parameter η_φ of the control signal. To realize the measurements of the degree of coherence we used two pinholes with diameter of $200 \mu\text{m}$ mounted on motorized translation stages. The experimental curves of the degree of coherence and the degree of polarization are shown in Fig. 3. During the measurements it was noticed that LC2002 specimen was not able to provide pure phase modulation in contraposition to model of Eq. (4). However, it was observed that this situation did not affect appreciably the theoretical predictions.

5. CONCLUSIONS

In this work, a novel method for modulating the degree of coherence and the degree of polarization of an electromagnetic beam using widely available 90° -twist LC-SLMs was presented. In the case of a linearly polarized Gaussian beam, the obtained degree of polarization depended solely on the angle of input polarization, while the output degree of coherence was controlled with the proper choice of the computational variable η_φ of the control signal $\varphi(\mathbf{x})$. Although the 90° -twist LC-SLM LC2002 did not provide pure phase modulation, the expected coherence and polarization curves were not affected significantly. In future tests, we can improve this situation changing the wavelength of the source or using another LC-SLM; nevertheless, the LC2002 Holoeye device achieved coherence modulation in the range from 0 to 1.

ACKNOWLEDGMENT

This work has been supported by the National Council for Science and Technology of Mexico under project 165142 and by the Autonomous University of Puebla under project OSA-EXC12-G.

REFERENCES

1. Shirai, T. and E. Wolf, "Coherence and polarization of electromagnetic beams modulated by random phase screens and their changes on propagation in free space," *J. Opt. Soc. Am. A*, Vol. 21, No. 10, 1907–1916, 2004.
2. Shirai, T., O. Korotkova, and E. Wolf, "A method of generating electromagnetic Gaussian Schell-model beams," *J. Opt. A: Pure Appl. Opt.*, Vol. 7, No. 5, 232–237, 2005.
3. Ostrovsky, A. S., G. Martínez-Nikonoff, V. Arrizón, P. Martínez-Vara, M. A. Olvera-Santamaría, and C. Rickenstorff-Parrao, "Modulation of coherence and polarization using liquid crystal spatial light modulators," *Opt. Express*, Vol. 17, No. 7, 5257–5264, 2009.
4. www.hamamatsu.com.
5. Lu, K. and B. E. A. Saleh, "Theory and design of the liquid crystal TV as an optical spatial phase modulator," *Opt. Eng.*, Vol. 29, No. 3, 240–246, 1990.
6. Ostrovsky, A. S., G. Rodríguez-Zurita, C. Meneses-Fabián, M. A. Olvera-Santamaría, and C. Rickenstorff-Parrao, "Experimental generating the partially coherent and partially polarized electromagnetic source," *Opt. Express*, Vol. 18, No. 12, 12864–12871, 2010.

Simple Technique for Generating a Secondary Electromagnetic Source with Desired Degrees of Coherence and Polarization

M. A. Olvera and A. S. Ostrovsky

Facultad de Ciencias Físico Matemáticas

Benemérita Universidad Autónoma de Puebla, Puebla 72000, México

Abstract— We propose and analyze a rather simple technique for generating a secondary electromagnetic source with desired degrees of coherence and polarization. Starting from a completely coherent and completely polarized electromagnetic source, two coupled Mach-Zehnder interferometers are used for the experimental synthesis and characterization of the electromagnetic partially coherent and partially polarized source. Due to the last and wide-scale availability of the required optical components we have succeeded in the physical realization and characterization of the proposed technique and have demonstrated its efficiency in physical experiments. The experimental results are in good agreement with theoretical predictions.

1. INTRODUCTION

In the last decade great attention has been given to the development of the unified theory of coherence and polarization. Many recent investigations have been devoted toward the problem of generating the partially coherent and partially polarized electromagnetic source [1]. One of the central problems in this theory is the capability of simultaneous control the statistical properties of an electromagnetic field. Very important advances have been reported specially in connection with the use of spatial light modulators (SLM) [2–4]. In the present paper, we propose a very simple technique for modulating the coherence and polarization of laser radiation which does not need any LC SLM. This technique bears some resemblance with the one reported in [5], but differs from it as by another action principle so by the simplicity.

In practice, together with theoretical results, experimental investigations are essential in the electromagnetic coherence theory. So, once the desired secondary partially coherent and partially polarized source has been created, it must be subject to experimental characterization. The idea of such a determination is well known [6–8], but its physical realization has not been yet reported. Here we propose also a rather simple technique for characterizing the coherence of electromagnetic source, which was used in our experiments.

2. BACKGROUND

As has been shown by Wolf [8], the second-order statistical properties of a random planar (primary or secondary) electromagnetic source can be completely described by the cross-spectral density matrix (for brevity we omit the explicit dependence of the considered quantities on frequency ν)

$$\mathbf{W}(\mathbf{x}_1, \mathbf{x}_2) = \begin{bmatrix} \langle E_x^*(\mathbf{x}_1)E_x(\mathbf{x}_2) \rangle & \langle E_x^*(\mathbf{x}_1)E_y(\mathbf{x}_2) \rangle \\ \langle E_y^*(\mathbf{x}_1)E_x(\mathbf{x}_2) \rangle & \langle E_y^*(\mathbf{x}_1)E_y(\mathbf{x}_2) \rangle \end{bmatrix}, \quad (1)$$

where $E_x(\mathbf{x})$ and $E_y(\mathbf{x})$ are the orthogonal components of the electric field vector $\mathbf{E}(\mathbf{x})$, asterisk denotes the complex conjugate, and the angle brackets denote the average over the statistical ensemble. Using this matrix, Wolf defines the following three fundamental statistical characteristics of the source: the power spectrum

$$S(\mathbf{x}) = \text{Tr}\mathbf{W}(\mathbf{x}, \mathbf{x}), \quad (2)$$

the spectral degree of coherence

$$\mu(\mathbf{x}_1, \mathbf{x}_2) = \frac{\text{Tr}\mathbf{W}(\mathbf{x}_1, \mathbf{x}_2)}{[\text{Tr}\mathbf{W}(\mathbf{x}_1, \mathbf{x}_1)\text{Tr}\mathbf{W}(\mathbf{x}_2, \mathbf{x}_2)]^{1/2}}, \quad (3)$$

and the spectral degree of polarization

$$P(\mathbf{x}) = \left[1 - \frac{4\text{Det}\mathbf{W}(\mathbf{x}, \mathbf{x})}{[\text{Tr}\mathbf{W}(\mathbf{x}, \mathbf{x})]^2} \right]^{1/2}. \quad (4)$$

In Equations (2)–(4) Tr stands for the trace and Det denotes the determinant.

It is not out of place to mention here that, equally with Wolf's definition of the degree of coherence, there are known the other definitions [9–11]. But, for our following analysis, the definition given by Equation (3) proves to be quite sufficient.

3. GENERATING AND CHARACTERIZING THE SECONDARY SOURCE

As the primary source the laser radiation, linearly polarized in some plane normal to the direction of propagation, is employed. The source correlations can be characterized by the cross-spectral density matrix

$$\mathbf{W}_{\text{PS}}(\mathbf{x}_1, \mathbf{x}_2) = S_0 \exp\left(-\frac{\mathbf{x}_1^2 + \mathbf{x}_2^2}{4\varepsilon^2}\right) \begin{bmatrix} \cos^2 \theta & \sin \theta \cos \theta \\ \sin \theta \cos \theta & \sin^2 \theta \end{bmatrix}, \quad (5)$$

where S_0 is the value of power spectrum at the source centre, ε is the effective (rms) size of the source, and θ is the angle that the direction of the linear polarized electric field makes with the x axis. It can be shown that in this case that such a source is completely coherent and completely polarized.

We can make use of a Mach-Zehnder interferometer starting with a polarizing beam splitter PBS that separates the orthogonal field components $E_x(\mathbf{x})$ and $E_y(\mathbf{x})$ so that each of them can be independently changed by means of two rotating ground glass plates GGP₁ and GGP₂ [12]. At the exit of the interferometer is placed a 50/50 beam splitter cube which is used for coupling the next Mach-Zehnder interferometer as is shown in Fig. 1.

The considered system can be seen as a thin phase screen with an amplitude transmittance given by

$$\mathbf{T}(\mathbf{x}) = \begin{bmatrix} \exp[i\varphi_1(\mathbf{x})] & 0 \\ 0 & \exp[i\varphi_2(\mathbf{x})] \end{bmatrix}, \quad (6)$$

where $\varphi_1(\mathbf{x})$ and $\varphi_2(\mathbf{x})$ are the position-dependent Gaussian-correlated random variables characterized by parameters γ and σ [2] for two different points \mathbf{x}_1 and \mathbf{x}_2 separated by a distance ξ .

The cross-spectral density matrix of the secondary source (SS) created just behind the interferometer can be calculated as

$$\mathbf{W}_{\text{SS}}(\mathbf{x}_1, \mathbf{x}_2) = \left\langle \mathbf{T}^\dagger(\mathbf{x}_1) \mathbf{W}_{\text{PS}}(\mathbf{x}_1, \mathbf{x}_2) \mathbf{T}(\mathbf{x}_2) \right\rangle, \quad (7)$$

where the dagger denotes the Hermitian conjugation. On substituting from Equations (5) and (6)

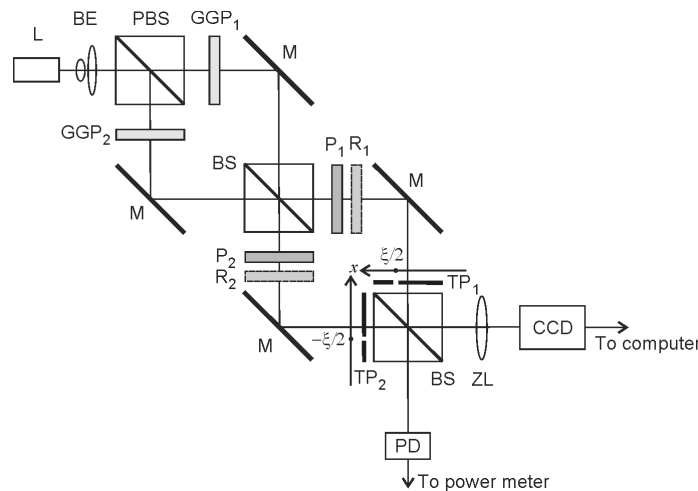


Figure 1: Schematic illustration of the technique for generating and characterizing the partially coherent and partially polarized source: L, laser; BE, beam expander; ZL, zoom-lens; PD, photodiode; BS, beam splitter; PBS, polarizing beam splitter; M, mirror; GGP₁, GGP₂, rotating ground glass plates; TP, translating pinhole; P₁, P₂, polarizers; R₁, R₂; polarization rotators.

into Equation (7), we find

$$\mathbf{W}_{SS}(\mathbf{x}_1, \mathbf{x}_2) = S_0 \exp\left(-\frac{\mathbf{x}_1^2 - \mathbf{x}_2^2}{4\varepsilon^2}\right) \times \begin{bmatrix} \exp\left\{-\sigma^2\left[1 - \exp\left(-\frac{\xi^2}{2\gamma^2}\right)\right]\right\} \cos^2\theta & \exp[-\sigma^2] \sin\theta \cos\theta \\ \exp[-\sigma^2] \sin\theta \cos\theta & \exp\left\{-\sigma^2\left[1 - \exp\left(-\frac{\xi^2}{2\gamma^2}\right)\right]\right\} \sin^2\theta \end{bmatrix} \quad (8)$$

Then, substituting this result into definitions given by Equations (3) and (4), we obtain, respectively,

$$\mu_{SS}(\mathbf{x}_1, \mathbf{x}_2) = \exp\left\{-\sigma^2\left[1 - \exp\left(-\frac{\xi^2}{2\gamma^2}\right)\right]\right\}, \quad (9)$$

$$P_{SS}(\mathbf{x}) = |1 - 2 \cos^2\theta|. \quad (10)$$

Equations (9)–(10) show that the generated source is partially coherent and partially polarized. As can be seen the degree of coherence and polarization changes in the full range from 1 to 0. To determine experimentally the elements W_{ij}^{SS} of the matrix \mathbf{W}_{SS} the Mach-Zehnder interferometer is employed. The polarizers P_1 and P_2 serve to cut off only one of the orthogonal field components. The removable rotators R_1 and R_2 serve to produce the rotation of one of the transmitted field component through 90° . For such a purpose a suitably oriented half-wave birefringent plate can be used. The power spectrum of the field observed at the output of the interference system in each experiment can be described by the spectral interference law [8]

$$S_{ij}(x') = S_i^{SS}\left(\frac{\xi}{2}\right) + S_j^{SS}\left(\frac{\xi}{2}\right) + 2 \left| W_{ii}^{SS}\left(\frac{\xi}{2}, -\frac{\xi}{2}\right) \right| \cos\left[\frac{k\xi}{z_0}x' + \alpha_{ij}\left(\frac{\xi}{2}, -\frac{\xi}{2}\right)\right] \quad (i, j = x, y), \quad (11)$$

where $S_{i,j}^{SS}$ are the power spectra of the field components in the pinhole position $\xi/2$, k is the wave number, z_0 is the geometrical path between the pinhole plane and the observation plane, and $\alpha_{ij} = \arg W_{ij}^{SS}$. As well known, the measure of the contrast of the interference fringes is the so-called visibility coefficient defined as

$$V_{ij}(\xi) = \frac{[S_{ij}(x')]_{\max} - [S_{ij}(x')]_{\min}}{[S_{ij}(x')]_{\max} + [S_{ij}(x')]_{\min}}. \quad (12)$$

On substituting from Equation (10) with $\cos(\cdot) = \pm 1$ into Eq. (12), we find that

$$|W_{ij}^{SS}(\xi)| = \frac{1}{2} \left[S_i^{SS}\left(\frac{\xi}{2}\right) + S_j^{SS}\left(\frac{\xi}{2}\right) \right] V_{ij}(\xi). \quad (13)$$

The spectra S_i^{SS} and S_j^{SS} can be measured when one of the pinholes is covered by an opaque screen and the degree of coherence and the degree of polarization of the generated source can be then calculated using definitions given by Equations (3) and (4).

4. EXPERIMENTS AND RESULTS

In the experimental setup as the primary source we used the He-Ne laser, so that the direction of its (linear) polarization made tilt of 45° with respect to the laboratory axes. To generate the secondary source with two different values of the transversal length of coherence, we used two pairs of ground glass plates with the diffusion angles of 10° and 30° . The interference pattern at the first output of the second interferometer was registered by the CCD camera and the corresponding power spectra were measured by the photodiode with optical power meter located at the second output. The results of the experiments for different pairs of ground glass plates are plotted in Fig. 2 together with their theoretical interpolations in accordance with Equation (8). As can be seen from Equation (10) the degree of polarization P depends only on the angle θ so that modulation is accomplished by rotating the plane of polarization of the primary source, i.e., by rotating the laser itself. By setting $\theta = \pi/4$ the calculated spectral degree of polarization was about zero for both experiments. As can be seen, the obtained experimental results are in a good correspondence with the theoretical predictions.

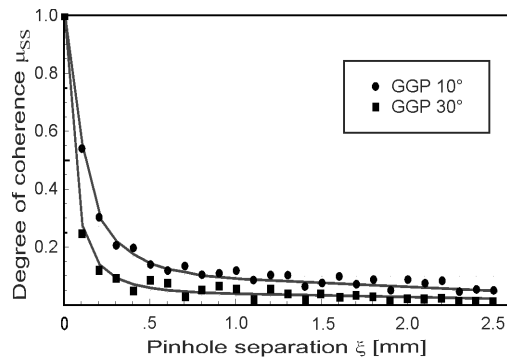


Figure 2: Experimental results for different pairs of GGP in dotted lines and its teoretical interpolations in solid lines.

5. CONCLUSIONS

We have proposed a rather simple technique for generating the partially coherent and partially polarized electromagnetic source using two rotating ground glass plates placed at the opposite arms of a Mach-Zehnder interferometer. The efficiency of the proposed technique has been confirmed with the physical experiment. We would like to stress particularly that such a source represents a special case of the well known Gaussian Schell-model uniformly polarized electromagnetic source, which appears here not as some handy mathematical construction but as a true product of physical experiment. The proposed techniques make possible a simultaneous synthesis and characterization procedure of physically realizable partially coherent and partially polarized electromagnetic fields.

ACKNOWLEDGMENT

The authors gratefully acknowledge the financial support from the Autonomous University of Puebla under project OSA-EXT-12-G.

REFERENCES

- Ostrovsky, A. S., P. Martínez, M. Á. Olvera, and G. Martínez, "Vector coherence theory: An overview of basic concepts and definitions," *Recent Research Developments in Optics*, S. G. Pandalai, Ed., Chapter 5, 113–142, Research Signpost, Kerala, 2009.
- Shirai, T. and E. Wolf, "Coherence and polarization of electromagnetic beams modulated by random phase screen and their changes on propagation in free space," *J. Opt. Soc. Am. A*, Vol. 21, No. 1, 1907–1916, 2004.
- Shirai, T., O. Korotkova, and E. Wolf, "A method of generating electromagnetic Gaussian Schell-model beams," *J. Opt. A: Pure Appl. Opt.*, Vol. 7, 232–237, 2005.
- Ostrovsky, A. S., G. Martínez, V. Arrizón, P. Martínez, M. A. Olvera, and C. Rickenstorff, "Modulation of coherence and polarization using liquid crystal spatial light modulators," *Opt. Express*, Vol. 17, 5257–5264, 2009.
- Piquero, G., F. Gori, P. Romanini, M. Satarsiero, R. Borghi, and A. Mondello, "Synthesis of partially polarized Gaussian Schell-model sources," *Opt. Commun.*, Vol. 208, 9–16, 2002.
- Gori, F., "Matrix treatment for partially polarized, partially coherent beams," *Opt. Lett.*, Vol. 23, 241–243, 1998.
- Wolf, E., *Introduction to the Theory of Coherence and Polarization of Light*, Cambridge University Press, Cambridge, 2007.
- Wolf, E., "Unified theory of coherence and polarization of random electromagnetic beams," *Phys. Lett. A*, Vol. 312, 263–267, 2003.
- Tervo, J., T. Setälä, and A. T. Friberg, "Degree of coherence for electromagnetic fields," *Opt. Express*, Vol. 11, 1137–1143, 2003.
- Luis, A., "Degree of coherence for vectorial electromagnetic fields as the distance between correlation matrices," *J. Opt. Soc. Am. A*, Vol. 24, 1063–1068, 2007.
- Réfrégier, P. and F. Goudail, "Invariant degrees of coherence of partially polarized light," *Opt. Express*, Vol. 13, 6051–6060, 2005.
- Shirai, T. and E. Wolf, "Coherence and Polarization of electromagnetic beams modulated by random phase screens and their changes on propagation in free space," *J. Opt. Soc. Am. A*, Vol. 21, 1907–1916, 2004.

Investigation of Electricity Quality in Ship Integrated Power System

N. F. Djagarov, S. Z. Zlatev, M. B. Bonev, and Z. G. Grozdev
Technical University of Varna, Bulgaria

Abstract— The increased requirements for efficiency allows the use of integrated electric power systems in ships. In the paper, is suggested a mathematical model of ship's integrated power system including ship power station 6 kV with three diesel generators, static and dynamic loads on 400 V, ship propulsion system consisting from Azipod with PMSM (Permanent Magnet Synchronous Motor), supplying by frequency converter. The different transient processes in static and dynamic operating mode are simulated also the quality of different point in power system is analyzed.

1. INTRODUCTION

Recently are built more complex and more powerful ship electrical power stations. On modern passenger, naval and cargo ships (floating cranes, dredgers, floating platforms and etc.) majority of electrical consumers are with adjustable electric power drives. Ship's power systems are characterized by commensurability of the power of generators and electric drives. Moreover, the generation and consumption of electricity (excluding additional ships needs) is performed without transformation. All this leads to a strong deterioration of electricity quality which, disturbing work such as electrical drives and other appliances.

For past years has been developing the Ship Integrated Power System (SIPS) to reduce ship acquisition and life cycle cost while still meeting all ship performance requirements. SIPS provide electrical power to ship service loads and electric propulsion for a wide range of ship applications [1]. SIPS consist from architecture and a family of modules from which affordable and high performance configurations can be developed for the full range of ship applications.

On some special ships is used DC power in the distribution of power onboard ships [2]. The decision to use DC instead of the more conventional AC is based on multiple investigations focused on electrical distribution system simplification and propulsion drive. The electrical distribution system simplification results were transitioned into the zonal architecture.

Most of cruise liners use a SIPS AC power. In these SIPS the adoption of the electrical propulsion systems makes it possible to design a unique, integrated electrical power system, which connects the electrical generators to all the consumers. Such new integrated ship's power system brings several advantages. Enhanced dynamics in propeller motion, flexibility of placing weights and designing spaces on board the ship, fuel savings, noise and vibration attenuation, comfort improvements, availability of high power propeller motors and possibility of using podded-drives are only some of the several benefits obtainable from the adoption of the integrated naval electrical system [3].

It is well know that propulsion converters are the main cause of harmonic disturbances injected into the electrical network. Load-side harmonics can impact over machine performance, insulation life and mechanical bearings. Currently, these effects are taken into account by designing the machine considering its feeding converter. On the supply-side instead, harmonic noise can affect sensitive loads, network controls and protections [4]. Sensitive ship loads include radar systems, communication systems, computer controls for navigation and other operative tasks, lighting plants and other services. The effects of harmonics on other nonsensitive equipment and loads (machinery, cables) are well known in literature.

In the article is developed full mathematical model of ship integrated AC electrical power system, with according suggested method [5, 6]. The studied of ship integrated power system is consisting from three diesel generators, electrical ship propulsion system (Azipod), controlled frequency converter, permanent magnet synchronous motor which drives ship propeller (Fig. 1). Furthermore ship's power supply station has step-down transformer supplies additional ships loads (simulated by two equivalent induction drives and static active-inductive load).

With so created a mathematical model were examined various operating and emergency operating modes of the ship's integrated electrical power system. Using the FFT was investigated absorbed electric current of ships propulsion system and the presence of harmonics in voltage at various points in the distribution network.

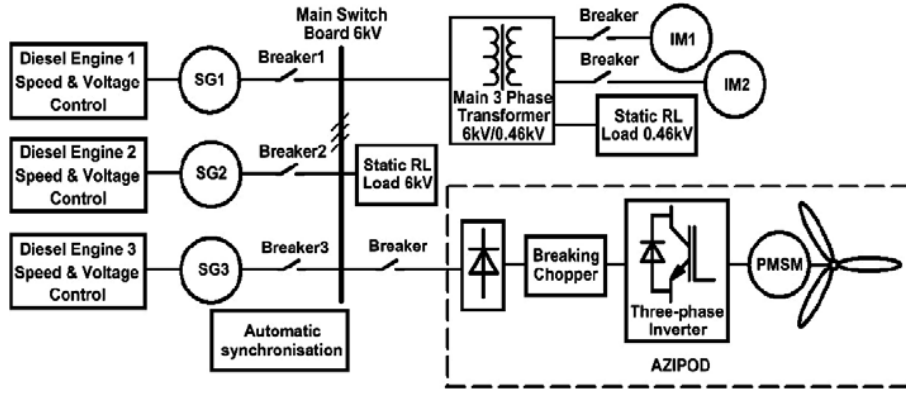


Figure 1: Investigated ship integrated power system.

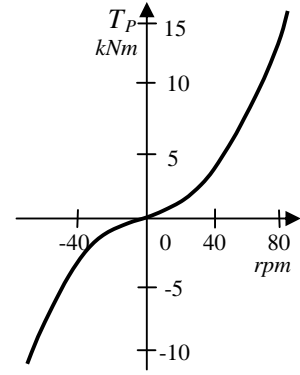


Figure 2: Dependence of propulsion motor torque from its rotor speed.

2. INVESTIGATED SHIP INTEGRATED POWER SYSTEM

On the Fig. 1 is shown diagram of studied ships integrated power system. The system is consist from three diesel-generators with power 3.1 MVA and voltage -6 kV connected to main switch board (MSB). The consumers of 6 kV are static RL load, and ship's propulsion system (Azipod) consisting from frequency converter (rectifier, breaking chopper, inverter) supplying ships propulsion electric motor — permanent magnet synchronous machine. Furthermore ship's power system has consumers on 400 V, supplied from step-down transformer 6 kV/400 V. the loads on 400 V are presented through two induction drives and static active/inductive load.

3. MATHEMATICAL MODEL OF INVESTIGATED SHIP INTEGRATED POWER SYSTEM

For creation of the mathematical model of studier SIPS are used noniterative method, suggested in [5, 6].

3.1. Mathematical Model of Synchronous Generator

$$\frac{d}{dt} \begin{bmatrix} \mathbf{I}_s \\ \mathbf{I}_r \end{bmatrix} = \begin{bmatrix} \mathbf{A}_{ss} & \mathbf{A}_{sr} \\ \mathbf{A}_{rs} & \mathbf{A}_{rr} \end{bmatrix} \cdot \begin{bmatrix} \mathbf{I}_s \\ \mathbf{I}_r \end{bmatrix} + \begin{bmatrix} \mathbf{B}_{ss} & \mathbf{B}_{sr} \\ \mathbf{B}_{rs} & \mathbf{B}_{rr} \end{bmatrix} \cdot \begin{bmatrix} \mathbf{U}_{MSB} \\ u_f \end{bmatrix} = \begin{bmatrix} \mathbf{H}_s \\ \mathbf{H}_r \end{bmatrix} + \begin{bmatrix} \mathbf{B}_{ss} & \mathbf{B}_{sr} \\ \mathbf{B}_{rs} & \mathbf{B}_{rr} \end{bmatrix} \cdot \begin{bmatrix} \mathbf{U}_{MSB} \\ u_f \end{bmatrix}; \quad (1)$$

$$\frac{d}{dt} \omega_k = \frac{1}{\tau_m} (T_{pm} + T_e);$$

where: through subscribes s and r note stator and rotor variables and parameters respectively; \mathbf{A} and \mathbf{B} are parameter-depended matrices; $\mathbf{I}_s = [i_d, i_q]^t$; $\mathbf{I}_r = [i_f, i_g, i_h]^t$; τ_m is the rotor mechanical time constant; T_{pm} is the prime mover torque (diesel-generator); $T_e = x_{ad} \cdot (i_d + i_f + i_g) \cdot i_q - x_{aq} \cdot (i_q + i_h) \cdot i_d$ is the electromagnetic torque; $\mathbf{U}_{MSB} = [u_d, u_q]^t$ — main switch board voltage.

3.2. Mathematical Model of Permanent Magnet Synchronous Motor

For simulation of processes in synchronous motor is used full mathematical model in axes d , q , 0 rotating with its rotor writing in Cauchy form:

$$\frac{d}{dt} \begin{bmatrix} i_d \\ i_q \end{bmatrix} = \begin{bmatrix} a_{11} & a_{12} \\ a_{21} & a_{22} \end{bmatrix} \cdot \begin{bmatrix} i_d \\ i_q \end{bmatrix} + \begin{bmatrix} b_{11} & 0 \\ 0 & b_{22} \end{bmatrix} \cdot \begin{bmatrix} u_d \\ u_q \end{bmatrix} = \mathbf{H}_M + \mathbf{B}_M \cdot \mathbf{U}_{MSB}; \quad (2)$$

$$\frac{d}{dt} \omega_r = \frac{1}{\tau_M} (T_m - T_P);$$

where: $a_{11} = r/l_d$; $a_{12} = l_q \cdot \omega_r/l_d$; $a_{21} = l_d \cdot \omega_r/l_q$; $a_{22} = r/l_q$; $b_{11} = 1/l_d$; $b_{22} = 1/l_q$; l_d , l_q — inductivity in direct and quadrature axes; r — resistance of stator winding; ω_r — angular rotor speed; τ_m is the rotor mechanical time constant; $T_m = i_q \cdot [\psi + (l_d - l_q) \cdot i_d]$ — electromagnetic torque of motor; T_P — mechanical torque of load (ship's propeller); ψ — amplitude of the flux induced by the rotor permanent magnets in the stator windings.

3.3. Mathematical Model of Induction Motor

$$\frac{d}{dt} \begin{bmatrix} \mathbf{I}_s \\ \mathbf{I}_r \end{bmatrix} = \begin{bmatrix} \mathbf{A}_{ss} & \mathbf{A}_{sr} \\ \mathbf{A}_{rs} & \mathbf{A}_{rr} \end{bmatrix} \cdot \begin{bmatrix} \mathbf{I}_s \\ \mathbf{I}_r \end{bmatrix} + \begin{bmatrix} \mathbf{B}_s \\ \mathbf{B}_r \end{bmatrix} \cdot \mathbf{U}_s = \begin{bmatrix} \mathbf{H}_s \\ \mathbf{H}_r \end{bmatrix} + \begin{bmatrix} \mathbf{B}_s \\ \mathbf{B}_r \end{bmatrix} \cdot \mathbf{U}_{MSB}; \quad (3)$$

$$\frac{d}{dt} \omega_r = \frac{1}{\tau_m} (T_e - T_l);$$

where: \mathbf{A} and \mathbf{B} are parameter-depended matrices; through subscribes s and r note stator and rotor variables and parameters respectively; $T_e = x_{ad} \cdot (i_{rd} \cdot i_q - i_{rq} \cdot i_d)$ is the electromagnetic torque; T_l is the load torque; τ_m is the rotor mechanical time constant.

3.4. Mathematical Model of Static R-L Load

$$\frac{d}{dt} \mathbf{I} = \mathbf{A} \cdot \mathbf{I} + \mathbf{B} \cdot \mathbf{U} = \mathbf{H} + \mathbf{B} \cdot \mathbf{U}; \quad (4)$$

where: \mathbf{A} and \mathbf{B} are load parameter-depended matrices.

Assuming that the resistances of the cable lines and transformers are included in the parameters of the elements of power system. Then the voltage of the main switch-boards will be calculated using Kirchkhoff's first law in differential form:

$$m_{SG1} \frac{d}{dt} I_{sSG1} + m_{SG2} \frac{d}{dt} I_{sSG2} + m_{SG3} \frac{d}{dt} I_{sSG3} + m_{Az} \frac{d}{dt} I_{Az} + m_{IM1} \frac{d}{dt} I_{sIM1} + m_{IM2} \frac{d}{dt} I_{sIM2} + m_{RL} \frac{d}{dt} I_{RL} = 0 \quad (5)$$

where: $m_j = S_j/S_{SG}$ — scale factor (relation of power of elements and power of generation power).

After replacing the derivatives by right part of (1), (3), (4), (5) we obtain algebraic equations for calculating the voltage of MSB

$$U_{MSB} = - \frac{m_{SG1} \cdot H_{sSG1} + m_{SG2} \cdot H_{sSG2} + m_{SG3} \cdot H_{sSG3} + m_{Az} \cdot H_{Az} + m_{IM1} \cdot H_{sIM1} + m_{IM2} \cdot H_{sIM2} + m_{RL} \cdot H_{RL}}{m_{SG1} \cdot B_{sSG1} + m_{SG2} \cdot B_{sSG2} + m_{SG3} \cdot B_{sSG3} + m_{Az} \cdot B_{Az} + m_{IM1} \cdot B_{sIM1} + m_{IM2} \cdot B_{sIM2} + m_{RL} \cdot B_{RL}}. \quad (6)$$

In this way is obtains noniterative method for calculation of processes in SIPS.

For speed and voltage regulators is used mathematical model which are suggested in [7]. On the Fig. 2 is shown the dependence of propulsion motor torque from its rotating rotor speed.

3.5. Study of Processes in Ship Integrated Power System

With so created a mathematical model of the studied system various normal and emergency modes were simulated: synchronization of diesel generators, connection on Azipod and alternation of its mechanical torque, variation of reference and direction of speed; connection/disconnection of loads on 400 V buses, short circuit and its disconnection from the protection device.

By FTT was studied the distortions of consumed current from Azipod and voltage from load side (PMSM) and MSB side. Below is shown part of the experimentally obtained results.

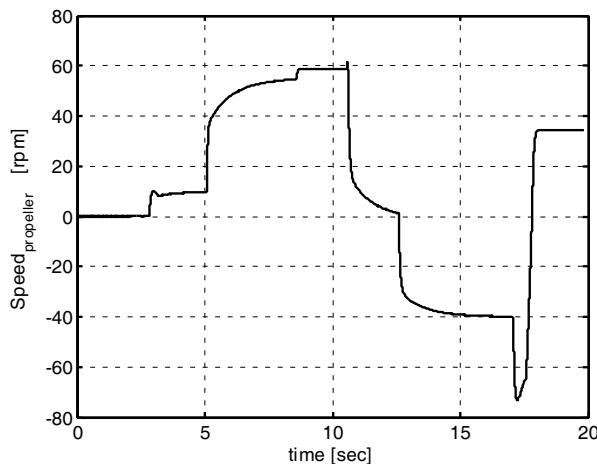


Figure 3: Propeller speed [rpm].

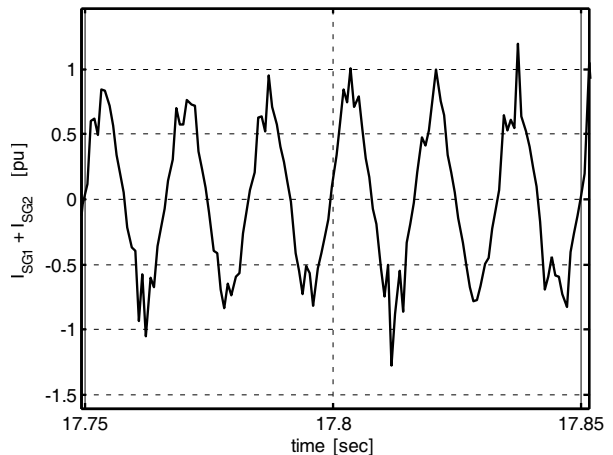


Figure 4: Generator current [pu].

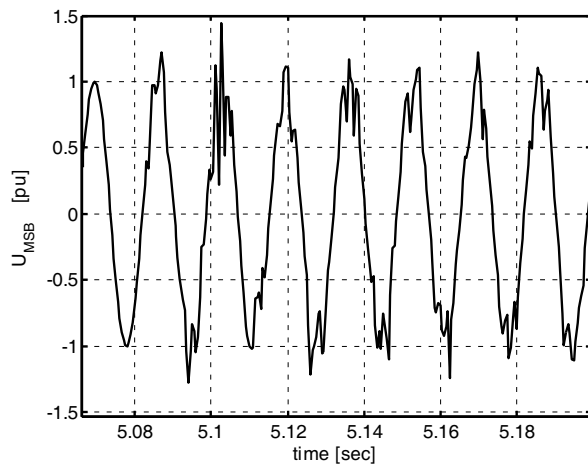


Figure 5: Voltage of MSB.

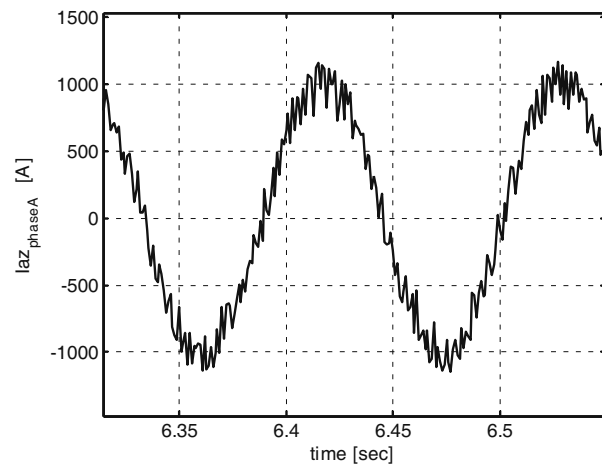


Figure 6: Phase current of PMSM.

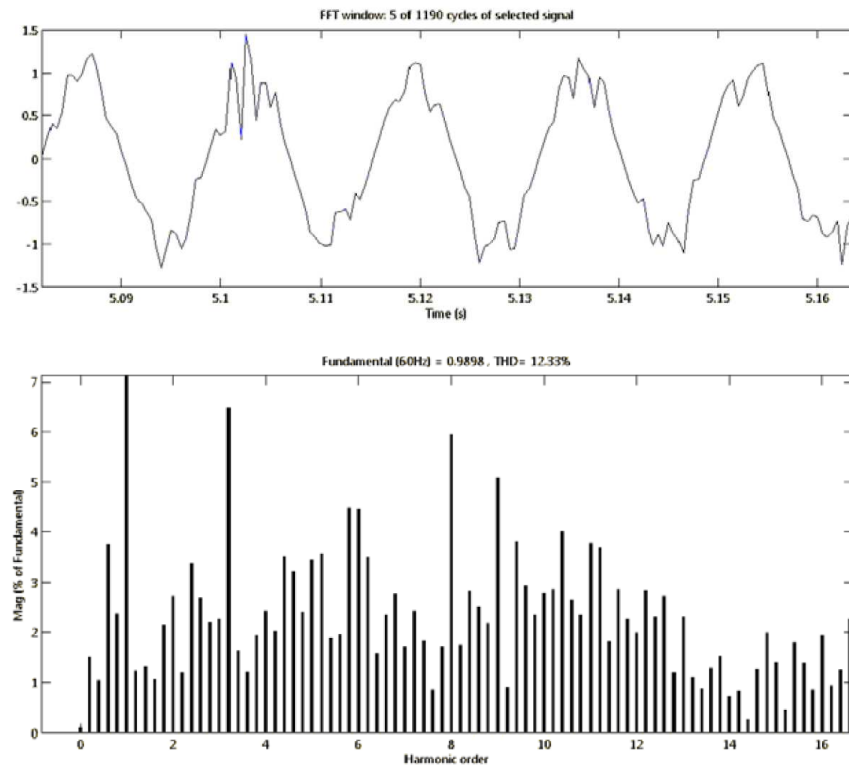


Figure 7: Voltage of main switch board MSB.

4. CONCLUSION

With suggested non iterative mathematical model of ship integrated power system were investigated different static and transient operating working modes at different disturbances. The power quality at different nodes from power system has been studied. The research has shown that appeared voltage harmonics reaches levels which disturbs operation of loads and the control of frequency converter for propeller motor PMSM. It should be provided the proper compensating devices that enhance the quality of electricity and the efficiency of all electrical equipment.

ACKNOWLEDGMENT

This article is published with help of project PD1/614-PD/21.04.2012 of Technical University of Varna.

REFERENCES

1. Doerry, N., H. Robey, J. Amy, and C. Petry, “Powering the future with the integrated power system,” *Naval Engineers Journal*, 267–279, May 1996.
2. Xie, Y., “Modeling, analysis and control of DC hybrid power systems,” 148, Ph.D. Dissertation, The University of Michigan, 2010.
3. Monti, A. and R. A. Dougal, “Integration of multidisciplinary systems into electric ship drives,” *Proceedings of SPEEDAM’04 Symposium*, 391–396, Capri, Italy, Jun. 2004.
4. Castellan, S., R. Menis, and G. Sulligoi, “EMTDC-based simulation of harmonic pollution in all-electric cruise liner: Analytical approach and experimental validation,” *Electrical Engineering Research Report*, No. 20, 78–83, Dec. 2005.
5. Djagarov, N. F., “Transient processes calculation in power system with complex grid topology,” *Electricity*, No. 1, 9–16, Moscow, 1990.
6. Djagarov, N. F., “A method of transient electromechanical processes modeling in power systems,” *2009 IEEE Bucharest Power Tech. Conference*, Bucharest, Romania, Jun. 28–Jul. 2, 2009, E-ISBN: 978-1-4244-2235-7.
7. SimPowerSystems 4 Reference, The MathWorks, Inc., 2007.

The All-optical Logic Gates Based on Mach-Zehnder Interferometer Photonic Crystal Waveguides

Yaw-Dong Wu, Teng-Huei Zou, Jian-Jang Lee, and Tien-Tsorng Shih

Department of Electronic Engineering

National Kaohsiung University of Applied Sciences, Kaohsiung 807, Taiwan, R.O.C.

Abstract— Photonic crystals (PCs) are periodic dielectric structure that has an important characteristic of PCs are photonic bandgap (PBG). Due to the property of PBG that wavelength within the bandgap cannot propagate through the crystal. We use the Mach-Zehnder interferometer (MZI) photonic crystal waveguide to design all-optical logic gates. We consider PCs with a triangular lattice of dielectric rods in the air. First, we compute the bandgap by the plan wave expansion method (PWE), and then we computer optimum coupling length with the finite-difference time-domain method (FDTD). Then we propose two logic gate structures. The state of input port determines the electric field at the output port. Changing one coupling length to $13a$ can cause the destructive interference, so we can use this property to design XOR gate. Changing two coupling length to $17a$ can cause the constructive interference, so we can use this property to design AND gate.

1. INTRODUCTION

Since the discovery by Eli Yablonovitch and Sajeev John [1, 2] in 1987, photonic crystals (PCs) based on optical devices has attracted many research groups attention due to their potential application [3, 4]. PCs are the periodic dielectric structure that can provide the property of photonic band gap (PBG) [5], and there is much kind of devices that have been designed. Due to the property of PBG that light propagation is completely localization in any direction, while the frequency ranges is in PBG. Mach-Zehnder interferometers (MZIs) are one type of interferometers, and there are many approaches to design the MZI structures [6, 7]. One is that changing the coupling length in on arm. Another is that changing the coupling length in two arms. By using these approaches, we can change the phase of the signal in one arm and make the phase of the signal in two arms are the same. In that way, we can get the constructive and destructive interference at the output port. Final, based on the characteristic of the MZIs, we will design a structure which consists of MZIs and two input ports. By changing the states of the two input ports, we can control signals to output port. According to the results, we will realize that the proposed devices could function as XOR and the AND logic gate.

2. ANALYSIS AND SIMULATION

Numerical method of the Finite-Difference Time-Domain (FDTD) [8–10] and the Plane Wave Expansion (PWE) [11–13] were used to design all-optical logic gates base on MZI photonic crystal

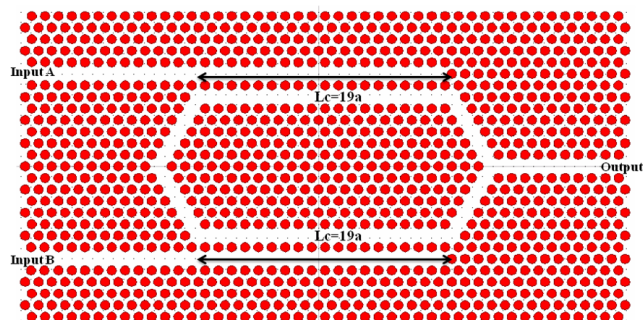


Figure 1: Schematic of Mach-Zehnder interferometer.

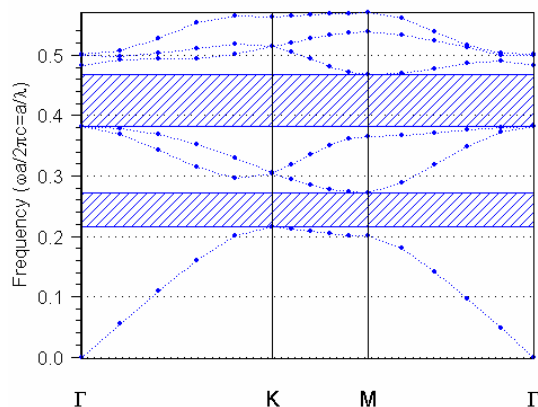


Figure 2: PBG of the Mach-Zehnder interferometer.

waveguides. We consider PC with a triangular lattice of dielectric rods in the air. The dielectric constant of the rods is $\epsilon = 11.56$ ($n = 3.4$) and the radius of the rod is $0.35a$, “ a ” is the lattice constant. First we design a MZI photonic crystal waveguide as show Figure 1. And then we utilized the PWE method to calculate the PBG of this structure as show in Figure 2. The structure consists of two inputs port and one output port. The coupling length of the MZI photonic crystal waveguide is $19a$. By changing the state of two input ports, the electric field at the output will be determined. In this simulation, the incident wave with the wavelength $\lambda = 1.55 \mu\text{m}$.

First we utilized FDTD methods to calculate with different coupling length. In the Figures 3(a), (b) and (c) is changing one coupling length, we show the graph of the normalized transmission efficiency with different coupling length from $5a$ to $19a$ in the structure when the wavelength is $1.55 \mu\text{m}$.

In our simulation result, we could find the best coupling length is $13a$. When the output port is “1”, the output transmission efficiency more than 92% and the feedback is less than 8%. When the output port is “0”, the output transmission efficiency 2%.

For the case 1: When the input port A is “OFF” and the input port B is “ON”, the output port is “ON”, as show in Figure 4(a). For the case 2: When the input port A is “ON” and the input port B is “OFF”, the output port is “ON”, as show in Figure 4(b). For the case 3: When the input port A is “ON” and the input port B is “ON”, the output port is “OFF”, as show in Figure 4(c). The truth table of the proposed XOR gate is shown in Table 1.

Second we utilized FDTD methods to calculate with different coupling length. In the Fig-

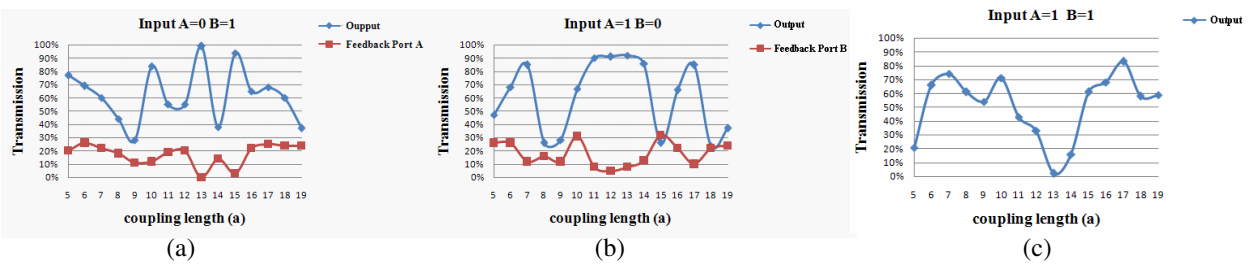


Figure 3: (a), (b), (c) Schematic diagram is changing one coupling length.

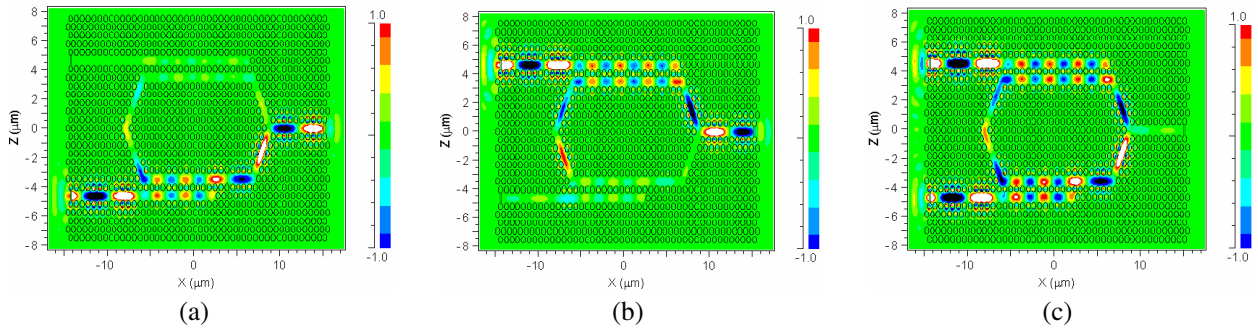


Figure 4: (a), (b), (c) Electric field distributions for XOR logic gate.

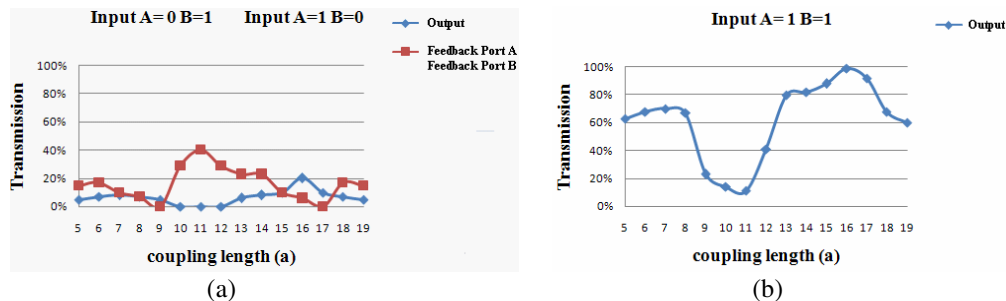


Figure 5: (a), (b) Schematic diagram is changing two coupling length.

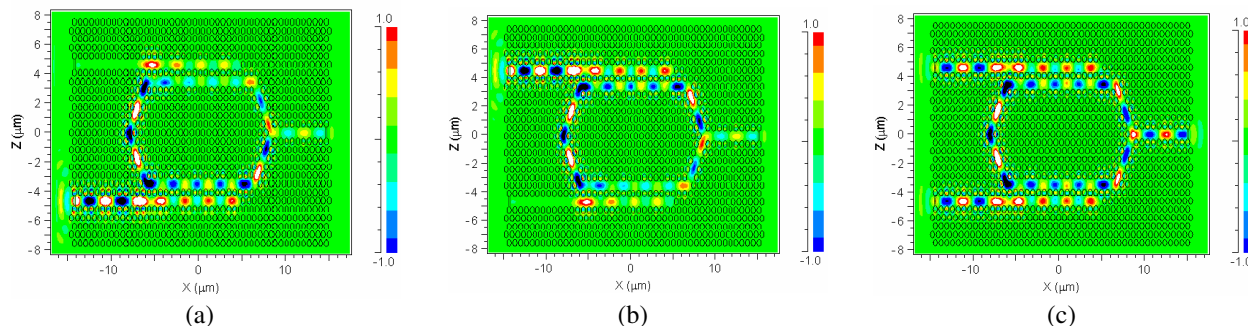


Figure 6: (a), (b), (c) Electric field distributions for AND logic gate.

Table 1: Truth table of the XOR gate and transmission efficiency (%).

Input port A	Input port B	Output	Transmission
0	0	0	0%
0	1	1	99%
1	0	1	92%
1	1	0	2%

Table 2: Truth table of the AND gate and transmission efficiency (%).

Input port A	Input port B	Output	Transmission
0	0	0	0%
0	1	0	10%
1	0	0	10%
1	1	1	92%

ures 5(a), (b) is changing two coupling length, we show the graph of the normalized transmission efficiency with different coupling length from $5a$ to $19a$ in the structure when the wavelength is $1.55 \mu\text{m}$.

In our simulation result, we could find the best coupling length is $17a$. When the output port is “1”, the output transmission efficiency 92%. When the output port is “0”, the output transmission efficiency 10% and feedback 0%.

For the case 1: When the input port A is “OFF” and the input port B is “ON”, the output port is “OFF”, as show in Figure 6(a). For the case 2: When the input port A is “ON” and the input port B is “OFF”, the output port is “OFF”, as show in Figure 6(b). For the case 3: When the input port A is “ON” and the input port B is “ON”, the output port is “ON”, as show in Figure 6(c). The truth table of the proposed AND gate is shown in Table 2.

3. SUMMARY

In this paper, we have proposed novel all-optical logic gates based on MZI photonic crystal waveguides. This device was analyzed and simulated by the PWE and the FDTD methods. When two arms of the MZI in length are the same, constructive interference will occur at output port. If two arms of the MZI in length are not the same, destructive interference will occur at output port. According to this property, we can propose two logic gate structures.

REFERENCES

1. Yablonovitch, E., “Inhibited spontaneous emission in solid-state physics and electrons,” *Phys. Rev. Lett.*, Vol. 58, 2059, 1987.
2. John, S., “Strong localization of phonics in certain disordered dielectric superlattice,” *Phys. Rev. Lett.*, Vol. 58, 2486, 1987.
3. Zhao, D., J. Zhang, P. Yao, X. Jiang, and X. Chen, “Photonic crystal Mach-Zehnder interferometer based on self-collimation,” *Appl. Phys. Lett.*, Vol. 90, 231114-1, 2007.

4. Miao, B., C. Chen, S. Shi, and D. W. Prather, "A high-efficiency in-plane splitting coupler for planar photonic crystal self-collimation devices," *IEEE Photon. Technol. Lett.*, Vol. 17, 61, 2005.
5. Johnson, S. G. and J. D. Joannopoulos, "Designing synthetic optical media: Photonic crystals," *Acta. Mater.*, Vol. 51, 5823, 2003.
6. Martinez, A., A. Griol, P. Sanchis, and J. Marti, "Mach-Zehnder interferometer employing coupled-resonator optical waveguide," *Opt. Lett.*, Vol. 28, 405, 2003.
7. White, T. P., C. Martijn de Sterk, R. C. McPhedran, and T. Huang, "Recirculation-enhanced switching in photonic crystal Mach-Zehnder interferometers," *Opt. Express*, Vol. 12, 3035, 2004.
8. Kunz, K. S. and R. J. Luebbers, *The Finite Difference Time Domain Method for Electromagnetics*, CRC Press, Boca Raton, FL, 1993.
9. Smith, G. S., M. P. Kesier, J. G. Maloney, and B. L. Shirely, "Antenna design with the use of photonic band-gap materials as all-dielectric planer reflectors," *Microwave Opt. Technol. Lett.*, Vol. 11, 169, 1996.
10. Maloney, J. G., M. P. Kesier, B. L. Shirely, and G. S. Smith, "A simple description for waveguiding in photonic bandgap materials," *Microwave Opt. Technol. Lett.*, Vol. 14, 261, 1997.
11. Zhang, Z. and S. Satpathy, "Electromagnetic wave propagation in periodic structure: Bloch wave solution of Mazwell's equations," *Phys. Rev. Lett.*, Vol. 65, 2650, 1990.
12. Leung, K. M. and Y. F. Liu, "Photon band structures: The plane-wave method," *Phys. Rev. B*, Vol. 41, 10188, 1990.
13. Ho, K. M., C. T. Chan, and C. M. Soukouils, "Existence of a photonic gap in periodic dielectric structures," *Phys. Rev. Lett.*, Vol. 65, 3152, 1990.

Proposal for Large Mode Area Photonic Crystal Fibers

Yaw-Dong Wu, Jian-Jang Lee, and Tien-Tsorng Shih

Department of Electronic Engineering
National Kaohsiung University of Applied Sciences
415 Chien Kung Road, Kaohsiung 807, Taiwan, R.O.C.

Abstract— Conventional single-mode fibers suffer from small core, leading to limited output power due to generally a single-mode fiber diameter about $8\ \mu\text{m} \sim 10\ \mu\text{m}$. In order to allow higher output power and improve the influence of external force, currently photonic crystal fibers (PCFs) have overcome the mentioned shortcomings, such as endlessly single-mode operation, large mode area (LMA), and high birefringence et al.. These properties provide scaling potential for fiber laser and amplifier systems. We present the results of numerical analysis showing that large period can be obtained in LMA PCFs. One of analysis methods corresponds to finite-element method (FEM) with perfectly matched layer boundary conditions. This method respects the sufficient reliability, efficiency, and accuracy for the PCFs. In this paper, we proposed several PCF models to increase the effective mode area up to $1000\ \mu\text{m}^2$. The confinement loss is reduced to $0.486\ \text{dB/km}$ at the wavelength of $1.064\ \mu\text{m}$ for the improved PCF with $d/\Lambda = 0.28$.

1. INTRODUCTION

Fiber lasers have attracted much interest in recent years. Ytterbium in particular is capable of high efficiency and may be pumped directly by diode lasers at 915 or $980\ \text{nm}$. For high power, the effective area of optical fiber is limited by the fact that an increasing core size requires a correspondingly decreasing index step between the core and the cladding in order to maintain single-mode operation. On the other hand, the intensity within the core of an optical fiber becomes very large and this can give rise to optical nonlinearity and physical damage. In order to avoid these effects, high power lasers based on conventional Ytterbium doped step-index fibers have used relatively large mode area [1]. Some literatures have reported the ytterbium-doped fiber lasers with output power beyond $1\ \text{kW}$ [2, 3]. The photonic crystal fiber (PCF) has attracted growing attention owing to its many unique properties, such as low nonlinearity, endlessly single-mode operation, large mode area (LMA), and high birefringence [4–6]. The development of LMA fibers is important for a wide range of practical applications most notably those requiring either the delivery or generation of high power optical beams. Thus, an interesting research of PCF is the realization high power laser applications by means of endlessly single mode PCFs with very LMA. These properties provide scaling potential for fiber laser and amplifier systems.

An all-silica PCF with the different ratio of hole diameter to pitch d/Λ was studied in this paper. One of important requirement is maintained low loss for a practical application to optical fiber. It is shown from our numerical results that it is possible to design a low loss PCF with LMA at $1.064\ \mu\text{m}$.

2. ANALYSIS AND SIMULATION

All the analyses of the PCF properties have been performed by using the finite-element method (FEM) [7]. This method respects the sufficient reliability, efficiency, and accuracy for the PCFs. In particular, the FEM is suited for studying fibers with non-periodic air-hole arrangements. As it has been previously shown, triangular-lattice PCFs present a wider effective area for large Λ value so that they can be practical applied for high power delivery. In order to successfully use triangular-lattice PCFs for this kind of applications, it is necessary to define their single-mode operation regime. Typically the PCF is operated close to cut-off where $V = \pi$, the V -parameter can be written as [8]:

$$V = \frac{2\pi}{\lambda} \Lambda \sqrt{n_{eff}^2 - n_{FSM}^2} \quad (1)$$

where n_{eff} and n_{FSM} are the effective indices, respectively. FSM is the fundamental guided mode of the fundamental space-filling mode (FSM) in the air-hole cladding. The Λ is the air-hole pitch that choices as the effective core radius can be adopted also for the PCF. In general, they consist of an ordered array of air-holes running along its length. PCFs can divide into two kinds of guiding mechanisms: one is photonic bandgap fibers [9], such a fiber with low loss and low nonlinearity

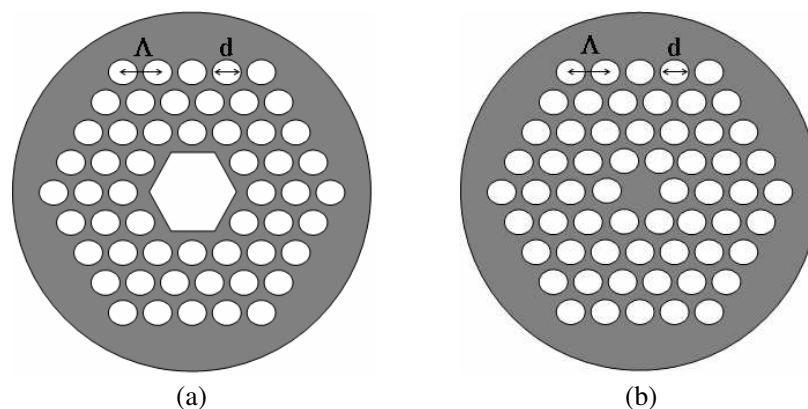


Figure 1: Schematic of the cross-section of the two kinds of PCFs: (a) Photonic bandgap fiber that guides in a hollow core by a band gap. (b) Holey fiber that confines light in a solid core by index guiding.

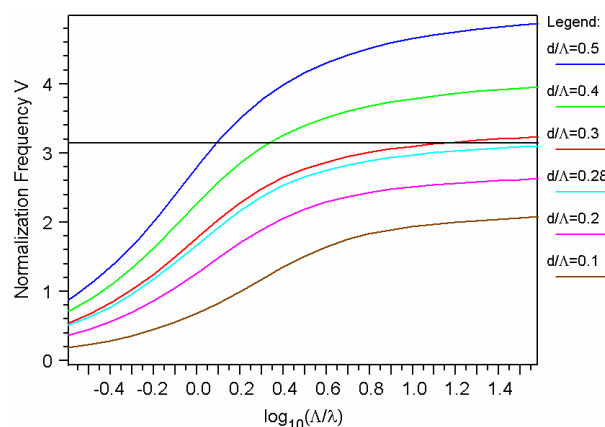


Figure 2: Cutoff value of the normalized frequency V according to the Λ/λ for the proposed PCF.

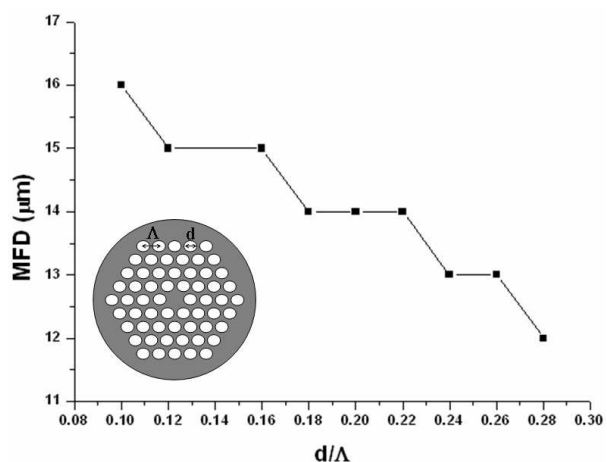


Figure 3: The MFD of the PCF with $\Lambda = 9 \mu\text{m}$ and different d/Λ .

transmission over a hollow core, which can not be obtained with conventional fibers based on total internal reflection (TIR), as shown in Figure 1(a). Band gap confinement is attractive because it allows light to be guided within a hollow core. Furthermore, the effective index of the guided mode is lower than unity, the electric field localizes in the hollow core. The other one is index-guiding fibers [10]. The air-holes arranged in a triangular lattice a PC in the cladding, and a defect is made in the core by replacing an air-hole with silica glass, as shown in Figure 1(b). Since the average refractive index at the defect is higher than that in PC, such a PCF operates via TIR.

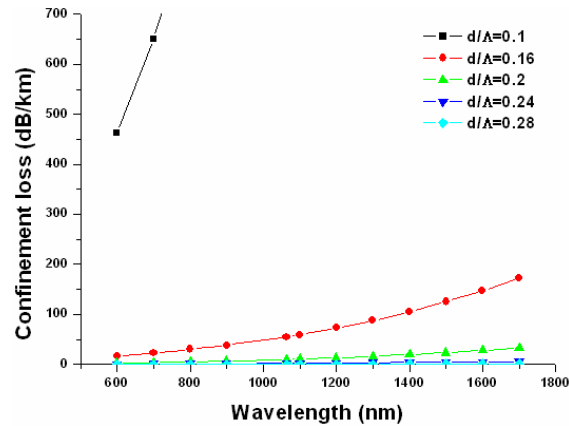
In this paper, we focus on all-silica holey fiber with large effective area at $1.064 \mu\text{m}$. In order to ensure at single-mode operation, the resulting curves of the normalized frequency V against Λ/λ for various relative hole sizes and hole pitches Λ are shown in Figure 2. The horizontal line corresponds to the single mode condition when V value of PCF is lower than π . Thus we further calculate the mode field diameter (MFD) of $d/\Lambda < 0.28$ with hole pitch $\Lambda = 9 \mu\text{m}$, as shown in Figure 3. However, the numerical results show the limited MFD by changing hole diameter. Table 1 shows the properties of several PCF models with different hole pitch Λ and d/Λ , increasing Λ can cause apparent an increase for MFD. The effective area of the fundamental mode is up to $\sim 1000 \mu\text{m}^2$, corresponding to a MFD larger than $26 \mu\text{m}$. The effective area A_{eff} of fiber is calculated as follows:

$$A_{eff} = \frac{\left(\iint |E|^2 dx dy \right)^2}{\iint |E|^4 dx dy} \quad (2)$$

where E is the propagation electrical field. The hole diameter increases opposite to decrease MFD, the model of MFD17-5 especially.

Table 1: The properties of several PCF models with different hole pitch Λ and d/Λ .

	Λ	d/Λ	MFD	A_{eff}
MFD15-1	15 μm	0.1	26 μm	1017 μm^2
MFD17-1	17 μm	0.1	28 μm	1256 μm^2
MFD17-5	17 μm	0.5	20 μm	531 μm^2
MFD21-1	21 μm	0.1	35 μm	1963 μm^2
MFD21-2	21 μm	0.2	32 μm	1425 μm^2

Figure 4: Confinement loss property of MFD21 with the different d/Λ .

According to the previous results, the PCF model of MFD21 is considered and further changes the geometry structure. Figure 4 shows the confinement loss property of the MFD21 with the different d/Λ from 600 nm–1700 nm. However, MFD21-1 is not available in high power delivering because acute loss. Besides, we have since reduced to 0.486 dB/km at the wavelength of 1.064 μm by increasing d/Λ . We proposed several PCFs with large effective area and low loss for further applications, such as polarization-maintaining fiber, amplifier, and fiber laser etc..

3. CONCLUSION

In this paper, we proposed several PCF models to provide an available in high power delivering. All the analyses of the PCF properties have been performed by using the FEM. The effective area of the fundamental mode is up to $\sim 1000 \mu\text{m}^2$, corresponding to a MFD larger than 26 μm . The numerical results show low loss and large effective area with the confinement loss of 0.486 dB/km at 1.064 μm . This is done by increasing d/Λ of MFD21 reduced effective index. These interesting properties may find applications for polarization-maintaining fiber, amplifier, and fiber laser.

REFERENCES

1. Dominic, V., S. MacCormack, R. Waarts, S. Sanders, S. Bicknese, R. Dohle, E. Wolak, P. S. Yeh, and E. Zucker, "110 W fiber laser," *Electron. Lett.*, Vol. 35, 1158–1160, 1999.
2. Jeong, Y., J. K. Sahu, D. N. Payne, and J. Nilsson, "Ytterbium-doped large-core fiber laser with 1 kW of continuous-wave output power," *Electron. Lett.*, Vol. 40, 470–471, 2004.
3. Liem, A., J. Limpert, H. Zellmer, A. Tunnermann, T. Reichel, K. Morl, S. Jetschke, S. Unger, H. R. Muller, J. Kirchhof, T. Ssndrock, and A. Harschak, "1.3 kW Yb-doped fiber laser with excellent beam quality," *Proc. Conference on Lasers and Electro-Optics 2004*, San Francisco, USA, May 2004, postdeadline paper CPDD2.
4. Schmidt, O., J. Rothhardt, T. Eidam, F. Roser, J. Limpert, and A. Tunnermann, "Single-polarization ultra-large-mode-area Yb-doped photonic crystal fiber," *Opt. Express*, Vol. 16, 3918–3923, 2008.
5. Birks, T. A., J. C. Knight, and P. Sr. J. Russell, "Endlessly single-mode photonic crystal fiber," *Opt. Lett.*, Vol. 22, 961–963, 1997.

6. Schreiber, T., F. Roser, O. Schmidt, and J. Limpert, “Stress-induced single-polarization single-transverse mode photonic crystal fiber with low nonlinearity,” *Opt. Express*, Vol. 13, 7621–7630, 2005.
7. Koshiba, M. and K. Saitoh, “Structural dependence of effective area and mode field diameter for holey fibers,” *Opt. Express*, Vol. 11, 1746–1756, 2003.
8. Mortensen, N. A. and J. R. Folkenberg, “Modal cutoff and the V parameter in photonic crystal fibers,” *Opt. Lett.*, Vol. 28, 1879–1881, 2003.
9. Roberts, P. J., D. P. Williams, H. Sabert, B. J. Mangan, D. M. Bird, T. A. Birks, J. C. Knight, and P. St. J. Russell, “Design of low-loss and highly birefringent hollow-core photonic crystal fiber,” *Opt. Express*, Vol. 14, 7329–7341, 2006.
10. Russell, P. St. J., “Photonic crystal fibers,” *Science*, Vol. 299, 358–362, 2003.

Cantor Dust Zone Plates

W. D. Furlan¹, V. Ferrando^{1,2}, A. Calatayud², F. Giménez³, and J. A. Monsoriu²

¹Departamento de Óptica, Universitat de València, Burjassot 46100, Spain

²Centro de Tecnologías Físicas, Universitat Politècnica de València, Valencia 46022, Spain

³I.U. Matemática Pura y Aplicada, Universitat Politècnica de València, Valencia 46022, Spain

Abstract— In this communication, we present a novel family of zone plates based on the Cantor dust fractal. Cantor dust is a two-dimensional version of the Cantor set. The pupil function, that defines the Cantor Dust Zone Plate (CDZP), can be written as a combination of rectangle functions. The axial irradiance provided by CDZPs of different fractal order is investigated, analysing the influence of the fractality.

1. INTRODUCTION

A renewed interest in diffractive focusing elements has been experienced by the scientific community in the last years because these elements are essential in image forming setups that are used in THz tomography [1], soft X-ray microscopy [2, 3], astronomy [4, 5], and lithography [6]. Following this trend, our group recently introduced a new type of 2D photonic-image-forming structures: the Fractal Zone Plates (FZPs) [7–9]. When illuminated by a plane wavefront, a FZP produces multiple foci along the optical axis. The internal structure of each focus exhibits a characteristic fractal structure reproducing the self-similarity of the originating FZP. We have shown that the number of foci and their relative amplitude can be modified with the FZP design [9]. It has been proved that this property can be profited in image forming systems to obtain an enhancement of the depth of field [10].

Square zone plates (SZPs) [11] are another kind of promising diffractive optical elements which are the result of the combination of two linear Fresnel zone plates. Under a monochromatic plane wave illumination this configuration produces a focalization pattern with a cross-like irradiance distribution. Based on the SZP fractal rectangular zone plates (FSZPs) [12] with an extended depth of focus have been recently introduced.

On the other hand the photon sieve (PS) is another diffractive optical element constructed by substitution of the transparent areas in a ZP by a great number of non overlapping holes of different sizes [13, 14]. The principal advantage of the PS is that it lends itself to apodization by simply changing the angular or radial density of holes, improving the diffraction efficiency.

In this work, we present a Cantor Dust based Zone plate (CDZP) as the combination of the concepts FSZP and PS.

2. PUPIL FUNCTION OF THE CDZP

The CDZP is based on the 2D Cantor dust distribution. This distribution can be represented by a 2D matrix that can be obtained recursively starting from a first 2D element,

$$t_1 = \begin{bmatrix} 1 & 0 & 1 \\ 0 & 0 & 0 \\ 1 & 0 & 1 \end{bmatrix},$$

and then recursively by applying to each element the following transformation rules:

$$[1] \rightarrow \begin{bmatrix} 1 & 0 & 1 \\ 0 & 0 & 0 \\ 1 & 0 & 1 \end{bmatrix} \quad \text{and} \quad [0] \rightarrow \begin{bmatrix} 0 & 0 & 0 \\ 0 & 0 & 0 \\ 0 & 0 & 0 \end{bmatrix}. \quad (1)$$

After an arbitrary number of iterations, S , we will obtain a binary array, t_S , with $3^S \times 3^S$ elements. We will refer to the t_S array elements as $t_{Sjj'}$, where j and j' take values from 1 to 3^S . This array can be geometrically represented as a square surface divided into $3^S \times 3^S$ squares where “1” represents a white square and “0” represents a black one.

From this geometrical representation we can construct the CDZP as a photon sieve with rectangular holes formed by the white squares but varying the distribution sides quadratically with

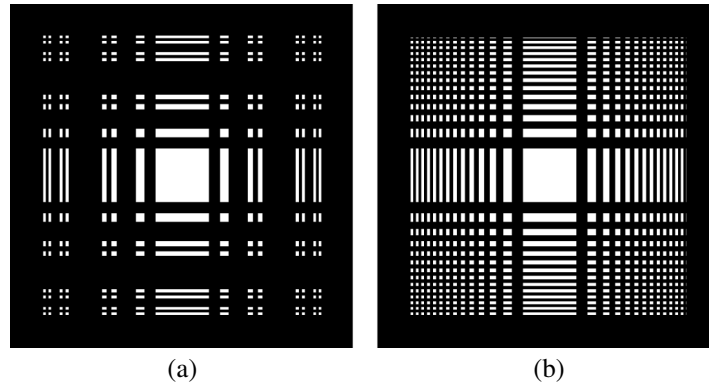


Figure 1: (a) CDZP of order $S = 3$ and (b) its periodic equivalent lens.

respect to the transverse coordinates (see Fig. 1(a)). In this way the pupil function that represents a CDZP can be written as:

$$q(\bar{x}_0, \bar{y}_0) = \sum_{j=1}^N \sum_{j'=1}^N t_{Sjj'} \left[\text{rect}\left(\sqrt{\frac{N}{j}} \bar{x}_0\right) - \text{rect}\left(\sqrt{\frac{N}{j-1}} \bar{x}_0\right) \right] \cdot \left[\text{rect}\left(\sqrt{\frac{N}{j'}} \bar{y}_0\right) - \text{rect}\left(\sqrt{\frac{N}{j'-1}} \bar{y}_0\right) \right], \quad (2)$$

where $N = 3^S$, $\{\bar{x}_0, \bar{y}_0\} = \left\{ \frac{x_0}{a}, \frac{y_0}{a} \right\}$ (being a the half-width of the zone plate and $\{x_0, y_0\}$ the cartesian coordinates at the pupil plane) and $\text{rect}()$ is the rectangle function defined as:

$$\text{rect}(x) = \begin{cases} 1 & \text{si } |x| \leq 1 \\ 0 & \text{si } |x| > 1 \end{cases} . \quad (3)$$

In Fig. 1(b), the equivalent periodic lens is shown for comparison.

3. FOCUSING PROPERTIES

Under a monochromatic plane wave illumination, the irradiance provided by a CDZP can be obtained, applying the Fresnel approximation, as:

$$I(\bar{x}, \bar{y}, u) = \frac{1}{16} \left| \sum_{j=1}^N \left\{ (ERF_{\bar{x},j}(u) - ERF_{\bar{x},j-1}(u)) \cdot \sum_{j'=1}^N t_{jj'} (ERF_{\bar{y},j'}(u) - ERF_{\bar{y},j'-1}(u)) \right\} \right|^2, \quad (4)$$

where $u = \frac{a^2}{2\lambda z}$ is the normalized axial coordinate and

$$ERF_{a,b}(u) = \text{Erf}\left[(1+i)\sqrt{\pi u} \left(\sqrt{\frac{b}{N}} + a\right)\right] + \text{Erf}\left[(1+i)\sqrt{\pi u} \left(\sqrt{\frac{b}{N}} - a\right)\right],$$

being $\text{Erf}[x] = \frac{2}{\sqrt{\pi}} \int_0^x e^{-t^2} dt$ the error function.

For the axial irradiance ($\bar{x} = 0, \bar{y} = 0$) Eq. (4) can be reduced to:

$$I(0, 0, u) = \left| \sum_{j=1}^N d_{Sj} \cdot \left(\text{Erf}\left[(1+i)\sqrt{\pi u} \sqrt{\frac{j}{N}}\right] - \text{Erf}\left[(1+i)\sqrt{\pi u} \sqrt{\frac{j-1}{N}}\right] \right) \right|^4, \quad (5)$$

Figure 2 shows the normalized axial intensity provided by CDZPs of orders 2 and 3 and by the equivalent periodic lens for $f = 10$ cm and $\lambda = 633$ nm, being $f = \frac{a^2}{\lambda 3^S}$. The characteristic fractal selfsimilarity can be observed in the CDZP irradiance.

The distribution of the diffracted energy, not only in the optical axis but over the whole transverse plane is of interest for the prediction of applications capabilities of CDZP. Thus, a two-dimensional analysis of the diffracted intensities is required. Eq. (4) has been used to calculate the

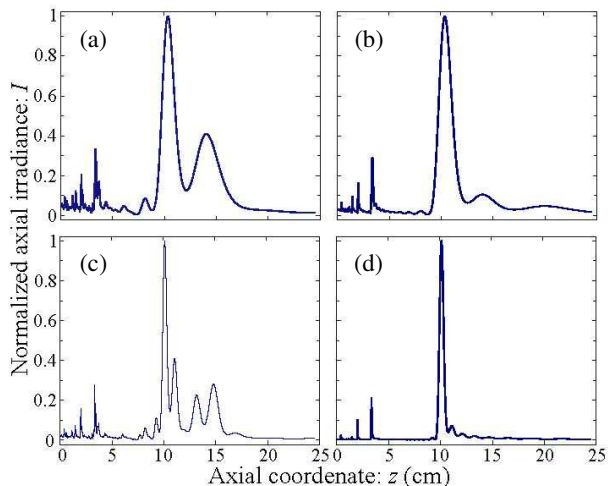


Figure 2: Normalized axial irradiance provided by the CDZP and its equivalent periodic lens of focal length, $f = 10$ cm ($\lambda = 633$ nm). (a) CDZP of order $S = 2$ and (b) its equivalent periodic lens. (c) CDZP of order $S = 3$ and (d) its equivalent periodic lens.

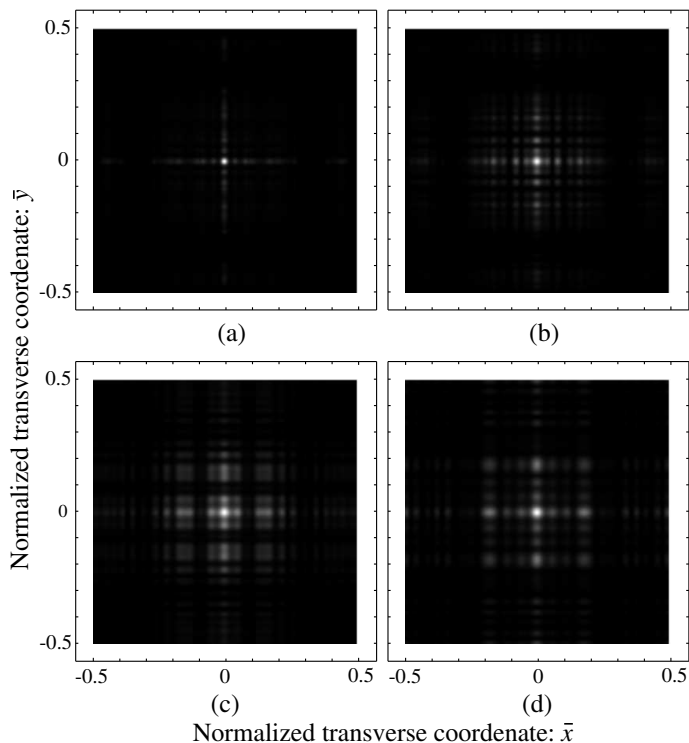


Figure 3: Transverse diffraction patterns of a CDZP with $S = 3$ at (a) the main focus located at $u = 13.38$, and at the three subsidiary foci localized at (b) $u = 12.23$, (c) $u = 10.26$ and (d) $u = 9.13$.

evolution of the diffraction patterns for a CDZP from near field to far field. Of particular interest are the intensities at transverse planes corresponding to the different maxima of the axial irradiance. Figure 3 shows the result obtained for $S = 3$ at the main focus located at $u = 13.38$ and at the three subsidiary foci located at $u = 12.23$, $u = 10.26$ and $u = 9.13$. In each case, the intensities are normalized to its maximum value.

4. CONCLUSION

A new fractal DOE is proposed. The focusing properties of these fractal diffractive lenses are analytically analyzed. The axial irradiances of CDZPs have been computed for different stages of fractal order S . The axial response for the CDZP exhibits a characteristic selfsimilar fractal

profile. Moreover, under monochromatic illumination a CDZP gives rise a focal volume containing a delimited sequence of two-arms-cross patterns that are axially distributed according to the self-similarity of the lens.

ACKNOWLEDGMENT

The financial support of the Spanish Ministry of Science and Innovation under the projects FIS2011-23175 and TRA2009-0215 is acknowledged. We also acknowledge the support from Generalitat Valenciana through the project PROMETEO2009-077 and from Universitat Politècnica de València through the project PAID-05-11.

REFERENCES

1. Wang, S. and X. Zhang, “Terahertz tomographic imaging with a Fresnel lens,” *Opt. Photon. News*, Vol. 13, No. 12, 59–59, 2002.
2. Wang, Y., W. Yun, and C. Jacobsen, “Achromatic Fresnel optics for wideband extreme-ultraviolet and X-ray imaging,” *Nature*, Vol. 424, 50–53, 2003.
3. Kipp, L., M. Skibowski, R. L. Johnson, R. Berndt, R. Adelung, S. Harm, and R. Seemann, “Sharper images by focusing soft x-rays with photon sieves,” *Nature*, Vol. 414, 184–188, 2001.
4. Hyde, R., “Eyeglass. 1. Very large aperture diffractive telescope,” *Appl. Opt.*, Vol. 38, No. 19, 4198–4212, 1999.
5. Andersen, G., “Large optical photon sieve,” *Opt. Lett.*, Vol. 30, No. 22, 2976–2978, 2005.
6. Menon, R., D. Gil, G. Barbastathis, and H. Smith, “Photon sieve lithography,” *J. Opt. Soc. Am. A*, Vol. 22, No. 2, 342–345, 2005.
7. Saavedra, G., W. D. Furlan, and J. A. Monsoriu, “Fractal zone plates,” *Opt. Lett.*, Vol. 28, No. 12, 971–973, 2003.
8. Furlan, W. D., G. Saavedra, and J. A. Monsoriu, “Fractal zone plates produce axial irradiance with fractal profile,” *Opt. Photon. News*, Vol. 14, No. 12, 31, 2003.
9. Monsoriu, J. A., G. Saavedra, and W. D. Furlan, “Fractal zone plates with variable lacunarity,” *Opt. Express*, Vol. 12, No. 18, 4227–4234, 2004.
10. Furlan, W. D., G. Saavedra, and J. A. Monsoriu, “White-light imaging with fractal zone plates,” *Opt. Lett.*, Vol. 32, No. 15, 2109–2111, 2007.
11. Janicijevic, L. J., “Diffraction characteristics of square zone plates,” *Journal of Optics-nouvelle Revue d’Optique*, Vol. 28, No. 4, 199–205, 1982.
12. Calatayud, A., V. Ferrando, F. Giménez, W. D. Furlan, G. Saavedra, and J. A. Monsoriu, “Fractal square zones plates,” *Optics Communications*, (submitted).
13. Giménez, F., J. A. Monsoriu, W. D. Furlan, and A. Pons, “Fractal photon sieve,” *Optics Express*, Vol. 14, No. 25, 11958–11963, 2006.
14. Giménez, F., W. D. Furlan, and J. A. Monsoriu, “Lacunar fractal photon sieves,” *Optics Communications*, Vol. 277, No. 1, 1–4, 2007.

Analysis and Design of a UHF-band Harmonic Meter

A. Naserialiabadi¹, Gh. Moradi¹, A. Kheirdoost¹, J. Rashed-Mohassel², and R. Sarraf Shirazi¹

¹Wave Propagation & Microwave Measurement Research Lab., Department of Electrical Engineering
Amirkabir University of Technology, 424 Hafez Avenue, Tehran 15914, Iran

²Center of Excellence on Applied Electromagnetic Systems
School of Electrical and Computer Engineering, University of Tehran, P. O. 14395-515, Iran

Abstract— Design and analysis of a system to measure the amplitude of harmonics of a signal in UHF band is presented. First we propose analytical consideration, then the results are used to validate the method. The proposed structure is so simple such that includes a single diode mixer. In mixer, harmonics of the desired signal to measure are fed into RF-port and we synthesize a comb signal to feed in LO-port. The bottle neck is amplitude of each harmonic in comb signal. The proposed design is validated and optimized by using a full-wave electromagnetic simulator. After optimization, bandwidth increased.

1. INTRODUCTION

Today spectrum analyzers are using widely to determine the frequency content of signals. These instruments are available in wide range of frequency and dynamic range. In all of them the method is to down convert signal, then determine frequency content (amplitude and phase) by digital processing (DSP instruments are using widely) instruments. Signal wanted to determine its frequency content is fed into a downconverter mixer and local oscillator's frequency is swept to ensure to down convert all of its content to frequency range that digital processing block works [1].

The problem we consider is that we have a single tone signal and its harmonics and we want to measure the amplitude of harmonics. This signal could be the output of a high power amplifier when input is a single tone signal, so we have harmonics of this signal in the output. We suppose we have the frequency of fundamental tone. We also suppose an attenuator is used to make the output signal to small signal.

2. THEORY

We represent the signal wanted to determine it's frequency content by (1).

$$RF = \sum_{n=1}^k A_n \cos(n\omega_{RF}t + \alpha_n) \quad (1)$$

To down convert (1) by a multiplier, we need LO signal such (2)

$$LO = \sum_{m=1}^k B_m \cos(m\omega_{LO}t + \beta_m) \quad (2)$$

$$\omega_{LO} - \omega_{RF} = \omega_{IF} \quad (3)$$

As said we Know ω_{RF} , we choose ω_{LO} so that

$$\frac{\omega_{IF}}{\omega_{LO}} = 1, \quad \frac{\omega_{IF}}{\omega_{RF}} = 1 \quad (4)$$

f_{RF} is in UHF band, we choose $f_{IF} = 10$ MHz, so in UHF band we have (5)

$$\frac{\omega_{IF}}{\omega_{RF}} \leq \frac{10}{300} = 1 \quad (5)$$

If we use an ideal multiplier to multiply (1) and (2), we have

$$\begin{aligned}
 RF \times LO &= \left(\sum_{n=1}^k A_n \cos(n\omega_{RF}t + \alpha_n) \right) \left(\sum_{m=1}^k B_m \cos(m\omega_{LO}t + \beta_m) \right) \\
 &= \sum_{n=1}^k \sum_{m=1}^k A_n B_m \cos(n\omega_{RF}t + \alpha_n) \cos(m\omega_{LO}t + \beta_m) \\
 &= \sum_{n=1}^k \sum_{m=1}^k \frac{A_n B_m}{2} (\cos(n\omega_{RF}t + \alpha_n + m\omega_{LO}t + \beta_m) + \cos(n\omega_{RF}t + \alpha_n - m\omega_{LO}t - \beta_m)) \quad (6)
 \end{aligned}$$

The low frequency content of (6) is

$$\sum_{m=1}^k \frac{A_m B_m}{2} \cos(m\omega_{IF}t + \alpha_m - \beta_m) \quad (7)$$

The maximum frequency content of (7) is $k f_{IF}$. We make LO signal, so we know B_m . If we detect (7) so we can determine A_m , the amplitude we want to measure, since we know B_m .

3. MIXER CONSIDERATION

In order to multiply (1), (2) these signals should fed to RF and LO ports of a mixer. In usual applications a single tone LO signal is used in downconvertor mixers, but we want to multiply two multi harmonic signals. If single tone LO signal is fed to LO port, nonlinear element (here diode) produces harmonics of this tone and frequencies which are linear combination of f_{LO} , f_{RF} , include desired IF frequency, will produced but conversion loss of harmonics of IF frequency will be so great and this can lower level of IF signal to noise level since we have supposed that RF signal is made to small signal by attenuator, so large conversion loss can lower level of IF signal to noise level.

To avoid falling off IF signal to noise level we can fed harmonics of f_{LO} two LO port. This makes conversion loss smaller than the case single tone LO signal ($\cos(\omega_{LO}t)$) fed to LO port. Power of different harmonics of LO signal should be tuned to make conversion loss of different IF harmonics as minimum as possible.

We should note that by considering more harmonics of RF signal, conversion loss of IF harmonics will increase.

Usual way to produce multi harmonic signal to make desired LO signal is to use comb generator, typically include SRD, but amplitude of harmonics in output signal of comb generators generally decrease by harmonic index increasing or remain approximately constant and we have no control on amplitude of output harmonics. But as mentioned we need to tune power of different harmonics of LO signal to make conversion loss of different IF harmonics as minimum as possible so we can use frequency multipliers with attenuators to control power of harmonics of LO signal.

4. MIXER IMPLEMENTATION

We use a single diode mixer, little complicate to consider a multi harmonic signal as LO signal. In single diode mixer we use a multisection Wilkinson coupler in UHF band to mix RF and LO signals. HSMS 8101 (Surface Mount Microwave Schottky Mixer Diode) is used as schottky diode to mix LO and RF signals. We set the resistor in IF section 50ohm ($Z_{IF} = 50 \text{ohm}$), the input resistance to digital processing block.

Comb generators could be used to make a multi harmonic signal but amplitude of harmonics decrease by harmonic index increase.

The Conversion Loss of mixer in different harmonics is important, Large Conversion Losses make dynamic range less and we try to make conversion loss for different harmonics as minimum as possible.

Conversion Loss of m th IF harmonic is:

$$ConvLoss_m = \text{Power of } m'\text{th RF harmonic} - \text{Power of } m'\text{th IF harmonic} \quad (8)$$

Conversion Loss of single diode mixer we designed, with a single tone RF signal and a single tone LO signal, is 8.4dB when power of LO signal is 8dBm. But if we fed the first two harmonics of LO

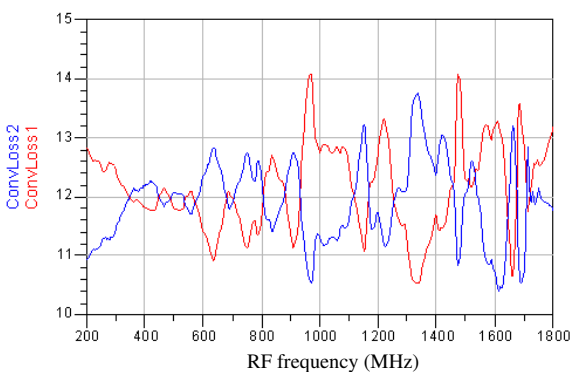


Figure 1: ConvLoss_{1,2} for two harmonics of RF signal.

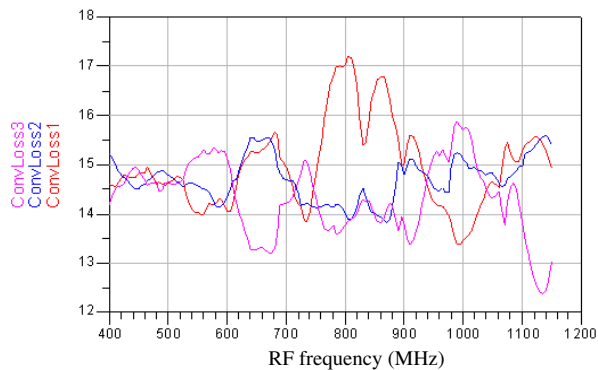


Figure 2: ConvLoss_{1,2,3} for three harmonics of RF signal.

signal in LO port and the first two harmonics of RF signal in RF port, ConvLoss₁ and ConvLoss₂ will be so larger than 8.4 dB. We can change power of LO harmonics to decrease conversion loss of different harmonics. But try to decrease ConvLoss₁, increase ConvLoss₂ and vice versa. Finally for two harmonics of RF signal we can reach ConvLoss_{1,2} \approx 12 dB and for three harmonics of RF signal we can reach ConvLoss_{1,2,3} \approx 15 dB. The variation of conversion loss by RF frequency for two and three harmonics is simulated by multitone harmonic balance method, are shown in Figures 1 and 2.

We should note that 3 dB of conversion loss is due to coupler and 1 dB is due to ohmic resistance of diode, here $R_s = 6$ ohm. In IF port we can detect the amplitude of IF harmonics and since we have conversion Loss of mixer for different harmonics we can determine amplitude of RF harmonics.

5. CONCLUSION

The method to measure harmonics amplitude introduced and mixer consideration and limitation described. Conversion loss of different harmonics were made as minimum as possible. It was mentioned that using usual comb generators cause large conversion losses since we have no complete control on amplitude and phase of different harmonics in comb signal so we changed power of LO harmonics to make conversion losses as minimum as possible and this makes dynamic range larger.

REFERENCES

1. Application Note 15, *Agilent Spectrum Analysis Basics*, Agilent Technologies, Inc., August 2006.
2. Gilmore, R. and L. Besser, *Practical RF Circuit Design for Modern Wireless Systems, Volume II, Active Circuits and Systems*, Artech House, 2003.
3. Barataud, D., A. Mallet, M. Campovecchio, J. M. Nebus, J. P. Villotte, and J. Verspecht, "Measurements of time domain voltage/current waveforms at R.F. and microwave frequencies for the characterization of nonlinear devices," *Proc. IEEE Instrum. Meas. Technol. Conf.*, Vol. 2, 1006–1010, May 1998.
4. Pozar, D. M., *Microwave Engineering*, 3rd Edition, Wiley, 2005.

A Fiber Optic Sensor Integrated with Fuzzy Similarity Analysis to Evaluate Hydrocarbon Pollutant in Water

I. Palamara, D. Pellicanó, and M. Versaci

Department of Mechanics and Materials, NDT-Lab, University “Mediterranea” of Reggio Calabria, Italy

Abstract— One of the main environmental problems is related to the amount and quality of water at our disposal. Many developed countries have adopted law that call for constant monitoring of water quality. Monitoring is an essential step to implement any procedures for purification from contaminants. A possible tool of detection is constituted by the employment of optical fibers having building features which allow an optimal use in liquid environments. By means of a sensor, a sample containing water with micro particles of pollutant is put through a light source evaluating the absorption of light at different frequencies. This research proposes a new methodology designed to detect and classify micro-particles of hydrocarbons, type C14 C40, in water. In particular, the obtained signals are subjected to a fuzzy similarity analysis in order to detect the presence of micro-pollution and classify its percentage. A sensor integrated with fuzzy similarity analysis represents a useful tool, easy to use and without implementation of complex procedures. Any technological production would also allow an “in situ” analysis.

1. INTRODUCTION

Clean and unpolluted water is undoubtedly the most precious natural resource existing on our planet. Water has life properties which are crucial to the world's global ecosystem. Water pollution can cause serious diseases to humans and animals; it can, also, destroy the habitats of many species of fish and other animals. In some nations, fishing or harvesting of other animals is the main source of income. With respect to human life, one of the most dangerous problems posed by water pollution is the infectious diseases. When water cannot be adequately treated, infectious diseases can spread very quickly through the water supply. Bacteria, parasites, and viruses can live in polluted water, allowing the spread of dangerous illnesses such as typhoid, intestinal parasites, and many other diseases [1]. Hydrocarbon compounds can be considered the major pollution problem in drinking water: the Environmental Protection Agency states that 33% of all water pollution is due to Hydrocarbon. Many developed countries have adopted law that call for constant monitoring of water quality. In 1997 the European Commission proposed a Directive to establish a common action in the field of water policy. The Directive, known as the Water Framework Directive, was adopted in September 2000. Currently water pollution is detected in laboratories, where small samples of water are analyzed. A possible different detection methodology is constituted by the employment of optical fibers. A simple sensor essentially constituted of optical fibers allows an in situ measures. This research proposes a fuzzy similarity analysis of the obtained signals [2] in order to improve the detection of micro-pollution and the classification of its percentage. The paper is organized as follows: in Section 2 it is given a basic description of the database and the fuzzy methodology; in Section 3 the results of the new approach are presented, while conclusions are given in Section 4.

2. MATERIALS AND METHODS

The sensor was developed by the Institute of Technology-Lecce-(IIT) (Figure 1). It is formed by a transmitter Tx and a receiver Rx , both in optic fiber; a sample containing water with microparticles of pollutant is put through a light source (broad white lamp source); the receiver is connected to a high sensitive Optical Multichannel Analyzer (OMA) to evaluate the absorption of light at different frequencies. Samples (Table 1) with different concentration of hydrocarbon (C14 and C40) are analyzed. The database is substantially structured in a set of five measures of samples without pollution and seven measures for each sample at a different pollution concentration. From the observation of the optical spectra we got information about how much energy was absorbed at each frequency (wavelength)(Figure 2(a)). In fact, when a light beam of intensity I_0 passes through a layer of thickness L of a mean, a part of it is absorbed by the same mean and a part is transmitted with a residual intensity I [3].

So, if the concentration of micro-particles is low, a bigger quantity of light will be collected at the output corresponding to a lower quantity of absorbed light of the liquid; as a consequence, with

Table 1: Sample of water polluted and respective concentration.

Sample	Concentration (mg/l)	Sample	Concentration (mg/l)
Nopollution	0	#5	0.45
#1	0.15	#6	0.53
#2	0.2	#7	0.75
#3	0.21	#8	1.42
#4	0.34		

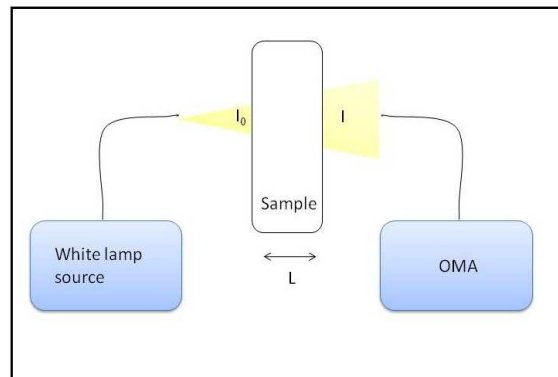


Figure 1: Schematic layout of sensor.

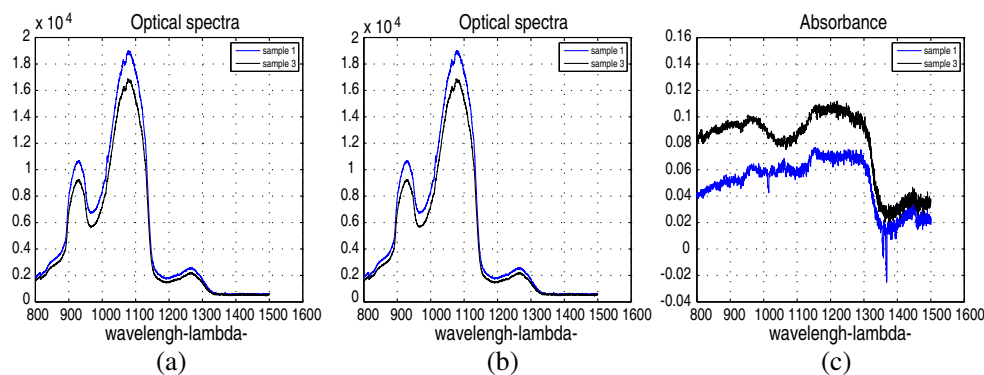


Figure 2: (a) Spectra of the sample at different pollution concentration, (b) transmittance and (c) absorbance respectively.

an increasing concentration a lower quantity of light will be collected, corresponding to a bigger quantity of absorbed light (Figures 2(b) and 2(c)). The relation between I_0 and I is $\frac{I}{I_0} = 10^{-\epsilon CL} = T = 10^{-A}$ where L is the path length, C is the concentration of the substance, ϵ is the absorption coefficient of the substance and A is the absorbance. The transmissivity can be expressed in terms of absorbance which, as for the liquids, is defined as $A = -\log T$. As comparison, the Lambert Beer Law $A = \epsilon CL$ is expressed. So, going through parameters of transmittance and absorbance allows to determine values of a concentration related to a determined species in a sample.

2.1. Fuzzy Similarities Measures to Evaluate Hydrocarbon Pollutants

2.1.1. Fuzzy Similarities Measures (FSM)

A fuzzy similarity measure is a fuzzy binary relation in $F(X)$, with X as the universe of items $S : F(X) \times F(X) \rightarrow [0, 1]$ satisfying the following properties:

- S is reflexive: $S(A, A) = [1, 1]$;
- S is symmetric: $S(A, B) = S(B, A)$;
- S is min-transitive: $S(A, C) > \min(S(A, B), S(B, C))$.

where A , B and C are fuzzy sets belonging to $F(X)$. In the literature a lot of measures [2] can be found to express the similarity between two fuzzy sets. In this work, we will use two different

approaches: the first one comes out from the computation of a distance:

$$S_1 = \frac{1}{n} \sum_{i=1}^n \frac{\min(\mu_A(x_i) - \mu_B(x_i))}{\max(\mu_A(x_i) - \mu_B(x_i))} \quad (1)$$

$$S_2 = \sum_{i=1}^n \frac{1 - |(\mu_A(x_i) - \mu_B(x_i))|}{n} \quad (2)$$

$$S_3 = 1 - \sum_{i=1}^n \frac{|(\mu_A(x_i) - \mu_B(x_i))|}{|(\mu_A(x_i) + \mu_B(x_i))|} \quad (3)$$

$$S_4 = 1 - \frac{1}{1 + |(\mu_A(x_i) - \mu_B(x_i))|} \quad (4)$$

where n is the number of elements contained in the fuzzy sets A and B ; $\mu_A(x_i)$ and $\mu_B(x_i)$ are the membership functions of the A and B fuzzy sets respectively. In the second approach the similarity [4] is judged by looking into the common and distinctive features of the two sets, so they are not considered the single elements as points in a metrical space but as sets of features (set of logic predicates).

$$S_5 = \frac{\sum_{i=1}^n (\mu_A(x_i), \mu_B(x_i))}{\sum_{i=1}^n (\mu_A(x_i), \mu_B(x_i)) + \alpha \min(\mu_A(x_i), 1 - \mu_B(x_i)) + \beta \min(1 - \mu_A(x_i), \mu_B(x_i))} \quad (5)$$

2.1.2. Membership Functions

For each polluted sample and for the one free from micro-pollutants, the Gaussian membership functions are “built” (Figure 3) in which the mean and the variance have been determined using the concentration values of the micro-pollutants present in the samples. For our goal the class of data referring to sample without pollution is A and the classes of data referring to samples with pollution are labelled with B_j , as many of the samples. Analyzing Figure 3, for concentration values near one another, the membership functions can be gathered together using a unique Gaussian with mean m equal to the mean of means, as *variance* value the maximum one of the single variances. In Figure 4 it can be observed how the fuzzy sets have been grouped together: the fuzzy set of reference is made up of the sample free from micro-pollutants (no poll set); the second set is made up of samples 1, 2 and 3 (first set); the third one, instead, by the samples 4, 5 and 6 (second set); in the last two fuzzy sets they’re present, respectively, the samples 7 and 8 (third and fourth set).

3. RESULTS

Before mapping the measures of similarity it has been taken into account the fuzziness level (Figure 5) of each set using the linear index $LI = \frac{2}{n} \sum_{i=1}^n \min(\mu_A(x_i)(1 - (\mu_A(x_i)))$ [5]. The measures of similarity (Figures 6 and 7) confirm the possibility to detect the presence of micro-pollutants. An analysis of the values’ range allows to make considerations also on the concentrations of the present pollutants. It is noticed, in fact, that the minor is the value of similarity the mayor is the concentration present in the sample.

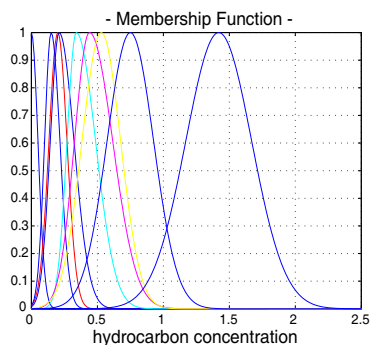


Figure 3: Membership functions of all the samples.

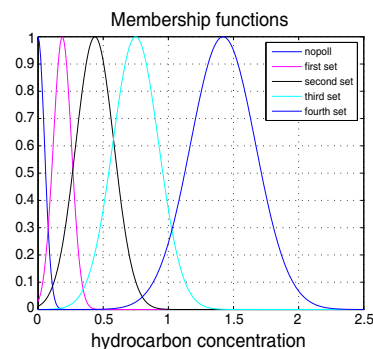


Figure 4: Membership functions of the five fuzzy sets.

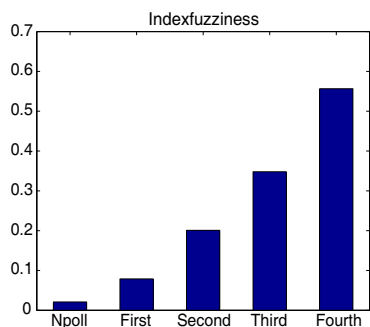


Figure 5: Evaluation of the Linear index for each fuzzy sets, no-poll represents samples without pollution.

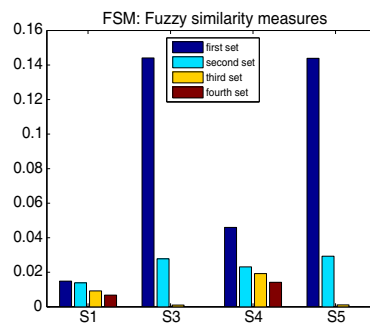


Figure 6: Fuzzy similarity measures S_1 - S_3 - S_4 - S_5 for each fuzzy set.

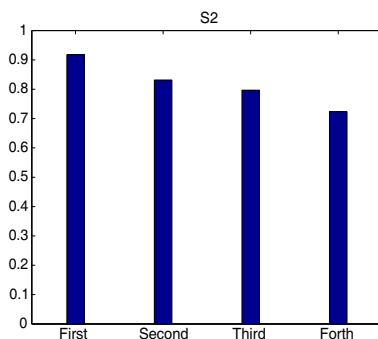


Figure 7: Fuzzy similarity measures S_2 for each fuzzy set.

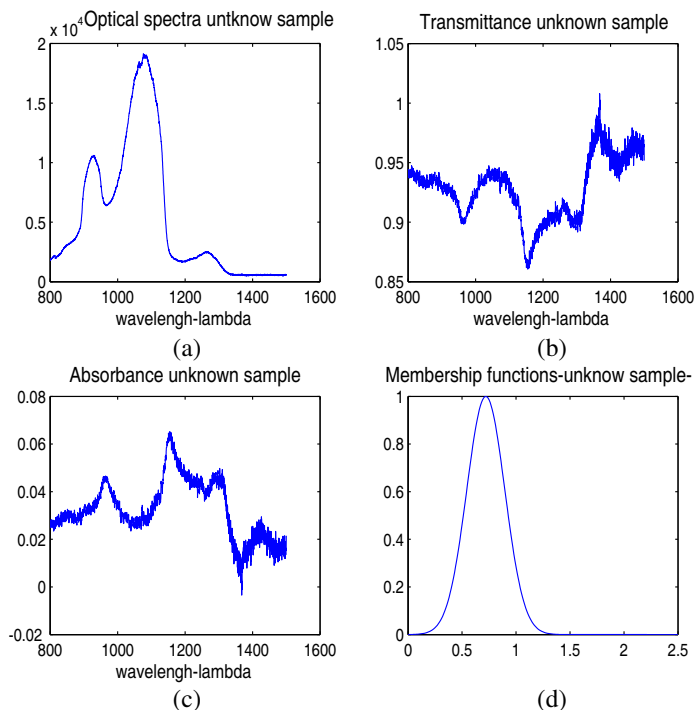


Figure 8: (a) Optical spectra of unknown samples, (b) respective transmittance and (c) absorbance. In Figure 7(c) it is shown the relative Gaussian membership function.

To test the methodology proposed as classifier, it is used an unknown sample. From the measurements through sensor (Figure 8(a)) it is possible to fix the transmittance and the absorbance (Figures 8(b) and 8(c)) and then build the Gaussian membership function (Figure 8(d)). The values of similarity (Figures 10(a) and 10(b)) are comparable with those related to the the third

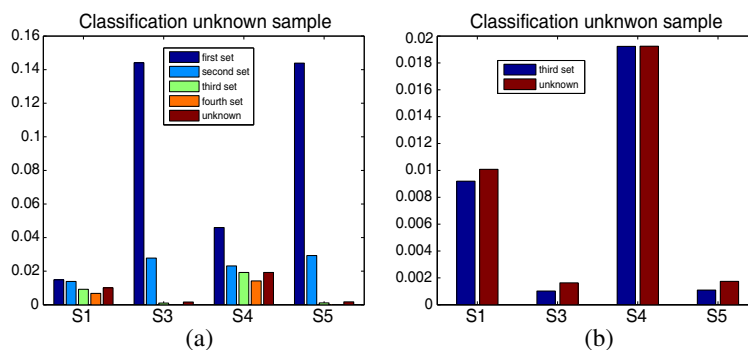


Figure 9: Classification of unknown samples (red bars). The system classifies it as belonging to the third fuzzy set.

fuzzy set: sample #7 with concentration 0.75 (Table 1). The system classifies the sample with a concentration close to 0.75, because the values of similarity are lightly higher than the ones of the sample #7; likely, the value of the concentration of the pollutant is a bit lower than 0.75.

4. CONCLUSION

In the present work, we propose an approach of fuzzy similarity for the detection and the classification of pollutants in water. Starting from measures obtained by using fiber optic sensors and the following optical analysis, they've been implemented five different similarity measures. The results obtained confirm good performances both in terms of detection and classification. A sensor integrated with a fuzzy similarity analysis could represent a useful tool: easy to use and without any implementation of complex procedures. Any technological production would also allow an "situ" analysis.

ACKNOWLEDGMENT

The authors would like to acknowledge Dr. Alessandro Massaro of the Italian Institute of Technology (IIT), for making available all the pollution data in our possession, and Eng. Aimeé Lay Ekaukille of the University of Salento for the useful conversation.

REFERENCES

1. Schwarzenbach, R., et all., "Global water pollution and human health," *Annual Review of Environment and Resources*, Vol. 35, 109–136, 2010.
2. Joniyak, Z. C., "Distance based similarity measures on fuzzy sets," *Proceedings of the third Slovakian-hungarian Joint Symposium on Applied Machine Intelligence, SAMI*, Herl'ani, Slovakia, 2005.
3. Udd, E. and W. B. Spillman, Jr., *Optic Sensors: An Introduction for Engineers and Scientists*, 2nd Edition, Wiley, 18th July 2010.
4. Tversky, A., "A Features of similarity," *Psychological Review*, Vol. 84, No. 4, 327–352, 1977.
5. Chaira, T. and A. K. Ray, *Fuzzy Image Processing and Applications with MatLabr*, CRC Press, 2010.

Uncertainty Calculation for Phase Noise Optoelectronic Metrology Systems

P. Salzenstein and E. Pavlyuchenko

Franche Comté Electronique Thermique Optique Sciences et Technologies (FEMTO-ST)
Centre National de la Recherche Scientifique (CNRS), Besançon, France

Abstract— This paper details how the global uncertainty is calculated for a phase noise optoelectronic system based on a pair of optical delay line and the use of a cross correlation method. The final global uncertainty on the spectral density of phase noise determined by this method is better than 2 dB.

1. INTRODUCTION

In this work, we focus on the determination of the uncertainty of phase noise measurements of signals delivered by optoelectronic oscillators [1, 2]. The developed system works for any Device under test (DUT) that delivers a frequency between 8.2 and 12.4 GHz [3]. It works with optical fiber based delay lines for a laser wavelength at 1.55 μm . The measured phase noise includes the DUT noise and the instrument background. It is interesting to notice that the use of a cross correlation decrease the cross spectrum terms of uncommon phase noise as $\sqrt{(1/m)}$, where m is the average number. When we use cross correlation on 500 samples that lead to the noise floor of the instrument typically in the order of $\mathcal{L}(f)$ is -170 dBc/Hz at 10 kHz from the 10 GHz microwave modulation signal with a 2 km delay lines. We briefly present how the phase noise is determined in the following part and then the estimation of the global uncertainty of this system is described. Two main categories of uncertainties terms are taken into consideration. “htype A”, statistic contribution such as repeatability and experimental standard deviation; “type B” due to various components and temperature control, but also to the asymmetry of the instrument. Uncertainty on $\mathcal{L}(f)$ strongly depends on propagation of uncertainties through the transfer function when the optical fiber are inserted into the system for operation.

2. PRESENTATION OF THE SYSTEM TO BE EVALUATED IN TERMS OF UNCERTAINTY

Full description of the system has been previously done [4], but we found interesting to describe the main aspect of such a system. In this system, the oscillator frequency fluctuation is converted to phase frequency fluctuation through the delay line. Short-term instabilities of signal are usually characterized in terms of the single sideband noise spectral density PSD $S_\varphi(f)$. S is typically expressed in units of decibels below the carrier per hertz (dBc/Hz) and is defined as the ratio between the one-side-band noise power in 1 Hz bandwidth and the carrier power. If the mixer voltage gain coefficient is K_φ (volts/radian), then mixer output rms voltage can be expressed as:

$$V_{out}^2(f) = K_\varphi^2 |H_\varphi(jf)|^2 S_\varphi(f) \quad (1)$$

where $|H_\varphi(jf)|^2 = 4 \cdot \sin^2(\pi f \tau)$ is the transfer function of optical delay line, and f is the offset frequency from the microwave carrier. Eq. (1) shows that the sensitivity of the bench depends directly on K_φ^2 and $|H_\varphi(jf)|$. The first is related to the mixer and the second essentially depends on the delay τ . In practice, we need an FFT analyzer to measure the spectral density of noise amplitude $V_{out}^2(f)/B$, where B is the bandwidth used to calculate $V_{out}(f)/B$. The phase noise of the DUT is finally defined by Eq. (2) and taking into account the gain of DC amplifier G_{DC} as:

$$\mathcal{L}(f) = [V_{out}^2(f)] / [2K_\varphi^2 \cdot |H_\varphi(jf)|^2 G_{DC}^2 B] \quad (2)$$

For the validation of the measure of our phase noise bench, we compare data sheet of the commercial frequency synthesizer Anritsu/Wiltron 69000B [5] with the phase noise we measure using our system. Our bandwidth is limited to 100 kHz ($\tau = 10 \mu\text{s}$) but the measured phase noise corresponds to the datasheet [4].

The background phase noise of the bench is determined after performing 500 averaged with cross-correlation method, when removing the 2 km optical delay line. In this case, phase noise of

the 10 GHz synthesizer is rejected. The noise floor (without optical transfer function) is respectively then better than -150 and -170 dBc/Hz at 10^1 and 10^4 Hz from the 10 GHz carrier. When optical fiber is introduced noise floor of such a system is up to -90 and -170 dBc/Hz at 10^1 and 10^4 Hz from the 10 GHz carrier [6].

3. UNCERTAINTY CALCULATION

For the evaluation of the uncertainty, we use the main guideline delivered by the *Bureau International des Poids et Mesures* (BIPM) in the guide “Evaluation of measurement data — Guide to the expression of uncertainty in measurement” [7]. According to this guideline, the uncertainty in the result of a measurement generally consists of several components which may be grouped into two categories according to the way in which their numerical value is estimated. The first category is called “type *A*”, is those which are evaluated by statistical methods such as reproducibility, repeatability, special consideration about Fast Fourier Transform analysis, and the experimental standard deviation. The components in category *A* are characterized by the estimated variances. Second family of uncertainties contributions is for those which are evaluated by other mean. They are called “type *B*” and due to various components and temperature control. Experience with or general knowledge of the behavior and properties of relevant materials and instruments, manufacturer’s specifications, data provided in calibration and other certificates (noted *BR*), uncertainties assigned to reference data taken from handbooks. The components in category *B* should be characterized by quantities which may be considered as approximations to the corresponding variances, the existence of which is assumed.

3.1. Statistical Contributions

Uncertainty on $\mathcal{L}(f)$ strongly depends on propagation of uncertainties through the transfer function as deduced from Eq. (2). We see here that “type *A*” is the main contribution. For statistical contributions aspects, the global uncertainty is strongly related to repeatability of the measurements. Repeatability (noted *A1*) is the variation in measurements obtained by one person on the same item and under the same conditions. Repeatability conditions include: the same measurement procedure, the same observer, the same measuring instrument, used under the same conditions, repetition over a short period of time, the same location. We switch on all the components of the instrument and perform a measurement keeping the data of the curve. Then we need to switch them off and switch them on again to obtain another curve. We must repeat this action several times until we have ten curves. Elementary term of uncertainty for repeatability is experimentally found to be equal to 0.68 dB.

Other elementary terms still have lower contributions.

Reproducibility, noted *A2*, is the variability of the measurement system caused by differences in operator behavior. Mathematically, it is the variability of the average values obtained by several operators while measuring the same item. The variability of the individual operators are the same, but because each operator has a different bias, the total variability of the measurement system is higher when three operators are used than when one operator is used. When the instrument is connected, there is no change of each component or device inside. That makes this term negligible because, for example, the amplifier is never replaced by another one. We remark that, if one or more of the components would be replaced, it will be necessary to evaluate the influence of the new component on the results of measurements. Main aspect is that operators are the same. In our case, operator don’t change. It means a first approximation we can take 0 dB for this uncertainty.

Uncertainty term due to the number of samples is noted *A3*. It depend on how many points are chosen for each decades. For this term, we check how works the Fast Fourier Transform (FFT) analyzer, it leads to an elementary term of uncertainty less than 0.1 dB.

Finally, statistical contribution can be considered as:

$$A = \sqrt{(\sum A_i)} \quad (3)$$

According to Eq. (3), it can then be considered that the whole statistical contribution is better than 0.69 dB.

3.2. Other Contributions Evaluated by Other Mean

Our system is not yet formally traceable to any standard. Phase noise measurement generally don’t need to be referenced to a standard as the method is intrinsic. So the data provided in calibration and other certificates, noted *BR*, are not applicable. It results that we can take 0 dB as a good approximation of *BR*.

Influence of the gain of the DC amplifier, noted $BL1$, is determined to be less than 0.04 dB.

Temperature effects, noted $BL2$, are less than 0.1 dB as optical fiber regulation system of temperature is turned on.

Resolution of instruments, noted $BL3$, is determined by the value read on each voltmeter when we need to search minimum and maximum for the modulator but also for wattmeter. Resolution is then no worse than 0.1 dB.

The influence of the variation of the power of the Dispositive Under Test (DUT) — oscillator to be characterized for instance during the measurement, noted $BL4$, is negligible while the variation stay limited. It results that we can keep 0 dB as a reasonable value for $BL4$ if the DUT is not too unstable.

Uncertainty on the determination of the coefficient K_φ (noted $BL5$) dependent for the slope expressed in Volt/rad is found to be lower than 0.08 dB.

For the contribution of the use of automatic/manual range, noted $BL6$, we can deduce from experimental curves that this influence is no more than 0.02 dB. In our case, all these terms were found lower than repeatability.

The influence of the chosen input power value of the DUT, noted $BL7$, is negligible as the input power in normal range, i.e., between -4 dBm and $+6$ dBm, has a very limited influence. We experimentally observe an influence. It stay better than 0.02 dB.

Other elementary terms still have lower contributions. BL is the arithmetic sum of each elementary contribution. It is determine to be 0.38 dB.

3.3. Estimation of the Global Uncertainty of This System

Uncertainty at 1 sigma interval of confidence is calculated as follows:

$$uc = \sqrt{A^2 + BR^2 + BL^2} \quad (4)$$

We deduce from Eq. (4) that uncertainty at 1 sigma, noted uc , is better than 0.79 dB. Its leads to a global uncertainty of 1.58 dB at 2 sigma. For convenience and to have an operational uncertainty in case of degradation or drift of any elementary term of uncertainty, it is wise to degrade the global uncertainty. That's why we choose to keep $U = 2$ dB at 2 sigma for a common use of the optoelectronic system for phase noise determination.

4. CONCLUSIONS

Elementary term of uncertainty for repeatability is found to be the main contribution and is up to 0.68 dB at 1 sigma at some Fourier frequency. Other elementary terms still have lower contributions. For instance, temperature effects, resolution of instruments are lower. Its leads to a global uncertainty better than 2 dB at 2 sigma.

ACKNOWLEDGMENT

The authors acknowledge the support of the French National Research Agency (ANR) grant #ANR 2010 BLAN 0312 02.

REFERENCES

1. Tavernier, H., P. Salzenstein, K. Volyanskiy, Y. K. Chembo, and L. Larger, "Magnesium fluoride whispering gallery mode disk-resonators for microwave photonics applications," *IEEE Photonics Technology Letters*, Vol. 22, No. 22, 1629–1631, 2010.
2. Volyanskiy, K., P. Salzenstein, H. Tavernier, M. Pogurmiski, Y. K. Chembo, and L. Larger, "Compact optoelectronic microwave oscillators using ultra-high Q Whispering Gallery mode disk-resonators and phase modulation," *Optics Express*, Vol. 18, No. 21, 22358–22363, 2010.
3. Salzenstein, P., J. Cussey, X. Jouvenceau, H. Tavernier, L. Larger, E. Rubiola, and G. Sauvage, "Realization of a phase noise measurement bench using cross correlation and double optical delay line," *Acta Physica Polonica A*, Vol. 112, No. 5, 1107–1111, 2007.
4. Salzenstein, P., E. Pavlyuchenko, A. Hmima, N. Cholley, M. Zarubin, S. Galliou, Y. K. Chembo, and L. Larger, "Estimation of the uncertainty for a phase noise optoelectronic metrology system," *Physica Scripta*, Vol. T149, 014025, 2012.
5. Typical Datasheet Anritsu 69B Serie Available on Page 8 at the Following Link: http://cem.inrets.fr/private/materiel-labo/images/m_011-doc_gene_65ghz.pdf.

6. Salzenstein, P., N. Cholley, M. Zarubin, E. Pavlyuchenko, A. Hmima, Y. K. Chembo, and L. Larger, “Optoelectronic phase noise system designed for microwaves photonics sources measurements in metrology application,” *Proc. SPIE 8071*, 807111, 2011.
7. GUM: Guide to the Expression of Uncertainty in Measurement, Fundamental Reference Document, JCGM100:2008 (GUM 1995 Minor Corrections): <http://www.bipm.org/en/publications/guides/gum.html>.

Electrophysical Investigation of the Ferroelectric Conductivity in BTO/LCMO Multilayers

A. M. Buryakov¹, M. S. Ivanov¹, E. D. Mishina¹, and V. T. Moshnyaga²

¹Moscow State Technical University of Radioengineering, Electronics and Automation (MSTU-MIREA)
 Prospekt Vernadskogo 78, Moscow 119454, Russia

²I-Physikalisches Institut, Friedrich-Hund-Platz 1
 Universitaet Goettingen, Goettingen D37077, Germany

Abstract— In this paper, we report the electric current and conductivity dependences of ferroelectric layer thickness are studied in a BaTiO₃/LaCaMnO₃ (BTO/LCMO) heterostructures. It is demonstrated that current through the heterostructures has tunneling part of conductivity. For the common current observed decreasing with the increasing ferroelectric layers thickness. Conductivity dependence on applied voltage demonstrated the polarization change with the hysteresis behavior. It is shown that ferroelectricity exists in ferroelectric layer up to four nanometers thickness.

1. INTRODUCTION

In recent years, interest in multiferroics (materials with coexisting magnetic and electrical ordering) has intensified [1–3]. Detailed investigations of a member of the multiferroic class, ferroelectric-magnetic layered structures, have renewed interest in the effect of tunneling electrons via a ferroelectric [4–8]. This effect was first considered in [9] as the basis for a polar switch. Tunnel junctions can be used in spintronic based on the transport properties of spin polarized electrons. Since many multiferroics crystallize to structures similar to magnetic semimetals, they can be combined to form multifunctional epitaxial heterostructures in which a multiferroic layer is used as a magnetic field driven ferroelectric tunnel junction or an electric field driven magnetic tunnel junction [10, 11]. Many multiferroic materials are characterized by high conductivity that could be used for applications in a number of electronic devices. In classification exist two groups of multiferroics: homogeneous and composite. Reporting heterostructures belongs to the group of composite multiferroics, because consist of double layers. The La_{1-x}CaxMnO₃ manganite layer and BaTiO₃ ferroelectric layer were fabricated by metal-organic aerosol deposition technique (MAD) on MgO (100) substrates [12]. In this work, an electrophysical method for investigating the conditions and characteristics of a tunnel current via ferroelectric barrier is proposed. It is shown that in the voltage dependence manifest two parts of current behavior: linear and nonlinear. Different mechanisms of the conductivity's contribution to nonlinear part in the ferroelectric/manganite heterostructure are discussed.

The BTO layer is considered as ferroelectric quantum barrier in BTO/LCMO heterostructures. Investigation heterostructures with the ferroelectric tunnel junction (FTJ) instead of conventional dielectric tunnel junction (DTJ) has some advantages [13]. One of the main and important advantages of FTJ is the spontaneous polarization and the ability to change it with electric field. Thus in multilayer structures provided the opportunity to directly influence on the transport properties in electronic structure of quantum barrier. Another functional feature of ferroelectric barrier is the switching of conductivity associated with depolarization ferroelectric films. When an electric field applied against the quantum barrier polarization the conductivity of a barrier is reduced until the coercive field. Arising shield of the electric field and depolarization ferroelectric film are point to the transport properties of the electron through the FTJ.

2. EXPERIMENT AND RESULTS

Structures LCMO/BTO with respective layer thicknesses of LCMO 12 nm and variable thicknesses of BTO layers (2, 4 and 6 nanometers) are investigated at 80 K temperature. We used this range because the LCMO film underwent a paramagnetic/ferromagnetic phase transition at Curie temperature $T_c = 190$ K and an insulator/conductor phase transition at temperature $T_{MI} = 157$ K. Below the metal-insulator transition temperature (TMI) the BTO layer is dielectric, while the LCMO layer becomes metallic. The ratio between the electric field components in the BTO and LCMO layers is determined by the boundary conditions for tangential field components: $E_{BTO} = E_{LCMO}$. Due

to the electrode configuration there is in-plane and out of plane experiment results are presented. Electrodes were deposited on the BTO film surface and on the LCMO film surface.

For the in plane configuration the electrodes were deposited on the BTO layer surface with a gap of $25\ \mu\text{m}$ as it show on the inset Figure 1. The distribution configuration of electric field is illustrated on the inset too. In that case the principal scheme present as metal — FTJ — manganite — FTJ — metal, i.e., serial connections of FTJ.

Following from the experiments data for all samples two ranges of applied electric field reveal different behavior of electrical parameters. For high fields (from 3 volts), the current-voltage dependence shows ohmic behavior. For low field (up to 3 volts), the current-voltage dependence shows nonlinear behavior. This kind of exponential growth indicates the tunneling current through thin ferroelectric layer. We tried to simulate the nonlinear current behavior with help of Sommerfeld-Bethe method. Unfortunately this method did not fitting enough all the nonlinear current features. Thus it requires an understanding the origins of transport mechanism through BTO layer as from FTJ.

From the voltage dependences follows that increasing of the ferroelectric layer thickness lead to the dramatically current decreasing trough BTO/LCMO heterostructures (Figure 1). As a result for FTJ properties follows if the quantum barrier thickness increasing the tunneling probability through the FTJ is exponentially decreasing.

Thus the nonlinear nature of the current-voltage dependence heterostructures demonstrates tunneling character of the conductivity. In heterostructures BTO/LCMO, the tunneling probabilities of electrons through ferroelectric barrier with a thickness more than 6 nm close to zero. For all of the dependencies there is a nonlinear current part of growth at low voltage. This range corresponds to the mechanism of the quantum tunneling through ferroelectric barrier. With increasing applied voltage dependence becomes a straight line, which corresponds to the contribution of the ohmic conductance through LCMO layer and conduction mechanism through the BTO layer different from the mechanism of quantum tunneling.

For the out of plane configuration the electrodes were deposited on the BTO layer surface and on the LCMO layer surface with a gap of 5 mm as it show on the inset Figure 2. The distribution configuration of electric field is illustrated on the inset too. In that case the principal scheme present as metal — FTJ — manganite, i.e., FTJ with ferromagnetic electrode (MFTJ).

The experimental results of current-voltage dependences the MFTJ heterostructures are shown on Figure 2. Compare the experimental data with the planar geometry experimental data note that tunneling current decreased in the transverse geometry. This fact can be explained by the differences in distance between the electrodes. Analysis of the ferroelectric layer thickness, as in case of serial barriers, the tunneling current shows a decrease with increasing thickness of the barrier. However, the nonlinear part of current-voltage dependences is rather weak and dominated by the linear part. Tunneling through a ferroelectric barrier is manifest in the initial moment of

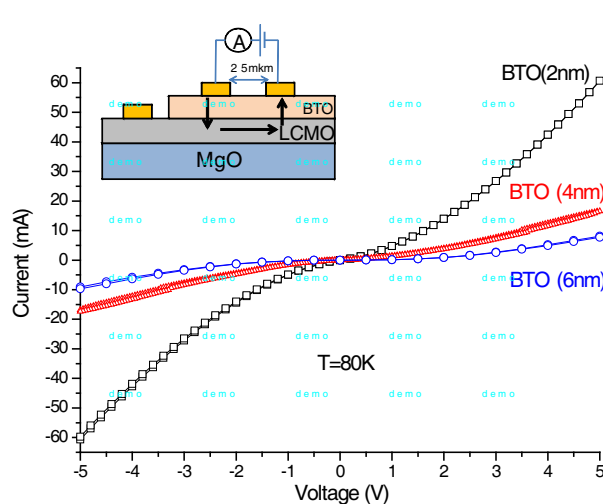


Figure 1: Current-voltage dependence of BTO/LCMO heterostructures (planar geometry of the electrodes).

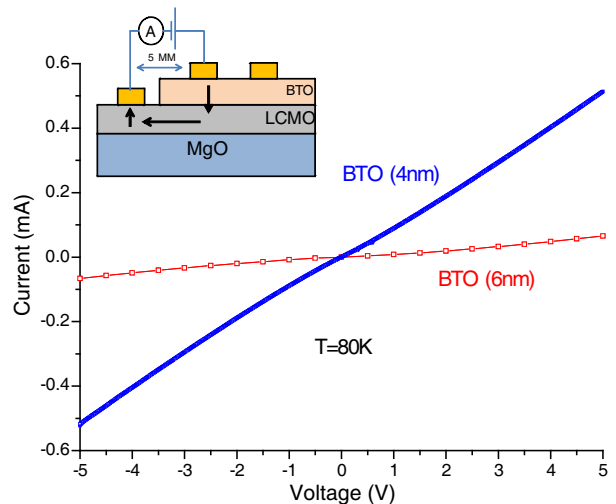


Figure 2: Current-voltage dependence of BTO/LCMO heterostructures (traditional lateral system of electrodes).

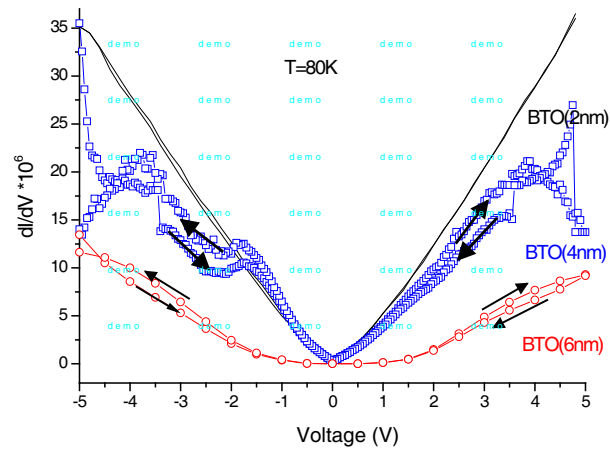


Figure 3: Differential conductivity of BTO/LCMO heterostructures (planar geometry of the electrodes).

applying an electric field, but with the increasing applied voltage the conductivity through LCMO layer becomes the main mechanism.

The question about the ferroelectric polarization arises when the electric field applies to the ferroelectric layer. It is known, that for depolarization ferroelectric polarization is required to apply electric field more than coercive field. However, remains an open question about the critical ferroelectric layer thickness in which there is still a spontaneous polarization exist. In case of existing spontaneous polarization, the next important point is about the possibility of changing the polarization under applied electric field. For the BTO/LCMO heterostructures the main indicator of the ferroelectric film polarization existing is the analysis of conductivity. For this aim differential conductivity of BTO/LCMO heterostructures is shown on Figure 3.

From the dependence follow that conductivity of BTO/LCMO heterostructures increase with the ferroelectric barrier thickness decreasing. Accordingly, the thinner tunnel junction thickness, the easier electrons tunneling through the quantum barrier. Differential conductance dependence is increasing with increase amplitude of the applied electric field. This behavior is explained by the fact that the form of the quantum barrier depends on the applied voltage, i.e., the shape of the barrier is distorted. In turn, the distortions of the quantum barrier shape directly influence on the conductivity properties of FTJ. Polarization properties of BTO/LCMO heterostructures appear with the ferroelectric layers thickness increasing. From the analysis of the differential conductance can be seen when the thickness of the layer BTO 4 nm and 6 nm the divergence at high voltage is observed. The arrows on the figure show the direction of the amplitude applied electric field. Because at the initial moment there was a decrease in the conductivity it follows that own ferroelectric polarization is directed against the direction of applied electric field. When the direction of the electric field changed the BTO/LCMO heterostructures conductivity was decrease, which testifies to the depolarization of a ferroelectric layer. Proceeding from the analysis of experimental results, we can speak about the influence of the ferroelectric quantum barrier polarization on the transport properties in ferroelectric/manganite heterostructure. In BTO/LCMO heterostructures is shown that the ferroelectric properties of the BTO film manifests with a thickness up to four nanometers.

Thus conductivity as well as current in the multilayer with the smallest BTO layer shows increasing with increasing voltage. Although in the samples with 4 nm and 6 nm thickness of the BTO layers the nonlinearity in electric current and conductivity dependences were not so pronounced, the switching of resistivity was found in that structures. We suppose that the observed effect appears due to the polarization formation in the ferroelectric films and the electric dipoles oriented along the electric field. After changes direction of electric field also observed change the polarization, but slowly up to coercive force. Thus we observed the hysteresis in differential conductivity dependence.

3. CONCLUSIONS

In this paper report an investigation of BTO/LCMO heterostructures with the variation of BTO layers is presented. Due to the electrodes configuration the serial connections of FTJ and MFTJ are discussed. For all samples two ranges of applied electric field reveal different behavior of electrical

parameters. For high fields, the current-voltage dependence shows ohmic behavior. For low field, the current-voltage dependence shows nonlinear behavior accompanied by conductance dependence with hysteresis. We attribute this exponential growth to the tunneling current through thin ferroelectric layer. Unfortunately the current-voltage dependence simulated by Sommerfeld-Bethe method was unsuccessful, so another mechanism of BTO film must be involve in the simulation. Conductivity dependence on applied voltage demonstrated the polarization change with the hysteresis behavior. It is shown that ferroelectricity exists in ferroelectric layer up to four nanometers thickness.

ACKNOWLEDGMENT

The authors thank Dr. V. Moshnyagu (University of Goettingen, Germany) for samples manufacturing opportunity provide.

REFERENCES

1. Spaldin, N. A. and M. Fiebig, *Science*, Vol. 309, 391, 2005.
2. Wang, J., H. Zheng, V. Nagarajan, et al., *Science*, Vol. 299, 1719, 2003.
3. Tokura, Y., *Science*, Vol. 312, 1481, 2006.
4. Esaki, L., R. B. Laibowitz, and P. J. Stiles, *IBM Tech. Discl. Bull.*, Vol. 13, 2161, 1971.
5. Qu, H., W. Yao, T. Garcia, et al., *Appl. Phys. Lett.*, Vol. 82, 4322, 2003.
6. Contreras, J. R., H. Kohlstedt, U. Poppe, et al., *Appl. Phys. Lett.*, Vol. 83, 4595, 2003.
7. Wang, J., S. Ju, and Z. Y. Li, *J. Appl. Phys.*, Vol. 105, 093920, 2009.
8. Zhuravlev, M. Y., R. F. Sabirianov, and S. S. Jaswal, *Phys. Rev. Lett.*, Vol. 94, 246802, 2005.
9. Gajek, M., M. Bibes, S. Fusil, et al., *Nature Mater.*, Vol. 6, 296, 2007.
10. Tsymbal, E. Y. and H. Kohlstedt, *Science*, Vol. 313, 181, 2006.
11. Sahoo, S., S. Polisetty, C. G. Duan, et al., *Phys. Rev. B*, Vol. 76, 092108, 2009.
12. Moshnyaga, V., A. Giske, K. Samwer, E. Mishina, et al., *Appl. Phys.*, Vol. 95, 7360, 2004.
13. Tsymbal, E. Y. and H. Kohlstedt, *Science*, Vol. 313, 2006.

Enhanced Magnetization and Second Harmonic Generation in Multiferroic BST/NBFO Superstructures

K. A. Brekhov¹, M. S. Ivanov¹, N. E. Sherstyuk¹, E. D. Mishina¹,
V. M. Mukhortov², and V. T. Moshnyaga³

¹Moscow State Technical University of Radioengineering, Electronics and Automation (MSTU-MIREA)
Prospekt Vernadskogo 78, Moscow 119454, Russia

²South Center RAS, Rostov-on-Don, Russia

³I-Physikalisches Institut, Friedrich-Hund-Platz 1, Universitaet Goettingen, Goettingen D37077, Germany

Abstract— Experimental studies were carried out using optical second harmonic generation (SHG) of the ferroelectric polarization switching process in a multilayer structure of barium strontium titanate/bismuth ferrite, neodymium-doped (BTO/NBFO). Multilayer structures were fabricated by layer-deposition high-frequency sputtering of ceramic targets. The structures reveal higher magnetization in comparison with NBFO film of the same total thickness. Ferroelectric polarization as it reveals itself in the SHG signal is higher than in pure NBFO but lower than in BST film.

1. INTRODUCTION

The practical importance of the multilayer multiferroic systems studying is associated with the prospect for developing devices that are controlled both by the electric and magnetic channel. Multiferroics may be in multiple states, capable of switching in magnetic and electric fields, for example, in polarized/magnetized state, in a state of mechanical stress, etc.. In the case of heterosystems there is an additional opportunity to regulate this interaction by varying the thickness of the films.

During the last decades bismuth ferrite as well as its compounds is the subject of intense interest for the developers of multiferroic structures and magnetoelectric devices. The main characteristics of the material, from a practical point of view, are the high temperatures of the electric ($T_c = 1083$ K) and magnetic ($T_N = 643$ K) ordering, as well as the relatively low conductivity [1, 2]. A giant (~ 3 V/(cm · Oe)) magnetoelectric effect was shown in thin films of bismuth ferrite [3], the observed value being several orders of magnitude higher than those values obtained at room temperature for other materials. Enhancement was also observed for a piezoelectric effect in BFO film as compared to lithium niobate LiNbO_3 and lead zirconate titanate $\text{Pb}(\text{Zr},\text{Ti})\text{O}_3$. The interest to thin films of bismuth ferrite is also explained in several papers (e.g., [4]) by the effect of increasing by more than one order of magnitude of spontaneous polarization as compared with the value in bulk material. Doping BiFeO_3 by different metals results in an enhancement of magnetization and electric polarization [5], piezoelectric and pyroelectric properties as well [6].

This paper presents the results of polarization switching processes investigation by optical second harmonic generation (SHG) in multilayer structures of $(\text{BST}/\text{NBFO})_N$ with different number of layers N and different layer thickness. Magnetization of the multilayer $(\text{BST}/\text{NBFO})_N$ structures is studied as well.

2. THE SAMPLE

Samples of multilayer structures containing alternating layers of ferroelectric ($\text{Ba}_{0.8}\text{Sr}_{0.2}\text{TiO}_3$) and multiferroic ($\text{Nd}_{0.02}:\text{BiFeO}_3$) materials were prepared by Rf sputtering of stoichiometric targets on MgO substrates [7] with the first layer being BST at high oxygen pressures (~ 1 torr) and high specific HF power ($70\text{--}100$ W/cm²) supplied to the sputtering target. The used conditions provide deposition of heteroepitaxial films of very high quality [7], which is confirmed by XRD. Fig. 1 shows the structure of the samples.

Total thickness for both samples was approximately the same. Sample 1 contains 20 alternating layers of BST/NBFO with the thickness of 6 nm, sample 2 consists of 34 layers of BST/NBFO with the thickness of 3 nm.

In [8] it was shown that the influence of BST on film NBFO system appears in changing orientation of the film NBFO relatively to the crystallographic directions of MgO substrate as compared to the case of the BST sublayer absence. For these films, regardless of the thickness of the single

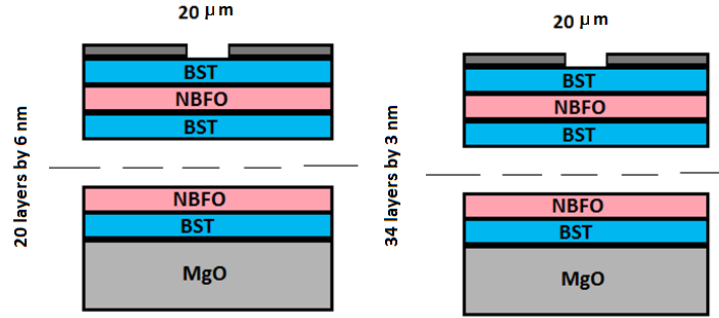


Figure 1: Schematic view of the samples.

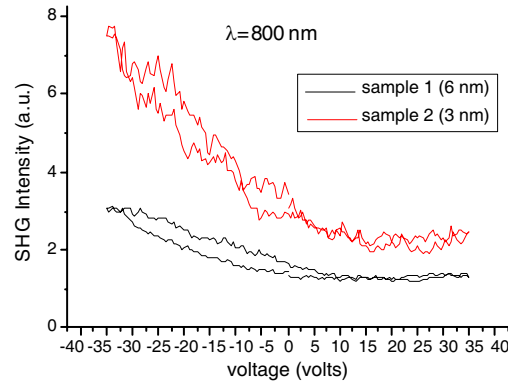


Figure 2: SHG intensity dependence on the applied voltage.

crystalline BST sublayer, a parallel orientation of the axes of the NBFO film and the MgO substrate in the intergrowth plane is observed [8].

To measure dielectric characteristics of the heterostructures, rectangular electrode system with a gap between the electrodes of 20 microns was formed by photolithography. The relatively large area of the electrodes (about 10 mm^2) has provided a higher field homogeneity in the gap. The resistance of the structure is about $10 \text{ M}\Omega$.

For SHG studies a tunable titanium-sapphire laser was used (“Avesta-Project”, Russia), with a pulse duration $\sim 100 \text{ fs}$, average power up to 0.5 W , repetition rate of $\sim 82 \text{ MHz}$ and wavelengths range of $750\text{--}800 \text{ nm}$. The measurements were performed in the transmission geometry. To register the SHG signal, a system consisted of a photomultiplier tube (PMT), an amplifier and photon counter (Stanford Research) was used.

3. THE SECOND HARMONIC GENERATION

Figure 2 shows experimental dependencies of the SHG intensity on the applied voltage which looks like parabola with its minimum shifted from zero voltage and raised on top of some background SHG signal.

In ferroelectrics, parabolic dependences $I_{2\omega}(U)$ can be fitted by equation

$$I_{2\omega} = (C + \alpha U)^2 \quad (1)$$

on top of incoherent background $E_{bg}^{2\omega}$, where C and α are constants [9].

On the other hand, coherent part of SHG intensity in dipole approximation is given by

$$I_{2\omega} = \left(f_{2\omega} \chi^{(2)} f_{\omega} E_{\omega} f_{\omega} E_{\omega} \right)^2, \quad (2)$$

where $\chi^{(2)}$ is second order susceptibility, E_{ω} is the electric field of the incident laser beam, and f_{ω} , $f_{2\omega}$ — appropriate Fresnel factors.

For ferroelectrics $\chi^{(2)}$ may consist of two parts: switchable and nonswitchable. The latter is associated with the constant C , the former can be written as [10] $\chi^{(2)} = \chi^{(0)} P_0 = \chi^{(0)} (\epsilon - 1) \frac{U}{d}$, where P_0 .

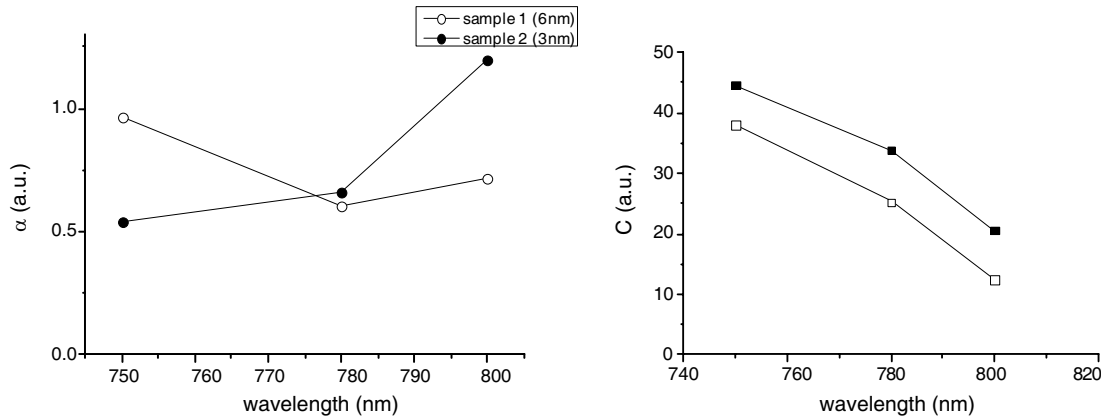


Figure 3: Fitting parameters dependencies on the wavelength.

By comparison (1) and (2) one can get

$$\alpha = \frac{\chi^{(0)}(\varepsilon - 1)}{d} (f_{\omega} E_{\omega} f_{\omega} E_{\omega}).$$

The second “field”-dependent part is the constant L for all experiments independently on the sample (for experiments carried out in the equal conditions), as well as the gap between the electrodes. Then, in arbitrary units $\alpha = \chi^{(0)}(\varepsilon - 1)$.

Figure 3 shows fitting parameters C (nonswitchable polarization) and α .

Figure 3(b) shows that thickness layer increase from 3 nm to 6 nm leads to decrease of non-switchable part of ferroelectric polarization. Also it is shown that coherent part of nonswitchable ferroelectric polarization decreases with increasing wavelength. At the same time a parameter depends on layer thickness: it is increasing for sample 1, and it is decreasing for sample 2.

Studies of nonlinear optical response of multilayer structures by applying the electric field were carried out in the wavelength range 750–800 nm. Increasing absorption at shorter wavelengths increases the contrast and SHG intensity, that allows us to investigate structures with lower layer thickness.

Magnetic properties of the structure have been measured with external field applied parallel to the film plane by SQUID technique. Both magnetic hysteresis loops and temperature dependences of magnetization was measured after the sample cooling down without an external field. Fig. 2 reveals the saturation magnetization of the structures to be about 60 emu/cm³ and coercive field to be about 200 Oe at 10 K. During the heating up to 300 K magnetization decreases about 2 times. Thus, we observed an order of magnitude enhancement of magnetization in the BST/BNFO superlattice structure in comparison with analogous BTO/BFO [11].

4. CONCLUSIONS

Thus, it is shown that BST/NBFO structures have considerable part of non-switchable ferroelectric polarization, analogously to NBFO thin films. Multilayer structures exhibit a much higher degree of asymmetry. This can be explained by the fact that with decreasing film thickness the contribution of non-switching polarization arising due to stress and strain deformation at the interface between layers increases. The difference between the intensities of the SH signal for samples 1 and 2 ($I_1^{2\omega} > I_2^{2\omega}$) is explained by the greater thickness of the layers in the sample 1.

Polarization hysteresis loop obtained by second harmonic generation technique reveals switchability that is lower than for pure BST film, but higher than for pure BNFO film. Sufficient part of nonswitchable polarization is found in superlattices analogously to the pure BNFO film. Both magnetization and ferroelectric polarization are found to possess bulk rather than interface localization.

ACKNOWLEDGMENT

This work was supported by the Russian Foundation of Basic Research and Ministry of Education and Science of Russian Federation (Center for collective users “UNO ‘Electronics’”).

REFERENCES

1. Teague, J. R., R. Gerson, and W. J. James, *Solid State Commun.*, Vol. 8, 1073, 1970.
2. Fischer, P. and M. Polomska, *J. Phys. C: Solid State*, Vol. 13, 1931, 1980.
3. Wang, J., H. Zheng, V. Nagarajan, et al., *Science*, Vol. 299, 1719, 2003.
4. Bai, F., J. Wang, M. Wuttig, J. F. Li, N. Wang, A. Pyatakov, A. K. Zvezdin, L. E. Cross, and D. Viehland, *Appl. Phys. Lett.*, Vol. 86, 032511, 2005.
5. Cheng, J., B. Ruetter, S. Dong, A. P. Pyatakov, A. K. Zvezdin, L. E. Cross, and D. Viehland, *Physical Review B*, Vol. 72, 104434, 2005.
6. Yuan, G. L. and S. W. Or, *Appl. Phys. Lett.*, Vol. 88, 062905, 2006.
7. ???
8. ???
9. ???
10. Dolino, G., J. Lajzerowicz, and M. Vallade, *Physical Review B*, Vol. 2, 2194, 1970.
11. Toupet, H., V. V. Shvartsman, F. LeMarrec, P. Borisov, W. Kleemann, and M. Karkut, “Enhanced magnetization in BiFeO₃/BaTiO₃ multilayers: An interface effect?,” *Integrated Ferroelectrics*, Vol. 100, 165, 2008.

Two Dimensional Nano Photonic Crystals with Metallic Rod and Dielectric Clad in Metallic Background

A. Gharaati and Z. Roozitalab

Department of Physics, Payame Noor University, Tehran, Iran

Abstract— In this paper, dispersion characteristic of two-dimensional metallo-dielectric nano photonic crystal with three refractive indices that containing two metallic-dielectric rods in metallic background is studied base on plane wave expansion method (PWEM). At first, the eigenvalue equation of TM mode is obtained. Then, the influences of radius of inner and thickness and dielectric constant of outer shell on the photonic band gap (PBG) is analyzed, respectively. Our results show that the PBG becomes larger when we use two metallic-dielectric concentric rods in metallic background with plasma frequency and damping constant different from the inner rods. The width of PBG will be increased by enhancement of radius of metal rod, but, whenever the thickness and dielectric constant of dielectric shell increases, this width in PBG has been decreased. All of our calculations have been done by using the Drude model of metal.

1. INTRODUCTION

Recently, great interest has been devoted to the study of two-dimensional (2D) Metallo-dielectric photonic crystals (MDPCs). MDPCs are defined as crystals such that consist of dielectric and metal elements. Compared with dielectric photonic crystals (PCs), the MDPCs have some interesting properties. There is a wide PBG between zero frequency and the cut-off frequency. The inclusion of metallic components can enlarge the size of the gaps and produce flat bands. These structures are interesting for different applications such as a practical filter, polarizer or waveguide, in which the dimensions of metallic 2D MDPCs can be kept much smaller than the minimum dimensions needed for a typical dielectric PC [1, 2]. In this paper, only the E -polarization (TM mode) band gap is considered since there is no band gap or very thin band gap for the H -polarization (TE mode). Here, the PBG formation in 2D MDPCs with three materials is investigated. The photonic structure of such 2D MDPC compose of elements that have three index of refraction, i.e., the background material is metal (silver) and the central rods is metal (copper) with plasma frequency and damping constant different from the background. The rods are covered by a dielectric shell.

The rest of the paper is organized as follows. It has been presented in Section 2, the theory which can modify PWEM for TM mode. In Section 3, it has been shown dispersion curve and influences of radius of copper rod and thickness of dielectric shell on the PBG. Finally the conclusions are given in Section 4.

2. THEORETICAL MODEL

Figure 1 shows the schematic structures of 2D MDPC with square lattice which contain copper rod with dielectric shell in metallic background. The parameters ε_{Cu} , ε_d and ε_{Ag} are dielectric constants of the internal, external rods and background, respectively. R_1 and R_2 are radius of external and internal rods, respectively and the thickness of the dielectric shell is then $R_1 - R_2$. Parameter a is the lattice constant. The photonic band structure calculations were performed along the Γ -X-M- Γ edges of the irreducible Brillouin zone (Figure 1(b)).

Metals are frequency dependent material. We have used the Drude model to describe the dielectric constant of copper and silver as follows [3]

$$\varepsilon_{Cu} = 1 - \frac{\omega_{pCu}^2}{\omega(\omega + i\gamma_{Cu})}, \quad (1)$$

$$\varepsilon_{Ag} = 1 - \frac{\omega_{pAg}^2}{\omega(\omega + i\gamma_{Ag})}, \quad (2)$$

where ω_{pCu} , ω_{pAg} and γ_{Cu} , γ_{Ag} are plasma frequency and damping constant of copper and silver,

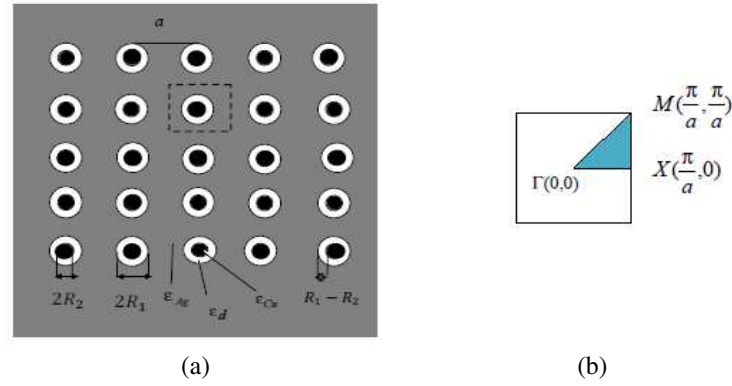


Figure 1: (a) Schematic structures of a unit cell for 2D MDPCs which contain two concentric rods in which the internal and external rods are copper and dielectric, respectively. They arranged in silver background. (b) Irreducible Brillouin zone of the square lattice. The structure of unit cell is indicated by a dashed line. The gray, white and black area represents silver, dielectric and copper, respectively.

respectively. The conventional eigenvalue equation for TM mode in PC can be written as [2, 4]

$$\begin{aligned} |\vec{k} + \vec{G}|^2 E_{z,k}(\vec{G}) &= \frac{\omega^2}{c^2} \sum_{G'} \kappa(\vec{G} - \vec{G}') E_{z,k}(\vec{G}') \\ &= \frac{\omega^2}{c^2} \kappa(0) E_{z,k}(\vec{G}) + \frac{\omega^2}{c^2} \sum_{G \neq G'} \kappa(\vec{G} - \vec{G}') E_{z,k}(\vec{G}'), \end{aligned} \quad (3)$$

where ω is wave frequency; c is the speed of light in vacuum; $E_{z,k}(\vec{G})$ and $\kappa(\vec{G})$ is the Fourier coefficient of electric field and dielectric constant, respectively. The Fourier coefficient of $\kappa(\vec{G})$ can be written as

$$\kappa(\vec{G}) = \begin{cases} (\varepsilon_d - \varepsilon_{\omega Ag})f_1 + (\varepsilon_{\omega Cu} - \varepsilon_d)f_2 + \varepsilon_{\omega Ag} & \text{if } \vec{G} = 0 \\ (\varepsilon_d - \varepsilon_{\omega Ag})2f_1 \frac{J_1(\vec{G}R_1)}{\vec{G}R_1} + (\varepsilon_{\omega Cu} - \varepsilon_d)2f_2 \frac{J_1(\vec{G}R_2)}{\vec{G}R_2} & \text{if } \vec{G} \neq 0 \end{cases}, \quad (4)$$

parameters f_1 and f_2 are $\pi R_1^2/a^2$ and $\pi R_2^2/a^2$. If Eq. (4) is substituted into Eq. (3) to make the transposition, the eigenvalue equation of TM mode can be obtained

$$\sum_{G'} \left\{ \frac{\omega^4}{c^4} + A_{TM} \frac{\omega^3}{c^3} - B_{TM} \frac{\omega^2}{c^2} - C_{TM} \frac{\omega}{c} + D_{TM} \right\} E_{z,k}(\vec{G}') = 0, \quad (5)$$

the complete solution of Eq. (5) is obtained by solving for the eigenvalues of following matrix by the diagonalization of this matrix, where the eigenvalues of this matrix is ω/c . For different wave vectors k , one can obtain a series of eigenfrequencies ω , which compose the band structures of 2D MDPC for TM mode. This matrix is

$$\begin{bmatrix} 0 & I & 0 & 0 \\ 0 & 0 & I & 0 \\ 0 & B_{TE} & -A_{TE} & I \\ -D_{TE} & C_{TE} & 0 & 0 \end{bmatrix} \quad (6)$$

where the elements of the matrices A_{TM} , B_{TM} and C_{TM} are given by

$$A_{TM} = \frac{(i\gamma_b + i\gamma_d)}{c} I, \quad (7a)$$

$$B_{TM} = (N^{-1})M + \frac{\gamma_d \gamma_b}{c^2} I, \quad (7b)$$

$$C_{TM} = \begin{cases} -\frac{i\gamma_d}{c} \frac{\omega_{pb}^2}{c^2} 2f_1 \frac{J_1(|\vec{G}-\vec{G}'|R_1)}{|\vec{G}-\vec{G}'|R_1} + \frac{i\gamma_b}{c} \frac{\omega_{pd}^2}{c^2} 2f_2 \frac{J_1(|\vec{G}-\vec{G}'|R_2)}{|\vec{G}-\vec{G}'|R_2} & \text{if } \vec{G} \neq \vec{G}' \\ \frac{(i\gamma_b+i\gamma_d)}{c} |\vec{k} + \vec{G}|^2 - \frac{i\gamma_d}{c} \frac{\omega_{pb}^2}{c^2} f_1 + \frac{i\gamma_b}{c} \frac{\omega_{pd}^2}{c^2} f_2 + \frac{i\gamma_d}{c} \frac{\omega_{pb}^2}{c^2} & \text{if } \vec{G} = \vec{G}' \end{cases}, \quad (7c)$$

$$D_{TM} = (N^{-1}) \frac{i\gamma}{c} |\vec{k} + \vec{G}|^2, \quad (7d)$$

$$N = \begin{cases} (\varepsilon_d - 1) 2f_1 \frac{J_1(|\vec{G}-\vec{G}'|R_1)}{|\vec{G}-\vec{G}'|R_1} + (1 - \varepsilon_d) 2f_2 \frac{J_1(|\vec{G}-\vec{G}'|R_2)}{|\vec{G}-\vec{G}'|R_2} & \text{if } \vec{G} \neq \vec{G}' \\ (\varepsilon_d - 1) f_1 + (1 - \varepsilon_d) f_2 + 1 & \text{if } \vec{G} = \vec{G}' \end{cases}, \quad (7e)$$

$$M = \begin{cases} -\frac{\omega_{pb}^2}{c^2} 2f_1 \frac{J_1(|\vec{G}-\vec{G}'|R_1)}{|\vec{G}-\vec{G}'|R_1} + \frac{\omega_{pd}^2}{c^2} 2f_2 \frac{J_1(|\vec{G}-\vec{G}'|R_2)}{|\vec{G}-\vec{G}'|R_2} & \text{if } \vec{G} \neq \vec{G}' \\ |\vec{k} + \vec{G}|^2 + \frac{\omega_{pb}^2}{c^2} - \frac{\omega_{pd}^2}{c^2} f_1 + \frac{\omega_{pd}^2}{c^2} f_2 & \text{if } \vec{G} = \vec{G}' \end{cases}, \quad (7f)$$

$$I = \delta_{\vec{G}, \vec{G}'}. \quad (7g)$$

3. RESULTS AND DISCUSSION

In this work, internal rod is taken to be copper (Cu) with the plasma frequency $\omega_{pCu} = 2\pi \times 1.194 \times 10^{15}$ rad/s and damping constant $\gamma_{Cu} = 2\pi \times 8.34 \times 10^{12}$ rad/s, external rod is Na_3AlF_6 in which dielectric constant is $\varepsilon_d = 1.7956$ and background is silver (Ag) with the plasma frequency $\omega_{pAg} = 2\pi \times 2.175 \times 10^{15}$ rad/s and damping constant $\gamma_{Ag} = 2\pi \times 4.35 \times 10^{12}$ rad/s [6]. Figure 2 has shown dispersion curves of TM mode in which radii of external and internal rods are $R_1 = 0.3a$ and $R_2 = 0.15a$, respectively. Lattice constant is $a = 300$ nm. In Figure 2, the structure with $R_1 = 0.3a$ and $R_2 = 0.15a$ can lead to five PBGs; TM_{0-1} (the gap between the zero frequency and cut-off frequency), TM_{1-2} , TM_{2-3} , TM_{4-5} and TM_{6-7} . We give the ranges of BGs (BGR) in Table 1.

3.1. Effect of Radius of Internal Rod and Thickness of the Shell on PBG

Figures 3(a) and 3(b) show the variation of the Radius of internal (copper) rod and thickness of the dielectric (Na_3AlF_6) shell on PBGs, respectively. We can see, when space averaged of copper rod becomes higher as radius of this rod increases; these PBGs seem to become large, see Figure 3(a), but when space averaged of dielectric shell increases the width of their decreases, see Figure 3(b).

Table 1: The BGR in Figure 2 for TM mode.

	TM_{0-1} $\omega a/2\pi c$	TM_{1-2} $\omega a/2\pi c$	TM_{2-3} $\omega a/2\pi c$	TM_{4-5} $\omega a/2\pi c$	TM_{6-7} $\omega a/2\pi c$
BGR	0-1.198	1.198-1.381	1.381-1.712	1.715-2.089	2.095-2.217

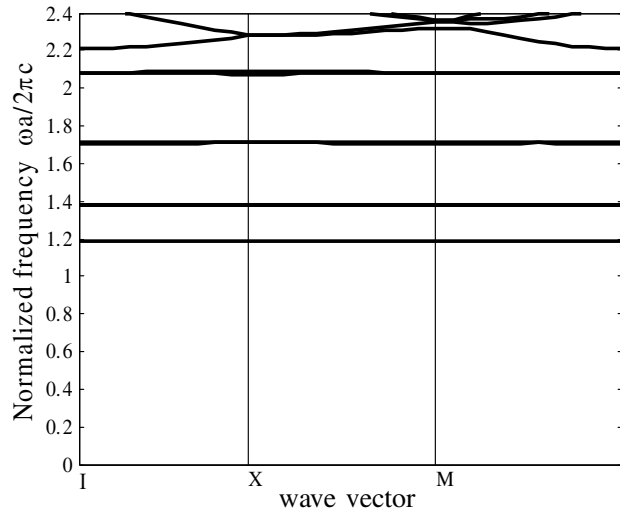


Figure 2: Dispersion curve for the above-mentioned structure.

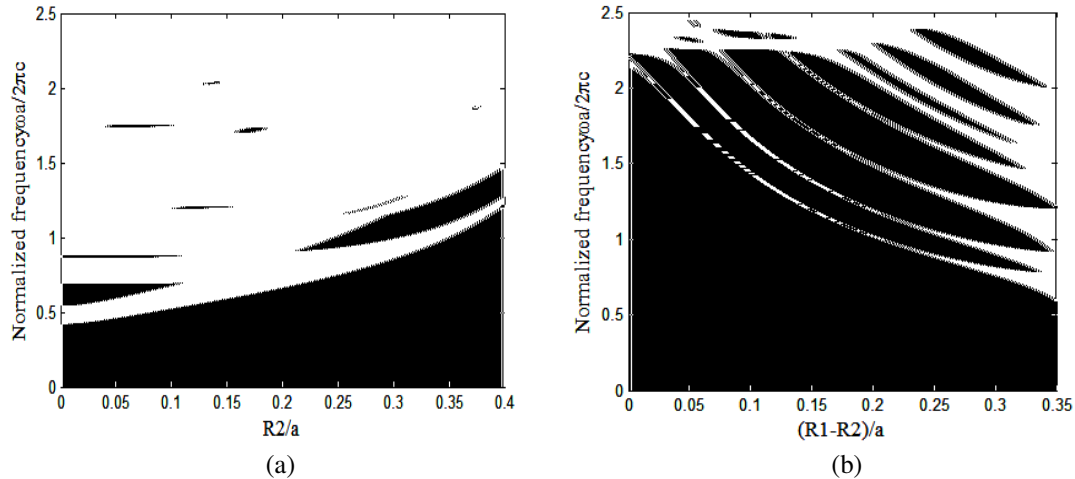


Figure 3: Gap maps; (a) the normalized frequency versus the radius of copper rod R_2/a , when the radius of dielectric (Na_3AlF_6) rod fixed at $R_1/a = 0.5$. (b) The normalized frequency versus the thickness of the dielectric (Na_3AlF_6) shell $(R_1 - R_2)/a$, when the radius of copper rod fixed at $R_2/a = 0.15$. In both figures, $a = 300$ nm.

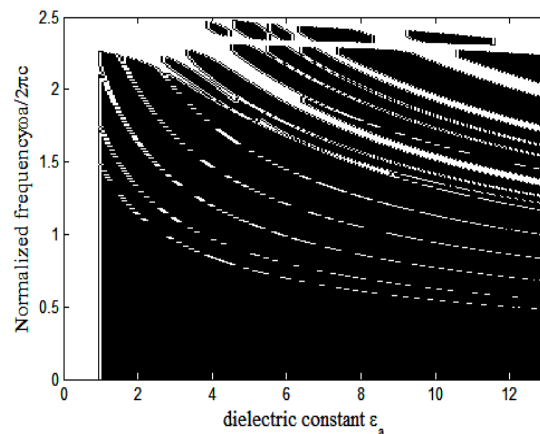


Figure 4: Gap map; the normalized frequency versus the dielectric constant of dielectric rod ϵ_d . Radii of external and internal rods fixed at $R_1/a = 0.35$ and $R_2/a = 0.15$, dielectric constant of internal rod and background are ϵ_{Cu} and ϵ_{Ag} , respectively.

3.2. Effect of Dielectric Constant on PBG

Figure 4 shows the effect of dielectric constant ϵ_d of dielectric shell on the PBG. We can see, when dielectric constant increases, the width of PBG without TM_{0-1} , has increased faster for lower ϵ_d , but when ϵ_d increases, they decrease, because of the higher dielectric contrasts between metal and dielectric will easily lead to large gaps [4].

4. CONCLUSIONS

In conclusion, different dispersion characteristic of 2D MDPC is studied based on modified PWEM. Results have shown that when we use two metallic-dielectric concentric rods in metallic background with plasma frequency and damping constant different from the inner rods; the gap width increased as compared to the same crystal made from simple dielectric rods. The width of PBG will be increased by enhancement of radius of metal rod, but, whenever the thickness and dielectric constant of dielectric shell increases, it has been decreased. These results may provide theoretical instructions for designing new PC devices using metallic-dielectric structure.

ACKNOWLEDGMENT

This work has been financially supported by the Payame Noor University (PNU) I. R. of Iran under the grant No. 1390/3/0/14/185.

REFERENCES

1. Sakoda, K., *Optical Properties of Photonic Crystals*, Springer-Verlag, Berlin, 2001.
2. Qi, L. and Z. Yang, “Modified plane wave method analysis of dielectric plasma photonic crystal,” *Progress In Electromagnetic Research*, Vol. 91, 319–330, 2009.
3. Jackson, J. D., *Classical Electrodynamics*, 3rd Edition, John Wiley & Sons, Inc., California University, NY, 1999.
4. Skorobogatiy, M. and J. Yang, *Fundamentals of Photonic Crystal Guiding*, Cambridge University Press, Cambridge, 2009.
5. El-Kady, I., M. M. Sigalas, R. Biswas, K. M. Ho, and C. M. Soukoulis, “Metallic photonic crystals at optical wavelengths,” *Physical Review B*, Vol. 62, No. 23, 15299–15302, 2000.

The Study of Two Dimensional Photonic Crystal Made of Two Concentric Cylindrical Nano-layers of Dielectric with Negative Refraction Index

A. Gharati and L. M. Ebrahimi

Department of Physics, Payame Noor University, Tehran, Iran

Abstract— In this paper, we study the propagation of electromagnetic wave in 2D photonic crystal (PC) made of two concentric cylinders of dielectric with the negative refraction index for TM mode in two kind structures. Applying the boundary conditions in Maxwell equation in periodic structures, we change this equation to Helmholtz equation. By solving this equation in two dimensions and using plane wave expansion method (PWEM), we can find the band gaps and allowed modes. We consider two structures with two concentric cylindrical rods; the external rod in the first structure consists of negative refraction index material while in the second structure it is made of a dielectric material. It is shown that by increasing the diameter of the cylinder which is composed of negative refraction index material in both structures, we can obtain wider band gaps in compare to the structures which there is no negative refractive index materials.

1. INTRODUCTION

In the past decade, there has been much research activity relating to PCs. They are periodic dielectric structures with an index of refraction periodicity of the order of the wavelength of light. There are three kinds of PCs: one-, two- and three dimensional (1D, 2D and 3D). They can prohibit the propagation of electromagnetic waves within a certain frequency range so the light can be totally reflected. Such forbidden band called PBGs which is similar to the electronic band gaps for electrons in semiconductors [1–3]. In 2000, Smith and coworkers [4] demonstrated in their work that it is possible to fabricate an artificial metamaterial with electrodynamic characteristics that can be described by a negative index of refraction. NRMs are artificial composites characterized by both negative dielectric permittivity and negative magnetic permeability in some frequency ranges [5]. In these metamaterials the direction of Poynting vector, $\vec{S} = \vec{E} \times \vec{H}$, is opposite to the wave vector \vec{k} , so the wave vector and refractive index should be negative then, \vec{k} , \vec{E} and \vec{H} form a left-handed set of vectors [6].

2. THEORETICAL MODEL

In this section, we investigate the negative refraction of electromagnetic waves in a 2D PC. We have considered two structures. The first consists of concentric cylindrical rod and shell in which the radius of the rod is R_1 ($R_2 > R_1$) and its dielectric permittivity is ε_{n1} and the radius of the shell is R_2 with dielectric permittivity ε_d , in a negative refractive index background ε_{n2} , Figure 1(a). The second one is the same as the first but the place of rod and shell has been interchanged, and this structure is in a dielectric background ε_{d2} , Figure 1(b).

Here we consider band gaps of 2D PC based on Helmholtz equation in which they are calculated by using well-known software such as Matlab based on PWEM method. we change the radii of cylinders and the refraction indexes of them then we study the band gaps. According to this point, the simulated results of the band structure for TM and TE modes of 2D PC are demonstrated. The plane wave expansion method leads to the following equations [7]:

$$TM : \sum_{G'} \kappa (G - G') |k_t + G'|^2 E_{z,k_t} (G') = \omega_{k_t}^2 E_{z,k_t} (G) \quad (1)$$

$$TE : \sum_{G'} \kappa (G - G') (k_t + G') (k_t + G) H_{z,k_t} (G') = \omega_{k_t}^2 H_{z,k_t} (G) \quad (2)$$

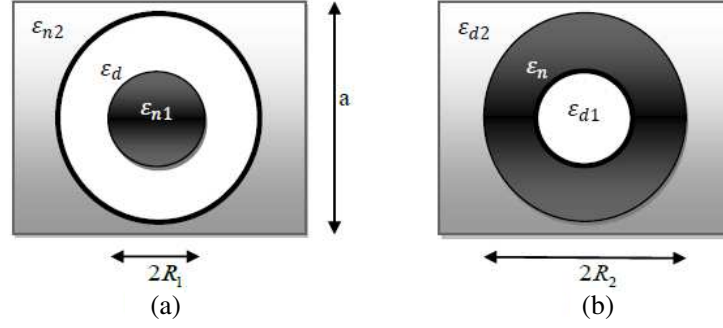


Figure 1: Schematic structures of concentric rod and shell with radius R_1 and R_2 , ($R_2 > R_1$) and (a) in the first structure the rod filled with negative refractive index, ε_{n1} and the shell with positive refractive index, ε_d , and the dielectric permittivity background is ε_{n2} but (b) in the second structure the rod filled with positive refractive index, ε_{d1} and the shell with negative refractive index, ε_n , and the dielectric permittivity background is ε_{d2} .

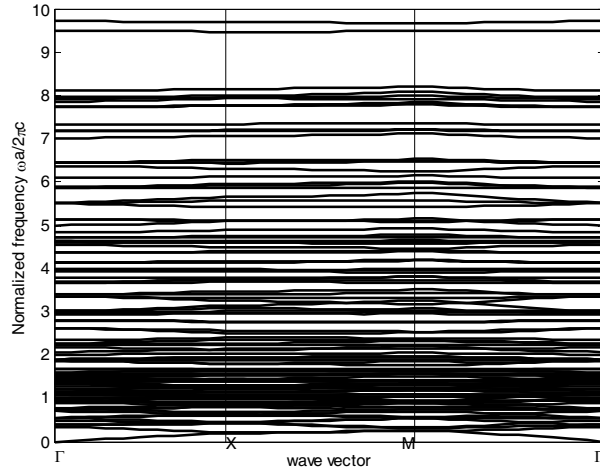


Figure 2: The band structure of the first structure for TM mode, $\varepsilon_d = 12$, $\varepsilon_{n1} = -1.4$, $\varepsilon_{n2} = -1$, $R_1 = 0.3a$ and $R_2 = 0.5a$.

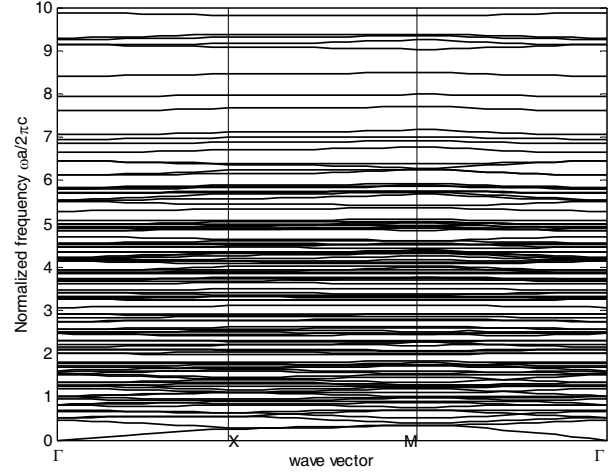


Figure 3: The band structure of the first structure for TM mode, $\varepsilon_d = 12$, $\varepsilon_{n1} = -1.4$, $\varepsilon_{n2} = -1$, $R_1 = 0.4a$ and $R_2 = 0.5a$.

in which Fourier coefficient for the first structure is the product of $\kappa_\varepsilon(G - G')$ to $\kappa_\mu(G - G')$

$$\kappa_\varepsilon(G - G') \equiv \left\{ \begin{array}{ll} (\varepsilon_{n1} - \varepsilon_d)f_1 + (\varepsilon_d - \varepsilon_{n2})f_2 + \varepsilon_{n2} & \text{if } G = G' \\ (\varepsilon_{n1} - \varepsilon_d)2f_1 \frac{J_1(GR_1)}{GR_1} + (\varepsilon_d - \varepsilon_{n2})2f_2 \frac{J_1(GR_2)}{GR_2} & \text{if } G \neq G' \end{array} \right\} \quad (3)$$

$$\kappa_\mu(G - G') \equiv \left\{ \begin{array}{ll} (\mu_{n1} - \mu_d)f_1 + (\mu_d - \mu_{n2})f_2 + \mu_{n2} & \text{if } G = G' \\ (\mu_{n1} - \mu_d)2f_1 \frac{J_1(GR_1)}{GR_1} + (\mu_d - \mu_{n2})2f_2 \frac{J_1(GR_2)}{GR_2} & \text{if } G \neq G' \end{array} \right\} \quad (4)$$

and for the second structure is a gain the product of $\kappa_\varepsilon(G - G')$ to $\kappa_\mu(G - G')$

$$\kappa_\varepsilon(G - G') \equiv \left\{ \begin{array}{ll} (\varepsilon_{d1} - \varepsilon_n)f_1 + (\varepsilon_n - \varepsilon_{d2})f_2 + \varepsilon_{d2} & \text{if } G = G' \\ (\varepsilon_{d1} - \varepsilon_n)2f_1 \frac{J_1(GR_1)}{GR_1} + (\varepsilon_n - \varepsilon_{d2})2f_2 \frac{J_1(GR_2)}{GR_2} & \text{if } G \neq G' \end{array} \right\} \quad (5)$$

$$\kappa_\mu(G - G') \equiv \left\{ \begin{array}{ll} (\mu_{d1} - \mu_n)f_1 + (\mu_n - \mu_{d2})f_2 + \mu_{d2} & \text{if } G = G' \\ (\mu_{d1} - \mu_n)2f_1 \frac{J_1(GR_1)}{GR_1} + (\mu_n - \mu_{d2})2f_2 \frac{J_1(GR_2)}{GR_2} & \text{if } G \neq G' \end{array} \right\} \quad (6)$$

where the radius of the cylindrical rod, shell and the lattice constant are R_1 , R_2 and a , respectively. Also, f_1 and f_2 are given by $f_1 = \pi R_1^2/a^2$ and $f_2 = \pi R_2^2/a^2$.

3. NUMERICAL RESULTS AND DISCUSSION

In this section, we have investigated band gaps for both structures in TM and TE modes by using of Equations (1) and (2). First structure consists of concentric cylindrical rod and shell with radii R_1 and R_2 , ($R_2 > R_1$), $\varepsilon_d = 12$, $\varepsilon_{n1} = -1.4$ and $\varepsilon_{n2} = -1$. We have changed the radius of the rod. We assume that $R_2 = 0.5a$ then we have changed R_1 from 0.1 to $0.5a$ by step 0.1. First, we have drawn the band structure for TM mode. We can observe that by increasing the radius of the rod, the number of the band gaps increase and we obtain wider band gaps in compare to the structure with positive refractive index (Figures 2 and 3).

Now, we have investigated the band structures for TE mode.

Again, we consider that $R_2 = 0.5a$ and we have changed R_1 from 0.1 to $0.5a$ by step 0.1. As we see, in Figures 4 and 5, by increasing the radius of the rode, the number of band gaps increase.

On the other hand, Second structure consists of concentric cylindrical rod and shell with radii R_1 and R_2 , ($R_2 > R_1$), $\varepsilon_{d1} = 12$, $\varepsilon_n = -1.4$ and $\varepsilon_{d2} = 8.9$. In this case, we consider $R_1 = 0.1a$ and we have changed R_2 from $0.2a$ to $0.5a$ by step 0.1. By increasing the radius of the shell which is made of negative refractive index material, we obtain many and width band gaps, as it has been shown in Figures 6, 7, 8 and 9.

Finally, we investigate the band structures of TE mode for the second structure. Again, we consider $R_1 = 0.1a$ and we have changed the radius of the shell R_2 from $0.2a$ to $0.5a$ by step 0.1.

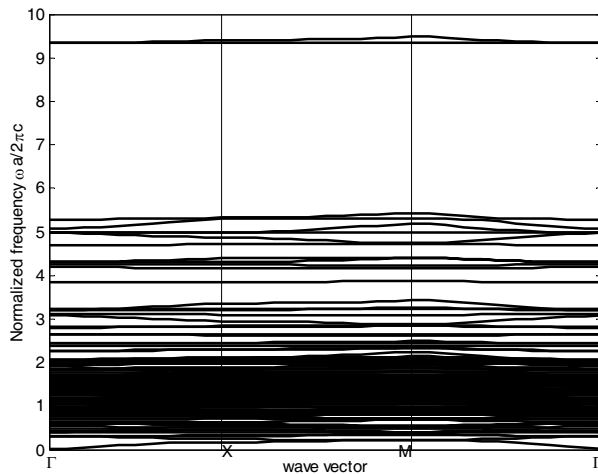


Figure 4: The band structure of the first structure for TE mode, $\varepsilon_d = 12$, $\varepsilon_{n1} = -1.4$, $\varepsilon_{n2} = -1$, $R_1 = 0.1a$ and $R_2 = 0.5a$.

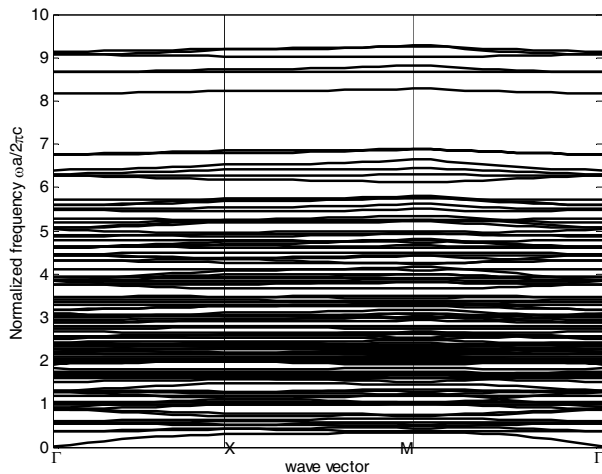


Figure 5: The band structure of the first structure for TE mode, $\varepsilon_d = 12$, $\varepsilon_{n1} = -1.4$, $\varepsilon_{n2} = -1$, $R_1 = 0.4a$ and $R_2 = 0.5a$.

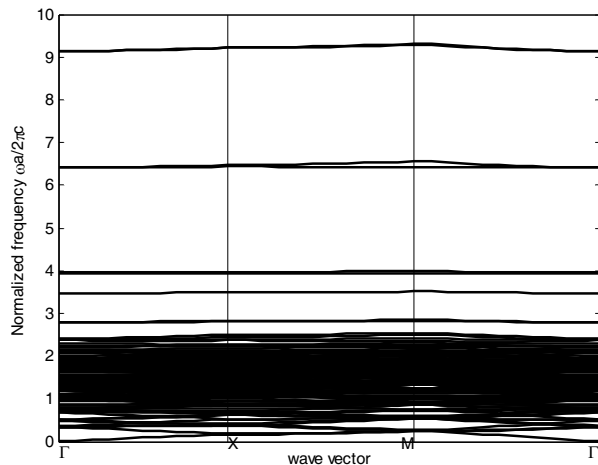


Figure 6: The band structure of the second structure for TM mode, $\varepsilon_d = 12$, $\varepsilon_{n1} = -1.4$, $\varepsilon_{d2} = 8.9$, $R_1 = 0.1a$ and $R_2 = 0.2a$.

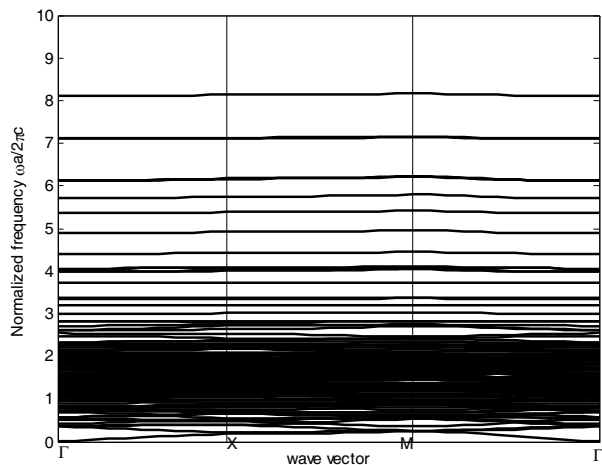


Figure 7: The band structure of the second structure for TM mode, $\varepsilon_d = 12$, $\varepsilon_{n1} = -1.4$, $\varepsilon_{d2} = 8.9$, $R_1 = 0.1a$ and $R_2 = 0.3a$.

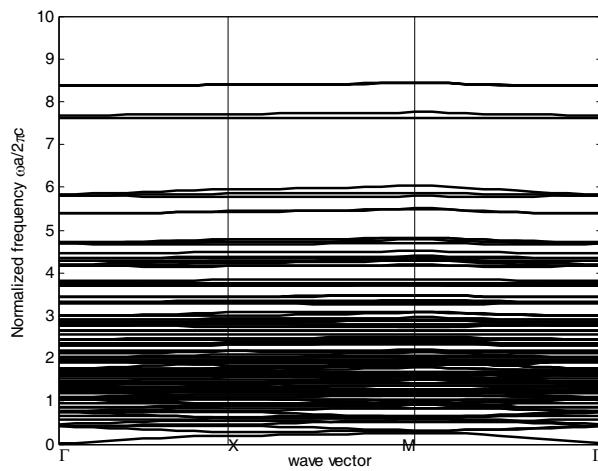


Figure 8: The band structure of the second structure for TM mode, $\varepsilon_d = 12$, $\varepsilon_{n1} = -1.4$, $\varepsilon_{d2} = 8.9$, $R_1 = 0.1a$ and $R_2 = 0.4a$.

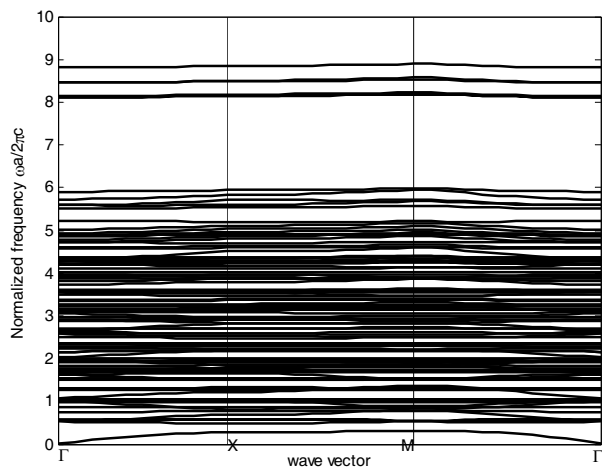


Figure 9: The band structure of the second structure for TM mode, $\varepsilon_d = 12$, $\varepsilon_{n1} = -1.4$, $\varepsilon_{d2} = 8.9$, $R_1 = 0.1a$ and $R_2 = 0.5a$.

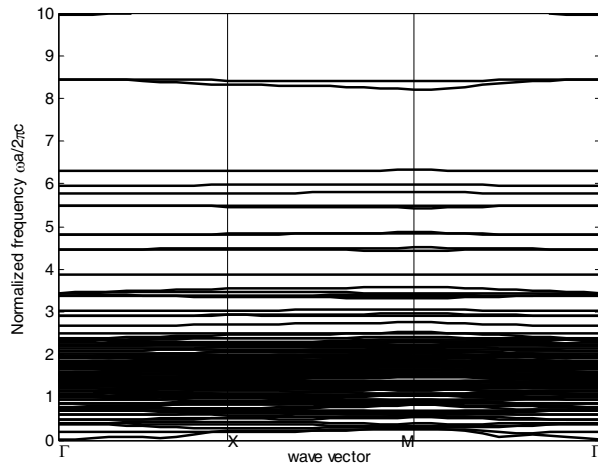


Figure 10: The band structure of the second structure for TE mode, $\varepsilon_d = 12$, $\varepsilon_{n1} = -1.4$, $\varepsilon_{d2} = 8.9$, $R_1 = 0.1a$ and $R_2 = 0.3a$.

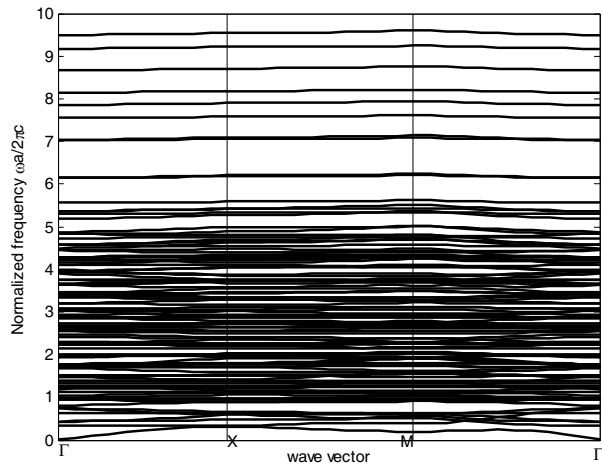


Figure 11: The band structure of the second structure for TE mode, $\varepsilon_d = 12$, $\varepsilon_{n1} = -1.4$, $\varepsilon_{d2} = 8.9$, $R_1 = 0.1a$ and $R_2 = 0.5a$.

As we expected, we see that by increasing the radius of the shell which is composed of meta-material, the number of band gaps increase (Figures 10 and 11).

4. CONCLUSION

In conclusion, by drawing the band structures of two special structures of 2D PCs, we observed that by increasing the radius of the rod and shell in the first and second structures, respectively, we have obtained more and wider band gaps in compare to the structures with positive refractive index material. And it is just because of the existing of negative refractive index material in these structures.

ACKNOWLEDGMENT

This work has been financially supported by the Payame Noor University (PNU) I. R. of Iran under the grant No. 1390/3/0/14/185.

REFERENCES

1. Saleh, B. E. A. and M. C. Teich, *Fundamental of Photonics*, 2nd Edition, Wiley, 2nd Edition, E' cole Polytechnique de Montre' al, Canada University of Vermont, USA, 2007.
2. Sukhovanov, A. and V. Guryev, *Photonic Crystals Physics and Practical Modeling*, Springer Series in Optical Science, New York, 2009.

3. Joannopoulos, J. D., P. R. Villeneuve, and S. Fan, “Photonic crystals: Putting a new twist on light,” *Nature*, Vol. 386, 143–149, London, 1997.
4. Smith, D. R., W. J. Padilla, D. C. Vier, S. C. Nemat-Nasser, and S. Schultz, “A composite medium with simultaneously negative permeability and permittivity,” *Phys. Rev. Lett.*, Vol. 84, No. 18, 4184–4187, 2000.
5. Pendry, J. B., A. J. Holden, W. J. Stewart, and I. Youngs, “Extremely low frequency plasmons in metallic mesostructures,” *Phys. Rev. Lett.*, Vol. 76, 4773–4776, 1996.
6. Marquardt, P. and C. M. Soukoulis, *Wave Propagation from Electrons to Photonic Crystals and Left-handed Materials*, Princeton University Press, Canada, 2008.
7. Skorobogatiy, M. and J. Yang, *Fundamentals of Photonic Crystal Guiding*, 1st Edition, Cambridge University Press, 2009.

Investigation of Defect Modes on One-dimensional Ternary Metallic-dielectric Nano Photonic Crystal with Metallic Defect Layer

Abdolrasoul Gharraati and Hadis Azarshab

Department of Physics, Payame Noor University, Tehran, Iran

Abstract— We investigate the characterization of defect mode in one-dimensional ternary metallic-dielectric photonic crystal structures. The defect layer is made of metallic material. We consider defect mode for both symmetric and asymmetric geometries. Additionally, we demonstrate reflectance in terms of wavelength and its dependence on different angles of incidence for both transverse electric (TE) and transverse magnetic (TM) waves. There is just one defect mode when we use metallic defect layer. All of our calculations have done with transfer matrix method (TMM) and the Drude model of metals.

1. INTRODUCTION

In recent years, advances in photonic technology have caused so much attention. The simplest possible photonic crystal consists of alternating layers of material with different dielectric constants [1]. A one dimensional ternary metallic-dielectric photonic crystal (1DTMDPC) is a periodic structure containing dielectric and metallic elements with different index of refraction. 1DPCs because of its simple fabrication has many applications such as multilayer's coatings [2], narrow band filters, and so on. A range of frequency in which light cannot propagate through the PC is called photonic band gaps (PBG). We have used TMM to calculate the transmitted and reflected coefficients of incident electromagnetic waves.

In this paper, using TMM, we calculate the defect mode wavelength. We apply this method to 1DPC consisting of periodically dielectric-metal-dielectric with metallic defect layer for both TE and TM waves.

2. THEORETICAL ANALYSIS

A 1DTMDPC with a structure of $A/(n_1n_2n_3)^N D(n_3n_2n_1)^N/A$, for symmetric geometry and $A/(n_1n_2n_3)^N D(n_1n_2n_3)^N/A$, for asymmetric geometry, where A and N mean the usual air and the number of periods, and n_1 , n_2 and n_3 are the refractive indices of dielectric, metal and dielectric layers, respectively. 1DTMDPC is made of N -period cells immersed in air ($n_A = 1$) in which the metallic layer 2 is sandwiched by two dielectric layers 1 and 3 in each cell. The Drude model [3] is invoked to characterize the wavelength dependence of metallic layer. We assume that the temporal part of the field to be $\exp(-i\omega t)$. So metal permittivity in Drude model is

$$\varepsilon_2(\omega) = 1 - \frac{\omega_p^2}{\omega^2 + i\gamma\omega} \quad (1)$$

where ω_p and γ are the plasma frequency and damping coefficient, respectively. Then metal refractive index is given by $n_2 = \sqrt{\varepsilon_2}$. A one layer in Fig. 2 along with the components of the electric and magnetic fields of the incident, reflected, and transmitted wave [7].

Using Maxwell equations we have the relations $k_0 = \omega\sqrt{\mu_0\varepsilon_0}$, where it is the wave vector in the air, $B = n\sqrt{\varepsilon_0\mu_0}E$, $p_\ell = n_\ell \cos \theta_\ell$, $\beta_\ell = k_0 n_\ell d_\ell \cos \theta_\ell$, where $\ell = 1, 2$, and 3. So, the electric fields become: $E_{i2} = E_{t1} \exp(-i\beta_\ell)$ and $E_{i1} = E_{r2} \exp(-i\beta_\ell)$ and when included in the boundary conditions, E_{t1} and E_{i1} can be solved in terms of E_a and B_b :

$$E_{i1} = \frac{(p_1 E_b + B_b)}{2p_1} \exp(-i\beta_\ell), \quad E_{t1} = \frac{(p_1 E_b + B_b)}{2p_1} \exp(i\beta_\ell). \quad (2)$$

And finally, substituting the above expressions in the initial fields components and written in matrix form, we have

$$\begin{pmatrix} E_a \\ B_a \end{pmatrix} = \begin{pmatrix} \cos \beta_\ell & \frac{-i}{p_\ell} \sin \beta_\ell \\ -ip_\ell \sin \beta_\ell & \cos \beta_\ell \end{pmatrix} \begin{pmatrix} E_1 \\ B_1 \end{pmatrix} = M_1 \begin{pmatrix} E_1 \\ B_1 \end{pmatrix} \quad (3)$$

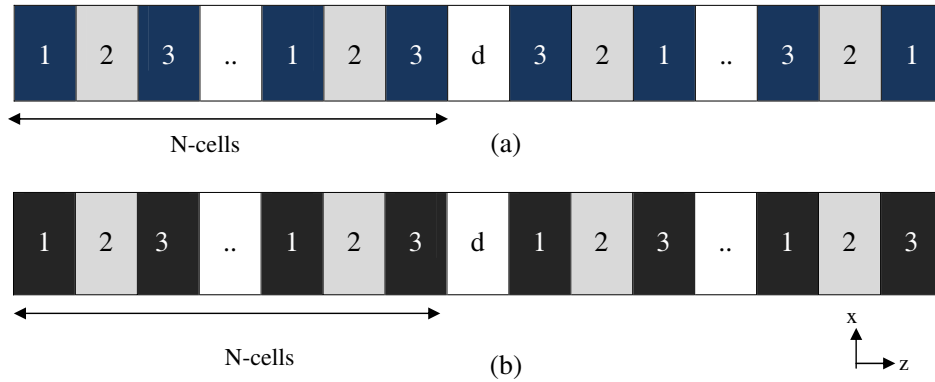


Figure 1: (a) The structure of symmetric 1DTMDPC. (b) The structure of asymmetric 1DTMDPCs.

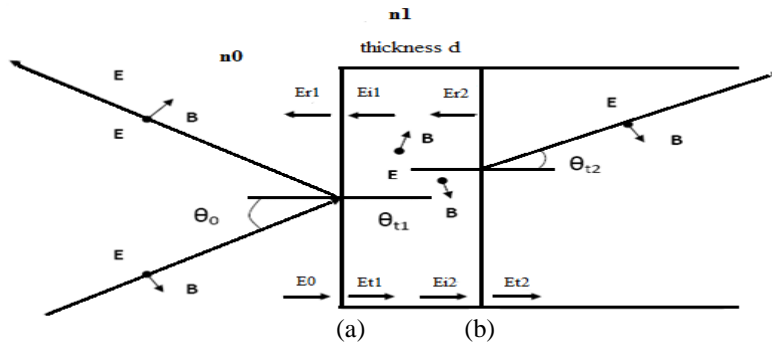


Figure 2: A schematic of one layer of 1DTMDPC.

Each layer of PC has its own transfer matrix and the overall transfer matrix of the system is the product of individual transfer matrices, so the characteristics matrix $M(\Lambda)$ for a single period is expressed as [4]

$$M(\Lambda) = \begin{bmatrix} M_{11} & M_{12} \\ M_{21} & M_{22} \end{bmatrix} = \prod_{\ell=1}^3 \begin{bmatrix} \cos \beta_{\ell} & \frac{1}{ip_{\ell}} \sin \beta_{\ell} \\ -ip_{\ell} \sin \beta_{\ell} & \cos \beta_{\ell} \end{bmatrix} \quad (4)$$

On the basis of Bloch theorem, the half trace is used to compute the Bloch wave vector [3, 4].

$$a = \frac{(M_{11} + M_{22})}{2} = \cos \beta_1 \cos \beta_2 \cos \beta_3 - \frac{1}{2} \left(\frac{p_1}{p_2} + \frac{p_2}{p_1} \right) \sin \beta_1 \sin \beta_2 \cos \beta_3 - \frac{1}{2} \left(\frac{p_2}{p_3} + \frac{p_3}{p_2} \right) \cos \beta_1 \sin \beta_2 \sin \beta_3 - \frac{1}{2} \left(\frac{p_1}{p_3} + \frac{p_3}{p_1} \right) \sin \beta_1 \cos \beta_2 \sin \beta_3 \quad (5)$$

Then, the total characteristic matrix of the total PC is given by [4]

$$M_T(N\Lambda) = \begin{bmatrix} m_{11} & m_{12} \\ m_{21} & m_{22} \end{bmatrix} = M(\Lambda)^N = \begin{bmatrix} M_{11} & M_{12} \\ M_{21} & M_{22} \end{bmatrix}^N, \quad (6)$$

The reflection coefficient r is given by [7]

$$r = \frac{(m_{11} + m_{12}p_0)p_0 - (m_{21} + m_{22}p_0)}{(m_{11} + m_{12}p_0)p_0 + (m_{21} + m_{22}p_0)} \quad (7)$$

where $p_0 = n_0 \cos \theta_0$. We can calculate the reflectance $R = |r|^2$. The above calculations can be used for TM wave by substituting $p_{\ell} = \cos \theta_{\ell}/n_{\ell}$ where $\ell = 0, 1, 2$, and 3, respectively. So the characteristic Matrix of Left and Right unit cells with the number of periods equal N in symmetric

and asymmetric geometry is given by [5]

$$M_{cellL} = (M_3 \cdot M_2 \cdot M_1)^N, \quad M_{cellR} = (M_1 \cdot M_2 \cdot M_3)^N \quad (8)$$

$$M_{cellL} = M_{cellR} = (M_3 \cdot M_2 \cdot M_1)^N \quad (9)$$

And therefore defect matrix (M_{def}) is given by Eq. (4).

Then the characteristics matrix of entire system is expressed as

$$M_{tot} = M_{cellR} \cdot M_{def} \cdot M_{cellL} \quad (10)$$

3. NUMERICAL RESULTS AND DISCUSSION

In this paper, the layers 1 and 3 are ZnSe and Na_3AlF_6 which refractive indices and thicknesses are $n_1 = 2.6$, $d_1 = 90$ nm, $n_3 = 1.34$, $d_3 = 90$ nm, respectively [6]. The metallic layer is taken to be silver (Ag) with the plasma frequency $\omega_p = 2\pi \times 2.175 \times 10^{15}$ rad/s [7], $d_2 = 10$ nm. The thickness of defect layer is $d_{def} = 10$ nm and its index of refraction is calculated with $n_d \cdot d_{def} = q\lambda_0/4$, with a design wavelength of $\lambda_0 = 1550$ nm in infrared region. The number of periods for right and left cells is equal. The substrate is assumed to be air with $n_A = 1$.

3.1. Defect Modes in 1DSTMDPC with Metallic Defect Layer

In Fig. 3, we plot the reflectance response for symmetric 1DTMDPC (1DSTMDPC) as shown in Fig. 1, at different angles of incidence at $d_{def} = 10$ nm, and $N = 5$ for TE wave. We see that defect mode move to the shorter wavelengths with increasing angle of incidence.

We now in Fig. 4 show wavelength-dependant reflectance of 1DSTMDPC with the structure of $(A/(n_1n_2n_3)^5 d(n_3n_2n_1)^5/A)$ for TM-wave. For normal incidence, that is at 0° , there is no difference between TE and TM waves. We see that resonant peak move to the left (shorter wavelengths) as the angle of incidence increases. We give the wavelength of the defect modes for different angles of incidence in TE and TM wave in Table 1.

As we see in Table 1 defect mode move to the shorter wavelengths for TE wave as compared with TM wave in 1DSTMDPC.

3.2. Defect Modes in 1DATMDPC with Metallic Defect Layer

In Fig. 5, we plot the reflectance response for asymmetric 1DTMDPC (1DATMDPC). We see defect mode move to the shorter wavelengths with increasing angles of incidence.

We show in Fig. 6 wavelength-dependant reflectance of 1DATMDPC with the structure of $(A/(n_1n_2n_3)^5 d(n_1n_2n_3)^5/A)$ for TM-wave. For normal incidence, that is at 0° , there is no difference between TE and TM wave. We see that resonant peak move to the left (shorter wavelengths) as

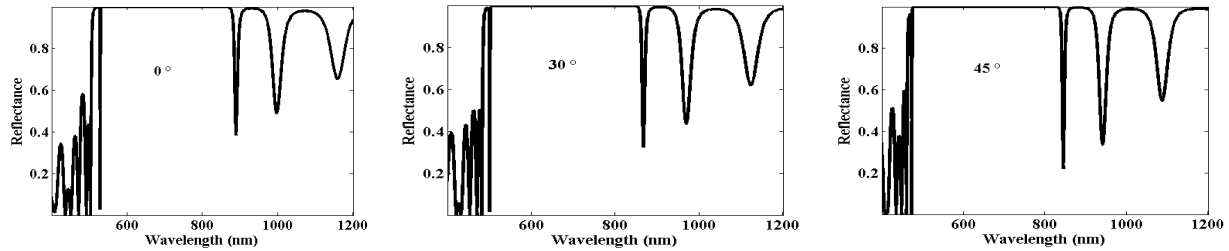


Figure 3: The calculated wavelength-dependant reflectance for the 1DSTMDPC for TE-wave.

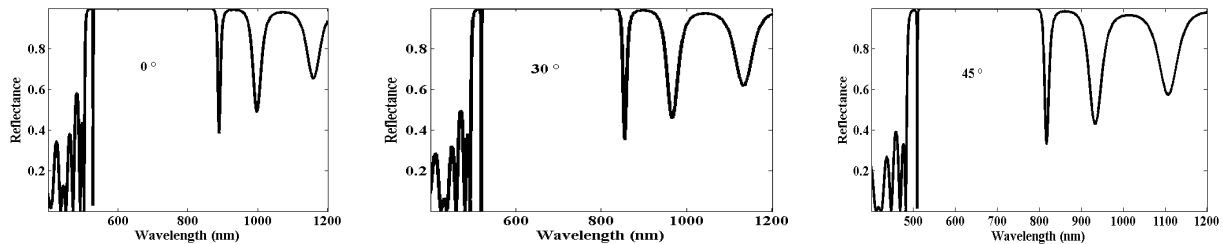


Figure 4: The calculated wavelength-dependant reflectance in 1DSTMDPC for TM-wave.

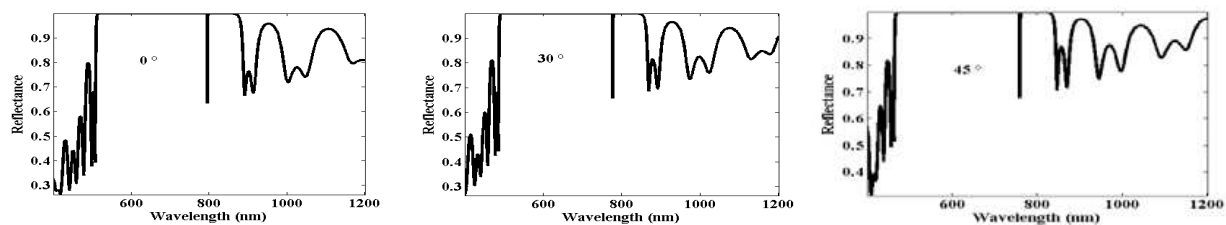


Figure 5: The calculated wavelength-dependant reflectance for the 1DATMDPC for TE-wave.

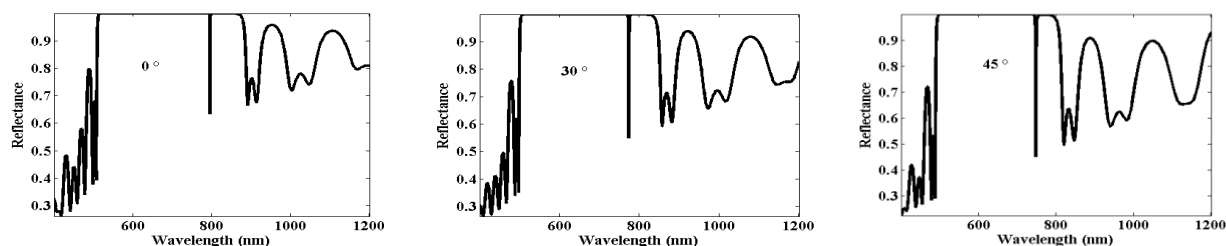


Figure 6: The calculated wavelength-dependant reflectance for the 1DATMDPC for TM-wave.

Table 1: The location of defect mode in 1DSTMDPC by changing angle of incidence.

Angels (degree)	Wavelength in TE wave (\sim nm)	Wavelength in TM wave (\sim nm)
0°	529	529
15°	521	526
30°	501	519
45°	473	509
60°	446	499
75°	427	490

Table 2: The location of defect mode in 1DATMDPC by changing angles of incidence.

Angels (degree)	Wavelength in TE wave (\sim nm)	Wavelength in TM wave (\sim nm)
0°	795	795
15°	790	790
30°	778	774
45°	759	748
60°	740	716
75°	726	690

the angle of incidence increases. We give the wavelength of the defect modes for different angles of incidence in TE and TM wave in Table 2.

As we see in Table 2 defect mode in 1DATMDPC move to the shorter wavelengths for TM wave as compared with TE wave.

4. CONCLUSION

In this paper, we have studied properties of defect modes in 1DTMDPC. Defect layer is made of metallic element with structure $A/(n_1n_2n_3)^5d(n_3n_2n_1)^5/A$ for symmetric geometry and $A/(n_1n_2n_3)^5d(n_1n_2n_3)^5/A$ for asymmetric geometry. As we have shown, there is just one defect mode for metallic defect layer. Moreover defect modes move to the shorter wavelengths for TE and TM waves, but, defect mode move to the shorter wavelengths for TE wave in 1DSTMDPC as compared with TM wave. Also, defect mode move to the shorter wavelengths for TM wave in 1DATMDPC as compared with TE wave in this structure.

REFERENCES

1. Joannopoulos, J. D., R. D. Meade, and J. N. Winn, *Photonic Crystals: Molding the Flow of Light*, Princeton University Press, Princeton, NJ, 1995.
2. Szipocs, R., K. Ferencz, C. Spielmann, and F. Krausz, “Chirped multilayer coatings for broadband dispersion control in femtosecond lasers,” *Optics Letters*, Vol. 19, No. 3, 201–203, 1994.
3. Wu, C. J., Y.-H. Chung, and B. J. Syu, “Band gap extension in a one-dimensional ternary metal-dielectric photonic crystal,” *Progress In Electromagnetics Research*, Vol. 102, 81–93, 2010.
4. Born, M. and E. Wolf, *Principles of Optics*, Cambridge, London, 1999.
5. Saleh, B. E. A. and M. C. Teich, *Fundamentals of Photonics*, Wiley, New York, 2007.
6. Orfanidis, S. J., *Electromagnetic Waves and Antennas*, Rutgers University, NJ, 2008.
7. Gharaati, A. and H. Azarshab, “Characterization of defect modes in one-dimensional ternary metallo-dielectric nanolayered photonic crystal,” *Progress In Electromagnetics Research B*, Vol. 37, 125–141, 2012.

Optimum Parameters for an Undersampled Digitally Heterodyned SFGPR

D. Adirosi¹, G. Alberti², and G. Galiero²

¹Thales Alenia Space Italia, Italy

²Consortium for Research on Advanced Remote Sensing Systems — CO.R.I.S.T.A., Italy

Abstract— A key aspect of a previously proposed undersampled digitally heterodyned stepped frequency GPR is the capability to generate and acquire a large band of frequencies. This is obtained by moving most of the analog domain functionalities of the SFGPR into the digital one. The necessity to generate a large bandwidth is to achieve high resolution. In this paper, an analysis of the aliased images generated by the needed digital frequency generator is performed. In this paper a procedure based on the method presented in [2] is developed. It allows to choose and to analyze the best set of values of the parameters characterizing the SFGPR. The analysis was performed with the aid of software tools developed ad hoc in a high level language. The key aspects of the analysis and its main results are discussed and illustrated.

1. INTRODUCTION

It is well known that the capability of electromagnetic waves to propagate beyond the physical discontinuities of propagation media makes it possible to exploit them to investigate internal features of dielectric bodies. From this property, an endless number of practical applications have been arisen, ranging from medical prospecting to detection of mines, nondestructive testing of industrial items and GPR applications.

In [1], a new architecture of an Undersampled Digitally Heterodyned SFGPR with variable sampling frequency was presented. The key aspects and the advantages of the new architecture were presented and discussed: signal generation by means of DAC; undersampling of the echoes by means of a large bandwidth ADC with a planned step by step varying sampling frequency; digital quadrature demodulation of the undersampled echoes.

In [2] an analysis of the proposed SFGPR's parameters set was performed to indicate a procedure to choose their best values. In this paper an analysis of the aliased images generated by the needed digital frequency generator is performed. Its necessity is dictated by the large bandwidth nature of the described SFGPR. The analysis has been performed with the aid of software tools developed ad hoc in a high level language (LabViewTM).

The key aspects of the performed analysis as well as its main results shall be discussed and illustrated.

2. ANALYSED ARCHITECTURE

The SFGPR architecture presented in [1] and analysed in this paper (shown in Figure 1) is an heterodyned GPR where the quadrature downconversion is performed digitally on the undersampled signals. This choice allows to alleviate not only the problems typical of homodyne GPR related to the flicker noise (in that the frequency of the signal to be sampled is always greater than 0 Hz, i.e., 1 MHz) and to the drift of DC values with the temperature but also the problems related to the quadrature demodulation in that it is performed in the digital domain instead of the analog one by direct acquisition of the IF signal. A brief description of the main blocks is given below:

Transmitting Chain (Tx Chain): the signal to be transmitted is generated by means of a DAC, its output is low pass filtered and amplified prior to be sent to the transmitting antenna. The clock of the DAC is provided by a frequency generation unit;

Receiving Chain (Rx Chain): the signal received by the antenna is amplified by an LNA and provided to a large band ADC; the signal is undersampled with sampling frequencies provided by the FGU. The samples acquired are transferred to an FPGA whose aim is to perform the quadrature downconversion in the digital domain; the local oscillator of this downconverter is chosen according to the frequency of the transmitted signal and to the planned sampling frequency; its phase takes into account the possibility of spectral inversion of undersampled signals also;

Frequency Generation Unit (FGU): aim of this unit is to generate all the frequencies employed in the SFGPR from a very low phase noise master oscillator: DAC and ADC clocks, FPGA reference clock.

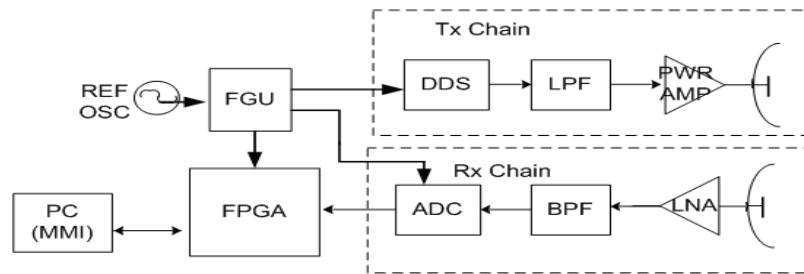


Figure 1: SFGPR architecture presented in this paper.

The SFGPR architecture presented has the following advantages:

- Absence of a synchronism chain, generally used in SFGPR to get a phase reference of the transmitted signal;
- Simplified RF front end: both Tx and Rx chains are substantially constituted by an amplifier and a filter; this is allowed by the undersampling of the received echoes;
- Simplified Frequency Generation Unit;
- Substantial reduction of the power consumption and weight due to the great simplification brought in the RF front end;
- Flexible architecture with respect of the possible frequency bands to use. In fact the constraints on which bands to use are mainly due to DAC and ADC 3-dB bandwidths; nowadays are present on the market DACs capable to generate frequencies even in the second and third Nyquist zone as well as ADC with input bandwidth as large as 3 GHz. This allows the employment of the same SFGPR in large band of investigation frequencies and with very large synthesized bandwidth. This peculiarity of the architecture presented will be even more enhanced in the near future with the advent of integrated circuits with increased input/output bandwidths as the trend of the last years has indicated.

In [1] it was also remarked that the achievement of the mentioned goals has been possible by moving SFGPR complexities from the analog domain into the digital one.

3. ALIASED IMAGES ANALYSIS PERFORMED

Due to the wide bandwidth nature of the described SFGPR an aliased images analysis is needed. The intrinsic advantages achievable by moving GPR complexities from the analog domain into the digital one have the side effect to potentially “move” aliased images into the useful intermediate frequency band if a suitable frequency plan is not performed in advance. The mentioned analysis has been performed with the aid of the “normalised acceptable bandpass sampling rates” map [3]: for each frequency step to be generated the first three aliased images are reported on it; these are $f_{s_DDS} - f_i$, $f_{s_DDS} + f_i$, $2f_{s_DDS} - f_i$ where f_i indicates the generic step frequency and f_{s_DDS} is the sampling frequency of the DDS. In order to filter out them once the digital quadrature downconversion shall be performed they have to fall outside the prohibited band; this is a band centered around the useful intermediate frequency and with a bandwidth related to the transition band desired for the digital LPF to be implemented. Generally these frequencies fall into regions different from the one the useful intermediate frequency falls in (both identified by different values of the parameter m [3]); this can lead to a different choice of the sampling frequency values due to the different slope of the map’s lines and it can solve the problem of aliased images falling into the useful intermediate frequency band when it happens.

In [4] this analysis was performed by following a sort of “brute force” approach, that is the results attainable were simulated and checked against the allowed bandwidth. This approach allowed to define a first attempt set of values for the procedures developed in this paper and to verify its validity but there was no way to show if the set chosen was the best one or not and if it was far from being an optimum choice. In this paper a completely different approach has been followed by using the “normalised acceptable bandpass sampling rates” map [3]. By plotting in this map the different frequencies steps to be generated as well as the aliased images digitally generated, it is possible to determine the best combination and the number of sampling frequencies to be used, where best means the values that allow to relax the requirements on the anti-alias filters in the

analog domain as well as the digital low pass filters following the digital quadrature demodulator. The outline of the procedure followed in this paper, and implemented with the aid of ad hoc software tools, is:

- a first attempt set of values is provided by the analysis performed previously [1, 4];
- for each sampling frequency of the interval provided in input, the following computations are performed on the “normalised acceptable bandpass sampling rates” map:
 1. for each frequency step to be generated its distance from the left boundary line of the mentioned map is computed;
 2. the same distances are computed for all the “spurious” frequencies associated to the step frequency of the previous point;
 3. differences among each distance of the point 2 with respect to the distance computed in point 1 are computed.
 4. the minimum of the differences of the previous point shall provide the final result for the couple of frequencies considered: sampling and step one.
- once all the computations of the previous step are performed the output will be a matrix representing (for each possible couple of step frequency and sampling one) the minimum distance among the step frequency and its “spurious”.

The procedure just described is based on the following property of the “normalised acceptable bandpass sampling rates” map: for a fixed normalised sampling frequency (K), it is possible to demonstrate that the extension of the allowed zone for the undersampled frequencies is constant and that it depends only on the values of K .

In the following table are reported the value of the SFGFPR parameters used for the analysis shown in the next paragraph.

4. ANALYSIS RESULTS

In order to clarify the above mentioned procedure the results of the analysis performed are reported in Figure 2. The parameters used to get the results shown are reported in Table 1. The results consist in a matrix on whose column and row indexes reports, respectively, the step frequency and the sampling ones set. Each element of this matrix reports the minimum distance among the correspondent frequency step and the “spurious” for the chosen sampling frequency (i.e., for the selected row); if a matrix cell reports -1 it means that the correspondent step frequency can not be sampled suitably by the chosen sampling frequency.

The best result is obtained by selecting the single sampling frequency (if available) or set of them that provide the highest distance for each step frequency allowing, in this way, to set an higher transition bandwidth for the antialiasing LPF filters. By looking at the results shown in Figure 2 different conclusions can be deduced:

- if for each step frequency it is chosen the sampling frequency producing the maximum distance, it can be observed that as transition bandwidth of the LPF can be chosen 2.5 MHz (if the maximum step frequency is limited to 240 MHz) or 2 MHz (by including the 250 MHz). For the mentioned step the sampling frequencies are: 21 MHz, 24 MHz, 26 MHz, 27 MHz, 29 MHz. The inclusion of the step frequency 260 MHz would reduce the transition bandwidth to 1 MHz.
- if as sampling frequencies are chosen 26 MHz and 27 MHz it is possible to see that the minimum distance reported for all step frequencies is 2 MHz (if the maximum step frequency is limited to 250 MHz), and this would be the transition bandwidth allowed for the LPF filters.

Table 1: SFPGR frequency generation main parameters.

PARAMETER	VALUE
F_Start	100 MHz
Step Frequency	10 MHz
Number of Steps	19
Sampling Frequencies	26 MHz/27 MHz
F_DDS	1100 MHz

Prediction of a New Superconductivity-like Effect in Galilean Reference Systems (Part II)

Namık Yener

Technology Faculty, Kocaeli University, Izmit, Kocaeli 41380, Turkey

Abstract— Prediction of a hitherto unknown superconductivity-like effect is made which is independent of temperature, but rather requires Galilean reference systems moving at the speed of light in vacuum. As the medium (I) to which the laboratory frame is attached, a Lorentz medium is selected whereas for medium (II) to which the rest frame is attached, a perfectly conducting medium is selected. The interface is an infinite plane perpendicular to the uniform rectilinear motion involved. The fact that the Lorentz medium appears as a metal when observed from the rest frame, is unearthed in a previously reported work by the same author. Next the limit condition which in effect requires attainment of speed of light in vacuum by the uniform rectilinear motions of the Galilean reference systems is considered, and the effective permittivity function of medium (I) observed from the rest frame is found to have a character similar to that of a superconductor. It should be stressed that the fundamental premise of the work is Lorentzian relativistic transformation and not Galilean relativistic transformation under which the permittivity function could have been invariant. This work is presented in a series of two papers. In Part (I) the models for medium (I) observed from the laboratory frame and the rest frame are presented. In Part (II) the prediction of the new superconductivity-like effect is made and equations with the same structure as London equations in a superconductor are presented. Also included in this Part is a discussion proving that the dispersion relation for medium (I) observed from the rest frame can be split as a permittivity function and a permeability that is equal to that observed from the laboratory frame, which is but the permeability of free space.

1. INTRODUCTION

Equation (23d) of Part I [1] has a two-fold significance. First differing from a dispersion relation it does not contain the wave number k_1' although it contains the frequency ω' . This aspect allows it to be sufficient to negate the Special Relativity Theory. Indeed variation of α and r with changing relative speeds of K and K' will force c and c' to vary as well because all other quantities appearing in (23d) of Part (I) are material properties or the frequency ω' . In the future publication mentioned in the Introduction section of Part I, we shall demonstrate that ω' is a free parameter that can be introduced through choice of boundary conditions of the electromagnetic system at hand, and the only alternative is that c and c' vary as relative speeds of K and K' do.

Secondly, if solved for $\frac{c}{c'}\omega'$ in which it is a cubic, (23d) of Part I yields three solution sets:

$$(i) \quad \frac{c}{c'}\omega' = -i\frac{1}{2\gamma} [\alpha\omega_0^2 + \gamma^2/\alpha + |\alpha\omega_0^2 - \gamma^2/\alpha + 2i\alpha r b\gamma|], \quad (1a)$$

$$(ii) \quad \frac{c}{c'}\omega' = -i\frac{1}{2\gamma} [\alpha\omega_0^2 + \gamma^2/\alpha - |\alpha\omega_0^2 - \gamma^2/\alpha + 2i\alpha r b\gamma|], \quad (1b)$$

$$(iii) \quad \frac{c}{c'}\omega' = 0 \quad (1c)$$

In the above $|\cdot|$ denotes the absolute value of a complex number. Solution (i) does not support $\omega' = 0$, because the right hand side is a sum of two strictly positive quantities. It supports all values of ω' other than zero (including infinity).

Solution (ii), at relativistic values of α and r (i.e., at values close to ∞ and -1 respectively) has a positive imaginary part, which is not physical when $\exp(-i\omega't')$ is considered for $t' \rightarrow \infty$. However we must choose a solution that is physical for all values of α and r . Therefore we discard (ii).

Solution (iii) clearly determines a (zero) value for ω' which should be attainable for all values of α . The finite values of α and the zero value of ω' clearly satisfy (23d) of Part (I) and in the above mentioned future publication we shall show that for any finite value of ω' (including zero), α can attain the infinite value. Thus solution set (iii) is acceptable while solution set (i) is also acceptable for non-zero values of ω' . We have then the solution for all combinations of α and ω' . It should be pointed out that the c/c' factor that ω' has in (1), takes on the change brought about by α while ω' can remain a free parameter.

Here clearly ω' is an imaginary frequency, as it is under the $\alpha^2/\gamma' \rightarrow \infty$ (or under the equivalent $\alpha \rightarrow \infty$ limit-which equivalence will be shown below) condition too, as discussed above.

The dispersion relation (23a) of Part (I) can be interpreted as follows in terms of a refractive index for medium (I) when observed from K' :

$$n'^2(\omega') = \varepsilon'_r(\omega') \cdot 1 = 1 - \frac{b^2 c'^2}{c^2} \frac{\alpha c/c'}{(\alpha c \omega'/c' + i\gamma)\omega'} \quad (2)$$

which is the same as Equation (11) of Part (I) that was sought for. Here it must be noted that we are not attempting to obtain the Lorentz transform of the dielectric permittivity function. We are only transforming the dispersion relation and then casting the transformed relation into a form which can be interpreted as representing an effective permittivity function. Conductivity [2] and dielectric constant [3] may be invariants only under Galilean transformation which is excluded from our assumptions in favor of the Lorentz transformation which dictates a transformation of the constitutive relations in general [4].

Notice that we do not invoke the pure imaginary property of ω' in (2), because (2) amounts to be the Fourier transform of the impulse response of the medium and any kind of frequency constraints of input functions must subsequently be implemented after the final form of the permittivity function has been established and when the responses to new inputs are considered.

2. PREDICTION OF A NEW SUPERCONDUCTIVITY-LIKE EFFECT

Using the relation $\sigma' = -i\omega'(\varepsilon'_r - 1)$ in (2) to obtain the conductivity, one gets

$$\sigma' = \left(\frac{bc'}{c}\right)^2 \frac{\alpha c/(c'\gamma)}{1 - i\omega'\alpha c/(c'\gamma)}, \quad (3)$$

which can be identified as Drude's model for electronic conduction at least when the structure of the expression is considered. Here $\Gamma = \alpha c/(c'\gamma)$ takes the role of the parameter τ which is the lifetime in Drude's model. The interesting result of [5] is therefore the transformation of the refractive index of a causally dispersive dielectric with absorption in the K frame (Equation (10) of Part I) to the refractive index of a metal represented by Drude model for medium (I) when it is observed from K' . Indeed in the transformation process ω_0 has at least formally disappeared from the new refractive index expression. This is similar to vanishing of the restoring force $m\omega_0^2 X$ in (2) of Part (I) in a metal establishing that the charge can move freely.

Let us separate the real and imaginary parts of the conductivity expression in (3),

$$\sigma' = \sigma'_R + i\sigma'_I = \frac{b^2 c'^2}{c^2} \frac{\Gamma}{(\omega'\Gamma)^2 + 1} + i \frac{b^2 c'^2}{c^2} \frac{\Gamma^2 \omega'}{(\omega'\Gamma)^2 + 1}. \quad (4)$$

If the limit $\Gamma = \alpha c/(c'\gamma) \rightarrow \infty$ is taken σ'_R will be zero everywhere except at $\omega' = 0$ where it is infinite. But

$$\frac{b^2 c'^2}{c^2} \int_{-\infty}^{+\infty} \frac{\Gamma}{(\omega'\Gamma)^2 + 1} d\omega' = \pi \frac{b^2 c'^2}{c^2} \quad (5)$$

is independent of $\alpha c/(c'\gamma)$. And this area under the curve represented by σ'_R is true for any value of $\Gamma = \alpha c/(c'\gamma)$. It is clear that,

$$\sigma'_{Rs} = \lim_{\Gamma \rightarrow \infty} \frac{b^2 c'^2}{c^2} \frac{\Gamma}{(\omega'\Gamma)^2 + 1} = \pi \frac{b^2 c'^2}{c^2} \delta(\omega'). \quad (6a)$$

where $\delta(\omega')$ is the Dirac delta function. On the other hand,

$$\sigma'_{Is} = \lim_{\Gamma \rightarrow \infty} \frac{b^2 c'^2}{c^2} \frac{\Gamma^2 \omega'}{(\omega'\Gamma)^2 + 1} = \frac{b^2 c'^2}{c^2} \frac{1}{\omega'}. \quad (6b)$$

where the subscript s represents the superconductivity-like state. Hence we have no loss in medium (I) from infinite down to zero frequency. Furthermore because of the Dirac delta function

the medium presents infinite conductivity at zero frequency. This is a type of superconductivity-like effect in which the gap bandwidth extends from zero frequency to infinite frequency.

Combining (2) with (6) we can write

$$k'_1 = \frac{\omega'}{c'} \sqrt{1 + i \frac{\pi}{\omega'} \frac{b^2 c'^2}{c^2} \delta(\omega') - \frac{b^2 c'^2}{c^2 \omega'^2}} \quad (7)$$

as the dispersion relation for medium (I) observed from K' in the superconductivity-like state.

It should also be pointed out that the $\Gamma = \alpha c / (c' \gamma) \rightarrow \infty$ condition that is required for the superconductivity-like effect, is essentially equivalent to $\alpha \rightarrow \infty$ if it is noted that c , c' and γ that are involved also, are all finite quantities.

3. EQUATIONS WITH THE SAME STRUCTURE AS LONDON EQUATIONS IN A SUPERCONDUCTOR

On the other hand $\vec{J}'_s = \sigma' \vec{E}'$ by definition in a conductor and

$$\nabla' \times \vec{J}'_s = \sigma' \nabla' \times \vec{E}' = -\sigma' \frac{\partial \vec{B}'}{\partial t'}, \quad (8)$$

follows. From the non-zero everywhere imaginary part of the conductivity (see Equations (6b) and (8)), we can write

$$\nabla' \times \vec{J}'_s = -i \frac{b^2 c'^2}{c^2} \frac{1}{\omega'} \left(-i \omega' \vec{B}' \right), \quad (9)$$

or

$$\nabla' \times \vec{J}'_s = -\frac{b^2 c'^2}{c^2} \vec{B}'. \quad (10)$$

Hence

$$\vec{E}' = \frac{c^2}{b^2 c'^2} \frac{\partial}{\partial t'} \vec{J}'_s \quad (11)$$

follows from Maxwell-Faraday equation. This relation is the version of the first London equation for the particular type of superconductivity-like effect that is predicted.

In the $\omega' = 0$ limit, combining (10) and the Maxwell-Ampere equation

$$\nabla' \times \vec{B}' = \mu_0 \vec{J}'_s \quad (12)$$

one can obtain the second London equation

$$\nabla' \times \left(\nabla' \times \vec{B}' \right) = -\mu_0 \frac{b^2 c'^2}{c^2} \vec{B}' = -\frac{1}{\lambda^2} \vec{B}',$$

where λ has dimensions of length, and is the penetration depth of medium (I) observed from K' . This depth can be written as

$$\lambda = \sqrt{\frac{1}{\mu_0} \frac{c^2}{b^2 c'^2}}. \quad (13)$$

This is the distance inside the surface over which an external magnetic field is expelled out to zero. In the bulk of medium (I) $\vec{B}' = 0$ [6] when observed from K' .

4. DISCUSSION

In this work, the Lorentz transformed dispersion relation represented by Equation (11) in Part (I) has been interpreted to yield a permittivity function given by Equation (2) of this paper. This entails the permeability of medium (I) observed from K' to be equal to that of the permeability observed for the same medium from K and namely that of free space. Indeed these assumptions are commensurate with the modified (or the classical) Lorentz transformations. One can check this by separating the permittivity given by Equation (2) into a conductivity part expressed by Equation (3) and a relative dielectric constant part obtained from the expression $\epsilon'_r - i \frac{\sigma}{\omega}$ which will be found to be 1. If these dielectric constant and conductivity values are used in the standard formulas for the transformation of the electromagnetic field according to the Lorentz transformation, it will be found that the vector fields support this splitting of the dispersion relation. This was verified on solutions of Maxwell's equations in K and K' that satisfied the boundary condition on the interface of medium (I) with the perfectly conducting medium, medium (II).

5. CONCLUSION

Prediction of a new superconductivity-like effect is made which is independent of temperature but requires attainment of speed of light in vacuum by the motion of Galilean reference systems. The laboratory frame medium must be selected as a Lorentz medium and the rest frame medium is selected as a perfect conductor to simplify imposition of boundary conditions. The Lorentz medium appears as a metal when observed from the rest frame for all values of relative speeds of involved Galilean reference systems, and the same medium has a permittivity function which is similar to that of a superconductor when these relative speeds reach speed of light in vacuum.

REFERENCES

1. Yener, N., “Prediction of a new superconductivity-like effect in Galilean reference systems (Part I),” *PIERS Proceedings*, Moscow, Russia, August 19–23, 2012.
2. Lorrain, P., et al., *Magneto-fluid Dynamics: Fundamentals and Case Studies of Natural Phenomena*, Springer, New-York, 2006.
3. Censor, D., “Non-relativistic electromagnetic scattering: ‘Reverse engineering’ using the Lorentz force formulas,” *Progress In Electromagnetics Research*, Vol. 38, 199–221, 2002.
4. Kong, J. A., *Electromagnetic Wave Theory*, EMW Publishing, Cambridge, USA, 2005.
5. Yener, N., “Non-constancy of speed of light in vacuum for different galilean reference systems in case of an impulsive plane wave,” *PIERS Proceedings*, 1638–1643, Xi’an, China, Mar. 22–26, 2010.
6. Annett, J. F., *Superconductivity Superfluids and Condensates*, Oxford University Press, New York, 2010.

Remote Sensing and Simulation Model for Crop Management

J. Soria-Ruiz¹, Y. Fernandez-Ordonez², A. Quijano-Carranza¹, J. Macías-Cervantes¹,
P. Saucedo¹, D. Gonzalez¹, and J. Quintana¹

¹Geomatics Lab, National Institute of Research for Forestry Agriculture and Livestock (INIFAP)
Toluca, Mexico

²Colegio de Postgraduados, Montecillo, Mexico

Abstract— When one considers the components involved in studying the worldwide supply and demand for agricultural products, the applications of remote sensing in general are many and varied. The scope of the physical, biological, and technological problems facing modern agriculture is an extremely broad one that is intimately related with worldwide problems of population, energy, environmental quality, climate and weather. The objective of this research was to determine maize acreage and to predict yield using SPOT images, weather data and field collected data for crop variables. The study area is located in the Corn Belt within the State of Sinaloa in northwestern Mexico. Sinaloa is the main producer of white maize in this country producing around 5 million tons per year. Yield prediction relies on determining extent acreage of the crop and on monitoring growth and developing using data on vegetation indexes (NDVI), on leaf area indexes (LAI) and on photosynthetic active radiation (PAR). For determining acreage and NDVI, multispectral and panchromatic scenes of SPOT-5 were processed using supervised classification techniques. NDVI data were obtained from the visible red and infrared bands. LAI and PAR data were gathered with canopy analyzers on 209 maize plots geo-located with GPS. Yield prediction was done with a mathematical model as a function of planting dates considering other relevant data such as crop genotype, crop vigor, phenological data of maize, climate and soil. The prediction yield was produced 40 days before harvest. Results indicate that, the total cultivated area of maize in State of Sinaloa, the agricultural cycle Fall-Winter 2011, was 383, 693 hectares, it predicted an average yield of $6.84 \text{ ton}\cdot\text{ha}^{-1}$, with a confidence interval of 95 percent, a range of 6.58 to $7.9 \text{ ton}\cdot\text{ha}^{-1}$ and an average output of 2.6 million tons of maize grain. In addition, we obtained an R^2 of 0.68 for the NDVI and LAI variables. The prediction yield model showed an effectiveness of 95%. This prediction of maize yields is already supporting decision makers from the Ministry of Agriculture and farmers as well.

1. INTRODUCTION

Producers and decision makers in the rural sector require reliable information about the expected production volumes of crops. Maize is a staple crop in Mexico, so it is important to predict yield on a yearly basis. The state of Sinaloa is located in northwestern Mexico, it is the main producer of white maize of this country and yields around 5 million tons per year. Production expectations in recent agricultural cycles have been uncertain for the spring-summer cycle, with a production potential significantly lower than in the autumn-winter cycle, primarily due to the high temperatures in this region which occur starting in the month of March and account for a shortening of the phenological cycle of maize. Both producers and decision makers in the rural sector require information about the expected production volumes of maize, so it is important to predict yields on a yearly basis.

To estimate the volume of production of corn ahead of harvest, we attempted a prediction for the 31st of May, approximately 40 days before the start of harvest, using surface data collected by the statistics office of the Ministry of Agriculture (SIAP) and applying prediction models based on weather and field data. The particular objective of this research was to estimate corn acreage and yield prediction in Sinaloa, Mexico, from SPOT images and prediction models.

2. MATERIALS

In order to realize a crop forecast, an first forecast approximation used a mathematical model, experimental data of maize yield produced by the National Institute of Research for Forestry Agriculture and Livestock (INIFAP) in the State of Sinaloa in Mexico, data of mean yield as a function of time of seeding for all the possible seeding dates in two agricultural cycles (spring-summer, autumn winter) and weather data furnished by the state automated agro meteorological stations network.

For the second and definitive maize crop volume forecast for the spring-summer cycle, surface data determined by the SIAP office and other data from INIFAP prediction models which were fed

with meteorological information, field data, vegetation indexes derived from satellite images, leaf area measurements from canopy analyzers, GPS and mobile map devices were used.

3. METHODS

The study area. This research was conducted in the corn belt of the State of Sinaloa, Mexico in 2011.

Determination of crop acreage. 17 multispectral and 17 panchromatic scenes of SPOT 5 were used in 2011, to determine the acreage and vegetation indexes (NDVI) for maize.

The satellite images were geometrically corrected and orthorectified; these processes were carried out with geographic information systems tools (GIS) (Soria et al., 2010). Acreage was determined from a supervised classification process. Normalized difference vegetation indices (NDVI) were obtained from the visible red and infrared image bands.

Crop monitoring. For monitoring the crop, GPS and canopy analyzers were used to determine leaf area (LAI) and PAR in 209 maize plots in the study area. The elements considered for predicting yields were:

- Cultivated area (area by planting date and as sown by agricultural region)
- Genotype (predominant genotype, component technologies and crop vigor at the flowering stage)
- Weather (heat units, climate scenarios and current weather conditions)
- Soil (soil texture and depth)

Prediction model. The performance prediction model used was obtained from information based on Sown surface (by date of planting and agro-climatic region), Corn (predominant genotypes, component technologies and health in the mature stage), Climate (climate scenarios and current weather conditions) and Soil (texture and depth).

Yield forecast. In order to estimate ahead of harvest time the production volumes of grain for maize (approximately 40 days ahead of the harvest date on May 31st) based on the official SIAP data for cultivated surfaces the forecast was produced with prediction models fed mainly with the aforementioned data of heat units, genotypes and field data. Figure 2 shows the schematized elements considered for crop forecast in Sinaloa.

Leaf Area Indices Sampling. With canopy analyzer equipment (*Accupar*) Leaf Area Indices were obtained in the flowering stage of the crop over 209 plots located over the entire state of Sinaloa.

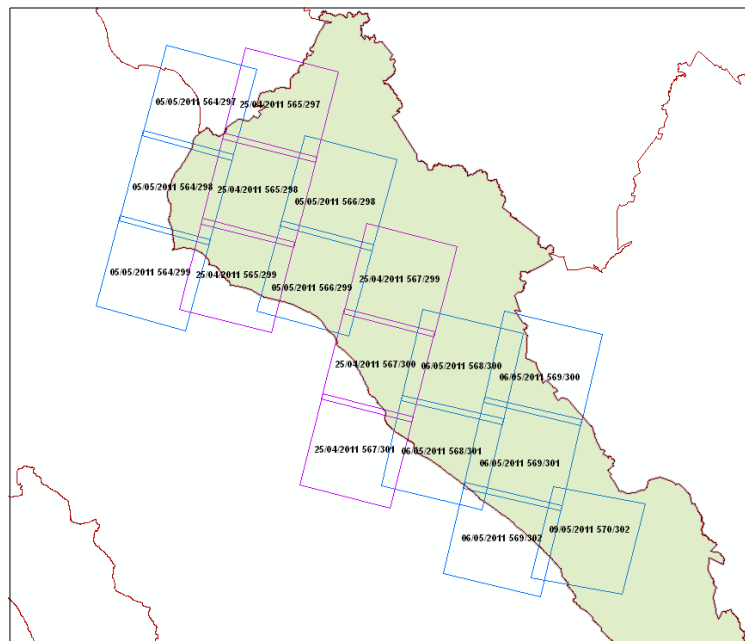


Figure 1: SPOT imagery used to determine the acreage of corn in Sinaloa, Mexico in 2011.

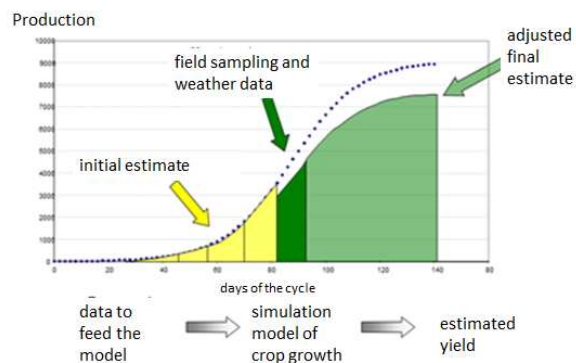


Figure 2: Procedure used for the prediction of corn yields in Sinaloa, Mexico.

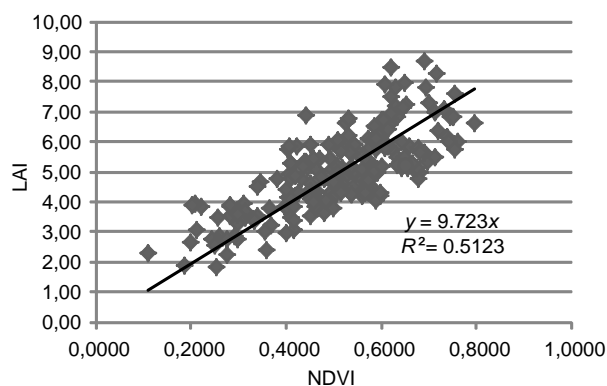


Figure 3: Dispersion of the values of LAI and NDVI in corn plots. Sinaloa, Mexico.

Vegetation Indices. To establish the behavior of vegetation and its relation to the leaf area indices in the flowering stage, the NDVIs were obtained from SPOT satellite images, corresponding to the same dates of collection of the foliar indexes on the field and over the same parcels.

Yield sampling. In order to know the degree of effectiveness of the yield and volume forecasts, sampling of yields was performed over 209 maize plots in the physiological maturity stage. These samplings were carried out on the same parcels where foliar area indexes in the flowering stage were measured.

4. RESULTS AND DISCUSSIONS

Leaf area indices — vegetation indices. These two indexes are directly related to plant vigor and to crop yield. The results which were obtained for both indexes LAI (leaf area index) and NDVI (normalized difference vegetation index) over the 209 sampled plots indicate that there is a variation in the values of these indicators, coincident with the fact that in the agricultural cycle Spring-Summer 2011 a bad year for agriculture and especially for maize in Sinaloa. Frost was present in February and suspect seed quality used in reseeded procedures are a possible explanation. Figure 3 shows a high variation in NDVI and LAI with a determination coefficient (R^2) of 0.51. This supports the conjecture that the different genotypes introduced in Sinaloa por reseeded in the Spring-Summer 2011 cycle were of different origin and thus different yield potential. Many of these seeds are not adapted to the conditions in the region. The observed relations in the values of these variables show a high dispersion.

Yield prediction. Mathematical models obtained from experimental data which allow the calculation of mean yield value in terms of seeding date, cultivated genotypes, heat units and leaf area indexes were used. The yield prediction model in terms of seeding date produces a determination coefficient of 0.83 for the seeding dated interval between November 1st and April 15.

Table 1 shows the yield prediction and expected production volumen for the Spting-Summer agricultural cycle for the sate of Sinaloa, with a confidence interval of 95%. A cultivated surface of 383, 693 ha is shown, which is the sum of the reseeded surface of 308,580 ha and of the undamaged surface of 75,113 ha, with an expected mean yield of 6.84 ton/ha, with a confidence interval of 95%,

Table 1: Corn acreage, average yield prediction and expected average production volume for the agricultural cycle PV 2011 in the State of Sinaloa.

SURFACE (ha)	YIELD (ton·ha ⁻¹)	CONFIDENCE INTERVAL (95%) (ton·ha ⁻¹)	PRODUCTION VOLUME (ton)	CONFIDENCE INTERVAL (95%) (ton·ha ⁻¹)
383,693	6.84 t·ha ⁻¹	6.58–7.09	2,624,460	2,524,924–2,721,191

and rank of 6.58 to 7.09 ton/ha, an average production value of 2.62 million tons of grain. It is important to mention that the mean forecasted yield may vary with a lower tendency; this due to the effect of plagues, to deficient water management or to heat waves in the grain filling stage, among other factors.

5. CONCLUSIONS

The prediction yield model showed an effectiveness of 95%. This prediction of maize yields in Sinaloa, Mexico provides important support information to farmers and to decision makers within the Ministry of Agriculture.

The low correlation between LAI and NDVI variables in maize, indicate that 2011 was a difficult year for agriculture in the northwestern part of Mexico, due to frost in February which led to the introduction of uncertified seeds for replanting.

REFERENCES

1. Demers, M., *Fundamentals of Geographic Information Systems*, 3rd Edition, John Wiley & Sons, Inc., USA, 2005.
2. ESRI, *ArcGis 10. Undersatending Our World*, Redlands, CA, USA, 2011.
3. Ferencz, C., P. Bognars, J. Lichtenbergger, D. Hamar, G. Tarcsai, G. Timars, G. Molnars, S. Pasztor, P. Steinbach, B. Szekely, O. Ferenkcz, and I. Ferencz-Arcos, "Crops yield estimation by remote sensing," *Int. Journal of Remote Sensing*, Vol. 25, No. 20, 4113–4149, 2004.
4. Soria-Ruiz, J., Y. Fernandez-Ordoñez, and H. Woodhouse, "Land-cover classification using radar and optical images: A case study in central Mexico," *Int. Journal of Remote Sensing*, Vol. 31, No. 12, 3291–3305, 2010.

A Microwave Optoelectronic Oscillator: Mach-Zehnder Modulator or VCSEL Based Layout Comparison

M. E. Belkin and A. V. Loparev

Joint Research Laboratory “Microwave and Optoelectronic Devices”

Moscow State Technical University of Radio-Engineering, Electronics and Automation (MSTU MIREA)
Vernadskogo Av., 78, Moscow, Russian Federation

Abstract— This work is focused on a most promising device of microwave photonics — optoelectronic oscillator. We consider two version of its layout: based on a semiconductor laser with an external intensity modulator using integrated Mach-Zehnder interferometer, or based on VCSEL with its direct modulation. A comparative simulation results in OE-CAD tool of the microwave-band optoelectronic oscillator’s spectral and phase noise characteristics and the results of the experimental verification are highlighted and discussed.

1. INTRODUCTION

An optoelectronic oscillator (OEO) studied in this paper is a most valuable example of microwave photonics breakthrough. As a matter of fact OEO opens up new horizons of highly stable RF oscillators in a frequency range from hundreds of MHz to hundreds of GHz [1]. The key advantage of an OEO in comparison with traditional RF and microwave oscillators is the higher spectral purity achievable [2].

The state of the art for OEOs is currently considered to be a single-frequency (within the X-band) OEO product from OEwaves Inc. with a class leading phase noise level of -163 dBc/Hz at a 10 kHz offset from the carrier [3]. The enhanced spectral purity of an OEO’s central mode occurs due to its well-known feature of improving with delay time, and very long delays can be easily achieved with a nearly lossless optical fiber line extending for several kilometers. At the other hand, OEO is able to combine successfully higher spectral purity and extremely wide frequency range of carrier tuning within the limits of some octaves [4] that is impossible for traditional microwave transistor oscillators.

Up-to-date in the most publications devoted to OEO a circuit arrangement with unmodulated laser source and feedback on Mach-Zehnder external modulator has been studied. But recently a version combined the functions of optical emitter and feedback control in one vertical cavity surface emitting laser (VCSEL) preferred by potential low cost, power consumption, and integrability has been also investigated [5]. Thus, there exists a need for detailed comparison of the above OEO design approaches. Following this, below spectral and phase noise characteristics of two microwave-band OEO layouts based on an unmodulated distributed feedback (DFB) laser and an external Mach-Zehnder intensity modulator, or based on a direct modulated VCSEL will be researched and compared.

2. OPTOELECTRONIC OSCILLATOR OE-CAD MODELS

The typical layout of an OEO scheme with external modulator [6] is presented in Figure 1(a). The OEO consists of two principal sections: optical and electrical. The optical section includes semiconductor laser module (SLM), electro-optical modulator (EOM), optical fiber line (OFL), and photo detector module (PDM). To ensure a reliable operation of the OEO with low laser noise levels and low loss for the optical section an optical isolator (OI) and polarization controller (PC) are introduced into the scheme. The electrical section includes a low-noise RF amplifier (LNA), tunable band-pass filter (BPF), power amplifier (PA), and electrical coupler (EC). The operating principle of the OEO is based on the conversion of the continuous optical radiation energy emitted from the SLM into periodical discrete energy bursts in the RF-band. To achieve this, the EOM is controlled by a positive-feedback optoelectronic loop (see Figure 1(a)). A current OEO carrier frequency in the RF band is determined by the BPF’s bandpass, while the overall energy storage time of OEO depends on the fiber delay. By managing the fiber length and gain of the LNA and PA one can ensure, for a given circuit, the amplitude and phase balance required for self-sustained oscillation.

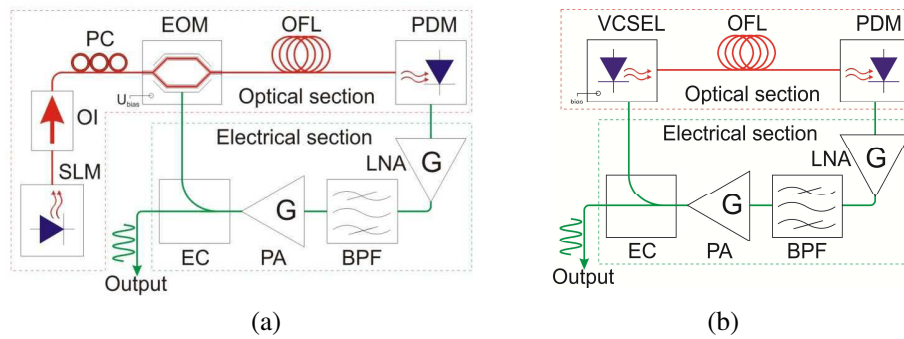


Figure 1: (a) External EOM-based and (b) VCSEL-based OEO layouts for comparison.

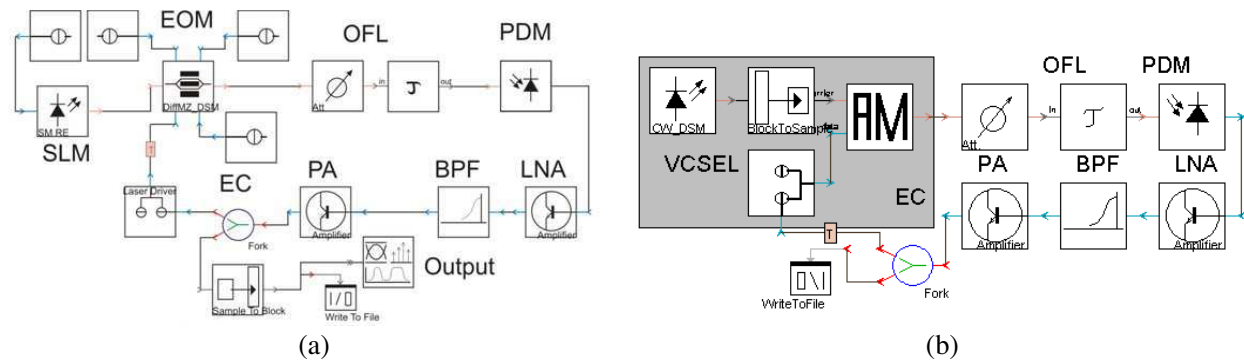


Figure 2: (a) EOM-based and (b) VCSEL-based OEO models in VPI transmission maker OE-CAD tool.

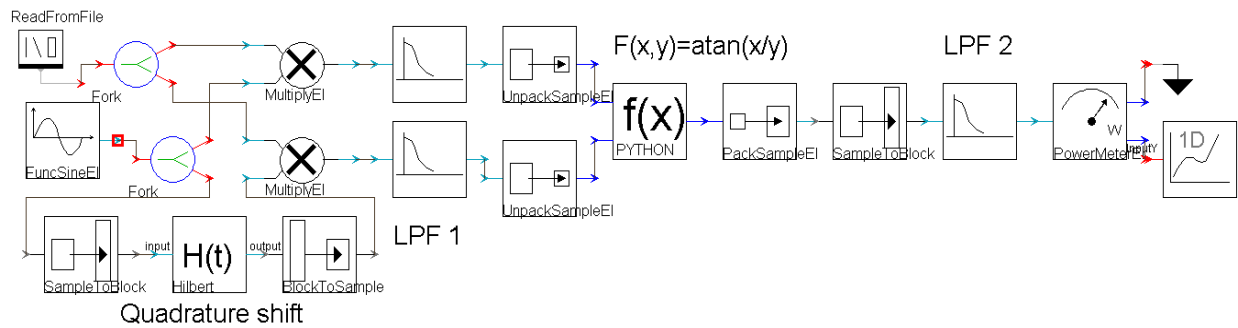


Figure 3: Arrangement for simulating OEO's phase noise measurement in VPI transmission maker.

The electrical section of the VCSEL-based OEO being simulated (Figure 1(b)) is similar to the same one of OEO with external modulator. But in optical section VCSEL is modulated directly by injection current from EC so the layout is far simpler.

Previously we worked out in detail optoelectronic computer-aided design (OE-CAD) based OEO model [4] by VPI System's VPI Transmission Maker software tool [7], which due to considering its self-excitation and large-signal steady-state operation modes allows simulating spectral and phase-noise characteristics for certain schematic. A single-loop EOM-based and VCSEL-based OEO computerized models are shown in Figures 2(a) and 2(b) correspondingly. In both cases the simulation is performed with aperiodic boundary conditions that allow concurrent simulation of the RF and optical elements of the OEO in object-oriented environment. Note that the library VCSEL model based on the rate equations does not work correctly in OEO's divergent oscillations regime, so we substituted it for a combination of equivalent laser model and ideal optical intensity modulator.

In the layouts of Figure 2 all the elements of Figure 1 have a specific interpretation. For example, the SLM is represented by single-mode rate equations-based DFB laser model, the EOM is based on

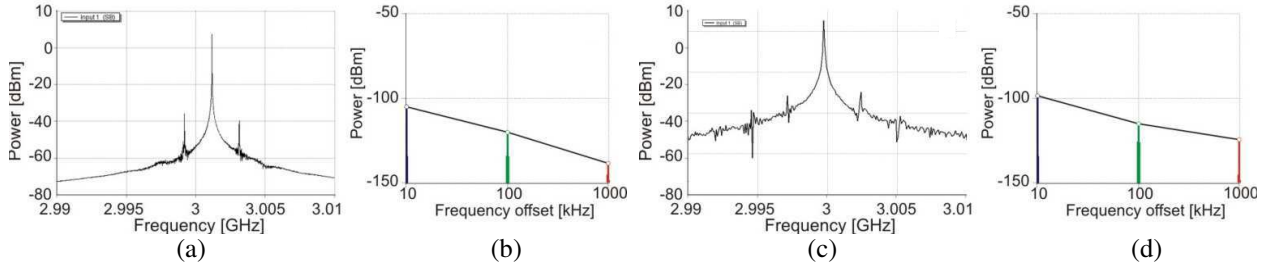


Figure 4: (a) EOM-based OEO spectral and (b) phase noise characteristics and (c) VCSEL-based OEO spectral and (d) phase noise simulated in VPI Transmission Maker OE-CAD.

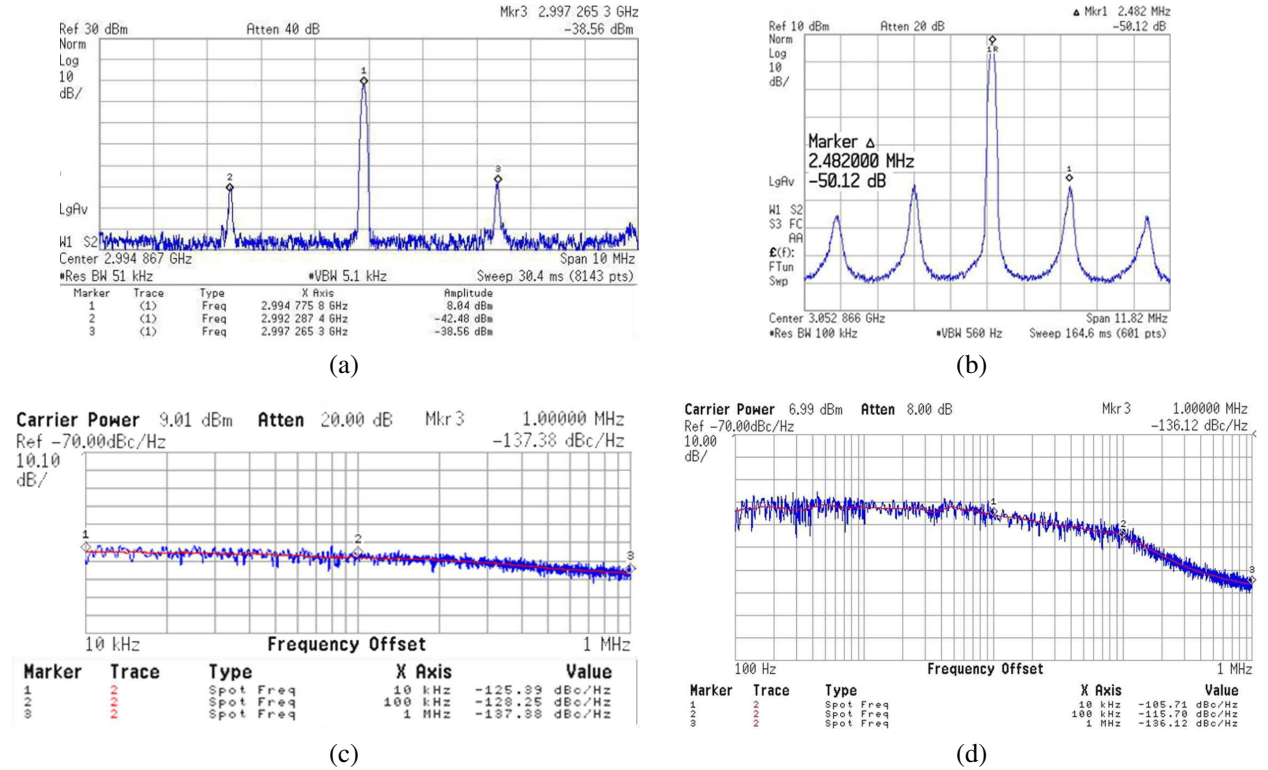


Figure 5: (a) Measured EOM-based OEO spectrum and (b) phase noise characteristics and (c) VCSEL-based OEO spectrum and (d) phase noise characteristics.

a differential Mach-Zehnder interferometer model, VCSEL module filled with gray color is imitated by the combination of CW_DSM laser, Amplitude Modulator (AM) and Laser Driver models; OFL is constructed by a combination of an optical attenuator and a delay line. The spectrum of the OEO output signal exports by a spectrum analyzer library model. The specific schematic realization for simulating in VPI Transmission Maker OEO's phase noise characteristics in the bandwidth of 100 Hz at offsets of 10 kHz, 100 kHz and 1 MHz from the carrier, is presented in Figure 3.

The simulation results of spectral and phase noises (in the bandwidth of 100 Hz) characteristic of EOM-based (a), (b) and VCSEL-based (c), (d) OEO at operation frequency near 3 GHz and 65 m of OFL length are showed in Figure 4.

As it shown on Figure 4(a), EOM-based OEO output power is +5 dBm, the side-mode suppression ratio is more than 45 dB. Also from Figure 4(b) the relative phase noise spectral density of the EOM-based OEO are: $S_{10\text{kHz}} = -120 \text{ dBc/Hz}$, $S_{100\text{kHz}} = -130 \text{ dBc/Hz}$ and $S_{1\text{MHz}} = -139 \text{ dBc/Hz}$. It is clear from Figure 4(c) that VCSEL-based OEO output power is +5.5 dBm, the side-mode suppression ratio more than 40 dB. As it depicted in Figure 4(d), the relative phase noise spectral density of the VCSEL-based OEO are: $S_{10\text{kHz}} = -110 \text{ dBc/Hz}$, $S_{100\text{kHz}} = -125 \text{ dBc/Hz}$ and $S_{1\text{MHz}} = -135 \text{ dBc/Hz}$.

Table 1: EOM-based vs. VCSEL-based OEO comparison.

	Frequency range (GHz)	Output power (dBm)	Side-mode suppression (dB)	Phase noise (dBc/Hz) at 3 GHz at offsets		
				10 kHz	100 kHz	1 MHz
EOM-based OEO	2.5–15	9	46.5	–125	–128	–138
VCSEL-based OEO	2.5–6	7	50	–106	–116	–136

3. EXPERIMENTAL VERIFICATION

For an experimental verification of simulated results, EOM- and VCSEL-based prototypes being in line with Figure 1’s layouts were created. The major prototype’s elements in the optical section are: MQW DFB laser diode LDI H-DFB-1550 (1.55 μm , power output up to 17 mW, RIN = –155 dB/Hz) from IIT Inc. as SLM; LiNbO₃ Mach-Zehnder optical modulator MATH-005-40 (1.55 μm , typical insertion loss 4.5 dB, 3-dB bandwidth of 35 GHz) from COVEGA Inc. as EOM; VCSEL module (1.55 μm , power output up to 1 mW, RIN = –140 dB/Hz) from Beam Express, LLC; pin-photodiode XPDV3120R (wavelength range 1480–1620 nm, responsivity 0.6 A/W, 3-dB bandwidth 75 GHz) from u2t Photonics, Inc. as PDM. For the electrical section a tunable band pass YIG-filter (tuning range 2.5–15 GHz, insertion loss 5 dB, 3-dB bandwidth 11 MHz at 2.5 GHz and 20 MHz at 15 GHz) from Magneton, Inc. is used as BPF. Besides, removable sets of two microwave amplifiers (total gain of near 50 dB, noise figure 3.5 dB) for the frequency bands 2.5–8 GHz and 8–15 GHz are employed.

The examples of the experimental results of EOM-based OEO spectrum and phase noise characteristics at the oscillation frequency of 3 GHz are presented in Figures 5(a) and 5(b) [8]. In addition, the VCSEL-based OEO spectrum and phase noise characteristics at the same oscillation frequency are showed in Figures 5(c) and 5(d).

Experimental results represented in Figure 5 are closely matched with the simulation results and confirm the feasibility of the proposed OEO models in VPI Transmission Maker software tool.

4. CONCLUSIONS

In the paper spectral and phase noise characteristics of two microwave-band OEO layouts based on an unmodulated DFB laser and an external Mach-Zehnder intensity modulator, or based on a direct modulated VCSEL were researched. Table 1 lists a brief parametrical comparison of the both OEOs.

Thus, simulating and experimental investigation of two versions of the microwave-band optoelectronic oscillator reveals that directly modulated VCSEL-based OEO, which offers a number of obvious advantages such as integrability, low cost and power consumption, has commensurable parameters compared to a typical external modulator-based layout excluding near-to-carrier phase noise. We predict that most probable cause of this defect lies in an increased radiation noise of VCSEL vs. DFB used in typical OEO layout. Another bottleneck of a VCSEL-based OEO is the relatively limited tuning range that is referred to more narrow modulation bandwidth of the VCSEL employed in comparison with the same of the Mach-Zehnder modulator.

ACKNOWLEDGMENT

The authors would like to express their thanks to Sergei Mingaleev and Thomas Feibig from VPI Systems for fruitful discussions regarding with OEO phase noise simulation singularities. This work was supported by the Russian Federation Ministry of Education and Science.

REFERENCES

1. Yao, X. S., “Opto-electronic oscillators,” *RF Photonic Technology in Optical Fiber Links*, W. S. C. Chang, Ed., 255–292, Cambridge University Press, 2002.
2. Maleki, L., “Recent progress in opto-electronic oscillator,” *Microwave Photonics International Topical Meeting*, 81–84, Oct. 12–14, 2005.
3. <http://www.oewaves.com>.
4. Belkin, M. E., A. V. Loparev, Y. Semenova, et al., “A tunable RF-band optoelectronic oscillator and OE-CAD model for its simulation,” *Microwave and Optical Technology Letters*, Vol. 53, No. 11, 2474–2477, 2011.

5. Rissons, A., N. Gromaire, A. Bacou, and J.-C. Mollier, “Phase noise reduction of 1.55 and 1.3 μm VCSEL based optoelectronic oscillator,” *Proceedings of MWP/APMP Conference*, 85–88, 2011.
6. Yao, X. S. and L. Maleki, “Optoelectronic oscillator for photonic systems,” *IEEE Journal of Quantum Electronics*, Vol. 32, No. 7, 1141–1149, Jul. 1996.
7. <http://www.vpisystems.com>.
8. Loparev, A. V., “Optoelectronic and microelectronic building principles of solid-state microwave oscillators,” Doctor’s Thesis, MSTU MIREA, 2011 (in Russian).

Passive Components Based on Two-dimensional Photonic Crystals

T. N. Bakhvalova and I. V. Khmel'nitsky

Joint Research Laboratory “Microwave and Optoelectronic Devices”
Moscow State Institute of Radio-Engineering, Electronics and Automation, MSTU MIREA
Moscow 119454, Russian Federation

Abstract— Possibilities of the use and the results of modeling of two-dimensional photonic crystal (PhC) spectral demultiplexer were proposed and investigated. Several spectral demultiplexers/multiplexers are designed: to separate the channels with wavelengths of 1490 and 1550 nm (Passive optical network, PON); 1270 and 1310 nm (IEEE 802.3 40GBASE-LR4); 1270 and 1290 nm (IEEE 802.3 40GBASE-LR4). Proposed two-channel demultiplexers based on PhC are designed to separate the channels with wavelengths which widely used in telecommunications. These demultiplexers consist of circular silicon rods in rectangular lattice surrounded by air with radius of circular is $0.2a$ (a — lattice constant). These devices are based on wavelength channel splitters by using different filters. One filter with three defective rods inside it and another filter with tapered region are placed at the T -junction. Selection of model geometric parameters is based on the analysis of photonic band gap maps. The computations were carried out using the Optiwave's OptiFDTD 8 software.

1. INTRODUCTION

A photonic crystal (PhC) with photonic band gap (PBG) is a promising candidate as a platform to construct devices with dimensions of several wavelengths for future photonic integrated circuits. PhCs are particularly interesting in all-optical systems to transmission and processing information due to the effect of light localization in the defect region of the periodic structure [1]. Because PBG structures allow strong control over the light propagation, some of the most exciting applications of these structures are based on the functionalities through the incorporation of defects in periodic lattice leading to the design of PhC heterostructure-based PBG waveguides and devices [2]. Defects influence on the PhC photonic band structure that can result in the flow or confinement of light along particular pathways in the crystal. Moreover, PBGs in these structures are polarization sensitive. These properties of PhC structures have been used to design various passive optical components, such as splitters [3], multiplexers, demultiplexers, polarizers [4], time delays [5], and so on. Two-dimensional (2D) PhC is most suitable for such devices creating. Currently dielectric rods in air and membrane are two basic types of PhC. In this paper the first PhC type was used as more suitable for proposed below structure of the spectral filters.

At present, it's known a series of publications on modeling two-dimensional PhC spectral filters and demultiplexers. In particular, in [6] were presented the simulation results of the fiber-optic transmission systems (FOTS) demultiplexer with WDM (wide wavelength-division multiplexing) for wavelength separating of 1310 and 1550 nm. PhC structure based on the set of silicon rods/pillars and made on a quartz substrate. To form the broadband filters were used rods with different radii (defects). Later this approach was developed in [1, 7]. Moreover, in [8] presented a model of so-called triplexer with reflector for working wavelengths of 1310, 1490 and 1550 nm. The total size of such device was only 16×20 microns. The rods material was InGaAsP. The effect of spectral channel separation was carried out by the addition of defects with different radii and refractive index (material of defective rods was Si_3N_4). Although in [8] were obtained a good result in the channel separation, the use of several materials complicates the technological process of the demultiplexer fabrication. Also the considerable interest is to study the possibility of using filters with a smaller spacing between the optical carriers, such as FOTS on IEEE 802.3 standard.

In view of the foregoing, in this article we propose and investigate PhC demultiplexers for separation optical channels, in which by introducing defects in a strictly periodic structure, as well as by changing the parameters of the elements, the conditions for the selective radiation distribution are created. This device consists of silicon rods surrounded by air, and can operate at a difference between the operating wavelengths below 100 nm (60 nm, 40 nm and 20 nm). The total size of such devices is less than 10×10 microns. Also we discussed the possibility of using 2D PhC as a polarizer.

2. MODEL CALCULATIONS AND RESULTS

2.1. Photonic Crystal Demultiplexer

Infinite, strictly periodic structure of the photonic crystal is characterized by photonic band gap, which depends on the ratio of the refractive indices of the elements and ground substance, as well as the geometric parameters of the structure. Due to creating a device through changing the structure, we break the strict periodicity, which forms the field with a modified photonic band gap [7]. So spectral filters of optical range based on the 2D PBG structure can be created by the correct selection of geometrical and physical parameters.

Figure 1 shows the structure of the demultiplexer comprising two ways to filter out. T-shaped waveguide is formed by removing the corresponding row of dielectric rods. First filter is formed by introducing three additional defects with smaller radii in the PhC waveguide. Radius of the defect is selected on the basis of analysis of photonic bandgap map. To select values of the rods radii is necessary so that at a certain radius r both operating frequencies were within the band gap, that corresponds to PhC waveguide channel, and at another value of the radius r_{def} only one frequency fell into photonic band gap, that corresponds to a PhC bandpass filter. This filter are broadband (~ 100 nm at 3 dB) and cannot be used in case of a small difference in the working wavelengths. Therefore, it is necessary to use an additional mechanism for spectral limiting.

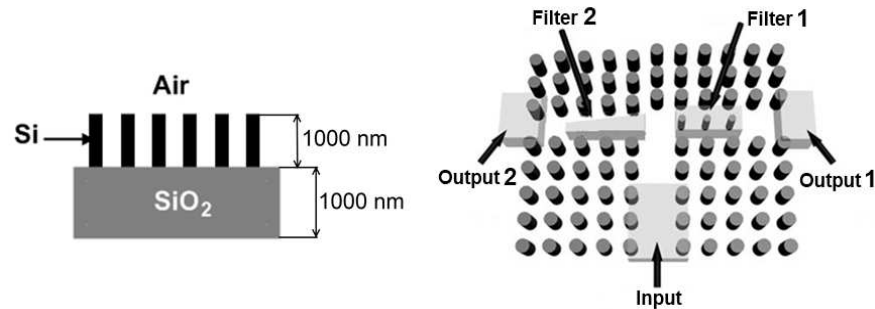


Figure 1: Schematic diagram of the optical Demultiplexer/Multiplexer based on a PhC waveguide.

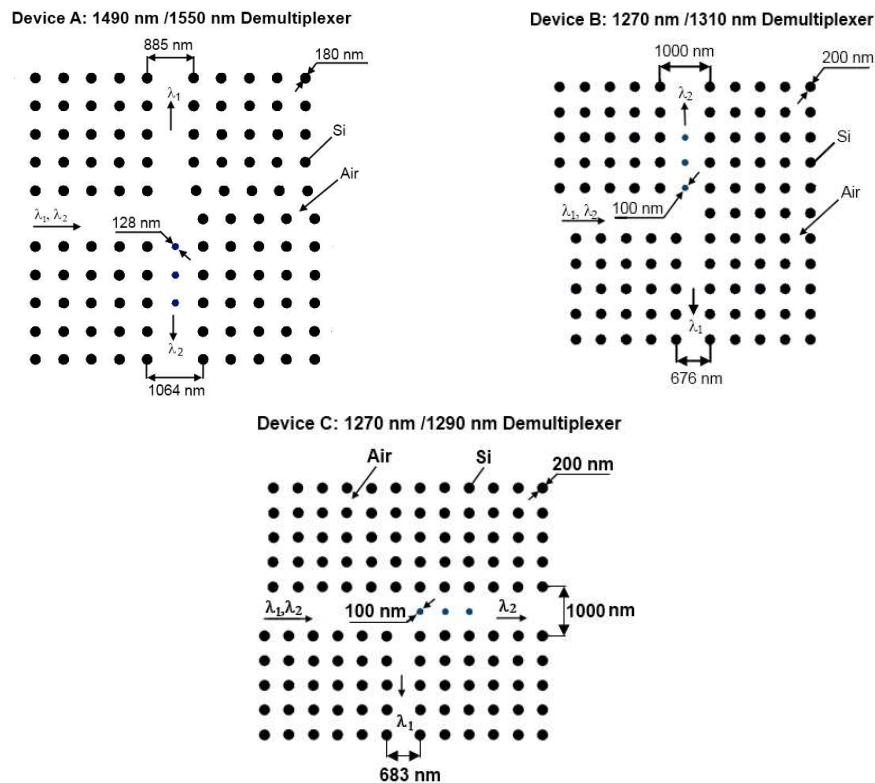


Figure 2: PhC demultiplexers for different wavelength ranges.

Table 1: Loss values for all three devices in both outputs.

	Device A		Device B		Device C	
	1490 nm	1550 nm	1270 nm	1310 nm	1270 nm	1290 nm
Output 1	14 dB	4 dB	14 dB	6 dB	10 dB	4 dB
Output 2	2 dB	16 dB	2 dB	13.5 dB	4 dB	12 dB

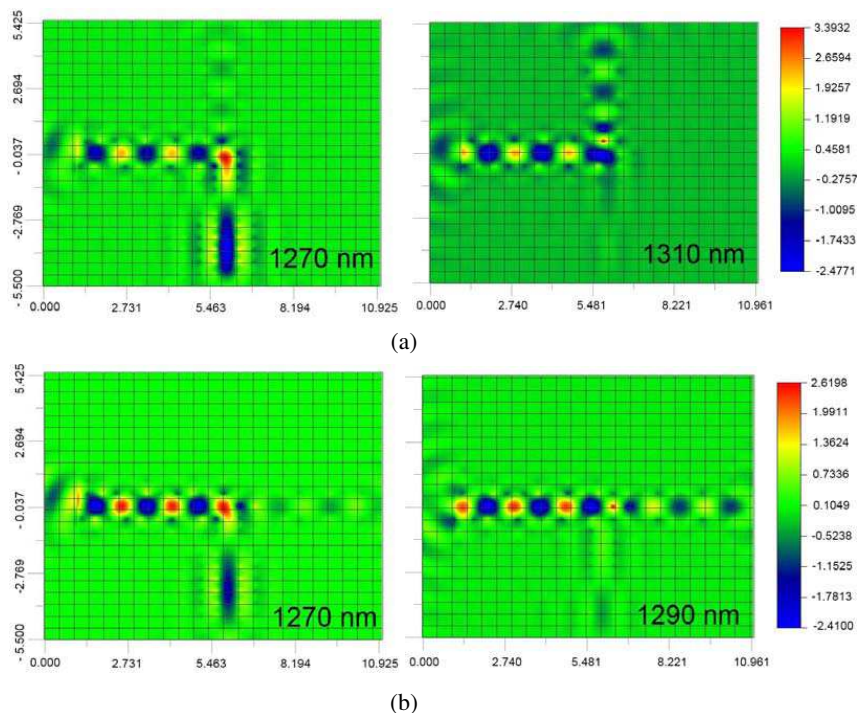


Figure 3: Results of FDTD simulation of wavelength channel splitting for (a) device B and (b) device C.

Second filter is formed by tapered region. With reducing of the PhC waveguide transverse dimension the operational wavelength shifts to shorter wavelength. For example, at a certain transverse dimension of the waveguide channel wavelength $\lambda_1 = 1550$ nm cannot spread it, while the $\lambda_2 = 1490$ nm will pass without significant attenuation. Thus, the narrower waveguide will be distributed to smaller wavelengths. The use of additional ways to filter can reduce losses and significantly improve the results for one of the operational wavelength.

Figure 2 shows the topology of demultiplexers for different telecommunication wavelength ranges. Device A designed for passive optical network PON; devices B and C designed for IEEE 802.3 40GBASE-LR4 [9]. All values of geometrical and physical parameters are presented on the figure. These devices are modeled on the basis of the above principles for spectral filtering.

The obtained results of computer simulation are shown in Fig. 3 and Table 1. Table 1 lists the numerical values of the output isolation of all three devices being considered. As can be seen from the table, the smaller spacing between the working wavelength, the more difficult to carry out spectral separation. This is primarily due to the broad-band of the first filter.

A similar modeling was carried out for a range of wavelengths 1510, 1530, 1550 and 1570 nm (ITU-T Rec. G.695). The model is based on the same principles for constructing photonic crystal filter, but for the channels separation of 20 nm. The simulation results were obtained of the same order as above (for 1270, 1290, 1310 and 1330 nm).

2.2. Photonic Crystal Polarizer

To form a polarizer, 2D PhC must have an overlapping band gap for both polarizations (complete band gap) and be easier to fabricate. TM band gaps are favored in a lattice of isolated high- ϵ (ϵ — dielectric constant) regions, and TE band gaps are favored in a connected lattice. For complete band gap is necessary to arrange a photonic crystal with both isolated spots and connected regions

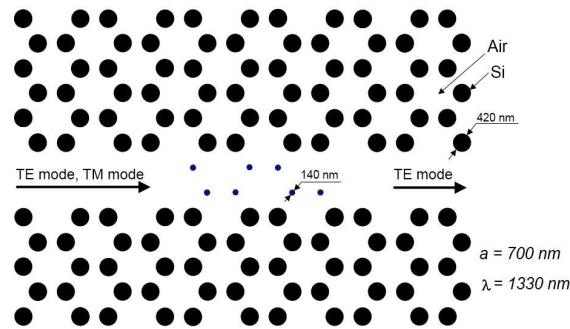
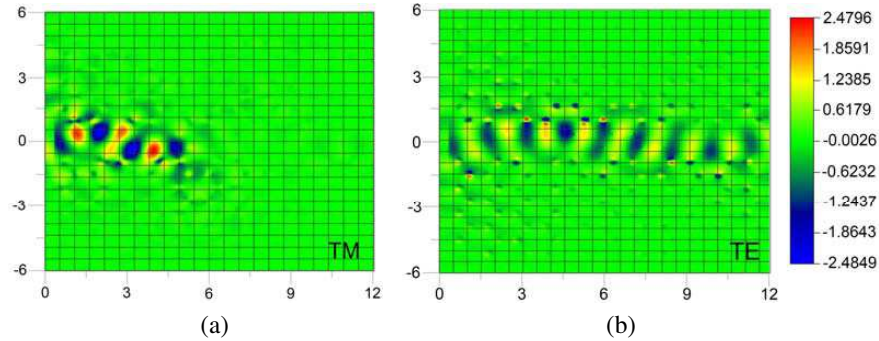


Figure 4: Schematic diagram of the PhC polarizer.

Figure 5: Snapshot of the PhC polarizer at $1.33 \mu\text{m}$ (a) for TM mode and (b) for TE mode.

of dielectric material. So it must be 2D PhC with high- ϵ regions that are both practically isolated and linked by narrow veins. In the case of triangular lattice of air columns: if the radius of the columns is large enough ($0.95a$), the spots between columns look like localized regions of high- ϵ material, which are connected (through a narrow squeeze between columns) to adjacent spots [10]. Thus, this structure has very thin dielectric veins of width $0.05a$ between the air columns. In fact, to fabricate such a structure is relatively difficult procedure. Another solution of this problem is to use a honeycomb structure. The gap map for this structure is of much larger extent than the complete PBG of the triangular lattice and the production of such 2D lattices less formidable.

To design a PBG polarizer, we consider 2D PhC structure composed of a honeycomb lattice of Si rods in air. Principles of modeling of the polarization filter are completely analogous to given above modeling principles of the first type spectral filter. Polarizing filter is based on introduction of additional defect rods in the PhC waveguide. The values of the radii of defects are selected from the analysis of a complete photonic band gap (investigate the variation of PBGs by changing the radius of defect rods in the linear defect waveguide using the PWE method). For example [2], for operating wavelength of $1.55 \mu\text{m}$ values of geometrical and physical parameters are: lattice constant $a = 0.885 \mu\text{m}$, rod radius $r = 0.24a$, the radius of the defect rods $r_1 = 0.08a$ (supports only TE modes but exhibits a PBG for TM mode) and $r_2 = 0.32a$ (supports only TM modes but exhibits a PBG for TE mode).

Thus it is possible to select the necessary geometric parameters (lattice constant, basic and defect radii) for a polarizer operating at any wavelength. Fig. 4 shows the scheme of the polarizer operating at a wavelength of $1.33 \mu\text{m}$ for blocked of TM-mode. Fig. 5 shows results of FDTD simulation for $1.33 \mu\text{m}$ PhC polarizer.

3. CONCLUSIONS

A new topology of a spectral demultiplexer based on 2D PhC with the formation of which one arm of the T-splitter is realized by means of tapered waveguide channel, which allowed an interval of operating wavelengths of 60 nm, 40 nm and 20 nm. The entire structure was made of Si on a substrate of SiO_2 , which provides relatively simple manufacturing process and the possibility of using these devices as part of standard optoelectronic integrated circuit. The obtained lower values of isolation between the arms in comparison with known results [1, 7, 8] explained by the use of homogeneous material (as opposed to [8]) and a narrow spectral interval (as opposed to [1, 7]).

The design of the PhC polarizer by utilizing the complete PBGs was also discussed. Modeling of polarizer for the required wavelength is carried out following proper selection of radius values of the defects.

The dimension of the PhC polarizers and demultiplexers lies in the microscale range leading to the design of ultra-compact passive components. Our future work aims to increase insulation and reduce losses in the proposed devices by further modification of the structure topology.

REFERENCES

1. Pal, B., *Frontiers in Guided Wave Optics and Optoelectronics*, 621–645, InTech, 2010.
2. Sinha, R. K. and Y. Kalra, “Design of a photonic band gap polarizer,” *Opt. Eng.*, Vol. 45, 110503, 2006.
3. Kim, S., I. Park, and H. Lim, “Design of PC splitters/combiners,” *Proceedings of SPIE*, No. 5597, 129–135, 2004.
4. Kalra, Y. and R. K. Sinha, “Design of ultra compact polarization splitter based on the complete photonic band gap,” *Opt. Quantum Electron.*, Vol. 37, 889–895, 2005.
5. Fakharzadeh, M., O. M. Ramahi, S. Safavi, and S. K. Chaudhuri, “Design and analysis of ultra-miniaturized meandering photonic crystals delay lines,” *IEEE Trans. Adv. Packag.*, Vol. 31, No. 2, 311–319, 2008.
6. Guryev, I., et al., “Demultiplexing with wide bandwidth filters based on 2D photonic crystals,” *Radiotekhnica*, No. 143, 125–131, 2005 (in Russian).
7. Sukhoivanov, I. and I. Guryev, *Photonic Crystals: Physics and Practical Modeling*, 152–242, Springer Verlag, 2009.
8. Shin, T.-T., Y.-D. Wu, and J.-J. Lee, “Proposal for compact optical triplexer filter using 2-D photonic crystals,” *IEEE Photonics Technology Letters*, Vol. 21. No. 1, 18–20, 2009.
9. Bakhvalova, T. and M. Belkin, “Modeling of photonic crystal demultiplexers,” *Nano- and Microsystem Technique*, No. 1, 27–30, 2012 (in Russian).
10. Joannopoulos, J. D., *Photonic Crystals: Molding the Flow of Light*, 286, Princeton University Press, 2008.

Low-phase Noise Photonic Millimeter Wave Generation Using a Nonlinear MZM and Four-wave Mixing in Ultra Long SOAs

André Garcia, Vitaly Rymanov, and Andreas Stöhr
 Zentrum für Halbleitertechnik und Optoelektronik (ZHO)
 Universität Duisburg-Essen, Germany

Abstract— We demonstrate an experimental study of the influence of the Semiconductor Optical Amplifier (SOA) interaction length on the four-wave mixing (FWM) efficiency. We furthermore propose and demonstrate a simple set-up for a frequency-tunable (up to 50 GHz) photonic microwave generator using nonlinearities in a Mach-Zehnder modulator (MZM) and the four-wave mixing (FWM) effect in an ultra-long semiconductor optical amplifier (UL-SOA). The operation principle of the photonic microwave generator is based on an external modulation scheme using a low phase noise local oscillator (LO) source to multiply the LO frequency in the optical domain. We experimentally characterized the influence of the SOA interaction length on the FWM efficiency using three types of SOAs, as well as, the overall Radio Frequency (RF) conversion efficiency at the different achieved multiplication levels to identify the optimal operation conditions for the SOA. Using a low frequency reference LO source fixed at 4 GHz, the generation of a tunable and low phase noise millimeter-wave (mm-wave) signal up to 50 GHz was demonstrated.

A maximum achievable multiplication factor (N) of twelve-times the LO frequency, 48 GHz, has been achieved resulting from the nonlinear behavior of the MZM and the UL-SOA. Additional phase noise measurements were performed for the fundamental LO frequency as well as of the generated mm-wave signal with a multiplication factor of $N = 8$. Those measurements revealed a phase noise level of -96 dBc/Hz and -78 dBc/Hz at 10 kHz offset from the carrier, respectively. By using novel high-output power double-mushroom PDs, output power levels up to about 0 dBm have been achieved.

1. INTRODUCTION

The concept of generating millimeter-wave (mm-wave) signal by optical means is an interesting alternative for providing frequency tunable and low phase noise continuous-wave (cw) signals. Such a photonic local oscillator (LO) would exhibit a number of unique features when compared to a purely electronic LO including wide frequency tunability, and broadband modulation capabilities as well as possibility of low-loss mm-wave signal transport via optical fiber. Several applications including broadband wireless links, radar systems, and earth-observation sensors would benefit from cost-effective photonic sources for low phase noise mm-wave cw signal generation.

Recently, several approaches for generating cw mm-wave signal by optical means were reported. One of the favorable approaches employs optical heterodyning of two optical waves with different frequencies in a high-frequency photodetector (PD), but is mainly limited by the bandwidth of the used PD and produces a signal with poor phase noise performances as long as the phases of the two optical waves are not locked to each other. Locking the phase of two optical waves using some techniques [1], improves the signal's phase noise but also increase system complexity. Another quite straight forward technique utilizes direct high speed external optical modulation using e.g., an Mach-Zehnder modulators (MZM) or an electro-absorption modulators (EAM). However, because of the bandwidth limitation of state-of-the-art external modulators (typically limited at around 50 GHz), photonic generation of frequencies higher than 80 GHz using double-sideband modulation presents a challenge [1].

To overcome these bandwidth limitations, several schemes have been demonstrated and proposed to achieve frequency multiplication [2], but the key limitation is the requirement of an ultra-narrow-band optical filter to remove undesired optical side-bands which significantly increases system complexity and cost. Recently in [3], we demonstrated a novel concept for a frequency tunable photonic synthesizer based upon exploiting nonlinear optical modulation in an MZM and four wave mixing in an SOA which does not require a narrow-band amplifier. In [3], we already demonstrated 50 GHz band operation with an eight times optical multiplication of the LO frequency.

In this paper, we present a low phase noise up to 50 GHz photonic synthesizer based upon external modulation in conjunction with the FWM effect in an UL-SOA. This technique achieves an optical multiplication factor of $N = 12$. Furthermore, low phase noise operation at a frequency

8-times the LO frequency showing a phase noise level of -78 dBc/Hz at 10 kHz offset from the carrier has been shown.

2. ULTRA-LONG SEMICONDUCTOR OPTICAL AMPLIFIERS (UL-SOAS)

Recently, novel ultra-long SOAs have been developed that are highly nonlinear, due to intra-band effects such as carrier heating (CH) and spectral hole burning (SHB), and these characteristics result in a high FWM efficiency [4]. In contrast to short SOAs, ultra-long-SOAs can be considered as comprising of two sections: a linear amplifying section and a nonlinear saturated section. The amplifying section has the same properties as a short SOA while in the lumped 3rd order nonlinear section, the carrier density is clamped to the net transparency level because of the high optical power after the amplifying section. Therefore, fast nonlinear intra-band effects can influence the signals and are expected to strongly interact with the original signals and thus UL-SOAs should exhibit tremendous four-wave mixing efficiency.

To identify optimal operation conditions for application on generation of optical millimeter-waves, experimental studies with respect to their nonlinearities are necessary.

3. EXPERIMENTAL SETUP AND RESULTS

The basic configuration of the photonic synthesizer is shown in Figure 1.

For the experimental characterization of the SOA's, we performed experiments using three different types of SOAs: An SOA with 1 mm interaction length (SOA-1 mm), one SOA with 2 mm interaction length (SOA-2 mm) and another SOA with an interaction length larger than 2 mm (SOA > 2 mm).

At first, the influence of the SOA's interaction length on the FWM efficiency was characterized using the setup shown in Figure 1 that includes a 1550 nm DFB laser source (LD) with a subsequent EDFA and polarization controller. An MZM biased at V_π used for generating a double side band optical signal with a suppressed carrier (DSB-SC) and driven by a Local Oscillator (LO) fixed to 4 GHz, an additional Erbium Doped Fiber Amplifier (EDFA) precedes the SOA to obtain the required optical input power necessary for operating the UL-SOA in the non-linear regime, a Single Mode Fiber (SMF), as the saturation optical output power of the SOAs were too high for the photo detector PD (+8 dBm maximum), an optical attenuator (ATT) was used to limit the optical input power to PD to ~ 5 dBm, corresponding to a photocurrent of ~ 2 mA, and a U2t photonics 50 GHz Photo Detector with responsivity @1550 nm of 0.65 A/W. The optical double-sideband signal was applied for all SOAs and after detection by a PD at an optical input power of 5 dBm, the electrical RF power of the optically multiplied higher-order frequency components were measured using an electrical spectrum analyzer (ESA). For the measurements, the SOA's optical input power was fixed to +8 dBm (saturation conditions).

We can see from Figure 2, for example, for a multiplication factor of $N = 8$ (eight times the LO frequency), the results show that the SOA with the longest interaction length (SOA > 2 mm) presented the best performance as expected, confirming that the nonlinearity increases with the device length. The power of the mm-wave generated is limited by the maximum optical input power of the used PD that is around +8 dBm, however by using novel high-output power double-mushroom PDs, output power levels up to about 0 dBm have been achieved [5]. The maximum achievable multiplication factor was also analyzed. Here, the MZM was driven at high LO power (+18 dBm) to achieve the maximum multiplication level possible, and biased at V_π .

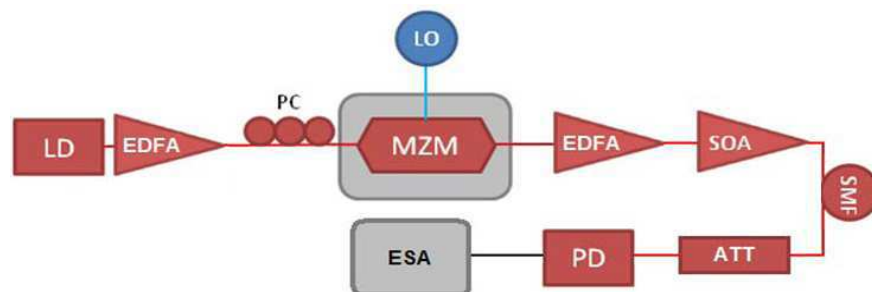


Figure 1: Photonic MW synthesizer to generate a MW frequency N -times the reference frequency of the LO.

As can be observed from Figure 3, efficient optical 12 times multiplication was achieved due to the nonlinear behavior of the UL-SOA. For the system operating without SOA only a multiplication factor of $N = 4$ has been achieved. Although twelve times optical multiplication is possible, as it was found experimentally, the conversion efficiency was improved by ~ 4 dB when using $N = 8$ instead of $N = 12$.

RF conversion efficiency as a function of the LO drive power was analyzed for three different multiplication levels, $N = 4$, $N = 8$ and $N = 12$, using the SOA > 2 mm that presented better performance, for identifying optimal operating conditions for the SOA. The LO frequency was fixed to 4 GHz and SOA in saturation conditions.

The Figure 4 illustrates that a multiplication of $N = 12$ has been achieved due to the nonlinear behavior of the SOA with an RF conversion efficiency at about -50 dB for the LO drive power from 8 to 12 dBm, showing the best operation point for this SOA.

Additional Phase noise measurements were performed for the fundamental LO frequency as well as for the generated MW signals with a multiplication factor of $N = 4$ and $N = 8$. Furthermore, the corresponding measurement noise floor for the different MW signals has also been measured. Based upon the theory, the phase noise for a multiplication factor of $N = 4$ and $N = 8$ should increase by 12 and 18 dB, respectively.

As can be seen from Figure 5, the phase noise performance degrades as expected, revealing phase noise levels of -96 dBc/Hz for LO frequency, and -78 dBc/Hz for $N = 8$ at 10 kHz offset from the carrier, respectively. At high offset frequencies, the measurement noise floor limits the measurement of the phase noise. Thus it is no surprise that the phase noise of the generated MW signals (at both low and high offset frequencies) demonstrates the same behavior as the LO signal, but with their corresponding degradation.

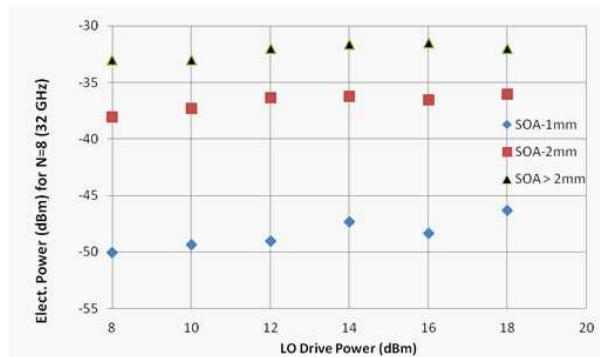


Figure 2: SOA interaction length influence on the FWM efficiency.

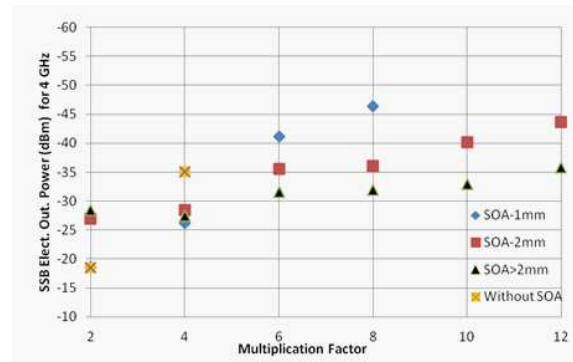


Figure 3: Maximum multiplication factor with high LO drive power.

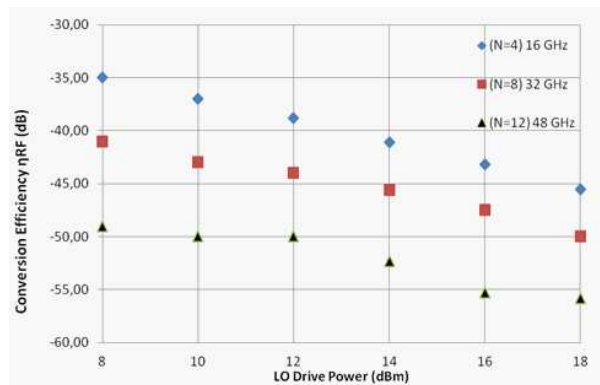


Figure 4: RF conversion efficiency.

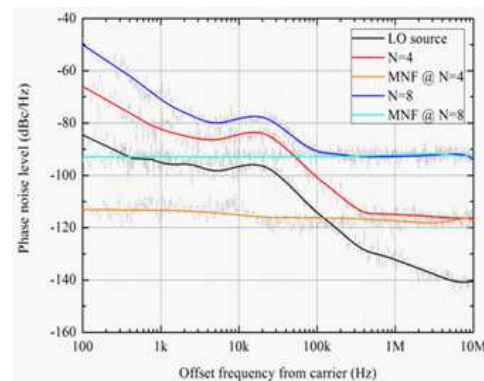


Figure 5: Phase noise measurements of the LO signal and the 4- and 8-times multiplied MW signal.

4. CONCLUSIONS

We could prove that the nonlinearity of the UL-SOA increase with length and we achieved a significant conversion efficiency improvement due to nonlinearity FWM in UL-SOA and the optical scheme using one MZM and a subsequent UL-SOA proved capable of generating low noise MW signals and the concept employing MZM and FWM in UL-SOA allows very high, up to at least 12 times optical multiplication level.

ACKNOWLEDGMENT

The author would like to thank the German Academic Exchange Service (DAAD) for their financial support.

REFERENCES

1. Bordonalli, A. C., C. Walton, and A. J. Seeds, “High-performance phase locking of wide linewidth semiconductor lasers by combined use of optical injection locking and optical phase-lock loop,” *Journal of Lightwave Technology*, Vol. 17, No. 2, 328–342, Feb. 1999.
2. Wang, Q., H. Rideout, F. Zeng, and J. Yao, “Millimeter-wave frequency tripling based on four-wave mixing in a semiconductor optical amplifier,” *IEEE Photon. Technol. Lett.*, Vol. 18, No. 23, 2460–2462, Dec. 1, 2006.
3. Garcia, A., S. Fedderwitz, and A. Stöhr, “Optical generation of low-phase noise microwave signals using nonlinear MZM and ultra-long SOA,” *IMOC 2011*, 255–259, IEEE Copyrights, 2011.
4. Runge, P., K. Petermann, W. Brinker, M. Schlak, and B. Sartorius, “Supercontinuum generating in ultralong SOAs — Theory and experiment,” *ECOC 2009*, 6.2.4, Vienna, Austria, Sep. 20–24, 2009.
5. Rymanov, V., T. Tekin, and A. Stöhr, “Double mushroom 1.55 μm waveguide photodetectors for integrated E-band (60–90 GHz) wireless transmitter modules,” *Proc. SPIE Photonics West 2012*, Vol. 8259, 82590E–82590E-7, San Francisco, California, USA, Jan. 2012.

Single Atom Trapping of Light

Raphael Tsu¹ and Michael A. Fiddy²

¹ECE Department, UNC Charlotte, USA

²Center for Optoelectronics, UNC Charlotte, USA

Abstract— Recently we revisited some of the questions frequently asked about the “size” of a photon and whether there is a satisfactory understanding of the absorption and emission of photons by atomic transitions. Adopting a dipolar model, one can draw analogies between the electromagnetic response of an atom and that of a sub-wavelength sized antenna, provided the constraints of quantum theory are included. By considering a photon as a unit of exchange of energy and momentum with an atom, we obtain some interesting and deeper insights.

1. INTRODUCTION

When discussing the absorption and emission of light by atomic transitions, it is customary to consider sizes such as the Bohr radius, the classical radius of an electron and the Compton wavelength. Whether light is absorbed or not is usually described by a vague concept we refer to as an interaction cross-section. For incident light of a given frequency, its effective wavelength in close proximity to the atom is held as a good measure of this cross-section. However, it is important to recognize the fundamental distinction between waves and particles. Strictly speaking particles all have potentials, including Yukawa potentials, and these have a r^{-1} singularity. This singularity defines them to be reasonably well localized in some region of space which we depict as somewhat fuzzy based on Heisenberg’s uncertainly principle. Waves have no mass but do transfer energy and momentum and we fully appreciate that this transfer or exchange of energy and momentum takes place in quantized units. Waves are not described in terms of being localized in space, and indeed, the only meaningful quantity one can usefully exploit in our models is an intensity operator which has the dimensions of some number of photons per unit volume. Simple optical experiments lead us to accept that electromagnetic waves are somewhat delocalized and our ignorance of their propagation path results in phenomena such as Young’s interference patterns and coherent wavefunction phenomena such as entanglement. Nevertheless, even while we might describe low light levels by plane waves, strong interactions with particles occur. A plane wave expanded into a series of spherical Hankel functions of the second kind, gives us some transitory spatial localization of the wave’s energy and momentum in space and time, but a physical process predisposing that choice of basis set remains elusive. We are more comfortable envisioning plane waves incident on boundaries that are locally flat (on the scale of the wavelength) but should not forget that any real boundary is made of agglomerations of atoms, more or less strongly coupled to each other, each of which we are happy to assume plays a role in the total electromagnetic response. We therefore consider justified in more carefully examining the interaction of an electromagnetic wave with a single atom. We can identify an interface between two piece-wise analytic regions associated with an atom, one inside and one outside of some interaction volume. In the same way as one would model a simple dipole antenna, we circumscribe the physical antenna and consider the possible response of dipole and higher order multipoles confined to that volume. We then match wave functions and their derivatives at the interface, which in turn create reflections and lead to confinement. Such a physical process is not instantaneous and takes time. Trapping with an increasingly high Q , is well understood to be the case for increasingly small antennas, [1]. Indeed Stuart and Pidwebetsky build on earlier work and give a model for extremely high polarizabilities and hence high Q -factors, is the region including the antenna has a negative permittivity [1]. In the case of an atomic transition, one has a number of electrons which will each be affected by the electric and magnetic fields of an incident wave in a very complex fashion. The interaction with this plasma may usually be considered to be weak because of the relatively long wavelength of the light compared to the interaction volume. However, if that volume exhibits a resonant behavior with the specific frequency or effective wavelength of the light inside the interaction volume, then a strong interaction can build up over time, which might be many millions of periods. When the volume’s plasma frequency equals the atomic transition frequency, strong interactions with particles occur. A plane wave expanded into a series of spherical Hankel functions of the second kind, gives us some transitory spatial localization of the wave’s energy and momentum in space and time, but a physical process predisposing that choice of

basis set remains elusive. We are more comfortable envisioning plane waves incident on boundaries that are locally flat (on the scale of the wavelength) but should not forget that any real boundary is made of agglomerations of atoms, more or less strongly coupled to each other, each of which we assume plays a role in the total electromagnetic response. We therefore consider justified in more carefully examining the interaction of an electromagnetic wave with a single atom. We can identify an interface between two piece-wise analytic regions associated with an atom, one inside and one outside of some interaction volume. In the same way as one would model a simple dipole antenna, we circumscribe the physical antenna and consider the possible response of dipole and higher order multipoles confined to that volume. We then match wave functions and their derivatives at the interface, which in turn create reflections and lead to confinement. Such a physical process is not instantaneous and takes time.

To summarize this section, whenever particles such as atoms interact with waves, we recognize that there are r^{-1} singularities to be dealt with involving the interaction of Schrodinger waves for the electrons and protons with light and its component electric and magnetic fields [2]. Coupling between the electrons and spatial modes of the incident field are inevitable. We note that the interaction of two electrons separated by Δd and emitting a photon can be estimated using the uncertainty relationship, $\Delta d \Delta k = 1$. Consequently the ratio of the interaction energy to the photon energy ($e^2/\Delta d$)/ $\hbar \Delta \omega = e^2/\hbar(\Delta \omega/\Delta k) = e^2/\hbar c = \alpha$, the fine structure constant, which describes the Coulomb interaction of a particle with photon. We argue that one cannot state that one has detected a single photon, until after reaching a build-up time, QT , where T is the period of the light and Q , the quality factor. For convenience, we next consider the simplest atomic interaction volume, which is a H atom.

2. THE HYDROGEN ATOM

We know interaction parameters very accurately for the H-atom, and taking the 1S-2P transition, $\hbar\omega = 10.2\text{ eV}$ with $\lambda = 1.215 \times 10^{-7}\text{ m}$. The relaxation time (due to spontaneous emission) is $\tau = 1.6 \times 10^{-9}\text{ s}$ and the period of the wave $T = 4.05 \times 10^{-16}\text{ s}$, giving $Q = \tau/T = 2.5 \times 10^7$. This is an exceptionally large Q and as far as we are aware, only a superconducting cavity can reach such a high Q value at low frequency. We are dealing with the incident light being trapped for more than 10^7 cycles of the optical field which in turn necessarily results in a very high degree of interaction between a single H-atom and light. H-atom and light. Let us start with the dielectric function for Lorentz model of resonant interaction between dipoles and light

$$\varepsilon(\omega) = 1 + (\omega_{es}^2) / [\omega_0^2 - \omega^2 - i\gamma\omega]$$

with ω_{es} expressed in terms of the plasma frequency $\omega_p^2 = ne^2/m\varepsilon_0$, in which n is replaced by a single dipole per unit volume of $4\pi a^3/3$, with a being the radius to be determined for a high overall gain. In essence, a single atom (a dipole) interacting with an electromagnetic wave defines a volume of interaction. The gain factor $Q = \omega_0\tau$ for a resonant system with $\tau = 1/\gamma$, the lifetime. Taking the 1s-2p transition of an H-atom with $\omega_0 = 1.55 \times 10^{16}\text{ s}^{-1}$ and the lifetime $\tau = 1.6 \times 10^{-9}\text{ s}$, giving $Q = 2.48 \times 10^7$, 25 million cycles represent the long build-up time involved with the interaction of a single atom with light. The remarkable feature of a single atom interacting with even very low intensities of background radiation is that it describes a resonating system with such a high Q . *We note that resonators with much higher values of Q are known, such as the Q of 2×10^{11} in a system using ^{133}Ce which is available commercially.* Equating $\omega_{es}^2 = \omega_0^2$, the radius of the spherical interaction volume to be $a = 0.6\text{ \AA}$, somewhat larger than the Bohr radius at 0.53 \AA . Following Fitzpatrick [3], using the dipole moment $d = 0.632 \times 10^{-29}$ the background electric field, $E = \hbar\gamma/d = 1.05 \times 10^4\text{ V/m}$, we can obtain the electric field for the dipole transition between 1s-2p at resonance is $E_{1s-2p} = Q^{1/2}E = 5.15 \times 10^7\text{ V/m}$, far lower than the Rydberg field is $5.14 \times 10^{11}\text{ V/m}$. We must realize the meaning of such high Q with reference to response and sensitivity. Detectors with high sensitivity, favor a high- Q system. However, in electronic applications, a Q over one million is too slow, for example, an atomic system is too slow compared to a solid state system.

The field builds up during these millions of cycles and one can calculate that after build up, the electric field of spontaneous emission is given by $5 \times 10^7\text{ V/m}$. In a given light field at the resonant frequency, the Rabi flopping between two eigenstates occurs at the Rabi frequency. With a relentless flux of light incident on our H atom, the Rabi frequency represents a fundamentally limited response determined by the properties of the high- Q cavity defined by the interaction volume. During trapping, one has a trapped oscillating electrostatic field similar to evanescent

modes which dominate when the radius of the volume is a lot less than the wavelength. Returning to Chu's high $Q \sim (kd)^{-3}$ factor for very small antennas [4], we can estimate d for the H-atom. Adopting the classical Lorentz model, and assuming one dipole within our interaction volume, a high gain or Q at the resonant frequency, chosen to be that of the 1S-2P transition, leads to $d = 0.6\text{\AA}$. This is to be expected as the field trapping takes place and it is smaller than the 2P orbital, but slightly larger than the Bohr radius. The Q factor for a small antenna is 3.4×10^7 which is within 30% of that observed.

In Fig. 1, we have plotted the typical real and imaginary parts of the dielectric function, ε_1 and ε_2 using the Lorentz model. Note that at the resonant frequency, ε_2 reaches the maximum value of Q and the FWHM at $Q/2$ as expected, while ε_1 reaches $\pm Q/2$ as shown. Fig. 2 shows what happens as the resonance bandwidth narrows. However, it is important to recognize that dielectric functions, as for any constitutive relationships, are defined assuming the random phase approximation (RPA) is applicable. The RPA requires situations where statistical averaging can be both physically justified and dominates as it does for solids having structures with translational symmetry, or liquids and gases. Obviously such an assumption does not apply to a single atom, nevertheless, our model relies on the principle that within the space-time of the interaction between light and the atom, it is indeed possible to consider the concept of constitutive relationships.

3. BOUNDARY CONDITION FOR HIGH- Q SYSTEM

Second order partial differential equations require two conditions to be matched over the boundary separating two analytic regions, allowing the unique specification of two constants for the two solutions. Let us discuss what sort of boundary conditions may be defined between a plane wave interacting with the field of an isolated emitter or absorber, represented by an atom, a molecule, or even a finite region of space-time. Such considerations are important for a number of situations, for example, a dipole antenna interacting with an incident wave, or emitting radiation into space all around the dipole. Let us create a model applicable to the case whenever the single atom, or molecule, or a single electron, is interacting with an electromagnetic plane wave. Let us take a plane wave interacting with a singular field such as the Coulomb field having a point singularity. Surely at a distance far from the point singularity, the far field of a single electron is almost indistinguishable from a plane wave. Whereas at very close distances, it would require the expansion of the plane wave into spherical harmonics to describe the interaction. In a radiation field when $r \gg \lambda$, we know that we may neglect higher order poles. However, for $r \ll \lambda$, the action is all controlled by the term involving $(ka)^3$, the origin of Chu's formula for high Q [4]. When $ka \ll 1$, interaction feeding back to the incident wave is minuscule for a single site. Therefore, in a typical solid, Avogadro's number helps to promote the interaction. When such a large number of interactions is averaged over a close range, phase coherence is lost because phonons are the major culprits in destroying phase coherence typically in times shorter than 10^{-14} s. This fact justifies the use of RPA for the description of the dielectric function. However, with a single atom interacting with light, when

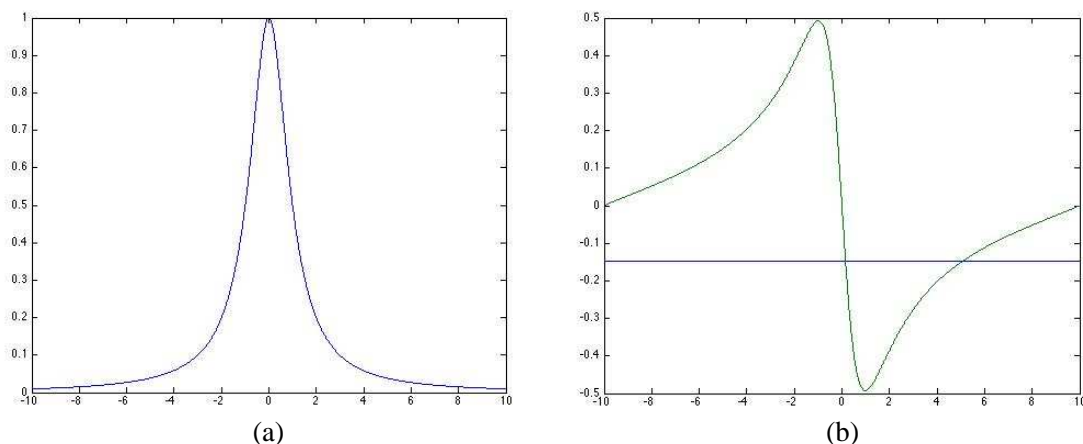


Figure 1: (a) The imaginary and (b) real parts of the Lorentz model oscillator for the spectral dependence of the permittivity. The imaginary part rises to a value of Q at resonance, which the real part extends to $\pm Q/2$ as shown.

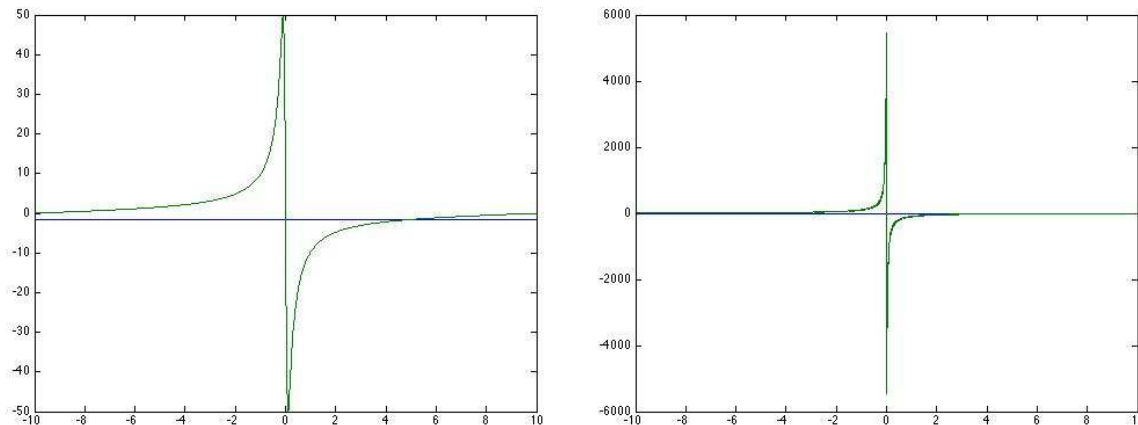


Figure 2: As the resonance bandwidth narrows, Q increases as illustrated in these plots of the real part of the permittivity.

$ka \ll 1$, the interaction between a wave and a single atom is weak and we need to wait for a very long time for the transfer of energy to reach a significant value. This is the reason why, formally, boundary conditions can only come into play after millions of cycles, because of the very slow build-up. For this reason, a high Q system only manifests itself in situations having where a single atom interacts with an incident wave. More importantly, we recognize that RPA is not applicable, and therefore, any devices having the same sort of logic cannot be made into a laser-like device. Rather, a high nonlinear interaction must be present for in-phase interaction in order to generate a useful device. Lastly, we may ask where is the origin of line broadening. By definition, line broadening implies nonlinearity to generate frequency components not present in the incident wave. Therefore, the very presence of line broadening is the result of nonlinear interaction. High Q is therefore a testament to a very weak interaction, but nonlinear in nature, channeling part of the incident wave into frequencies not originally present.

4. CONCLUSIONS

The mechanism of the trapping of an incident electromagnetic wave's energy by an atom, is argued here to be quite similar to that for a small antenna. The Lorentz oscillator model for an atomic resonance and for an antenna that is much smaller than a wavelength both leads to similar estimates for the Q of an atom. We illustrated this for the special case of the 1s-2p transition of a H-atom. One can expect that for atoms with large atomic numbers, the number of electrons in the interaction volume will increase and their various wavefunctions will predispose them to a much more complicated set of coupling phenomena with the spherical Hankel (or other choice) basis functions representing the incident electromagnetic wave. The same mechanism will be at play however, namely the transfer of energy into the interaction volume over some millions of cycles of the electromagnetic wave until the local electric field equals that of an eigenstate. At that moment, a rapid emission of a quantized packet of energy $\hbar\omega$ with an unpredictable momentum $\hbar k$ will occur. In high intensity fields, one can expect coherent emission at the Rabi frequency.

REFERENCES

1. Stuart, H. R. and A. Pidwebetsky, "Electrically small antenna elements using negative permittivity resonators," *IEEE Trans. Antenna & Propagation*, Vol. 54, 1644, 2006.
2. Tsu, R., *Superlattice to Nanoelectronics*, 2nd Edition, Elsevier, 2011.
3. Fitzpatrick, R., *Lectures on Quantum Mechanics*, Complete Version on Google, Dec. 12, 2006.
4. Chu, L. J., *J. Appl. Phys.*, Vol. 19, 1163, 1948.
5. Kraus, J. D., *Antennas*, McGraw-Hill, 1950.

Gold Nanoparticles Chain Waveguide with Enhanced Transmission Method and Spectral Coding

C. Cinar and T. Sengor

Electrical & Electronics Engineering, Yıldız Technical University, Turkey

Abstract—In this study a known waveguide consisting of fifteen gold cubic nanoparticles is examined using 3D FDTD method with Drude model and auxiliary differential method. The magnitude of transmission rate to the end point of the waveguide is managed to be increased by using total fourteen particles without changing the length of the chain by just removing the 4th particle, where all the other parameters are unchanged. By not deploying 4th particle there became two separate chain which enlightened by single gauss laser beam at the same time and this effect makes surface plasmon polarizations boosted twice like a cascade amplifier. In addition to one removal, two and three removal of particles at a time is studied and their spectral transmission rate characteristics are given as a communication coding or data storage information placement location.

1. INTRODUCTION

In recent years, plasmonics has attracted a great deal of attention due to its important potential toward applications in sensing, medical imaging, and information processing. This branch of photonics develops new concepts to confine light beyond the diffraction limit and enhance the electromagnetic field at the nanoscale. The synthesis and fabrication of disperse noble metal nanoparticles with a variety of shapes, from cubes to spheres and branched multipods. Energy transport in ordered arrays of closely spaced noble metal nanoparticles plasmon waveguides relies on near-field coupling between surface plasmon-polariton modes of neighboring particles [1]. This type of guiding due to near-field coupling was demonstrated experimentally in macroscopic structures operating in the microwave regime [2]. At the submicron scale, a theoretical analysis of plasmon waveguides was done using a point-dipole model in [3, 4].

The chain consists of fifteen gold dots with a square base ($l \times l = 100 \times 100 \text{ nm}^2$) and 40 nm high is modeled in [5] and spectral transmission rates are given for the 600 nm–800 nm wavelength range for three different spacing distance between nanodots. Moreover the behavior of the transmittance spectrum of a chain against its length has been demonstrated in a previously published work [6], where the length of the chain was changed by controlling the number of metallic dots and letting the others parameters unchanged. So that it is shown that the position and the shape of the narrow band in the transmission rate spectrum do not depend on the length of the chain and only the mean value of the transmittance is modified with the varying of the chain's length.

In this work the chain of metallic nanoparticles studied in [5] is obtained and developed by using 3D FDTD technique [7] with drude model and auxiliary differential method [8]. For the dispersive properties of the gold, Drude parameters are chosen like $\epsilon_b = 10.48$, $w_p = 1.3755e16 \text{ ve}$ $\gamma = 1.177e14$ [9]. Waveguide is enlightened with Gaussian laser beam as in [5] and its formulations are obtained from [10].

2. ENHANCED TRANSMISSION

Schematic structure of original structure modeled in [5] is shown in Figure 1(a). This structure consists of fifteen cubic particles with height $h = 40 \text{ nm}$ and $100 \times 100 \text{ nm}^2$ cross section area. The nanoparticles are gold metallic sorted cubes of length and height smaller than the incident wavelength along the x axis.

It is aimed to determine the propagation conditions of a local excitation along the nanoparticles waveguide by computing the near-field distribution above the chain when one end is locally illuminated by a focused gaussian beam. The chain lies on a glass substrate ($\epsilon_1 = 2.25$) and is surrounded by air ($\epsilon_2 = 1$). The illumination light is a Gaussian laser beam focused at its input end. The beam waist is set to $W_0 = 1.5 \mu\text{m}$ and the electric field polarization is aligned along the x -axis.

To visualize the guiding efficiency of the waveguide chain, a study of the near-field optical transmittance versus the incident wavelength λ of the excitation beam is carried out. The spectra have been plotted for wavelength range from 600 nm to 800 nm. Results of the 3D FDTD simulations

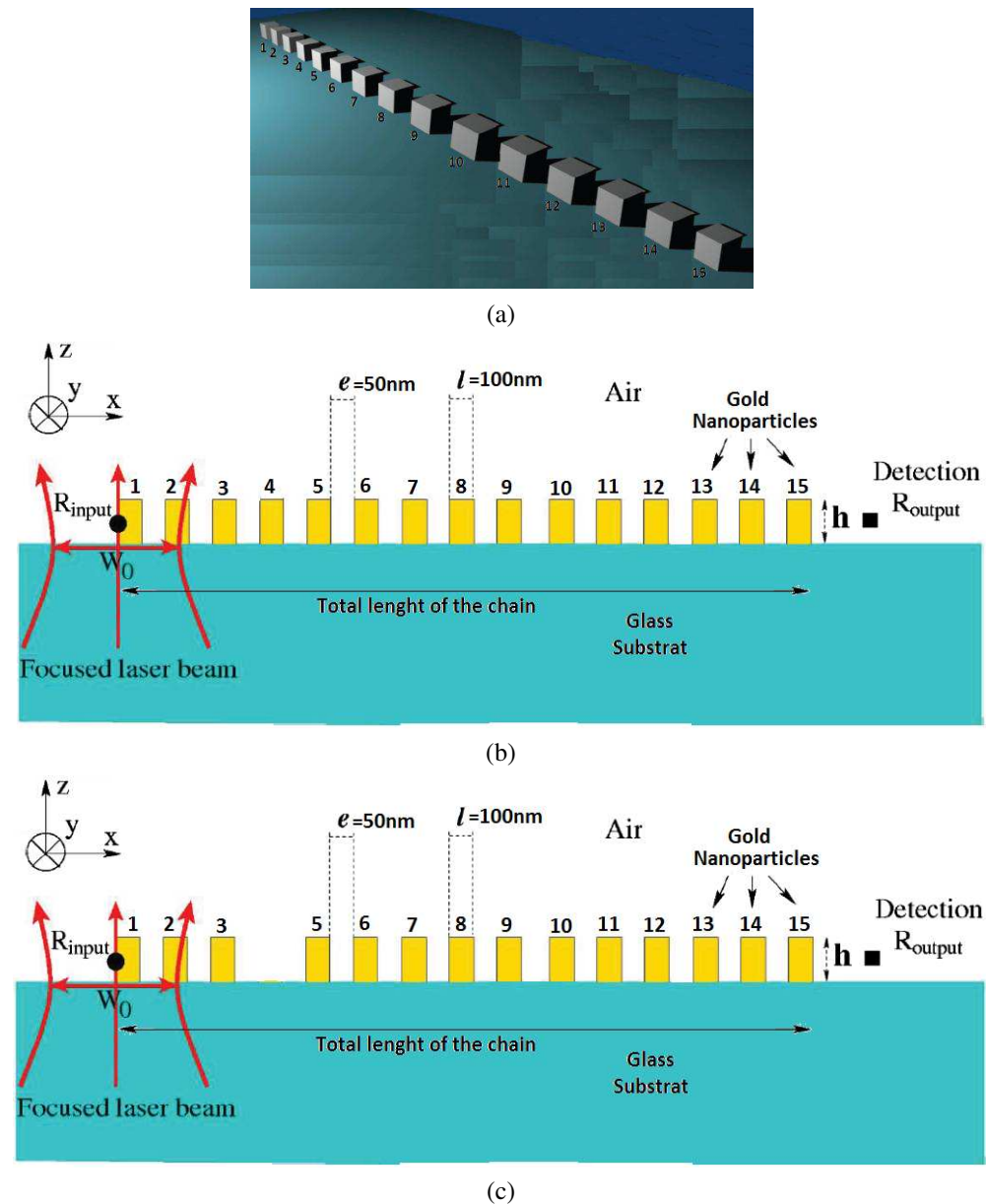


Figure 1: (a) 3D image of waveguide chain. (b) Original structure consists of fifteen particles spaced 50 nm apart from each other [5]. (c) Proposed structure consists of total 14 particles (only 4th of them are removed), total length of the chain and all other parameters unchanged.

for both original structure in Figure 1(b) and proposed structure in Figure 1(b) are depicted Figure 1(c). The near-field optical transmittance can be defined by the dimensionless quantity

$$T(\lambda) = \frac{I_{output}}{I_{input}} = \frac{|E(R_{output}, \lambda)|^2}{|E(R_{input}, \lambda)|^2} \quad (1)$$

Here $E(R_{output}, \lambda)$ represents the electric field computed at the chain exit (R_{output}) and $E(R_{input}, \lambda)$ the incident electric field computed at R_{input} in the absence of the chain. The position of the vector R_{input} has been placed at the center of the enter side of the waveguide while the output observation point R_{output} has been shifted of 100 nm from its exit side.

As seen at Figure 2, proposed structure has the same transmission band character as original structure's but new structure's transmission rate magnitude has a gain approximately twice the original structure's magnitude. It can be said that by just removing 4th particle and remaining all other things especially length of the chain unchanged, the amount of the energy transported to the end of the chain can be boosted efficiently without effecting spectral transmission band

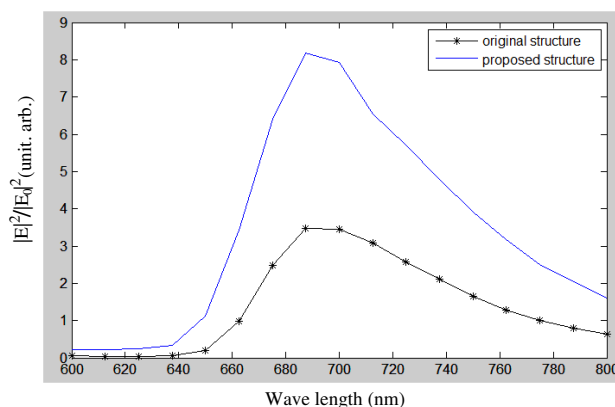


Figure 2: Spectral transmission rates of original structure consists of fifteen particles [5] and proposed structure consists of total 14 particles (only 4th removed, total length of the chain and all other parameters unchanged.)

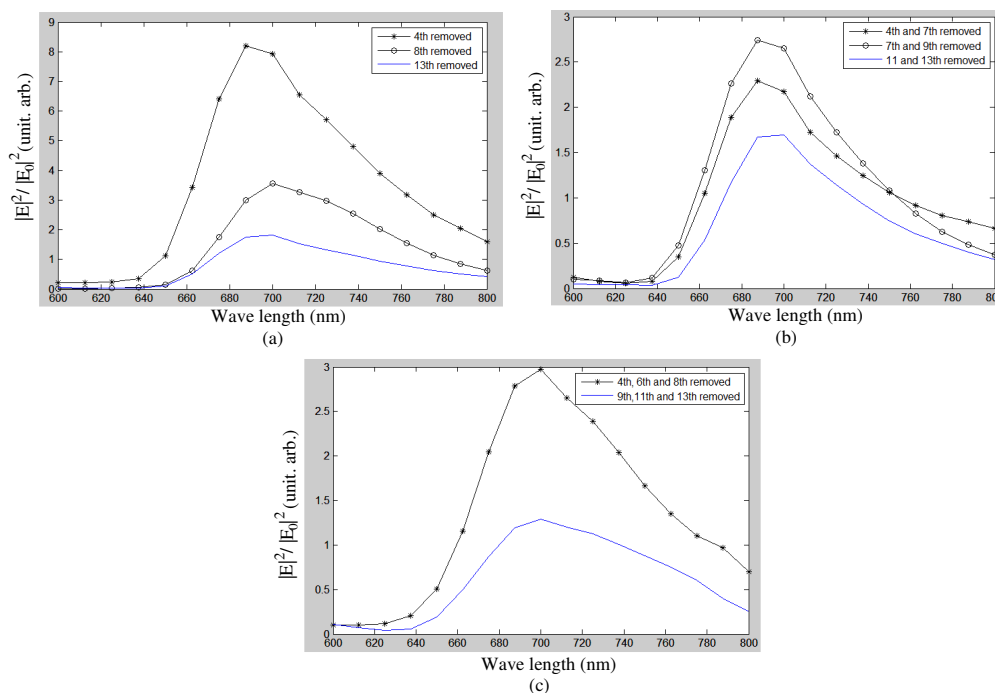


Figure 3: Spectral transmission rate of (a) one particle removed structures, (b) two particles removed structures, (c) three particles removing structures.

properties. Laser waist radius is 750 nm and so that it can enlighten first seven particles adequately when 4th particle is removed there became two separate chains (particles 1, 2, 3 and particles 5, 6, 7, ..., 15). Both chains' total lengths are so enough that they can produce their own surface plasmon polarizations and these SPP's are efficiently coupled and transmitted to the output point by particles.

3. SPECTRAL CODING PATTERNS

In addition to above structure (removing 4th particle), one particle removed: 8th and 13th; two particle removed: 4th–6th, 7th–9th and 11th–13th; three particle removed: 4th–6th–8th and 9th–11th 13th totally eight structures are simulated. In Figure 3(a) spectral transmission rate of one particle removed structures, in Figure 3(b) spectral transmission rate of two particles removed structures and in Figure 3(c) spectral transmission rate of three particles removing structures are given.

As seen in Figure 3(a), when the removed particle gets closer to the output end, magnitude of spectral transmission rate decreases. It can be thought that as the removed particle gets closer to

the output point, coupled and transmitted SPP's by particles get weaker. But the characteristic of spectral transmission rate does not change significantly. Therefore, from these one particle removed structures, spectral transmission rate patterns proportion to magnitude can be obtained obviously. At the output point spectral transmission rate can be controlled by just removing one particle from its place. The location of removed particle directly influences the output spectra. Consequently these patterns can be used as coding information for optical communication or nanodevices. Same things can be said for two particles removed structures as seen in Figure 3(b) and three particles removed structures as seen in Figure 3(c).

When all structures are compared, as long as one particle exists between them, increasing number of removed particles near the output end does not affect the magnitude of transmission rate. But when particles which are close to first seven particles are removed, output spectra can be different from what is expected because first seven particles are close to focus point of laser light.

4. CONCLUSIONS

In this work, a known waveguide chain structure as called original structure [5] consists of fifteen gold nanoparticles is examined and its output spectral transmission rate is improved significantly by just removing 4th particle and remaining all other parameters especially length of the chain unchanged as called proposed structure. By not deploying 4th particle there became two separate chain which enlightened by single gauss laser beam at the same time and this effect makes surface plasmon polarizations boosted twice like a cascade amplifier. The amount of the SPP's energy transported to the end of the chain can be boosted efficiently without effecting spectral transmission band properties.

In addition to one particle removed structure; two particle removed and three particle removed structures are simulated. From these one, two, and three particle removed structures, spectral transmission rate patterns proportion to magnitude can be obtained obviously. The location of removed particle directly influences the output spectra. Consequently these patterns can be used as coding information for optical communication or nanodevices.

REFERENCES

1. Maier, S. A., "Observation of coupled plasmon-polariton modes in Au nanoparticle chain waveguides of different lengths: Estimation of waveguide loss," *Applied Physics Letters*, Vol. 81, No. 9, 1714–1716, 2002.
2. Maier, S. A., M. L. Brongersma, and H. A. Atwater, *Appl. Phys. Lett.*, Vol. 78, No. 16, 2001.
3. Brongersma, M. L., J. W. Hartman, and H. A. Atwater, *Phys. Rev. B*, Vol. 62, 16356–16359, 2000.
4. Maier, S. A., M. L. Brongersma, P. G. Kik, S. Meltzer, A. A. G. Requicha, and H. A. Atwater, *Adv. Mater.*, Vol. 13, No. 19, 1501–1505, 2001.
5. Larochea, T. and C. Girard, "Near-field optical properties of single plasmonic nanowires," *Applied Physics Letters*, Vol. 89, No. 23, 2006.
6. Girard, C. and R. Quidant, "Near-field optical transmittance of metal particle chain waveguides," *Opt. Express*, Vol. 12, 6141–6146, 2004.
7. Sullivan, D. M., *Electromagnetic Simulation Using the FDTD Method*, IEEE Press, 2000.
8. Ung, B., "Interference of surface waves in a metallic nanoslit," *Optics Express*, OSA, 2007.
9. Palik, E. D., ed., *Handbook of Optical Constants of Solids*, Vol. 2, Academic Press, 1991.
10. McDonald, K. T., "Axicon gaussian laser beams," *Princeton University*, Princeton, NJ 08544, March 14, 2000.

Turbulent Parameters Estimation through the Phase Decomposition into the Zernike Polynomials

V. A. Kulikov¹, M. S. Andreeva², and V. I. Shmalhausen²

¹A. M. Obukhov Institute of Atmospheric Physics, Russian Academy of Sciences, Russia

²Department of Physics, M. V. Lomonosov Moscow State University, Russia

Abstract— We propose a method for estimation of turbulence characteristics that is based on the sequential analysis of normalized correlation functions of Zernike coefficients. This method has been applied for analysis of the experimental data from turbulence modeling in a water cell with a laser beam passing through it. We show presence of the anisotropy of the turbulence in some regimes.

1. INTRODUCTION

The wavefront phase [1, 2] of a laser beam as well as the amplitude [3–5] is used for the analysis of turbulent characteristics. Different methods of the wavefront phase analyses exist [6–8]. Usually estimating such parameters as inner and outer scales and the structural constant C_n^2 of refractive index [5–10], these methods provide significantly different results. These differences result from a variety of temperature regimes as well as from the diversity of methodologies. As the experimenters are not able to control the weather conditions in the real atmosphere, there are good reasons for using the numerical and the physical modeling to analyze the effects and to perfect the estimation methods of the main turbulent parameters.

Most of the theories suppose that the turbulence is isotropic, which doesn't necessarily occur.

In this work, some of the results of the experiment carried out in a water cell to simulate the turbulence are suggested [14, 15]. The wavefront phase of a laser beam was analyzed after it has propagated through the random layer of water. The evident advantage of such a model is the opportunity to control the turbulent parameters and analyze them in the constant temperature, temporal and spatial conditions.

The proposed method of turbulent parameters estimation is based on the phase decomposition by Zernike polynomials [16]. The correlation functions of Zernike coefficients of the experimental data phase decomposition are investigated and both the inner and the outer scale are estimated sequentially. The key feature of the method is the mentioned sequential of turbulent scales estimation results from the turbulence physical properties and allows to eliminate the indeterminacy that usually appears in the solution of the two-parametric problem.

2. EXPERIMENTAL DESIGN AND PHASE ANALYSIS

In the experiment the turbulence was created by the temperature gradient between the heater and the cooler plates in a water cell. The cell was made of optical glass, 34 cm in length and 21 cm in width. the heater and the cooler plates were held at constant temperatures. The distance between them was 10 cm. The experimental design scheme is presented by Figure 1.

A 30 mm wide collimated laser beam was propagated through the turbulent layer as showed in Figure 1. The semiconductor laser with the wavelength of 780 nm was used. The Shack-Hartmann

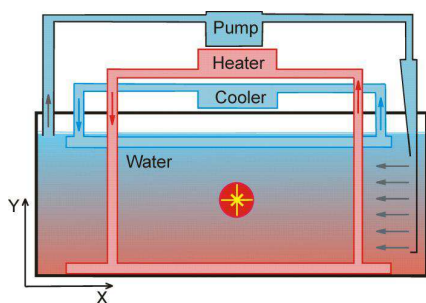


Figure 1. Design of the experimental assembly.

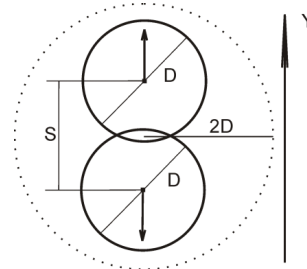


Figure 2. The direction of aperture shifting.

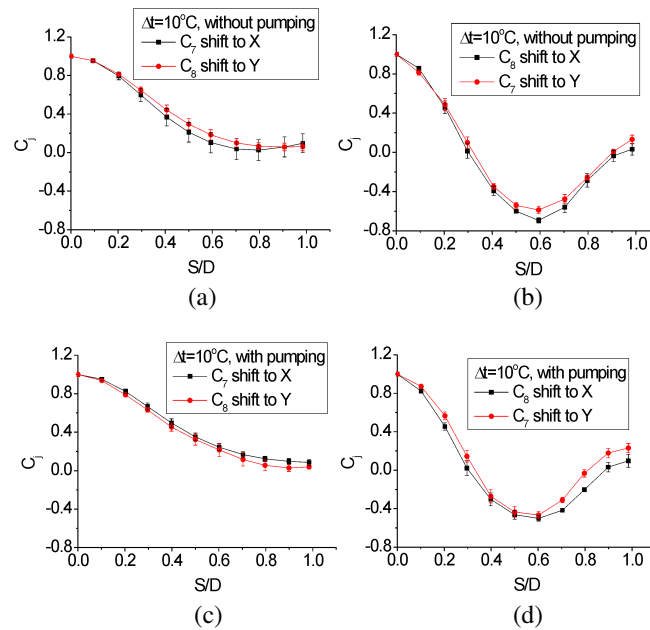


Figure 3. Correlation functions for Zernike modes ($j = 7, 8$) with aperture shifting in x direction (square curves) or y direction (circular curves): (a) C_7 (X axis) and C_8 (Y axis), $\Delta t = 10^\circ\text{C}$ without pumping; (b) C_8 (X axis) and C_7 (Y axis), $\Delta t = 10^\circ\text{C}$ without pumping; (c) C_7 (X axis) and C_8 (Y axis), $\Delta t = 10^\circ\text{C}$ with pumping; (d) C_8 (X axis) and C_7 (Y axis), $\Delta t = 10^\circ\text{C}$ with pumping.

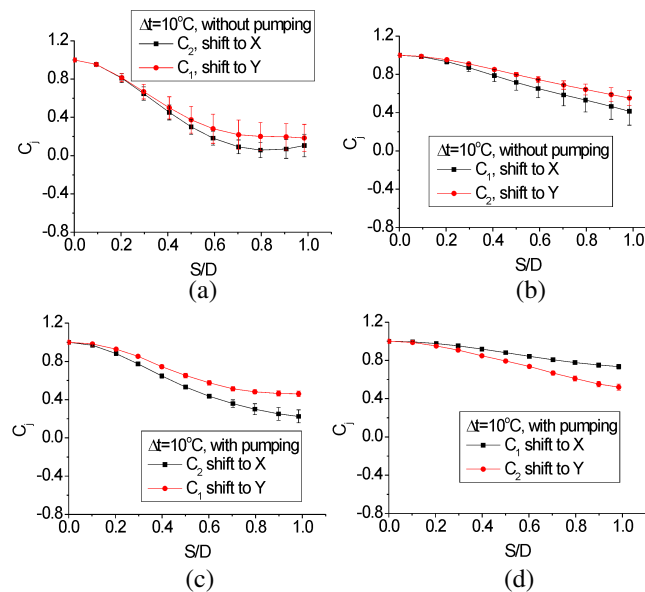


Figure 4. Correlation functions for Zernike modes ($j = 1, 2$) with aperture shifting in x direction (square curves) or y direction (circular curves): (a) C_2 (X axis) and C_1 (Y axis), $\Delta t = 10^\circ\text{C}$ without pumping; (b) C_1 (X axis) and C_2 (Y axis), $\Delta t = 10^\circ\text{C}$ without pumping; (c) C_2 (X axis) and C_1 (Y axis), $\Delta t = 10^\circ\text{C}$ with pumping; (d) C_1 (X axis) and C_2 (Y axis), $\Delta t = 10^\circ\text{C}$ with pumping.

sensor with 30-mm input aperture was the detector which measured the local slopes of wavefront then they were restored to the laser beam wavefront phase. In order to calculate the Zernike coefficients of the phase correlation functions two virtual circular apertures, both 15 mm in diameter, were allocated in the reconstructed distribution. It was possible to advance the relative position of these apertures to each other a distance of S in the Y direction as it is shown in Figure 2(a) (along the temperature gradient). In addition, the apertures shift along the X direction was also carried out for anisotropy controlling.

Zernike coefficients had been calculated in each aperture before the correlation functions of Zernike coefficients were counted. They were averaged over many realizations. The normalized

correlation functions are given

$$C = \frac{\langle a_{1j}a_{2j} \rangle}{\langle a_1 \rangle^2} \quad (1)$$

where a_{1j} is the Zernike coefficients in the first aperture, a_{2j} is the Zernike coefficients in the second aperture, in assumption that $\langle a_{1j} \rangle^2 = \langle a_{2j} \rangle^2$.

The isotropy checking showed that it is possible to create the anisotropy turbulence in a water cell.

In this paper, the turbulent scale estimations in isotropy and anisotropy cases is estimated and the derived results are discussed.

3. THEORY AND METHOD OF ANALYSIS

The two-dimensional spectral density of the phase fluctuation in the von Karman-Tatarskii model is

$$\Phi(k) = \frac{A \exp(-(k/k_m)^2)}{k(k^2 + k_0^2)^{11/6}}, \quad (2)$$

where $A = 0.0096(2\pi/\lambda)^2 \int_0^\infty C_n^2(z) dz$, C_n^2 is structural constant of refractive index, λ is the wavelength of the propagating light, k is wave vector, $k_0 = 1/L_0$, L_0 is the outer scale of turbulence; $l_m = \alpha/k_m$, l_m is the inner scale of turbulence, $\alpha = 5.92$.

In this cause the form of the Zernike modes correlation functions derived analogously [8] is

$$\langle a_{1j}a_{2j}(S) \rangle = A(n+1) \int_0^\infty e^{-\frac{k^2}{k_m^2}} \times (J_0(2Sk) + pJ_{2m}(2Sk)) \frac{J_{n+1}^2}{k(k^2 + k_0^2)^{11/6}} dk \quad (3)$$

where n is the radial order of the j -th Zernike polynomial, J is the Bessel functions of an appropriate order; $p = 0, -1, +1$ depending on Zernike mode number.

Expression (3) was used for numerical calculations and shows that the correlation functions of the Zernike coefficients of different modes order depend differently on the changes of inner or outer scales. For the analysis the modes of the first three orders were taken. The dependence character is very close for modes of the same order.

The opportunity to estimate sequentially the turbulent scales is based on the independence of the third order Zernike modes of the outer scale L_0 in the cause $L_0/D > 1$, in other words when the diameter of the receiving aperture D is less than the outer scale L_0 . The first order Zernike modes appreciably depend on both the inner and the outer scales. The inner scale influences all the investigated orders in the case $l_m/D \sim 1$.

The idea of the method is to estimate first the inner scale using the correlation functions of the third order as they depend only on the inner scale. Then to estimate the value of the outer scale using the first order correlation functions considering the inner scale known. The second order modes are not analyzed as they depend on both scales in an approximately similar way but with different sign.

4. RESULTS

The turbulent scales in the case of temperature difference between the cooler and the heater $dt = 10^\circ\text{C}$ with and without wind were estimated. In these regimes the value of Rayleigh $Ra = 2.36 * 10^8$ and Prandtl $Pr = 6.27$ which means that the turbulence is developed.

In the presence of the wind the Reynolds number value is $Re = (1 - 1.5) * 10^3$ which is below the critical value which allows to conclude that the flow should not be turbulent.

The isotropy was controlled with the use of observation of the correlation function of four Zernike coefficients. According to the isotropic theory, some of the correlation functions (e.g., $j = 1$ and $j = 2$, $j = 7$ and $j = 8$) fit each other when the direction of aperture shifting changes from y to x . We show that the third-order modes meet this requirement in all the studied modes of turbulence.

The first-order modes demonstrate such a fit only at $\Delta t = 10^\circ\text{C}$. Along with the introduction of the flow the isotropy becomes disturbed.

As it can be seen on Fig. 3 the turbulence isn't isotropy in the case of the flow presence. One shouldn't use the isotropy theories for estimating such regimes. All that can be seen is that there is more correlation along Y axe than along the X one.

Table 1.

Δt , °C	pumping	l_m , cm	along Y ; L_0 , cm	along X L_0 , cm
10	no	1–2	4–9	6–10
10	yes	1–2	28–33	8–9

Resulting estimates are given in Table 1.

We estimate both turbulent scales at $\Delta t = 10^\circ\text{C}$ without pumping. In other cause, we can't estimate outer scale because anisotropy is present.

5. CONCLUSIONS

Both isotropy and anisotropy turbulent regimes can be created in the cell. The described above method provides the correct estimation only in the case of isotropy turbulence. The outer scale estimations of $L_0 = 4\text{--}10$ cm and $l_m = 1\text{--}2$ cm by $\Delta t = 10^\circ\text{C}$ without flow were received as the result of the research. It should be noted that the inner scale estimations are equal in both regimes which is probably connected with the small-scale perturbations isotropy. In order to receive the correct turbulence parameters estimations in the anisotropy case the anisotropy theory of turbulence is more likely needed.

REFERENCES

- Bertolotti, M., M. Carnevale, L. Muzii, and D. Sette, "Atmospheric turbulence effects on the phase of laser beams," *Applied Optics*, Vol. 13, No. 7, 1582–1585, 1974.
- Goodwin, M., C. Jenkins, and A. Lambert, "Improved detection of atmospheric turbulence with SLODAR," *Optics Express*, Vol. 15, No. 22, 14844–14860, 2007.
- Kleen, R. H. and G. R. Ochs, "Measurements of the wavelength dependence of scintillation in strong turbulence," *J. Opt. Soc. Am.*, Vol. 60, No. 12, 1695–1697, 1970.
- Gurvich, A. S., M. A. Kallistratova, and F. É. Martvel, "An investigation of strong fluctuations of light intensity in a turbulent medium at a small wave parameter," *Radiophysics and Quantum Electronics*, Vol. 20, No. 7, 705–714, 1977.
- Frehlich, R. G., "Estimation of the parameters of the atmospheric turbulence spectrum using measurements of the spatial intensity covariance," *Applied Optics*, Vol. 27, No. 11, 2194–2198, 1988.
- Hu. P. H., J. Stone, and T. J. Stanley, "Application of Zernike polynomials to atmospheric propagation problems," *J. Opt. Soc. Am. A*, Vol. 6, No. 10, 1595–1608, 1989.
- Consortini, A. and K. A. O'Donnell, "Measuring the inner scale of atmospheric turbulence by correlation of lateral displacements of thin parallel laser beams," *Waves in Random Media*, Vol. 3, 85–92, 1993.
- Takato, N. and I. Yamaguchi, "Spatial correlation of Zernike phase-expansion coefficients for atmospheric turbulence with finite outer scale," *J. Opt. Soc. Am. A*, Vol. 12, No. 5, 958–963, 1995.
- Ochs, G. R. and R. J. Hill, "Optical-scintillation method of measuring turbulence inner scale," *Appl. Applied Optics*, Vol. 24, No. 15, 2430–2432, 1985.
- Wilson, R. W., "SLODAR: Measuring optical turbulence altitude with a Shack-Hartmann wavefront sensor," *Mon. Not. R. Astron. Soc.*, Vol. 337, 103–108, 2002.
- Kolmogorov, A. N., "Local structure of turbulence in an incompressible fluid at very high Reynolds number," *Dokl. Akad. Nauk. USSR*, Vol. 30, 299–303, 1941.
- Von Kármán, T., "Progress in the statistical theory of turbulence," *J. Mar. Res.*, Vol. 7, 252–264, 1948.
- Tatarski, V. I., *Wave Propagation in a Turbulent Medium*, McGraw-Hill, New York, 1961.
- Maccioni, A. and J. C. Dainty, "Measurement of thermally induced optical turbulence in a water cell," *J. of Modern Opt.*, Vol. 44, No. 6, 1111–1126, 1997.
- Gurvich, A. S., M. A. Kallistratova, and F. É. Martvel, "An investigation of strong fluctuations of light intensity in a turbulent medium at a small wave parameter," *Radiophysics and Quantum Electronics*, Vol. 20, No. 7, 705–714, 1977.
- Noll, R. J., "Zernike polynomials and atmospheric turbulence," *J. Opt. Soc. Am.*, Vol. 66, 207–211, 1976.

Possibility of O^+/H^+ Transition Level Determination from Irkutsk Incoherent Scatter Data and GPS Total Electron Content

B. G. Shpynev and D. S. Khabituev

Institute of Solar-Terrestrial Physics, Irkutsk, Russia

Abstract— Experimental data obtained on Irkutsk Incoherent Scatter Radar (ISR) and GPS Total Electron Content (TEC) were used for estimation of the O^+/H^+ transition level and electron density distribution in the upper topside ionosphere and in the plasmasphere. As model description we use modified Chapman function where O^+/H^+ transition level is used as parameters. On the base of the model the estimation was made for electron density distribution in the upper topside ionosphere and in the plasmasphere, as well as for O^+/H^+ transition level dynamics in different geophysical conditions. It is shown that plasmasphere can contribute more than 30% to GPS TEC, and input from plasmasphere should be taken into account when GPS TEC variations are analyzed.

1. INTRODUCTION

The interest to the topside ionosphere structure and dynamics is supported by practical needs of astronautics and space weather forecasting, which require the developing of theoretical and empirical models. Different techniques of electron density $n_e(h)$ measurements at altitudes above F2-layer maximum provide information about $n_e(h)$ and ion composition with different space-time resolution. For example, low-orbital (600–1000 km) satellites can produce direct measurements of n_e and ion composition along their orbit and give wide latitude-longitude coverage. However, pure time resolution of satellite measurements does not give a chance for investigation of fast dynamical processes in this region. Also, direct satellite measurements can't provide altitudinal distribution of $n_e(h)$ as it possible to do by spectrometers in mesosphere and stratosphere, because of specific properties of atomic gases. This problem can be solved by using ionosonde onboard satellites with few thousands kilometers orbits, but such equipment requires significant power supply and complicated antenna design, so only few such projects (as IMAGE/RPI and ISIS [7]) can be called as successful.

Another example is the incoherent scatter technique, which provides excellent time and altitude resolution, but only a few radars operate worldwide, these measurements are very expensive and only two of radars: Arecibo and Jicamarca can make observation above 1000 km. So, the investigation of upper ionosphere and plasmasphere dynamics on time intervals of hour and less is very difficult task. Experimental data, derived by different techniques are generalized in semi-empirical models, some of which are commonly used separately or as parts of more complex models [2–6].

Wide possibilities for ionospheric studies are given by navigation systems GPS/GLONAS, which provide integral electron content along satellite-receiver beam. Due to relatively large number of satellites multi-positional reception of GPS/GLONAS signals is used for reconstruction of ionosphere structure [8], however the sensitivity of these techniques is not sufficient for plasmasphere.

In present study we try to combine GPS TEC data with incoherent scatter data, collected on Irkutsk ISR during period of high solar activity (1998–2000). Such analysis is possible due to technical peculiarities of Irkutsk ISR and gives new information additionally to usual ISR observations.

2. METHOD AND MODEL

The main idea of the method presented here is the estimation of the difference between GPS TEC and total content of ionospheric electrons derived from Irkutsk's ISR $n_e(h)$ profiles. Technical features and frequency range (154–162 MHz) of Irkutsk ISR make possible to do Faraday rotation measurements with absolute calibration which don't require ionosonde information about F0F2 [9].

In brief, this technique uses the property of HF radio waves when polarization plane of the wave rotates in the magnetized plasma with angular speed depended on local electron density. Derivative of rotational phase is proportional to n_e and it is used for calculation of $n_e(h)$ profile. Total electron content along the radar beam may be calculated from formula

$$TEC_{ISR} = \frac{1}{\gamma} \int_0^{h_x} n_e(h) dh, \quad (1)$$

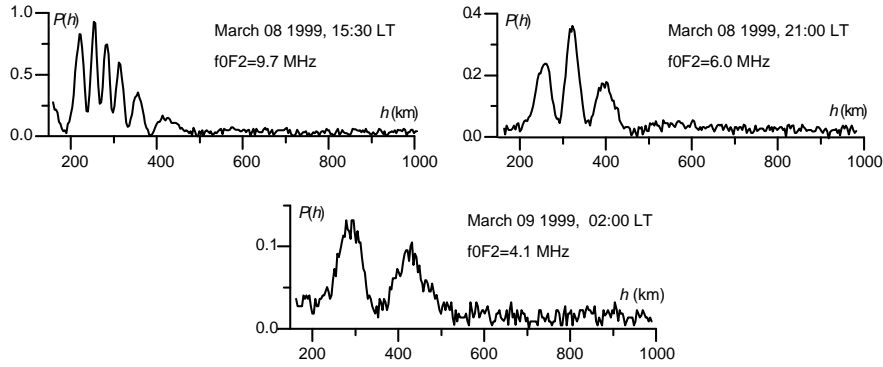


Figure 1: Examples of power profiles, measured by Irkutsk ISR.

where h_x is the top altitude to which TEC is calculated. Coefficient of proportionality γ can be supposed constant for midlatitudes and it is equal to $\gamma = \frac{e^3 B_0 \cos \alpha}{2 \varepsilon_0 m_e^2 \omega^2 c}$. Here e is the electron charge, B_0 is the geomagnetic field strength, α is the field inclination, ε_0 is the dielectric permittivity of vacuum, m_e is the electron mass, ω is the radio wave frequency and c is the speed of light. The antenna of Irkutsk ISR can emit and receive only single linear polarization, so that received signal fades when polarization of signal and antenna are perpendicular. Typical examples of power profiles, registered by Irkutsk ISR are shown on Figure 1. Distance to points of fading is uniquely defined by TEC from ground (expression (1)), and these points may be used as markers of Faraday fading TEC, which is:

$$TEC_F = 0.901 \times (0.5 + n) \times \pi, \quad (2)$$

Here n is the number of Faraday minimums after the first minimum which has polarization phase equal to $\pi/2$. Even with the presence of ground clutter, which limits low altitude of observation by 165 km, the first minimum always presents in Faraday profile of Irkutsk ISR and TEC_F may be calculated. Every Faraday hump after the first minimum contributes 2.83 TECU. Practically, at least one minimum always presents in power profile and we know altitude and TEC_F from the ground to this point. Accuracy of calculation for Faraday minimum altitude depends on noise, but it is better than 0.5 TECU. In this study we use GPS IONEX maps and TEC_F calculation accuracy is better than typical errors (~ 1 TECU) of GPS mapping technique [10].

To combine GPS and ISR data we need a model of $n_e(h)$ distribution in the topside ionosphere and in the plasmasphere. It may be modified Chapman layer model [6], where altitude of O^+/H^+ transition level is included as parameter. We also will suppose that atmosphere conditions below and above O^+/H^+ transition level are the same and scale heights of oxygen and hydrogen ions differ by only the mass factor 16. The altitude range of transition area is supposed to be small relatively the size of F2 layer. Such conditions are very probable in quiet geomagnetic conditions. As scale height of atomic oxygen ions H_{O^+} we will use the vertical scale height (not plasma scale height) which can be found from logarithmic $n_e(h)$ profile in lower topside ionosphere. Such scale height depends both from plasma temperature and from ion-neutral drag effect induced by neutral wind. If we denote by h_m and h_T altitudes of F2 maximum and O^+/H^+ transition level, the model can be written as

$$N_{O^+} = N_m \exp \left\{ 1 - \frac{h - h_m}{H_{O^+}} - \exp \left(-\frac{h - h_m}{H_{O^+}} \right) \right\} \quad (3)$$

$$N_{H^+} = N_{O^+}(h_T) \cdot \exp \left(-\frac{h - h_T}{H_{H^+}} \right) \quad (4)$$

$$H_{H^+} = 16 \cdot H_{O^+} \quad (5)$$

Figure 2 shows schematically denotations used in (3)–(5) and three altitude ranges where different methods of TEC calculation are used. The altitude h_F corresponds to Faraday minimum which is used for calculation of TEC_F . In logarithmic coordinates $n_e(h)$ distribution inside TEC2 area will be presented by linear functions

$$\ln n_e \cong ah + b \quad (6)$$

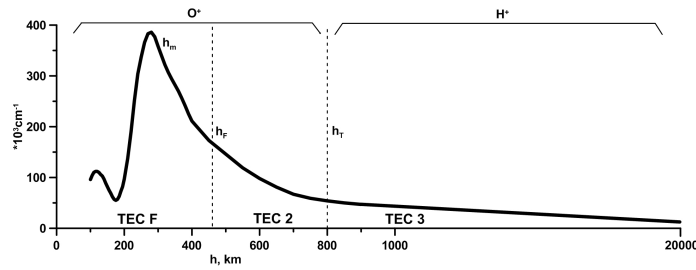


Figure 2: Basic denotations and scheme of calculations for model.

Coefficients a and b can be easily calculated from linear regression formula. Logarithmic electron density in the plasmasphere (TEC3) can be also presented by linear function with first coefficient $a_H = a/16$. Coefficient b_H is calculated from condition of equality of two distributions at h_T altitude.

$$a_H h_T + b_H = a h_T + b, \quad (7)$$

This gives:

$$b_H = (a + a/16)h_T + b, \quad (8)$$

Then TEC2 may be written as

$$Tec2 = H_{O^+} \times \left(\exp\left(-\frac{h_T}{H_{O^+}} + b\right) - \exp\left(-\frac{h_F}{H_{O^+}} + b\right) \right), \quad (9)$$

TEC3 in the plasmasphere will be

$$Tec3 = 16H_{O^+} \times \exp\left(-\frac{h_T}{16H_{O^+}} + b_{H^+}\right), \quad (10)$$

Total electron content GPS is equal to sum of these values in three areas:

$$TEC_{GPS} = TEC_F + Tec2 + Tec3, \quad (11)$$

Then from formulas (7)–(11) we can get the altitude h_T :

$$h_T = -H_{O^+} \ln \left(\frac{\left(\frac{TEC_{GPS} - TEC_F}{H_{O^+}}\right) \cdot 10^4 - \exp(a h_F)}{15} \right) \quad (12)$$

Condition of the model (3)–(5) requires that $h_T < b \cdot H_{O^+}$, and this criteria is the control parameter for experimental data processing. Typical error of the method may be estimated if we will vary TEC_{GPS} by ± 1 TECU. It is ± 20 km in daytime when TEC_{GPS} is ~ 30 – 40 TECU, and it is ± 40 km in nighttime when TEC_{GPS} is ~ 15 TECU. Standard deviation of scale height calculation lies in ± 10 km range. So, if suggestions used in model are valid, then the accuracy of h_T calculation lies in interval of few tens of meters.

3. EXPERIMENT

For estimation of model quality we have analyzed the Irkutsk ISR data collected at high solar activity (years 1998–2000) when every power profile has multiple Faraday fading and all parameters needed may be calculated with good accuracy. We have examined the dynamics of h_T in different seasons and geomagnetic conditions, and we also have estimated the dynamics of relative contribution of the plasmasphere to total electron content.

As an example Figure 3 shows variation of topside ionosphere parameters during September 24–26, 2000. Figure 3 (top plot) shows variations of h_T for September 24, 25 and 26, 2000 (solid, dashed and dot dashed lines). Bottom plot shows in the same manner relative contributes of ionosphere and plasmasphere (above h_T) to GPS TEC, calculated by Formulas (2), (9) and (10). Summed daily indexes $C_p = \sum a_p$ for these days are 130, 191 and 241 respectively. The first day: September

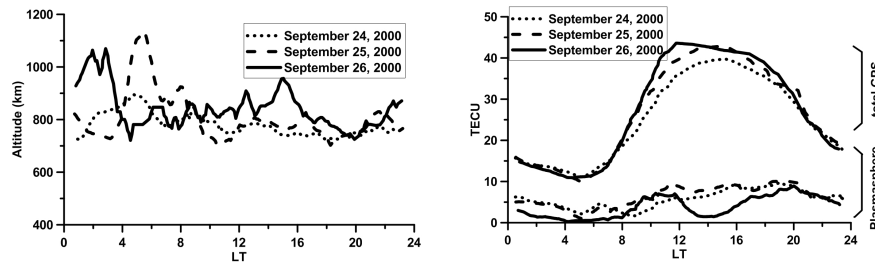


Figure 3: O^+/H^+ transition level, GPS TEC and plasmasphere TEC on September 24–26, 2000.

24 we can consider as quiet. Top panel of Figure 3 presents typical dynamic of O^+/H^+ transition level which slightly changes from day to day. Bottom panel shows relative contribution of the ionosphere and plasmasphere to total electron content.

Variations of O^+/H^+ transition level on Figure 3 show the good repeatability from day to day in quiet geomagnetic conditions, but in other days their daily variations may be very specific and they depend on local neutral wind and geomagnetic conditions. The climatology of h_T variations is the subject for additional study.

The relative contribution of plasmasphere electrons during different experiments of year 1998–2000 can be as much as 50%, and this should be taken into account when GPS TEC data or data from occultation experiments are used for restoration of ionosphere structure and for explanation of ionospheric dynamics.

ACKNOWLEDGMENT

The work was supported by Russian Found of Basic Research (Grant RFBR 11-05-00822) and RF Ministry of Education and Science Project 16.518.11.7097.

REFERENCES

1. Kutiev, I., R. A. Heelis, and S. Aananian, "The behavior of the O^+-H^+ transition level at solar maximum," *J. Geophys. Res.*, Vol. 85, 2366–2372, 1980.
2. Kutiev, I. and P. Marinov, "Topside sounder model of scale height and transition height characteristics of the ionosphere," *Adv. Space Res.*, Vol. 39, No. 4, 759–766, 2007.
3. Kutiev, I. S., P. G. Marinov, and S. Watanabe, "Model of topside ionosphere scale height based on topside sounder data," *Adv. Space Res.*, Vol. 37, 943–950, 2006.
4. Stankov, S. M. and N. Jakowski, "Topside ionospheric scale height analysis and modeling based on radio occultation measurements," *J. Atmos. Solar-Terr. Phys.*, Vol. 68, 134–162, 2006.
5. Luan, X., L. Liu, W. Wan, J. Lei, S.-R. Zhang, J. M. Holt, and M. P. Sulzer, "A study of the shape of the topside electron density profile derived from incoherent scatter radar measurements over Arecibo and Millstone Hill," *Radio Sci.*, Vol. 41, RS4006, 2006, doi:10.1029/2005RS003367.
6. Strangeways, H. J., I. Kutiev, L. R. Cander, S. Kouris, V. Gherm, D. Marin, B. De La Morena, S. E. Pryse, L. Perrone, M. Pietrella, S. Stankov, L. Tomasik, E. Tulunay, Y. Tulunay, N. Zernov and B. Zolesi, "Near-Earth space plasma modeling and forecasting," *Annals of Geophysics*, Vol. 52, Nos. 3–4, 2009.
7. Reinisch, B. W., P. Nsumei, X. Huang, D. K. Bilitza, "Modeling the F2 topside and plasmasphere for IRI using IMAGE/RPI and ISIS data," *Advances in Space Research*, Vol. 39 731–738, 2007, doi:10.1016/j.asr.2006.05.032.
8. Kunitsyn, V. E., A. M. Padokhin, A. E. Vasiliev, G. P. Kurbatov, V. L. Frolov, and G. P. Komrakov, "Study of GNSS-measured ionospheric total electron content variations generated by powerful HF heating for a special issue: GNSS remote sensing," *Advances in Space Research* Vol. 47, 1743–1749, 2011.
9. Shpynev, B. G., "Incoherent scatter Faraday rotation measurements on a radar with single linear polarization," *Radio Sci.*, Vol. 39, No. 3, RS3001, 2004, doi: 10.1029/2001RS002523.
10. Mannucci, A. J., B. D. Wilson, D. N. Yuan, C. M. Ho, U. J. Lindqwister, and T. F. Runge, "A global mapping technique for GPS-derived ionospheric total electron-content measurements," *Radio Sci.*, Vol. 33, No. 2, 565–582, 1998.

Radiosounding of Ionospheric Disturbances Generated by Exhaust Streams of the Transport Spacecraft “Progress” Engines

V. V. Khakhinov, B. G. Shpynev, V. P. Lebedev, D. S. Kushnarev,
S. S. Alsatkin, and D. S. Khabituev

Institute of Solar-Terrestrial Physics, SB, RAS
Lermontov st. 126a, P. O. Box 291, Irkutsk 664033, Russia

Abstract— Results of series of active experiments, when transport cargo spacecraft “Progress” engines work in the field of Irkutsk’s Incoherent Scattering Radar (ISR) view, allow us to conclude that artificial disturbances, associated with exhaust gases, can produce observable changes in the ionosphere and in the radar signal, even with relatively small amount of exhaust product is used. Changes in ionospheric and radar characteristics strongly depend on geometry of the experiment. The most significant changes are observed when the engine burn is directed towards the Irkutsk ISR. Electron density depression (“hole”) can reach up to $\sim 20\text{--}30\%$ compared with background values. The hole life-time is about 10–15 minutes. Angular characteristics of reflected signals and radar cross-section are very sensitive to these artificial disturbances.

1. INTRODUCTION

A sequence of “Plasma-Progress” Active Space Experiments (ASE) was carried out in years 2007–2012. The main goal of these experiments is to study spatial-temporal characteristics of the plasma disturbances caused by the engine burns of orbital maneuvering subsystem (OMS) engines of “Progress’s” spacecrafts. All “Progress” spacecrafts were used after their mission on the International Space Station during reduction of their orbit and destruction in the Pacific Ocean. The “Progress” orbit altitude was usually about 340 km. Two types of engines were used in different combinations. First were eight Orientation and Mooring Engines, 47 gram/sec exhaust product each, which ran simultaneously (8 flights total). Second was the Approach and Correction engine (ACE, 53 flights total) with 1 kg/sec exhaust product. Amount of engine exhaust products was relatively small and did not exceed 11 kg.

The main ground based research tool was the Irkutsk Incoherent Scatter Radar operated by Institute of Solar-Terrestrial Physics. Each burn took place exactly when spacecrafts crossed radar diagram field of view. Exhaust directions and amount of injected products were changed for each flight. As diagnostic technique we used the standard ionosphere observation mode by Incoherent Scatter method which was adapted to technical features of Irkutsk ISR [7]. Also, special technique was used for precise diagnostic of spacecraft radiolocation cross-section, including angular characteristic of reflected signal [9]. Incoherent scatter technique was used for studying of ionosphere response to electron density ($Ne(h)$) irregularities associated with exhaust products (mainly these are $Ne(h)$ depletions with 5–20 minutes lifetime). Radiolocation measurements let us study space-temporal refractive effects caused by exhaust stream.

Artificial ionospheric disturbances associated with spacecraft engine exhaust were investigated during some experiments, which were performed with the NASA Space-Shuttle programmer and ISR (Millstone-Hill, Jicamarca and Arecibo) [1–6]. During these experiments large portions of exhaust products injected into the ionosphere almost simultaneously and produced large area of ionization depletion. The amount of exhaust products varied from 87 kg [2] up to 830 kg [3]. These experiments produced large disturbances observed in the ionosphere for the period of one hour or more along the Shuttle track near the F2 layer maximum.

According to [1–3], exhaust products in the ionosphere initiate two observable effects: first is the production of local peak in radar received power, with tens of second duration; second is the reaction of exhaust gases (H_2O , H_2 , and CO_2) with the ambient ionospheric plasma, which make dominant atomic ions (O^+) convert to molecular ions which, in their turn, recombine rapidly with the ambient electrons to form neutral species. The second process under consideration depends both on the stream direction and geometry, and it can be of different duration depending on the background plasma density. In the experiments [1–6] the depletion areas were significantly wider than radars diagram patterns, and changing in electron density could be easily observed. The peculiarity of present study is the localization of exhaust cloud in the space, which means that this cloud can overlay only a part of the radar diagram or can be moved from the diagram by neutral

wind. This requires careful estimates of external factors when direction and time of each burn are chosen. Despite on these problems, the advantage of these experiments is their repeatability.

2. EXPERIMENT RESULTS

Till present time we carried out 11 experimental ASE sessions (3–7 days each), with 61 experimental flights total. The times of experiments correspond to different ionospheric conditions day/night, seasons, solar activity etc. [8,9]. First session in September 2007 showed observable (15–30%) depletions of ionization during three experiments, however, other four days we did not observe significant effects. Similar result was obtained in year 2008 [9].

Ionospheric conditions during the ASE experiment in 2007–2008 corresponded to very low solar activity. Geomagnetic conditions were also quiet ($K_p < 4$). While quiet geomagnetic conditions were the advantage of the experiment, the low solar activity was the disadvantage because it produced very low background electron density. It caused low radar signal/noise ratio (especially in nighttime) and, hence, the bad experimental data quality. However, low background N_e is the chance for relatively small exhaust mass to make $N_e(h)$ depletion in significant volume. This is why some experiments showed observable effects.

Later experiments in years 2010–2011 were carried out at higher solar activity level, and as result at higher background $N_e(h)$. These experiments confirm previously founded conclusion that scale of artificial irregularities depend on background ionization. Figures 1 shows $N_e(h)$ profiles for September 1, 2010 experiment when ACE exhaust stream was directed northward. Blue curve corresponds to conditions before burning, next curves are $N_e(h)$ after: 5 min. (green); 9 min. (red); 14 min. (light-blue); and 19 min. (black). The maximal depletion was about $\sim 28\%$ after 8–10 minutes. Figure 2 shows in the same manner the result of September 4, 2010 experiment where maximal depletion was about $\sim 12\%$ also after 8–10 minutes.

It should be mentioned that during some flights with similar conditions (mass of fuel, burn direction, local time) significant ionospheric disturbances were not observed. Figures 3 and 4 show that in similar conditions differences between $N_e(h)$ profiles can't be distinguished from regular variations and statistical errors. Similar results were obtained in April 2010 experiment. In each of five flights ACE worked “on braking” or “toward the radar” with total exhaust from 5.7 to 9.8 kg.

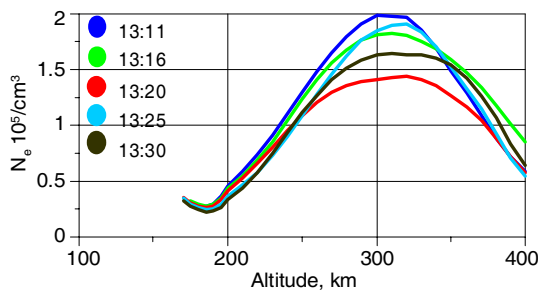


Figure 1: $N_e(h)$ during the 01.09.2010 experiment. ACE run northward at 13:20:02 UT. Amount of fuel was 7.5 kg.

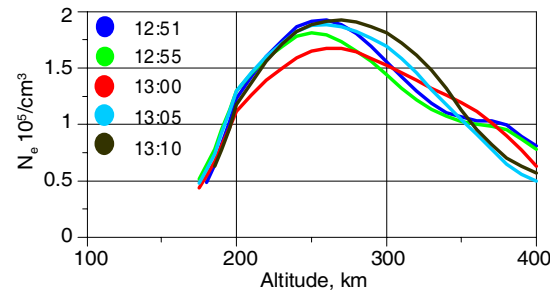


Figure 2: $N_e(h)$ during the 04.09.2010 experiment. ACE run northward at 12:59:30 UT. Amount of fuel was 7.44 kg.

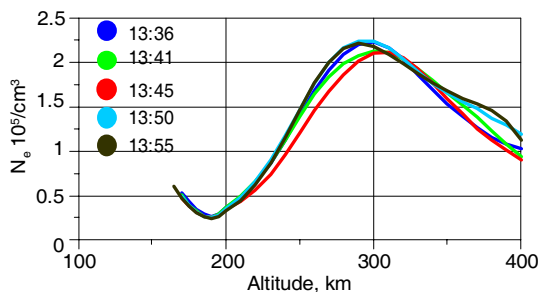


Figure 3: $N_e(h)$ during the 02.09.2010 experiment. ACE run northward at 13:44:57 UT. Amount of fuel was 7.0 kg.

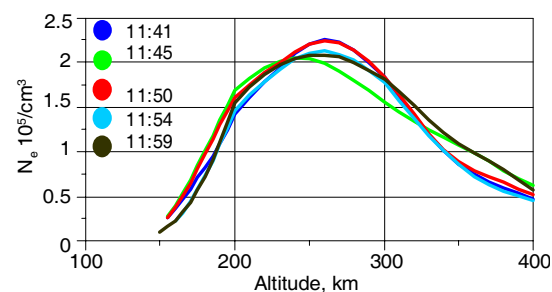


Figure 4: $N_e(h)$ during the 05.09.2010 experiment. ACE run northward at 11:49:08 UT. Amount of fuel was 7.52 kg.

Local time of these experiments was from 01 : 30 LT to 03 : 30 LT. Clear response to these burns was not founded. The most probable reason for unsuccessful experiments are the differences of flight orbits from ISR antenna diagram position which has 0.5° size in north-south direction and $\sim 10^\circ$ in west-east direction. Angle between spacecraft orbit and long axes of radar diagram is changed from one flight to other, and only flights when orbit and diagram coincide or are very close to each other can produces clouds which significantly overlay the diagram pattern.

Disturbances generated by burn streams make changes in power and phase characteristics of “Progress” radar signals. Figure 5 shows temporal variations of “Progress” radar power during two April 2010 experiments. Black and gray lines correspond to radar beam positions shifted by 0.5° . All curves show clear changing of signal in reply to engine running. Curves on Figure 5 show both depletion of total power and noise-like variations caused by refraction on irregularities generated by burn. This noise-like behavior of the radar signal continues a few seconds after engine switches off.

Some experiments when burn stream was pointed toward ISR show extremely large depletion of radar signal. Figure 7 shows variation of “Progress” radar signal (a) and calculated radar cross-section (b) during 07.09.2008 experiment. Dash line on left plot shows typical variations of radar signal when “Progress” passes through ISR antenna diagram. Radar cross-section shows the

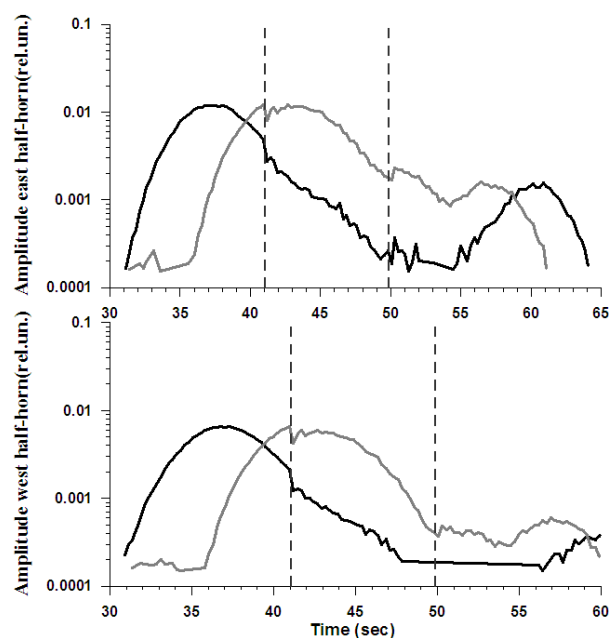


Figure 5: “Progress” radar power during the 23.04.2012 experiment. ACE runs “on radar”, vertical dashed lines are time of ACE switch on and switch off. Amount of fuel 8.88 kg.

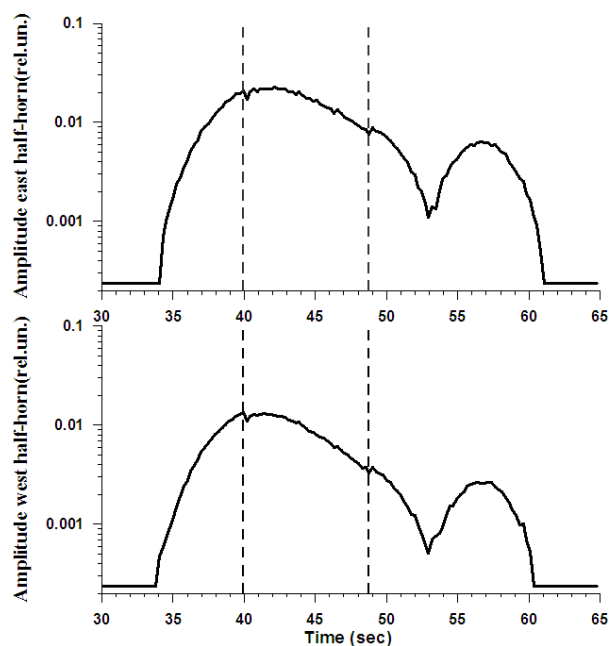


Figure 6: As on Figure 5 for the 26.04.2012. ACE runs “on radar” with 8.83 kg exhaust.

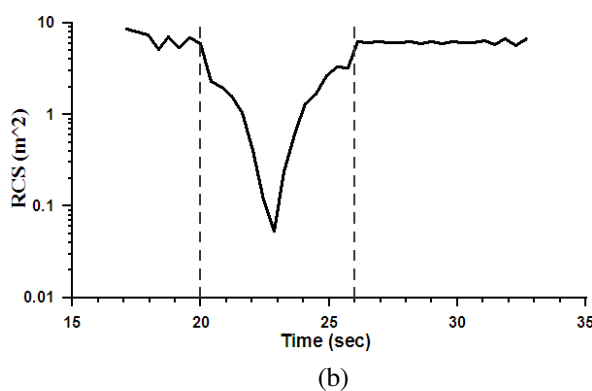
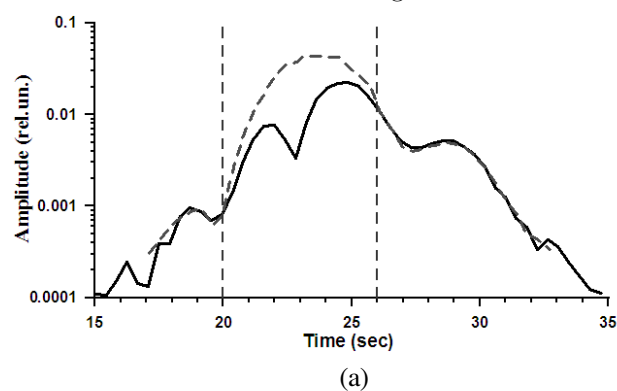


Figure 7: Variation of the “Progress” radar signal (a) during 07.09.2008 experiment. Dash line shows signal without burn. (b) is the actual radar cross-section of “Progress”. Exhaust product was 11 kg.

changing of “visible” “Progress’s” size during the burn. We should mentioned that Irkutsk ISR has carrier frequency ~ 160 MHz. Strong depletion of radar cross-section in this experiment can be caused by two reasons: the refraction of radar signal on stream edge or absorption (or sporadic partial reflections) of the signal by irregularities of ~ 2 meter size which are generated inside the burn stream.

In such experiments the signal reflected by “Progress” may be used as indicator of stream size and dynamics. As antenna system of Irkutsk ISR has two half-horn structure in east-west direction and independent receiver for both half-horn it is possible to make interferometric measurements of reflected signal by using phase difference between these receiving channels. This technique is now developed for estimation of stream size both along and across stream direction.

3. CONCLUSIONS

Results of active experiments show that small portions of exhaust gases from spacecraft engines can produce irregularities in the ionospheric plasma, which can be observed and study by incoherent scatter facilities. In the cases when cloud of exhaust gases occupies significant part of radar diagram pattern the depletion of ionization can be observed. Typically it can be 10–30% of background electron density with life-time about 10–20 minutes. Some experiments were unsuccessful, and this means that procedure of forming of irregularity clouds is not yet perfect because it depends on many external factors.

Small-scale irregularities, generated by exhaust stream moving and expansion, are also the subject for further investigations. Effects of diffraction or absorbing on these irregularities are regularly observed during ACE experiments and they provide the information about exhaust stream dynamics.

ACKNOWLEDGMENT

Authors are grateful to Dr. E. M. Tverdokhlebova and Dr. M. Yu. Kurshakov, the Central Research Institute for Machine-Building, A. I. Manzheley and T. I. Timofeyeva, the Mission Control Center, for collaboration in the “Plasma-Progress” program. Work has been supported by the grant 10-05-01099-a of the Russian Foundation for Basic Research and of the RF Ministry of Education and Science Project 16.518.11.7097.

REFERENCES

1. Bernhardt, P. T., J. D. Huba, W. E. Swartz, and M. C. Kelly, “Incoherent scatter from space shuttle and rocket engine plumps in the ionosphere,” *Journal Geophysical Research*, Vol. 103, No. A2, 2239–2251, 1998.
2. Bernhardt, P. T., J. D. Huba, E. Kudeki, R. F. Woodman, L. Condori, and F. Villanueva, “Lifetime of a depression in the plasma density over Jicamarca produced by space shuttle exhaust in the ionosphere,” *Radio Science*, Vol. 36, No. 5, 1209–1220, 2001.
3. Foster, J. C., J. M. Holt, and L. J. Lanzerotti, “Mid-latitude ionospheric perturbation associated with the spacelab-plasma depletion experiment at Millstone Hill,” *Annals of Geophysics*, Vol. 18, 111–119, 2000.
4. Mendillo, M., J. Baumgardner, D. P. Allen, J. Foster, J. Holt, G. R. A. Ellis, A. Klekociuk, and G. Reber, “Spacelab-2 plasma depletion experiments for ionospheric and radio astronomical studies,” *Science*, Vol. 238, 1260–1264, 1987.
5. Mendillo, M. and J. M. Forbes, “Artificially created holes in the ionosphere,” *Journal of Geophysical Research*, Vol. 83, 5785–5792, 1991.
6. Mendillo, M., G. S. Hawkins, and J. A. Klobuchar, “A sudden vanishing of the ionospheric F region due to the launch of Skylab,” *Journal of Geophysical Research*, Vol. 80, 2217–2228, 1975.
7. Shpynev, B. G., “Incoherent scatter Faraday rotation measurements on a radar with single linear polarization,” *Radio Science*, Vol. 39, No. 3, RS3001, 2004, doi: 10.1029/2001RS002523.
8. Shpynev, B. G., V. V. Khakhinov, A. V. Medvedev, A. P. Potekhin, V. P. Lebedev, E. M. Tverdokhlebova, and A. I. Manzheley, “Ionospheric perturbation associated with the “Plasma-Progress” experiment at Irkutsk,” *Proc. XXIX URSI General Assembly*, GP2-05.3, Chicago, USA, 2008.
9. Potekhin, A. P., V. V. Khakhinov, A. V. Medvedev, D. S. Kushnarev, V. P. Lebedev, and B. G. Shpynev, “Active space experiments with the use of the transport spacecraft “Progress” and Irkutsk IS Radar,” *PIERS Proceedings*, 223–227, Moscow, Russia, August 18–21, 2009.

Investigation of Ionospheric Slab Thickness and Plasmaspheric TEC Using Satellite Measurements

Photos Vryonides, Christos Tomouzos, Giannis Pelopida, and Haris Haralambous
Frederick University, 7 Y. Frederickou St., Palouriotisa, Nicosia 1036, Cyprus

Abstract— The ionospheric slab thickness (τ) is a parameter which provides information about the nature of the distribution of ionization at a specific location and is defined as the ratio of the vertical Total Electron Content (vTEC) measured in TEC units (1 TECu = 10^{16} electrons m^{-2}) to the maximum ionospheric electron density in the F-region (NmF2). Slab thickness provides substantial information on the shape of the electron density profile as well as the neutral and ionospheric temperatures/gradients, composition and dynamics. On the other hand the electron content in the plasmasphere, termed plasmaspheric electron content (PEC) has received increasing interest in the last few years due to its significance in measuring and modeling the ionosphere to altitudes lower than GPS, in the context of transionospheric signal propagation.

An investigation of the characteristics of these two parameters (τ and PEC) is carried out based on 650 values of vTEC and NmF2 retrieved by a space-based technique (radio occultation measurements from the Constellation Observing System for Meteorology, Ionosphere, and Climate-FORMOSAT-3/COSMIC) and vTEC values based on a ground-based technique (IGS dual frequency GPS receivers facilitating monitoring of the ionosphere) taking advantage of the inherently excellent spatial coverage achieved by the satellite constellation and the relatively uniform distribution of GPS stations operating over European latitudes. To ensure that simultaneous measurements of GPS derived vTEC and COSMIC derived vTEC and NmF2 are used, the distance between the GPS stations and GPS occultation at the peak of the F layer is limited to 1° within a time interval of 5 min. In addition only data during geomagnetically quiet conditions have been taken into account, as ionospheric electron density irregularities give rise to erroneous determination of the peak density and height from GPS occultations due to significant fluctuations of the electron density profile.

1. INTRODUCTION

The ionospheric slab thickness is a physical parameter that is related closely to the shape of the ionospheric electron density profile [1]. Slab thickness is also helpful in understanding the nature of variations of the upper atmosphere, since it can be related directly to the vertical scale height [2]. In addition the temporal and spatial distribution of slab thickness provides possibilities for more accurate calculation of the signal delay of radio wave propagating through the ionosphere. Based on long-time series of vTEC and of F2 peak electron density (NmF2), numerous analyses of the climatological behavior of the slab thickness have been made where it was recognised that slab thickness shows diurnal, day-to-day, seasonal, spatial, solar, and geomagnetic activity variations [3]. In this study, 1800 slab thickness values were calculated based on ground-based GPS_TEC measurements over Europe and GPS/COSMIC radio occultation measurements for the period 2007–2010.

The ionospheric slab thickness (τ) is a parameter which provides information about the nature of the distribution of ionisation at a specific location and is defined as the ratio of the vTEC to the maximum ionospheric electron density in the F-region (NmF2) [3].

$$\tau = \frac{TEC}{NmF2} \quad (1)$$

2. DIURNAL AND SEASONAL BEHAVIOUR OF SLAB THICKNESS

The slab thickness database used in this study consists of measurements from January 2007 to December 2010 covering three years of low to medium solar activity period. These measurements were retrieved by combining the simultaneous and co-located LEO_TEC (FORMOSAT-3/COSMIC) and ground GPS_TEC measurements over the European sector. The FORMOSAT-3/COSMIC satellite system consists of six small satellites deployed at a height of about 800 km to form a constellation with circular orbit. Figure 1 shows the diurnal profile of monthly median values of slab thickness where the seasonal variation of τ is characterised by rather higher night-time values (from 20UT to 06UT) in comparison with the daytime values (from 08UT to 18UT).

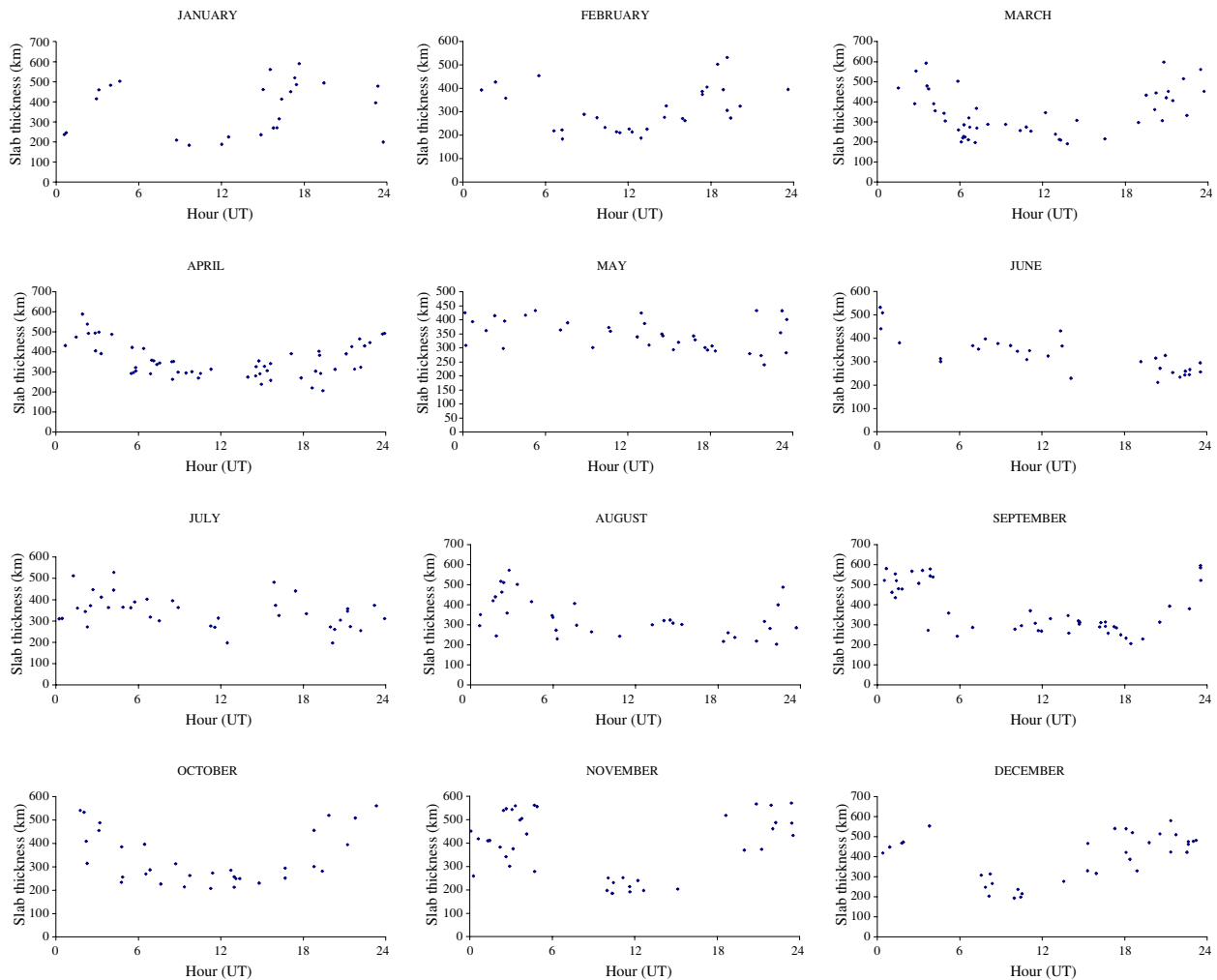


Figure 1: Diurnal profile of monthly median values of slab thickness over Europe for 2007–2010.

In addition it can also be observed that slab-thickness shows a strong pre-sunrise peak. This morning peak in slab-thickness may be attributed to the lowering of the ionospheric F layer immediately before sunrise to regions of greater neutral density, leading to increased ion loss due to recombination [4]. The effect is considered to be particularly evident in the bottomside ionosphere that encompasses the density peak. As a result, the decrease in NmF2 and the bottomside density is much faster than the topside ionosphere where the loss rate is lower and thus, an enhancement occurs. Furthermore, plasmaspheric fluxes can also play a role in the increase. The pre-sunrise peak is a regular feature reported to appear during solar minimum in all seasons and latitudes, while during solar maximum it is still preserved for high and low latitudes but not evident in middle latitudes [5].

3. PLASMASPHERIC INVESTIGATION USING SATELLITE MEASUREMENTS

Plasmaspheric electron content (PEC) is an elusive component of GPS-TEC. It is significant in measuring and modeling the ionosphere to altitudes much lower than GPS, such as for ground-based transionospheric radars that must detect and track orbital and ballistic objects [6]. In this study, we present results based on ν TEC values from a chain of GPS stations over the European sector and LEO-TEC retrieved by radio occultation measurements from FORMOSAT-3/COSMIC satellites.

In Figure 2(b) PEC with respect to latitude is plotted outlining a clear trend (continuous trend line) for decreasing towards the poles as expected. This is due to the fact that the GPS raypaths traverse different distances through the plasmasphere at different latitudes. The raypath length through the plasmasphere decreases with increasing latitude and therefore so does PEC. A good correlation between GPS-TEC and LEO-TEC is shown in Figure 2(a) which represents a scatter

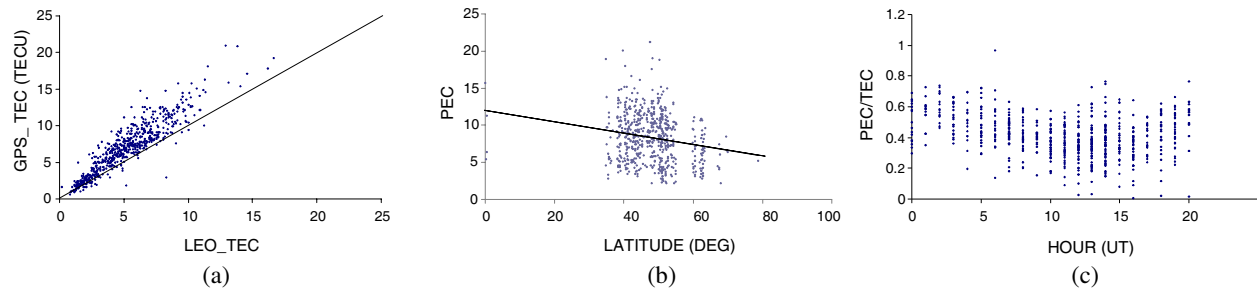


Figure 2: (a) GPS_TEC versus LEO_TEC, (b) PEC versus latitude over the European sector and (c) Diurnal profile of PEC contribution to GPS_TEC.

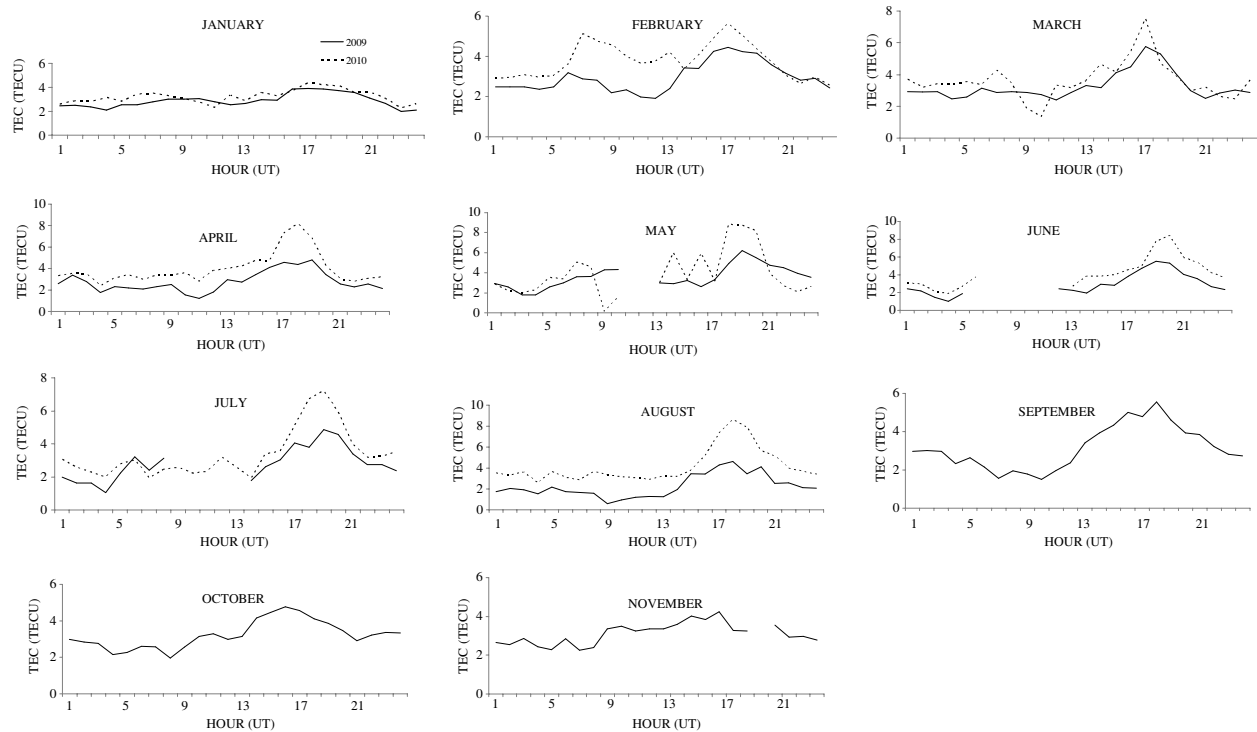


Figure 3: Monthly median variation of PEC over Cyprus from January 2009 to August 2010.

diagram between the two datasets with the GPS_TEC overestimating the LEO_TEC values as expected (emphasised by the $\text{GPS_TEC} = \text{LEO_TEC}$ line) since it includes the plasmaspheric contribution (PEC). In addition from Figure 2(c) it is evident that the percentage contribution of PEC to the GPS_TEC varies from a minimum of about 20% during daytime to a maximum of about 60% during nighttime. The night-time PEC percentage contribution is much higher because ionospheric electron content is low at that time of the day whereas during daytime, the ionosphere electron content is much higher, corresponding to a lower plasmasphere contribution as expected since the electron density below the F2 layer peak varies significantly according to local time and is higher during daytime than at night-time. These findings are in general agreement with the average plasmaspheric contribution reported at various studies [7–9].

To evaluate the behaviour of PEC over a single European location we used $v\text{TEC}$ values obtained from GPS satellite signals (GPS_TEC) and we evaluated PEC by subtracting these values from total electron content derived from ionograms (ITEC) obtained simultaneously from the digisonde (DPS-4D) located in Nicocia Cyprus. The difference of $\text{GPS_TEC} - \text{ITEC}$ can be considered as a measure of PEC over Cyprus and by making use of the good temporal resolution we can get a better insight on its diurnal and annual variability. Figure 3 demonstrates the monthly median diurnal pattern of this contribution from January 2009 to August 2010. It is obvious that the shapes of the monthly median patterns are similar for each month of 2009 and 2010 and also that the PEC values are greater for 2010 implying an increasing trend with increasing solar activity. The greater

PEC occurs characteristically towards sunset.

4. CONCLUSIONS

The estimation of percentage contribution of the plasmaspheric electron (PEC) content and slab thickness (τ) obtained by combining the simultaneous and co-located LEO_TEC-NmF2 and GPS_T-EC measurements over the European sector has been presented. The diurnal pattern of PEC contribution and τ in the European sector for years 2007 to 2010 has been presented. A conclusion that can be drawn from this investigation is that the plasmasphere contributes significantly to total TEC at 20% during daytime to 60% during night-time and therefore can have significant effect on our communication and navigation systems. In addition we observe that τ has a very distinctive diurnal pattern which varies in accordance to the month of the year with a very characteristic pre-sunrise peak which seems to gradually diminish from winter to summer.

REFERENCES

1. Gulyaeva, T. L., B. Jayachandran, and T. N. Krishnankutty, "Latitudinal variation of ionospheric slab thickness," *Adv. Space Re.*, Vol. 33, No. 6, 862–865, 2004.
2. Stankov, S. M. and N. Jakowski, "Topside ionospheric scale height analysis and modeling based on radio occultation measurements," *J. Atmos. Terr. Phys.*, Vol. 68, No. 2, 134–162, 2006.
3. Stankov, S. M. and R. Warnant, "Ionospheric slab thickness-analysis, modeling, and monitoring," *Adv. Space Re.*, Vol. 44, 1295–1303, 2009.
4. Davies, K. and X. M. Liu, "Ionospheric slab thickness in middle and low latitudes," *Radio Sci.*, Vol. 26, 1991.
5. Jayachandran, B., T. N. Krishnankutty, and T. L. Gulyaeva, "Climatology of ionospheric slab thickness," *Ann. Geophys.*, Vol. 22, 25–33, 2004.
6. Bishop, G. J., A. Secan, and S. H. Delay, "GPS TEC and the plasmasphere: Some observations and uncertainties," *Radio Sci.*, Vol. 44, 2009.
7. Lunt, N., L. Kersley, G. J. Bishop, and A. J. Mazzella, Jr., "The contribution of the protonosphere to GPS total electron content: Experimental measurements," *Radio Sci.*, Vol. 34, No. 5, 1273–1280, 1999.
8. Belehaki, A., N. Jakowski, and B. W. Reinisch, "Plasmaspheric electron content derived from GPS TEC and digisonde ionograms," *Adv. Space Re.*, Vol. 33, 833–837, 2004.
9. Breed, A. M. and G. L. Goodwin, "Ionospheric slab thickness and total electron content determined in Australia," *Radio Sci.*, Vol. 32, No. 4, 1635–1643, 1997.

The Doppler Effect at the Propagation of the Signal through the Multipath Radio Channel in HF Wave Band

N. V. Ilyin and M. S. Penzin

Institute of Solar-Terrestrial Physics of the Siberian Branch of the RAS, Russia

Abstract— The Doppler frequency shift is usually equal to a part of hertz or several hertz at pulse vertical or oblique ionospheric sounding at carrier frequency of several megahertz. Usually the duration of the probe pulse is hundreds of microseconds and the propagation time is milliseconds. Thus the spectral width of a single pulse is about 10 kHz. It is impossible to measure the frequency shift of a part of hertz. One of the approaches for detecting Doppler frequency shift is that a coherent sequence of pulses is emitted. In this case the spectrum of the pulse sequence is line one. If the sequence length is large enough so that the width of the line was comparable to the frequency shift then the normal spectral analysis of the entire sequence allow us to measure this shift if it does not change during the analysis.

Another approach also uses the coherent pulse sequence but instead the spectrum of the entire sequence we record the shift of the average phase of each pulse in relation to the previous one. This requires a coherent processing, for example, with synchronous phase detector. If the analog outputs of the phase detector are inputted to an oscilloscope then the single pulse reflected from the ionosphere will be represented by the oval whose width is about 10% of its length (the phase distortion due to dispersion of the absorption). The position of such oval will change due to changes in the phase of the propagation function. The oval rotates and at the same time practically the speed of the rotation is not constant. It is the average speed of the rotation that is interpreted as a Doppler frequency shift.

It is shown, using results of modeling with the normal wave method, that the most sensitive characteristic of the signal in relation to the parameters of the radio channel is the phase at propagating the signal in the multipath radio channel in comparison with amplitude, the angle of coming, the time delay.

The results of modeling the propagation of the monochromatic signal through a quasi-stationary multipath radio channel are presented. The behavior of the phase of each beam individually and the quadrature-components behavior of the total signal is shown.

1. INTRODUCTION

The Doppler frequency shift is usually equal to a part of hertz or several hertz at vertical or oblique ionospheric pulse sounding at carrier frequency of several megahertz. Usually the duration of the probe pulse is hundreds of microseconds and the propagation time is milliseconds. Thus the spectral width of a single pulse is about 10 kHz. It is impossible to measure the frequency shift of a part of hertz. One of the approaches for detecting Doppler frequency shift is that a coherent sequence of pulses is emitted. In this case the spectrum of the pulse sequence is line one. If the sequence length is large enough so that the width of the line is comparable to the frequency shift then the normal spectral analysis of the entire sequence allow us to measure this shift if it does not change during the analysis.

Another approach also uses the coherent pulse sequence but instead of the spectrum of the entire sequence we record the shift of the average phase of each pulse in relation to the previous one. This requires a coherent processing, for example, with synchronous phase detector. If the analog outputs of the phase detector are inputted to an oscilloscope then the single pulse reflected from the ionosphere will be represented by the oval which width is about 10% of its length (the phase distortion due to dispersion of the absorption). The position of such oval will change due to changes in the phase of the propagation function. The oval rotates and at the same time practically the speed of the rotation is not constant. It is the average speed of the rotation that is interpreted as a Doppler frequency shift. It is shown, using results of modeling with the normal wave method that the most sensitive characteristic of the signal in relation to the parameters of the radio channel is the phase at propagating the signal in the multipath radio channel in comparison with amplitude, an angle of coming, a time delay.

There is presented results of modeling the propagation of the monochromatic signal through a quasi-stationary multipath radio channel with the normal-wave method [1]. The behavior of the

phase of each beam individually and the quadrature-components behavior of the total signal is shown.

The normal-wave methods allow us to see the fine structure of the spectral signal changes at propagating through the multipath channel. Other methods measure a average Doppler shifts along the path [2, 3].

2. THE PULSE SEQUENCE

For simplicity, we'll consider a narrow-band amplitude-modulated pulses with a carrier frequency ω_0 and amplitude $a(t)$. The pulses are repeated after a time interval T .

The separate emitted amplitude-modulated narrowband pulse is given by

$$u(t) = a(t) \cos(\omega_0 t), \quad (1)$$

and the coherent sequence of emitted pulses is given by

$$f(t) = \sum a(t - kT) \cos(\omega_0 t). \quad (2)$$

We believe that the period is proportional to the pulse repetition period of the carrier frequency. The spectrum of such a sequence is

$$\begin{aligned} F(\omega) &= U(\omega) \sum \exp(i\omega kT), \\ U(\omega) &= (A(\omega + \omega_0) + A(\omega - \omega_0))/2, \end{aligned} \quad (3)$$

here $A(\omega)$ is the spectrum of $a(t)$.

$$\left| \sum \exp(ik\omega T) \right|^2 = \left(\frac{\sin N\omega T}{\sin \omega T} \right)^2$$

The sum of exponents tends to a sum of δ functions when the number of terms is increasing. The coherence of the sequence of signals is needed that exponents in the sum have not the phase shift. In fact, the finite sum is different from δ functions and looks like repeating narrow peaks with a period $2\pi/T$. The smaller peaks are grouped on short distance around those peaks.

Thus the spectrum of the coherent pulse becomes the line spectrum with an envelope equal to the spectrum of the single pulse.

3. THE PROPAGATION OF THE PULSE SEQUENCE THROUGH THE MULTIPATH RADIO CHANNEL

Let us now consider the propagation of a sequence of pulses through single-beam quasi-stationary channel, a channel which parameters vary slowly with time. Channel in the signal band is characterized by a transfer function

$$H(\omega) = |H(\omega)| e^{i\Phi(\omega)} = H_0(1 + \gamma(\omega - \omega_0)) e^{i\Phi_0 + i\tau_0(\omega - \omega_0)}, \quad (4)$$

here H_0 is the module of the transfer function at the carrier frequency, γ is the logarithmic frequency derivative of the transfer function that represents the slope of the module in the signal band, the value that determines the distortion of the pulse in the first order in the bandwidth, Φ_0 is phase of the transfer function at the carrier frequency τ , τ_0 is the group delay of the pulse signal, which is equal to the frequency derivative of the phase of the transfer function.

In this case, we assume that all the four parameters of the transfer function may depend on time, but their influence is considered separately. Suppose, at first, that only the phase of the transfer function is changing over time, and the time dependence is linear.

Timing selected parameters of the signal correspond to vertical pulse sounding of the ionosphere in the shortwave range. The frequency $f = \omega_0/2\pi$ is about 2 MHz, pulse duration is 100 microseconds, the frequency of pulse repetition is 50 Hz, i.e., 50 pulses per second. The bandwidth of a single pulse in this case is of the order of 10 kHz. The distance between the peaks of the spectrum of a sequence is 50 Hz.

When the single pulse propagates through such a channel the signal at the output will look like

$$u_0(t) = H_0 \left[a(t - \tau) \cos(\omega_0 t + \Phi_0) - \gamma \frac{d}{dt} a(t - \tau) \sin(\omega_0 t + \Phi_0) \right] \quad (5)$$

in complex form

$$u_0(t) = H_0 c(t - \tau) \exp(i(\omega_0 t + \Phi_0)) \quad (6)$$

here $c(t) = a(t) - i\gamma a(t)$.

Let's consider the effect of various channel parameters on the characteristics of the received signal:

- 1) We believe that from pulse to pulse phase Φ_0 varies linearly

$$\Phi_0(k) = k\Delta\Phi$$

The spectrum a coherent received sequence of pulses will be of the form

$$F_0(\omega) = U_0(\omega) \sum \exp(i(k\omega T + k\Delta\Phi)) = U_0(\omega) \sum \exp\left(i\left(\omega + \frac{\Delta\Phi}{T}\right)kT\right). \quad (7)$$

Thus, the visible frequency shift in the received sequence of pulses is $\Delta\omega = \Delta\Phi/T$.

- 2) Let's consider the effect of shifting the group delay. Let the delay of each pulse is shifted by $\Delta\tau$ but it means that at the point of the reception time difference between adjacent pulses is $T + \Delta\tau$ (not T) which will give the spectrum of the coherent sequence

$$F_0(\omega) = U_0(\omega) \sum \exp(i(\omega k(T + \Delta\tau))). \quad (8)$$

That is, the distance between the maxima of the spectrum is changed. Line shape is not changed.

- 3) Effect of changes in amplitude H_0

$$F_0(\omega) = U_0(\omega) \sum (H_0 + ka) \exp(i\omega kT) = U_0(\omega) \left(\sum H_0 \exp(i\omega kT) + a \sum k \exp(i\omega kT) \right). \quad (9)$$

Thus, the dynamics of the modulus of the transfer function distorts the shape of the spectral lines and does not change frequency shift.

- 4) The damping effect of dispersion is reduced to a change in the shape of the spectral lines and an increase in distant peaks in the spectrum. The position of the central line does not change.

Thus, the observed shift in the spectrum of quasi-monochromatic signal as a whole can lead only to a change of the phase transfer function over time. In this case, the phase is the most rapidly changing value.

4. THE PROPAGATION OF THE PULSE SEQUENCE THROUGH THE MULTIPATH RADIO CHANNEL WITH THE NORMAL-WAVE METHOD

Multipath channel is the sum of the single beam channels. Therefore, the transfer function is the sum of the transfer functions of separate rays.

If the monochromatic signal is emitted in the presence of multipath then it will also be monochromatic

$$u(t) = a \cos(\omega_0 t). \quad (10)$$

Suppose that there are a few rays, each ray has the form

$$a_i \cos(\omega_0 t + \varphi_i) + b_i \sin(\omega_0 t + \varphi_i) \quad (11)$$

then the sum of rays is

$$\cos(\omega_0 t) \left[\sum (a_i \cos \varphi_i + b_i \sin \varphi_i) \right] + \sin(\omega_0 t) \left[\sum (-a_i \sin \varphi_i + b_i \cos \varphi_i) \right]. \quad (12)$$

In the stationary case, we have a pure harmonic oscillation with certain amplitude and phase. The vector amplitude of the resulting oscillations is the vector sum of the amplitudes of separate rays. Since each vector changes slowly over time (this is conjecture) then the sum also changes.

Thus, if the emitted monochromatic signal then quadrature components of the received signal have the form:

$$\begin{aligned} a(t) &= \sum (a_i(t) \cos \phi_i(t) + b_i(t) \sin \phi_i(t)) \\ b(t) &= \sum (-a_i(t) \sin \phi_i(t) + b_i(t) \cos \phi_i(t)) \end{aligned} \quad (13)$$

Note that if all the phases are constant and only the amplitude of the separate ray changes then spectral analysis of the quadrature components shows the presence of Doppler effect, although the pulse sounding does not show it.

In the method of normal waves the channel transfer function is:

$$H(\omega) = A \sum_i R_i(\omega, x_1) R_i(\omega, x_2) \exp \left(ika \int_{\theta_1}^{\theta_2} \gamma_i(\omega, \theta) d\theta \right). \quad (14)$$

Here ω is frequency, x_1 is height of the emitting point, x_2 is height of the receiving point, θ is angular distance, limits on integral is angular coordinates of the receiving point and the emitting point on earth surface, γ_i is spectrum parameter, the number of the spectrum parameter corresponds to the number of normal wave of order of 10^5 , A is radius of Earth.

5. THE MODELING RESULTS OF THE PROPAGATION OF THE SIGNAL THROUGH THE MULTIPATH CHANNEL WITH NORMAL-WAVE METHOD

For quantitative estimates of the possibility of using this approach the current method of calculating the field in the method of normal waves was modified, currently used for prediction of the propagation in the stationary ionosphere.

Phase of the normal waves is of the order of 10^5 , the absolute phase of individual pulses has the same order. Moreover, for fixed points of emission and reception for the quasi-monochromatic signal at the carrier frequency ω_0 the sum divides into several sums corresponding to the geometrical optics rays. The module of the partial transfer function and the phase are analytic functions of the parameters of the ionosphere, in particular they depends on the critical frequency. Accordingly, the phase of the pulse (average phase) is also analytic function of the parameters of the medium. It means that if variations in the critical frequency of the layer is small then the phase variation of the pulse is proportional to variations in the critical frequency but the proportionality factor (in fact, the factor ka is the ratio of the radius of the earth to the wavelength) is very large, about 10^5 . So, when modeling the dynamics of the phases of individual pulses it is necessary to go with a time step such that the critical frequency during this time does not change by more than $10^{-3}\%$.

The modeling shows that if critical frequency changes to 2% then the linearity of the phase change on changes of the critical frequency is preserved. In fact, a separate phase of the beam monitors changes in the plasma frequency at the point of reflection.

Illustrations of each phase changes of the rays on the road 3500 km are presented on Figures 1–4 at the critical frequency 6 MHz, operating frequency of 10 MHz. The behavior of the total signal for a change the one parameter (critical frequency) and the two parameters (the critical frequency and height of the beginning of the layer) are presented too. Variations of the critical frequency are up to 0.1%, the height variation of the beginning of the layer is up to 0.5 km.

For the modeling was taken the model layer, which is homogeneous along the path and is define by three parameters: the critical frequency of the layer, the maximum height, and the height of the beginning of the layer. Such a model is chosen from those considerations that it has the small number of parameters characterizing the medium; hence, it is the easiest way to determine the influence of each parameter separately.

The Figures 1–4 show the following: the time pulses sweep receiving at the observation point is in the top right part, the time behavior of the phase of each pulse is in the right bottom part, either the phase diagram of the total monochromatic signal or its quadrature components and the envelope is in the top left.

Variations of medium parameters were specified in the form of a modulated harmonic addition to the critical frequency:

$$f_{cr}(t) = f_{cr0} \left(1 + a \cos \left(2\pi \frac{t}{T} \right) \sin \left(10\pi \frac{t}{T} \right) \right), \quad (15)$$

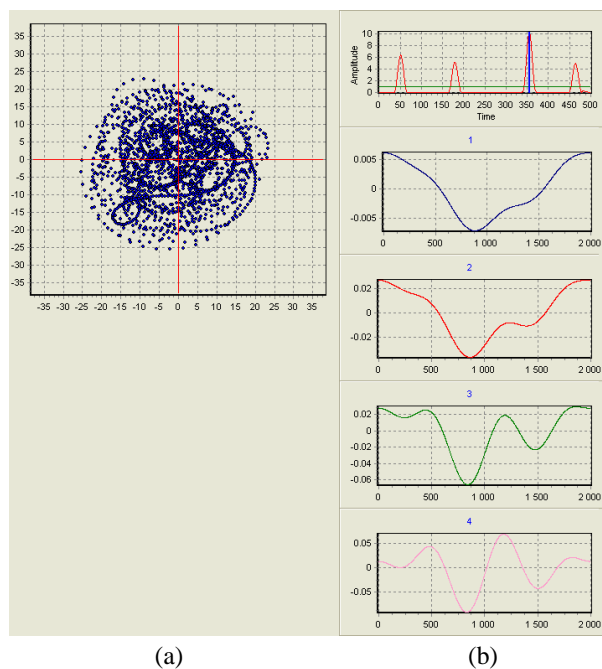


Figure 1: Phase diagram of the (a) received signal and (b) phase of the separate rays, a four-beam channel.

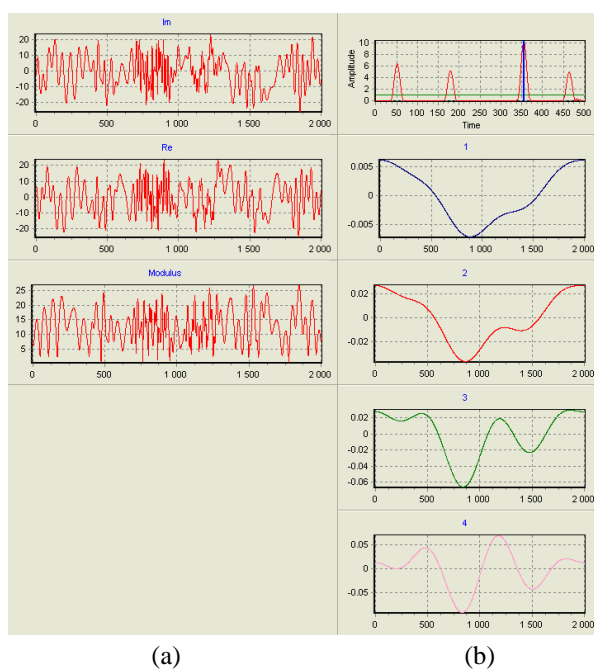


Figure 2: Quadrature components of the (a) received signal and (b) phase of the separate rays, a four-beam channel.

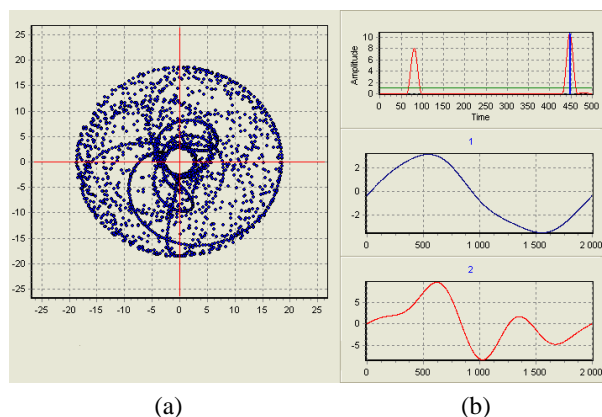


Figure 3: Phase diagram of the (a) received signal and (b) phase of the separate rays, a two-beam channel.

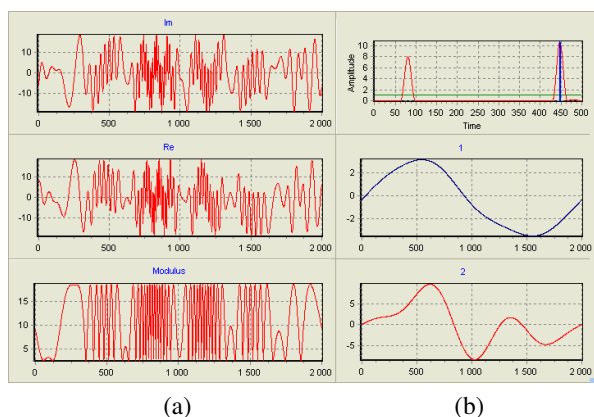


Figure 4: Quadrature components of the (a) received signal and (b) phase of the separate rays, a two-beam channel.

here a is the amplitude of the variation, T is the duration of the perturbation.

Thus, the application of the method of normal waves allows us to develop a new approach to modeling of propagation of the radio waves in the weak-stationary ionosphere and, in particular, allows us to analyze the fine structure of the spectral signal changes in the multipath channel. This in turn provides the prerequisites for creating a detailed theory of spectral distortions of the signal in the non-stationary ionosphere and a new interpretation of experimental data and new methods of analysis of the received signal.

Conducting such a modeling of the fine structure in the Doppler Effect in the geometrical optics is not possible. Shift of the receiving point is equal to several meters leads to the fact that a phase changes by tens of degrees, which completely distorts the picture of the temporal behavior of the phase of the separate pulse.

6. CONCLUSIONS

It is shown that the most sensitive characteristic of the signal in relation to the parameters of the radio channel is the phase at the propagation of the signal in the multipath radio channel in

comparison with amplitude, an angle of coming, a time delay. Also it is shown that the phase change is determined by the parameters of the medium. In fact, the phase of each beam monitors the changes of the plasma frequency at the reflection point.

There are presented results of modeling the propagation of the quasi-stationary signal through a quasi-stationary multipath radio channel in the report. The behavior of the phase of each beam individually and the phase behavior of the total signal is shown.

REFERENCES

1. Kurkin V. I., I. I. Orlov, and V. N. Popov, *Normal-wave Method in Problem of Short-wave Radio*, Nauka, Moscow, 1981.
2. Dyatlov, A. P., P. A. Dyatlov, and B. H. Kulbikayan, “Estimation doppler frequency shift of signals of the satellite navigation system ‘NAVSTAR’,” No. 4, 35–39, News of Higher Educational Institutions, Natural Sciences, North-Caucasian Region, 2004.
3. Batuhin, V. I., V. A. Ivanov, A. A. Kolchev, and S. V. Rozanov, “Measurement of Doppler frequency shifts on individual rays using chirp sounder,” Vol. 43, No. 12, 1044–1054, New of Universities, Radio, 2000.

The Real-time Forecast of HF Radio Channel on the Base of Ionosphere Sounding Data

S. N. Ponomarchuk, V. P. Grozov, M. S. Penzin, and G. V. Kotovich
Institute of Solar-Terrestrial Physics SB RAS, Irkutsk, Russia

Abstract— We propose a technique for ionograms interpretation by means of significant signal amplitude relief points, the identification of propagation modes, the operative definition of modes composition, maximal usable frequencies for each propagation mode and forecast of radio channel working frequencies ranges on the base of techniques and algorithms for radio physical information secondary processing with a help of chirp sounder data in vertical and oblique sounding regimes. The reliability of results depends on ionogram registration accuracy, the presence diagnostically complex binding to uniform time system and accuracy characteristics of forecast techniques. We show that it is necessary to choose the working frequencies for decameter radio communication due to signals propagation conditions along radio path and noise situation in receiving point. This procedure needs the noise measurements problem solving for given frequency range, the determination of signal/noise ratio in accordance with receiving band width, the determination of time and frequency scattering intervals, the choice of calculation criteria for optimal working frequencies ranges due to signal propagation ranges and noise situation.

1. INTRODUCTION

Ionospheric communication lines are a component part of radio technical information transfer systems which use radio waves of decameter range. Modern information transfer systems are supposed to process in big variety of noise situations quite often in condition of a priori information insufficiency. Thus the construction of adaptive systems with maximal effectiveness of signal detection in noise situation presents big interest.

In this paper, we propose a technique for ionograms interpretation by means of significant signal amplitude relief points, the identification of propagation modes, the operative definition of modes composition, maximal usable frequencies for each propagation mode and forecast of radio channel working frequencies ranges on the base of techniques and algorithms for radio physical information secondary processing with a help of chirp sounder data in vertical and oblique sounding regimes. The reliability of results depends on ionogram registration accuracy, the presence diagnostically complex binding to uniform time system and accuracy characteristics of forecast techniques. We show that it is necessary to choose the working frequencies for decameter radio communication due to signals propagation conditions along radio path and noise situation in receiving point. This procedure needs the noise measurements problem solving for given frequency range, the determination of signal/noise ratio in accordance with receiving band width, the determination of time and frequency scattering intervals, the choice of calculation criteria for optimal working frequencies ranges due to signal propagation ranges and noise situation.

2. THE TECHNIQUES AND ALGORITHMS OF SECONDARY PROCESSING

Here we shall select the main features of secondary processing. On the basis of spectral analysis we form ionogram. On ionogram we may select four main object types: useful signal, background noise, concentrated hindrances and isolated surges. The main problem of automatic ionogram processing is the selection of tracks on ionogram which satisfy some criteria with following determination of points with significant amplitude. By considering the ionogram as a complex image we may use the techniques of image processing theory.

The secondary ionogram processing is reduced to solving of two independent problems:

- a) conducting preprocessing of ionograms to remove noise from images and to improve the amplitude characteristics;
- b) data compression to allow a significant reduction in their volume without significant loss of useful information;

The ionogram pre-processing is concluded in clearness from noise components [1], i.e., it is necessary to select useful signal on noise and stationary hindrances background as well as to delete isolated surges which has an intensity comparable with useful signal and can inflict malfunctions

in algorithms for ionosphere parameters determination. The analysis of filters which can be used for ionogram processing has shown that for removing the noise from image and signal restoring on pre-processing stage one can use local filters built on the use of ordinal additive statistics which connected with processed fragment characteristics.

The data compression technique [2] is used for selection of points with significant amplitude which physically corresponds to signal receipts moments determining by signal front or amplitude relief maximum. For sitting out the single artifacts, the partial data reconstruction and revealing ionogram primary track one can use effective cellular automaton technique. Cellular automata are the discrete dynamical systems which completely defined by local mutual connection of their elements. The whole data space is divided on elementary cells which afterwards evolves under discrete time. The law of the dynamics of such a system is expressed by a set of rules by which each cell changes its state depending on the state of neighboring entering into a local area.

The implemented algorithm is allowed to achieve a compression ratio of the initial information up to 5–10 times depending on the level of noise and speckle [2].

3. VERTICAL SOUNDING IONOGRAM INTERPRETATION TECHNIQUE

The ionogram interpretation technique is based on using of height-frequency characteristic (HFC) modeling results in long-run forecast mode and experimental ionograms processing results. By using ionosphere models (for example, IRI as a standard ionosphere model [3]) one can calculate height-frequency characteristic for vertical propagation. Under modeling of this dependence we can obtain the value of integral on the base of general formulas. This problem pertains to direct problems class and its solving does not form big difficulty [4].

The obtained height-frequency characteristic is superimposed on experimental ionogram and is used for model mask building. Then by scanning of model mask along the ionogram one can construct the histogram of coincidences for model and real tracks. After that we change the slope of model tracks and repeat the scanning process.

After the termination of the process we select the histogram with maximal number of points with significant amplitude falling into model mask. On Fig. 1, we present the results of automatic interpretation for vertical sounding ionogram: input ionogram (the 11/17/2005 Usol'ye-Irkutsk path) with (a) secondary processing results and (b) interpretation results.

4. OBLIQUE SOUNDING IONOGRAM INTERPRETATION TECHNIQUE

The technique is based on using of modeling results for distance-frequency characteristic (DFC) on given path in long-run forecast regime, adiabatic relations and experimental ionogram data processing matrix of points with significant amplitude $A(f_i, P_j)$. For oblique sounding ionogram interpretation problem one can formulate the following background suggestions [5]. Under the ionosphere parameters variations within the accuracy of long-run forecast are saved the following values:

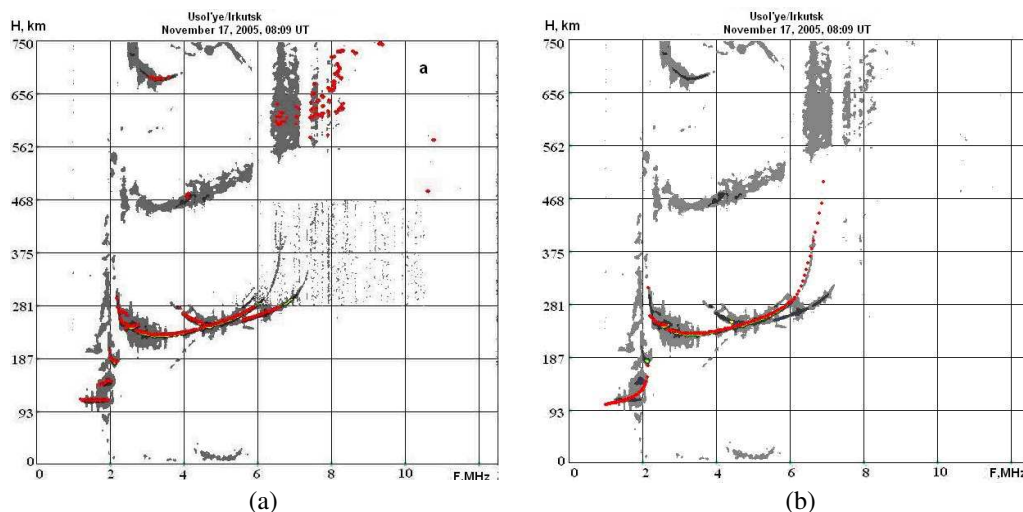


Figure 1: (a) Vertical sounding ionogram and (b) the interpretation results, November 17, 2005, 08 : 09 UT.

- the ratio of group path P_m in joining point of lower and upper rays for some mode on path length;
- the ratio of maximal usable frequency (MUF) for modes of different multiplicity which propagates in one of waveguide channels (with lower wall as Earth surface but upper wall as E, F1 or F2 layer);
- distance frequency characteristic for one mode with multiplicity 1, on relative frequency grid $\beta = f/f_{m,l}$,

where $f_{m,l}$ — mode of maximal usable frequency for given range.

The algorithm of oblique sounding ionogram interpretation in automatic mode is built as follows. The calculation of oblique sounding distance-frequency characteristic for given path in the regime of long-term prediction are cried out. Coming thereof, one can construct the model mask for minimal multiplicity mode of F layer, which includes two bands of width ΔP km (on vertical) and extent on frequency from μf_m^p to f_m^p , where f_m^p — forecast maximal usable frequency of supporting mode for upper ray and with extent from νf_m^p to f_m^p for upper ray. The algorithm of supporting trace on ionogram is concluded in count of point number for signal receipts moments under moving of model mask along experimental points on relative frequency grid. The mask moves on points of the matrix $A(f_i, P_j)$ by joining the “nose” with point A_{ij} . Under moving the mask we count the number of points $A(f_i, P_j)$ which falls into mask within rectangle $[\Delta f \times \Delta P]$, where Δf and ΔP are selected due to ionosounder resolution on range and frequency. The maximal values of experimental points count are saved. In the case of f_m^r and P_m^r determination the remained experimental points which correspond to mode of first multiplicity are identified by lengthening of mask bands to lower frequencies range along model distance-frequency characteristic scaled by multiplier f_m^r/f_m^p and searching for elements P_{ij} falling in these bands. After than we carry out linear interpolation of tracks in order to turn on uniform frequency grid. The identification of modes with greater multiplicity is conducted by above-mentioned procedure.

Figure 2 shows the results of automatic interpretation of an oblique sounding ionogram for the 02/01/2009 Magadan-Irkutsk path.

5. THE OPERATIVE DIAGNOSTICS OF RADIO CHANNEL

Under serving of regional decameter radio communication systems with radio path length not exceeded limit range of one leap (~ 3000 km) the real-time calculation of optimal working frequencies is possible on the base of diagnostics characteristics for vertical sounding data. In the framework of Smith-Kazantsev technique we carry out direct recalculation of height-frequency characteristic (HFC) in the radio path middle point into range-frequency characteristic (RFC) for oblique sounding. Since the radius of space correlation for ionosphere parameters is about 1000 km then in first approximation for radio paths with length less than two correlation radiuses we may transfer HFC

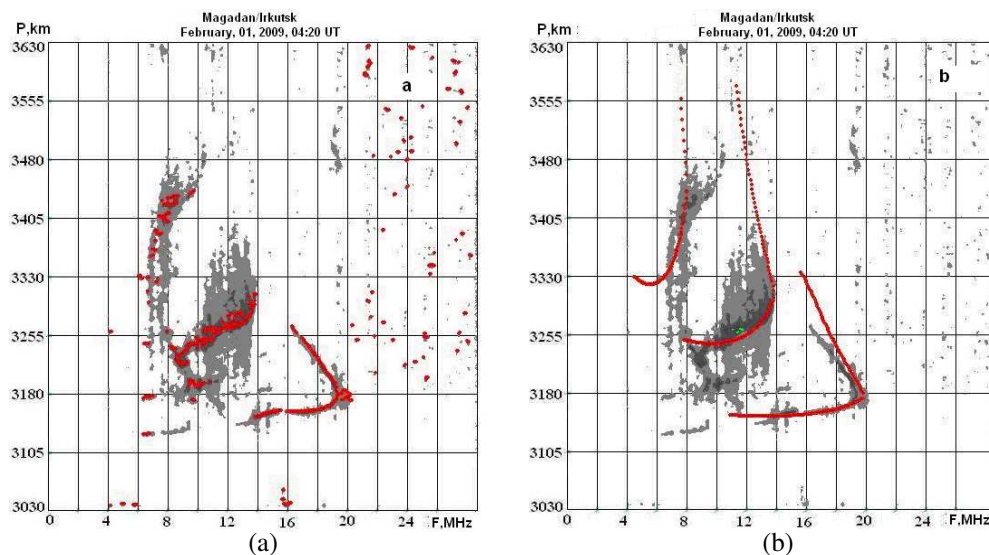


Figure 2: (a) Oblique sounding ionogram and (b) the interpretation results, February 17, 2009, 04 : 20 UT.

in sounding point to radio path middle point. This assumption corresponds to spherically symmetric ionosphere model and valid for quiet medium conditions in absence of sharp gradients and disturbances.

The algorithm of radio path characteristics calculation in real-time mode on the base current vertical sounding data is carried out by the next scheme. We conduct automatic processing of VS ionograms in order to select signals with significant amplitude. After that we cut off reflected signals with multiplicity greater than 1, carry out the tracks identification and construct tracks. After tracks selection we carry out the calculation of ionosphere parameters: critical frequencies and minimal reflection heights for each ionosphere layer. If we have right identification for all HFC layers on the base of tracks, then we calculate the oblique propagation characteristics: range-frequency characteristic, maximal usable frequencies (MUF) of propagation modes and signal level at receiver input.

On the base of OS station current data after secondary processing we have a set of tracks which characterized different modes corresponding to different reflection regions. The maximal observed frequency of each selected tracks is coincides with maximal frequency in that track. Each selected track is corresponds to fixed signal propagation mode. So the minimal observed frequency is the initial track point.

6. THE ALGORITHM OF OPTIMAL FREQUENCIES CHOICE

There exist several approaches to choice of optimal working frequencies (OWF) for radio communication. The most simple is the approach based on OWF choice by means of maximal frequency for all modes which as a rule is corresponds to MUF of mode with minimal multiplicity in F-channel. We subscribe to OWF the value which is equal to 0.85 MUF . On short paths under that OWF choice in many cases the received signal can be multi-rayed. For these cases we may correct by means of given radio line protection coefficient which defines the minimal possible signal/noise ration for given radio communication reliability. For given radio line parameters (transmitter power, antenna, and band of signal) we determine the intervals of radio communication working frequencies for which signal/noise ratio exceeds the value of protection coefficient. The noise level is calculated on the base well-known station and atmosphere noise models [6] or can be measured by means of ionosphere sounding process.

Under using modems and wide-band SW radio communication it is better to use choice criterion for optimal working frequencies based on functional relation between error probability averaged by random signal parameters and characteristics of information transfer channel. In this case, it is necessary to carry our detailed analysis of oblique sounding signals structure with definition of inter-mode delays, accounting of signal coherency band due to signal frequency dispersion in ionosphere.

7. CONCLUSIONS

Thus the techniques and algorithms of secondary processing for ionograms and interpretation of vertical and oblique ionosphere sounding signals allows us to select tracks on ionograms and to carry out theirs identification. For vertical sounding we conduct the calculation of ionosphere parameters; critical frequencies and minimal reflection heights for each ionosphere layer. In the case of right identification of all HFC layers with a help of obtained tracks we can calculate the characteristics of oblique propagation: range-frequency characteristic, maximal usable frequencies (MUF) for each propagation mode and signal level at receiver input. In OS case these techniques allows us to carry out operative definition of modes composition, MUF for each mode, to build signal RFC by significant points of signal amplitude relief and to conduct the identification of propagation modes. On the base of developed techniques we construct the algorithms of direct diagnostics of decameter radio channel with a help of OS and VS data and this information allows us to carry out operative choice of working frequencies for connected radio channel.

ACKNOWLEDGMENT

This work is supported by the Ministry of Education and Science of the Russian Federation (government contract 14.740.11.0078) and the Russian fund of basic research (grant No. 11-05-00892).

REFERENCES

1. Grozov, V. P., "Processing of ionograms — Statistical approach," *Proceedings of International Symposium on Radio Propagation, (ISRP'97)*, 225–228, Qingdao, China, 1997.

2. Grozov, V. P., V. E. Nosov, G. A. Ososkov, and E. G. Zaznobina, “Artificial neural networks for computer-aided ionogram analysis,” *Computer Aided Processing of Ionograms and Ionosonde Records*, P. J. Wilkinson, Ed., 30–34, Boulder, USA, 1998.
3. Bilitza, D. and D. D. Reinisch, “International reference ionosphere 2007: Improvements and new parameters,” *Advances in Space Research*, Vol. 42, 599–609, 2008.
4. Mikhailov, S. Y., “Ambiguity of recovering plasma frequency profiles by the given HFC and their discernibility for oblique propagation of short radiowaves in the isotropic ionosphere,” *Izvestiya Vuzov. Radiophysics*, Vol. XLII, No. 10, 855–872, 2000 (in Russian).
5. Grozov, V. P., V. I. Kurkin, V. E. Nosov, and S. N. Ponomarchuk, “An Interpretation of data oblique-incidence sounding using the chirp-signal,” *Proc. ISAP’96*, 693–696, Chiba, Japan, 1996.
6. *Documents of the VIII Plenary Assembly CCIR*, Geneva, Vol. VII, Doc. 65, 1957.

A Novel Microstrip-fed Dielectric ROD Antenna Array with High Gain

Y. Liu and X. Chen

College of Electronics and Information Engineering, Sichuan University, Chengdu 610064, China

Abstract— A low cost and simple structure dielectric rod antenna array is proposed. It is composed of cylindrical dielectric rods acting as the radiation elements, which are made of low cost Teflon with relative permittivity of 2.08 rather than high permittivity dielectric that are commonly used in dielectric resonator antennas. To achieve high gain, dielectric rods form an array and are connected with a microstrip corporate feeding network. After optimized by a parallel genetic algorithm (GA) on a cluster system, a prototype 4×4 array is fabricated and tested. The simulation and measurement results are in good agreement and show the proposed antenna possesses encouraging properties, i.e., good end-fire radiation performances with a high gain up to 20.3 dBi at the working frequency 8.0 GHz and a $|S_{11}| < 10$ dB impedance bandwidth of 7.7% (from 7.70 GHz to 8.32 GHz).

1. INTRODUCTION

In recent years, the dielectric resonator antennas have become an attractive alternative for many modern wireless communications systems. The dielectric resonator antennas offer several advantages for some applications such as small size [1], wide impedance bandwidth [2], high radiation efficiency [3]. But so far in the large numbers of previous researches, dielectric resonator antennas are commonly made of high permittivity materials [4, 5] that are often expensive, and some are with complicated configurations [6, 7].

In this work, a novel dielectric rod antenna array is presented. Its geometry is very simple, e.g., using cylindrical dielectric rods acting as its radiation elements, and is low cost by employing a low permittivity material Teflon to fabricate the dielectric rods. To achieve high gain, a 4×4 array is formed and fed by a microstrip corporate feeding network that allows the use of low cost and accurate planar print techniques. Structural parameters of the dielectric rods and the microstrip corporate feeding network are optimized by a parallel Genetic Algorithm (GA) on a cluster system.

2. ANTENNA CONFIGURATION

The side view of proposed dielectric rod antenna array is shown Figure 1. It consists of 4×4 cylindrical dielectric rods fabricated by using widely available Teflon with relative permittivity $\epsilon = 2.08$. Each cylindrical dielectric rod is glued on a PCB (printed circuit board) with permittivity 2.65 and thickness 2.0 mm, and hold by a circular metallic waveguide located at the bottom end, which is designed to guide and propagate electromagnetic energy.

As illustrated in Figure 2, a microstrip corporate feeding network etched on the PCB is used to provide equal amplitude and phase excitation to all the cylindrical dielectric rods. Each terminal circular patch located right under the cylindrical dielectric rod. The feed network comprises series T-junctions power to deliver electromagnetic energy uniformly and multiple-section quarter-wavelength impedance transformers to achieve impedance match.

3. ANTENNA OPTIMIZATION

The GA is a powerful and efficient optimization technique and has been widely applied in the optimization of various antennas [8–10]. In this work, we employ the GA in conjunction with FDTD to optimize structural parameters of the proposed dielectric rod antenna array for achieving high gain and good impedance match at the working frequency.

Taking into account robustness of the Teflon, the length of the rods which is the main determinant of the radiation gain is kept fixed at $L_d = 80$ mm. So there are a total of 12 structural parameters needed to optimized, i.e., $R_s, D_x, D_y, L_1, L_c, L_p, L_q, L_t, L_r, W_1, W_2, W_3$. The fitness function of the GA is defined as

$$F = C_1 * \text{Gain} + C_2 * S_{11}, \quad (1)$$

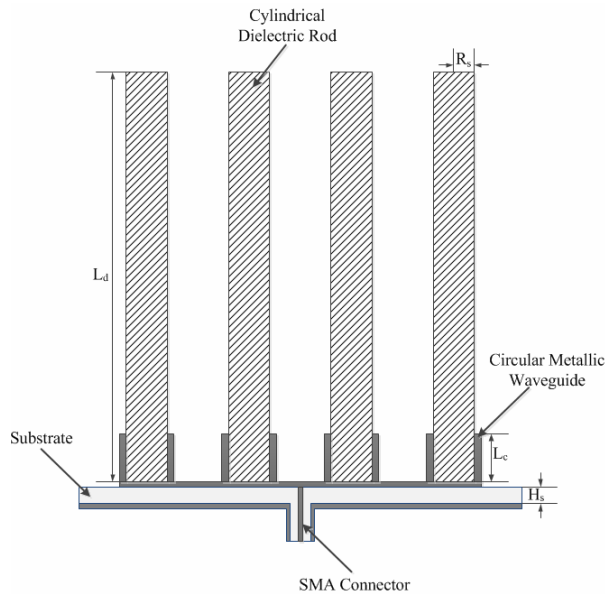


Figure 1: The side view of proposed dielectric rod antenna array.

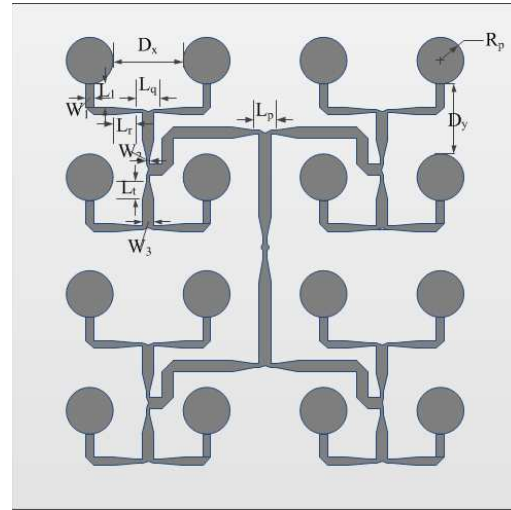


Figure 2: The top view of the corporate feeding layer.

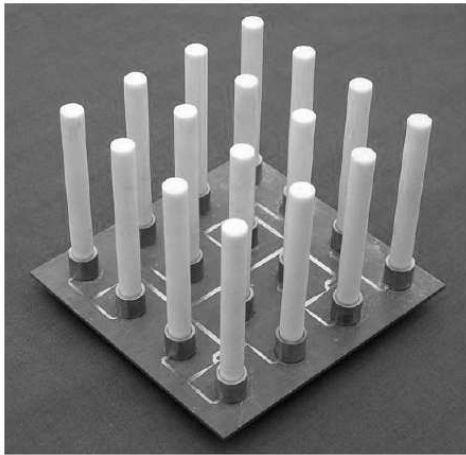


Figure 3: The fabricated dielectric rod antenna array.

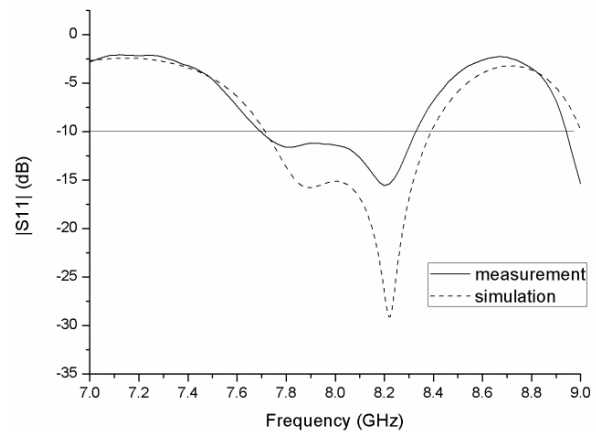


Figure 4: The measured and simulated return loss of the prototype antenna.

where F is the fitness value, Gain and S_{11} refer the radiation gain in dBi and return loss in dB of the dielectric rod antenna array at its working frequency of 8 GHz. C_1 and C_2 are weight factors and set to be 0.025 and -0.03 , respectively.

In the optimization, the GA employs tournament selection with elitism, single-point crossover with probability $P = 0.5$, jump mutation with probability $P_m = 0.2$, and it uses 100 generations, 120 chromosomes, and 100 individuals in a population.

4. RESULTS AND ANALYSIS

The structural parameters determined by the GA-based optimization are as follows (unit: mm): $R_s = 4.4$, $D_x = 17.4$, $D_y = 18.4$, $L_1 = 2.6$, $L_c = 10.5$, $L_p = 6.1$, $L_q = 3.3$, $L_t = 6.2$, $L_r = 3.9$, $W_1 = 1.4$, $W_2 = 0.4$, $W_3 = 2.0$. A prototype antenna as shown in Figure 3 has been fabricated and measured. Figure 4 compares the measured and simulated return loss of the prototype antenna. The measured bandwidth is about 7.7% (from 7.70 GHz to 8.32 GHz). At its center frequency of 8 GHz, the antenna has an input return loss of -11.4 dB, which estimates a good impedance match has been achieved.

Measured and simulated radiation patterns on the XZ plane and YZ plane at the center fre-

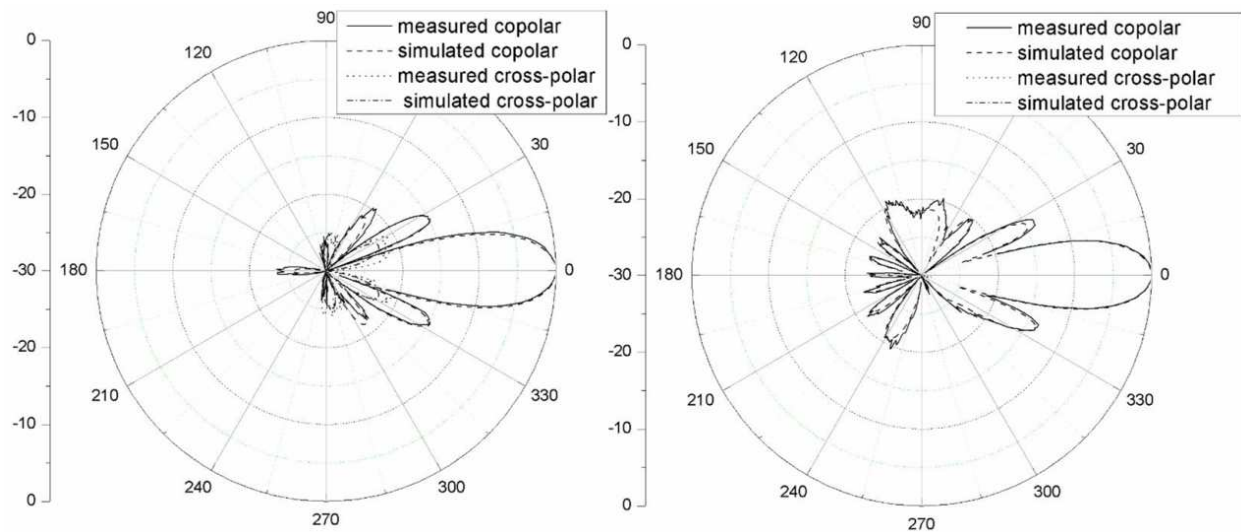


Figure 5: Measured and simulated radiation patterns on the XZ Plane and YZ plane.

quency of 8 GHz are illustrated in Figure 5. It's obvious that the measured and simulated radiation patterns agree very well. The gain at 8 GHz is up to 20.3 dBi. The measured side-lobes are approximately 13.5 dB below the main lobe. The simulation and measurement show the antenna radiates in linear polarization with the main polarization in the direction of Y axis and the cross-polarization level less than -20 dB.

5. CONCLUSION

A novel microstrip-fed dielectric rod antenna array with high gain is presented. The dielectric antenna array is composed of cylindrical dielectric rods, which are made of Teflon. The microstrip corporate feeding network has been chosen to provide matched phase and electromagnetic energy to all the dielectric rod elements. After optimized by the GA in parallel on a cluster system, a prototype antenna was fabricated and measured. The measured results agree with the simulated results well and show that the antenna achieves a high radiation gain up to 20.3 dBi at its working frequency of 8 GHz. Future work will focus on the design and fabrication of significantly larger arrays of profiled dielectric rods and raise the working frequency of the antenna.

ACKNOWLEDGMENT

The work was supported by the New Century Excellent Talent Program in China (Grant No. NCET-08-0369).

REFERENCES

1. Saed, M. A. and R. Yadla, "Microstrip-FED low profile and compact dielectric resonator antennas," *Progress In Electromagnetics Research*, Vol. 56, 151–162, 2006.
2. Rezaei, P., M. Hakkak, and K. Forooghi, "Design of wide-band dielectric resonator antenna with a two-segment structure," *Progress In Electromagnetics Research*, Vol. 66, 111–124, 2006.
3. Mongia, R. K., A. Ittipiboon, and M. Cuhaci, "Measurement of radiation efficiency of dielectric resonator antennas," *IEEE Microwave Guided Wave Lett.*, Vol. 4, 80–82, Mar. 1994.
4. Ain, M. F., S. I. S. Hassan, J. S. Mandeep, M. A. Othman, B. M. Nawang, S. Sreekantan, S. D. Hutagalung, and Z. A. Ahmad, "2.5 GHz BaTiO₃ dielectric resonator antenna," *Progress In Electromagnetics Research*, Vol. 76, 201–210, 2007.
5. Saed, M. A. and R. Yadla, "Microstrip-FED low profile and compact dielectric resonator antennas," *Progress In Electromagnetics Research*, Vol. 56, 151–162, 2006.
6. Kumar, C., V. V. Srinivasan, V. K. Lakshmeesha, and S. Pal, "Design of short axial length high gain dielectric rod antenna," *IEEE Transactions on Antennas and Propagation*, Vol. 58, No. 12, 4066–4069, 2010.
7. Chung, J. and C. Chen, "Two-layer dielectric rod antenna," *IEEE Transactions on Antennas and Propagation*, Vol. 56, 1541–1547, Jun. 2008.

8. Su, D. Y., D.-M. Fu, and D. Yu, “Genetic algorithms and method of moments for the design of PIFAS,” *Progress In Electromagnetics Research Letters*, Vol. 1, 9–18, 2008.
9. Panduro, M. A., C. A. Brizuela, L. I. Balderas, and D. A. Acosta, “A comparison of genetic algorithms, particle swarm optimization and the differential evolution method for the design of scannable circular antenna arrays,” *Progress In Electromagnetics Research B*, Vol. 13, 171–186, 2009.
10. Xu, Z., H. Li, Q.-Z. Liu, and J.-Y. Li, “Pattern synthesis of conformal antenna array by the hybrid genetic algorithm,” *Progress In Electromagnetics Research*, Vol. 79, 75–90, 2008.

On the Velocities of Motion of the Electromagnetic Field in the Near Zone of Elementary Radiators

O. V. Missevich¹, A. L. Kholmetskii², V. A. Permyakov³, and D. V. Sorokovik⁴

¹Institute of Nuclear Problems, Minsk 220030, Belarus

²Department of Physics, Belarus State University, Minsk 220030, Belarus

³National Research University “Moscow Power Engineering Institute”
Krasnokazarmennaya Str. 14, Moscow 111250, Russia

⁴OAo “RusHydro”, Architektov Vlasov Str., Moscow 117393, Russia

Abstract— In a number of experimental works the phenomenon of an anomalously small delay of the electromagnetic field in the near and intermediate zones of antennas has been discovered and analyzed. In order to interpret this effect, in this report, the space-time evolution of the fields in the near zone of elementary dipoles is studied analytically. We studied the instantaneous velocities of motion of the extrema and zeros of the electric and magnetic fields as well as the Poynting vector in the near and intermediate zones of an electric dipole. This approach was applied to the quasi-harmonic and pulse excitation modes of the electric dipole. Using the principle of permutational duality, one can transfer the obtained results to the case of a magnetic dipole, which allows us to apply them for the interpretation of the experiments performed by O. V. Missevich a.o.

1. INTRODUCTION

Propagation of electromagnetic pulses in a uniform medium has become a subject of research since the time of publication of pioneering studies performed by Heinrich Hertz [1]. This problem was theoretically analyzed in works of A. Sommerfeld and L. Brillouin [2]. A review of the state-of-the-art of these studies by the mid-1970s was published by L. A. Vainshtein [3]. It has been found that the pulse front moves with the velocity of light in vacuum c , a forerunner is formed behind the front, and the main body of the pulse follows the forerunner. In the case of narrowband (quasi-monochromatic) pulses, the group velocity v_g , which is equal to the velocity of motion of the main body of the pulse, is usually less than c . However, there are specific cases in which $v_g > c$. Propagation of pulses in a lossy medium, a supercritical plasma, and evanescent waveguides are even more complicated situations. In these media, the amplitude deformation of pulses may be very substantial and the velocity of motion of the maximum of the pulse amplitude may exceed the velocity of light in vacuum or even may be negative [3]. It follows from [3] that implementation of the group velocity of the pulse main body exceeding the velocity of light in vacuum does not mean that the causality principle is violated, because the pulse main body moves behind the front and cannot approach it.

In recent years, a large number of experimental studies of the processes related to propagation of electromagnetic waves through sections of evanescent waveguides and, in optics, through a system of prisms under the conditions of violated total internal reflection were performed. In these experiments, the propagation time of the pulse passing through irregular system parts in which nonuniform (evanescent) electromagnetic waves are formed becomes less than the propagation time of a uniform purely transverse (TEM) wave. From the physical viewpoint, these phenomena are similar to the processes related to propagation of the pulse main body in dispersive media with a velocity exceeding the velocity of light in vacuum [3]. These effects are discussed in review [4] in a broader context, which includes tunneling effects in quantum mechanics.

In the microwave band, motion of the pulse main body with a supraluminal velocity was experimentally found in [5]. The phenomenon of anomalously small retardation of the electromagnetic field in the near and Fresnel zones of antennas was experimentally studied in [6–13]. The theoretical analysis of these phenomena is behind the experimental studies. Physical processes of formation of pulsed fields in the near and Fresnel zones of antennas have not yet been adequately analyzed.

2. ON THE CONCEPTS OF THE VELOCITY OF THE ELECTROMAGNETIC FIELD

Let us discuss the concepts related to the velocity of motion of a nonstationary field.

We consider electromagnetic fields in a nondispersive medium (vacuum). It is known that electromagnetic waves in vacuum far away from sources propagate with the speed $c = 299970$ km/s.

In a dispersive medium, there concepts of the phase and group velocities of modulated waves. The concepts of the group and phase velocities were used for description of propagation of the near field of an electric dipole in vacuum [14]. This raises the question of whether application of these concepts to the case of antennas located in vacuum is justifiable.

Our viewpoint is as follows. The concept of the phase velocity, which is rigorously valid for an isolated harmonic wave, is extended to a superposition of harmonic waves with variable amplitudes in the following form: it relates to the velocity of motion of phase fronts corresponding to the zeros of the components of the electric and magnetic fields.

The situation concerning the concept of the group velocity is more complicated. Radiation of a small antenna in vacuum can be treated as excitation of a spherical waveguide. From this viewpoint, an antenna in vacuum is a structure with frequency dispersion. The group velocity of a superposition of waves is usually introduced as the velocity of motion of the envelope. In this case, it is assumed that the envelope varies slowly as compared to the high-frequency filling [15]. This definition is used in [14]. Near a point antenna, the envelope varies rapidly and the approach used in [14] is, strictly speaking, is unjustified. The surprising thing is that, in [14], this approach was used for the analysis of individual group velocities of electric and magnetic field components and not the Poynting vector.

We will analyze the instantaneous velocities of motion of the zeros and extrema of the electric and magnetic fields and the Poynting vector. Instantaneous velocities of the zeros of the electric and magnetic fields are the phase velocities (which coincides with [14]) and instantaneous velocities of extrema of the Poynting vector are the analogues of the group velocities.

3. A TECHNIQUE FOR THE ANALYSIS OF THE EVOLUTION OF THE FIELD LINES OF THE ELECTROMAGNETIC FIELD AND THE VECTOR LINES OF THE POYNTING VECTOR FOR AN ELECTRIC DIPOLE

Let us consider an electric dipole excited by a pulsed current and directed along the z axis of the Cartesian coordinate system. Length l of the dipole is small as compared to the duration of the pulse exciting the the antenna and the dipole diameter is substantially lesser than the dipole length. Expressions for the fields excited by the dipole are well known [16]:

$$\begin{aligned} \mathbf{E}(R, \theta, t) &= \frac{\cos \theta}{2\pi\epsilon_0} \left[\frac{p(t')}{R^3} + \frac{p'(t')}{cR^2} \right] \mathbf{e}_R + \frac{\sin \theta}{4\pi\epsilon_0} \left[\frac{p''(t')}{c^2 R} + \frac{p'(t')}{cR^2} + \frac{p(t')}{R^3} \right] \mathbf{e}_\theta \\ \mathbf{H}(R, \theta, t) &= \frac{1}{4\pi} \mathbf{rot} \left[\frac{1}{R} p'(t') \mathbf{e}_z \right] \end{aligned} \quad (1)$$

In formula (1), $p(t) = q(t)l$ is the time dependence of the dipole moment and primes above function $p(t')$ denote derivatives with respect to the argument $t' = t - R/c$.

Let us introduce variable $\tau = ct - R$ and write field components in the following form:

$$E_R(R, \theta, t) = \frac{\cos \theta}{2\pi\epsilon_0 R^3} f_1, \quad f_1 = p(\tau) + Rp'(\tau), \quad (2)$$

$$E_\theta(R, \theta, t) = \frac{\sin \theta}{4\pi\epsilon_0 R^3} f_2, \quad f_2 = p(\tau) + Rp'(\tau) + R^2 p''(\tau), \quad (3)$$

$$H_\varphi(R, \theta, t) = \frac{c}{4\pi} \sin \theta \left(\frac{p''(\tau)}{R} + \frac{p'(\tau)}{R^2} \right) \quad (4)$$

The analysis of the dipole fields is simplified due to the fact that the time dependence of these fields is parametric and the field structure is axially symmetric. This allows us to use vector analysis in a plane and apply well-known methods of the qualitative theory of first-order ordinary differential equations. A qualitative analysis was performed for the electric field and the Poynting vector in the cylindrical coordinate system. The results of the qualitative analysis were reported in [17–20].

4. SOME RESULTS OF THE ANALYSIS OF THE NEAR-ZONE FIELDS OF AN ELECTRIC DIPOLE

A feature of the applied analysis of nonstationary fields is the possibility of studying the field evolution for sources with arbitrary time dependences of the charge and current. For this reason, we consider in detail harmonic excitation of a dipole.

We will analyze evolution of field component E_R at $\theta = 0$ and components E_θ , H_φ , and S_R at $\theta = 90^\circ$. Instantaneous phase velocities of the field components are determined by equating to zero the field components [17–20] and instantaneous velocities of the field extrema and the Poynting vector are determined from conditions $\frac{\partial U}{\partial R} = 0$, where U are the corresponding components of the field or the Poynting vector.

Trajectories of the zeros (dashed lines) and extrema (bold solid lines) of field components E_R , E_θ , and H_φ , respectively, in plane $(\omega t, k_0 R)$ are shown in Figs. 1(a), 1(b), and 1(c). Thin straight lines depict corresponding velocities of light in vacuum.

As follows from Fig. 1(a), the zeros and local extrema of E_R originate at the point of the dipole with infinite velocities. These velocities monotonically decrease with time and tend to the velocity of light in vacuum.

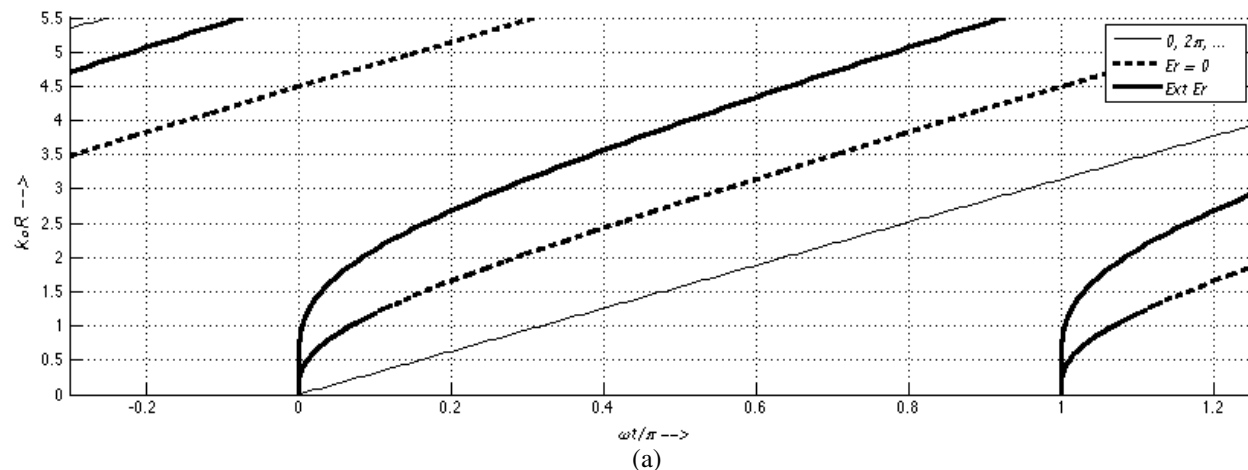
As follows from Figs. 1(b) and 1(c), the process of formation of the zeros and extrema of components E_θ and H_φ is qualitatively different. Local extrema of E_θ and H_φ arise at a finite distance from the dipole with infinite velocities. Then, the extrema are split into two extrema. One extremum moves toward infinity with a decreasing velocity tending to the velocity of light in vacuum. The other extremum moves toward the dipole. Zeros of E_θ demonstrate similar behavior. Zeros of H_φ originate at the point of the dipole with an infinite velocity; then they move toward infinity and their velocities tend to the velocity of light in vacuum.

Trajectories of the zeros of E_θ (dashed lines) and H_φ (dotted lines) and the extrema of the Poynting vector (bold solid lines) in plane $(\omega t, k_0 R)$ are shown in Fig. 1(d). It follows from the analysis of Fig. 1(d) that formation and motion of the extrema of the Poynting vector are similar to those of the extrema of E_θ and H_φ . Thus, we can say that the instantaneous velocities of the extrema of component S_R of the Poynting vector are larger than the velocity of light in vacuum in a certain time interval.

Comparison of our results with the results of study [14] shows that they coincide for the phase velocities. As to the group velocities of field components determined in [14], their behavior qualitatively agrees with the velocities of motion of the extrema of E_R , E_θ , and H_φ . Evolution of the Poynting vector was not analyzed in [14].

Along with the harmonic excitation of the dipole, we also analyzed particular variants of excitation of this dipole by pulses with a finite duration and a small number of oscillations of the charge and current. It has been shown that evolution of the zeros and extrema of the field components and the Poynting vector is more complicated than in the case of harmonic excitation. In this case, local extrema of the fields and the Poynting vector in the near zone may move with velocities exceeding the velocity of light in vacuum; however, they cannot leave behind the pulse fronts.

The results obtained can be extended to the case of radiation of a magnetic dipole or an electric loop with the use of the principle of the principle of permutational duality. Whence, the performed analysis qualitatively explains the experimental results presented in [11–13].



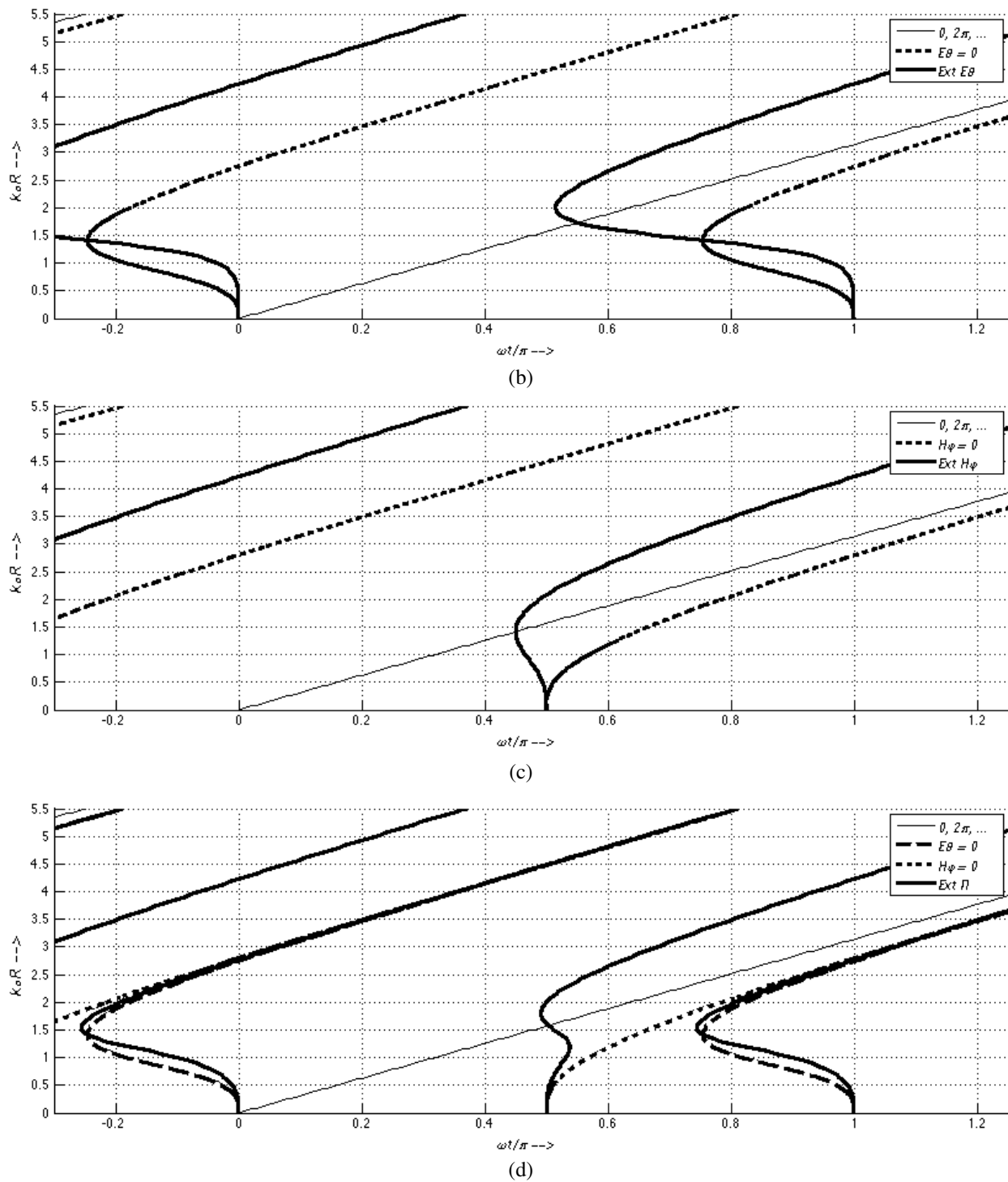


Figure 1: Evolution of the extrema and zeros of components E_R , E_θ , H_φ , and S_R in plane $(\omega t, k_0 R)$.

REFERENCES

1. Hertz, H., *Ann. d. Phys. B*, Vol. 36, No. 1, 1889.
2. Brillouin, L., *Wave Propagation and Group Velocity*, Academic Press, New York, London, 1960.
3. Wainstein, L. A., *Sov. Phys. Usp.*, Vol. 118, No. 2, 1976.
4. Shvartsburg, A. B., *Phys. Usp.*, Vol. 50, No. 37, 2007.
5. Enders, A. and G. Nimitz, *J. Phys. I France*, Vol. 2, No. 9, 1992.
6. Ranfagni, A. and D. Murnai a.o., *Phys. Rev. E*, 1998.
7. Ranfagni, A. and D. Murnai a.o., *Phys. Rev. E*, 2004.

8. Ranfagni, A. and D. Murnai a.o., *Phys. Letters A*, Vol. 247, 1998.
9. Ranfagni, A. and D. Murnai a.o., *Phys. Letters A*, Vol. 352, 2006.
10. Ranfagni, A. and D. Murnai a.o., *Phys. Letters A*, Vol. 372, 2008.
11. Missevitch, O. V., A. L. Kholmetskii, and R. Smirnov-Rueda, *J. Appl. Phys.*, Vol. 101, 023532, 2007.
12. Missevitch, O. V., A. L. Kholmetskii, and R. Smirnov-Rueda, *J. Appl. Phys.*, Vol. 102, 013529, 2007.
13. Missevitch, O. V., A. L. Kholmetskii, and R. Smirnov-Rueda, *EPL*, Vol. 93, 64004, 2011.
14. Walker, W., *Lorentz Group, CPT and Neutrios*, A. Chubucalo, V. Dvoeglazov, D. Ernst, V. Kadyshevsky and Y. S. Kim, Eds., 327, World Scientific, Singapore, 2000.
15. Crawford, Jr, F. S., *Waves*, Vol. 3, Mc Graw-Hill Book Company, 1968.
16. Feynman, R. P., R. B. Leighton, and M. Sands, *The Feynman Lectures on Physics*, Vol. 2, Addison-Wesley Publishing Company, Inc. Reading, Massachusetts, Palo Alto, London, 1964.
17. Permyakov, V. A., D. V. Sorokovik, and A. N. Korykin, *The Third International Conference Ultrawideband and Ultrashort Impulse Signals, UWBUSIS-2006*, Sevastopol, Ukraine, Sep. 18–22, 2006.
18. Permyakov, V. A. and D. V. Sorokovik, *Nonlinear World*, Vol. 5, No. 12, 2007 (in Russian).
19. Permyakov, V. A. and D. V. Sorokovik, *Nonlinear World*, Vol. 6, No. 4, 2008 (in Russian).
20. Permyakov, V. A., D. V. Sorokovik, and A. N. Korykin, “Qualitative analysis of dipole antennas impulse radiation,” *Progress In Electromagnetics Research Symposium Abstracts*, Moscow, Russia, Aug. 18–21, 2009.

Design of Array Synthesis Horn Antenna for High Power Microwave Applications

Jae-Min Lee and Jong-Myung Woo

Department of Radio Science and Engineering, Chungnam National University
99 Daehak-ro, Yuseong-gu, Daejeon 306-764, Korea

Abstract— In this paper, an array synthesis horn antenna was designed for high power microwave applications. For the high power microwave applications, an antenna should have high gain and small back lobe to focus the beam. Four horn antennas with TE₁₀ mode and 10 dBi of gain were arrayed to 2 × 2. The horn of 2 × 2 arrayed horn antenna was extended to increase the gain. A higher order mode in the arrayed horn antenna with extended horn occurred because of the array distance. This higher order mode reduced the gain and broadened the beamwidth. Therefore, the vertical junction between arrayed horns was controlled to eliminate higher order mode. For small back lobe, two stepped-corrugated structures were attached on the aperture in the 2 × 2 arrayed synthesis horn antenna. The size of the array synthesis horn antenna is 500 × 500 × 836 mm³ (4.08 × 4.08 × 6.83λ³, where λ is free space wavelength at 2.45 GHz). The gain and front to back ratio was measured as 21.1 dBi and 38 dB respectively. The beam width of *E*- and *H*-plane is 14° and 13.6°. The designed antenna would be appropriate for high power microwave applications.

1. INTRODUCTION

In the field of high power microwave (HPM) applications, antenna design is important because the antenna has to handle high power energy efficiently and high gain is also needed to focus beam. Antennas for HPM applications have been investigated. Reflector antennas [1, 2] are mainly used in this applications due to high gain characteristics. Helical array antenna with circular polarization was proposed in [3] for HPM applications. Reflector antennas have back lobe by spill over. This back lobe causes personnel hazards and equipment interference possibilities. Handling HPM system is difficult because high power source generator has large size [4]. Therefore, it is needed to reduce back lobe in HPM antenna design and one big source generator is needed to substitute to several small size sources to generate high power.

This paper presents an array synthesis horn antenna for high power microwave applications. First, a horn antenna with corrugated structures is investigated to suppress back lobe. Next, four horn antennas are arrayed to 2 × 2 in order to use several power sources. To achieve high gain, the horn of 2 × 2 arrayed horn antenna was extended. Split mode was occurred due to the array distance and the extended horn in this arrayed horn antenna. The mode of the arrayed horn antenna is synthesized by controlling vertical junction between the arrayed horn antennas and split mode is eliminated. Finally corrugated structures are attached on the aperture of the array synthesis horn antenna to reduce back lobe. These results are presented in the next section.

2. A HORN ANTENNA WITH CORRUGATED STRUCTURE

A basic horn antenna with corrugated structure was simulated to reduce back and side lobe before designing an array synthesis horn antenna. It is needed to analyze back lobe reducing method in single horn antenna because the results are applied to the array synthesis horn antenna to suppress back lobe.

Figure 1 shows structure and radiation pattern of horn antenna with one corrugated structure. Probe-fed waveguide with cut-off frequency of 1.75 GHz is used for horn antenna. The horn antenna is designed at 2.45 GHz and it has aperture size of 122.5 mm (1λ) × 122.5 mm (1λ), where λ is wavelength in free space at 2.45 GHz. The horn antenna without corrugated structure has gain of 10.3 dBi, *E*- and *H*-plane beamwidth are 50°, 60° respectively. Corrugated structure attached on the horn aperture and its depth is 92 mm (0.75λ) width is 162 mm (1.32λ) to reduce back lobe. Gap (*g*) between aperture and corrugated structure was varied from 10 mm to 20 mm. As shown in Figures 1 (b) and (c), they are radiation pattern of *E*- and *H*-plane for *g* = 10, 15, 20 mm and no corrugated structure. For increasing the gap back lobe is decreased but side lobe is slightly increased because creeping waves are not suppressed perfectly. Gap between horn aperture and corrugated structure is chosen to be *g* = 20 mm because it has optimum Front to Back Ratio (FBR). When the

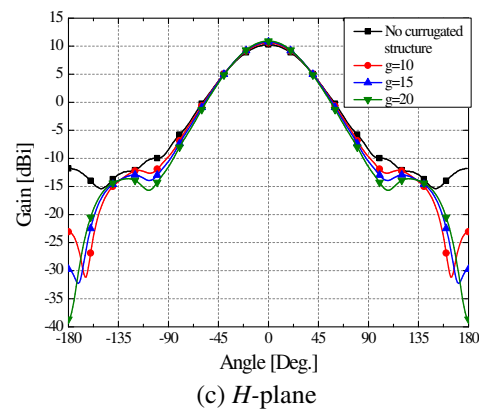
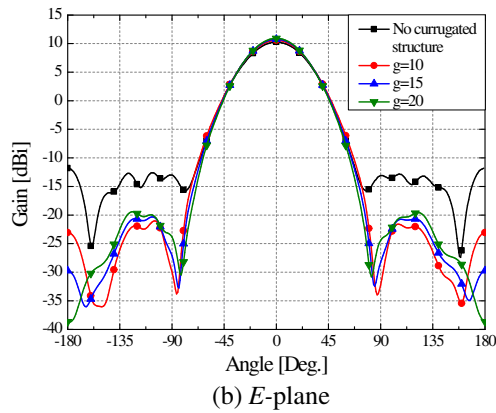
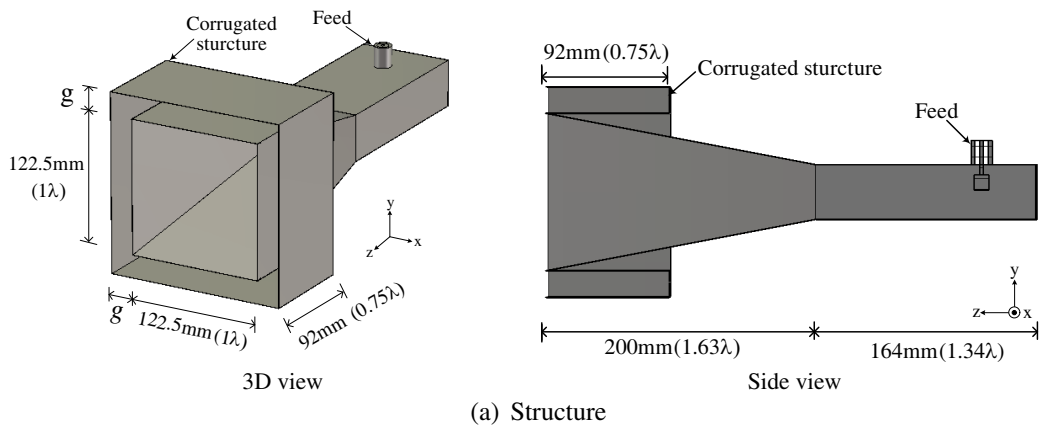


Figure 1: Structure and radiation pattern of horn antenna with one corrugated structure.

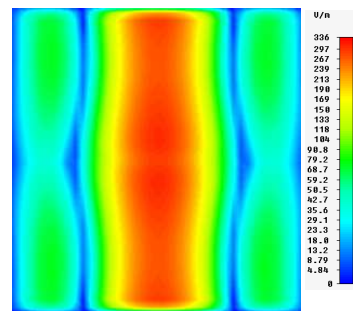
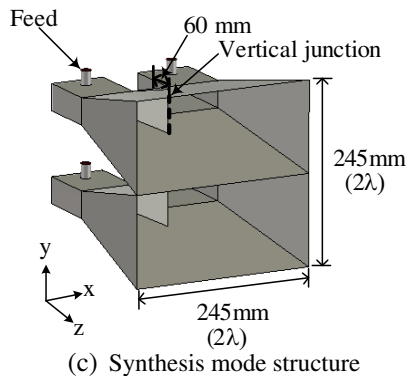
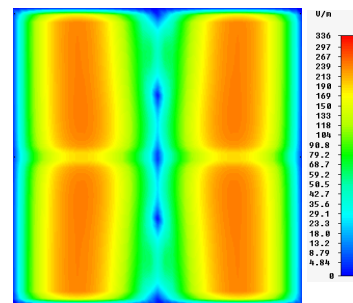
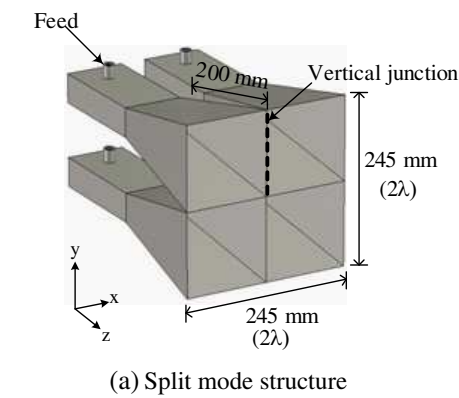


Figure 2: Structure and *E*-field distribution of split mode and synthesis mode.

g is 20 mm, gain is 10.9 dBi and E - and H -plane beam width are 50° , 60° respectively. These results represent that radiation pattern is similar to basic horn antenna. FBR is improved from 22.1 dB to 49.5 dB. Thus we confirmed that backward radiation is largely suppressed by corrugated structure. This corrugated structure can be applied to the array synthesis horn aperture to suppress back lobe.

3. ARRAY SYNTHESIS HORN ANTENNA

The horn antenna for HPM applications is needed to enlarge aperture for high gain. However in the case of single high power excitation a source must be high power, physical size is big and there are many challenges for fabrication. Therefore array horns need to be synthesized to obtain high gain by use of several sources. Figure 2 shows the geometry of 2×2 array antenna to apply four sources and they are partial illustrations of overall array synthesis horn antenna.

In the case of 2×2 array horn antenna as shown in Figure 2(a), gain was decreased by split mode occurred as shown in Figure 2(b). Therefore vertical junctions between arrayed horns are controlled to remove split mode. Figure 2(c) shows synthesis mode structure, length from waveguide aperture to vertical junction part is shorter than split mode structure. Consequently, E -field distribution is synthesized as shown in Figure 2(d). Then synthesis horn extended on the edge of arrayed horn to increase the gain. Furthermore 2-step corrugated structures have to attach on the synthesis horn aperture in order to suppression of back lobe. The size of the array synthesis horn antenna is $500 \times 500 \times 836 \text{ mm}^3$ ($4.08 \times 4.08 \times 6.83\lambda^3$). The gain and front to back ratio was measured as 21.1 dBi and 38 dB respectively. The beam width of E - and H -plane is 14° and 13.6° .

4. CONCLUSIONS

In this paper, we designed 2×2 array synthesis horn antenna for high power microwave applications. A single horn antenna with corrugated structure was investigated to reduce back lobe. Four horn antennas are arrayed to divide high power and array synthesis horn is extended on the aperture of 2×2 arrayed. When synthesis horn is attached on the aperture, split mode occurred in array synthesis horn. This split mode is suppressed by controlling vertical junction between arrayed horns. Thus gain is increased. Moreover, 2-step corrugated structure is added on the aperture of array synthesis horn and back lobe is decreased. Therefore proposed antenna would be appropriate for high power microwave applications.

REFERENCES

1. Giri, D. V., *High-power Electromagnetic Radiators, Non-lethal Weapons and Application*, Harvard University Press, 2004.
2. Rahmat-Samii, Y. and D. V. Giri, "Canonical examples of reflector antennas for high-power microwave applications," *IEEE Trans. Electromagn. Compat.*, Vol. 34, No. 3, 197–205, Aug. 1992.
3. Li, X.-Q., Q.-X. Liu, J.-Q. Zhang, and L. Zhao, "16-element single-layer rectangular radial line helical array antenna for high-power applications," *IEEE Antennas Wireless Propag. Lett.*, Vol. 9, 708–711, 2010.
4. Cousin, R., J. Larour, J. Gardelle, B. Cassany, P. Modin, P. Gouard, and P. Raymond, "Gigawatt emission from a 2.4-GHz compact magnetically insulated line oscillator (MILO)," *IEEE Trans. on, Plasma Science*, Vol. 35, No. 5, 1467–1475, Oct. 2007.

A Symmetrical Theory of Electromagnetism

P. E. Munhoz-Rojas

LACTEC — Instituto de Tecnologia Para o Desenvolvimento, Brasil

Abstract— An axiomatic reformulation of Maxwell’s theory of electromagnetism is presented that permits to deduce Maxwell’s theory and, also, most of the well known theories of classical electromagnetism. As a result it is shown that these theories are not fully equivalent.

It is shown that, independently of the existence or inexistence of free magnetic poles, Maxwell-Hertz’s equations are valid microscopically. It is also shown that all interaction processes involve an “electric quantity” and a “magnetic quantity”.

Using these concepts, a theory of the interaction between fields and macroscopic matter is presented, which extends the well known Maxwell-Lorentz’s theory. As a result, it is shown that Maxwell’s theory of light propagation in a non-conducting medium concerns the interaction between bound magnetic charges and bound electric charges, which is a phenomenon totally different from the electromagnetic perturbations that are attached to metallic conductors, where the excitation is due to free electric charges moving inside the conductor.

It is believed that these results, besides its academic interest, could be useful for the design and interpretation of the functioning principle of antennas and sensors.

1. INTRODUCTION

Maxwell [1] established that the field (**D**) that emanates from “free electricity” is a field different from the field (**E**) responsible for the “**electromotive** force” and, also, that the field (**H**) that is the potential for the flow of electricity (the “true electric currents”) is a field different from the field (**B**) responsible for the **mechanical** force on electric circuits, force that he called “electromagnetic force”.

Hertz [2, 3] introduced the idea of the existence of two types of vector potentials in order to explain the existence of two forces, of similar nature, one that is produced by electric currents and another that is produced by magnetic currents.

Assuming the existence of magnetic monopoles and the existence of two four-dimensional potentials, one that has its source in the movement of the free electric charges and the other that has its source in the movement of the magnetic monopoles, generalized Maxwell’s equations have been put forward [4, 5], which nowadays are assumed to be well known [6, 7].

2. SYMMETRICAL THEORY OF ELECTROMAGNETISM

We will extend Hertz theory [2, 3] by assuming the existence of two four-dimensional potentials, or equivalently, one four-dimensional complex potential field, which produce four three-dimensional fields, two of electric nature and two of magnetic nature:

$$-\frac{\partial \vec{A}_e}{\partial t} - \nabla \phi_e \equiv \frac{\vec{\Gamma}_m}{\mu_0}; \quad \nabla \times \left(\frac{\vec{A}_m}{\mu_0} \right) \equiv \frac{\vec{B}_m}{\mu_0} \left[\frac{A}{m} \right]; \quad -\frac{\partial \vec{A}_m}{\partial t} - \nabla \phi_m \equiv \frac{\vec{\Gamma}_e}{\varepsilon_0} \equiv \vec{E}_m; \quad \nabla \times \left(\frac{\vec{A}_e}{\varepsilon_0} \right) \equiv -\frac{\vec{B}_e}{\varepsilon_0} \left[\frac{V}{m} \right] \quad (1)$$

The combinations of these fields define two four-dimensional complex fields, the first of them, which will be called “matter field”, is defined as:

$$\begin{bmatrix} \mu_0 \frac{\partial \phi_e}{\partial t} + \nabla \cdot \left(\frac{\vec{A}_e}{\varepsilon_0} \right) \\ \varepsilon_0 \frac{\partial \phi_m}{\partial t} + \nabla \cdot \left(\frac{\vec{A}_m}{\mu_0} \right) \\ - \left(\mu_0 \frac{\partial}{\partial t} \left(\frac{\vec{A}_m}{\mu_0} \right) + \nabla \phi_m \right) + \nabla \times \left(\frac{\vec{A}_e}{\varepsilon_0} \right) \\ - \left(\varepsilon_0 \frac{\partial}{\partial t} \left(\frac{\vec{A}_e}{\varepsilon_0} \right) + \nabla \phi_e \right) - \nabla \times \left(\frac{\vec{A}_m}{\mu_0} \right) \end{bmatrix} \equiv \begin{bmatrix} f_m c^2 \\ f_e c^2 \\ \frac{\vec{\Gamma}_e}{\varepsilon_0} - \frac{\vec{B}_e}{\varepsilon_0} \\ \frac{\vec{\Gamma}_m}{\mu_0} - \frac{\vec{B}_m}{\mu_0} \end{bmatrix} \equiv \begin{bmatrix} f_m c^2 \\ f_e c^2 \\ \frac{\vec{E}_e}{\varepsilon_0} \\ \frac{\vec{E}_m}{\mu_0} \end{bmatrix} \begin{bmatrix} \left[\frac{V}{m} \right] \\ \left[\frac{A}{m} \right] \\ \left[\frac{V}{m} \right] \\ \left[\frac{A}{m} \right] \end{bmatrix} \quad (2)$$

And the second one, which will be called “electromagnetic field”, is defined as:

$$\begin{bmatrix} \mu_0 \frac{\partial \phi_e}{\partial t} + \nabla \cdot \left(\frac{\vec{A}_e}{\varepsilon_0} \right) \\ \varepsilon_0 \frac{\partial \phi_m}{\partial t} + \nabla \cdot \left(\frac{\vec{A}_m}{\mu_0} \right) \\ - \left(\mu_0 \frac{\partial}{\partial t} \left(\frac{\vec{A}_m}{\mu_0} \right) + \nabla \phi_m \right) - \nabla \times \left(\frac{\vec{A}_e}{\varepsilon_0} \right) \\ - \left(\varepsilon_0 \frac{\partial}{\partial t} \left(\frac{\vec{A}_e}{\varepsilon_0} \right) + \nabla \phi_e \right) + \nabla \times \left(\frac{\vec{A}_m}{\mu_0} \right) \end{bmatrix} \equiv \begin{bmatrix} f_m c^2 \\ f_e c^2 \\ \frac{\vec{I}_e}{\varepsilon_0} + \frac{\vec{B}_e}{\varepsilon_0} \\ \frac{\vec{I}_m}{\mu_0} + \frac{\vec{B}_m}{\mu_0} \end{bmatrix} \equiv \begin{bmatrix} f_m c^2 \\ f_e c^2 \\ \frac{\vec{G}_e}{\varepsilon_0} \\ \frac{\vec{G}_m}{\mu_0} \end{bmatrix} \begin{bmatrix} \frac{[V]}{[m]} \\ \frac{[A]}{[m]} \\ \frac{[V]}{[m]} \\ \frac{[A]}{[m]} \end{bmatrix} \quad (3)$$

The time derivative of the “matter field” is:

$$\begin{bmatrix} \nabla \cdot \left(\frac{\vec{F}_e}{\varepsilon_0} \right) \\ \nabla \cdot \left(\frac{\vec{F}_m}{\mu_0} \right) \\ - \varepsilon_0 \frac{\partial}{\partial t} \left(\frac{\vec{F}_e}{\varepsilon_0} \right) - \nabla \times \left(\frac{\vec{F}_m}{\mu_0} \right) \\ - \mu_0 \frac{\partial}{\partial t} \left(\frac{\vec{F}_m}{\mu_0} \right) + \nabla \times \left(\frac{\vec{F}_e}{\varepsilon_0} \right) \end{bmatrix} = \begin{bmatrix} \left(\frac{1}{c^2} \frac{\partial^2}{\partial t^2} - \nabla^2 \right) \phi_m - \frac{\partial}{\partial t} \left(\frac{f_e}{\varepsilon_0} \right) \\ \left(\frac{1}{c^2} \frac{\partial^2}{\partial t^2} - \nabla^2 \right) \phi_e - \frac{\partial}{\partial t} \left(\frac{f_m}{\mu_0} \right) \\ \left(\frac{1}{c^2} \frac{\partial^2}{\partial t^2} - \nabla^2 \right) \left(\frac{\vec{A}_m}{\mu_0} \right) + \nabla (f_e c^2) \\ \left(\frac{1}{c^2} \frac{\partial^2}{\partial t^2} - \nabla^2 \right) \left(\frac{\vec{A}_e}{\varepsilon_0} \right) + \nabla (f_m c^2) \end{bmatrix} \equiv \begin{bmatrix} \frac{\rho_{et}}{\varepsilon_0} \\ \frac{\rho_{mt}}{\mu_0} \\ \vec{J}_{et} \\ \vec{J}_{mt} \end{bmatrix} \begin{bmatrix} \frac{[V]}{[m^2]} \\ \frac{[A]}{[m^2]} \\ \frac{[A]}{[m^2]} \\ \frac{[V]}{[m^2]} \end{bmatrix}. \quad (4)$$

And the time derivative of the “electromagnetic field” is:

$$\begin{bmatrix} \nabla \cdot \left(\frac{\vec{G}_e}{\varepsilon_0} \right) \\ \nabla \cdot \left(\frac{\vec{G}_m}{\mu_0} \right) \\ - \varepsilon_0 \frac{\partial}{\partial t} \left(\frac{\vec{G}_e}{\varepsilon_0} \right) + \nabla \times \left(\frac{\vec{G}_m}{\mu_0} \right) \\ - \mu_0 \frac{\partial}{\partial t} \left(\frac{\vec{G}_m}{\mu_0} \right) - \nabla \times \left(\frac{\vec{G}_e}{\varepsilon_0} \right) \end{bmatrix} = \begin{bmatrix} \left(\frac{1}{c^2} \frac{\partial^2}{\partial t^2} - \nabla^2 \right) \phi_m - \frac{\partial}{\partial t} \left(\frac{f_e}{\varepsilon_0} \right) \\ \left(\frac{1}{c^2} \frac{\partial^2}{\partial t^2} - \nabla^2 \right) \phi_e - \frac{\partial}{\partial t} \left(\frac{f_m}{\mu_0} \right) \\ \left(\frac{1}{c^2} \frac{\partial^2}{\partial t^2} - \nabla^2 \right) \left(\frac{\vec{A}_m}{\mu_0} \right) + \nabla (f_e c^2) \\ \left(\frac{1}{c^2} \frac{\partial^2}{\partial t^2} - \nabla^2 \right) \left(\frac{\vec{A}_e}{\varepsilon_0} \right) + \nabla (f_m c^2) \end{bmatrix} \equiv \begin{bmatrix} \frac{\rho_{et}}{\varepsilon_0} \\ \frac{\rho_{mt}}{\mu_0} \\ \vec{J}_{et} \\ \vec{J}_{mt} \end{bmatrix} \begin{bmatrix} \frac{[V]}{[m^2]} \\ \frac{[A]}{[m^2]} \\ \frac{[A]}{[m^2]} \\ \frac{[V]}{[m^2]} \end{bmatrix}. \quad (5)$$

Equation (5), in the case where the electric current represents the movement of free electric charges and the magnetic current represents the movement of magnetic monopoles, are the generalized Maxwell's equations of Rohrlich [4] and Schwinger [5]. In the case of the inexistence of magnetic charges, Equation (5) reduces to the Feynman version of Maxwell's equations [8] or, if the electric current represents the movement of free electric charges, they reduce to the classical “microscopic Maxwell's equations” [7, 9].

Using standard procedures to obtain energy and momentum flow equations [7, 8], from Equation (5) we obtain:

$$\begin{aligned} & \begin{bmatrix} \frac{\partial}{\partial t} \left(\frac{1}{2} \left(\vec{G}_e \cdot \frac{\vec{G}_e}{\varepsilon_0} + \vec{G}_m \cdot \vec{G}_m \right) \right) + \nabla \cdot \left(\frac{\vec{G}_e}{\varepsilon_0} \times \frac{\vec{G}_m}{\mu_0} \right) \\ - \frac{\partial}{\partial t} \left(\vec{G}_e \times \vec{G}_m \right) + \nabla \cdot \left(\vec{G}_e \frac{\vec{G}_e}{\varepsilon_0} + \frac{\vec{G}_m}{\mu_0} \vec{G}_m - \vec{I} \left(\frac{1}{2} \left(\vec{G}_e \cdot \frac{\vec{G}_e}{\varepsilon_0} + \frac{\vec{G}_m}{\mu_0} \cdot \vec{G}_m \right) \right) \right) \end{bmatrix} \\ &= \begin{bmatrix} \frac{\partial U_{mech}}{\partial t} \\ \frac{\partial \mathcal{P}_{mech}}{\partial t} \end{bmatrix} = \begin{bmatrix} -\vec{J}_{et} \cdot \frac{\vec{G}_e}{\varepsilon_0} - \vec{J}_{mt} \cdot \frac{\vec{G}_m}{\mu_0} \\ \rho_{et} \frac{\vec{G}_e}{\varepsilon_0} + \vec{J}_{et} \times \vec{G}_m + \rho_{mt} \frac{\vec{G}_m}{\mu_0} - \vec{J}_{mt} \times \vec{G}_e \end{bmatrix} \begin{bmatrix} \frac{[VA]}{[m^3]} \\ \frac{[VAS]}{[m^4]} \end{bmatrix}. \quad (6) \end{aligned}$$

It must be noted that **all interaction terms** are the product of an “electric quantity” and a “magnetic quantity”.

3. DIFFERENT FORMS OF THE FIELDS EQUATIONS

The matter field can be separated into the field produced by free charges (\mathbf{f}_e and \mathbf{f}_m) and the field produced by bound charges (\mathbf{M}_e and \mathbf{M}_m). Then, making the following definitions: $\vec{F} \equiv \vec{f} - \vec{M}$; $\rho_t \equiv \rho_{fr} + \rho_b$; $\vec{J}_t \equiv \vec{J}_{fr} + \vec{J}_b$; Equation (4) can be written as:

$$\begin{aligned} \nabla \cdot \vec{f}_e &= \rho_{fre} \quad \frac{[As]}{[m^3]} & \nabla \cdot \vec{f}_m &= \rho_{frm} \quad \frac{[Vs]}{[m^3]} \\ -\nabla \times \frac{\vec{f}_m}{\mu_0} &= \vec{J}_{fre} + \frac{\partial \vec{f}_e}{\partial t} \quad \frac{[A]}{[m^2]} & \nabla \times \frac{\vec{f}_e}{\varepsilon_0} &= \vec{J}_{frm} + \frac{\partial \vec{f}_m}{\partial t} \quad \frac{[V]}{[m^2]} \end{aligned} \quad (7)$$

And

$$\begin{aligned} \nabla \cdot \vec{M}_e &= -\rho_{be} \left[\frac{As}{m^3} \right] & \nabla \cdot \vec{M}_m &= -\rho_{bm} \left[\frac{Vs}{m^3} \right] \\ \nabla \times \frac{\vec{M}_m}{\mu_0} &= \vec{J}_{be} - \frac{\partial \vec{M}_e}{\partial t} \left[\frac{A}{m^2} \right] & -\nabla \times \frac{\vec{M}_e}{\varepsilon_0} &= \vec{J}_{bm} - \frac{\partial \vec{M}_m}{\partial t} \left[\frac{V}{m^2} \right] \end{aligned} \quad (8)$$

Also, the electromagnetic field and the matter field can be separated into a part that is produced by the presence of electric charges ($\vec{\Gamma}_e$ and \vec{B}_m), and a part that is produced by the presence of magnetic charges (\vec{B}_e and $\vec{\Gamma}_m$). We obtain:

$$\begin{aligned} \nabla \cdot \vec{\Gamma}_e &= \rho_{et} \left[\frac{As}{m^3} \right] & \nabla \cdot \vec{B}_e &= 0 \left[\frac{As}{m^3} \right] \\ \nabla \times \frac{\vec{\Gamma}_e}{\varepsilon_0} &= -\frac{\partial \vec{B}_m}{\partial t} \left[\frac{V}{m^2} \right] & \nabla \cdot \vec{\Gamma}_m &= \rho_{mt} \left[\frac{Vs}{m^3} \right] \\ \nabla \cdot \vec{B}_m &= 0 \left[\frac{Vs}{m^3} \right] & \nabla \times \frac{\vec{\Gamma}_m}{\mu_0} &= \frac{\partial \vec{B}_e}{\partial t} \left[\frac{A}{m^2} \right] \\ \nabla \times \frac{\vec{B}_m}{\mu_0} &= \vec{J}_{et} + \frac{\partial \vec{\Gamma}_e}{\partial t} \left[\frac{A}{m^2} \right] & \nabla \times \frac{\vec{B}_e}{\varepsilon_0} &= -\vec{J}_{mt} - \frac{\partial \vec{\Gamma}_m}{\partial t} \left[\frac{V}{m^2} \right] \end{aligned} \quad (9)$$

Equation (9) shows that electric charges produce two fields of magnetic nature and that magnetic charges produce two fields of electric nature. In each case, one of the fields is of a solenoidal nature and this solenoidal field is related to the other field by a Faraday's law. This result is independent on the existence or inexistence of free magnetic charges.

A grouping of the fields that is frequently utilized [1, 8, 10] is the following:

$$\begin{aligned} \vec{D}_e &\equiv \vec{\Gamma}_e + \vec{M}_e = \vec{B}_e + \vec{f}_e = \varepsilon_0 \vec{E}_{mf} + \vec{B}_{eb}; \\ \vec{D}_m &\equiv \vec{\Gamma}_m + \vec{M}_m = \vec{B}_m + \vec{f}_m = \vec{\Gamma}_{mf} + \vec{B}_{mb}; \\ \varepsilon_0 \vec{H}_m &\equiv \vec{B}_e - \vec{M}_e = \vec{\Gamma}_e - \vec{f}_e = \varepsilon_0 \vec{E}_{mb} + \vec{B}_{ef}; \\ \mu_0 \vec{H}_e &\equiv \vec{B}_m - \vec{M}_m = \vec{\Gamma}_m - \vec{f}_m = \vec{\Gamma}_{mb} + \vec{B}_{mf}; \end{aligned} \Rightarrow \begin{aligned} \vec{G}_e &= \vec{D}_e + \varepsilon_0 \vec{H}_m \\ \vec{G}_m &= \vec{D}_m + \mu_0 \vec{H}_e \end{aligned} \quad (10)$$

Then, from Equations (7), (8) and (9) we obtain:

$$\begin{aligned} \nabla \cdot \vec{D}_e &= \rho_{fre} \left[\frac{As}{m^3} \right] & \nabla \cdot (\mu_0 \vec{H}_e) &= \rho_{bm} \left[\frac{Vs}{m^3} \right] \\ \nabla \times \vec{H}_e &= \vec{J}_{fre} + \frac{\partial \vec{D}_e}{\partial t} \left[\frac{A}{m^2} \right] & \nabla \times \frac{\vec{D}_e}{\varepsilon_0} &= -\vec{J}_{bm} - \frac{\partial}{\partial t} (\mu_0 \vec{H}_e) \left[\frac{V}{m^2} \right]. \end{aligned} \quad (11)$$

And

$$\begin{aligned} \nabla \cdot (\varepsilon_0 \vec{H}_m) &= \rho_{be} \left[\frac{As}{m^3} \right] & \nabla \cdot \vec{D}_m &= \rho_{frm} \left[\frac{Vs}{m^3} \right] \\ \nabla \times \frac{\vec{D}_m}{\mu_0} &= \vec{J}_{be} + \frac{\partial}{\partial t} (\varepsilon_0 \vec{H}_m) \left[\frac{A}{m^2} \right] & \nabla \times \vec{H}_m &= -\vec{J}_{frm} - \frac{\partial \vec{D}_m}{\partial t} \left[\frac{V}{m^2} \right] \end{aligned} \quad (12)$$

Equations (11) say that \vec{D}_e and \vec{H}_e are the fields produced by the free electric charges and the bound magnetic charges. And, Equation (12) says that \vec{D}_m and \vec{H}_m are the fields produced by the free magnetic charges and the bound electric charges.

The following set of selected equations, which take as the representative of the “magnetic world” the second and third equations from the first part of Equation (9) and as the representative of the “electric world” the first part of Equation (11), corresponds to the famous Hertz version of Maxwell's theory [10]:

$$\begin{aligned} \nabla \cdot \vec{B}_m &= 0 \left[\frac{Vs}{m^3} \right] & \nabla \cdot \vec{D}_e &= \rho_{fre} \left[\frac{As}{m^3} \right] \\ \nabla \times \vec{E}_m &= -\frac{\partial \vec{B}_m}{\partial t} \left[\frac{V}{m^2} \right] & \nabla \times \vec{H}_e &= \vec{J}_{fre} + \frac{\partial \vec{D}_e}{\partial t} \left[\frac{A}{m^2} \right]. \end{aligned} \quad (13)$$

It must be emphasized that, independently of the existence or inexistence of free magnetic poles, Maxwell-Hertz's equations are valid microscopically.

From Equation (11) and Equation (12), the interaction energy and momentum flow equations can be obtained:

$$\begin{aligned} &\left[\begin{aligned} &\frac{\partial}{\partial t} (\vec{H}_m \cdot \vec{D}_e + \vec{D}_m \cdot \vec{H}_e) + c^2 \nabla \cdot (\vec{D}_e \times \vec{D}_m + \varepsilon_0 \vec{H}_m \times \mu_0 \vec{H}_e) \\ &\frac{\partial}{\partial t} (\vec{D}_e \times \vec{D}_m + \varepsilon_0 \vec{H}_m \times \mu_0 \vec{H}_e) + \\ &-\nabla \cdot (\vec{H}_m \vec{D}_e + \vec{D}_e \vec{H}_m + \vec{D}_m \vec{H}_e + \vec{H}_e \vec{D}_m - \vec{I} (\vec{H}_m \cdot \vec{D}_e + \vec{D}_m \cdot \vec{H}_e)) \end{aligned} \right] \\ &= - \left[\begin{aligned} &\frac{\partial U_{mech}}{\partial t} \\ &\frac{\partial \mathcal{Q}_{mech}}{\partial t} \end{aligned} \right] = - \left[\begin{aligned} &\vec{J}_{fre} \cdot \vec{H}_m + \vec{J}_{bm} \cdot \frac{\vec{D}_m}{\mu_0} + \vec{J}_{be} \cdot \frac{\vec{D}_e}{\varepsilon_0} + \vec{J}_{frm} \cdot \vec{H}_e \\ &\rho_{fre} (\vec{H}_m + \vec{v}_{fre} \times \vec{D}_m) + \frac{\rho_{bm}}{\mu_0} \vec{D}_m - \vec{J}_{bm} \times \varepsilon_0 \vec{H}_m + \\ &+ \frac{\rho_{be}}{\varepsilon_0} \vec{D}_e + \vec{J}_{be} \times \mu_0 \vec{H}_e + \rho_{frm} (\vec{H}_e - \vec{v}_{frm} \times \vec{D}_e) \end{aligned} \right] \begin{aligned} &\left[\frac{VA}{m^3} \right] \\ &\left[\frac{VA_s}{m^4} \right] \end{aligned} \quad (14) \end{aligned}$$

Equation (14) contains an expression for the energy density that is slightly different from Maxwell's expression [1], but, they show that this expression for the energy density has a very interesting property: the fields that provoke forces on the free electric charges and bound magnetic charges are “ \mathbf{H}_m and \mathbf{D}_m ”, which are produced by bound electric charges and free magnetic charges, and vice versa, the fields that provoke forces on the bound electric charges and free magnetic charges are “ \mathbf{D}_e and \mathbf{H}_e ”, which are produced by free electric charges and bound magnetic charges.

4. MACROSCOPIC FIELDS

Maxwell [1], to use the macroscopic concept of medium, assumed that the macroscopic fields $\langle \mathbf{D}_e \rangle$ and $\langle \mathbf{H}_e \rangle$ could be considered as “excitation fields” [10] and the macroscopic fields $\langle \mathbf{E}_m \rangle$ and $\langle \mathbf{B}_m \rangle$ could be considered as “response fields”. Also, he assumed that the relationship between $\langle \mathbf{D}_e \rangle$ and $\langle \mathbf{E}_m \rangle$ and the relationship between $\langle \mathbf{H}_e \rangle$ and $\langle \mathbf{B}_m \rangle$ was a characteristic of each medium; and he also added a relationship between $\langle \mathbf{j}_{fre} \rangle$ and $\langle \mathbf{E}_m \rangle$.

In our case, we will choose as “excitation fields” $\langle \mathbf{H}_m \rangle$ and $\langle \mathbf{H}_e \rangle$, and we will assume that the constitutive relations are:

$$\begin{bmatrix} \langle \vec{D}_e \rangle \\ \langle \vec{D}_m \rangle \end{bmatrix} = \begin{bmatrix} \varepsilon_D & \frac{v_{eD}}{c^2} \\ \frac{v_{mD}}{c^2} & \mu_D \end{bmatrix} \begin{bmatrix} \langle \vec{H}_m \rangle \\ \langle \vec{H}_e \rangle \end{bmatrix}; \quad \begin{bmatrix} \langle \vec{f}_e \rangle \\ \langle \vec{f}_m \rangle \end{bmatrix} = \begin{bmatrix} -\varepsilon_f & \frac{v_{ef}}{c^2} \\ \frac{v_{mf}}{c^2} & -\mu_f \end{bmatrix} \begin{bmatrix} \langle \vec{H}_m \rangle \\ \langle \vec{H}_e \rangle \end{bmatrix} \quad (15)$$

Then,

$$\begin{aligned} \begin{bmatrix} \langle \vec{B}_e \rangle \\ \langle \vec{B}_m \rangle \end{bmatrix} &= \begin{bmatrix} \varepsilon_D + \varepsilon_f & \frac{v_{eD} - v_{ef}}{c^2} \\ \frac{v_{mD} - v_{mf}}{c^2} & \mu_D + \mu_f \end{bmatrix} \begin{bmatrix} \langle \vec{H}_m \rangle \\ \langle \vec{H}_e \rangle \end{bmatrix}; \quad \begin{bmatrix} \varepsilon_0 \langle \vec{E}_m \rangle \\ \langle \vec{\Gamma}_m \rangle \end{bmatrix} = \begin{bmatrix} \varepsilon_0 - \varepsilon_f & \frac{v_{ef}}{c^2} \\ \frac{v_{mf}}{c^2} & \mu_0 - \mu_f \end{bmatrix} \begin{bmatrix} \langle \vec{H}_m \rangle \\ \langle \vec{H}_e \rangle \end{bmatrix}; \\ \Rightarrow \begin{bmatrix} \langle \vec{M}_e \rangle \\ \langle \vec{M}_m \rangle \end{bmatrix} &= \begin{bmatrix} \varepsilon_D + \varepsilon_f - \varepsilon_0 & \frac{v_{eD} - v_{ef}}{c^2} \\ \frac{v_{mD} - v_{mf}}{c^2} & \mu_D + \mu_f - \mu_0 \end{bmatrix} \begin{bmatrix} \langle \vec{H}_m \rangle \\ \langle \vec{H}_e \rangle \end{bmatrix}. \end{aligned} \quad (16)$$

In the case of a non-conducting medium, which was the case studied by Maxwell in his “Electromagnetic theory of light” [1], we have:

$$\begin{aligned} \begin{bmatrix} \varepsilon_0 \langle \vec{E}_m \rangle \\ \langle \vec{\Gamma}_m \rangle \end{bmatrix} &= \begin{bmatrix} \varepsilon_0 & 0 \\ 0 & \mu_0 \end{bmatrix} \begin{bmatrix} \langle \vec{H}_m \rangle \\ \langle \vec{H}_e \rangle \end{bmatrix}; \quad \begin{bmatrix} \langle \vec{B}_e \rangle \\ \langle \vec{B}_m \rangle \end{bmatrix} = \begin{bmatrix} \langle \vec{D}_e \rangle \\ \langle \vec{D}_m \rangle \end{bmatrix} = \begin{bmatrix} \varepsilon_D & \frac{v_{eD}}{c^2} \\ \frac{v_{mD}}{c^2} & \mu_D \end{bmatrix} \begin{bmatrix} \langle \vec{H}_m \rangle \\ \langle \vec{H}_e \rangle \end{bmatrix}; \\ \Rightarrow \begin{bmatrix} \langle \vec{M}_e \rangle \\ \langle \vec{M}_m \rangle \end{bmatrix} &= \begin{bmatrix} \varepsilon_D - \varepsilon_0 & \frac{v_{eD}}{c^2} \\ \frac{v_{mD}}{c^2} & \mu_D - \mu_0 \end{bmatrix} \begin{bmatrix} \langle \vec{H}_m \rangle \\ \langle \vec{H}_e \rangle \end{bmatrix} \rightarrow \begin{bmatrix} \langle \vec{M}_e \rangle \\ \langle \vec{M}_m \rangle \end{bmatrix} = \begin{bmatrix} \varepsilon_D - \varepsilon_0 & \frac{v_{eD}}{c^2} \\ \frac{v_{mD}}{c^2} & \mu_D - \mu_0 \end{bmatrix} \begin{bmatrix} \langle \vec{E}_m \rangle \\ \langle \vec{H}_e \rangle \end{bmatrix}. \end{aligned} \quad (17)$$

It can be seen that Equation (17) predicts the “magnetolectric effect” [11], which is proportional to the velocities v_{eD} and v_{mD} (optical activity coefficients [12]). If the velocities v_{eD} and v_{mD} are taken equal to zero, we obtain the relationships assumed by Maxwell [1].

Introducing the relationships assumed by Maxwell into the average of Equation (11) and Equation (12), for a homogeneous time-invariant medium we have:

$$\begin{aligned} \mu_D \varepsilon_D \frac{\partial^2 \langle \vec{D}_e \rangle}{\partial t^2} - \nabla^2 \langle \vec{D}_e \rangle &= 0; & \mu_D \varepsilon_D \frac{\partial^2 \langle \vec{H}_m \rangle}{\partial t^2} - \nabla^2 \langle \vec{H}_m \rangle &= 0; \\ \mu_D \varepsilon_D \frac{\partial^2 \langle \vec{D}_m \rangle}{\partial t^2} - \nabla^2 \langle \vec{D}_m \rangle &= 0; & \mu_D \varepsilon_D \frac{\partial^2 \langle \vec{H}_e \rangle}{\partial t^2} - \nabla^2 \langle \vec{H}_e \rangle &= 0. \end{aligned} \quad (18)$$

Equation (18) says that the free oscillations of the fields in a homogeneous time-invariant non-conducting medium propagate with a velocity that is different from “ c ”. Maxwell [1] asserted that this velocity should be equal to the velocity of light in that medium and “that light is an electromagnetic disturbance, propagated in the same medium through which other electromagnetic actions are transmitted”.

From Equation (17), we can see that these free oscillations result from the interplay of the bound electric charges (which produce $\langle \mathbf{D}_m \rangle$ and $\langle \mathbf{H}_m \rangle$) with the bound magnetic charges (which produce $\langle \mathbf{D}_e \rangle$ and $\langle \mathbf{H}_e \rangle$). We conclude that bound magnetic currents and bound electric currents must exist in a non-conducting medium and the effect of its macroscopic average in a homogeneous medium is equivalent to a change in the time scale.

5. CONCLUSIONS

The symmetrical theory of electromagnetism presented in this paper start from the explicit recognition of the existence of four different three-dimensional fields and contains, as particular cases, the classical Maxwell's theory and also other well known theories of classical electromagnetism. As a result it is shown that these theories are not fully equivalent. Among the theories with one vector potential ($\mathbf{A}_e = 0$) the classical Maxwell's theory is the most general, the Feynman's version of Maxwell's equations can be obtained by making also $\varphi_e = 0$, and the "microscopic Maxwell's equations" are obtained by making also $\rho_{be} = 0$ and $\mathbf{J}_{be} = 0$. Among the theories with two vector potentials the "classical generalized Maxwell's equations" are obtained by making $\rho_{be} = \rho_{bm} = 0$ and $\mathbf{J}_{be} = \mathbf{J}_{bm} = 0$, and, the Hertz's theory, as described by C. T. Tai, is obtained by making $\varphi_e = \varphi_m = 0$ and $\text{div } \mathbf{A}_e = \text{div } \mathbf{A}_m = 0$.

For macroscopic media where the number of independent fields is reduced to two, by means of the "constitutive relations", a theory of the interaction between fields and macroscopic matter is presented, which extends the well known Maxwell-Lorentz's theory. As a result, it is shown that Maxwell's theory of light propagation in a non-conducting medium concerns the interaction between bound magnetic charges and bound electric charges.

ACKNOWLEDGMENT

The author thanks to LACTEC for providing the funds to develop this work and, also, gratefully thanks to his colleagues at LACTEC for providing key reference material and to his students at UTFPR for their very interesting questions.

REFERENCES

1. Maxwell, J. C., *A Treatise on Electricity and Magnetism*, 2nd Edition, Clarendon Press, Oxford, 1881.
2. Hertz, H., "On the relations between Maxwell's fundamental electromagnetic equations and the fundamental equations of opposing electromagnetics (in German), *Wiedemann's Annalen*, Vol. 23, 84–103, 1884. (English translation in *Miscellaneous Papers by Heinrich Hertz*, Translated by D. E. Jones MacMillan and Co., London, 1893; Reprinted by Dover, New York, 1962).
3. Tai, C. T. and J. H. Bryant, "New insights into Hertz's theory of electromagnetism," *Radio Science*, Vol. 29, 685–690, 1994.
4. Rohrlich, F., "Classical theory of magnetic monopoles," *Physical Review*, Vol. 150, 1104–1111, 1966.
5. Schwinger, J., "Magnetic charge and quantum field theory," *Physical Review*, Vol. 144, 1087–1093, 1966.
6. Costa-Quintana, J. and F. Lopez-Aguilar, "Propagation of electromagnetic waves in material media with magnetic monopoles," *Progress In Electromagnetic Research*, Vol. 110, 267–295, 2010.
7. Jackson, J. D., *Classical Electrodynamics*, 3rd Edition, John Wiley & Sons, Inc., New York, 1999.
8. Feynman, R. P., R. Leighton, and M. Sands, *The Feynman Lectures on Physics — Vol. II: The Electromagnetic Field*, Addison-Wesley, Reading, Massachusetts, 1965.
9. Landau, L. D. and E. M. Lifshitz, *Theoretical Physics — Vol. II: Field Theory*, 6th Edition, Mir, Moscow, 1980.
10. Sommerfeld, A., *Electrodynamics*, Academic Press, New York, 1952.
11. Dzyaloshinskii, I. E., "On the magneto-electrical effect in antiferromagnets," *JETP*, Vol. 10, 628–629, 1959.
12. Krowne, C. M., "Electromagnetic theorems for complex anisotropic media," *IEEE Trans. Antennas Propagat.*, Vol. 32, No. 11, 1224–1230, 1984.